國立臺灣大學工學院土木工程學系

碩士論文

Department of Civil Engineering

College of Engineering

National Taiwan University

Master Thesis

鋼筋混凝土柱構件於反覆側推與

振動台實驗下之耐震行為研究

Study of Reinforced Concrete Columns under Cyclic

Loading and Shaking Table Tests for Seismic Behavior

戴瀚呈

Han-Cheng Tai

指導教授：黃世建 博士

Advisor: Shyh-Jiann Hwang, Ph.D.

中華民國 112 年 6 月

June 2023

ii

國立臺灣大學碩士學位論文
口試委員會審定書
MASTER'S THESIS ACCEPTANCE CERTIFICATE
NATIONAL TAIWAN UNIVERSITY

鋼筋混凝土柱構件於反覆側推與振動台實驗下之耐震行為研究

Study of Reinforced Concrete Columns under
Cyclic Loading and Shaking Table Tests for Seismic Behavior

本論文係戴瀚呈 R10521207 在國立臺灣大學土木工程學系結構工程組完成之碩士學位論文，於民國 112 年 06 月 28 日承下列考試委員審查通過及口試及格，特此證明。

The undersigned, appointed by the Department/Institute of Civil Engineering, Structural Engineering Division on 28, June, 2023 have examined a Master's thesis entitled above presented by Han-Cheng, Tai R10521207 candidate and hereby certify that it is worthy of acceptance.

口試委員 Oral examination committee:

（指導教授 Advisor）

系主任/所長 Director:

iv

ACKNOWLEDGEMENT

First, I would like to thank my advisor, Professor Hwang, for motivating me to write my thesis in English. It was a tough process, and I cherish the experience deeply. I would also like to thank Sri for providing me with valuable advice and encouragement throughout my research.
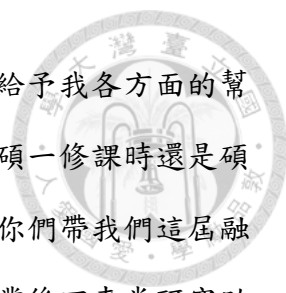
時光飛逝，兩年的研究所生涯即將邁入尾聲。如果說大學的四年讓我學會了進入社會前所需要的自我獨立的能力，那研究所的兩年就是讓我領悟了進入社會後所需要的認真負責的態度。如今要為自己的學生身份劃下句點，期許自己能攜帶著就讀研究所一路以來獲得的寶貴經驗，邁向人生的下一個階段。

謝謝我的指導教授黃世建老師，給予我研究上的指引與做事態度上的教誨。很慶幸研究所能在老師的指導下學習，老師對事情認真負責的態度，以及為人處事的用心，是身為學生的我們的最佳榜樣。老師給予我的教誨，我會銘記在心，時刻勉勵自己。

謝謝論文口試委員蔡克銓教授與廖文正教授，教授們寶貴的建議讓我的研究得以更加完整，對整體研究內容有更好的收斂與結論。

謝謝我大專生時期的指導教授洪崇展教授，帶領我進入鋼筋混凝土學的領域，啟發我對研究的興趣，並鼓勵我持續精進自己。

謝謝黃世建老師研究團隊的學長們，感謝文成學長、侑呈學長，在我遇到問題時總能不吝嗇的給予幫助；感謝于哲學長細心的教導，提供我研究資料，讓我的研究能更加深入；感謝樸文學長一路上的幫助，總是用心的跟我討論問題，給予我很多寶貴的意見，讓我能更順利的完成研究。

謝謝研究室的各位，謝謝學長姐紹愷、香芸、郁玫、承哲，給予我各方面的幫助，在我遇到問題時總是熱情的給予我建議與經驗分享，不管是碩一修課時還是碩二做研究時，因為有你們我才能順利的完成這兩年的學業。謝謝你們帶我們這屆融入研究室這個溫暖的家庭，創造了許多快樂的回憶。特別謝謝畢業後回來當研究助理的紹愷學長，有了你的回歸，我們研究室更是熱鬧，去了好多地方，也吃了好多不一樣的東西，總算有人跟我一起看風景跟嘴能仁。謝謝學弟黃強、家瑋、奕承、士鈞，在我們需要幫忙時總是大力相助，祝福你們接下來的研究仕途順遂！

謝謝研究室同屆的夥伴們能仁、榕玲、自強，很高興這段時間能跟你們一起度過，因為有你們我的研究所生活更加精采多姿，回憶滿滿。謝謝能仁做為研究室的開心果與精神支柱，不管做任何事都讓人覺得好笑，總是被犧牲來為研究室帶來歡樂的氣氛，以你無堅不摧的個性做為我們的好榜樣；謝謝榕玲做為研究室的彈藥庫，從剛開始認識時的安靜樣，到後來時不時開火來一發飛彈，開始跟我能南北呼應，建立起研究室的歡樂戰場。謝謝自強做為研究室的人生導師，用歷練豐富的人生經驗，啟發我們對現在的自我實現與對未來的期許展望，同時讓我們學會說話的藝術與為人處事上的韌性。

謝謝我的好友/室友宇筌、怡璋，在研究所期間互相給予的陪伴與勉勵，一起相處了六年，一起度過了人生轉變的重要階段，我想我們深厚的友情已不言而喻。謝謝好友采霏、宜庭，每次生日的相聚，遊玩，都為研究所生活增添了繽紛的色彩。

謝謝我的女友菀軒，這兩年來時不時的鼓勵我前進與化解我的煩惱，在我忙碌疲憊的時候給予我照顧與陪伴，還幫我的論文校稿，沒有你我絕對無法順利的完成這份論文。

最後要感謝我最重要的家人，做為最溫暖的避風港，時時刻刻支持著我追逐自己夢想的同時，又給予我最好的後勤支柱，讓我能自信的面對一切問題，知道背後有著最讓人安心的後盾。謝謝父親一直做為我人生的榜樣，謝謝母親對我為人處事的教導，我將這篇論文獻給你們，謝謝你們。

摘要

　　鋼筋混凝土柱構件為結構物中非常重要之構件，在地震力作用下，柱構件需提供良好的軸向與側向承載能力，以及一定程度之變形能力，維持結構物之安全性與使用性。剪力控制之鋼筋混凝土柱構件具有較差之變形能力，易於發生脆性剪力破壞，因此了解剪力破壞控制之柱構件於地震力下之行為是非常重要的研究議題。為了瞭解其行為，學界已大量針對此類構件進行實驗研究，然而基於振動台實驗之限制性與複雜性，大多數實驗研究皆以反覆載重實驗進行。同時，為了進行結構之耐震評估與設計，大量以反覆載重實驗結果為基礎之數值模型已被開發供使用。然而，結構物於真實情況下乃受到具有不同受力機制與作用時間之地震力，而這些反覆載重實驗結果與以反覆載重實驗為基礎之數值模型是否能有效且正確的代表與模擬桿件於真實地震力下之行為，仍有待驗證。本文之研究目的著重於對剪力控制鋼筋混凝土柱桿件之研究，驗證文內試體於反覆載重實驗下之結果與以反覆載重實驗為基礎之數值模型用於代表與模擬真實地震反應之可行性。

　　本研究比較了剪力控制鋼筋混凝土柱於振動台實驗與於反覆載重實驗下之反應，其比較結果顯示，反覆載重實驗之反應能有效的代表振動台實驗之反應，提供了保守的強度與一致的勁度與位移反應。本研究亦將以反覆載重實驗為基礎之側力位移模型與遲滯模型分別建立於結構分析軟體 ETABS 與 OpenSees 內以進行非線性動力歷時分析，並與振動台實驗結果進行比較以驗證其於模擬真實地震反應之可行性。其比較結果顯示，以反覆載重實驗為基礎之強度、勁度、位移與遲滯模型能有效的模擬振動台實驗之反應，提供了保守亦不失精準性之強度、位移與遲滯反應。
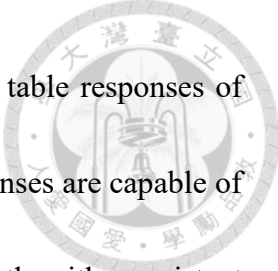
關鍵字:鋼筋混凝土、柱構件、剪力破壞、反覆載重實驗、振動台實驗、遲滯行為、動力歷時分析

ABSTRACT

Reinforced concrete columns are significant members in a structure, providing the structure with axial and lateral resistance with sufficient deformability when subjected to ground motions, ensuring the safety and serviceability of the structure. Shear-dominant reinforced concrete columns are prone to possess brittle failure behavior, and their behavior under dynamic loading conditions are necessary to be clarified. Experiments have been conducted to understand the behavior of shear-dominant reinforced concrete columns, while most of the experiments are based on cyclic loading tests instead of shaking table tests due to the limitation and complexity of the instrumentations and test setups. In the meantime, analytical models have been developed based on the cyclic loading responses for seismic assessment and design of reinforced concrete structures. However, structures are subjected to earthquake forces under practical conditions, and whether these cyclic loading responses and analytical models can represent shaking table responses is yet to be investigated. The objective of this research is to validate the feasibility of the cyclic loading-based responses and cyclic loading-developed analytical models to represent and simulate actual ground motion responses, and to promote the implementation of nonlinear time domain analysis.
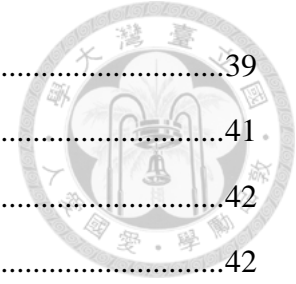
The comparison between cyclic loading responses and shaking table responses of RC intermediate-short columns indicates that the cyclic loading responses are capable of representing shaking table responses, providing conservative strength with consistent stiffness and lateral displacement behavior. Column models are developed in structural analysis program ETABS and OpenSees through different modeling concepts based on cyclic loading-developed flexural and shear backbone curves and hysteresis models. Time history analysis is performed on the column models and compared with the shaking table responses. The results indicate that the introduced column models, which consist of cyclic loading-developed analytical strength, stiffness, displacement, and hysteresis behaviors, are capable of simulating shaking table responses, providing both conservative and well simulated force-displacement relationship and hysteresis behavior.

Key words: Reinforced concrete, Columns, Shear failure, Cyclic loading tests, Shaking table tests, Hysteresis modeling, Time history analysis
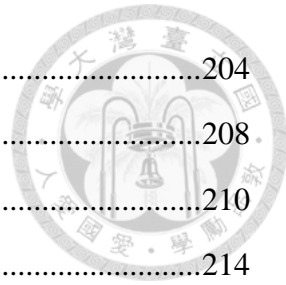
TABLE OF CONTENTS

LIST OF TABLES

LIST OF FIGURES

xvii

xxviii

CHAPTER 1: INTRODUCTION

1.1 Background

Located on the Pacific Ring of Fire, Taiwan is constantly hit by earthquakes due to collisions between the Philippine Sea Plate and the Eurasian Plate. The Chi-Chi Earthquake in 1999 struck Taiwan with a Richter scale of 7.3, causing severe property damage and numerous casualties. According to the Post-Earthquake Investigation Report on Chi-Chi Earthquake of National Center for Research on Earthquake Engineering (NCREE) (1999), the earthquake caused significant damage on reinforced concrete buildings in Taiwan, while mostly concentrated on the failure and collapse of column members, especially for low-rise reinforced concrete buildings which is common for buildings built in Taiwan around 1980s. It is observed that large window openings were built for the sake of lighting and ventilation, inducing short columns to be formed on the windowsills. These design layouts enhance the flexural strength of the short columns, leading to the failure mode of the columns being governed by shear failure behavior. With the occurrence of brittle shear failure, the lateral strength of the column drops rapidly, inducing the loss of gravity load carrying capacity and eventually leading to collapse of the building. Therefore, research on the shear failure behavior of these intermediate-short to short reinforced concrete columns is vital for the sake of the comprehension of building

1

seismic resistance capacity and collapse behavior.
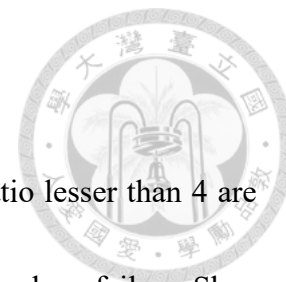
According to ACI 318-19 (2019), beams with span to depth ratio lesser than 4 are defined as deep beams, with their behavior mainly governed by brittle shear failure. Shen et al. (2021) indicates that columns with height to depth ratio larger than 4 can be considered as typical columns, with their behaviors mainly governed by flexural failure, but possibly by shear without sufficient shear reinforcement. Li et al. (2019) indicates that columns with height to depth ratio ranging from 2 to 4 can be defined as intermediate-short columns, and Li et al. (2014) indicates that columns with height to depth ratio lesser than 2 can be considered as short columns, with their behaviors prone to be governed by brittle shear failure. Columns being the major vertical component in a structure, it is necessary to define the force-displacement relationship for the column when performing static pushover analysis, and to define the hysteresis behavior for the column when performing nonlinear time domain analysis.

Shen et al. (2021), Li et al. (2019), and Li et al. (2014) developed trilinear force-displacement relationships for columns with height to depth ratio ranging from lesser than two to larger than four, Ling et al. (2021) developed hysteresis models for columns governed by flexure and by shear behavior separately. NCREE/TEASDA (2021) takes the recommendation of the above researches into consideration and developed the column model for nonlinear time domain analysis. Due to the experimental complication of

2

shaking table tests, the above analytical models of RC columns including force-displacement relationships and hysteresis models were developed based on a wide range of column specimens tested through cyclic loading tests on strong floors. However, actual RC members under practical conditions are subjected to dynamic ground motions, which consist of distinct force mechanisms and applied time steps. Therefore, it is necessary to compare the cyclic loading test results with shaking table test results of same column specimens to distinguish the discrepancies and similarities between their behaviors, while having comprehensive understanding of column dynamic behaviors beforehand. Furthermore, verification of the analytical models that were developed under cyclic loading tests by dynamic loading situations is also required to demonstrate their feasibility, and the application of the developed analytical models into different structural analysis program is necessary for the promotion of nonlinear time domain analysis.

1.2 Objectives

The overall objective of this research is to study the dynamic behaviors of flexural and shear-dominant reinforced concrete columns, investigate the discrepancies and similarities between the behaviors of cyclic loading and shaking table test results of the same specimens, and to verify the cyclic loading-developed analytical models through dynamic loading situations by detailed comparison through strength, stiffness, lateral

3

displacement, and hysteresis behavior, and by overall comparison through simulations on nonlinear time history responses.
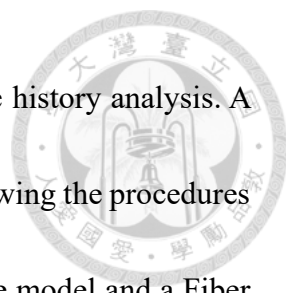
Weng (2007) conducted cyclic loading tests on eight full scale intermediate-short RC columns with different design and test parameters, while Su (2007) conducted shaking table tests on four half-scale RC frames consisted of nine intermediate-short columns, with seven of the specimens having the same design and test parameters as the full-scale columns tested by Weng (2007). In order to take the shaking table test results into account for further research, it is necessary to understand the behaviors of the shaking table tests in a detailed manner. Su (2007) presented the shaking table test results, but lack thorough investigations on the member and structural failure behaviors. This research conducts a detailed investigation on the shaking table test result of intermediate-short RC columns tested by Su (2007), providing conclusions on the column behaviors of shaking table tests, and extending relevant researches regarding the effect of varying axial load due to overturning moment on shear and flexure strengths. With thorough understanding of the shaking table test behavior, the half-scale columns are then compared with the corresponding full-scale columns under cyclic loading tests to investigate the discrepancies and similarities between strengths, stiffness, and deformations of cyclic loading and shaking table tests results, verifying the feasibility for cyclic loading test behaviors to represent shaking table test phenomena, allowing for simpler experimental

4

setups to achieve the same result.

On the other hand, Taiwan Earthquake Assessment for RC Structures by Dynamic Analysis Handbook (TEASDA 2021) developed force-displacement relationships for RC columns governed by flexure and shear behavior, while Ling et al. (2021) developed hysteresis models for columns with different design parameters. The above behavior models are necessary for engineers to perform nonlinear time domain analysis, but the models are developed based on cyclic loading tests, lacking thorough verification with practical dynamic loading behaviors. Also, ETABS version 2016 (2016) provided PMM flexural hinge to consider the change in axial load due to overturning moments of high-rise buildings, but constant axial load hinges for shear hinges. It is necessary to study the influence of the varying axial load on flexure and shear-dominant column behaviors through shaking table test results, and propose recommendation on the consideration of varying axial load effect for different backbone curves on different hinges.

This research compares current strength prediction models provided by NCREE/TEASDA (2021) with the shaking table test results conducted by Su (2007) with the consideration of different axial load influences, and investigates the feasibility of the column backbone curve models in NCREE/TEASDA (2021) and different effective stiffness models. Three different column analytical models were constructed based on backbone curve models in NCREE/TEASDA (2021) and hysteresis models in Ling et al.

5

(2021) inside structural analysis programs to perform nonlinear time history analysis. A Concentrated Plastic Hinge model is constructed inside ETABS following the procedures provided by NCREE/TEASDA (2021). A Concentrated Plastic Hinge model and a Fiber model are developed inside OpenSees by this research. All three models are constructed with analytical foundations regarding seismic parameters such as strength, deformation, stiffness, and hysteresis behavior, allowing for engineers to perform nonlinear time domain analysis through blind prediction, enhancing the accuracy and capability of current structural analysis methods. The time history analysis results of the above three models are then compared with the shaking table test results conducted by Su (2007) to evaluate their feasibility, and to compare the pros and cons within one another.

In conclusion, the first part of this research studies the shaking table test results of RC intermediate-short columns to investigate the behavior of flexural and shear-dominant members under dynamic loadings, while also evaluating the feasibility for cyclic loading test results to represent dynamic loading test results for the sake of simpler experimental setups. The second part of this research validates the analytical models developed based on cyclic loading tests with dynamic loading test results with or without the consideration of varying axial load effect. Lastly, time history analysis by different column models in different structural analysis programs is performed, in order to verify the feasibility and accuracy of the analytical models, and to promote the utilization of nonlinear time domain

analysis for clearer understanding on structural and member behaviors.

1.3 Organization

This thesis consists of seven chapters and the Appendix, the main text describes: literature reviews on previous researches, cyclic loading test setup and results, shaking table test setup and results, comparison of cyclic loading and shaking table test responses as well as evaluation of analytical models, and finally comparison of nonlinear time history analysis results with the test responses. The thesis has been organized as described below:

Chapter 1, "Introduction," describes the background and objective of this research, expecting to promote the utilization of nonlinear time domain analysis of reinforced concrete structures.

Chapter 2, "Literature Review," reviews previous studies relevant to this research. Force-displacement relationships and hysteresis modeling of columns governed by flexure and shear behaviors are introduced in this chapter. An introduction on performing structural analysis through finite element structural analysis program OpenSees is also introduced. More shaking table experimental tests of RC columns are introduced as a comparison with the shaking table test of Su (2007) to investigate the dynamic behavior of RC columns. Research on the consideration of varying axial load on column hinges is

7

introduced. Current available models for predicting the effective stiffness of columns are also discussed in this chapter.
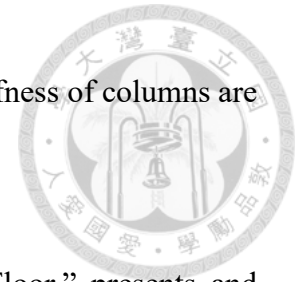
Chapter 3, "Cyclic Loading Tests of Columns on Strong Floor," presents and discusses the cyclic loading tests on RC intermediate-short columns conducted by Weng (2007). Weng (2007) and Li et al. (2019) have had thorough and detailed investigation and explanation of the cyclic loading test results, no further investigation is performed for this chapter in this research.

Chapter 4, "Dynamic Tests of Columns by Shaking Table," presents and discusses the shaking table tests on RC intermediate-short columns conducted by Su (2007). Su (2007) presented the test results but due to the complication of shaking table tests, more detailed researches should be performed to investigate the behavior of the shaking table test results thoroughly, and provide with conclusions regarding the observed behaviors. The results presented in this chapter are analyzed and investigated by this research based on the tests conducted by Su (2007).

Chapter 5, "Comparison of Cyclic Loading and Shaking Table Test Response," compares the cyclic loading test results of full-scale column specimens with the shaking table test results of half-scale column specimens. Varying axial load phenomenon on column strength observed in the previous chapter is discussed and investigated in this chapter. Evaluation of current models on the prediction of strength, effective stiffness,

8

and overall force-displacement relationship of the specimens with or without consideration of varying axial load under dynamic loadings is presented in this chapter.

Chapter 6, "Hysteresis Modeling of Shaking Table Tests," presents the proposed method to construct a Concentrated Plastic Hinge Model and a Fiber Section Model for columns inside finite element structural analysis program OpenSees. A Concentrated Plastic Hinge Model recommended by NCREE/TEASDA (2021) is also introduced in addition to the two mentioned models to perform nonlinear time history analysis. The accuracy of the analytical results is then evaluated with the test results by Su (2007), further discussion and comparison of the results are presented in this chapter.

Finally, **Chapter 7**, "Conclusion and Future Work," summarizes the overall conclusions of this research throughout each chapter, and provides recommendations for future research.

As for the **Appendix**, a database of additional 10 shaking table-tested reinforced concrete columns governed by flexural behavior is collected in the **Appendix** for the research of shaking table test varying axial load on column flexural strengths.

10
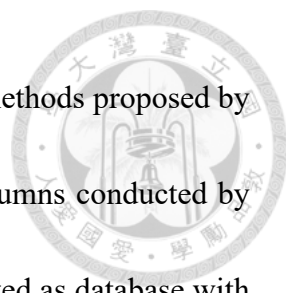
CHAPTER 2: LITERATURE REVIEW

2.1 Introduction

This research takes into account the result of cyclic loading tests on intermediate-short RC columns conducted by Weng (2007) and shaking table tests on intermediate-short RC columns conducted by Su (2007), and performs further research based on the test data and observed behaviors. These two tests will be further introduced in chapter 3 and chapter 4 with complete information on the test setups and results, thus will not be introduced in this chapter.

Section 2.2 references the introduction of shear and flexure backbone curves of columns recommended by NCREE/TEASDA (2021), which will then be implemented onto the Concentrated Plastic Hinge models inside program ETABS and OpenSees. Section 2.3 introduces the Finite Element Structural Analysis program OpenSees and the corresponding constitutive materials, elements, and springs used to construct the Fiber Section model (Fiber Model for abbreviation) and the Concentrated Plastic Hinge model (CPH Model for abbreviation) inside OpenSees, which the overall models would be further introduced in chapter 6. The first two sections define the force-displacement relationship of columns, Section 2.4 continues to introduce the model to define the hysteresis behavior such as unloading stiffness and pinching phenomenon proposed by

Dowell et al. (1998) and the corresponding optimization parameter methods proposed by

Ling et al. (2022). Section 2.5 introduces shaking table tests on columns conducted by

Elwood and Moehle (2003) and Guo (2008). The test results are treated as database with

Su (2007) for researches on column dynamic behaviors. Section 2.6 introduces research

on column strength by Yeh and Chou (2017) considering the large varying axial load on

columns for high-rise buildings. Lastly Section 2.7 introduces available analytical models

for simulating the effective stiffness of columns for comparison with the shaking table

test results by Su (2007).

2.2 Modeling Column Behavior with Concentrated Plastic Hinge

When conducting static pushover or dynamic time domain analysis of reinforced

concrete (RC) structures, engineers often use structural analysis software such as ETABS

or SAP2000 for analysis. These software use elements and nodes to form the analytical

models of the members and the structures, while setting up nonlinear concentrated plastic

hinges to simulate the nonlinear behavior of structural components. Therefore, it is

necessary to understand the nonlinear behavior of structural components such as columns,

beams, and walls, in order to assign corresponding hinges to the structural components to

simulate the overall behavior of the structure.

The most direct method to determine the overall behavior of structural components

is to use the force-displacement curves obtained through actual experiments or analytical simulations. To achieve blind analysis and design of structures, analytical simulations on force-displacement curves are required. From previous research, the shear strength of columns decreases with the increase in lateral displacement, limiting the column strength and deformability. When subjecting to axial and lateral load, shear failure, flexure-shear failure or flexure failure of RC columns can occur. This section describes in detail the analytical model recommended by NCREE/TEASDA (2021) for lateral force-displacement relationships of RC columns controlled by shear and flexure-shear failure behavior, which will then be implemented by this research as concentrated plastic hinges in analysis software ETABS and OpenSees.

2.2.1 Shear Failure Backbone Curve for Column

According to Section 3.1.1 of NCREE/TEASDA (2021), Li et al. (2019) proposed a trilinear curve to simulate the shear failure backbone curve of RC columns (see **Figure 2-1**) consisted of a shear cracking point, a strength point, and an axial failure point. The first segment simulates the effective linear stiffness of column up to the shear cracking point, the shear cracking strength is indicated as V_{cr}, and the corresponding deformation as Δ_{cr}. The second segment simulates the behavior after shear cracking up to the strength point, the corresponding shear strength and deformation are indicated as V_n and Δ_n. The

13
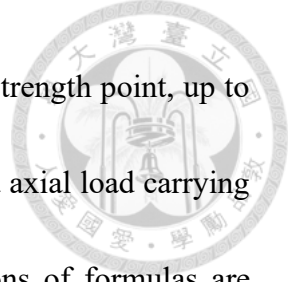
third segment simulates the strength degradation behavior after the strength point, up to the condition where the column completely loses the lateral load and axial load carrying capacity, where the deformation is indicated as Δ_a. The derivations of formulas are described below.

Shear Cracking Point (V_{cr}, Δ_{cr})

NCREE/TEASDA (2021) takes the recommendation of ACI 318-14 (2014) on the calculation of cracking strength of RC wall into consideration, and propose the calculation for cracking strength of RC columns as follows:

$$V_{cr} = 0.87\sqrt{f'_c}b_c d + \frac{Pd}{4h_c} \qquad \text{(kgf/cm}^2) \qquad (2.1)$$

$$V_{cr} = \left[0.16\sqrt{f'_c} + \frac{h_c(0.33\sqrt{f'_c} + \frac{P}{5b_c h_c}}{M_u/V_u - h_c/2}\right] b_c d \qquad \text{(kgf/cm}^2) \qquad (2.2)$$

In which f'_c is the concrete compressive strength, b_c is the column width, d is the effective depth which can be taken as $0.8h_c$, h_c is the column depth, P is the axial load subjected on the column, M_u/V_u is the ratio of the acting moment to shear force at that section of concern. The cracking strength is taken as the smaller of Eqs. (2.1) and (2.2), if $(M_u/V_u - h_c/2)$ is smaller than zero, then Eq. (2.2) isn't applicable, and Eq. (2.1) should be taken as the cracking strength.

The deformation at cracking point is the summation of shear deformation $\Delta_{s,cr}$ and flexural deformation $\Delta_{f,cr}$ as shown in Eqs. (2.3) to (2.5).

14

$$\Delta_{cr} = \Delta_{s,cr} + \Delta_{f,cr} \tag{2.3}$$

$$\Delta_{s,cr} = \frac{V_{cr}H}{0.4E_c b_c d} \tag{2.4}$$

$$\Delta_{f,cr} = \frac{V_{cr}H^3}{12E_c I_{eff}} \tag{2.5}$$
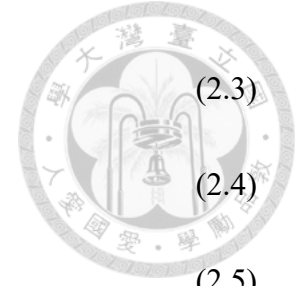
In which I_{eff} is the column sectional effective moment of inertia, which varies with the change in axial load subjected, the calculation is shown in **Table 2-1**, I_g is the moment of inertia of the column, and A_g is the gross area of the column section. For axial loads between $0.1f'_c A_g$ and $0.5f'_c A_g$, linear interpolation of the values in **Table 2-1** is used to calculate the effective moment of inertia.

Shear Strength Point (V_n, Δ_n)

According to the research of Li et al. (2019), it was observed from the crack patterns that for columns with higher height to depth ratio, the concrete strut could not directly transfer the applied force from the top to the bottom end, and that the shear strength of the column is decided by the smaller of the shear strength of the internal support and the shear strength of the inclined concrete strut. The force transfer mechanism is as shown in **Figure 2-2**, recommended by MacGregor (1997).

For the shear strength of the internal support for RC columns, NCREE/TEASDA (2021) takes the recommendation of ASCE/SEI 41-17 (2017) on the calculation of the strength of diagonal cracks, indicated as $V_{n,t}$. The calculation of $V_{n,t}$ is shown as follows:

15

$$V_{n,t} = \frac{A_{st}f_{yt}d}{s} + \left(\frac{1.6\sqrt{f'_c}}{M/_{Vd}} \sqrt{1 + \frac{P}{1.6\sqrt{f'_c}A_g}} \right) \times 0.8A_g \qquad (\text{kgf/cm}^2) \qquad (2.6)$$

In which, s is the spacing of transverse reinforcement, A_{st} is the total transverse reinforcement area within a spacing, f_{yt} is the yielding strength of the transverse reinforcement, $M/_{Vd}$ is the ratio of the maximum moment to the shear times effective depth d, the value is limited between 2 to 4.

For the shear strength of the concrete strut for RC columns, NCREE/TEASDA (2021) takes the recommendation of Hwang et al. (2017) (Softened Strut-and-Tie Model, SST Model) on the calculation of the crushing strength of concrete struts, indicated as $V_{n,c}$. The calculation of $V_{n,c}$ is shown as follows:

$$V_{n,c} = K\zeta f'_c A_{str} \cos\theta \qquad (2.7)$$

In which, K is the strut-and-tie index, ζ is the reinforced concrete softening coefficient, A_{str} is the effective area of the concrete strut end, and θ is the inclination angle between the concrete strut and the horizontal axis.

The calculation for the strut-and-tie index is shown as follows:

$$K = tan^A\theta + cot^A\theta + 0.14B - 1 \leq 1.64$$

$$A = 12\frac{\rho f_{yt}}{f'_c} \leq 1 \,; B = 30\frac{\rho f_{yt}}{f'_c} \leq 1$$

$$\theta \geq 45°; \; \rho = \rho_h, f_y = f_{yh}$$

$$\theta < 45°; \; \rho = \rho_v, f_y = f_{yv}$$

(2.8)

16

For conditions of inclination angle (θ) larger than 45 degrees, the horizontal ties are more effective, thus the horizontal reinforcement ratio ρ_h and corresponding yielding strength f_{yh} is used. For conditions of inclination angle (θ) lesser than 45 degrees, the vertical ties are more effective, thus the vertical reinforcement ratio ρ_v and corresponding yielding strength f_{yv} is used.

Zhang and Hsu (1998) proposed the softening coefficient ζ for reinforced concrete members subjected to shear cracking. Due to the complexity of the proposed equation, Hwang and Lee (2002) simplified the equation as follows:

$$\zeta = \frac{10.7}{\sqrt{f'_c}} \leq 0.52 \qquad (\text{kgf/cm}^2) \qquad (2.9)$$

The effective area of the concrete strut is calculated as Eq. (2.10), while NCREE/TEASDA (2021) recommends using the compression zone depth, a_c, developed by Paulay and Priestly (1992).

$$A_{str} = b_c a_c \qquad (2.10)$$

$$a_c = (0.25 + 0.85 \frac{P}{b_c h_c f'_c}) h_c \qquad (2.11)$$

The calculation of strut inclination angle θ requires iteration through force equilibrium. It is recommended to start the iteration at an angle of $\theta = 63.4°$, the procedure is shown in **Figure 2-3**.

The determination of column shear strength V_n is also shown in **Figure 2-3**, the value can be calculated after the iteration of strut inclination angle θ. The deformation at

strength point Δ_n is the summation of shear deformation $\Delta_{s,n}$ and flexural deformation $\Delta_{f,n}$ as shown in Eqs. (2.12) to (2.14).

$$\Delta_n = \Delta_{f,n} + \Delta_{s,n} \tag{2.12}$$

$$\Delta_{f,n} = \frac{V_n H^3}{12 E_c I_{eff}} \tag{2.13}$$

The calculation of shear deformation $\Delta_{s,n}$ includes the contribution from fan shaped strut (**Figure 2-2(a)** D-Region) at the top and bottom ends of the column, i.e. Δ_D, and contribution from non-fan shaped strut (**Figure 2-2(a)** B-Region) at the center of the column, i.e. Δ_B. Therefore, the total shear deformation of columns with height to depth ratio larger 2 can be indicated as follows:

$$\Delta_{s,n} = 2 \times \Delta_D + \Delta_B \tag{2.14}$$

$$L_D = d \times tan\theta \tag{2.15}$$

$$\Delta_D = 0.006 sin2\theta \times L_D \tag{2.16}$$

$$L_B = H - 2 \times L_D \geq 0 \tag{2.17}$$

$$\Delta_B = \frac{V_n L_B}{0.4 E_c b_d d} \tag{2.18}$$

In which L_D is the D-Region height and L_B is the B-Region height.

For columns with height to depth ratio lesser than 2, which can be considered as short columns, Li and Hwang (2017) stated that the concrete strut can directly transfer the force from top to bottom of the column through observations of crack patterns, as shown in **Figure 2-2(b)**. Therefore, the strength provided by internal support $V_{n,t}$ can be

18
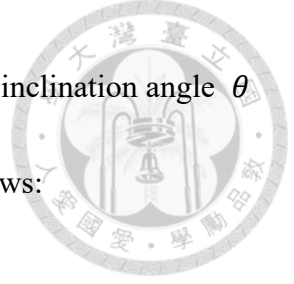
neglected, and the shear strength can be taken as Eq. (2.7), while the inclination angle θ and total deformation at strength point Δ_n can be calculated as follows:

$$\theta = \tan^{-1}\left(\frac{H}{h_c - \frac{2a_c}{3}}\right) \tag{2.19}$$

$$\Delta_n = \Delta_{f,n} + \Delta_{s,n} = \frac{V_n H^3}{12 E_c I_{eff}} + 0.006 sin2\theta \times H \tag{2.20}$$

Axial Collapse Point (V_a, Δ_a)

After reaching the strength point, the shear strength of the column is assumed to degrade linearly up to the point of the axial collapse point, where the column completely loss its lateral load carrying capacity, i.e. $V_a = 0$, the deformation at axial collapse point is calculated as follows:

$$\Delta_a = \Delta_n + rH \tag{2.21}$$

NCREE/TEASDA (2021) takes the recommendation of ASCE/SEI 41-17 (2017) into consideration for the coefficient of deformation r at the axial collapse point of columns. The coefficient r is determined through axial load ratio $(P/A_g f'_c)$ and transverse reinforcement ratio $(A_{st}/b_c s)$ as shown in **Table 2-2**, for ratios within the provided values, linear interpolation should be performed.

2.2.2 Flexural-Shear Failure Backbone Curve for Column

With sufficient stirrups, the shear strength V_n of columns would be higher than the nominal flexural strength V_{mn}, allowing the failure mode of the column to be prone to

19
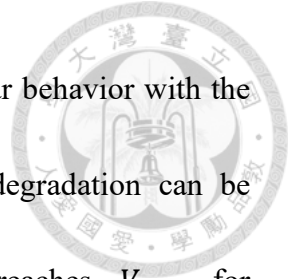
flexure failure. As shown in **Figure 2-4**, the column enters nonlinear behavior with the

yielding of longitudinal reinforcement and significant stiffness degradation can be

observed. Strength point is reached when the lateral force reaches V_{mn}, for

conservativeness and simplification, NCREE/TEASDA (2021) assumes that strain

hardening can be neglected and the lateral force can be retained up to the point of

longitudinal reinforcement fracturing or buckling and concrete crushing, the flexural

strength would degrade afterwards but the column would be able to retain the gravity load

carrying capacity.

Yielding Point (V_y, Δ_y) and Strength Point (V_{mn}, Δ_{mn})

According to mechanics of materials, the flexural strength of a double curvature

column V_{mn} can be calculated as follows:

$$V_{mn} = 2M_n/H \tag{2.22}$$

In which M_n is the nominal moment strength of the column. As for the strength at

yielding of the outmost longitudinal reinforcement of the column V_y, the calculation

procedure is same as Eq. (2.22), while taking the yielding moment strength M_y as the

input moment value.

The deformation at yielding strength Δ_y can be calculated using Eq. (2.23), while

taking V_y as the input strength value, and I_{eff} can be calculated using **Table 2-1** for

pre-yielding condition. The deformation at nominal strength Δ_{mn} can be calculated

20

using Eq. (2.23), and I_{eff} can be calculated using **Table 2-1** for post-yielding condition.

$$\Delta_{mn} = \Delta_{f,mn} + \Delta_{s,mn} = \frac{V_{mn}H^3}{12E_c I_{eff}} + \frac{V_{mn}H}{0.4E_c b_c d} \qquad (2.23)$$

The failure mode for flexure failure and flexural-shear failure are considered as ductile failure, and they both occur after the column enters nonlinear behavior, which results in problem when distinguishing between the two failure behaviors during analysis. For existing buildings built before seismic requirement codes, it is common for the RC columns of these buildings to have lower transverse reinforcement ratio, limiting the columns to develop full ductile failure behavior. For conservativeness and simplification, NCREE/TEASDA (2021) recommends to define flexural-shear failure backbone curves for all columns to consider their flexure behaviors, the backbone curve is shown in **Figure 2-5**.

Shear Failure Point (V_{mn}, Δ_s)

NCREE/TEASDA (2021) takes the recommendation of Elwood and Moehle (2005a) on the drift ratio of shear-critical columns at the point of shear failure Δ_s into consideration, the equation is as follows:

$$\Delta_s = \left(\frac{3}{100} + 4\rho'' - \frac{1}{133}\frac{v_m}{\sqrt{f'_c}} - \frac{1}{40}\frac{P}{A_g f'_c} \right) H \geq \frac{1}{100}H \qquad (2.24)$$

In which $\rho'' = \frac{A_{st}}{b \times s}$ is the transverse reinforcement ratio and $v_m = \frac{V_{mn}}{b_c d}$ is the shear stress.

Axial Collapse Point (V_a, Δ_a)

21

NCREE/TEASDA (2021) takes the recommendation of Elwood and Moehle (2005b) on the drift ratio of columns at the point of axial failure Δ_a, the equation is as follows:
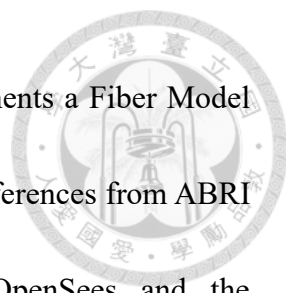
$$\Delta_a = \left(\frac{4}{100} \frac{1 + (\tan\theta)^2}{\tan\theta + P \frac{S}{A_{st} f_{yt} d_c \tan\theta}} \right) H \qquad (2.25)$$

In which d_c is the depth of the concrete core, calculated by center-to-center distance of stirrups, θ is the angle between the shear crack and horizontal axis, assumed to be 65° for flexural-shear failure columns, but limited below $\tan^{-1}\left(\frac{H}{h_c}\right)$.

According to NCREE/TEASDA (2021), the overall failure pattern of flexural-shear failure columns can be illustrated as shown in **Figure 2-6**. With the increase in lateral deformation, either the shear cracking point Δ_c or the yielding point Δ_y is reached with the formation of shear cracks and flexural cracks. Up to the point of shear failure Δ_s, the dominant shear crack is widened and could not sustain the lateral force, therefore strength degradation is initiated. Reaching to the point of axial collapse Δ_a, the lateral load carrying capacity of the column degrades to zero, and the shear friction mechanism on the dominant shear cracks is left to sustain the axial load subjected on the column. It is after the sliding on the dominant shear crack that the column completely loss its gravity load carrying capacity and thus collapse occurred.

2.3 Modeling Column Behavior with Fiber Section

Apart from the Concentrated Plastic Hinge models constructed in ETABS and

22

OpenSees using flexure and shear hinges, this research also implements a Fiber Model constructed in OpenSees for the analysis of the tests. This section references from ABRI (2021) and introduces the finite element analysis program OpenSees and the corresponding models implemented in this research.

2.3.1 OpenSees Introduction

OpenSees (Open System for Earthquake Engineering Simulation) (McKenna et al. 2000) is a structural analysis program for earthquake engineering research. It was developed by the Pacific Earthquake Engineering Research Center (PEER) at the University of California, Berkeley in 1999, and is mainly used to simulate the seismic behavior of structures. Its open-source design allows users to add and replace program objects without modifying the main program, providing a high degree of freedom during construction of analytical models and analysis procedures. The core of OpenSees is a finite element analysis software, which is composed of over a hundred object classes written by C++ object-oriented programming languages. For the operation face, TCL (Tool Command Language) is used to create models and perform analyses, aiming to provide a simple text interface for operation of the program itself and combination with subroutines, most importantly to be outputted in the form of an application program.

The operation of OpenSees is mainly divided into two stages: the establishment of

analytical models and the simulation of the analytical models. In terms of establishing the

analytical models, OpenSees provides various truss elements, beam-column elements,

linear plane elements, connection elements, and damper models for usage. In terms of

materials that are implemented in the elements, OpenSees provides linear elastic materials,

elastic-perfect-plastic materials, hardening materials, hysteretic materials, and concrete

materials. In terms of analysis methods, OpenSees provides static and dynamic linear

elastic analysis, nonlinear analysis, various time-history dynamic integration methods,

modal analysis, and various linear and nonlinear substitution methods.

The operational procedure for OpenSees is as follows:

(1) Input the parameters for definition of the model, including degrees of freedom,

dimensions of elements, nodes, and boundary conditions.

(2) Input the material definitions, section definitions, geometry definitions, and element

definitions, then construct and store the structure.

(3) Read the constructed structure, define the loading types, input the force analysis

commands according to requirements, and output the analysis results.

2.3.2 OpenSees Fiber Section

The nonlinear analysis of reinforced concrete structures inside OpenSees is mainly

based on the finite element analysis of fiber sections of specific sections of reinforced

concrete members. The establishment of a reinforced concrete fiber section consists of steel fibers and concrete fibers to simulate the moment curvature relationship (i.e. flexure behavior) of the section, where the concrete fibers can be separated into confined concrete and unconfined concrete. **Figure 2-7** shows a layout of a common fiber section of a reinforced concrete beam section, the circular black sections are the steel fibers, the outmost grey section is the unconfined concrete fiber, and the interior dark grey section is the confined concrete fiber. The steel fibers are generated on the section using "*fiber layer straight*" command, which allows users to generate a straight layer of steel fibers from the defined starting point to the ending point. The concrete fibers are generated on the section using "*fiber patch rect*" command, which allows users to generate a rectangular patch of defined number of fibers from the defined starting point to the ending point. The fiber section can then be defined onto elements to create a fiber element.

2.3.3 OpenSees Element

OpenSees contains a various range of elements, the nonlinear behaviors of the tests in Su (2007) are mainly concentrated on the columns, therefore, "Nonlinear Beam-Column Elements" are used to simulate the columns, and "Elastic Beam-Column Elements" are used to simulate the top steel beams with the assumption of linear behavior for members aside from the columns. On the other hand, "Zero-Length Elements" are
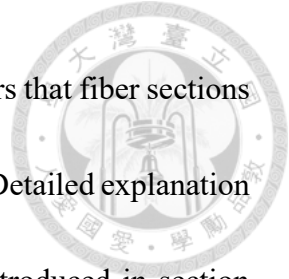
implemented on the column ends to simulate other nonlinear behaviors that fiber sections are not able to consider, such as shear and axial behavior of columns. Detailed explanation of application of Zero-Length Elements on column ends will be introduced in section 2.3.6.

The Nonlinear Beam-Column Elements are defined using "*element forceBeamColumn*" command, the object is based on the iterative force-based formulation which encompasses distributed plasticity integration and assumes Gauss-Lobatto integration with a copy of the same sectional force-deformation model at each integration point. It is required for users to input the number of Gauss-Lobatto integration points defined along the element. The user-defined fiber section is then defined onto the Nonlinear Beam-Column Element to form a whole fiber element of the column, mainly to simulate its flexure behavior.

The Linear Beam-Column Elements are defined using "*element elasticBeamColumn*" command. The input of cross-sectional area, Young's Modulus, shear modulus, torsional moment of inertia, and second moment of inertia are required for the definition of a Linear Beam-Column Element.

2.3.4 OpenSees Constitutive Material Model

OpenSees contains a various range of constitutive material models for steel, concrete,

and other materials. In this research, "Concrete07" material model is used for confined and unconfined concrete, "Pinching4" material model is used for steel material, shear hinge, and flexural hinge, this section would introduce the two material models. In addition, "Hysteretic" material model is also introduced.

Concrete07 Material Model

The concrete material model is defined using "*uniaxialMaterial Concrete07*" command, it is an implementation of Chang & Mander's (1994) concrete model with simplified unloading and reloading curves. The model requires eight input parameters to define the monotonic envelope of concrete, the parameters and calculation procedure for some of the parameters are provided on the OpenSees official website (https://opensees.berkeley.edu/). The stress-strain relationship of the material model and corresponding definitions of the parameters are shown in **Figure 2-8**.

Pinching4 Material Model

The reinforcement steel material, shear and flexural force-displacement hinges are defined through Pinching4 material model onto the column analytical model in this research, using "*uniaxialMaterial Pinching4*" command. It is used to construct a uniaxial material that represents a pinched load-deformation response and exhibits degradation under cyclic loading. The force-displacement relationship of the material model and corresponding definition of the parameters are shown in **Figure 2-9**. The implementation
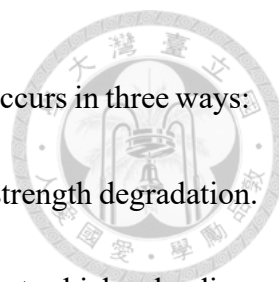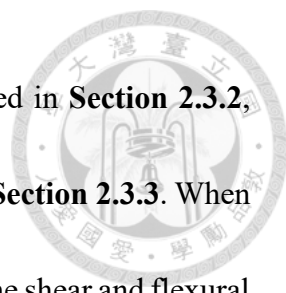
of cyclic degradation of strength and stiffness for the material model occurs in three ways: unloading stiffness degradation, reloading stiffness degradation, and strength degradation. The pinching behavior is defined through: ratio of the deformation at which reloading occurs to the maximum historic deformation demand, ratio of the force at which reloading begins to the force corresponding to the maximum historic deformation demand, and ratio of strength developed upon unloading from negative load to the maximum strength developed under monotonic loading.

The overall hysteresis behavior is controlled by the cyclic unloading stiffness degradation and pinching behavior mentioned above, taking the recommendation from Ling (2022) on the Pivot Model, this research limits the definition for hysteresis behavior into two phenomena: the unloading stiffness degradation (*$gK1*, *$gK2*, *$gK3*, *$gK4*, *$gKLim parameters*) and the pinching point for ratio of force at which reloading begins corresponding to the maximum historic deformation demand (*$rForceP*, *$rForceN parameters*), therefore, only the research on the two parameters mentioned would be introduced further through this research, the rest of the parameters remain their default values. Detailed explanation on the parameter research performed by this research would be introduced in **Section 6.2.1**.

When implemented as constitutive material model for longitudinal steel reinforcement, the stress-strain relationship of steel is input onto the Pinching4 material

model and defined onto the steel fiber on the fiber section introduced in **Section 2.3.2**, then defined onto the nonlinear beam-column element introduced in **Section 2.3.3**. When implemented as force-displacement relationship backbone curve for the shear and flexural hinge, the force-displacement relationship mentioned in **Section 2.2** is input onto the Pinching4 material model and defined onto the Zero-Length elements (**Section 2.3.6**) on column ends. The quadrilinear input curve of Pinching4 material model allows for input of the trilinear shear backbone curve in **Figure 2-1**, and input of the quadrilinear flexural-shear backbone curve in **Figure 2-5**. Therefore, Pinching4 material model is chosen as the input model for the implementation of the column-end hinges, and for consistency, the model is also used as the input model for steel material.

Hysteretic Material Model

The Hysteretic material model is defined using "*uniaxialMaterial Hysteretic*" command. It is used to construct a uniaxial trilinear hysteretic material object with pinching of force and deformation, damage due to ductility and energy, and degraded unloading stiffness based on ductility. The stress-strain relationship of the material model and corresponding definition of the parameters are shown in **Figure 2-10**. The input behaviors of stress-strain relationships or force-displacement relationships are defined by the user. Taking the recommendation from Ling (2022) on the Pivot Model, this research limits the definition for hysteresis behavior into two phenomena: the unloading stiffness

29

degradation due to ductility (*$beta parameter*) and the pinching point for ratio of force

(*$pinchy parameter*), therefore, only the research on the two parameters mentioned would

be introduced, the rest of the parameters remain their default values.
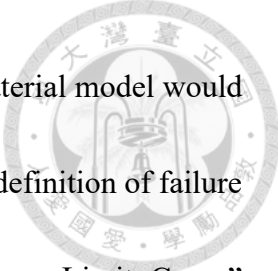
It is mentioned in the section for Pinching4 material model that this research employs

Pinching4 material model for steel constitutive material model and column-end hinge

backbone curve models, for the purpose of complete research and wider application of

hysteresis modeling, Hysteretic material model is also introduced, and detailed

explanation on the parameter research performed by this study would be introduced in

Section 6.2.2.

2.3.5 OpenSees Limit State Material Model

"Limit State Uniaxial Material Model" is a series of material models developed by

Elwood and Moehle (2003) based on the existing Hysteretic material model in OpenSees.

Three limit curves have been implemented in OpenSees by Elwood and Moehle (2003),

one to define shear failure (**Figure 2-11**), another to define axial failure (**Figure 2-12**),

and a trilinear general purpose limit curve that can be used to approximate any capacity

model.

The limit curve acts as a capacity limit for the applied member, when the behavior

of the member reaches the capacity limit defined on the limit curve, the limit curve would

30

then activate the corresponding limit state material model, and the material model would

be implemented onto the overall member behavior, thus allowing for definition of failure

behavior after the capacity limit is reached. For example, a "Shear Limit Curve"

implements Eq. (2.24) as the capacity curve (dark dashed lines in **Figure 2-11**) for

detection of shear failure. After the detection of shear failure, a "Shear Limit State

Material Model" that is defined on a shear spring is activated. The material performs the

strength degradation behavior of flexural-shear columns due to shear failure, thus is

implemented as a negative slope for its force-displacement relationship as shown in the

shear spring response in **Figure 2-13**. The analytical model setup for the shear spring

(with implementation of shear limit state material and shear limit curve) in series with the

beam-column element is shown in **Figure 2-13**. The total response is also shown in

Figure 2-13, which is the combination of the shear spring response and the beam-column

response. According to **Figure 2-13**, before the detection of shear failure, the shear spring

responses on its black dashed lines without strength degradation behavior, and the beam-

column element responses on its yielding plateau (black solid lines), no strength

degradation is observed for the overall behavior. After the detection of shear failure, the

shear spring responses on its grey solid lines with strength degradation behavior, and the

beam-column element would unload (grey solid lines), transferring the strength

contribution to the shear spring, and strength degradation behavior would be implemented

on the overall behavior of the column (grey solid lines). A simplified lateral force-displacement response of failure detection is shown in **Figure 2-14**.

The "Axial Limit Curve" implements Eq. (2.25) as the capacity curve (dark dashed lines in **Figure 2-12**), and the response procedure of "Axial Limit State Material Model" is same as the "Shear Limit State Material Model" mentioned previously, but governed by axial load-lateral deformation relationship. The analytical model setup for the axial spring (with implementation of axial limit state material and axial limit curve) in series with the beam-column element and the shear spring mentioned above is shown in **Figure 2-15**. It can be observed that the gravity load carrying capacity decreases with the increase in lateral deformation.

An example on the input parameters and command procedures for the above two material models is provided by Kakavand (2012). Several parameters are still required to be calculated for the establishment of the shear limit state material model (e.g. K_{deg}), which Elwood (2004) provides a detailed explanation on the behavior and calculation procedure. **Figure 2-16** shows the stiffness for strength degradation slope for the shear spring response K_{deg} and total response $K^t{}_{deg}$ in **Figure 2-13**. The Eqs. are as follows:

$$K^t{}_{deg} = \frac{V_u}{(\Delta_a - \Delta_s)} \tag{2.26}$$

$$K_{unload} = \frac{12EI_{eff}}{H^3} \tag{2.27}$$

32

$$K_{deg} = \left(\frac{1}{K^t_{deg}} - \frac{1}{K_{unload}} \right)^{-1}$$

(2.28)

In which V_u is the ultimate shear capacity of the column, Δ_a is calculated by Eq. (2.25), Δ_s is calculated by Eq. (2.24), and K_{unload} should be used for double curvature boundary conditions. Further details on how the material models are implemented in OpenSees and applied for analysis can be found in Elwood and Moehle (2003).

This research implements the "Shear Limit State Material Model" on each column to consider the flexure-shear failure behavior for columns without sufficient transverse reinforcement to reach full ductility. "Axial Limit State Material Model" is also implemented on each column to consider the loss of gravity load carrying capacity after shear failure with the increase in subjected axial load and lateral deformation. Setup of the material models onto the column analytical models would be explained in detail further through this research.

2.3.6 OpenSees Column End Hinge

"Zero-Length Elements" are defined using "*element zeroLength*" command on column ends, which can be considered as column end hinges. Zero-length elements are defined between two nodes at identical positions, which indicates that the elements do not contribute to any structural geometry. The numbers of degrees of freedom that the elements possess depends on the dimensions that users define for the analytical models,

33
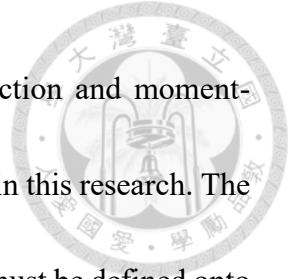
definition for force-displacement relationships on the x and y direction and moment-rotation relationship on the z direction are required for the 2D model in this research. The force-displacement relationships and moment-rotation relationships must be defined onto the material models of own choice prior to defining onto each degree of freedom on the zero-length elements.

Zero-length elements can simulate behaviors that aren't considered by fiber sections of the columns such as bond slip of low axial load columns and shear failure behavior. With the contribution from zero-length elements, the analytical models of columns in OpenSees can capture the overall behavior of columns more precisely. Elwood (2004) developed the Limit State Material Model mentioned in **Section 2.3.5**, and introduces the procedure for the implementation of the two material models onto the zero-length elements and onto the column ends, in addition with a rotational material to consider bond slip on column ends.

Elastic rotational slip springs are implemented onto the top and bottom zero-length elements of the columns to consider the flexibility due to slip of the longitudinal bars between the columns and foundations. The rotational stiffness of the slip spring (K_{slip}) can be determined by Eqs. (2.29) and (2.30).

$$K_{slip} = \frac{8u}{d_b f_s} EI_{flex} \tag{2.29}$$

$$u = 0.8\sqrt{f'_c} \qquad \text{(MPa)} \tag{2.30}$$

In which u is the constant bond stress assumed along the column longitudinal reinforcement.

Kakavand (2012) provided a manual for the establishment of three materials onto zero length elements on column ends, indicated as the Limit State Material Manual. The analytical model setup recommended by Kakavand (2012) is shown in **Figure 2-17**. According to Elwood (2004) and Kakavand (2012), "Shear Limit State Material Model" is a lateral force - lateral displacement relationship material implemented on the uniaxial spring of a zero-length element on the global x direction to consider flexural-shear failure behavior of columns. "Axial Limit State Material Model" is an axial force – lateral displacement relationship material implemented on the uniaxial spring of a zero-length element on the global y direction to consider gravity load carrying capacity of columns after flexural-shear failure. "Bondslip Material" is a moment-rotation relationship material implemented on the rotational springs of zero-length elements on the global z rotational direction to consider bond slip of longitudinal reinforcements at column ends. This research takes the recommendation of Elwood (2004) and Kakavand (2012) on the establishment of the above material models, and develops own column analytical models considering additional shear cracking and shear failure behavior. The developed column analytical models would be introduced in **Section 6.3**.

35

2.4 Modeling Hysteresis Behavior of Columns
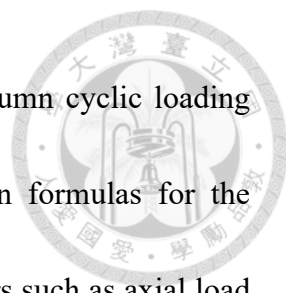
Accurate hysteresis modeling of columns is essential in order to carry out nonlinear time domain analysis for existing non-seismic RC buildings and irregular newly build RC structures. The Hysteretic material model and Pinching4 material model introduced in **Section 2.3.4** are capable of simulating the unloading and reloading hysteresis response of columns through OpenSees. This section introduces the Pivot hysteresis model provided by ETABS and SAP2000 for definition of member hysteresis behaviors.

2.4.1 Pivot Model

The Pivot hysteresis model (Pivot Model) is developed by Dowell et al. (1998) based on hysteresis behaviors of bridge columns, it is capable of simulating the unloading stiffness degradation of RC members after cracking and the pinching behavior. The unloading stiffness is governed by the parameter α, which defines the primary pivot point where the unloading stiffness curves intersect each other. The pinching behavior is governed by the parameter β, which defines the pinching pivot point where the reloading stiffness curves intersect each other, the parameters are shown in **Figure 2-18**.

The parameters defined in Dowell et al. (1998) are for bridge columns, considering the difference between building columns and bridge columns, Sharma et al. (2013) proposed another recommendation on the two parameters for rectangular columns.

36

Sharma et al. (2013) fitted the hysteresis curves of rectangular column cyclic loading experiments with the Pivot Model and regressed recommendation formulas for the calculation for α and β. The formulas are regressed with parameters such as axial load ratio, longitudinal reinforcement ratio, and transverse reinforcement ratio. However, Sharma et al. (2013) regressed columns governed by flexural failure and shear failure behavior together, the results were not able to reflect the actual failure mode of RC columns. Ling et al. (2022) proposed calculation formulas which considers flexure failure and shear failure behavior of columns separately. The optimization of the formulas is based on the energy dissipation capacity of the hysteresis curves of the columns, and developed through methods including simulated annealing algorithm, regression analysis, and numerical verification. The two parameters are calculated based on the axial load ratio, longitudinal reinforcement ratio, and transverse reinforcement ratio of each column, therefore, the Pivot Model can exhibit different hysteresis behaviors through different values of α and β.

According to ASCE/SEI 41-13 (2014), the failure criteria of columns can be distinguished by the ratios between the nominal flexural strength V_{mn} and the shear strength V_n, i.e. V_{mn}/V_n. For ratios larger than 1, shear failure is defined. For ratios lesser than 1 but larger then 0.6, flexural-shear failure is defined. For ratios lesser than 0.6, flexure failure is defined. Ling et al. (2022) classified flexure failure and flexural-shear

37
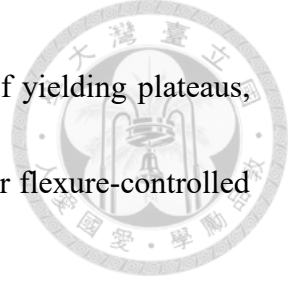
failure columns under the same criteria owing to their possession of yielding plateaus, and developed formulas for the calculation on the two parameters for flexure-controlled columns as shown below:

$$\alpha_F = 0.30 \times \left(\frac{N}{A_g f_c'}\right)^{-2.8} \times \left(\frac{\rho_l f_{y\ell}}{f_c'}\right)^{1.0} \times \left(\frac{\rho_t f_{yt}}{f_c'}\right)^{0.65} + 2.20 \le 10 \qquad (2.31)$$

$$\beta_F = 0.62 \times \left(\frac{N}{A_g f_c'}\right)^{0.1} \times \left(\frac{\rho_l f_{y\ell}}{f_c'}\right)^{0.1} \times \left(\frac{\rho_t f_{yt}}{f_c'}\right)^{-0.15} \le 1 \qquad (2.32)$$

For shear-controlled columns, the formulas are shown below:

$$\alpha_S = 1.0 \times \left(\frac{N}{A_g f_c'}\right)^{-3.0} \times \left(\frac{\rho_\ell f_{y\ell}}{f_c'}\right)^{2.3} \times \left(\frac{\rho_t f_{yt}}{f_c'}\right)^{1.5} + 2.10 \le 10 \qquad (2.33)$$

$$\beta_S = 0.13 \times \left(\frac{N}{A_g f_c'}\right)^{0.16} \times \left(\frac{\rho_\ell f_{y\ell}}{f_c'}\right)^{-0.37} \times \left(\frac{\rho_t f_{yt}}{f_c'}\right)^{-0.35} \le 1 \qquad (2.34)$$

In which ρ_ℓ is the longitudinal reinforcement ratio and $f_{y\ell}$ is the corresponding yielding strength, ρ_t is the transverse reinforcement ratio and f_{yt} is the corresponding yielding strength.

Since the model only focuses on the modeling of hysteresis behavior, thus it does not consider strength degradation due to increased displacement. However, the in-cycle strength degradation, which can be considered as hysteresis behavior, is neglected by the model. Based on the research results of Ling et al. (2022), focusing on the pinching behavior and unloading stiffness behavior while neglecting the in-cycle strength degradation behavior can provide test-to-model energy ratios of 0.95 for flexural-dominant columns, and 0.85 for shear-dominant columns, indicating sufficient accuracy

38

and simpler modeling by the proposed technique. Thus, the model will only focus on simulating the pinching and unloading stiffness behavior.
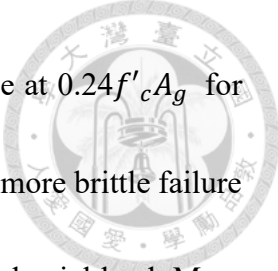
2.5 Shaking Table Experimental Studies on Behavior of Columns

Dynamic collapse tests of RC columns have been performed by researchers to study the strength and post failure behavior of columns. Elwood and Moehle (2003) conducted shaking table tests on two RC single story three-column frames with circular and rectangular sections. Guo (2008) conducted shaking table tests on three RC single story four-column frames. This research aims to study the dynamic behavior of flexure-dominant and shear-dominant columns due to overturning moment. To increase the test database in addition to Su (2007)'s test results, this research takes the test results of single column responses of Elwood and Moehle (2003) and Guo (2008) into consideration for more comprehensive research and comparison result. The column design parameters and responses are summarized in the **Appendix**.

2.5.1 Elwood and Moehle (2003)

Figure 2-19 shows the test specimen design layout for the three-column frame in Elwood and Moehle (2003). The two frames conducted by Elwood and Moehle (2003), i.e. S1 and S2, have identical design layout, but different applied axial load for the center column while remaining the same applied axial load for the outer columns. The applied

39

axial load for the center column in specimen S1 is at $0.1f'_cA_g$, while at $0.24f'_cA_g$ for

specimen S2. It is expected for the center column of S2 to experience more brittle failure

behavior and significant axial load redistribution due to higher applied axial load. More

information on the test setup and test results are provided in Elwood and Moehle (2003)

and Elwood (2004).

Since this research aims to study the dynamic behaviors of flexure controlled and

shear controlled columns due to overturning moment, it is mainly the outer columns on a

frame that are subjected to large varying axial loads due to overturning moment, with

increased axial load on one direction and decreased axial load on another (compared to

the initial axial subjected on the column). For center columns on odd numbered column

frames, being on the center position of the overturning moment, instead of increasing

axial load on one direction and decreasing axial load on another, slight decreasing of axial

load on both direction is observed, as shown in the center column axial load – lateral

displacement response of S2 in **Figure 2-20**. To perform research on the effect of large

varying axial load due to overturning moment on column strength, the test results of the

two outer columns on the three-column frame of Elwood and Moehle (2003)'s test are

taken into consideration. A total of four column responses from the research of Elwood

and Moehle (2003) are added into the database. The hysteresis curves of the four columns

are shown from **Figure 2-21** to **Figure 2-24**.

2.5.2 Guo (2008)

Figure 2-25 and **Figure 2-26** shows test specimen design layout for the four-column frames in Guo (2008). **Figure 2-25** is the design layout for specimen P1 and P2, and **Figure 2-26** is the design layout for specimen L, the three specimens have the same design layout and test parameters except that specimen L has lap splicing at the bottom of two non-ductile columns. More information on the test setup and test results are provided in Guo (2008).

As explained in **Section 2.5.1**, outer columns on a frame are prone to subject to large varying axial loads due to overturning moment, with increased axial load on one direction and decreased axial load on another. **Figure 2-27** shows the axial load – lateral displacement response of outer column C1 of specimen P1. The figure indicates that when the frame drifts to the negative direction, which is the direction of column C1, the axial load increases by around 80 percent, and decreases by around 80 percent to the positive direction, which is the direction of column C4. The test results of the two outer columns on the four-column frame of Guo (2008)'s tests are taken into consideration. A total of six column responses from the research of Guo (2008) are added into the database. The hysteresis curves of the six columns are shown from **Figure 2-28** to **Figure 2-33**.

41

2.6 Consideration of Varying Axial Load on Column Strength

Yeh and Chou (2017) observed the phenomenon of varying axial loads on framed structures due to overturning moment under dynamic forces, and even larger varying axial loads for high-rise buildings. Increased axial load would enhance the strength and lower the ductility from previous researches on RC members, therefore, it is necessary to perform research on the effect of varying axial load on member strength and ductility behavior. Yeh and Chou (2017) constructed analytical models of high-rise RC buildings, performed analysis, and proposed corresponding conclusions. This research studies shaking table test behaviors of single-story framed columns and references Yeh and Chou (2017)'s research as evidence.

2.6.1 Yeh and Chou (2017)

Yeh and Chou (2017) constructed analytical models for a three-story conventional school building (**Figure 2-34** and **Figure 2-35**) and a ten-story dual system residential building (**Figure 2-36**), with moment resisting frame on one direction and shear wall dual system on another, inside structural analysis program ETABS. ETABS version 2016 (2016) provided PMM flexural hinge to consider the change in axial load due to overturning moments of high-rise buildings. For the flexural hinges of the above buildings, Yeh and Chou (2017) constructed the hinges with M3 (or M2, depends on the

direction) nonlinear hinges (constant initial axial load) and PMM nonlinear hinges (varying axial load) in separate models according to TEASPA (2018) recommendations, to observe the differences on structural and member response with or without the consideration of varying axial load. The pushover analysis results of the models show the different responses for the effect of varying axial load on column strength for low-rise buildings with low varying axial load and for mid-to-high-rise buildings with higher varying axial load.

Figure 2-37 shows the moment-rotation response of the first-floor outmost column on the compression side for the school building, and Figure 2-38 shows the response on the tension side. It is observed that the moment strength of the PMM hinge model increased slightly on the compression side and decreased slightly on the tension side compared with the M3 hinge model with constant axial load. The responses of axial load with increasing moment of the PMM hinges are shown in Figure 2-39, which moderate increase and decrease in the axial load can be observed. The capacity curves of the overall response of the whole building are shown in Figure 2-40, it can be observed that the ultimate strength of the structure is increased considering varying axial load with the PMM hinge model, but the difference with the M3 hinge model is subtle. It can be concluded that the PMM hinge model can reflect the change in strength due to varying axial load, but not severe due to small varying axial load for the three-story structure, and

43

using the M3 hinge model predicts slightly lesser strength, which is more conservative.
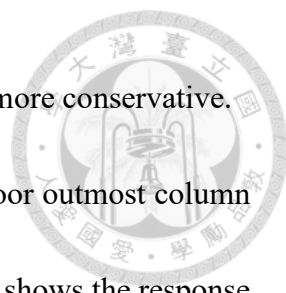
Figure 2-41 shows the moment-rotation response of the first-floor outmost column on the compression side for the residential building, and **Figure 2-42** shows the response on the tension side. It is observed that the moment strength of the PMM hinge model increased significantly on the compression side and decreased significantly on the tension side compared with the M2 hinge model with constant axial load. The responses of axial load with increasing moment of the PMM hinges are shown in **Figure 2-43**, which significant increase and decrease in the axial load can be observed. The capacity curves of the overall response of the whole building are shown in **Figure 2-44**, it can be observed that the difference in the ultimate strength of the structure is almost neglectable for the two models, which shows that the enhanced strength on the compression side can make up the decreased strength on the tension side even for such structure with large varying axial load. It can be concluded that the PMM hinge model can reflect the change in strength due to varying axial load, while using the M2 hinge model with constant axial load can still simulate the overall behavior with sufficient accuracy and consume much lesser analysis time. It is still recommended by Yeh and Chou (2017) to perform analysis for mid-to-high-rise buildings with PMM nonlinear hinges to reflect the effect of varying axial load on column strength, and for more accurate force distribution of members.

44

2.7 Effective Stiffness of Column

The simulated stiffness of members influences the response of the structures significantly, therefore, the development of accurate analytical models for predicting the stiffness of members is necessary. The effective stiffness is used to predict the initial linear stiffness behavior of RC columns. Researchers and structural codes have developed their own models to predict the effective stiffness. This section introduces the effective stiffness recommended by ASCE/SEI 41-17 (2017), Elwood and Eberhard (2006), and Elwood and Eberhard (2009), which will then be compared with the measured stiffness of RC columns from Su (2007)'s test results.

2.7.1 ASCE/SEI 41-17 (2017)

According to ASCE/SEI 41-17 (2017), component stiffness shall be calculated considering shear, flexure, axial behavior, and reinforcement slip deformations. It is recommended by ASCE/SEI 41-17 (2017) to use the following equation to calculate the flexural rigidity, which considers the flexure behavior, axial behavior, and slip deformations.

$$E_c I_{eff}/E_c I_g \quad \begin{cases} = 0.3 & \dfrac{P}{A_g f'_c} \leq 0.1 \\[2mm] = 0.7 & 0.5 < \dfrac{P}{A_g f'_c} \end{cases} \tag{2.35}$$

In which E_c is the concrete elastic modulus, I_g is the column section gross moment of

45

inertia. Linear interpolation is permitted for axial load ratios between 0.1 to 0.5. For the calculation of shear rigidity, the following equation is recommended:

$$0.4E_c A_w \tag{2.36}$$

In which A_w can be taken as $b_c d$. The total effective stiffness of the column is the summation of contributions from flexure rigidity and shear rigidity.

2.7.2 Elwood and Eberhard (2006)

Elwood and Eberhard (2006) proposed an effective stiffness model which concludes that the yield displacement of the column can be considered as the sum of the displacements due to flexure, bar slip, and shear. The equation is shown below:

$$\Delta_y = \Delta_{flex} + \Delta_{slip} + \Delta_{shear} = \frac{L^2 M_{0.004}}{6EI_{flex}} + \frac{L d_b f_s \phi_y}{8u} + \frac{2M_{0.004}}{(AG)_{eff}} \tag{2.37}$$

In which $M_{0.004}$ is the flexural moment at maximum concrete compressive strain of 0.004, EI_{flex} can be determined from the moment curvature at first yield, d_b is the diameter of the longitudinal reinforcement, f_s is the stress in tension reinforcement, and u is the average bond stress.

Elwood and Eberhard (2006) then proposed a simplified formula based on the above research for estimating the effective stiffness of rectangular reinforced concrete columns with normal-strength concrete, which considers displacements due to flexure, bar slip, and shear. The equation is as follows:

46

$$E_c I_{eff}/E_c I_g \quad \begin{matrix} = 0.2 & \frac{P}{A_g f'_c} \le 0.2 \\ \\ = 0.7 & 0.5 < \frac{P}{A_g f'_c} \end{matrix} \tag{2.38}$$

In which linear interpolation is permitted for axial load ratios between 0.2 to 0.5.

2.7.3 Elwood and Eberhard (2009)

A three-component model that explicitly accounts for deformations due to flexure, shear, and anchorage-slip was proposed by Elwood and Eberhard (2009) to provide a more accurate estimate of the effective stiffness of RC columns. The model took into consideration of additional circular sections, high strength concretes, and spiral transverse reinforcement columns into a database of 366 columns compared to the model in Elwood and Eberhard (2006), which is based on a database of 120 columns, to develop its equation. A detailed equation and a simplified equation for practice is provided. The simplified equation for practice is as follows:

$$\frac{EI_{eff\,calc}}{EI_g} = \frac{0.45 + 2.5\,{}^P/_{A_g f'_c}}{1 + 110\left(\frac{d_b}{D}\right)\left(\frac{D}{a}\right)} \le 1.0 \; and \; \ge 0.2 \tag{2.39}$$

In which $\frac{d_b}{D}$ can be approximated as 1/18 for building columns, D is the column depth in direction of loading, and a is the shear span of the column.

47

CHAPTER 3: CYCLIC TESTS OF COLUMNS ON STRONG FLOOR

3.1 Introduction

This chapter introduces the cyclic loading tests on intermediate-short (aspect ratio of 2 to 4) reinforced concrete columns conducted by Weng (2007). Li et al. (2019) discussed the test results of Weng (2007) and compared with proposed analytical models. The tests were conducted to investigate the influence of different parameters on the seismic behaviors of RC intermediate-short columns, therefore, a total of eight columns were tested with different aspect ratios, transverse reinforcement ratios, and axial load ratios at full-scale design. As mentioned in Chapter 1, cyclic-tested full-scale columns work as a comparison with shaking table-tested half-scale columns by Su (2007) to study the differences between cyclic and shaking table test behaviors. Among the eight types of design parameters in the cyclic tests, which each represents one type of column, three types of design parameters (i.e. three columns) can be used for comparison with shaking table-tested columns, but designed in full-scale, therefore, this chapter would focus on the introduction of the three columns. Weng (2007) and Li et al. (2019) have provided detailed discussion on the test behaviors, this chapter will introduce the results briefly for comparison usage. It is to mention that this research references from Weng (2007) and Li

49

et al. (2019) for the test results, figures of test setups, figures of crack patterns, and tables for specimen information.

3.2 Test Program

This section introduces the specimen design layout of the three columns designed by Weng (2007) which are referenced by this research. The test program setup and instrumentation are also mentioned.

3.2.1 Specimen Design

For all the intermediate-short column specimens, the cross section is 500×500 mm, the design concrete strength is 21 MPa, the longitudinal reinforcement ratio is designed at 3.24% with 16 No.8 reinforcement at design yield strength of 420 MPa, and No.3 reinforcement is used for the column transverse reinforcement at design yield strength of 420 MPa. The tested material strengths are shown in **Table 3-1**. As mentioned in the introduction, the research parameters of the cyclic tests are the aspect ratio, transverse reinforcement ratio, and axial load ratio. The aspect ratios of the columns are designed at 3 and 4 to indicate intermediate-short columns, the transverse reinforcement ratio can be separated into ductile (135° stirrups and 90-135° cross ties with 10 cm spacing) and nonductile (90° stirrups with 30 cm spacing) reinforcement design, while the axial load ratio can be separated as high axial load ($0.3 f_c' A_g$) and low axial load ($0.1 f_c' A_g$). The

50
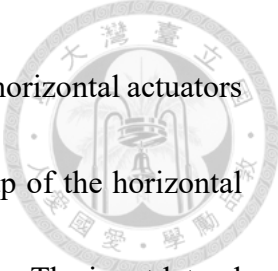
naming of the specimens follows the sequence of aspect ratio, ductile or nonductile reinforcement design, and lastly high or low axial load ratio.
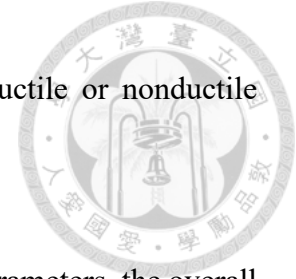
A total of eight columns are designed with different research parameters, the overall information of the specimens is shown in **Table 3-2**. Three of them are referenced by this research to compare with the shaking table tests, and this section will be focusing on the introduction of the three specimen designs and corresponding test results. The first specimen is the 4NL specimen, which has an aspect ratio of four, nonductile transverse reinforcement ratio designed at 0.1%, and low applied axial load ratio under $0.1 f_c' A_g$, the design layouts are shown in **Figure 3-1**. The second specimen is the 3DL specimen, which has an aspect ratio of three, ductile transverse reinforcement ratio designed at 0.43%, and low applied axial load ratio under $0.1 f_c' A_g$, the design layouts are shown in **Figure 3-2**. The third specimen is the 3NL specimen, which has an aspect ratio of three, nonductile transverse reinforcement ratio designed at 0.1%, and low applied axial load ratio under $0.1 f_c' A_g$, the design layouts are shown in **Figure 3-3**.

3.2.2 Experimental Setup

In order to perform double curvature condition for testing, two vertical actuators are set up as shown in **Figure 3-4**. The vertical actuators apply axial loads on the columns, with values of either $0.1 f_c' A_g$ or $0.3 f_c' A_g$, deforming at the same vertical deformation

to remain the columns under perfect double curvature condition. Two horizontal actuators are set up to provide lateral forces, as shown in **Figure 3-4**, the setup of the horizontal forces of the actuators pass through the inflection point of the columns. The input lateral displacements follow the test sequence for displacement cycles shown in **Figure 3-5**, which follows the loading protocol of ACI 374.1-05 (2006) as the drift ratio works as the controlling parameter in increasing order. For the loading time rate, 0.5 mm/s is applied for drift ratios of 0.25% and 0.5%, 1.0 mm/s for drift ratios of 0.75% and 1.5%, 1.5 mm/s for 2% and 4%, 2 mm/s for 5% and 8%, and 2.5 mm/s after 8%. The measurements used for the test include a linear variable differential transducer (LVDT), dial gages, and a tiltmeter to measure deformations during the loading. The installation setup for the above-mentioned instrumentations is shown in **Figure 3-6**.

3.3 Test Result

This section presents the overall hysteresis response of the columns 4NL, 3DL, and 3NL, while also providing the crack patterns of each column at strength point and before collapse.

3.3.1 Hysteresis Response

Figure 3-7 shows the hysteresis response for specimen 4NL under cyclic loading. The maximum lateral strength is developed at 0.85% drift ratio with a value of 476.2 kN.

After reaching the strength point, the lateral strength of the column drops immediately with a degrading slope of -12 kN/mm. With nonductile transverse reinforcement design, the column loses its lateral strength at 5% drift ratio, and loses its gravity load carrying capacity at 6% drift ratio, collapse occurs with significant drop in the column's vertical deformation correspondingly.

Figure 3-8 shows the hysteresis response for specimen 3DL under cyclic loading. The maximum lateral strength is developed at 1.15% drift ratio with a value of 781.3 kN. After reaching the strength point, the lateral strength of the column drops immediately with a degrading slope of -15.3 kN/mm. With ductile transverse reinforcement design, the lateral strength of the column degrades to 16% of the maximum value at 4% drift ratio, and loses its gravity load carrying capacity at 9.6% drift ratio, collapse occurrs with significant drop in the column's vertical deformation correspondingly.

Figure 3-9 shows the hysteresis response for specimen 3NL under cyclic loading. The maximum lateral strength is developed at 0.538% drift ratio with a value of 480.2 kN. After reaching the strength point, the lateral strength of the column drops immediately with a degrading slope of -54 kN/mm. With nonductile transverse reinforcement design, the column loses its lateral strength at 6% drift ratio, and loses its gravity load carrying capacity at 8% drift ratio, collapse occurrs with significant drop in the column's vertical deformation correspondingly.

53

The crack patterns and failure definition for each of the column will be presented in the next section.

3.3.2 Crack Pattern

For specimen 4NL, minor shear cracks appear on the column top and bottom hinge regions at 0.3675% drift ratio. Large dominant shear cracks form at column center at 0.621% drift ratio with a maximum width of 1.3 mm. At strength point, the dominant shear cracks are widened to 3 mm at an inclination angle of 64 degrees as shown in **Figure 3-10**. At 3% drift ratio, concrete cover spalling is observed. At 6% drift ratio, significant concrete cover spalling and yielding of stirrups is observed with the concrete core losing its integrity, as shown in **Figure 3-11**. Longitudinal reinforcement buckling and loosen of stirrups cause collapse of the column at the end of the test. The overall crack patterns show development of significant shear cracks, and the hysteresis curve in **Figure 3-7** shows brittle shear failure behavior. As a result, shear failure is defined for specimen 4NL.
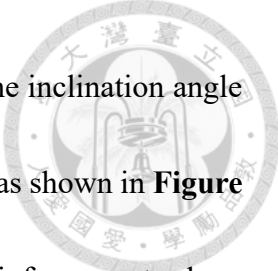
For specimen 3DL, minor shear cracks appear on the column top and bottom hinge regions at 0.314% drift ratio. Shear cracks form on column center at 0.512% drift ratio with maximum width of 0.1 mm. At strength point, the dominant shear cracks continue to form throughout the whole column, with maximum width of 0.55 mm at an inclination angle of 58 degrees as shown in **Figure 3-12**. At 5% drift ratio, concrete cover spalling is

54

observed. At 8% drift ratio, most of the concrete cover has spalled off, and the concrete core has lost its integrity as it is crushed into smaller pieces, as shown in **Figure 3-13**. The broken of stirrups causes collapse of the column at the end of the test. The overall crack patterns show development of numerous shear cracks, and the hysteresis curve in **Figure 3-8** shows brittle shear failure behavior. As a result, shear failure is defined for specimen 3DL.

For specimen 3NL, dominant shear cracks appear on the column center at 0.318% drift ratio with maximum width of 0.8 mm. At strength point, the dominant shear cracks are rapidly widened to 2 mm at an inclination angle of 66 degrees as shown in **Figure 3-14**. At 1.912% drift ratio, concrete cover spalling is observed. At 5% drift ratio, significant concrete cover spalling and yielding of stirrups is observed with the concrete core losing its integrity, as shown in **Figure 3-15**. The broken of stirrups causes collapse of the column at the end of the test. The overall crack patterns show development of significant shear cracks, and the hysteresis curve in **Figure 3-9** shows brittle shear failure behavior. As a result, shear failure is defined for specimen 3NL.

According to Thurlimann (1979), the inclination angle of a concrete primary strut should not be larger than $\tan^{-1}(2)$ and smaller than $\tan^{-1}(\frac{1}{2})$. For reinforced concrete columns, the lower bound of the crack is limited to 45 degrees, therefore, the inclination angle of a column concrete strut with the horizontal axis is bounded between 63.4 and 45

55

degrees based on analytical concepts. According to Li et al. (2019), the inclination angle of the column concrete strut is determined through force equilibrium, as shown in **Figure 2-3**. When the column is designed with insufficient transverse reinforcement, shear tension failure due to insufficient internal support to provide force equilibrium would occur, limiting the concrete strut inclination angle to its maximum value. When provided with sufficient transverse reinforcement, balanced failure between shear tension and shear compression behavior may occur, decreasing the strut inclination angle. The force transfer mechanism is shown in **Figure 2-2**. The above-mentioned behaviors can be verified by the crack inclination angles presented in this section.

It can be observed from the crack patterns of the above specimens that with lower transverse reinforcement ratio (specimens 4NL & 3NL), insufficient internal support is provided, limiting the strut inclination angle to its maximum value (64° & 66°), which varies slightly due to measurement deviation and concrete variability. With increased transverse reinforcement ratio (specimen 3DL), more internal support is provided and the inclination angle is lowered to 58°. The overall test behaviors correspond with the above-mentioned phenomenon, and Li et al. (2019) provides comparison results for more reinforced concrete intermediate-short columns.

CHAPTER 4: DYNAMIC TESTS OF COLUMNS BY SHAKING TABLE

4.1 Introduction

This chapter introduces the dynamic shaking table tests on intermediate-short (aspect ratio of 2 to 4) reinforced concrete columns conducted by Su (2007). The tests were originally conducted to study the shear failure behavior of intermediate-short RC columns under dynamic loadings to observe the dynamic collapse behavior of single column specimens and overall frame specimens, and to investigate the influence of different parameters on the seismic behaviors of RC intermediate-short columns. Therefore, a total of four frames which consist of nine columns were tested with different aspect ratio and transverse reinforcement ratios under half-scale design.

As mentioned in **Chapter 1**, shaking table-tested half-scale columns work as a comparison with cyclic tested full-scale columns (Weng 2007) to study the differences between cyclic and shaking table test behaviors. Three types of design parameters are used for comparison between cyclic loading and shaking table-tested columns (i.e. category 4NL, 3DL, and 3NL). The shaking table tests contributed a total of seven columns, with three in the category of 4NL, two in the category of 3DL, and two in the category of 3NL, all designed in half-scale. This research not only focuses on the

57

comparison of cyclic and shaking table test behaviors, but also holds a large portion on the research of column dynamic behaviors. Therefore, the overall column and frame test behaviors will be presented in this chapter in a detailed manner. It is to mention that this research references from Su (2007) for the test results, figures of test setups, figures of crack patterns, and tables for specimen information, the rest of the presented and discussed contents are conducted by this research.

4.2 Test Program

This section introduces the specimen design layouts of all four frames conducted by Su (2007) which are referenced by this research. The test program setup, instrumentation, and input ground motions are also mentioned.

4.2.1 Specimen Design
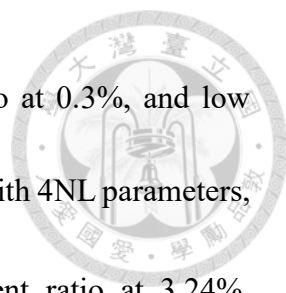
A total of four frames are designed for the shaking table tests at half-scale due to the limitation in size for the shaking table, and named by their testing sequence from T1 being the first test to T4 being the last test. T1 is a three-column frame and T2 to T4 are two-column frames. For all the intermediate-short column specimens, the cross section is 250×250 mm, the design concrete strength is 21 MPa, No. 4 steels are used for the column longitudinal reinforcement at design yield strength of 420 MPa, and D4 (4mm diameter) steels are used for the column transverse reinforcement at design yield strength of 600

58

MPa. The tested material strengths are shown in **Table 4-1**. As mentioned in the introduction, the research parameters of the shaking table tests are the aspect ratio and transverse reinforcement ratio. The aspect ratios of the columns are designed at 3 and 4 to indicate intermediate-short columns, while the transverse reinforcement ratio can be separated into ductile (135° stirrups and 90-135° cross ties with 5 cm spacing) and nonductile (90° stirrups with 15 cm spacing) reinforcement design.

The naming of the four frames is mentioned previously, and when installed on the shaking table, the columns in a particular frame are named in the order of: C1 being the column on the north side when installed on the shaking table, C2 being the column in the center, and C3 being the column on the south side. For two-column specimens, the two columns are named with C1 and C3. The designed parameter naming of each column follows the sequence of aspect ratio, ductile or nonductile reinforcement design, and lastly high or low axial load, same as the sequence in the cyclic loading tests. Detailed information on the naming and design of each frame and column will be presented later in this section.

The design parameters of the specimens can be separated into four categories, specimen 4DL, 4NL, 3DL, and 3NL. The properties of each category are shown in **Table 4-2**. Specimen T1 is a three-column frame, the north and south columns (C1 and C3) are designed with 4DL parameters, which has an aspect ratio of four, low longitudinal
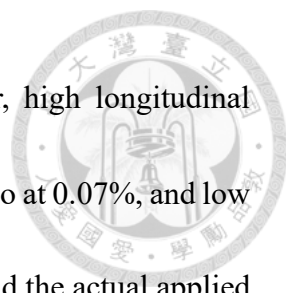
reinforcement ratio at 1.62%, ductile transverse reinforcement ratio at 0.3%, and low

applied axial load at 0.1 $f'_c A_g$. The center column (C2) is designed with 4NL parameters,

which has an aspect ratio of four, high longitudinal reinforcement ratio at 3.24%,

nonductile transverse reinforcement ratio at 0.07%, and low applied axial load at 0.1

$f'_c A_g$. The design parameters of frame T1 and the actual applied axial load are shown in

Table 4-3, while the specimen design layout is shown in **Figure 4-1**.

Specimen T2 is a two-column frame, the north and south columns (C1 and C3) are

designed with 3DL parameters, which has an aspect ratio of three, high longitudinal

reinforcement ratio at 3.24%, ductile transverse reinforcement ratio at 0.3%, and low

applied axial load at 0.1 $f'_c A_g$. The design parameters of frame T2 and the actual applied

axial load are shown in **Table 4-4**, while the specimen design layout is shown in **Figure**

4-2.

Specimen T3 is a two-column frame, the north and south columns (C1 and C3) are

designed with 3NL parameters, which has an aspect ratio of three, high longitudinal

reinforcement ratio at 3.24%, nonductile transverse reinforcement ratio at 0.07%, and low

applied axial load at 0.1 $f'_c A_g$. The design parameters of frame T3 and the actual applied

axial load are shown in **Table 4-5**, while the specimen design layout is shown in **Figure**

4-3.

Specimen T4 is a two-column frame, the north and south columns (C1 and C3) are

designed with 4NL parameters, which has an aspect ratio of four, high longitudinal

reinforcement ratio at 3.24%, nonductile transverse reinforcement ratio at 0.07%, and low

applied axial load at 0.1 $f'_c A_g$. The design parameters of frame T4 and the actual applied

axial load are shown in **Table 4-6**, while the specimen design layout is shown in **Figure**

4-4.

Three of the columns are designed under the category of 4NL (T1C2, T4C1, T4C3),

two of the columns are designed under the category of 3DL (T2C1, T2C3), and two of

the columns are designed under the category of 3NL (T3C1, T3C3), which provides seven

shaking table-tested columns to be compared with the three cyclic tested comlumns

mentioned in **Chapter 3**.

4.2.2 Experimental Setup

A total of four frames are tested on the shaking table (**Figure 4-5**) in National Center

for Research on Earthquake Engineering (NCREE) Taipei Lab for the shaking table tests.

The columns are casted separately as shown in **Figure 4-6**, then locked together with

prestress using steel beams to form framed structures (**Figure 4-7**). For T1 frame which

consists of three columns, the c.t.c. span is 135 cm, while for T2 to T4 frame which

consists of two columns, the c.t.c. span is 270 cm. Lead packet weights are installed on

the top steel beam (**Figure 4-8**) to simulate axial loads for the columns and to induce

lateral force as mass blocks for the reaction of ground motions. The initial designed axial load is 0.1 $f_c'A_g$ for all specimens, while the actual applied axial load ranges between 2.84% to 10.22%, the values are provided from **Table 4-3** to **Table 4-6**. The reason for the difference in applied axial loads for columns on the same frame can be induced by two reasons. The first reason may be that the columns are casted separately and locked together afterwards, the slight difference in axial length of the columns may lead to uneven gravity load distribution. The second reason may be contributed by the difference in applied prestress to lock the top foundation of the columns onto the top steel beam, and the uneven prestress may lead to unbalanced internal forces. Overall, the gravity load distribution can be seen sensitive to the axial length of specimens as well as the experimental setup.

Accelerometers are installed on the top steel beam and bottom foundation of the specimens (**Figure 4-8**) on horizontal and vertical directions to measure the corresponding accelerations. Load cells below column foundations are instelled to provide measurements for axial loads and base shears during test procedures. In order to measure the deformations, temposonics (LDT) are installed on the top steel beams and top foundations of the columns to measure the overall horizontal displacements of the frame (**Figure 4-9**). String pots are installed within each column (**Figure 4-9**), and pulleys are combined with the usage of string pots to measure vertical and oblique displacements

62

(LVDT), which can then be used to calculate the lateral and vertical deformations of the columns.
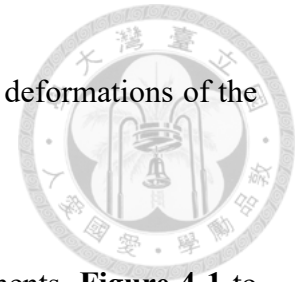
Strain gages are also used to measure the strains of reinforcements. **Figure 4-1** to **Figure 4-4** shows the setup of strain gages, with blue-colored symbols indicating the position of strain gages on stirrups, and red-colored symbols indicating the position of strain gages on longitudinal reinforcements.

4.2.3 Input Ground Motion

The measured ground acceleration of TCU082 station during the 1999 Chi-Chi earthquake on the east-west direction is chosen as the input ground motion for the shaking table tests. TCU082 station is located around the center part of Taiwan, with the maximum measured ground acceleration of 221.16 gal.

Each run of input ground motions within the same test procedure is conducted with the same acceleration time history, but magnified to different peak ground acceleration (PGA) values, ranging between 500 gal and 1g. All tests start the runs with lower PGAs to simulate slight member failure behaviors for minor earthquakes, and increase to higher PGAs for following runs to simulate structural collapse behaviors for major earthquakes. If collapse hasn't occurred, it is determined by the test conductor whether to continue with other ground motions or terminate the tests. To record the natural periods of the

63
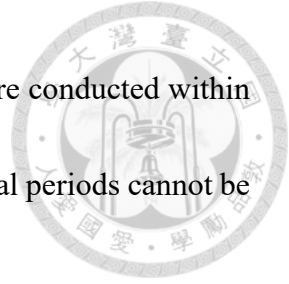
frames at initial conditions and after failure, 30 gal of white noises are conducted within

the major runs of ground motions. For collapsed specimens, the natural periods cannot be

measured.

All the ground motions are compressed with a value of $\frac{1}{\sqrt{2}}$ on the time steps to

prevent over-enhancing the strain rate effect compared with typical ground motions, since

the specimens are designed at half-scale. For shaking table tests, the achieved acceleration

for ground motion may not be same as the input acceleration due to instrumental accuracy

limitations. Accelerations are much more complicate to simulate considering its various

influencial factors. The input ground motion information, the input PGAs, and the

achieved PGAs of each run during each test are provided in **Table 4-7**, and the response

spectra for each test are shown in **Figure 4-10**.

4.3 Test Result
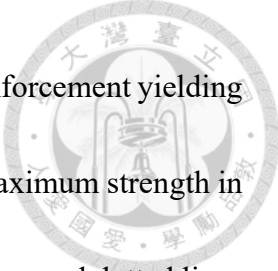
The first part of this section presents the fundamental properties of each test. In order

to take the test results into consideration for further research, it is necessary to understand

the behaviors of the shaking table tests in a detailed manner. This section presents the

measured responses such as lateral deformation, vertical deformation, base shear, axial

load, and strain gage readings to better investigate test behaviors. Based on the presented

results, this section then describes the failure development sequence and provide

discussions on observed column behaviors. It is to mention that the tests and results are conducted and processed by Su (2007), the figures and researches in this section are conducted by this research.

The presented results follow the sequence starting from individual columns to overall frames. For each member, the introduction starts from R2 to later runs, and follows the sequence of crack patterns, hysteresis responses, and time history responses for each specific run. The sequence may change for better presentation of test results. All the time history responses are enlarged to focus on the time period that is of concern.
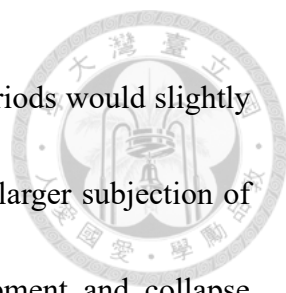
The required information and plotted figures for investigating the column responses is mentioned prior to the main content in each section. For all the plotted figures, the black lines indicate the test results, the square symbols indicate the points of longitudinal reinforcement yielding, the triangular symbols indicate the points of maximum strength development, the circular symbols indicate the point of axial failure, and the cross symbols indicate the point of collapse. Axial failure is defined when the column loses its vertical deformation stability, which indicates the initiation of a prompt and significant drop in the measured vertical deformation. The collapse point is defined when the top steel beam of the frame falls onto the shaking table after axial failure or when the vertical deformation reaches a stable measurement value. The condition that occurs first defines the collapse point of the column. For the stirrup strain gage readings, the red lines indicate

65

the response for all runs. The horizontal dotted black lines indicate reinforcement yielding

limits, while the vertical dotted black lines indicate the drift ratio at maximum strength in

both directions. For all the figures, solid lines indicate correct responses, and dotted lines

indicate broken and un-referenceable responses. **Table 4-8** provides the maximum

measured lateral strengths for all columns. The values are defined as measured/developed

maximum lateral strengths in this section rather than flexural or shear strengths by the

following reasons. First, since shaking table tests are not displacement-controlled, which

can observe the full backbone curve of specimens with strength degradation behavior, and

define the maximum strength points as the flexural or shear strengths of the specimens.

Shaking table tests apply small to large earthquake forces on the specimens, the forces

does not necessary induce the specimens to develop their maximum strengths. Second,

the specimens have not yet been defined as flexural or shear-dominant, thus the measured

lateral strength values cannot yet be defined as shear strengths or flexural strengths.

4.3.1 Test Fundamental Properties

The natural periods and damping ratios of the frames measured at each white noise

ground motion are presented in **Table 4-9**. The initial natural period of Test 1 is around

0.13 seconds, while values for the three other frames are lower at around 0.1 seconds.

With the subjection of smaller earthquake forces, crack formations on the column body

lead to slight softening of the structural stiffness, thus the natural periods would slightly increase after the first run, as observed from Test 2 to Test 4. With larger subjection of earthquake forces which may lead to maximum strength development and collapse behavior, the structural stiffness would be damaged severely, thus the natural periods would increase significantly, as observed in Test 1 and Test 2 during following runs. For frames subjected to collapse behavior after strength development, no natural periods could be measured, as observed in Test 3 and Test 4. The test periods are plotted on the response spectra in **Figure 4-10** to observe the specimen response when subjected to ground motions. With RC column members and steel top beams locked together to form frames, the damping ratios of each frame locates between 2 % to 5 %, which 2 % is the common value for steel structures and 5 % is for RC structures.

4.3.2 Behavior of Test 1

As shown in **Table 4-7**, there are a total of four runs of ground motions subjected on Frame T1. R2 and R3 have an input PGA of 500 gal to simulate linear behaviors of structures under small-to-medium earthquakes. R4 has an input PGA of 1g to simulate strength developments and collapse behaviors of structures under large earthquakes. Since strength development has been observed but structural collapse hasn't occurred, R6, which has an input PGA of 800gal, is subjected on the frame to induce collapse of the

frame. The test terminates with collapse of all columns after R6.
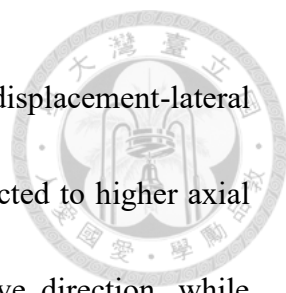
Column C1

Column C1 is located on the north side of frame T1. The crack patterns at different stages of the column are shown in **Figure 4-11**. The lateral displacement and base shear time history responses are shown in **Figure 4-12** and **Figure 4-13**. The hysteresis responses are shown in **Figure 4-14**, with positive axial loads indicating compression, while the stirrup strain gage readings are shown in **Figure 4-18**. The failure sequence of the column is shown in **Table 4-10**. The actual applied initial axial load is 157 kN in compression.

The crack pattern at the initial stage for column C1 before the input of ground motions is shown in **Figure 4-11**. Due to the application of the top steel beam onto the top foundation of column C1 through prestress, several flexural cracks have been induced throughout the column body, therefore, it can be expected that the initial stiffness of the column might be softened.

Figure 4-12 and **Figure 4-13** show the overall time history response for lateral displacement and base shear, with the failure sequence plotted as symbols on the test curves. No development of failure sequence can be seen occurring during R2 and R3.

From the hysteresis curve in **Figure 4-14**, it can be observed that column C1 is under linear behavior during R2 and R3 (grey lines).

The axial load-lateral displacement plot and vertical displacement-lateral displacement plot in **Figure 4-14** indicates that the column is subjected to higher axial load and shortened axial deformation when drifted to the negative direction, while subjecting to lower axial load and lengthened axial deformation when drifted to the positive direction. This varying axial load phenomenon is caused by the overturning moment of the overall frame acting on the column member, which would be explained more in detail in the frame discussion part in this section.

For R4, which has an input PGA of 1g, **Figure 4-11** shows the crack patterns of the column at the points of maximum strength development in both directions. Due to initial cracking on the column body, not much flexural cracks have formed when the column reaches maximum strength, while shear cracks have formed on the plastic hinge section on the top of the column.

The time history responses in **Figure 4-12** and **Figure 4-13** indicate that at 24.16 second through R4, longitudinal reinforcement yielding (red square symbol) is observed in the negative direction, then at 24.295 second in the positive direction. At 24.525 second, the maximum strength (red triangular symbol) in the negative direction is developed, then at 25.135 second in the positive direction.
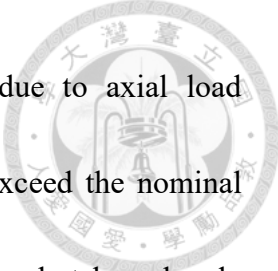
The hysteresis curve in **Figure 4-14** shows that the column longitudinal reinforcements yield (red square symbol) at a strength value of 69.73 kN in the negative

direction and 80.78 kN in the positive direction, while significant stiffness softening can be observed through the curve due to reinforcement yielding. The column then develops its maximum strength (red triangular symbol) in the negative direction with a value of 136.12 kN under higher axial load of 614.74 kN in compression, and in the positive direction with a value of 130.86 kN under lower axial load of 403.71 kN in compression. As yielding of the longitudinal reinforcements are indicated by the strain gage readings, the lateral strength of the column develops exceeding the value of flexural strength V_{mn} (orange dotted lines in the figure), thus it can be concluded that the strength development behavior is flexure-dominated.

The axial load-lateral displacement plot and vertical displacement-lateral displacement plot in **Figure 4-14** indicate the phenomenon of varying axial load. The axial load response shows that during R4, a residual drift to the positive direction induces a gravity load redistribution phenomenon, leading to the axial load on column C1 to increase by a large value, but still responses under varying axial load phenomenon. The initial axial load is applied at 8.40 %, the high varying axial load is applied at 32.90 %, and the low varying axial load is applied at 21.60 %. The low varying axial load is higher than the initial axial load due to the load redistribution phenomenon.

The moment-axial load response during R4 is plotted on the P-M curve of the column as shown in **Figure 4-15**. The axial load during zero moment (black line) is

different from the initial axial load value (orange dotted line) due to axial load redistribution during R2 and R3. The moment response does not exceed the nominal moment strengths at their corresponding subjected axial load values, but has already exceeded the nominal moment strength at the initially subjected axial load value, and responses below the balance point. This may be due to that the significantly increased axial load through axial load redistribution is not shown to be able to fully enhance the flexural strength of the column up to its ideal value. To sum up, the moment-axial load behavior of the column indicates the development of flexural strength.

For R6, which has an input PGA of 800gal, the hysteresis curve in **Figure 4-14** shows that the column develops a very large yielding plateau with the strength maintained up to 8% of drift ratio, and continues with rapid strength degradation with increasing lateral displacement. Axial failure (red circular symbol) and collapse (red cross symbol) occurred around the value where the lateral strength of the column degrades to zero.

Figure 4-11 shows the crack pattern of the column at the point before collapse. During R6, the ground motion continues to damage the shear crack on the plastic hinges that are formed during R4. When the column is subjected to a large lateral displacement up to 10% of drift ratio, the dominant shear crack is widened and the concrete and stirrup could not sustain the lateral deformation and force. As a result, sliding occurs on the dominant shear crack, which leads to the collapse of the column.

71

The time history responses in **Figure 4-12** and **Figure 4-13** indicate that at 37.53 second through R6, axial failure (red circular symbol) of the column is defined, then at 38.18 second, collapse (red cross symbol) occurred and rest of the data aren't referenceable.

The vertical displacement-lateral displacement plot in **Figure 4-14** indicates a severe drop in the axial displacement at the axial failure point, which represents the condition when the column loses its structural stability. The axial load-lateral displacement plot in **Figure 4-14** indicates a significant boost in the axial load at the collapse point, which is measured by the transducer when the upper part of the dominant shear crack (the column body and the top steel beam) slides through the crack and falls the bottom foundation.

The longitudinal reinforcement readings are plotted with the lateral drifts of the column as shown in **Figure 4-16** and **Figure 4-17**. The readings indicate that all reinforcements have yielded in tension before reaching their lateral displacements at maximum strengths, and have yielded significantly when reached, which indicates contribution of flexural behavior to the development of column strength. For the stirrup strain gage readings in **Figure 4-18**, the results show that no stirrups have yielded throughout all the runs for column C1.

The strength development is concluded to be mainly governed by flexural-shear behavior through the observation of strain gage readings, crack pattern developments, and

overall hysteresis behaviors, thus flexural-shear failure is defined for column C1.

Column C2
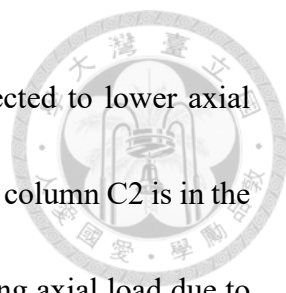
Column C2 is located on the center of frame T1. The crack patterns at different stages of the column are shown in **Figure 4-19**. The lateral displacement and base shear time history responses are shown in **Figure 4-20** and **Figure 4-21**. The hysteresis responses are shown in **Figure 4-22**, with positive axial loads indicating compression, while the stirrup strain gage readings are shown in **Figure 4-24**. The failure sequence of the column is shown in **Table 4-10**. The actual applied initial axial load is 53 kN in compression. Only the results from R2 to R4 are plotted in the above figures since the column completely loses its lateral load carrying capacity at the end of R4, and that the results in R6 are not referenceable.

The crack pattern at the initial stage for column C2 before the input of ground motions is shown in **Figure 4-19**, no initial cracks can be observed.

Figure 4-20 and **Figure 4-21** show the overall time history response for lateral displacement and base shear, with the failure sequence plotted as symbols on the test curves. No development of failure sequence occurs during R2 and R3.

From the hysteresis curve in **Figure 4-22**, it can be observed that column C2 is under linear behavior during R2 and R3 (grey lines).

The axial load-lateral displacement plot and vertical displacement-lateral

73

displacement plot in **Figure 4-22** indicates that the column is subjected to lower axial load and slight lengthened axial deformation in both directions. Since column C2 is in the center of the three-column frame, it is the least sensitive to the varying axial load due to overturning moment, and is slightly lengthened when the whole frame drifts to both directions, which leads to an induce in tensile force on the column, and decreases the applied axial load or even turns into a tensile load as a result.
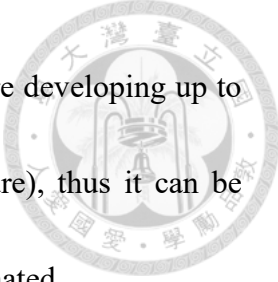
For R4, which has an input PGA of 1g, **Figure 4-19** shows the crack patterns of the column at the points of maximum strength development in both directions and at the end of R4. No significant shear cracks can be observed when the column develops its maximum strength in the positive direction, while a significant and dominant shear crack appears on the lower part of the column when reaching maximum strength in the negative direction. Since column C2 is designed with nonductile transverse reinforcement and 90-degree hooks, the stirrups could not provide sufficient internal support to sustain the shear force and are opened without seismic hook design. The confinement for the concrete core and anchorage for longitudinal reinforcements are lost with the damage of stirrups on the lower part of the column, thus the cover concrete spalls and longitudinal reinforcements buckle with the concrete core losing its integrity at the end of R4.

The time history responses in **Figure 4-20** and **Figure 4-21** indicate that at 24.175 and 24.18 second through R4, maximum strength development (green triangular symbol)

74

and longitudinal reinforcement yielding (green square symbol) is observed in the negative direction. Yielding in the positive direction occurs at 24.29 second, and maximum strength is developed at 24.3 second. Axial failure is defined at 24.305 second. Since column C2 was held up by the two outer columns after axial failure, collapse for the column is defined when the whole frame collapses, which is controlled by the collapse behavior of the two outer columns during R6.

The hysteresis curve in **Figure 4-22** shows that the column longitudinal reinforcements yield (green square symbol) at a strength value of 156.93 kN in the negative direction and 123.72 kN in the positive direction, while significant stiffness softening can be observed through the curve due to reinforcement yielding. The column then develops its maximum strength (green triangular symbol) in the negative direction with a value of 163.14 kN under axial load of 86.17 kN in tension, and in the positive direction with a value of 152.68 kN under axial load of 87.41 kN in tension. Axial failure (green circular symbol) is defined after strength development in the positive direction. The hysteresis curve shows rapid strength degradation behavior after strength point in the positive direction, and the lateral load carrying capacity degrades to zero with the following drifts at the end of R4, which indicates brittle failure behavior. Complete failure is defined for column C2 in this run, thus the results in R6 are not referenceable. Although yielding of the longitudinal reinforcements are indicated by the strain gage readings, the

75

lateral strength of the column experiences strength degradation before developing up to the value of flexural strength V_{mn} (orange dotted lines in the figure), thus it can be concluded that the strength development behavior isn't flexure-dominated.

The axial load-lateral displacement plot in **Figure 4-22** indicates that the column is subjected to axial load around the same value in tension when reaching maximum strength in both directions. After strength development in the positive direction, the axial load increases significantly in tension, and axial failure is defined after the initiation of the axial load increase. This is due to the loss of lateral load carrying capacity of the column, which should have collapsed directly after shear failure since the column has nonductile transverse reinforcement design, but its structural stability is held by the two ductile outer columns due to the setup of the three-column frame. With collapse behavior prevented and the axial length of column C2 forced to remain under the same deformation with the outer columns by the top steel beam, column C2 thus turned into an increasing tensile force acting on the whole frame, with significantly increased values subjecting on the column when drifted to both directions. The initial axial load is applied at 2.84 %, the high varying axial load is applied at -4.61 %, and the low varying axial load is applied at -4.68 %. The varying axial loads are lower than the initial axial load due to the load redistribution phenomenon.
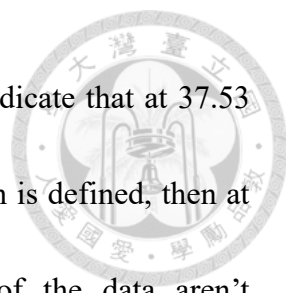
The moment-axial load response during R4 is plotted on the P-M curve of the

76

column as shown in **Figure 4-23**. The axial load during zero moment (black line) is different from the initial axial load value (orange dotted line) due to axial load redistribution during R2 and R3. The moment response has reached the nominal moment strengths at their corresponding subjected axial load values, but has not exceeded the nominal moment strength at the initially subjected axial load value, and responses below the balance point. This may indicate development of flexural strength, and should be combined with other observations to conclude.

For the stirrup strain gage readings in **Figure 4-24**, the top (C01 and D01) and bottom (C03) strain gages show lower readings while the center strain gages (C02 and D02) show relatively larger readings. This indicates that transverse reinforcements (stirrups) do transfer shear force in intermediate-short columns. In addition, the tensile strain of transverse reinforcements near the column ends are relatively small, which indicates that transverse reinforcements near column ends have lower force transfer efficiencies. Based on the observed transverse reinforcement behavior on shear-dominant intermediate-short RC columns by Li et al. (2019), the transverse reinforcements should be more effective on the center part of the column, and less effective on the column ends. The readings for this specimen show shear-dominant behavior.

Based on the observations of strain gage readings, crack pattern developments, and overall hysteresis behaviors, column C2 is concluded to be dominated by shear behavior,

and thus shear failure is defined for column C2.
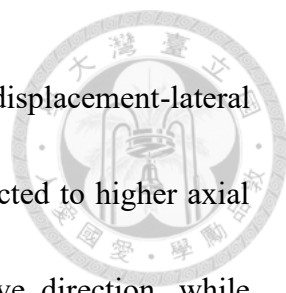
Column C3

Column C3 is located on the south side of frame T1. The crack patterns at different stages of the column are shown in **Figure 4-25**. The lateral displacement and base shear time history responses are shown in **Figure 4-26** and **Figure 4-27**. The hysteresis responses are shown in **Figure 4-28**, with positive axial loads indicating compression, while the stirrup strain gage readings are shown in **Figure 4-32**. The failure sequence of the column is shown in **Table 4-10**. The actual applied initial axial load is 167 kN in compression.

The crack pattern at the initial stage for column C3 before the input of ground motions is shown in **Figure 4-25**. Due to the application of the top steel beam onto the top foundation of column C3 through prestress, several flexural cracks have been induced throughout the column body, therefore, it can be expected that the initial stiffness of the column may be softened.

Figure 4-26 and **Figure 4-27** show the overall time history response for lateral displacement and base shear, with the failure sequence plotted as symbols on the test curves. No development of failure sequence can be seen occurring during R2 and R3.

From the hysteresis curve in **Figure 4-28**, it can be observed that column C1 is under linear behavior during R2 and R3 (grey lines).

78

The axial load-lateral displacement plot and vertical displacement-lateral displacement plot in **Figure 4-28** indicates that the column is subjected to higher axial load and shortened axial deformation when drifted to the positive direction, while subjecting to lower axial load and lengthened axial deformation when drifted to the negative direction. This varying axial load phenomenon is due to the overturning moment of the overall frame acting on the column member.

For R4, which has an input PGA of 1g, **Figure 4-25** shows the crack patterns of the column at the points of maximum strength development in both directions. Due to initial cracking on the column body, not much flexural cracks have formed when the column reaches maximum strength, while shear cracks have formed on the plastic hinge section on the top of the column.

The time history responses in **Figure 4-26** and **Figure 4-27** indicate that at 24.155 second through R4, longitudinal reinforcement yielding (blue square symbol) is observed in the negative direction, then at 24.29 second in the positive direction. At 24.495 second, the maximum strength (blue triangular symbol) in the negative direction is developed, then at 25.105 second in the positive direction.
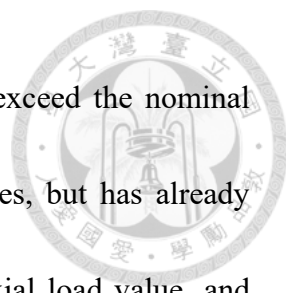
The hysteresis curve in **Figure 4-28** shows that the column longitudinal reinforcements yield (blue square symbol) at a strength value of 67.29 kN in the negative direction and 92.99 kN in the positive direction, while significant stiffness softening can

79

be observed through the curve due to reinforcement yielding. The column then develops

its maximum strength (blue triangular symbol) in the negative direction with a value of

127.21 kN under lower axial load of 407.39 kN in compression, and in the positive

direction with a value of 135.21 kN under higher axial load of 607.69 kN in compression.

As yielding of the longitudinal reinforcements are indicated by the strain gage readings,

the lateral strength of the column develops exceeding the value of flexural strength V_{mn}

(orange dotted lines in the figure), thus it can be concluded that the strength development
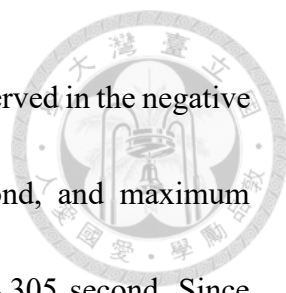
behavior is flexure-dominated.

The axial load-lateral displacement plot and vertical displacement-lateral

displacement plot in **Figure 4-28** indicates the phenomenon of varying axial load. The

axial load response shows that during R4, a residual drift to the positive direction induces

a gravity load redistribution phenomenon, leading to the axial load on column C3 to

increase by a large value, but still responses under varying axial load phenomenon. The

initial axial load is applied at 8.94 %, the high varying axial load is applied at 32.52 %,

and the low varying axial load is applied at 21.80 %. The low varying axial load is higher

than the initial axial load due to the load redistribution phenomenon.

The moment-axial load response during R4 is plotted on the P-M curve of the

column as shown in **Figure 4-29**. The axial load during zero moment (black line) is

different from the initial axial load value (orange dotted line) due to axial load

80

redistribution during R2 and R3. The moment response does not exceed the nominal moment strengths at their corresponding subjected axial load values, but has already exceeded the nominal moment strength at the initially subjected axial load value, and responses below the balance point. This may be due to that the significantly increased axial load through axial load redistribution is not shown to be able to fully enhance the flexural strength of the column up to its ideal value. To sum up, the moment-axial load behavior of the column indicates the development of flexural strength.

For R6, which has an input PGA of 800gal, **Figure 4-25** shows the crack pattern of the column at the point before collapse. During R6, the ground motion continues to damage the shear crack on the plastic hinges that are formed during R4. When drifted to the positive direction (to the left of the photo), the column is subjected to higher axial load due to varying axial load, which combines with the lateral force to induce larger force acting to open the dominant shear crack on the top of the column, which induces earlier and constant degradation for the concrete materials on the shear crack. The stiffness of the column is thus softened with spalling of concrete cover and widening of the crack, as a result, sliding occurs on the dominant shear crack, which leads to the collapse of the column and induces a large lateral displacement on the overall frame.

The time history responses in **Figure 4-26** and **Figure 4-27** indicate that at 35.195 second through R6, axial failure (blue circular symbol) of the column is defined, then at

81
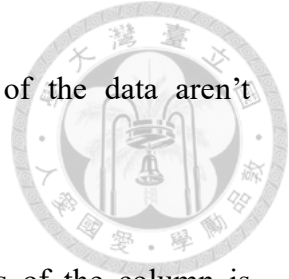
35.485 second, collapse (blue cross symbol) occurred and rest of the data aren't referenceable.

The hysteresis curve in **Figure 4-28** shows that the stiffness of the column is significantly softened during R6. At a large lateral drift of 8% drift ratio, the reloading stiffness could not reload to the yielding plateau and the strength directly degrades to zero. Axial failure (blue circular symbol) and collapse (blue cross symbol) occurred around the value where the lateral strength of the column degrades to zero.

The vertical displacement-lateral displacement plot in **Figure 4-28** indicates a severe drop in the axial displacement at the axial failure point, which represents the condition when the column loses its structural stability. The axial load-lateral displacement plot in **Figure 4-28** indicates a significant boost in the axial load after a large drift ratio up to 8%, which is measured by the transducer when the upper part of the dominant shear crack (the top part of the column and the top steel beam) slides through the crack and falls onto the bottom part of the column. The collapse point is not plotted due to the extreme value of measured axial load which exceeds the axis upper limit.

The longitudinal reinforcement readings are plotted with the lateral drifts of the column as shown in **Figure 4-30** and **Figure 4-31**. The readings indicate that all reinforcements have yielded in tension before reaching their lateral displacements at maximum strengths, and have yielded significantly when reached, which indicates

contribution from flexural behavior to the development of column strength. For the stirrup strain gage readings in **Figure 4-32**, the results show that no stirrups have yielded throughout all the runs for column C3.

The strength development is concluded to be mainly governed by flexural-shear behavior through the observation of strain gage readings, crack pattern developments, and overall hysteresis behaviors, thus flexural-shear failure is defined for column C3.

Frame T1
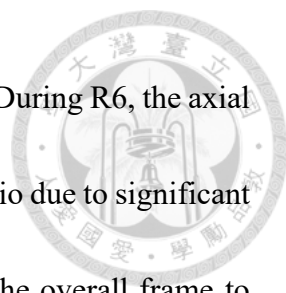
The crack patterns at different stages of the frame are shown in **Figure 4-33**. The lateral displacement, base shear, and axial load time history responses are shown in **Figure 4-34** ,**Figure 4-35**, and **Figure 4-36**, with positive axial loads indicating compression. The hysteresis curves are shown in **Figure 4-37** and the failure sequence of the frame is shown in **Table 4-10**.

The actual applied initial axial loads are provided in **Table 4-3**. Since the columns are casted separately and locked together with a steel beam which has a smooth surface to apply mass blocks, very slight difference in the casted column axial length can affect the axial load distribution. On the other hand, different applied prestress in the vertical direction on different columns to lock the top foundation with the top steel beam can also affect the axial load distribution, and may even induce unwanted residual forces. **Table 4-3** shows higher axial loads for the outer columns and much lower value for the center

83

one. It is inferred that this phenomenon is induced by the above-mentioned conditions.

The overall crack patterns at the end of each run are shown in **Figure 4-33**. From the initial condition to R3, several flexural cracks can be observed on column C1 (right) and C3 (left) as mentioned previously, and no failure can be observed. At the end of R4, more flexural cracks and some shear cracks have formed on the column body and on the plastic hinge regions. The concrete on the lower part of column C2 (center) has lost its integrity with severe cover concrete spalling. At the end of R6, sliding of the dominant shear cracks on the bottom plastic hinge section occurs for column C1, and on the top plastic hinge section for column C3, which leads to an overall collapse of the frame to the left direction in the figure. The longitudinal reinforcements on the already-damaged column C2 buckle with the collapse of the frame.

From the hysteresis curve in **Figure 4-37**, it can be observed that frame T1 is under linear behavior during R2 and R3 (grey lines). During R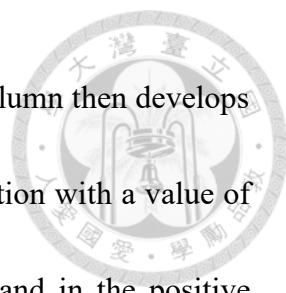4, column C2 (green triangular symbols) governs the maximum strength development for the frame at both directions for smaller drift ratios. With larger drift ratios, it is column C1 (red triangular symbols) and C3 (blue triangular symbols), which has better ductility, that contributes to the maximum strength developments. The responses show that for a frame which has columns dominated by different failure patterns, it would be the brittle shear-controlled columns that governs the strength development at smaller drift ratios, and the ductile flexure-

controlled columns that contributes to behaviors at larger drift ratios. During R6, the axial

failure of column C3 (blue circular symbol) occurs first at 2% drift ratio due to significant

stiffness degradation, which induces a large lateral deformation of the overall frame to

the positive direction and leads to the axial failure of column C1 at a drift ratio exceeding

12%. Strength degradation of the overall frame can be observed from the hysteresis curve

afterwards, and the test is then terminated after the overall collapse.

The time history responses of the overall frame and the three columns are plotted

together to compare between their behaviors. Since the development of failure sequence

is mainly focused during R4 and R6 as explained in previous sections, **Figure 4-34** and

Figure 4-35 only presents the lateral displacement and base shear time history responses

during R4 and R6. **Figure 4-36** presents additional axial load response during R3 for

discussion on responses before failure development. The failure time sequence of the

frame is shown in **Table 4-10** and can be illustrated by **Figure 4-34** and **Figure 4-35**.

Figure 4-34 shows that during R4, column C2 (green line) develops maximum

strength (green triangular symbols) first in both directions at lower drift ratios and axial

failure (green circular symbol) follows, then for column C1 (red triangular symbols) and

C3 (blue triangular symbols) together in the negative direction first and positive direction

later at larger drift ratios. During R6, it is the axial failure of column C3 (blue circular

symbol) that leads to a large lateral deformation to the positive direction, which stops

after reaching collapse point (blue cross symbol). With column C1 not being able to withstand the large lateral deformation, axial failure (red circular symbol) occurs first and collapse (red cross symbol) follows. The results are then shown in dotted lines to indicate un-referenceable data after collapse of the frame.

Figure 4-35 shows that before 24 second, since column C2 (green line) has higher longitudinal reinforcement ratio and a more shear-dominated behavior, the higher stiffness of the center column takes up more of the lateral force generated by the input ground motion on the top mass blocks, with the two outer columns (red and blue lines) subjecting to lesser force. Column C2 then develops maximum strength (green triangular symbols) in both directions and shear failure occurs with strength degradation down to zero value. The generated earthquake force is redistributed to the two outer columns as a trend of increasing lateral force can be observed after the shear failure of column C2. During R6, column C3 (blue line) showed a limited strength development behavior in the positive direction due to stiffness degradation as explained previously, while most of the lateral force is taken by column C1 (red line). Axial failure (blue circular symbol) and collapse (blue cross symbol) of column C3 occurs when the column could not contribute to lateral load carrying capacity anymore in the positive direction. Strength degradation of column C1 leads to axial failure (red circular symbol) and collapse (red cross symbol) after the column is left alone to sustain all of the gravity and lateral loads. The results are

86

then shown in dotted lines to indicate un-referenceable data after collapse of the frame.
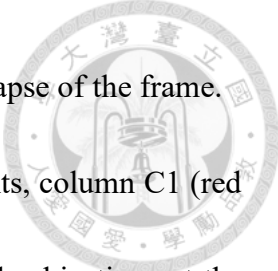
Figure 4-36 shows that during R3, without failure developments, column C1 (red lines) and C3 (blue lines) are able to response in opposite axial load subjections at the same time, with one under higher axial load and lower for another due to the effect of varying axial loads. This varying axial load is induced by overturning moments of the overall frame. When subjected to ground motions, lateral force is induced on the mass blocks on the top of the frame, and this lateral force responses as both base shear and moments on the bottom base of the frame. This moment is defined as the overturning moment. On the compression side of the moment, the compressive force adds up with the initial axial load of the column to result in an increase in the subjected axial load on the column section. On the tension side of the moment, the tensile force subjects the initial axial load of the column to result in a decrease in the subjected axial load. This overall behavior is defined as the varying axial load. The axial load response for column C2 (green lines) remains constant with a slight decrease in value down to zero. This is due to the formation and enlargement of the flexural cracks on the two outer columns, which increases their axial lengths. With longer axial lengths, the outer columns are prone to take up more gravity loads, decreasing the gravity load carried by the center column. The axial response of the overall frame (black lines) remains constant since the mass blocks that are applied on the top of the frame remain unchanged. After 24 second into R4, the

87

shear failure (green triangular symbols) and axial failure (green circular symbol) of

column C2 occurs, which should have induced axial shortening and collapse behavior.

The setup of the specimen prevents collapse of the center column, but the relative axial

deformation between the center and outer columns on opposite directions induces a large

tensile force on column C2, which can be observed in the significant drop in axial load to

the tensile direction in the figure. The additional induced axial load is distributed evenly

to the two outer columns (blue and red lines), enlarging their subjected axial load by two

times compared with the initial axial load value. Varying axial load phenomenon can still

be observed after the axial load redistribution, with column C1 subjecting to higher axial

load during first maximum strength development, and column C3 under the same

condition during second maximum strength development. During R6, the collapse of

column C3 (blue cross symbol) occurs first with the top section of the dominant shear

crack slides through and falls onto the bottom section, which leads to a boost in the

measured axial load. The collapse of column C1 (red cross symbol) occurs with the same

phenomenon. The results are then shown in dotted lines to indicate un-referenceable data

after collapse of the frame.

4.3.3 Behavior of Test 2

As shown in **Table 4-7**, there are a total of two runs of ground motions subjected on

Frame T2. R2 has an input PGA of 500 gal to simulate linear behaviors of structures under small-to-medium earthquakes. R4 has an input PGA of 1g to simulate strength development and collapse behaviors of structures under large earthquakes. Although the frame does not collapse after R4, the lateral strength of column C3 has already degraded significantly, as a result, the test is then terminated.

Column C1

Column C1 is located on the north side of frame T2. The crack patterns at different stages of the column are shown in **Figure 4-38**. The lateral displacement and base shear time history responses are shown in **Figure 4-39** and **Figure 4-40**. The hysteresis responses are shown in **Figure 4-41**, with positive axial loads indicating compression, while the stirrup strain gage readings are shown in **Figure 4-43**. The failure sequence of the column is shown in **Table 4-11**. The actual applied initial axial load is 177 kN in compression.

The crack pattern at the end of R2 is shown in **Figure 4-38**. Flexural cracks have formed on the left side of the column body during R2, and are marked as red lines.

Figure 4-39 and **Figure 4-40** show the overall time history response for lateral displacement and base shear, with the failure sequence plotted as symbols on the test curves. No development of failure sequence occurs during R2.

From the hysteresis curve in **Figure 4-41**, it can be observed that column C1 is under

89

linear behavior during R2 (grey lines).

The axial load-lateral displacement plot and vertical displacement-lateral displacement plot in **Figure 4-41** indicate that that the column is subjected to higher axial load and slight shortened axial deformation when drifted to the negative direction, while subjecting to lower axial load and lengthened axial deformation when drifted to the positive direction. This varying axial load phenomenon is due to the overturning moment of the overall frame acting on the column member.
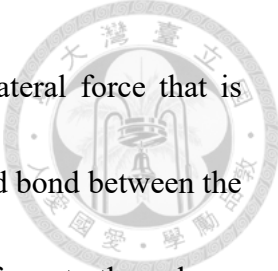
For R4, which has an input PGA of 1g, **Figure 4-38** shows the crack patterns of the column at the points of maximum strength development in the positive direction and at the end of R4. A significant shear crack appears on the upper part of the column when reaching maximum strength in the positive direction. Provided with sufficient shear strength and ductility due to ductile transverse reinforcement design and 135-degree hooks, the column did not collapse after R4. Dominant shear cracks indicating force transmission in both directions can be observed on the top and bottom body of the column through the photo at the end of the run.

The time history responses in **Figure 4-39** and **Figure 4-40** indicate that at 24.46 and 24.51 second through R4, longitudinal reinforcement yielding (red square symbol) and maximum strength development (red triangular symbol) is observed in the negative direction, then yielding and maximum strength development at 35.21 and 35.22 second

90
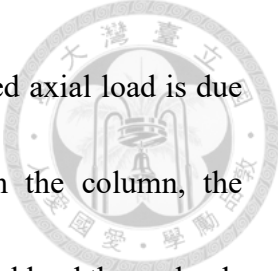
respectively in the positive direction. It is originally expected for the column to develop

its maximum strengths around 25 second when the ground motion reaches maximum

acceleration, due to slip, it is until 35 second that the maximum strength is reached in the

positive direction. The base shear response shows oscillations under high frequency at

larger base shear values, which is also due to slip. Originally, when the bond is fixed, the

base shear is able to develop. Up to a point when slip occurs, the base shear suddenly

unloads and the measured value decreases. When the slip reaches another fixed condition,

the base shear is then able to develop again. Repeating occurrence of the slip situation

causes the oscillation in the measured base shear values, while the phenomenon can also

be observed in the lateral displacement response.

The hysteresis curve in **Figure 4-41** shows that the column longitudinal

reinforcements yield (red square symbol) at a strength value of 182.39 kN in the negative

direction and 176.28 kN in the positive direction, while significant stiffness softening can

be observed through the curve due to reinforcement yielding. The column then develops

its maximum strength (red triangular symbol) in the negative direction with a value of

225.85 kN under axial load of 371.36 kN in compression, and in the positive direction

with a value of 187.87 kN under axial load of 186.63 kN in compression. The hysteresis

curve doesn't show much nonlinear behavior except for the slight degraded reloading

stiffness in the positive direction due to limited lateral deformation. This is due to slip

91

between the column top foundation and the top steel beam. The lateral force that is induced from the ground motion on the top mass blocks requires fixed bond between the column top foundation and the top steel beam to transfer the lateral force to the column body. Insufficient prestress applied between the foundation and steel beam of this specimen leads to slip on the interface whenever the transferred lateral load exceeds the interface frictional strength. This indicates that whenever the column is developing its strength with increasing lateral deformation, slip would occur on the interface, which limits the lateral deformation and strength development of the column, leading to undeveloped nonlinear behavior. The problem will be further discussed and quantified later in the overall frame T2 section. Although yielding of the longitudinal reinforcements are indicated by the strain gage readings, the lateral strength of the column experiences strength degradation before developing up to the value of flexural strength V_{mn} (orange dotted lines in the figure), thus it can be concluded that the strength development behavior isn't flexure-dominated.

The axial load-lateral displacement plot and vertical displacement-lateral displacement plot in **Figure 4-41** indicates the phenomenon of varying axial load. The axial load response shows that during R4, the measured axial load oscillates severely within a small change in drift ratio. This is due to slip between the column top foundation and the top steel beam. The measured axial load suddenly unloads when the bond between

92

the top foundation and the steel beam slips through. Since the induced axial load is due to overturning moment, without lateral force transferring through the column, the measured axial load would return to its initial value. The measured axial load then reloads again when the slip reaches another fixed point and the overturning moment re-induces the varying axial load. Although the measured values are interfered by the slip situation, the overall trend still shows varying axial load phenomenon. The initial axial load is applied at 9.47 %, the high varying axial load is applied at 19.87 %, and the low varying axial load is applied at 9.99 %.

The moment-axial load response during R4 is plotted on the P-M curve of the column as shown in **Figure 4-42**. The moment response has not exceeded the nominal moment strength at the varying axial load and the initially subjected axial load value, and responses below the balance point. This indicates that the flexural strength has not been developed fully.

For the stirrup strain gage readings in **Figure 4-43**, the results indicate that the stirrups are mostly undeformed before strength development, as shear cracks open with larger drift ratios, the measured strain values start to increase with increasing contribution to the lateral strength, but no yielding has been observed. Based on the observed transverse reinforcement behavior on shear-dominant intermediate-short RC columns by Li et al. (2019), the transverse reinforcements should be more effective on the center part

of the column, and less effective on the column ends. The readings for this specimen do not show significant difference between the ends and center stirrups, which may be due to severe slip that leads to the center stirrups not being able to develop larger strains. The readings still show transferring of shear force in the specimen.

Based on the observations of strain gage readings, crack pattern developments, and overall hysteresis behaviors, column C1 is concluded to be dominated by shear behavior, and thus shear failure is defined for column C1.

Column C3

Column C3 is located on the south side of frame T2. The crack patterns at different stages of the column are shown in **Figure 4-44**. The lateral displacement and base shear time history responses are shown in **Figure 4-45** and **Figure 4-46**. The hysteresis responses are shown in **Figure 4-47**, with positive axial loads indicating compression, while the stirrup strain gage readings are shown in **Figure 4-49**. The failure sequence of the column is shown in **Table 4-11**. The actual applied initial axial load is 178 kN in compression.

The crack pattern at the end of R2 is shown in **Figure 4-44**. Shear and Flexural-shear cracks have formed initiating on the left side to the center of the column body during R2, and are marked as red lines.

Figure 4-45 and **Figure 4-46** show the overall time history response for lateral

94

displacement and base shear, with the failure sequence plotted as symbols on the test curves. No development of failure sequence occurs during R2.
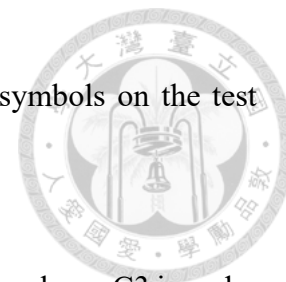
From the hysteresis curve in **Figure 4-47**, it can be observed that column C3 is under linear behavior during R2 (grey lines).

The axial load-lateral displacement plot and vertical displacement-lateral displacement plot in **Figure 4-47** indicate that that the column is subjected to higher axial load and slight shortened axial deformation when drifted to the positive direction, while subjecting to lower axial load and lengthened axial deformation when drifted to the negative direction. This varying axial load phenomenon is due to the overturning moment of the overall frame acting on the column member.
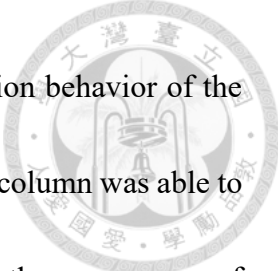
For R4, which has an input PGA of 1g, **Figure 4-44** shows the crack patterns of the column at the points of maximum strength development in the positive direction and at the end of R4. No additional shear cracks appear on the column body when reaching maximum strength in the positive direction. Provided with sufficient shear strength and ductility due to ductile transverse reinforcement design and 135-degree hooks, the column did not collapse but is severely damaged after R4. Although large amounts of shear cracks have formed, it can still be observed that dominant shear cracks indicating force transmission in both directions appear on the top and bottom body of the column. With several shear cracks passing through the center part of the column, the concrete loses its

95

integrity and the cover spalls. Slight expansion on the center part of the column can be observed, which might indicate yielding and plastic deformation of transverse reinforcements.
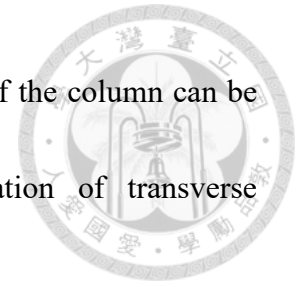
The time history responses in **Figure 4-45** and **Figure 4-46** indicate that at 24.265 and 24.295 second through R4, longitudinal reinforcement yielding (blue square symbol) and maximum strength development (blue triangular symbol) is observed in the positive direction, then yielding and maximum strength development at 24.44 and 24.445 second respectively in the negative direction. With better bond on the top interface, the column develops maximum strength after 24 second in both directions, which corresponds with the time of larger ground accelerations. The base shear response shows minor oscillations under high frequency at larger base shear values, which is also due to slip. The phenomenon can also be observed in the lateral displacement response.

The hysteresis curve in **Figure 4-47** shows that the column longitudinal reinforcements yield (blue square symbol) at a strength value of 186.35 kN in the positive direction and 178.87 kN in the negative direction, while significant stiffness softening can be observed through the curve due to reinforcement yielding. The column then develops its maximum strength (blue triangular symbol) in the positive direction with a value of 211.21 kN under axial load of 210.98 kN in compression, and in the negative direction with a value of 185.28 kN under axial load of 166.64 kN in compression. The

96

hysteresis curve shows complete strength development and degradation behavior of the column in both directions. Due to ductile reinforcement detailing, the column was able to sustain larger lateral drifts under post-strength conditions, without the occurrence of collapse. Slip still exists due to insufficient prestress between the top foundation of the column and top steel beam for this column, but with higher prestress and better bond on the interface compared with column C1, column C3 is able to deform with the top steel beam more consistently and develop larger lateral deformations. The problem will be further discussed and quantified later in the overall frame T2 section. Although yielding of the longitudinal reinforcements are indicated by the strain gage readings, the lateral strength of the column experiences strength degradation before developing up to the value of flexural strength V_{mn} (orange dotted lines in the figure), thus it can be concluded that the strength development behavior isn't flexure-dominated.

The axial load-lateral displacement plot and vertical displacement-lateral displacement plot in **Figure 4-47** indicates the phenomenon of varying axial load. The axial load response shows that during R4, the measured axial load oscillates severely within a small change in drift ratio. This is due to slip between the column top foundation and the top steel beam as explained in the section of column C1. Although the measured values are interfered by the slip situation, the overall trend still shows varying axial load phenomenon. The initial axial load is applied at 9.53 %, the high varying axial load is

97

applied at 11.92 %, and the low varying axial load is applied at 8.92 %.

The moment-axial load response during R4 is plotted on the P-M curve of the column as shown in **Figure 4-48**. The moment response has not exceeded the nominal moment strength at the varying axial load and the initially subjected axial load value, and responses below the balance point. This indicates that the flexural strength has not been developed fully.

For the stirrup strain gage readings in **Figure 4-49**, the results indicate that the stirrups are mostly undeformed before strength development, as shear cracks open with larger drift ratios, the measured strain values start to increase with increasing contribution to the lateral strength. Based on the observed transverse reinforcement behavior on shear-dominant intermediate-short RC columns by Li et al. (2019), the transverse reinforcements should be more effective on the center part of the column, and less effective on the column ends. The strain gage readings for this specimen corresponds well with the shear transfer mechanism, since less slip occurs for the column, yielding of the center stirrups (C02 and D02) can be observed while the end stirrups show relatively lesser effective readings. The readings for this specimen show shear-dominant behavior.

Based on the observations of strain gage readings, crack pattern developments, and overall hysteresis behaviors, column C3 is concluded to be dominated by shear behavior, and thus shear failure is defined for column C3.

Frame T2

The lateral displacement, base shear, and axial load time history responses are shown in **Figure 4-50**, **Figure 4-54**, and **Figure 4-55**, with positive axial loads indicating compression. The slip behavior is explained through **Figure 4-51** to **Figure 4-53**. The failure sequence of the frame is shown in **Table 4-11**.

As explained previously, the distributed axial load from mass blocks is affected by the axial length and applied prestress of individual columns. **Table 4-4** provides the actual applied initial axial loads for columns C1 and C3. With even axial lengths and applied prestress, the two columns are subjected to even axial loads.
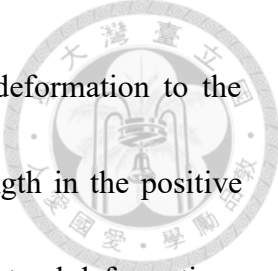
With slip problems occurring for columns C1 and C3, they behave with different lateral deformations at the same time period. As a result, it is unable to plot the overall hysteresis curve of the frame. **Figure 4-50** shows the comparison on lateral deformations of the frame (black line), i.e. the top steel beam, column C1 (red line), and column C3 (blue line). It can be observed that after 24 second, with increasing lateral deformation, the three members do not deform together consistently. The frame is observed to have a much larger deformation, with column C3 developing a smaller value, and column C1 having the least lateral deformation. This corresponds with the behavior of each columns introduced previously. When slip occurs, the top steel beam slides through the top foundations of the two columns, leading to a larger deformation. With the least prestress

99

applied, column C1 is not able to deform with the top steel beam consistently since slip occurs continuously, while column C3 is at slight better condition with larger deformation induced. The green lines in **Figure 4-51** and **Figure 4-52** indicate the quantified slip values for columns C1 and C3. Whenever there is a change in magnitude on the green lines, slip occurs, and the changed magnitude indicates the slip deformation. **Figure 4-53** compares the slip curves for the two columns. It can be observed that before 30 second, slip on the two columns are about the same, with column C1 (red line) having slight larger values. After 30 second when strength degradation initiates for column C3, it requires lesser interface strength to transfer the lateral force from the top steel beam to the column body. Therefore, slip is slightly eased on column C3, while it is column C1 that still possesses severe slip phenomenon.

The time history responses of the overall frame and the two columns are plotted together to compare between their behaviors. Since the development of failure sequence is mainly focused in R4 as explained in previous sections, the figures below only present the responses during R4.

Figure 4-50 shows that during R4, column C3 (blue line) develops maximum strength (blue triangular symbols) first in the positive direction and follows up in the negative direction during the next drift. The maximum strength for column C1 (red triangular symbol) is immediately reached afterwards in the negative direction. It is when

100

the strength of column C3 degrades and develops a large lateral deformation to the positive direction that column C1 then develops its maximum strength in the positive direction after 35 second. Without collapse of the overall frame, the lateral deformations of the columns are able to return back to smaller values.

Figure 4-54 shows that the two columns take up the lateral force evenly before the occurrence of slip. After maximum strength development of column C3 (blue triangular symbols) around 24 second, its lateral strength starts to degrade. After 34 second, the column could not sustain large lateral forces and column C1 finally develops its maximum strength in the positive direction (red triangular symbol) to contribute to the lateral load carrying capacity of the overall frame.

Figure 4-55 shows that during R2, without failure developments and slip phenomenon, column C1 (red lines) and C3 (blue lines) are able to response in opposite axial load subjections, with one in higher axial load and lower for another due to the effect of varying axial loads from overturning moments. The axial response of the overall frame remains constant since the mass blocks that are applied on the top of the frame remain unchanged. After 24 second into R4, the measured axial load values start to oscillate at high frequencies due to the occurrence of slip as explained previously in this section, and it even affects the measured axial load values for the overall frame. Distinct varying axial load phenomenon can still be observed within smaller drifts where slip does not occur,

101

and the maximum strength development of the two columns still behaves with one direction under higher axial load and lower for another.

4.3.4 Behavior of Test 3

As shown in **Table 4-7**, there are a total of two runs of ground motions subjected on Frame T3. R2 has an input PGA of 500 gal to simulate linear behaviors of structures under small-to-medium earthquakes. R4 has an input PGA of 1g to simulate strength development and collapse behaviors of structures under large earthquakes. The frame collapses after R4, and the test is then terminated.

Column C1

Column C1 is located on the north side of frame T3. The crack patterns at different stages of the column are shown in **Figure 4-56**. The lateral displacement and base shear time history responses are shown in **Figure 4-57** and **Figure 4-58**. The hysteresis responses are shown in **Figure 4-59**, with positive axial loads indicating compression, while the stirrup strain gage readings are shown in **Figure 4-61**. The failure sequence of the column is shown in **Table 4-12**. The actual applied initial axial load is 170 kN in compression.

The crack pattern at the initial stage is shown in **Figure 4-56**. Shear cracks have formed on the top of the column, which may be induced by internal forces due to applied

102

prestress to lock the top foundation with the top steel beam. At the end of R2, the shear cracks are slightly extended, and are marked as red lines. A short flexural crack is also formed during the run.
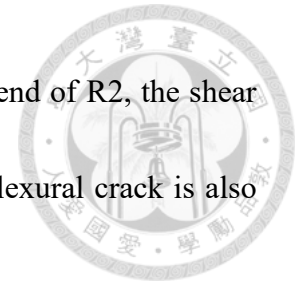
Figure 4-57 and **Figure 4-58** show the overall time history response for lateral displacement and base shear, with the failure sequence plotted as symbols on the test curves. No development of failure sequence occurs during R2.

From the hysteresis curve in **Figure 4-59**, it can be observed that column C1 is under linear behavior during R2 (grey lines).

The axial load-lateral displacement plot in **Figure 4-59** indicates that the column is subjected to higher axial load when drifted to the negative direction, while subjecting to lower axial load when drifted to the positive direction. This varying axial load phenomenon is due to the overturning moment of the overall frame acting on the column member. Due to the high frequency noise on the measured vertical displacement responses, vertical displacement-lateral displacement plot in **Figure 4-59** could not show referenceable responses.

For R4, which has an input PGA of 1g, **Figure 4-56** shows the crack patterns of the column at the points of maximum strength development in the positive direction and at the point before collapse. In addition to the initially-formed cracks, shear cracks have formed with an inclination angle around 45 degrees on the top and bottom plastic hinge

regions of the column during maximum strength development in the positive direction. The crack pattern of the column at the time before collapse is also shown in the figure. After the formation of a dominant shear crack in the negative direction, the crack couldn't sustain the lateral and gravity force, thus sliding on the crack and collapse of the column occurs afterwards. It can be observed that the crack formations for the column in both directions of the drift are not identical.

Based on the shear strength calculation procedure in **Figure 2-3**, it can be concluded that when insufficient transverse reinforcements are provided, the shear strength of a column is governed by its shear tension strength, indicating that the concrete strut does not develop to its maximum value, and the transverse reinforcements could not provide sufficient shear strength, thus failure occurs on the reinforcements. The strut inclination angle during shear tension failure will reach its maximum value at 63.4 degrees. When sufficient transverse reinforcements are provided, the shear strength of a column is governed by its shear compression strength, indicating that the concrete strut has developed to its maximum value, and the transverse reinforcements over-provide shear strength, thus failure occurs on the concrete strut. The strut inclination angle during shear compression failure will reach its minimum value at 45 degrees. The change from shear tension to shear compression failure indicates that shear strength of the column is enhanced, and the strut inclination angle is lowered.

104
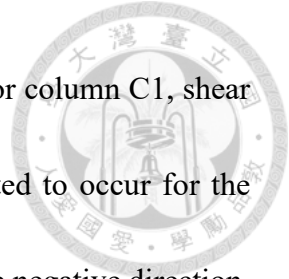
With nonductile reinforcement detailing and 90-degree hooks for column C1, shear tension failure and 63.4 degrees of strut inclination angle is expected to occur for the column, which corresponds to the behavior on the crack pattern in the negative direction. The crack pattern in the positive direction indicates two 45-degree inclined struts on the column ends, indicating enhanced shear strength and possible shear compression failure. It is inferred that the prestress in the top steel beam is applied unevenly, leaving a residual internal force in the column, enhancing the shear strength development, and changing the strut inclination angle in the positive direction. After entering nonlinear behavior in the positive direction, the residual force is then dissipated and the column returns to its original-designed shear behavior. The column then develops a significant shear crack with much larger inclination angle and collapses in the negative direction. The above discussion is yet to be verified through the following test results.
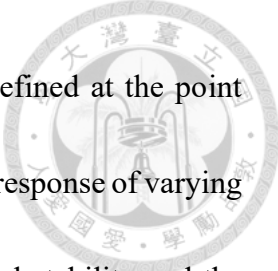
The time history responses in **Figure 4-57** and **Figure 4-58** indicate that at 24.28 and 24.295 second through R4, longitudinal reinforcement yielding (red square symbol) and maximum strength development (red triangular symbol) is observed in the positive direction, then maximum strength development and axial failure at 24.43 second in the negative direction. Collapse is then defined at 24.995 second as the column drifts to the negative direction. The lateral displacement response shows that after the point of maximum strength development, the lateral deformation of the column is still drifting to

105

the corresponding direction, which indicates the occurrence of strength degradation behavior in both directions.

The hysteresis curve in **Figure 4-59** shows that the column longitudinal reinforcements yield (red square symbol) at a strength value of 203.88 kN in the positive direction, while significant stiffness softening can be observed through the curve due to reinforcement yielding. The column then develops its maximum strength (red triangular symbol) in the positive direction with a value of 204.14 kN under axial load of 105.69 kN in compression, and in the negative direction with a value of 156.96 kN under axial load of 276.19 kN in compression. The longitudinal reinforcements yielded in the positive direction and develops a larger drift ratio at strength point but remain unyielded in the negative direction with a smaller drift ratio. The column then directly collapses to the negative direction after developing its maximum strength without any post-strength behavior. Although yielding of the longitudinal reinforcements are indicated by the strain gage readings, the lateral strength of the column experiences strength degradation before developing up to the value of flexural strength V_{mn} (orange dotted lines in the figure), thus it can be concluded that the strength development behavior isn't flexure-dominated.
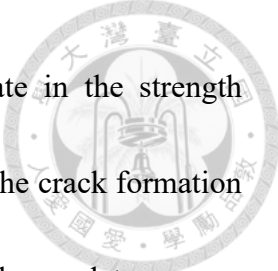
The axial load-lateral displacement plot in **Figure 4-59** indicates the phenomenon of varying axial load. The axial load response shows that during R4, the axial load response still demonstrates varying axial load behavior after reaching maximum strength

in both directions. The axial failure point (red circular symbol) is defined at the point when the axial load reaches maximum value, which indicates extreme response of varying axial load. After the axial failure point, the column loses its structural stability and the axial load unloads to its initial value since the phenomenon of varying axial load has been released. The initial axial load is applied at 9.10 %, the high varying axial load is applied at 14.78 %, and the low varying axial load is applied at 5.66 %.

The moment-axial load response during R4 is plotted on the P-M curve of the column as shown in **Figure 4-60**. The moment response has not exceeded the nominal moment strength at the varying axial load and the initially subjected axial load value, and responses below the balance point. This indicates that the flexural strength has not been developed fully.

For the stirrup strain gage readings in **Figure 4-61**, the results indicate that the stirrups are mostly undeformed before strength development. When reaching maximum strength in the positive direction, the center strain gages (C02 and D02) show ineffective readings, while the top and bottom strain gages (D01, C03, and D03) show increase in the measured values even up to yielding point (D03). When reaching maximum strength in the negative direction, the center and top strain gages (C01, D01, and C02) show increased readings without yielding, while the bottom strain gages (C03 and D03) show relatively ineffective readings. This shows that the strength development in both

107

directions is uneven since stirrups on different locations participate in the strength development respectively. The strain gage readings correspond with the crack formation on the column in **Figure 4-56** in both directions. Based on the observed transverse reinforcement behavior on shear-dominant intermediate-short RC columns by Li et al. (2019), the transverse reinforcements should be more effective on the center part of the column, and less effective on the column ends. The strain gage readings in the negative direction corresponds well with the shear transfer mechanism overall. The increased readings on the top stirrups may be caused by opening and crossing of the dominant shear crack. The strain gage readings in the positive direction vary from the shear transfer mechanism, indicating unexpected shear behavior. The difference in strain gage readings may explain the inferred phenomenon on residual internal forces due to applied prestress, as discussed in the crack pattern section. Initial readings of axial loads and base shears are required to quantify the residual force due to applied prestress. Since all the data are reset to zero at the start of each run, this phenomenon is unable to be verified. The concept and phenomenon should be kept in mind when utilizing the test data for further research.

Based on the observations of strain gage readings, crack pattern developments, and overall hysteresis behaviors, column C1 is concluded to be dominated by brittle-shear behavior, and thus shear failure is defined for column C1.

Column C3

Column C3 is located on the south side of frame T3. The crack patterns at different stages of the column are shown in **Figure 4-62**. The lateral displacement and base shear time history responses are shown in **Figure 4-63** and **Figure 4-64**. The hysteresis responses are shown in **Figure 4-65**, with positive axial loads indicating compression, while the stirrup strain gage readings are shown in **Figure 4-67**. The failure sequence of the column is shown in **Table 4-12**. The actual applied initial axial load is 191 kN in compression.
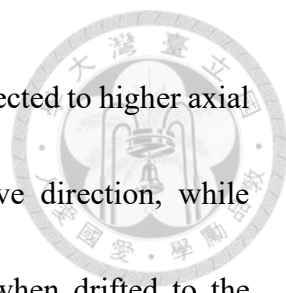
The crack pattern at the initial stage and at the end of R2 is shown in **Figure 4-62**. No cracks have formed on the column body after R2.

Figure 4-63 and **Figure 4-64** show the overall time history response for lateral displacement and base shear, with the failure sequence plotted as symbols on the test curves. The maximum strength is reached for the column at 24.425 second in the negative direction during R2.

From the hysteresis curve in **Figure 4-65**, it can be observed that column C3 is under linear behavior during R2 (grey lines). The column develops its maximum strength (blue triangular symbol) in the negative direction during R2 with a value of 122.81 kN under axial load of 110.97 kN in compression.

The axial load-lateral displacement plot and vertical displacement-lateral

109

displacement plot in **Figure 4-65** indicate that that the column is subjected to higher axial load and shortened axial deformation when drifted to the positive direction, while subjecting to lower axial load and lengthened axial deformation when drifted to the negative direction. This varying axial load phenomenon is due to the overturning moment of the overall frame acting on the column member.

For R4, which has an input PGA of 1g, **Figure 4-62** show the crack patterns of the column at the points of maximum strength development in the positive direction and at the point before collapse. A dominant shear crack formed from the top to the bottom of the column during maximum strength development in the positive direction. Another dominant shear crack formed crossing the previous crack when the column drifts to the negative direction before collapse. Sliding on the dominant shear crack leads to collapse of the column. It can be observed that the crack formations for the column in both directions of the drift are identical on behaviors and inclination angles. With nonductile reinforcement detailing and 90-degree hooks for column C1, brittle shear behavior is expected to occur for the column, which corresponds with the behavior in both directions.

The time history responses in **Figure 4-63** and **Figure 4-64** indicate that at 24.24 second through R4, maximum strength development (blue triangular symbol) is observed in the positive direction. Axial failure is defined at 24.44 second when the column drifts to the negative direction, and collapse is then defined at 24.935 second. The lateral
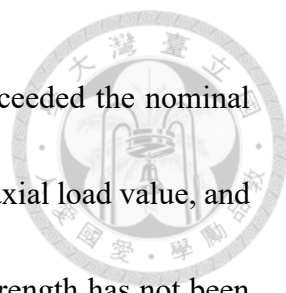
110

displacement response shows that after the point of maximum strength development, the lateral deformation of the column is still drifting to the corresponding direction, which indicates the occurrence of strength degradation behavior in the positive direction.

The hysteresis curve in **Figure 4-65** shows that the column develops its maximum strength in the positive direction with a value of 119.97 kN under axial load of 249.01 kN in compression. The column then directly collapses to the negative direction after axial failure (blue circular symbol) without any post-strength behavior.

The axial load-lateral displacement plot and vertical displacement-lateral displacement plot in **Figure 4-65** indicates the phenomenon of varying axial load. The axial load response shows that during R4, the response still demonstrates varying axial load behavior after reaching maximum strength in both directions. The axial failure point (blue circular symbol) is defined at the point when the vertical displacement reaches maximum value and the axial load reaches minimum value, which indicates extreme response of varying axial load. After the axial failure point, the column loses its structural stability and the vertical displacement drops rapidly inducing collapse behavior, while the axial load unloads to its initial value since the phenomenon of varying axial load has been released. The initial axial load is applied at 10.22 %, the high varying axial load is applied at 13.32 %, and the low varying axial load is applied at 5.94 %.

The moment-axial load response during R4 is plotted on the P-M curve of the

111

column as shown in **Figure 4-66**. The moment response has not exceeded the nominal moment strength at the varying axial load and the initially subjected axial load value, and responses below the balance point. This indicates that the flexural strength has not been developed fully.

For the stirrup strain gage readings in **Figure 4-67**, the results indicate that the stirrups are mostly undeformed before strength development. When reaching maximum strength in the positive direction, the center strain gages (C02 and D02) show increase in their measured values, and even yielded when passing the strength point (D02), while the others show ineffective readings. When reaching maximum strength in the negative direction, the center strain gages show relatively effective readings compared with the top and bottom strain gages. It is when the displacement at maximum strength is exceeded that the other strain gages start to show effective readings, which may be caused by opening and crossing of the dominant shear crack. The strain gage readings correspond with the crack formation in **Figure 4-62** as presented previously. Based on the observed transverse reinforcement behavior on shear-dominant intermediate-short RC columns by Li et al. (2019), the transverse reinforcements should be more effective on the center part of the column, and less effective on the column ends. The strain gage readings for this specimen corresponds well with the shear transfer mechanism in both directions, and this specimen shows shear-dominant behavior.

112

Based on the observations of strain gage readings, crack pattern developments, and overall hysteresis behaviors, column C3 is concluded to be dominated by brittle-shear behavior, and thus shear failure is defined for column C3.

Frame T3

The lateral displacement, base shear, and axial load time history responses are shown in **Figure 4-68**, **Figure 4-69**, and **Figure 4-70**, with positive axial loads indicating compression. The hysteresis curve is shown in **Figure 4-71** and the failure sequence of the frame is shown in **Table 4-12**.

As explained previously, the distributed axial load from mass blocks is affected by the axial length and applied prestress of individual columns. **Table 4-5** provides the actual applied initial axial loads for columns C1 and C3. With slightly different axial lengths and applied prestress, the two columns have slightly different applied axial loads.

From the hysteresis curve in **Figure 4-71**, it can be observed that frame T3 is under linear behavior during R2 (grey lines), and column C3 contributed to a maximum strength development (blue triangular symbol) in the negative direction. During R4, column C3 (blue triangular symbols) develops its maximum strength at a smaller drift ratio in the positive direction, followed by column C1 (red triangular symbol) at a larger drift ratio due to interference of flexure behavior. After strength development for column C1 (red triangular symbol) in the negative direction, axial failure (circular symbol) is defined for

113

both columns and strength degradation initiates. Brittle shear failure controls the failure behavior of the frame. The test is then terminated after the overall collapse.

The time history responses of the overall frame and the two columns are plotted together to compare between their behaviors. Since the development of failure sequence is mainly focused in R4 as explained in previous sections, the figures below only present the responses during R4.

Figure 4-68 shows that during R4, column C3 develops maximum strength (blue triangular symbols) first in the positive direction and the maximum strength for column C1 (red triangular symbol) is reached afterwards. Since the maximum strength in the negative direction has already been reached during R2 for column C3, only column C1 shows maximum strength development in the negative direction in this run. The axial failure of both columns occurs continuously. The displacement comparisons show that the two columns and the frame drifts together consistently.

Figure 4-69 shows that the two columns take up the lateral force evenly up to the point of maximum strength development in the positive direction. The base shear of column C3 suddenly drops with occurrence of shear failure (blue triangular symbols), while the base shear of column C1 continues to increase due to interference from flexure behavior. Both columns show broken strength development in the negative direction afterwards, indicating shear failure behavior. Collapse of the overall frame occurs at

114

around 25 second after a significant drop in the base shear.

Figure 4-70 shows that during R4, columns C1 (red lines) and C3 (blue lines) are able to response in opposite axial load subjections before 24 second, with one in higher axial load and lower for another due to the effect of varying axial loads from overturning moments. The axial response of the overall frame remains constant since the mass blocks that are applied on the top of the frame remain unchanged. After 24 second, maximum strength development occurs for both columns in both directions, which leads to slight oscillations during the peak points. The measured axial load for the overall frame is also affected in this time period. The varying axial load phenomenon can still be observed during the maximum strength development of the two columns, with one direction under higher axial load and lower for another.

4.3.5 Behavior of Test 4

As shown in **Table 4-7**, there are a total of two runs of ground motions subjected on Frame T4. R2 has an input PGA of 600 gal to simulate linear behaviors of structures under small-to-medium earthquakes. R4 has an input PGA of 900 gal to simulate strength development and collapse behaviors of structures under large earthquakes. The frame collapses after R4, and the test is then terminated.

Column C1

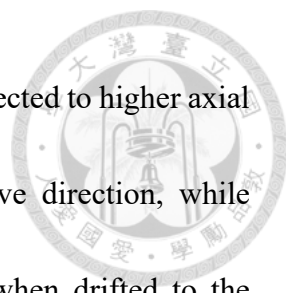Column C1 is located on the north side of frame T4. The crack patterns at different stages of the column are shown in **Figure 4-72**. The lateral displacement and base shear time history responses are shown in **Figure 4-73** and **Figure 4-74**. The hysteresis responses are shown in **Figure 4-75**, with positive axial loads indicating compression, while the stirrup strain gage readings are shown in **Figure 4-77**. The failure sequence of the column is shown in **Table 4-13**. The actual applied initial axial load is 102 kN in compression.

The crack pattern at the initial stage is shown in **Figure 4-72**. Shear cracks have formed throughout the column body, which may be induced by internal force due to applied prestress to lock the top foundation with the top steel beam. At the end of R2, more shear cracks have formed on the bottom part of the column, and are marked as blue lines.

Figure 4-73 and **Figure 4-74** show the overall time history responses for lateral displacement and base shear, with the failure sequence plotted as symbols on the test curves. No development of failure sequence occurs during R2.

From the hysteresis curve in **Figure 4-75**, it can be observed that column C3 is under linear behavior during R2 (grey lines).

The axial load-lateral displacement plot and vertical displacement-lateral

116

displacement plot in **Figure 4-75** indicate that that the column is subjected to higher axial load and shortened axial deformation when drifted to the negative direction, while subjecting to lower axial load and lengthened axial deformation when drifted to the positive direction. This varying axial load phenomenon is due to the overturning moment of the overall frame acting on the column member.

For R4, which has an input PGA of 1g, **Figure 4-72** shows the crack patterns of the column at the points of maximum strength development in the negative direction and at the point before collapse. A dominant shear crack formed from the top to the center of the column during maximum strength development in the negative direction. Sliding on the dominant shear crack leads to collapse of the column as indicated in the figure. With nonductile reinforcement detailing and 90-degree hooks for the column, brittle shear behavior is expected to occur for the column, which corresponds with the observed crack patterns.
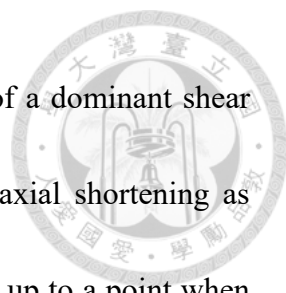
The time history responses in **Figure 4-73** and **Figure 4-74** indicate that at 24.265 and 24.27 second through R4, longitudinal reinforcement yielding (red square symbol) and maximum strength development (red triangular symbol) is observed in the positive direction, then maximum strength development occurs in the negative direction at 24.423 second. Axial failure is defined at 25.475 second after a few drifts under post-strength condition, and collapse occurs at 26.04 second as the column drifts to the negative

117

direction.

The hysteresis curve in **Figure 4-75** shows that the column longitudinal reinforcements yield (red square symbol) at a strength value of 143.88 kN in the positive direction. The column immediately develops its maximum strength (red triangular symbol) in the positive direction with a value of 145.54 kN under axial load of 24.58 kN in compression, and then in the negative direction with a value of 139.71 kN under axial load of 169.91 kN in compression. Severe strength degradation occurs but the column is able to unload and reload for a few times before reaching axial failure point at a strength value around zero. Collapse to the negative direction occurs after axial failure (red circular symbol). Although yielding of the longitudinal reinforcements are indicated by the strain gage readings, the lateral strength of the column experiences strength degradation before developing up to the value of flexural strength V_{mn} (orange dotted lines in the figure), thus it can be concluded that the strength development behavior isn't flexure-dominated.

The axial load-lateral displacement plot and vertical displacement-lateral displacement plot in **Figure 4-75** indicate the phenomenon of varying axial load. The axial load response shows that during R4, the response still demonstrates varying axial load behavior after reaching maximum strength in both directions. The varying axial load behavior is slightly interfered after severe strength degradation of the column. Since the

118

column unloads and reloads for a few times during the formation of a dominant shear crack, the drifts cause slight sliding on the crack which leads to axial shortening as observed on the vertical displacement-lateral displacement plot. It is up to a point when the shear crack could not sustain the lateral and gravity load, axial failure (red circular symbol) is then defined at the point when the column loses its structural stability and the vertical displacement drops rapidly. The measured varying axial load response after strength degradation is interfered by the axial shortenings and the results are not referenceable. The initial axial load is applied at 5.51 %, the high varying axial load is applied at 9.09 %, and the low varying axial load is applied at 1.32 %.

The moment-axial load response during R4 is plotted on the P-M curve of the column as shown in **Figure 4-76**. The moment response has not exceeded the nominal moment strength at the varying axial load and the initially subjected axial load value, and responses below the balance point. This indicates that the flexural strength has not been developed fully.

For the stirrup strain gage readings in **Figure 4-77**, the results indicate that the stirrups are mostly undeformed before strength development in both directions. It is after maximum strength point in the negative direction that the center stirrups (C02 and D02) develop larger readings. Yielding of the stirrups isn't observed. The strain gage readings correspond with the crack formation in **Figure 4-72** as presented previously. Based on

the observed transverse reinforcement behavior on shear-dominant intermediate-short RC columns by Li et al. (2019), the transverse reinforcements should be more effective on the center part of the column, and less effective on the column ends. The strain gage readings for this specimen corresponds well with the shear transfer mechanism in the negative direction, and this specimen shows shear-dominant behavior.

Based on the observations of strain gage readings, crack pattern developments, and overall hysteresis behaviors, column C1 is concluded to be dominated by brittle-shear behavior, and thus shear failure is defined for column C1.

Column C3

Column C3 is located on the south side of frame T4. The crack patterns at different stages of the column are shown in **Figure 4-78**. The lateral displacement and base shear time history responses are shown in **Figure 4-79** and **Figure 4-80**. The hysteresis responses are shown in **Figure 4-81**, with positive axial loads indicating compression, while the stirrup strain gage readings are shown in **Figure 4-83**. The failure sequence of the column is shown in **Table 4-13**. The actual applied initial axial load is 152 kN in compression.

The crack pattern at the initial stage is shown in **Figure 4-78**. Flexural-shear cracks have formed on the upper part of the column body, which may be induced by internal force due to applied prestress to lock the top foundation with the top steel beam. At the

120

end of R2, additional shear cracks have formed on the top and bottom of the column, and are marked as blue lines.

Figure 4-79 and Figure 4-80 show the overall time history responses for lateral displacement and base shear, with the failure sequence plotted as symbols on the test curves. No development of failure sequence occurs during R2.

From the hysteresis curve in Figure 4-81, it can be observed that column C3 is under linear behavior during R2 (grey lines).

The axial load-lateral displacement plot and vertical displacement-lateral displacement plot in Figure 4-81 indicate that that the column is subjected to higher axial load and shortened axial deformation when drifted to the positive direction, while subjecting to lower axial load and lengthened axial deformation when drifted to the negative direction. This varying axial load phenomenon is due to the overturning moment of the overall frame acting on the column member.

For R4, which has an input PGA of 1g, Figure 4-78 shows the crack patterns of the column at the points of maximum strength development in the negative direction and at the point before collapse. A dominant shear crack formed from the top to the center of the column during maximum strength development in the negative direction. Sliding on the dominant shear crack leads to collapse of the column as indicated in the figure. With nonductile reinforcement detailing and 90-degree hooks for column C3, brittle shear

121

behavior is expected to occur for the column, which corresponds with the observed crack patterns.
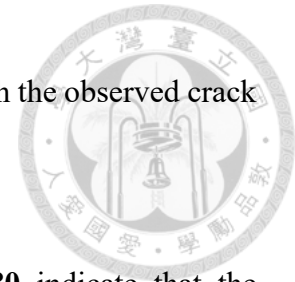
The time history responses in **Figure 4-79** and **Figure 4-80** indicate that the maximum strength development occurs in the positive direction at 24.27 second, then yielding of longitudinal reinforcements (blue square symbol) and development of maximum strength (blue triangular symbol) is observed at the same time in the negative direction at 24.435 second. Axial failure is defined at 25.49 second after a few drifts under post-strength condition, and collapse occurs at 26.095 second as the column drifts to the negative direction.

The hysteresis curve in **Figure 4-81** shows that the column develops its maximum strength in the positive direction with a value of 124.28 kN under axial load of 220.46 kN in compression. The longitudinal reinforcements then yield (blue square symbol) at a strength value of 159.46 kN in the negative direction with the column reaching its maximum strength (blue triangular symbol) in the negative direction at the same time under axial load of 59.55 kN in compression. Severe strength degradation occurs and the column is able to unload and reload for a few times before reaching axial failure point at a strength value around zero. Collapse to the negative direction occurs axial failure (blue circular symbol). Although yielding of the longitudinal reinforcements are indicated by the strain gage readings, the lateral strength of the column experiences strength

degradation before developing up to the value of flexural strength V_{mn} (orange dotted lines in the figure), thus it can be concluded that the strength development behavior isn't flexure-dominated.

The axial load-lateral displacement plot and vertical displacement-lateral displacement plot in **Figure 4-81** indicate the phenomenon of varying axial load. The axial load response shows that during R4, the response still demonstrates varying axial load behavior after reaching maximum strength in both directions. The varying axial load behavior is slightly interfered after severe strength degradation of the column. Since the column unloads and reloads for a few times during the formation of a dominant shear crack, the drifts cause slight sliding on the crack which leads to axial shortening as observed on the vertical displacement-lateral displacement plot. It is up to a point when the shear crack could not sustain the lateral and gravity load, axial failure (blue circular symbol) is then defined at the point when the column loses its structural stability and the vertical displacement drops rapidly. The measured varying axial load response after strength degradation is interfered by the axial shortenings and the results are not referenceable. The initial axial load is applied at 8.14 %, the high varying axial load is applied at 11.80 %, and the low varying axial load is applied at 3.19 %.

The moment-axial load response during R4 is plotted on the P-M curve of the column as shown in **Figure 4-82**. The moment response has not exceeded the nominal

123

moment strength at the varying axial load and the initially subjected axial load value, and responses below the balance point. This indicates that the flexural strength has not been developed fully.

For the stirrup strain gage readings in **Figure 4-83**, the results indicate that the stirrups are mostly undeformed before strength development in both directions. It is after maximum strength point in the negative direction that the center stirrups (C02 and D02) develop larger readings. The increased reading in strain gage D01 may be caused by opening and crossing of the dominant shear crack. Yielding of the stirrups isn't observed. The strain gage readings correspond with the crack formation in **Figure 4-78** as presented previously. Based on the observed transverse reinforcement behavior on shear-dominant intermediate-short RC columns by Li et al. (2019), the transverse reinforcements should be more effective on the center part of the column, and less effective on the column ends. The strain gage readings for this specimen corresponds well with the shear transfer mechanism in the negative direction, and this specimen shows shear-dominant behavior.

Based on the observations of strain gage readings, crack pattern developments, and overall hysteresis behaviors, column C3 is concluded to be dominated by brittle-shear behavior, and thus shear failure is defined for column C3.

Frame T4

The lateral displacement, base shear, and axial load time history responses are shown

in **Figure 4-84**, **Figure 4-85**, and **Figure 4-86**, with positive axial loads indicating compression. The hysteresis curve is shown in **Figure 4-87** and the failure sequence of the frame is shown in **Table 4-13**.

As explained previously, the distributed axial load from mass blocks is affected by the axial length and applied prestress of individual columns. **Table 4-6** provides the actual applied initial axial loads for columns C1 and C3. With unneglectable difference in axial lengths and applied prestress, the two columns have quite different applied axial loads.

From the hysteresis curve in **Figure 4-87**, it can be observed that frame T4 is under linear behavior during R2 (grey lines). During R4, both columns develop their maximum strength (triangular symbols) at the same lateral drift in the positive direction, then column C1 contributed to a maximum strength development of the frame first and followed up by column C3 in the negative direction at a larger drift ratio. After maximum strength development, axial failure (circular symbol) is defined for both columns after the strength degrades to almost zero. Brittle shear failure controls the failure behavior of the frame. The test is then terminated after the overall collapse.

The time history responses of the overall frame and the two columns are plotted together to compare between their behaviors. Since the development of failure sequence is mainly focused in R4 as explained in previous sections, the figures below only present the responses during R4.
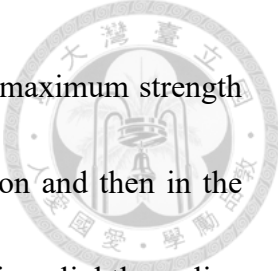
125

Figure 4-84 shows that during R4, both columns develop their maximum strength (triangular symbols) at around the same time in the positive direction and then in the negative direction, with column C1 (red triangular symbol) developing slightly earlier. The axial failure of both columns occurs at the same time. The displacement comparisons show that the two columns and the frame drifts together consistently.

Figure 4-85 shows that the two columns take up the lateral force evenly up to the point of maximum strength development in the negative direction. Both columns show broken strength development in the negative direction due to shear failure behavior. The residual strength for both columns behaves slightly differently after the initiation of strength degradation. Collapse of the overall frame occurs at around 26 second after the strength of both columns drops to zero.
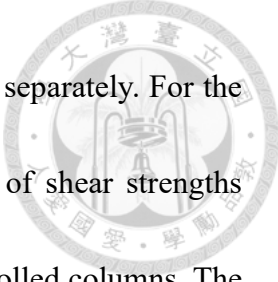
Figure 4-86 shows that during R4, columns C1 (red lines) and C3 (blue lines) are able to response in opposite axial load subjections before 24 second, with one in higher axial load and lower for another due to the effect of varying axial loads from overturning moments. The lines do not intersect each other due to the significant difference in applied initial axial loads. The axial response of the overall frame remains constant since the mass blocks that are applied on the top of the frame remain unchanged. After 24 second, maximum strength development occurs for both columns in both directions, which leads to slight oscillations during the peak points. The measured axial load for the overall frame

126

is slightly affected in this time period. The varying axial load phenomenon can still be observed during the maximum strength development of the two columns, with one direction under higher axial load and lower for another.

4.4 Discussion on Test Result

This section discusses the strength behaviors, stiffness behaviors, and collapse points of columns based on the presented shaking table test results. For strength behaviors, the flexural-dominant and shear-dominant columns are discussed separately. Axial loads have been concluded to have their effects on enhancing the lateral strengths of RC members and lowering their ductility. As introduced in **Section 4.2**, the shaking table-tested columns are subjected to initial axial loads at values of $0.1 f_c' A_g$. This initial axial load is applied on the column constantly and uniformly throughout the whole column body, thus can also be defined as the sustained axial load. **Section 4.3** presents that the columns are subjected to varying axial loads due to overturning moments on the overall frame when subjected to ground motions, inducing higher axial loads on one direction of the drift and lower on another. This varying axial load is applied on the column within a very short time period during a lateral drift, and increases from its sustained axial load to the maximum value with the increase in lateral displacement. This section discusses and compares the effect of both the sustained and the varying axial load on the development

127

of flexural and shear strengths of RC columns by shaking table tests separately. For the

shear strengths, this section provides discussions on the definition of shear strengths

based on the measure maximum lateral strength values of shear-controlled columns. The

strengths are then used for further comparison with analytical models in following

chapters. For stiffness behaviors, this section presents the stiffness time history response

of all columns and discusses the stiffness softening behavior. The test effective stiffness

is also measured to compare with analytical models in following chapters. The last part

of this section presents the lateral displacements at the collapse points of the shaking

table-tested columns.

The maximum strength developed by each column are presented in **Section 4.3**, and

it is concluded that two of the columns (T1C1, T1C3) are dominated by flexural behavior

and seven of the columns (T1C2, T2C1, T2C3, T3C1, T3C3, T4C1, T4C3) are dominated

by shear behavior. For columns dominated by flexural behavior, the definition of flexural

strength is used to represent the maximum strengths, and for columns dominated by shear

behavior, the definition of shear strength is used.

4.4.1 Flexural Strength Behavior

Section 4.3.1 introduces the hysteresis curves for columns T1C1 and T1C3, both

columns show yielding of longitudinal reinforcements and reaching of yielding plateaus

128
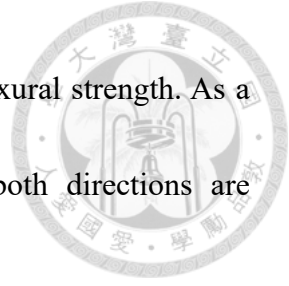
in both directions, and the strength values exceed the calculated flexural strength. As a result, the maximum strength developed for both columns in both directions are considered as the flexural strength of the columns.
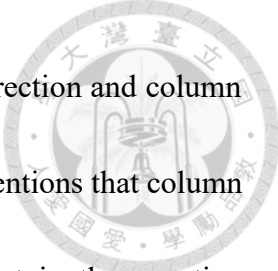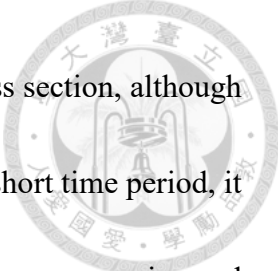
Sustained Axial Load

To investigate the enhancement of sustained axial loads on column flexural strengths by test results, the flexural strengths of flexural dominant columns applied with different initial axial loads should be compared. The columns introduced in **Section 4.3** are all designed with an initial axial load of $0.1 f_c' A_g$. The actual applied axial loads on the columns are 8.40 % and 8.94 % respectively. The very slight difference in applied axial load values between the two columns may not provide good comparison on the enhancemwnt of flexural strengths, thus will not be further discussed.

Varying Axial Load

To investigate the enhancement of varying axial loads on column flexural strengths by test results, the flexural strengths of individual flexural dominant columns on both directions with one under higher varying axial load and other under lower varying axial load should be compared.

Figure 4-88 plots the flexural strength of the two columns in the order of direction, where the strength in the negative direction is plotted on the left within each column and in the positive direction on the right. The strength values are rationalized by $\sqrt{f'_c}bd$.

Column T1C1 is shown to develop higher strength in the negative direction and column T1C3 shows the same trend in the positive direction. **Section 4.3.1** mentions that column T1C1 is subjected to higher axial load due to overturning moment in the negative direction and column T1C3 under the same condition in the positive direction. Based on this concept, the original figure is replotted in the order of subjection of axial load, with higher axial load on the left and lower axial load on the right as shown in **Figure 4-89** to observe the trend of strength development due to varying axial load. From various researches on RC column members and concepts on development of analytical models, the conclusions indicate that increase in axial load applied on columns would enhance the strength and reduce the ductility. However, the mentioned axial load is the constant axial load that is applied constantly on the column member, while for shaking table test specimens, the varying axial load is induced by the overturning moment, which induces increased or decreased axial load within a second and unloads to the initial condition directly afterwards. Whether the varying axial load phenomenon can affect strength development of columns is yet to be investigated. Based on the trend in **Figure 4-89**, it can be concluded that for flexure-dominant columns, the varying axial load does have its effect on the column flexural strength. Since the columns in this research response below the balance point on the P-M curve, the varying axial load enhances the flexural strength under higher axial load and the opposite condition under lower axial load. The flexural

130

strength of a column is contributed by the moment strength of its cross section, although

the varying axial load is subjected on the cross section within a very short time period, it

is still subjected orthogonally on the cross section, paralleled with the compressive and

tensile forces on the section, and it is observed through shaking table test responses that

this varying axial load is capable to sensitively affect the flexural strength development

of the section.

More test results should be taken into consideration for stronger verification on the

conclusion provided, and to what degree can the varying axial load enhance the column

strength is yet to be investigated. This research takes into account of shaking table tests

on flexure-controlled columns by Elwood and Moehle (2003) and Guo (2008) to propose

further researches. The specimen design parameters and the test results are provided in

the **Appendix** as mentioned in **Section 2.5**, which would be discussed in detail in

Chapter 5.
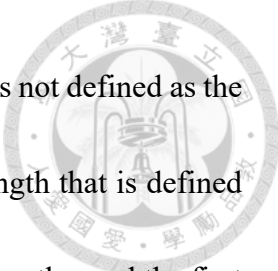
4.4.2 Shear Strength Behavior

Section 4.3 introduces the hysteresis curves for the shear-controlled columns. Since

the input forces of shaking table tests are based on ground motions and top mass blocks,

which is force controlled, the transducers are able to measure the maximum base shear

values that are subjected on the columns, but that may not be the maximum strength that

131
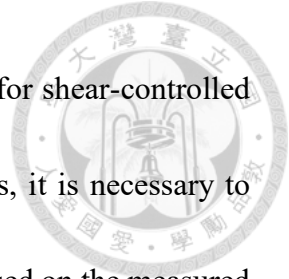
the columns are able to develop, which is defined as shear strength for shear-controlled columns. In order to investigate the strength development behaviors, it is necessary to define the shear strength values for the columns in both directions based on the measured values. To distinguish the shear strengths from the measured maximum strengths, a method/concept should be established to process all the data. The method is as follows:

1. By observation on the hysteresis curve, when strength degradation with increasing lateral displacement is observed after the development of maximum strength on one direction, the maximum strength value can be defined as the shear strength of this specimen.

2. The columns can develop their shear strengths in both directions through shaking table tests. The strength that is reached first is defined as the first shear strength, and second shear strength for the second one.

3. The first shear strength should develop a larger value than the second shear strength due to better integrity of the concrete section and material bonds without formation of shear cracks.

4. When maximum strength is developed in one direction, but strength degradation does not occur, the strength value is not defined as the shear strength. If the specimen continues to develop maximum strength in the other direction and strength degradation occurs, then the strength value is defined as the shear strength. However,
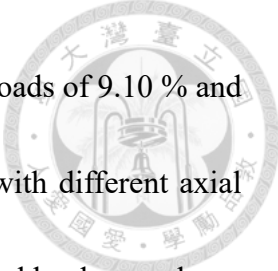
for conditions when the first measured maximum strength value is not defined as the shear strength but has a higher value than the defined shear strength that is defined in the other direction, both values will be considered as shear strengths, and the first maximum developed strength is redefined as the first shear strength, and the original first shear strength is redefined as the second shear strength.

Through processing of all the measured maximum strengths, the values in **Table 4-8** for columns T1C2, T2C1, T2C3, T3C1, T3C3, and T4C1 can be defined as shear strengths in both directions, while T4C3 only develops its shear strength in the negative direction. The measured strength values for all columns in both directions will still be taken into consideration for the following researches. It is to keep in mind that the first developed strength for column T4C3 is not defined as the shear strength.
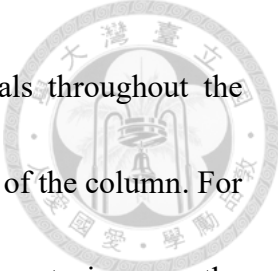
Sustained Axial Load

To investigate the enhancement of sustained axial loads on column shear strengths by test results, the shear strengths of shear dominant columns applied with different initial axial loads should be compared. The columns introduced in **Section 4.3** are all designed with an initial axial load of 0.1 $f'_c A_g$. Columns T1C2, T4C1, T4C3 are designed in the category of 4NL, with actual applied initial axial loads of 2.84 %, 5.51 % and 8.14 % respectively. Columns T2C1 and T2C3 are designed in the category of 3DL, with actual applied initial axial loads of 9.47 % and 9.53 % respectively. Columns T3C1 and T3C3

133
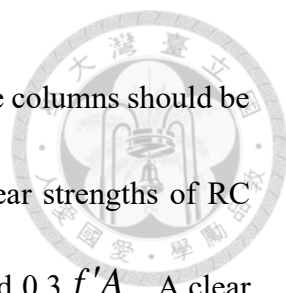
are designed in the category of 3NL, with actual applied initial axial loads of 9.10 % and 10.22 % respectively. The columns designed in the same category with different axial loads can be compared to investigate the enhancement of sustained axial loads on column shear strengths.

To take out the effect of damaged concrete integrity on the column shear strengths, only the first shear strengths of each column are compared. The shear strengths of each specimen and their corresponding sustained axial loads are summarized in **Table 4-14**. For 4NL specimens, the specimen with the lowest axial load is shown to develop the highest shear strength. Column T1C2 is the center column of a three-column frame with two flexural-dominant columns on the outside, since they are locked together with a top steel beam, the strength development of T1C2 may be affected by the two ductile columns. Focusing on the two remaining columns, the increase of 2.63 % on the sustained axial load enhanced the shear strength by 9.6 %. For both 3DL and 3NL specimens, the very slight difference in applied axial load values between the two columns in each category may not provide good comparison on the enhancemwnt of shear strengths, thus will not be further discussed. The comparison results conclude that increased sustained axial load does have its enhancement on column shear strength for shaking table-tested response. The columns in this research are only applied under low axial load of $0.1 f_c' A_g$ and only vary under 3 %. To observe the enhancement of sustained axial loads on column shear

134
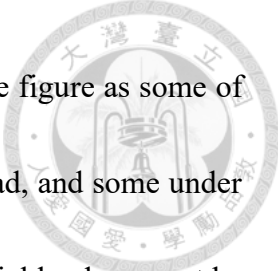
strengths clearly, significant change in applied initial axial load on the columns should be conducted. Li et al. (2019) provides cyclic loading test data for shear strengths of RC intermediate-short columns under initial axial loads of $0.1 f'_c A_g$ and $0.3 f'_c A_g$. A clear trend is observed as the sustained axial loads significantly increase the shear strength of the specimens. This section only focuses on the discussion of specimens presented in this chapter, thus will not provide further introduction and discussions.

Varying Axial Load

To investigate the enhancement of varying axial loads on column shear strengths by test results, the shear strengths of individual shear dominant columns on both directions with one under higher varying axial load and other under lower varying axial load should be compared.

Figure 4-90 plots the shear strength of the seven columns in the order of direction, where the strength in the negative direction is plotted on the left and in the positive direction on the right. The strength values are rationalized by $\sqrt{f'_c} bd$. **Section 4.3** mentions that for columns C1 in all the frames, they subject to higher axial load in the negative direction. For columns C3 in all the frames, they subject to higher axial load in the positive direction. Based on this concept, **Figure 4-90** is replotted in the order of subjection of axial load, with higher axial load on the left and lower axial load on the right as shown in **Figure 4-91** to observe the trend of strength development due to varying

135

axial load. However, no consistent behavior can be observed from the figure as some of the columns show higher strength when subjecting to higher axial load, and some under opposite behavior. As a result, it can be concluded that the varying axial load may not be the main factor that dominates the shear strength development for individual shear-dominant columns. As mentioned previously, the first shear strength should develop a larger value than the second shear strength due to better integrity of the concrete section and material bonds without formation of shear cracks. Based on this concept, the figure is again replotted in the order of strength development sequence, with the first shear strength on the left and the second shear strength on the right as shown in **Figure 4-92** to observe the trend of strength development based on failure sequence. Excluding the first measured base shear value for T4C3, based on the trend in the figure, it can be concluded that for individual shear-dominant columns, the first shear strength would be higher than the second shear strength due to damaged material integrity no matter the subjection of varying axial load.

Since the shear strength of RC columns is governed either by the concrete compressive zone strength, dowel action strength, aggregate interlock strength, together with the lateral strength provided by transverse reinforcements, indicated as shear tension strength, or by the crushing strength of concrete strut end, indicated as shear compression strength. For shear tension failure conditions, increased axial load would have to affect

136

all the above-mentioned strength contributions by different materials throughout the whole region of the shear crack in order to enhance the shear strength of the column. For shear compression failure conditions, increased axial load would have to increase the compression zone of the concrete strut or change the strut inclination angle to enhance the crushing strength of the strut. For sustained axial loads, the loads are constantly applied on the columns, providing sufficient time for concrete material to develop its change in strain concentration behaviors, and enhance the maximum strength development when lateral force is applied. For the varying axial loads, the increased axial loads are subjected on the columns within a very short time period. The shortly-applied axial loads must affect all the strength contributions throughout the shear crack within the short time period, allowing for the changed force-transfer mechanism to reflect on its strength, in order to enhance the shear strength of the column. It is concluded that for the flexural strength behavior, the axial load is subjected perpendicular to the section of strength development and parallel with all the forces that contribute to the flexural strength, thus even the shortly-applied varying axial load can affect its strength development. Unlike the flexural strength behavior, the shear strength behavior is concluded that the axial load has to penetrate throughout the whole region where the inclined shear crack passes through, and affects the different types of materials that contribute to the shear strength, which are not necessary parallel to the axial load, in order

137

to enhance the shear strength of the column. It is observed from the shaking table test responses that the shortly-applied varying axial load cannot sensitively affect the shear strength development due to insufficient applied time, and requires constant applied axial load to enhance its behaviors, thus the varying axial load is shown to not govern the strength development behavior of shear-dominant columns.

This conclusion provides a strong backup for the development of analytical models. On the one hand, when performing seismic assessment for shear-critical columns, shear failure is always prevented and the second shear strength wouldn't have to be taken into consideration. Therefore, the developed analytical models should always shoot for the condition of the first shear strength when comparing with shaking table test results. On the other hand, since the development of shear strength is shown to be governed by both the sustained axial load and the failure sequences instead of the effect of varying axial loads, the shear strength of columns can be inputted as constant values based on the sustained axial loads on column models when performing nonlinear structural analysis, neglecting the effect of varying axial loads. The evaluation of strength prediction models with or without the consideration of sustained and varying axial load the column flexural and shear strengths would be presented in **Chapter 5**.

138

4.4.3 Stiffness Behavior

The stiffness time history responses for all nine columns is presented in this section. The measured stiffnesses are plotted as circular symbols on the figures. The data points are the secant stiffness values, which is the slope of the line connecting the data point and the zero point, for linear behaviors, the secant stiffness is the column's actual stiffness. For shaking table tests, numerous small lateral forces are subjected on the columns before and after the large forces that induce development of strength, which leads to numerous small lateral displacements. For the processing of data points, drifts smaller than 1 mm are neglected since they may lead to error readings, and those larger than 1 mm are calculated to observe the stiffness time history response of columns subjecting to ground motions.

For the strength development of flexure-controlled RC columns with increasing lateral deformations, the sequence can be explained in the following order:

1. Elastic condition where plain-remain-plain can be assumed.

2. Flexural cracking of concrete material subjected to tensile force.

3. Nonlinear behavior of concrete material subjected to compressive force.

4. First yielding of longitudinal reinforcement.

5. Development of nominal moment strength.

For the strength development of shear-controlled RC columns with increasing lateral

deformations, the sequence can be explained in the following order:

1. Elastic condition where plain-remain-plain can be assumed.

2. Nonlinear behavior of concrete material subjected to compressive force.

3. Web shear cracking or flexural shear cracking of column body.

4. Development of shear strength.

Based on researches on column behaviors, the elastic condition only exists under small lateral deformations when no cracks have formed on the column body. The overall behavior from the development of flexural cracks to concrete compressive nonlinearity and up to the yielding of longitudinal reinforcements or shear crack formation is developed roughly under linear behavior. Combining with the elastic section, the development of strength from zero point up to the point of yielding of longitudinal reinforcements or shear crack formation can be represented by a linear relationship, which is defined as the effective stiffness of columns. Analytical models have taken the concept of effective stiffness to simulate the initial behavior of RC columns through a linear slope. Since this research processes the column stiffness by their time history response, the elastic stiffness can be evaluated solely, and the effective stiffness can be calculated as the overall average of the pre-yielding and pre-shear cracking stiffness. The responses will be presented frame by frame.
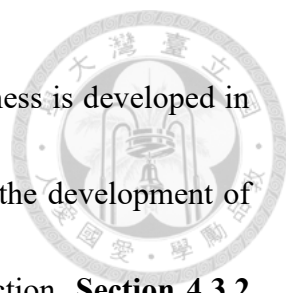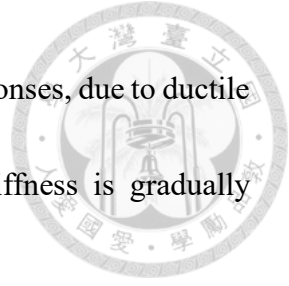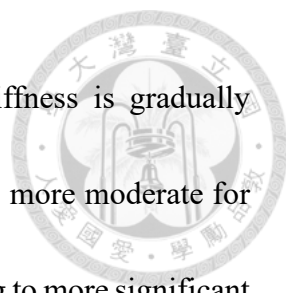
Frame T1

Figure 4-93 shows the response for column C1. A higher stiffness is developed in the negative direction before 24 second during R2, which indicates the development of elastic stiffness. This behavior is not observed in the positive direction. **Section 4.3.2** indicates that initial cracks have formed on the column, which may be the reason that the elastic stiffness in the positive direction is softened. The average measured elastic stiffness is 113.69 (kN/cm) in the positive direction and 276.85 (kN/cm) in the negative direction. After 24 second into R2, the stiffness of the column is softened in both directions, but remains under constant value through the whole run. This indicates the development of effective stiffness, and the average measured effective stiffness is 118.26 (kN/cm) in the positive direction and 143.71 (kN/cm) in the negative direction. Although slightly softened after each run, this constant stiffness behavior is able to maintain up to 24 second into R4 when maximum strength (grey triangular symbols) is developed. The stiffness in this time period can still be considered as effective stiffness, but are separated with the value during R2 since they are slightly softened by numerous small lateral drifts and may not be referenceable. The measured effective stiffness during R2 will be used to compare with current stiffness prediction models in **Chapter 5**. The measured elastic and effective stiffness values are provided in **Table 4-15**. For the post-strength stiffness responses, the stiffness is severely softened due to yielding of longitudinal reinforcements,

141

and keeps on degrading until reaching the collapse point (grey cross symbol).

Figure 4-94 shows the response for column C2. No higher stiffness is shown before 24 second during R2, which indicates no values for the measured elastic stiffness. Since the column has higher longitudinal reinforcement ratio (see **Table 4-3**), it is expected for the column to develop a much higher elastic and effective stiffness. As mentioned previously, drifts smaller than 1 mm would be neglected, with higher stiffness, the column is prone to enter nonlinear behavior even during smaller drift ratios. Therefore, this may be the reason that no elastic stiffness is measured. After 24 second into R2, the stiffness remains under constant value through the whole run. This indicates the development of effective stiffness, and the average measured effective stiffness is 349.26 (kN/cm) in the positive direction and 339.35 (kN/cm) in the negative direction. Although slightly softened after each run, this constant stiffness behavior is able to maintain up to 23 second into R4 when shear cracks form and the maximum strength (grey triangular symbols) is developed. As explained previously, the measured stiffness in this time period would not be taken into consideration, and the measured effective stiffness during R2 will be used to compare with current stiffness prediction models in **Chapter 5**. The measured effective stiffness values are provided in **Table 4-15**. For the post-strength stiffness responses, due to nonductile reinforcement detailing, the stiffness is severely softened and directly reaches the collapse point (grey cross symbols).
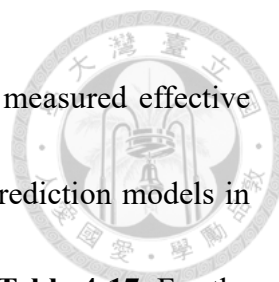
Figure 4-95 shows the response for column C3. A higher stiffness is developed in the positive direction before 24 second during R2, which indicates the development of elastic stiffness. This behavior is not observed in the negative direction. **Section 4.3.2** indicates that initial cracks have formed on the column, which may be the reason that the elastic stiffness in the negative direction is softened. The average measured elastic stiffness is 254.57 (kN/cm) in the positive direction and 154.47 (kN/cm) in the negative direction. After 24 second into R2, the stiffness of the column is softened in both directions, but remains under constant value through the whole run. This indicates the development of effective stiffness, and the average measured effective stiffness is 135.55 (kN/cm) in the positive direction and 138.77 (kN/cm) in the negative direction. Although slightly softened after each run, this constant stiffness behavior is able to maintain up to 24 second into R4 when maximum strength (grey triangular symbols) is developed. As explained previously, the measured stiffness in this time period would not be taken into consideration, and the measured effective stiffness during R2 will be used to compare with current stiffness prediction models in **Chapter 5**. The measured elastic and effective stiffness values are provided in **Table 4-15**. For the post-strength stiffness responses, the stiffness is severely softened due to yielding of longitudinal reinforcements, and degrades significantly due to opening of a dominant shear crack during R6 as mentioned in **Section 4.3.2**. Sliding on the dominant shear crack causes collapse of the column (grey cross

143

symbols), the measured stiffness response corresponds with the described failure pattern
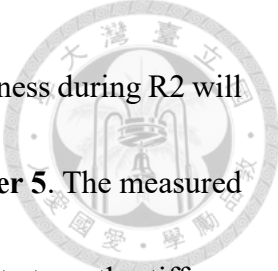
in **Section 4.3.2**.

Frame T2

Figure 4-96 shows the response for column C1. Higher stiffness is developed in both

directions before 24 second during R2, which indicates the development of elastic

stiffness. The average measured elastic stiffness is 629.17 (kN/cm) in the positive

direction and 658.87 (kN/cm) in the negative direction. After 24 second into R2, the

stiffness of the column is softened in both directions, but remains under constant value

through the whole run. This indicates the development of effective stiffness, and the

average measured effective stiffness is 407.74 (kN/cm) in the positive direction and

461.85 (kN/cm) in the negative direction. Although slightly softened after each run, this

constant stiffness behavior is able to maintain up to 24 second into R4 in the negative

direction when shear cracks form and the maximum strength (grey triangular symbol) is

developed. It is up to 34 second into R4 that the maximum strength is developed in the

positive direction and significant stiffness degradation can be observed. The degradation

of stiffness corresponds well with the development of maximum strengths. As explained

previously, the measured stiffness in this time period would not be taken into

consideration, and the measured effective stiffness during R2 will be used to compare

with current stiffness prediction models in **Chapter 5**. The measured effective stiffness

144

values are provided in **Table 4-16**. For the post-strength stiffness responses, due to ductile

reinforcement detailing, the column does not collapse and the stiffness is gradually

softened with degradation on the shear cracks.

Figure 4-97 shows the response for column C3. Higher stiffness is developed in both

directions before 24 second during R2, which indicates the development of elastic

stiffness. The average measured elastic stiffness is 624.12 (kN/cm) in the positive

direction and 640.75 (kN/cm) in the negative direction. After 24 second into R2, the

stiffness of the column is softened in both directions, but remains under constant value

through the whole run. This indicates the development of effective stiffness, and the

average measured effective stiffness is 443.77 (kN/cm) in the positive direction and

324.73 (kN/cm) in the negative direction. Although slightly softened after each run, this

constant stiffness behavior is able to maintain up to 24 second into R4 in the negative

direction when shear cracks form and the maximum strength (grey triangular symbols) is

developed in both directions and significant stiffness degradation can be observed. The

degradation of stiffness corresponds well with the development of maximum strengths.

As explained previously, the measured stiffness in this time period would not be taken

into consideration, and the measured effective stiffness during R2 will be used to compare

with current stiffness prediction models in **Chapter 5**. The measured effective stiffness

values are provided in **Table 4-16**. For the post-strength stiffness responses, due to ductile

reinforcement detailing, the column does not collapse and the stiffness is gradually

softened with degradation on the shear cracks. Since slip behavior is more moderate for

column C3, it is able to develop a larger lateral deformation, subjecting to more significant

post-strength stiffness softening due to increasing lateral deformation. As for column C1,

which severe slip behavior is observed, the post-strength stiffness softening is more

moderate due to smaller lateral deformation developed.

Frame T3
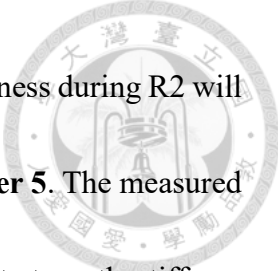
Figure 4-98 shows the response for column C1. No higher stiffness is developed in

the positive direction and no stiffness can be measured in the negative direction before 24

second during R2. **Section 4.3.4** indicates that initial cracks have formed on the column,

which may be the reason that the elastic stiffness in the positive direction is softened. The

reason that no stiffness can be measured is mentioned previously. The average measured

elastic stiffness is 620.93 (kN/cm) in the positive direction. After 24 second into R2, the

stiffness of the column remains under constant value through the whole run. This indicates

the development of effective stiffness, and the average measured effective stiffness is

552.56 (kN/cm) in the positive direction and 484.66 (kN/cm) in the negative direction.

Although slightly softened after each run, this constant stiffness behavior is able to

maintain up to 24 second into R4 when shear cracks form and the maximum strength

(grey triangular symbols) is developed. As explained previously, the measured stiffness

146

in this time period would not be taken into consideration, and the measured effective

stiffness during R2 will be used to compare with current stiffness prediction models in

Chapter 5. The measured effective stiffness values are provided in **Table 4-17**. For the

post-strength stiffness responses, due to nonductile reinforcement detailing, the column

directly collapses (grey cross symbols) with zero measured stiffness values after strength

development.

Figure 4-99 shows the response for column C3. Higher stiffness is developed in the

positive direction before 24 second during R2, which indicates the development of elastic

stiffness. No stiffness can be measured in the negative direction and the reason is

mentioned previously. The average measured elastic stiffness is 745.5 (kN/cm) in the

positive direction. After 24 second into R2, the stiffness of the column is softened in the

positive direction, but remains under constant value through the whole run, while the

maximum strength (grey triangular symbol) is developed in the negative direction but the

stiffness also remains under constant value through the whole run. This indicates the

development of effective stiffness, and the average measured effective stiffness is 547.14

(kN/cm) in the positive direction and 528.96 (kN/cm) in the negative direction. Although

slightly softened after each run, this constant stiffness behavior is able to maintain up to

24 second into R4 when shear cracks form and the maximum strength (grey triangular

symbol) is developed. As explained previously, the measured stiffness in this time period

147

would not be taken into consideration, and the measured effective stiffness during R2 will

be used to compare with current stiffness prediction models in **Chapter 5**. The measured

effective stiffness values are provided in **Table 4-17**. For the post-strength stiffness

responses, due to nonductile reinforcement detailing, the column directly collapses (grey

cross symbols) with zero measured stiffness values after strength development.

Frame T4

Figure 4-100 shows the response for column C1. Higher stiffness is developed in

the negative direction and slightly higher stiffness is developed in the positive direction

before 24 second during R2, which indicates the development of elastic stiffness. **Section**

4.3.5 indicates that initial cracks have formed on the column, which may be the reason

that the elastic stiffness in the positive direction is softened. The average measured elastic

stiffness is 286.18 (kN/cm) in the positive direction and 419.42 (kN/cm) in the negative

direction. After 24 second into R2, the stiffness of the column is softened in both

directions, but remains under constant value through the whole run. This indicates the

development of effective stiffness, and the average measured effective stiffness is 256.53

(kN/cm) in the positive direction and 233.22 (kN/cm) in the negative direction. Although

slightly softened after each run, this constant stiffness behavior is able to maintain up to

24 second into R4 when shear cracks form and the maximum strength (grey triangular

symbols) is developed. As explained previously, the measured stiffness in this time period

148

would not be taken into consideration, and the measured effective stiffness during R2 will

be used to compare with current stiffness prediction models in **Chapter 5**. The measured

effective stiffness values are provided in **Table 4-18**. For the post-strength stiffness

responses, due to nonductile reinforcement detailing, the column directly collapses (grey

cross symbol) with zero measured stiffness values after strength development.

Figure 4-101 shows the response for column C3. Higher stiffness is developed in

the negative direction and slightly higher stiffness is developed in the positive direction

before 24 second during R2, which indicates the development of elastic stiffness. **Section**

4.3.5 indicates that initial cracks have formed on the column, which may be the reason

that the elastic stiffness in the positive direction is softened. The average measured elastic

stiffness is 376.07 (kN/cm) in the positive direction and 443.05 (kN/cm) in the negative

direction. After 24 second into R2, the stiffness of the column is softened in both

directions, but remains under constant value through the whole run. This indicates the

development of effective stiffness, and the average measured effective stiffness is 290.76

(kN/cm) in the positive direction and 283.70 (kN/cm) in the negative direction. Although

slightly softened after each run, this constant stiffness behavior is able to maintain up to

24 second into R4 when shear cracks form and the maximum strength (grey triangular

symbols) is developed. As explained previously, the measured stiffness in this time period

would not be taken into consideration, and the measured effective stiffness during R2 will

be used to compare with current stiffness prediction models in **Chapter 5**. The measured

effective stiffness values are provided in **Table 4-18**. For the post-strength stiffness

responses, due to nonductile reinforcement detailing, the column directly collapses (grey

cross symbol) with zero measured stiffness values after strength development.

To sum up, effective stiffness values have been processed by each test during

different runs, and only the values during the first run in each test are taken into

consideration as the actual effective stiffness of the columns to minorize the softening of

stiffness due to accumulating drifts. The effective stiffness values of each column are

summarized in **Table 4-19**.

4.4.4 Collapse Point

This section summarizes the collapse point lateral drifts of all specimens. To define

a more organized procedure on processing the collapse point lateral drifts of all specimens,

this research refers to the approach of ASCE/SEI 41-13 (2014) on estimating the plastic

rotation at the loss of gravity load support, that is the axial load failure. For RC columns

subjected to shear failure, ASCE/SEI 41-13 (2014) provides that the point at the loss of

gravity load support is on the maximum lateral displacement of a column backbone curve

that the lateral strength degrades to zero. Based on this concept, this research processes

all the collapse point lateral drifts as the maximum lateral drift on the backbone curve of

150

the specimen that the lateral strength degrades to zero.

Column T1C2 does not experience collapse when it loses its lateral strength capacity, while columns T2C1 and T2C3 do not experience collapse. The drift ratio at collapse points for the rest of the columns are summarized in **Table 4-20**. Columns T1C1 and T1C3 provides collapse points for flexural-shear dominant columns, while columns T3C1, T3C3, T4C1, and T4C3 provide collapse points for shear dominant columns.

151
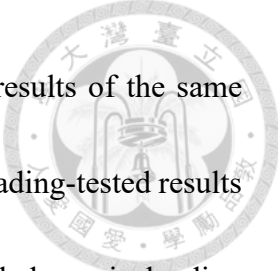
CHAPTER 5: COMPARISON OF CYCLIC LOADING AND SHAKING TABLE TEST RESPONSE

5.1 Introduction

This chapter presents the comparison on responses between cyclic loading and shaking table-tested RC columns, and between cyclic loading-based analytical models and shaking table test responses. It is mentioned in the introduction that the objective of this research is to validate the feasibility for utilizing cyclic loading test results to represent shaking table test results for simpler and more economic test setups. Thus, the strength, stiffness, collapse point, and overall lateral load-displacement relationship should be compared between these two types of tests for verification. As for the analytical models, they are developed mostly based on the cyclic loading test results, whether these cyclic loading-based analytical models can simulate actual shaking table-tested behaviors for strength, stiffness, and overall backbone curve is yet to be investigated.

For strength development, it has already been concluded that the difference in loading rate of tests would affect the strength development. For reinforced concrete members, with higher loading rate, the strain rate effect on reinforcement steel materials and the crack prevention dynamic effect on concrete materials would enhance the member strength. Shaking table tests subject lateral forces on members with much higher loading

rate compared to cyclic loading tests. Thus, the cyclic loading test results of the same specimen would develop lower strength values, allowing the cyclic loading-tested results to always be on the conservative side and able to represent actual dynamic loading situations since the higher loading rate is a bonus on strength behavior. To quantify the effect of loading rate on strength development for RC members, Hsu et al. (2023) collected test data on RC shear wall with openings loaded under different loading rates for same specimens. The higher loading rate tests of all specimens are loaded 100 times higher than the lower loading rate tests. The strengths of each specimen under different loading rates are summarized in **Table 5-1**. Under a 100 times-faster loading rate, the walls can develop an average $V_{t,high}/V_{t,low}$ ratio of 1.11, with a coefficient of variation of 0.05. This indicates that with a 100 times higher loading rate, the strength of RC shear wall with openings can be enhanced up to an average value of 11%.

For stiffness development, the softening of reinforced concrete members is due to formation of cracks on concrete sections. Shaking table tests subject to lateral forces within a very short time period before unloading of the forces due to oscillations of ground motions. As a result, when the section is about to develop lateral deformation and cracks are about to form, the force suddenly unloads and the above phenomena are not able to develop. Based on this concept, cyclic loading tests provide sufficient time for lateral deformations to develop and cracks to form, thus it is expected that the stiffness of shaking

154

table-tested columns should be higher than or around the same value as cyclic loading-tested columns.
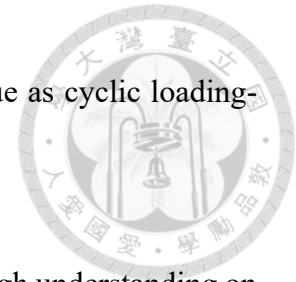
For collapse point development, it is necessary to have a thorough understanding on the collapse deformation of brittle-shear dominated columns to investigate collapse behavior of structures. Collapse point can be defined through cyclic loading tests by applying lateral deformations up to the point of loss of gravity load carrying capacity. The collapse point research for shaking table tests is much more dangerous and prone to damage instrumental setups since it is required for the sliding on dominant shear cracks and falling of the top mass blocks onto the ground for the column to develop sufficient lateral deformation to reach the collapse point. The shaking table test results in Su (2007) are conducted carefully and provide the chance to compare the collapse points of the same column under shaking table tests and cyclic loading tests. Due to inertia force of the top mass blocks when falling to the lateral direction, it is expected for the shaking table-tested columns to have the chance to develop larger collapse point lateral deformations.

Varying axial loads are subjected on columns due to overturning moments, it is discussed in **Section 4.4.1** that the test results in Su (2007) indicate that the flexural strength of columns is affected by the varying axial load, and the shear strength is governed by the failure sequence. This chapter takes into account the shaking table tests on RC columns by Elwood and Moehle (2003) and Guo (2008) as provided in the

155

Appendix to clarify the effect of varying axial load on column flexural strength based on a larger database of column responses.
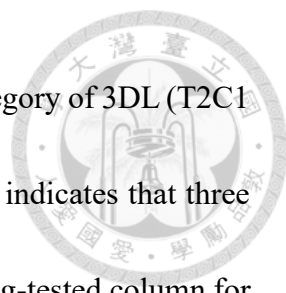
The modeling of column strength, stiffness, and overall lateral load-displacement relationship provided by NCREE/TEASDA (2021) is compared with the shaking table test results. The modeling of column strength with or without the consideration of the sustained axial load and with or without the consideration of varying axial load is discussed in this section and corresponding conclusion is provided. Additional effective stiffness models of columns (Elwood and Eberhard 2006, and Elwood and Eberhard 2009) are also compared with the shaking table test results.

5.2 Cyclic Loading and Shaking Table Test Response Comparison

This section presents the comparison on strength, stiffness, collapse point, and overall lateral load-displacement relationship of the RC intermediate-short columns through cyclic loading (Weng 2007) and shaking table tests (Su 2007).

5.2.1 Introduction

As mentioned in **Chapter 4**, three types of design parameters are used for the comparison between cyclic loading and shaking table-tested columns (i.e. category 4NL, 3DL, and 3NL). The cyclic loading tests contributed three columns, column 4NL, column 3DL, and column 3NL. The shaking table tests contributed a total of seven columns, with

three in the category of 4NL (T1C2, T4C1, and T4C3), two in the category of 3DL (T2C1 and T2C3), and two in the category of 3NL (T3C1 and T3C3). This indicates that three shaking table-tested columns can be compared with one cyclic loading-tested column for category 4NL, two shaking table-tested columns can be compared with one cyclic loading-tested column for category 3DL, and two shaking table-tested columns can be compared with one cyclic loading-tested column for category 3NL.

Due to the limitation of the shaking table, the shaking table-tested specimens must be designed in half-scale, while the cyclic loading-tested specimens can be designed at full-scale. **Table 3-2** and **Table 4-2** show the design parameters for the columns under different tests. For the differences on full-scale and half-scale design parameters and consideration on test procedures to allow for full-scale and half-scale behavior comparison, the following points are considered:

1. The concrete strength remains the same.

2. The longitudinal reinforcement ratio and yielding strength remain the same.

3. The design axial load remains the same.

4. The value for transverse reinforcement ratio times yielding strength remains the same. (Due to limitation on size for half-scale stirrups at 4 mm diameter, it is difficult to solely remain the transverse reinforcement ratio the same)

5. The length and width of the column is reduced by half.

6. The coarse aggregate size in concrete is reduced by half.

7. The input ground motion is compressed by $\frac{1}{\sqrt{2}}$.

8. The strength values are rationalized by $\sqrt{f'_c}bd$ for comparison.

9. The deformations are rationalized by their height (drift ratios) for comparison.

5.2.2 Strength Comparison

As mentioned in **Section 4.4.1**, the shear strength development of RC columns is governed by failure sequence. The ratios in this section are summarized in **Table 5-2**. **Figure 5-1** plots the shear strengths of the seven shaking table-tested columns and their corresponding cyclic loading-tested results in their failure sequence, with first shear strength to the left and second shear strength to the right. The results show good consistency where all the shaking table-tested strengths are larger than the cyclic loading-tested strengths. The average value for the $V_{shaking}/V_{cyclic}$ ratio is 1.25.

It is previously mentioned that the higher loading rates for shaking table tests can contribute to enhancement in strength for reinforced concrete shear wall with openings up to 11%. The applied time rate for the cyclic loading tests in Weng (2007) is 0.5 mm/s for 0.5% drift ratios, and approximate time rate for the shaking table tests in Su (2007) is 50 mm/s, this leads to a 100 times of time step difference for the input of lateral force, which has the same enhanced loading rate ratio with the RC shear wall with openings

158

introduced in **Section 5.2.1**, but results with a 25 % enhancement in strength compared with the 11 %. The much higher value of 25% enhancement for the columns may be contributed by other additional phenomena.

First, dynamic effect occurs when RC members are subjected to ground motions and the lateral forces are subjected on the members within a very short time period before unloading. For RC members, cracking and nonlinearity of materials lead to development of strength. The applied lateral force within a very short time period for the shaking table tests is not sufficient for the RC section to react and develop its cracks and its nonlinearity. It is usually up to the point when the applied force either just exceeds or has already exceeded the actual member strength that the RC section would develop its nonlinearity. Although able to be explained in concept, it is very hard to quantify the dynamic effect since concrete itself is a material with high variance due to its formation of cracks, leading to high variance for the dynamic effect as well. It can still be concluded that the dynamic effect is an enhancement on the shear strength of RC columns, since the development of shear strength is based on formation of shear cracks.

Secondly, since the shaking table-tested columns are not tested alone just like the cyclic loading-tested columns, they are tested together with other columns as a frame, just as actual RC structures. The lateral deformations and strength developments can be affected by other columns. Take frame T1 for example, the center shear-dominated

159
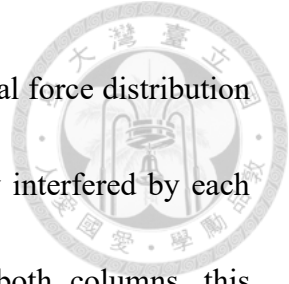
column C2 is locked with two flexure-dominated columns. The lateral force distribution and the lateral deformation development of the columns are highly interfered by each other. Since frame T2, T3, and T4 have identical designs for both columns, this phenomenon might not be dominant, but should still have its effect on each other.

As for column T3C1, it is mentioned in **Section 4.3.4** that the shear strength of the column is enhanced unexpectedly due to induction of residual force during application of prestress to lock the top steel beam with its top foundation. When comparing between dynamic loading and cyclic loading responses, strengths which might be interfered should be taken out of consideration.
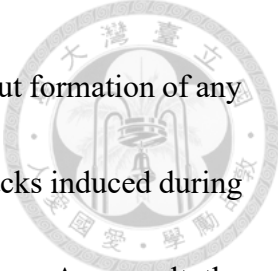
After taking out the values for columns T1C2 and T3C1, the average value for the $V_{shaking}/V_{cyclic}$ ratio is lowered to 1.16 with a COV of 0.12. The ratio is shown to have 16% in strength enhancement. Compared with the AVE of 1.11 and COV of 0.05 for shear wall with openings, in addition to the 11% enhancement from higher loading rates, the variance of the dynamic effect and interference from adjacent columns may also contribute to the enhancement. To sum up, the various enhancement phenomena from shaking table tests are shown to have their positive effect on the column shear strength development, and the cyclic loading test shear strengths, which would always be on the conservative side, are validated to be able to represent shaking table test shear strengths when researching on the responses of shear-dominated RC columns and members.

160

5.2.3 Stiffness Comparison

The ratios in this section are summarized in **Table 5-3**. **Figure 5-2** plots the effective stiffness of cyclic loading-tested columns and shaking table-tested columns in the order of direction, with negative direction to the left and positive direction to the right. The effective stiffness measurement procedure and results for shaking table tests are presented in **Section 4.4.2**, while the effective stiffness for cyclic loading tests is calculated by the secant stiffness of the shear cracking point ($\Delta_{test}, V_{cracking,calculated}$) on the actual test data during the first drift. The cracking strength value is calculated by Eqs. (2.1) and (2.2). The shaking table-tested effective stiffness is shown to be lower than or around the same value as the cyclic loading-tested effective stiffness for all the columns. The average value for the ${S_{shaking}}/{S_{cyclic}}$ ratio is 0.86.

As mentioned previously, the effective stiffness for the shaking table-tested columns is calculated as the average value of all the measured effective stiffness throughout the first run. On the one hand, this indicates that the stiffness may be softened due to continuous opening and closing of concrete minor cracks during accumulating drifts. On the other hand, the column is subjected to varying axial load with compression on one direction and tension on the other, the continuous change in axial load may also damage the minor cracks in the concrete. The effective stiffness for cyclic loading-tested columns is calculated as the secant stiffness of the shear cracking point during the first drift, which

161
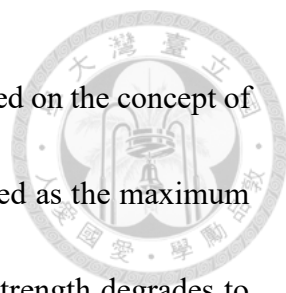
indicates that the stiffness is developed based on a column body without formation of any cracks. It is presented in **Chapter 4** that some columns have initial cracks induced during assemblage of the top steel beam before the subjection of ground motions. As a result, the measured stiffness for shaking table-tested columns is shown to be lower than the cyclic loading-tested columns, which is different from the expectation of the effects of strain rate and dynamic effect to stiffen the column stiffness.

When taking out the columns with severe initial cracking that may soften the effective stiffness severely (T2C3, T4C1, and T4C3), the average value for the $S_{shaking}/S_{cyclic}$ ratio can be increased to 0.94. In conclusion, although the average stiffness is slightly lower for the shaking table-tested columns due to the initial cracks and measurement method, the stiffness values are still shown to be around the same level for the overall results and same for some columns, and the cyclic loading test results provide good accuracy and consistency on stiffness behavior with the shaking table test results.

5.2.4 Collapse Point Comparison

The ratios in this section are summarized in **Table 5-4**. **Figure 5-3** plots the collapse point for the cyclic loading-tested columns and shaking table-tested columns, since only one collapse point can be reached for the shaking table tests, only one value is plotted for

162

each column. Following the definition discussed in **Section 4.4.4** based on the concept of ASCE/SEI 41-13 (2014), the collapse point lateral drifts are processed as the maximum lateral drift on the backbone curve of the specimen that the lateral strength degrades to zero. Columns T2C1 and T2C3 are designed with ductile reinforcement design, and the occurrence of slip does not allow the lateral displacements to develop fully, thus collapse does not occur for the columns. Only the columns with nonductile reinforcement design experiences collapse behavior, while the collapse of column T1C2 is prevented by the two outer ductile columns, therefore, only four columns (T3C1, T3C3, T4C1, and T4C3) are plotted in the figure. The shaking table-tested collapse displacement is shown to be higher than or just around the same value as the cyclic loading-tested collapse displacement for all the columns. The average value for the $D_{shaking}/D_{cyclic}$ ratio is 1.14.

Due to the inertia force of the top mass blocks when falling to the lateral direction during collapse, the shaking table-tested columns could develop larger lateral deformations at collapse point. The instant strength degradation leading to collapse behavior of the shaking table-tested columns could also vary the drift at collapse point. All in all, the collapse points between the two types of tests are shown to be around the same value for three columns, while having larger difference for one. The comparison indicates that the cyclic loading test results provide good accuracy and consistency on

163

collapse point behavior with the shaking table test results.

5.2.5 Lateral Load Displacement Relationship Comparison

Figure 5-4 to **Figure 5-6** plot the hysteresis curves of the shaking table tests and the backbone curves for the cyclic loading tests for all the seven columns to compare the overall lateral load-displacement relationship between cyclic loading and shaking table tests. This comparison also sums up the overall comparison results in this section.

For 4NL specimens in **Figure 5-4**, the stiffness behavior corresponds well for the two types of tests. The strength developments for cyclic loading tests are on the conservative side. Columns T4C1 and T4C3 develop direct strength degradation curves and the displacement responses correspond well with the cyclic loading test backbone curves. Column T1C2 does not show a direct curve but the trend of displacement development during strength degradation also corresponds well.

For 3DL specimens in **Figure 5-5**, the stiffness behavior corresponds well for the two types of tests. The strength developments are just around the same values. Columns T2C3 develops various drifts after reaching shear strength, and the strength degradation curve as well as the displacement response corresponds well with the cyclic loading test backbone curves.

For 3NL specimens in **Figure 5-6**, the stiffness behavior corresponds well for the

164

two types of tests. The strength development for column T3C3 is just around the same value. Column T3C1 develops a much higher strength and slight ductile behavior in the positive direction, as discussed in **Section 4.3.4**, its shear strength is enhanced unexpectedly. The comparison result also verifies that the column has developed strength and displacement exceeding its actual shear-dominant behavior. Columns T3C1 and T3C3 develop direct strength degradation curves and the displacement responses correspond well with the cyclic loading test backbone curves.

Based on the overall comparison results in **Section 5.2**, the cyclic loading test results are shown to be capable to represent shaking table test results. On the one hand, the cyclic loading test results provide good consistency and accuracy with shaking table test stiffness, collapse deformation, and displacement behavior. On the other hand, the shear strength values are lower for the cyclic loading test results. This indicates that the shear strength is enhanced when subjecting to actual ground motions, and the tested strengths from cyclic loading tests will always be more conservative than the actual strength of shaking table test responses.

5.3 Behavior of Column Strength Due to Varying Axial Load

This section presents the flexural strength development of flexural-dominated columns under varying axial load based on the test data in the **Appendix**.

165

5.3.1 Effect of Varying Axial Load on Flexural Strength

Section 4.4.1 presents the observations on column flexural strength due to varying axial loads for the two flexural-dominant columns in Su (2007) as shown in **Figure 4-89**, which concludes that the varying axial load does have its effect on enhancing the column flexural strength under higher axial load and developing lower strength under lower axial load for columns responding below the balance point on the P-M curve, even for a very short time period of increased or decreased axial load subjection. In order to validate this observed behavior more thoroughly, the database in the **Appendix** is constructed to include shaking table tests on columns by Elwood and Moehle (2003) and Guo (2008). All the columns are flexural-dominated to focus the comparison of this section on flexural strength.

Figure 5-7 plots the flexural strength of each column in the order of subjection of axial load, with higher axial load on the left and lower axial load on the right. The strength values are rationalized by $\sqrt{f'_c}bd$. The results show consistent behavior where the flexural strength is higher in directions of high axial load and lower in directions of low axial load. This validates the conclusion on the varying axial load having its effect on the strength development of flexural-dominated columns. This conclusion extends further researches on whether to consider the varying axial load effect when estimating column flexural strengths when performing nonlinear pushover or time domain analysis, or is

166

remaining using initial axial load to estimate the column flexural strength accurate enough. The main consideration between the two methods is the model complexity and time consumed for analysis. If the varying axial load effect is considered, the P-M curve must be constructed for each flexural-dominated column, and the model has to detect the current axial load during each time step and response with the varied strength, which is much more complex and time-consuming comparing with fixed axial load models. **Section 5.4** will be focusing on comparing the above-mentioned strength modeling methods.
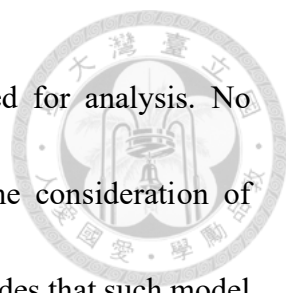
5.3.2 Effect of Varying Axial Load on Shear Strength

Section 4.4.2 presents the observations on column shear strength due to varying axial loads for the seven shear-dominant columns in Su (2007) as shown in **Figure 4-92**. Since sufficient shear-dominant column test data have been provided, no additional tests are taken into consideration. It is concluded that for individual shear-dominant columns, the first shear strength would be higher than the second shear strength due to damaged material integrity no matter the subjection of varying axial load.

This conclusion extends further researches on the feasibility for using initial axial load to estimate the column shear strengths by analytical models, or is the consideration of varying axial load required. The main consideration between the two methods, as

167
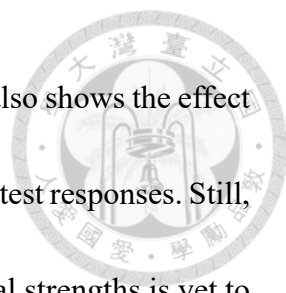
explained previously, is the model complexity and time consumed for analysis. No structural analysis software has provided models or hinges for the consideration of varying axial loads on column shear strengths. If this research concludes that such model is required, the analysis software should be recommended to take it into consideration. **Section 5.4** will be focusing on comparing the above-mentioned strength modeling methods.
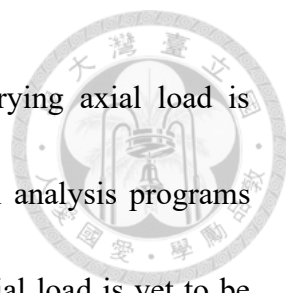
5.4 Modeling of Column Strength Considering Varying Axial Load

ETABS version 2016 (2016) provides the original M2 or M3 flexural hinge to model flexural behaviors of columns based on the strength of fixed initial axial load, which is the sustained axial load that is constantly applied on the column member. ETABS (2016) also provides the P-M-M flexural hinge to consider the change in axial load on the effect of flexural strength due to overturning moments of high-rise buildings, which is the varying axial load that is only applied on the column member when the structure is subjected to lateral loads. If the P-M-M hinge is used to simulate flexural behavior of columns, the P-M curve must be constructed for each column, and the model has to detect the current axial load during each time step and response with the varied strength. Although the strength response would be more accurate, the model setup is much more complicated and the analysis is more time-consuming. The large varying axial load on

168

columns for high-rise buildings is a recognized fact, and **Section 5.3** also shows the effect

of the varying axial load on column flexural strength based on various test responses. Still,

whether to consider the varying axial load to simulate column flexural strengths is yet to

be investigated. If fixed initial axial load strength is used to construct the column flexural

hinge, the simulated strength might be conservative for high axial load conditions and

might overestimate for low axial load conditions. If the varying axial load is considered,

the simulated strength might be more accurate. The first part of this section presents the

result comparison on using the initial axial load model (sustained axial load) and varying

axial load model to estimate the strength of the flexural-dominated columns in the

Appendix. In addition, the results of a zero axial load model (neglecting the sustained

axial load) is also compared with the two models above to observe the strength

enhancement effect of the sustained axial load and the varying axial load on flexural

strengths of RC columns.

On the other hand, ETABS version 2016 (2016) also provides the V2 or V3 shear

hinge to model shear behaviors of columns based on the strength of fixed initial axial load.

No shear hinge with the consideration of varying axial load is provided. **Section 4.4.1** has

shown that the shear strength development of shear-dominated columns is governed by

the failure sequence instead of the varying axial load, which indicates that the fixed initial

axial load should be used to construct the shear hinges to provide conservative and

169

consistent analysis results. Still, whether the consideration of varying axial load is required to simulate column shear strengths and whether structural analysis programs should provide shear hinges that consider the change in varying axial load is yet to be investigated and recommended. The second part of this section presents the result comparison of using initial axial load model (sustained axial load) or varying axial load model to estimate the strength of the shear-dominated columns in Su (2007). In addition, the results of a zero axial load model (neglecting the sustained axial load) is also compared with the two models above to observe the strength enhancement effect of the sustained axial load and the varying axial load on shear strengths of RC columns.

The sustained axial load values and the high and low axial load values during varying axial load for each column are summarized in **Table 5-5**.

5.4.1 Flexural Strength

The flexural strength of columns in this section are calculated by Eq. (2.22), and the ratios are summarized in **Table 5-6** and **Table 5-7**. Zero axial load is used to calculate the flexural strengths of the zero axial load model, the initial applied axial load is used to calculate the flexural strengths of the initial axial load model, and the measured axial loads at the point of maximum strength development on both directions are used to calculate the flexural strengths of the varying axial load model. **Figure 5-8** to **Figure 5-**

170
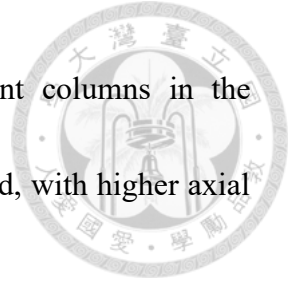
10 plot the measured flexural strengths for the flexural-dominant columns in the **Appendix** as red star symbols in the order of subjection of axial load, with higher axial load on the left and lower axial load on the right.

Figure 5-8 shows the comparison of strength values between the test results and the zero axial load model. The calculated flexural strength using zero axial load is plotted on the figure as orange circular symbols. It can be observed from the figure that when predicting the flexural strength under high axial load conditions, all the estimated strengths show very conservative results, with an average $V_{test}/V_{initial}$ ratio of 1.52. When predicting the flexural strength under low axial load conditions, most of the values are conservative and some are accurate, with an average $V_{test}/V_{initial}$ ratio of 1.17. If compared altogether, the initial axial load model provides an average $V_{test}/V_{initial}$ ratio of 1.34 with coefficient of variation (COV) of 0.17.
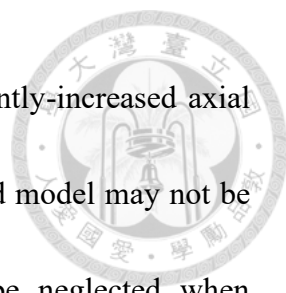
Figure 5-9 shows the comparison of strength values between the test results and the initial axial load model. The calculated flexural strength using initial axial load is plotted on the figure as green square symbols. It can be observed from the figure that when predicting the flexural strength under high axial load conditions, all the estimated strengths show conservative results, with an average $V_{test}/V_{initial}$ ratio of 1.32. When predicting the flexural strength under low axial load conditions, some are conservative, some are accurate, and some overestimate the values, with an average $V_{test}/V_{initial}$ ratio

171
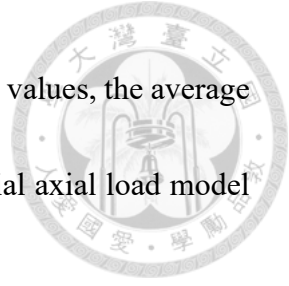
of 1.00. Since some models overestimate and some underestimate the values, the average

of the ratios is calculated to be 1.00. If compared altogether, the initial axial load model

provides an average $V_{test}/V_{initial}$ ratio of 1.16 with COV of 0.16.

Figure 5-10 shows the comparison of strength values between the test results and

the varying axial load model. The calculated flexural strength using varying axial load is

plotted on the figure as blue triangular symbols. It can be observed from the figure that

the trend of higher strength during higher axial load and lower strength during lower axial

load corresponds for the test behaviors and the model estimations. When predicting the

flexural strength under high axial load conditions, all the estimated strengths except T1C1

and T1C3 in Su (2007) show conservative results, with an average $V_{test}/V_{varying}$ ratio

of 1.15. When predicting the flexural strength under low axial load conditions, all the

columns except T1C1 and T1C3 in Su (2007) show accurate and conservative results,

with an average $V_{test}/V_{varying}$ ratio of 1.02. If compared altogether, the varying axial

load model provides an average $V_{test}/V_{varying}$ ratio of 1.09 with COV of 0.14.

For the two columns in Su (2007), **Section 4.3.2** mentioned that the failure of T1C2

turns into a large tensile force, leading to a significant increase on the axial load of the

two outer columns. This large inducement in axial load is not generated by the overturning

moments. Although the columns still show varying axial load phenomenon and flexural

strengths of the columns still show the trend of higher value when subjecting to higher

172

axial load and lower for the opposite condition, using the significantly-increased axial load to estimate the flexural strengths through the varying axial load model may not be feasible, and thus the responses on the two columns should be neglected when investigating the phenomenon. Taking out the ratios for the two columns, the average ratio of $V_{test}/V_{varying}$ during high axial load conditions is increased to 1.22, while increased to 1.05 during low axial load conditions. If compared altogether, the varying axial load model provides an average $V_{test}/V_{varying}$ ratio of 1.14 with COV of 0.10.

Figure 5-11 plots the estimated strength of the three models together, with the orange line indicating the zero axial load strength, the green line indicating the initial axial load strength, and the blue line indicating the varying axial load strength. The zero axial load strength is shown to be the lowest without the consideration of axial load, and the varying axial load strength is shown to oscillate above and below the initial axial load strength due to its consideration of varying axial load, except for columns T1C1 and T1C3 as explained previously. The test results are plotted as red star symbols on the figure to observe the correlation of the actual response with different models. When the column is subjected to higher axial load, the blue line (varying axial load strength) would be higher than the green line (initial axial load strength), and otherwise when subjected to lower axial load. The trend correlates well between the test response and the varying axial load model. Taking out the results for columns T1C1 and T1C3 and compared between each

173

other, the zero axial load model has an AVE of 1.32 and COV of 0.18, the initial axial

load model has an AVE of 1.17 and COV of 0.18, while the varying axial load model has

an AVE of 1.14 and COV of 0.10. The zero axial load model shows a very conservative

result compared to the two other models, which indicates that the strength enhancement

of sustained axial loads should be taken into consideration when estimating column

flexural strengths. Between the initial and varying axial load models, the average ratio is

just about the same, since the average of high and low axial load values is same as the

concept of using initial (averaged) axial load, while the COV shows that the varying axial

load model provides a more converged estimation. Taking out the results for columns

T1C1 and T1C3, if the high axial load and low axial load conditions are compared

separately, the average ratios of 1.35 and 0.99 in the initial axial load model can be

improved to 1.22 and 1.05 respectively by the varying axial load model, which shows a

more accurate improvement for the high axial load condition and a more conservative

improvement for the low axial load condition. It is to mention that remain using the initial

axial load model can still provide just enough accuracy for the estimation of column

strength in average. The comparison results indicate that the strength enhancement of

sustained axial loads should be considered when estimating column flexural strengths,

and the varying axial load effect should be considered to provide a more accurate and

conservative estimation for column flexural strengths when the structure is subjected to

174

earthquake forces, which induce varying axial loads.

5.4.2 Shear Strength

The shear strength of columns in this section is calculated by the procedure in **Figure 2-3**, and the ratios are summarized in **Table 5-8** and **Table 5-9**. Zero axial load is used to calculate the shear strengths of the zero axial load model, the initial applied axial load is used to calculate the shear strengths of the initial axial load model, and the measured axial loads at the point of maximum strength development on both directions are used to calculate the shear strengths of the varying axial load model. **Figure 5-12** to **Figure 5-14** plots the measured shear strength for the shear-dominant columns in the Su (2007) as red star symbols in the order of strength development sequence, with the first shear strength on the left and the second shear strength on the right.

Figure 5-12 shows the comparison of strength values between the test results and the zero axial load model. The calculated shear strength using zero axial load is plotted on the figure as orange circular symbols. It can be observed from the figure that when estimating the first shear strength by the zero axial load model, all the columns show very conservative results, with an average $V_{test}/V_{initial}$ ratio of 1.59. When predicting the second shear strength, all the columns show conservative results as well, with an average $V_{test}/V_{initial}$ ratio of 1.49. As mentioned in **Section 4.4.1**, the first shear strength is the
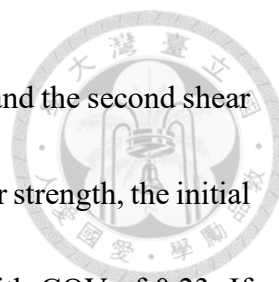
condition of concern since the first shear failure should be prevented and the second shear strength would not be developed, thus, when focusing on the first shear strength, the initial axial load model provides an average $V_{test}/V_{initial}$ ratio of 1.59 with COV of 0.23. If compared altogether, the initial axial load model provides an average $V_{test}/V_{initial}$ ratio of 1.54 with COV of 0.23.
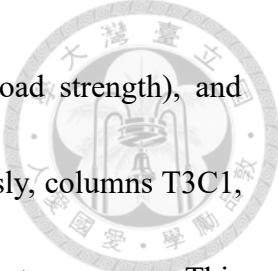
Figure 5-13 shows the comparison of strength values between the test results and the initial axial load model. The calculated shear strength using initial axial load is plotted on the figure as green square symbols. It can be observed from the figure that when estimating the first shear strength by the initial axial load model, all the columns show accurate or conservative results, with an average $V_{test}/V_{initial}$ ratio of 1.36. When predicting the second shear strength, some are conservative, some are accurate, and some overestimate the values, with an average $V_{test}/V_{initial}$ ratio of 1.19. Since the first shear strength is the condition of concern, when focusing on the first shear strength, the initial axial load model provides an average $V_{test}/V_{initial}$ ratio of 1.36 with COV of 0.23. If compared altogether, the initial axial load model provides an average $V_{test}/V_{initial}$ ratio of 1.27 with COV of 0.24.

Figure 5-14 shows the comparison of strength values between the test results and the varying axial load model. The calculated shear strength using varying axial load is plotted on the figure as blue triangular symbols. It can be observed from the figure that

176
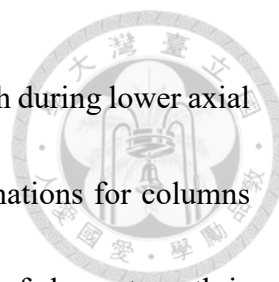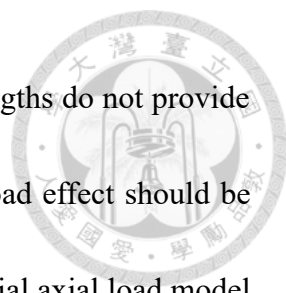
the trend of higher strength during higher axial load and lower strength during lower axial

load does not correspond for the test behaviors and the model estimations for columns

T3C1, T3C3, T4C1, and T4C3. This indicates that the development of shear strength is

not varying axial load dominant. When predicting the first shear strength, all the columns

show accurate or conservative results, with an average $V_{test}/V_{varying}$ ratio of 1.53.

When predicting the second shear strength, some are conservative and some overestimate

the values, with an average $V_{test}/V_{varying}$ ratio of 1.24. Since the first shear strength is

the condition of concern, when focusing on the first shear strength, the varying axial load

model provides an average $V_{test}/V_{varying}$ ratio of 1.53 with COV of 0.35. If compared

altogether, the varying axial load model provides an average $V_{test}/V_{varying}$ ratio of 1.40

with COV of 0.38.

Figure 5-15 plots the estimated strength of the three models together, with the

orange line indicating the zero axial load strength, the green line indicating the initial

axial load strength, and the blue line indicating the varying axial load strength. The zero

axial load strength is shown to be the lowest without the consideration of axial load, and

the varying axial load strength is shown to oscillate above and below the initial axial load

strength due to its consideration of varying axial load. The test results are plotted as red

star symbols on the figure to observe the correlation of the actual response with different

models. When the column is subjected to higher axial load, the blue line (varying axial

177
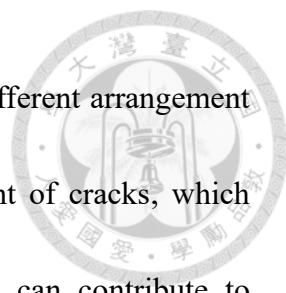
load strength) would be higher than the green line (initial axial load strength), and otherwise when subjected to lower axial load. As mentioned previously, columns T3C1, T3C3, T4C1, and T4C3 do not correlate with this trend on their test responses. This indicates that estimating the column shear strength based on a constant axial load should provide a more conservative and consistent result. Compared between each other, the zero axial load model has an AVE of 1.54 and COV of 0.23, the initial axial load model has an AVE of 1.27 and COV of 0.24, while the varying axial load model has an AVE of 1.40 and COV of 0.38. The zero axial load model shows a very conservative result compared to the two other models, which indicates that the strength enhancement of sustained axial loads should be taken into consideration when estimating column shear strengths. Between the initial and varying axial load models, both values show significant improvement in accuracy and convergence for the initial axial load model. As for the estimation of the first shear strength for the two models, the initial axial load model has an AVE of 1.36 and COV of 0.23, while the varying axial load model has an AVE of 1.53 and COV of 0.35. Both values show significant improvement in accuracy and convergence for the initial axial load model. The comparison results indicate that the strength enhancement of sustained axial loads should be considered when estimating column shear strengths. Combining with the conclusions of Section 5.3.2, to consider the varying axial loads on column shear strengths do not provide a consistent behavior, and

178

to consider the varying axial loads when estimating the column strengths do not provide

a correct and consistent estimation result. Thus, the varying axial load effect should be

neglected when estimating column shear strengths, and using the initial axial load model

can provide estimations with good accuracy and conservativeness.

Based on the above conclusion, the accuracy of the initial axial load model can be

discussed separately for the ductile and nonductile reinforcement design columns in Su

(2007). For the first shear strength of the columns with ductile reinforcement design

(T2C1 and T2C3), the initial axial load model provides an average $V_{test}/V_{initial}$ ratio of

1.07 with COV of 0.05. For the first shear strength of the columns with nonductile

reinforcement design (T1C2, T3C1, T3C3, T4C1, and T4C3), the initial axial load model

provides an average $V_{test}/V_{initial}$ ratio of 1.43 with COV of 0.20.
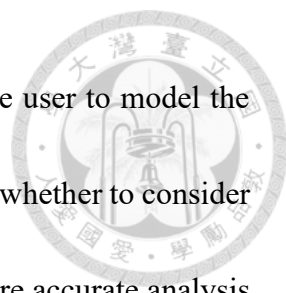
The model shows good estimation result for both categories. The significant

difference in both the average ratio and the coefficient of variation is due to the difference

in contribution from different materials. For columns with ductile reinforcement design,

the shear reinforcements contribute to a larger portion of the shear strength and

deformation development. Since reinforcement steel is a uniform material, it can

contribute to behaviors with higher uniformity, thus the COV of the ductile columns is

very low at a value of 0.05. For columns with nonductile reinforcement design, the

concrete material contributes to a larger portion of the shear strength and deformation

development. Concrete itself is a material with high variance, the different arrangement in aggregates, cement pastes, and voids can affect the development of cracks, which dominates the strength development significantly. As a result, it can contribute to behaviors with higher variance, thus the COV of the nonductile columns is higher but acceptable at a value of 0.20.

5.4.3 Conclusion

As mentioned previously, ETABS version 2016 (2016) provides the fixed axial load flexural hinge and the varied axial load flexural hinge for simulation of flexural nonlinear behavior, while only providing the fixed axial load shear hinge for simulation of shear nonlinear behavior. This section conducts a thorough investigation on the modeling of column strengths with or without the consideration of the sustained initial axial load, and with or without the consideration of the varying axial load induced by overturning moments based on comparison with shaking table test results. Both the flexural and shear strength comparison results indicate that the sustained axial load should be considered when estimating column strengths due to its enhancement on strength development. The flexural strength development is concluded to be more accurate with the consideration of varying axial load, but conservative enough if fixed axial load is used, and the shear strength development is concluded to be more accurate without the consideration of

varying axial load. ETABS program provides different hinges for the user to model the columns by their own decision. On the one hand, the user can choose whether to consider the varying axial load for flexural hinges for time-consuming but more accurate analysis results or remain using fixed axial load (constant flexural strength) flexural hinges. On the other hand, the user is only provided with the fixed axial load (constant shear strength) shear hinge when simulating nonlinear shear behaviors for shear-dominated RC members.

Section 2.6.1 introduces the research on the consideration of varying axial load on column flexural hinges for low-rise and high-rise RC buildings by Yeh and Chou (2017). It is concluded that the difference in flexural strength for columns on the compressive and on the tensile side can vary significantly when the P-M-M hinge is used, but the overall capacity curve with or without the consideration of varying axial load on the flexural hinges are the same. It is recommended by Yeh and Chou (2017) to still consider the varying axial load effect on the flexural hinges to reflect the effect of varying axial load on column strength, and for more accurate force distribution of members.

This section presents the difference in accuracy when estimating the column flexural strength with or without the consideration of varying axial load based on comparison with shaking table test results. It is concluded that the varying axial load effect should be considered to provide a more accurate and conservative estimation for column flexural strengths, while remain using the initial axial load model can still provide just enough

accuracy for the estimation of column flexural strengths in average. For the modeling of

columns in the following sections and chapters of this research, initial axial loads would

be used to estimate the column flexural and shear strengths since the columns are

subjected to low initial axial loads, and for a more efficient time history analysis.
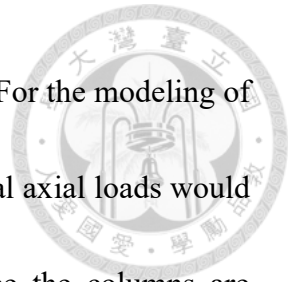
5.5 Modeling of Column Stiffness
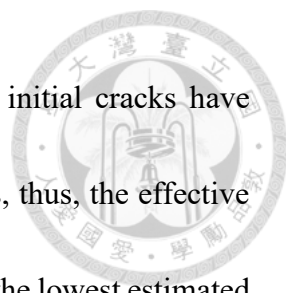
Section 2.7 introduces three effective stiffness models provided by ASCE/SEI 41-

17 (2017), Elwood and Eberhard (2006), and Elwood and Eberhard (2009). The effective

stiffness models are used to compare with the measured effective stiffness of the nine

columns in Su (2007) as presented in **Section 4.4.2**, the test values are provided in **Table

4-19** and the estimated values are summarized in **Table 5-10** for flexural-dominant

columns and in **Table 5-11** and **Table 5-12** for shear-dominant columns. Elwood and

Eberhard (2006) and ASCE/SEI 41-17 (2017) provide the same estimation of effective

stiffness for columns subjected to higher axial loads, but Elwood and Eberhard (2006)

provides a lower estimation than ASCE/SEI 41-17 (2017) during low axial loads. Elwood

and Eberhard (2009) is an improvement based on the Elwood and Eberhard (2006) model,

which provides a more sensitive estimation of column effective stiffness with different

axial loads and column shear spans in a wider range. The models for ASCE/SEI 41-17

(2017) and Elwood and Eberhard (2006) are simpler and can be calculated by constant
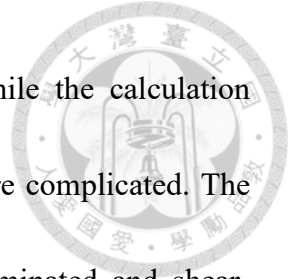
values and interpolation according to the applied axial loads, while the calculation

formula for the Elwood and Eberhard (2009) model is slightly more complicated. The

section first discusses the stiffness comparison of the flexural-dominated and shear-

dominated columns separately, and then compares the three stiffness models together for

the nine columns.

Figure 5-16 to **Figure 5-18** plot the measured effective stiffness for the flexural-

dominant columns (T1C1 and T1C3) and **Figure 5-19** to **Figure 5-21** plot the measured

effective stiffness for the shear-dominant columns (T1C2, T2C1, T2C3, T3C1, T3C3,

T4C1, and T4C3) from Su (2007) as red star symbols in the order of direction, with

negative direction on the left and positive direction on the right.

The results of the flexural-dominated columns are discussed first. **Figure 5-16** shows

the comparison of effective stiffness between the test results and the ASCE/SEI 41-17

(2017) model, with an average S_{test}/S_{model} ratio of 0.58 and COV of 0.08. **Figure 5-17**

shows the comparison of effective stiffness between the test results and the Elwood and

Eberhard (2006) model, with an average S_{test}/S_{model} ratio of 0.83 and COV of 0.08.

Figure 5-18 shows the comparison of effective stiffness between the test results and the

Elwood and Eberhard (2009) model, with an average S_{test}/S_{model} ratio of 0.59 and

COV of 0.08. The coefficients of variation are the same for all models. The average ratios

indicate that the Elwood and Eberhard (2006) model provides the best estimation of
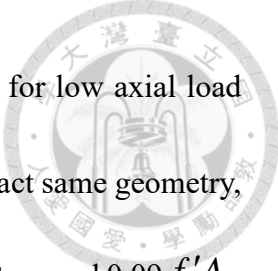
effective stiffness. However, it is mentioned in **Section 4.3.2** that initial cracks have formed on the two columns before the subjection of ground motions, thus, the effective stiffness values might be softened. This leads to the model which has the lowest estimated effective stiffness value be the one with the highest accuracy, but still overestimated. As a result, the comparison for the flexural-dominated columns may not be referenceable.

For the shear-dominated columns, **Figure 5-19** shows the comparison of effective stiffness between the test results and the ASCE/SEI 41-17 (2017) model, with an average S_{test}/S_{model} ratio of 1.05 and COV of 0.24. **Figure 5-20** shows the comparison of effective stiffness between the test results and the Elwood and Eberhard (2006) model, with an average S_{test}/S_{model} ratio of 1.47 and COV of 0.26. **Figure 5-21** shows the comparison of effective stiffness between the test results and the Elwood and Eberhard (2009) model, with an average S_{test}/S_{model} ratio of 1.22 and COV of 0.29. The ASCE/SEI 41-17 (2017) model provides the estimation with best accuracy and convergence. However, **Figure 5-19** shows that the model overestimates the effective stiffness for some columns. These columns correspond to those that have formation of initial cracks before the subjection of ground motions as mentioned in **Section 4.3**. Neglecting the columns with initial cracks, the average ratio and COV of the ASCE/SEI 41-17 (2017) model can be improved to 1.16 and 0.17 respectively. The average ratio and COV of the Elwood and Eberhard (2006) model can be improved to 1.63 and 0.19

184

respectively. The average ratio and COV of the Elwood and Eberhard (2009) model can be improved to 1.35 and 0.24 respectively. Overall, the ASCE/SEI 41-17 (2017) model is still shown to provide the estimation with best accuracy and convergence.

Between the ASCE/SEI 41-17 (2017) and the Elwood and Eberhard (2006) models, both models provide constant effective stiffness ratios for columns under low axial loads, and the former provides a higher estimation to prevent being too conservative. The comparison results also show that they have around the same values of coefficients of variation since both models have constant ratios for low axial load conditions, while the former provides better estimation results. Since the Elwood and Eberhard (2009) model varies with the change in axial loads and column shear spans, it has a higher coefficient of variation, while providing improved accuracy compared with the Elwood and Eberhard (2006) model. **Figure 5-22** plots the estimated effective stiffness for the three models together. It can be observed that the effective stiffness is governed by the column geometry and axial load instead of shear or flexure behavior, since the 4DL and 4NL specimens have the same effective stiffness, and the 3DL and 3NL specimens have the same effective stiffness. Since the applied axial loads for all columns are below or around $0.1 f_c' A_g$, the effective stiffness for the ASCE/SEI 41-17 (2017) and the Elwood and Eberhard (2006) models and only vary with the change in column height, with the former one having higher estimated values. The effective stiffness for the Elwood and Eberhard

185
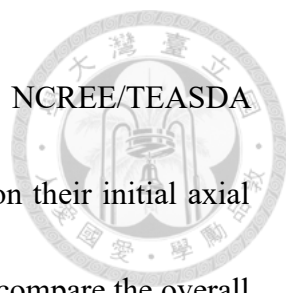
(2009) model is shown to be sensitive to changes in axial load even for low axial load conditions. Take frame T1 for example, the three columns have the exact same geometry, but the two outer columns (T1C1 and T1C3) have applied axial loads at around $0.09 f_c' A_g$ and the center column (T1C2) has an applied axial load at around $0.03 f_c' A_g$. The figure shows that the Elwood and Eberhard (2009) model estimated stiffness around the same value with the ASCE/SEI 41-17 (2017) model for the outer columns which has higher axial loads, and estimated stiffness around the same value with the Elwood and Eberhard (2006) model for the center column which has a lower axial load.

Overall, the ASCE/SEI 41-17 (2017) model is shown to be simple and accurate, while the Elwood and Eberhard (2009) model is shown to provide elaborate estimations for low axial load conditions, and the Elwood and Eberhard (2006) model is shown to be conservative. NCREE/TEASDA (2021) takes into account the effective stiffness model recommended by ASCE/SEI 41-17 (2017) for the development of shear and flexural backbone curves for RC columns in **Section 2.2**. The comparison results in this section show the accuracy and feasibility of the model on predicting the effective stiffness of shaking table-tested RC columns.

5.6 Modeling of Column Backbone Curve

Figure 5-23 to **Figure 5-26** plot the hysteresis curves of the shaking table tests and

their corresponding analytical backbone curves recommended by NCREE/TEASDA (2021) (**Section 2.2.1** and **Section 2.2.2**), and are estimated based on their initial axial load. The curves are plotted for all the nine columns in Su (2007) to compare the overall lateral load-displacement relationship between the analytical models and shaking table test responses. As mentioned in the introduction, these cyclic loading-based analytical models are yet to be verified for the estimation of shaking table test behaviors. The comparison in this section sums up the overall comparison results in this chapter, and the model backbone curves are plotted as blue lines on the figures.

For the columns in frame T1, the comparisons are provided in **Figure 5-23**. Columns T1C1 and T1C3 are flexural-dominated columns and are estimated with the flexural-shear backbone curve presented in **Section 2.2.2**. Column T1C2 is a shear-dominated column and is estimated with the shear backbone curve presented in **Section 2.2.1**. The strength estimations for the outer columns are accurate, and conservative for the center column. The stiffness estimations for the outer columns are too stiff, since initial cracks have formed on the column before the input of ground motions, the test initial stiffness is expected to be softened. The stiffness estimation for the center column is accurate. Column T1C1 develops a very large lateral deformation due to the collapse of column T1C3, this behavior is not simulated by the backbone curve. Column T1C3 experiences a reloading stiffness degradation due to the opening of shear cracks, this behavior is not

187

simulated by the backbone curve. Overall, the pre-failure behaviors are still simulated well by the analytical models. The backbone curve predicts a much smaller collapse point displacement for the center column, which is more conservative.

For the columns in frame T2, the comparisons are provided in **Figure 5-24**. Columns T2C1 and T2C3 are shear-dominated columns and are estimated with the shear backbone curve presented in **Section 2.2.1**. The strength and stiffness estimations for the two columns are accurate. Column T2C1 doesn't develop much post-strength behavior. Column T2C3 develops clear strength degradation behavior, and the displacement of the analytical model corresponds well with the test behavior.

For the columns in frame T3, the comparisons are provided in **Figure 5-25**. Columns T3C1 and T3C3 are shear-dominated columns and are estimated with the shear backbone curve presented in **Section 2.2.1**. The strength estimation is very conservative for column T3C1, as column T3C1 is explained to be interfered by flexural behavior. The strength estimation for column T3C3 is accurate. The stiffness estimations for the two columns are accurate. The backbone curves slightly overestimate the displacement at strength point, while predicting a much smaller collapse point displacement for the two columns, which is more conservative.

For the columns in frame T4, the comparisons are provided in **Figure 5-26**. Columns T4C1 and T4C3 are shear-dominated columns and are estimated with the shear backbone

188

curve presented in **Section 2.2.1**. The strength estimations are slightly conservative for both columns. The stiffness estimations for the two columns are accurate. The backbone curves predict the displacement at strength point accurately, while predicting a smaller collapse point displacement for the two columns, which is more conservative.

The strength point and collapse point displacements are complicated to simulate for the shear-dominant columns. It can be observed that for the columns with ductile reinforcement design (T2C1 and T2C3), the analytical model predicts the overall displacement development accurately. While for columns with nonductile reinforcement design (T1C2, T3C1, T3C3, T4C1, and T4C3), the actual test result varies quite significantly from the predicted displacement behavior. The significant difference in the accuracy is due to the difference in contribution from different materials. With the uniform steel reinforcements being the dominant material, the analytical model can predict displacement behaviors more accurately with smaller variance. With concrete being the dominant material, the test responses may vary significantly with the analytical models due to the variance of the material. Overall, the cyclic loading-based analytical models provided by NCREE/TEASDA (2021) (**Section 2.2**) for simulating the flexural-dominant or shear-dominant lateral load-displacement behavior of RC columns are shown to be capable of simulating actual shaking table-tested responses.

CHAPTER 6: HYSTERESIS MODELING OF SHAKING TABLE TESTS

6.1 Introduction
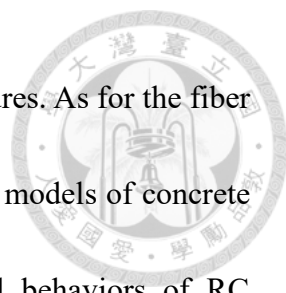
In order to perform seismic assessment for low-rise RC structures, NCREE published the "Technology Handbook for Seismic Evaluation and Retrofit of School Buildings" (NCREE 2008, 2009, 2013) handbooks to provide guidance for engineers on the seismic assessment of school buildings. To consider the large varying axial load of high-rise buildings when performing seismic assessment, NCREE published TEASPA V3.1 (2018) and TEASPA V4.0 (2020) to include recommendation procedures on the setup of PMM flexural hinges in structural analysis program ETABS. However, the mentioned guidance for seismic assessments are all based on nonlinear static pushover analysis, which holds its accuracy for low-rise buildings, but could not take into account the higher mode effects and torsional effects of medium-to-high-rise structures. Based on this drawback, NCREE then published the "Taiwan Earthquake Assessment for RC Structures by Dynamic Analysis" (NCREE/TEASDA 2021) handbook to provide guidance on dynamic analysis of RC structures.

Backbone curves of RC columns have already been developed for monotonic pushover analysis in TEASPA V3.1 (2018), however, it is required for the definition of
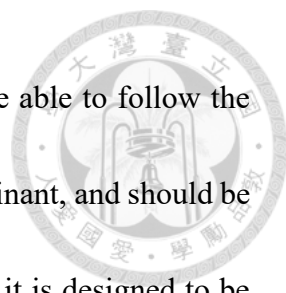
unloading and reloading stiffness behavior if cyclic loading analysis and nonlinear time domain analysis are to be performed. NCREE/TEASDA (2021) recommended using Pivot model (Dowell et al. 1998) to define the hysteresis behavior of RC columns using the optimized parameter calculation formula proposed by Ling et al. (2022) in structural analysis software ETABS. **Section 2.4.1** introduces the Pivot model and the optimized formulas by Ling et al. (2022). Ling et al. (2022) develops the formulas based on the hysteresis behavior of cyclic loading tests of RC columns. The feasibility for the proposed hysteresis parameters to model actual shaking table test behaviors is yet to be verified. The test results in Su (2007) provide a good chance to verify the cyclic loading-based hysteresis parameters by Ling et al. (2022) with shaking table-tested column responses governed by shear or flexural behaviors.

NCREE/TEASDA (2021) only provided guidance for column modeling in structural analysis software ETABS and SAP2000, which constructs the numerical models through nodes and elements, and simulates nonlinear behaviors by nonlinear hinges. OpenSees (Open System for Earthquake Engineering Simulation) (McKenna et al. 2000) is a structural analysis program for earthquake engineering research. Its open-source design provides a high degree of freedom during construction of analytical models and analysis procedures. As introduced in **Section 2.3**, OpenSees provides a wide range of elements, materials, and analysis methods, and is utilized by researches worldwide when

192
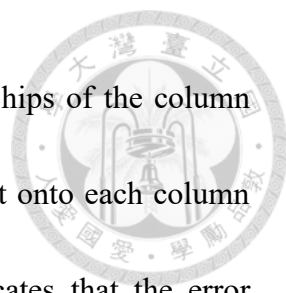
performing seismic analyses on a wide range of members and structures. As for the fiber

section in OpenSees, it is constructed based on constitutive material models of concrete

and reinforcement steel, which allows users to simulate flexural behaviors of RC

members accurately. The flexural behavior of a fiber section is simulated based on the

assumption of plane remain plane of continuous sections throughout the whole member.

However, discontinuities may form in sections of abrupt changes in cross-sectional

dimensions, or with the presence of concentrated loads or reactions that may cause

disturbances in the flow of internal forces. In these discontinuous regions, the shear

stresses are no longer uniform over the depth of the member, and the shear strength should

not be estimated with continuous sections. In this case, the fiber section may not estimate

the shear strength of these discontinuous regions well, and an additional lateral load-

displacement relationship that simulates shear behavior of RC members should be

implemented with the fiber section to consider both behaviors. To conclude,

NCREE/TEASDA (2021) provides a good guidance on the modeling of RC columns by

concentrated plastic hinges. To promote this modeling method for wider applications,

research can be performed to transform the concentrated plastic hinge model in

NCREE/TEASDA (2021) into OpenSees software. On the other hand, a RC column

numerical model that can simulate both the flexural and shear behavior, based on the fiber

section in OpenSees, should be developed for accurate simulation on flexural behavior

and considers shear behavior at the same time. The model should be able to follow the fiber section flexural behavior when it is designed to be flexural-dominant, and should be able to follow the shear lateral load-displacement relationship when it is designed to be shear-dominant.

Based on the above objectives, this chapter introduces the concentrated plastic hinge column model (ETABS model) recommended by NCREE/TEASDA (2021) in ETABS program, and the proposed concentrated plastic hinge column model (CPH model) and fiber section column model (Fiber model) inside OpenSees program. The backbone curves for flexural-dominant columns and shear-dominant columns for each model will be compared together to observe their differences.

To validate the hysteresis modeling by Ling et al. (2022) with shaking table-tested column responses, the overall energy dissipation capacity of the test hysteresis curve and the model hysteresis curve should be calculated and compared. Several factors can contribute to differences between the hysteresis curves of test results and analytical results, such as: differences in lateral load-displacement relationship, differences in unloading stiffness for each drift, differences in reloading stiffness for each drift, and differences in developed lateral displacement. To validate the analytical hysteresis models, the main factors in concern are the accuracy of unloading and reloading stiffness, therefore, the errors contributed from lateral load-displacement relationship and modeled lateral
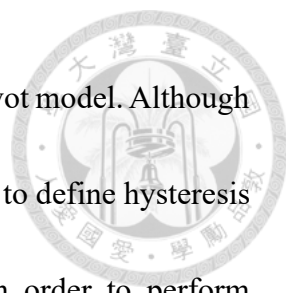
displacement should be taken out. The force-displacement relationships of the column

models are calculated based on provided backbone curves and input onto each column

prior to the implementation of time history analysis, which indicates that the error

contribution could not be neglected. As for the error from modeled lateral displacement,

the lateral displacement time history results of column models may not be same as the

actual test behavior, this may contribute to large errors when calculating the overall

energy dissipation capacities of the hysteresis curves. To take out this error, displacement

history analysis is performed on the column models based on actual lateral displacement

time history response from the test results. To simplify this analysis procedure, only the

drifts which contribute to large lateral deformations and development of energy

dissipation capacities would be taken into consideration. The energy dissipation

capacities of each hysteresis curve are then calculated and compared.

Lastly, the corresponding nonlinear time history analysis results of each model are

presented and compared with the shaking table test results presented in **Chapter 4** in

detail. The accuracy of each model is compared. The stiffness time history response of

the models and overall behaviors would be discussed at the last section in this chapter.

6.2 Conversion of Pivot Model Parameters into OpenSees

Ling et al. (2022) provided optimized equations to calculate parameters for the

definition of unloading and reloading stiffness degradations on the Pivot model. Although

Pivot model is widely applied by various structural analysis software to define hysteresis

behavior of RC members, it is not implemented in OpenSees. In order to perform

nonlinear time history analysis on the CPH and Fiber models in OpenSees, alternative

and applicable hysteresis models should be chosen in OpenSees to represent Pivot model.

OpenSees provides users with a variety of hysteresis models, but doesn't provide

validated equations to calculate the hysteresis behaviors of each model. To develop new

optimized equations for the hysteresis model parameters inside OpenSees would be time

consuming. As a result, this research proposes to transform the well-validated hysteresis

parameter equations by Ling et al. (2022) into chosen hysteresis models inside OpenSees.

The Pinching4 material model (Pinching4 model) provides a quadrilinear input for force-

displacement relationship, and allows for definition on the pinching point and unloading

stiffness degradation, which is the most direct model for the input of NCREE/TEASDA

(2021) backbone curves (**Figure 2-1** and **Figure 2-5**) and transformation for the Pivot

model hysteresis parameters. To promote hysteresis modeling inside OpenSees, the

conversion for Pivot model parameters into the Hysteretic material model (Hysteretic

model) is also shown in this section. The Hysteretic model provides a trilinear input for

force-displacement relationship, and allows for definition on the pinching point and

unloading stiffness degradation. This section introduces the hysteresis behavior of the two

196

models, and provides transformation equations for the analytical definition of their hysteresis behaviors.

Figure 6-1 shows the test hysteresis curves (black lines) for three categories of failure patterns for RC columns, flexural failure, flexural-shear failure, and shear failure. The simulated hysteresis behavior through Pivot model is plotted on the figure as magenta curves. The pinching points and unloading stiffness degradations of the model are shown to correspond with the test responses well. To quantify and compare the accuracy of the simulation on hysteresis behaviors for the Pivot model with test responses, the overall energy dissipation capacity is measured and calculated in ratios. For the flexural-dominant column, the ratio of E_{test}/E_{Pivot} is 1.11. For the flexural-shear-dominant column, the ratio of E_{test}/E_{Pivot} is 1.05. For the shear-dominant column, the ratio of E_{test}/E_{Pivot} is 0.76. The values are summarized in **Table 6-1**. Ling et al. (2022) provided analytical procedure to define the hysteresis behavior of RC columns based on their design parameter, and the results show that the equations provide good accuracy on test responses. The hysteresis curves for the Pinching4 model and Hysteretic model would be plotted in the same manner and the ratio of energy dissipation capacity would be compared within the same model in this section.
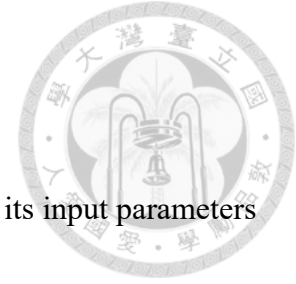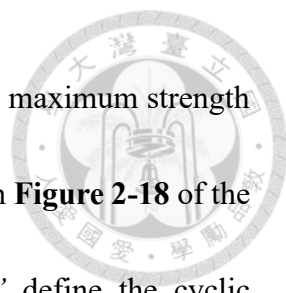
6.2.1 Pinching4 Material Model

Section 2.3.4 introduces the Pinching4 model in OpenSees and its input parameters are shown in **Figure 2-9**. Pinching4 model allows for a quadrilinear input for the force-displacement relationship of the model, which can be used as input for the quadrilinear flexural-shear backbone curve (**Figure 2-5**) and trilinear shear backbone curve (**Figure 2-1**) of RC columns. The input command for Pinching4 model is as follows:

uniaxialMaterial Pinching4 $matTag $ePf1 $ePd1 $ePf2 $ePd2 $ePf3 $ePd3 $ePf4

$ePd4 $rDispP $rForceP $uForceP $gK1 $gK2 $gK3 $gK4 $gKLim $gD1 $gD2 $gD3

$gD4 $gDLim $gF1 $gF2 $gF3 $gF4 $gFLim $gE $dmgType

The command *"$matTag"* defines the number tag of this specific material model. The commands *"$ePf1 $ePd1"* define the first point on the force-displacement curve in the positive direction, and the rest from 2 to 4 follows. For symmetric backbone curves, only definition in the positive direction is required. The command *"$rDispP"* defines the ratio of the deformation at which reloading occurs to the maximum historic deformation demand, which corresponds to the deformation at the pinching pivot point (parameter β) in **Figure 2-18** of the Pivot model. The command *"$rForceP"* defines the ratio of the force at which reloading begins to force corresponding to the maximum historic deformation demand, which corresponds to the force at the pinching pivot point (parameter β) in **Figure 2-18** of the Pivot model. The command *"$uForceP"* defines the

<div align="center">198</div>

ratio of strength developed upon unloading from negative load to the maximum strength

developed under monotonic loading, which is defined as zero value in **Figure 2-18** of the

Pivot model. The commands *"$gK1 $gK2 $gK3 $gK4 $gKLim"* define the cyclic

degradation model for unloading stiffness degradation, which corresponds to the

definition of the primary pivot point (parameter α) in **Figure 2-18** of the Pivot model.

The commands *"$gD1 $gD2 $gD3 $gD4 $gDLim"* define the cyclic degradation model

for reloading stiffness degradation, which is not simulated by the Pivot model. The

commands *"$gF1 $gF2 $gF3 $gF4 $gFLim"* define the cyclic degradation model for

strength degradation, which is not simulated by the Pivot model. The commands *"$gE*

$dmgType" define the ratio of maximum energy dissipation capacity and the type of

damage for the model.

Based on the above introduction, the commands *"$rDispP $rForceP"* are shown to

simulate the same behavior as the parameter β of the Pivot model, and the commands

"$gK1 $gK2 $gK3 $gK4 $gKLim" are shown to simulate the same behavior as the

parameter α of the Pivot model. The transformation of hysteresis parameters of Pivot

model to Pinching4 model would focus on the above commands, while the rest remain

their default values.

Ling et al. (2022) proposed the parameter β as the ratio to the force of the yielding

strength or cracking strength at which the reloading curves intersect. For flexural-

dominant columns, the yielding strength is used, and is taken as $0.75V_{mn}$. For shear-dominant columns, the shear cracking strength is used, and is taken as $0.6V_n$. Since the parameter β is governed by force, the command *"$rDispP"* is simplified as zero to focus the reloading behavior of the Pinching4 model on force. For the Pivot model, the parameter β is defined between 1.0 to 0.0, with 1.0 indicating full development of reloading strength and 0.0 indicating full degradation of reloading strength. Detailed explanation of the parameter is provided in Ling et al. (2022). For the Pinching4 model, the command *"$rDispP"* is defined between 1.0 to 0.0, with 1.0 indicating full development of reloading strength and 0.0 indicating full degradation of reloading strength. The values seem straightforward for direct transformation from β to *$rDispP*. However, full development of reloading strength of the Pivot model is up to the yielding point or the shear cracking point, and full development of reloading strength of the Pinching4 model is up to the maximum strength. As a result, the command *"$rDispP"* should be degraded and calculated separately for flexural and shear-dominant columns as follows:

$$\$rDispP_F = \beta_F \times 0.75 \tag{6.1}$$

$$\$rDispP_S = \beta_S \times 0.6 \tag{6.2}$$

The calculation of parameter β is provided in **Eqs. (2.32)** and **(2.34)**.

Ling et al. (2022) proposed the parameter α as the ratio to the extended point of the yielding strength or cracking strength at which the extended unloading curves intersect. For flexural-dominant columns, the yielding strength is used, and is taken as $0.75V_{mn}$. For shear-dominant columns, the shear cracking strength is used, and is taken as $0.6V_n$. For the Pivot model, the parameter α is defined between 10.0 to 0.0, with 10.0 indicating no degradation of unloading stiffness and 0.0 indicating full degradation of unloading stiffness. This indicates the unloading stiffness degradation is slightly degraded even when the parameter α is set to its upper limit at a value of 10. Detailed explanation of the parameter is provided in Ling et al. (2022). For the Pinching4 model, the unloading stiffness degradation rule is defined below:

$$k_i = k_0(1 - \delta k_i) \tag{6.3}$$

$$\delta k_i = \left[gK1(d_{max})^{gK3} + gK2 \left(\frac{E_i}{E_{monotonic}} \right)^{gK4} \right] \leq gKLim \tag{6.4}$$

The unloading stiffness is shown to be a portion of the initial stiffness of the Pinching4 model, and the degradation behavior is governed by maximum deformation and energy dissipated. To simplify the model, values for *$gK1 $gK2 $gK3 $gK4* are set to 1.0 which allows for *$gKLim* to govern the unloading stiffness behavior for the model, with 0.0 indicating no degradation of and 1.0 indicating full degradation. Since the unloading stiffness is shown to be a portion of the initial stiffness, if the backbone curves in **Figure**

201

2-1 and **Figure 2-5** are directly input into Pinching4 model, no modifications are required.

The command *"$gKLim"* should be calculated separately for flexural and shear-dominant

columns as follows:

$$\$gKLim_F = 1 - 0.1\alpha_F \tag{6.5}$$

$$\$gKLim_S = 1 - 0.1\alpha_S \tag{6.6}$$

However, if changes have been made on the initial stiffness for further modeling purposes,

consideration on the changed initial stiffness should be taken. The unloading stiffness

should be remained as the same portion of the initial stiffness before the change in the

initial stiffness value. The modified command *"$gKLim_{modified}"* should be calculated

separately for flexural and shear-dominant columns as follows:

$$\$gKLim_{modified,F} = 1 - 0.1\alpha_F \frac{k_{initial}}{k_{modified}} \tag{6.7}$$

$$\$gKLim_{modified,S} = 1 - 0.1\alpha_S \frac{k_{initial}}{k_{modified}} \tag{6.8}$$

The calculation of parameter α is provided in **Eqs. (2.31)** and **(2.33)**. $k_{initial}$ is the

original input initial stiffness for the column backbone curves in Pinching4 model, and

$k_{modified}$ is the modified input initial stiffness.

Based on the above transformation parameters, the simulated hysteresis behavior for

the three categories of failure patterns of RC columns through Pinching4 model is plotted

on **Figure 6-2** as green curves, and the test hysteresis curves are plotted as black curves.
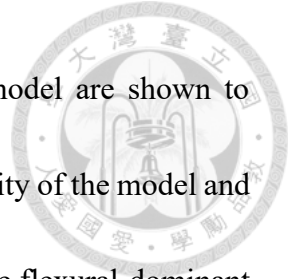
The pinching points and unloading stiffness degradations of the model are shown to correspond with the test responses well. The energy dissipation capacity of the model and test are calculated for each column for quantified comparison. For the flexural-dominant column, the ratio of $E_{test}/E_{Pinching4}$ is 0.91. For the flexural-shear-dominant column, the ratio of $E_{test}/E_{Pinching4}$ is 0.94. For the shear-dominant column, the ratio of $E_{test}/E_{Pinching4}$ is 0.72. The values are summarized in **Table 6-1**. The results show that the transformed parameters provide good accuracy with test responses. Since the hysteresis parameters are transformed from Pivot model to Pinching4 model, the ratios between their energy dissipation capacity can also be compared. For the flexural-dominant column, the ratio of $E_{Pivot}/E_{Pinching4}$ is 0.82. For the flexural-shear-dominant column, the ratio of $E_{Pivot}/E_{Pinching4}$ is 0.90. For the shear-dominant column, the ratio of $E_{Pivot}/E_{Pinching4}$ is 0.96. The values are summarized in **Table 6-2**. The results show good correspondence between the two models. To sum up, the behavior for the transformed hysteresis parameters in Pinching4 model show good consistence with the original Pivot model behavior, and the analytically defined energy dissipation capacity of Pinching4 model is shown to capture the actual test hysteresis behavior well. This research will implement the Pinching4 model as an input for the column backbone curves in **Figure 2-5** and **Figure 2-1** into OpenSees for the modeling of column hysteresis behaviors.
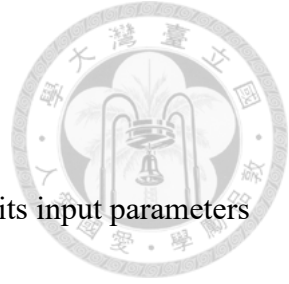
6.2.2 Hysteretic Material Model

Section 2.3.4 introduces the Hysteretic model in OpenSees and its input parameters

are shown in **Figure 2-10**. Hysteretic model allows for a trilinear input for the force-

displacement relationship of the model, which can be used as input for the trilinear shear

backbone curve (**Figure 2-1**) but not suitable for the quadrilinear flexural-shear backbone

curve (**Figure 2-5**) of RC columns. **Section 6.2.1** concluded that the Pinching4 model

would be used as input for the column backbone curves due to its capability for the input

of quadrilinear force-displacement relationships. The transformation equations for Pivot

model hysteresis parameters to Hysteretic model hysteresis parameters will still be

developed to provide for wider applications of hysteresis behavior in OpenSees. The input

command for Hysteretic model is as follows:

uniaxialMaterial Hysteretic $matTag $s1p $e1p $s2p $e2p $s3p $e3p $s1n $e1n

$s2n $e2n $s3n $e3n $pinchX $pinchY $damage1 $damage2 $beta

The command *"$matTag"* defines the number tag of this specific material model. The

commands *"$s1p $e1p"* define the first point on the force-displacement curve in the

positive direction, and the rest from 2 to 3 follows. The definition is also the same in the

negative direction. The command *"$pinchX"* is the pinching factor for deformation

during reloading, which corresponds to the deformation at the pinching pivot point

(parameter β) in **Figure 2-18** of the Pivot model. The command *"$pinchY"* is the

pinching factor for deformation during reloading, which corresponds to the force at the

pinching pivot point (parameter β) in **Figure 2-18** of the Pivot model. The command

"$damage1 $damage2" defines the reloading strength degradation due to ductility and

energy for the model. The command *"$beta"* defines the degraded unloading stiffness

based on ductility, which corresponds to the definition of the primary pivot point

(parameter α) in **Figure 2-18** of the Pivot model.

Based on the above introduction, the commands *"$pinchX $pinchY"* are shown to

simulate the same behavior as the parameter β of the Pivot model, and the command

"$beta" is shown to simulate the same behavior as the parameter α of the Pivot model.

The transformation of hysteresis parameters of Pivot model to Hysteretic model would

focus on the above commands, while the rest remain their default values.

Ling et al. (2022) proposed the parameter β as the ratio to the force of the yielding

strength or cracking strength at which the reloading curves intersect. For flexural-

dominant columns, the yielding strength is used, and is taken as $0.75V_{mn}$. For shear-

dominant columns, the shear cracking strength is used, and is taken as $0.6V_n$. Since the

parameter β is governed by force, the command *"$pinchX"* is simplified to its default

value at 0.5 to focus the reloading behavior of the Hysteretic model on force. For the

Pivot model, the parameter β is defined between 1.0 to 0.0, with 1.0 indicating full

development of reloading strength and 0.0 indicating full degradation of reloading
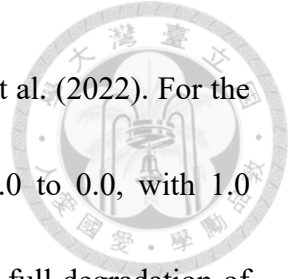
strength. Detailed explanation of the parameter is provided in Ling et al. (2022). For the

Hysteretic model, the command *"$pinchY"* is defined between 1.0 to 0.0, with 1.0

indicating full development of reloading strength and 0.0 indicating full degradation of

reloading strength. The values seem straightforward for direct transformation from β to

$pinchY. However, full development of reloading strength of the Pivot model is up to the

yielding point or the shear cracking point, and full development of reloading strength of

the Hysteretic model is up to the maximum strength. As a result, the command *"$pinchY"*

should be degraded and calculated separately for flexural and shear-dominant columns as

follows:

$$\$pinchY_F = \beta_F \times 0.75 \tag{6.9}$$

$$\$pinchY_S = \beta_S \times 0.6 \tag{6.10}$$

The calculation of parameter β is provided in **Eqs. (2.32)** and **(2.34)**.

Ling et al. (2022) proposed the parameter α as the ratio to the extended point of the

yielding strength or cracking strength at which the extended unloading curves intersect.

For flexural-dominant columns, the yielding strength is used, and is taken as $0.75V_{mn}$.

For shear-dominant columns, the shear cracking strength is used, and is taken as $0.6V_n$.

For the Pivot model, the parameter α is defined between 10.0 to 0.0, with 10.0 indicating

no degradation of unloading stiffness and 0.0 indicating full degradation of unloading

206

stiffness. This indicates the unloading stiffness degradation is slightly degraded even

when the parameter α is set to its upper limit at a value of 10. Detailed explanation of

the parameter is provided in Ling et al. (2022). For the Hysteretic model, the unloading

stiffness degradation is defined below:

$$k_i = k_0 m_u^{-beta} \tag{6.11}$$
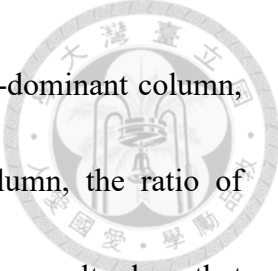
The unloading stiffness is shown to be a portion of the initial stiffness of the Hysteretic

model, and the degradation behavior is governed by the input command *"$beta"* with 0.0

indicating no degradation of and 1.0 indicating full degradation. The command *"$beta"*

should be calculated separately for flexural and shear-dominant columns as follows:

$$\$beta_F = 1 - 0.1\alpha_F \tag{6.12}$$

$$\$beta_S = 1 - 0.1\alpha_S \tag{6.13}$$

The calculation of parameter α is provided in **Eqs. (2.31)** and **(2.33)**.

Based on the above transformation parameters, the simulated hysteresis behavior for

the three categories of failure patterns of RC columns through Hysteretic model is plotted

on **Figure 6-3** as blue curves, and the test hysteresis curves are plotted as black curves.

The pinching points and unloading stiffness degradations of the model are shown to

correspond with the test responses well. The energy dissipation capacity of the model and

test are calculated for each column for quantified comparison. For the flexural-dominant

column, the ratio of $E_{test}/E_{Hysteretic}$ is 0.94. For the flexural-shear-dominant column, the ratio of $E_{test}/E_{Hysteretic}$ is 1.11. For the shear-dominant column, the ratio of $E_{test}/E_{Hysteretic}$ is 0.84. The values are summarized in **Table 6-1**. The results show that the transformed parameters provide good accuracy on test responses. Since the hysteresis parameters are transformed from Pivot model to Hysteretic model, the ratios between their energy dissipation capacity can also be compared. For the flexural-dominant column, the ratio of $E_{Pivot}/E_{Hysteretic}$ is 0.85. For the flexural-shear-dominant column, the ratio of $E_{Pivot}/E_{Hysteretic}$ is 1.06. For the shear-dominant column, the ratio of $E_{Pivot}/E_{Hysteretic}$ is 1.11. The values are summarized in **Table 6-2**. The results show good correspondence between the two models. To sum up, the behavior for the transformed hysteresis parameters in Hysteretic model show good consistence with the original Pivot model behavior, and the analytically defined energy dissipation capacity of Hysteretic model is shown to capture the actual test hysteresis behavior well. The Hysteretic model would not be used on the modeling of hysteresis behavior of columns in this research, but the transformation equations provide wider applications for the implementation of the Hysteretic model in OpenSees.

6.3 Description of the Analytical Model

Analytical models are constructed in ETABS and OpenSees to perform nonlinear
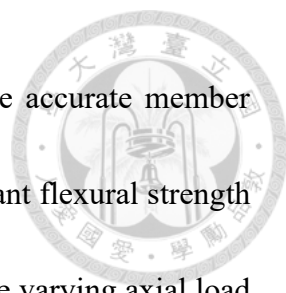
time history analysis. As mentioned in the introduction, a concentrated plastic hinge model (ETABS model) is constructed in ETABS following NCREE/TEASDA (2021) recommendations, a concentrated plastic hinge model (CPH model) and a fiber section model (Fiber model) is developed in OpenSees by this research. This section introduces the setup of each model. **Figure 4-9** shows the design drawing of the specimen setup for the shaking table test specimens in Su (2007). The setup of the top steel beam and the columns are simulated by the column model in **Figure 6-4**. The circles in the figure indicate the location of nodes, the top steel beam is simulated by rigid beam-column elements indicated as wide black lines in the figure, and the column bodies are simulated by nonlinear beam-column elements indicated as thin black lines in the figure. The bottom foundations of the column specimens are not simulated, and the bottom nodes of the column models are fixed on the floor where ground motions are applied. All three column models share the same setup on the position of nodes and elements, the top steel beams are all simulated with rigid elements, and it is the column bodies that vary with different models. **Figure 6-5** shows a simplified indication of the three models. The two node elements with different modeling setups are input onto the nonlinear elements on the frame in **Figure 6-4** to form different frame models, and these frame models are then subjected to ground motions to perform nonlinear time history analysis. This section will introduce all three models.

209
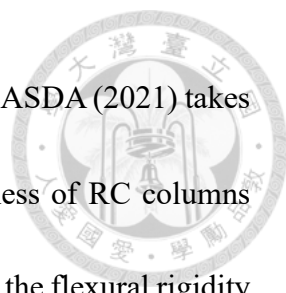
6.3.1 ETABS Concentrated Plastic Hinge Model

The concentrated plastic hinge model introduced in this section is constructed in structural analysis program ETABS following the procedure recommended by NCREE/TEASDA (2021). The model will be abbreviated as ETABS model for the following contents. **Figure 6-5 (c)** shows the setup of ETABS model. Two flexural hinges are setup at the top and bottom of the column with moment-rotation relationship to consider the change in curvature due to the column boundary conditions, and a shear hinge is setup at the center of the column with force-displacement relationship. It is concluded in **Chapter 5** that considering the varying axial load on flexural strength and neglecting the varying axial load on shear strength can provide with a better strength estimation result, while neglecting the varying axial load for both flexural strength and shear strength can provide just enough accuracy. It is mentioned in **Chapter 2** that ETABS provided the P-M-M hinge to consider the effect of varying axial load on the column flexural strength, and that this varying axial load hinge could be implemented on the column model to provide a more accurate analysis result. This concept can be easily implemented in pushover analysis, where the analysis is monotonic and the flexural strength can be updated within each monotonic step due to change in subjected axial load. Although the analysis procedure to update the flexural strength due to change in axial load for each monotonic step when using the P-M-M hinge is more time-consuming

210

compared with a constant flexural strength model, to achieve more accurate member simulation behaviors, both the increased time compared to the constant flexural strength model and the overall time taken is acceptable. However, to apply the varying axial load hinge into nonlinear time domain analysis is impracticable. Numerous lateral drifts in both directions develop during nonlinear time domain analysis, indicating that the flexural strength would have to be updated for numerous times under different axial loads throughout the time history response, leading to severely time-consuming analysis procedure. Since it is concluded in **Chapter 5** that neglecting the varying axial load for both flexural strength and shear strength can provide just enough accuracy, as a result, the ETABS model is constructed with constant axial load (constant strength) flexural and shear hinges.

The concept of ETABS model focuses the linear behavior of the column on the element section, indicated by the black line in **Figure 6-5 (c)**, and distributes the nonlinear flexural behavior onto the flexural hinges and the nonlinear shear behavior onto the shear hinge. The nonlinear hinge which has the lower strength will dominate the nonlinear behavior of the column. This concept allows the failure pattern of the column to not be pre-defined, since the initial linear behavior is simulated by the same column element. It is up to the point when the force demand exceeds the nonlinear strength of either hinges that the nonlinear behavior will be governed either by flexural or shear behavior.

211

The column element is defined with a linear section. NCREE/TEASDA (2021) takes the recommendation of ASCE/SEI 41-13 (2014) on the linear stiffness of RC columns into consideration. For columns with axial loads lower than $0.1 f_c' A_g$, the flexural rigidity and shear rigidity should be taken as follows:

$$Flexural\ Rigidity = 0.3 E_c I_g \tag{6.14}$$

$$Shear\ Rigidity = 0.4 E_c A_w \tag{6.15}$$

Where E_c is the concrete elastic modulus, I_g is the sectional moment of inertia, and A_w can be taken as bd. The flexural rigidity is contributed by flexural deformations and reinforcement slips between the column body and the foundations or joints. The shear rigidity is contributed by shear deformations. The above parameters are input into the column section in ETABS to define the linear behavior of the column model.

The flexural hinge is defined by the flexural backbone curve in **Figure 2-5** as introduced in **Section 2.2.2**. Since the axial loads of the specimens in this research varies under low axial load values, the fixed axial load flexural hinge (M2, M3) is used for efficient analysis process. The column model focuses the linear behavior on the column element, and focuses the nonlinear behavior on the hinges. However, he backbone curve in **Figure 2-5** includes the linear section, and should be taken out if the hinge is to be applied on the linear column model otherwise the linear deformations would be
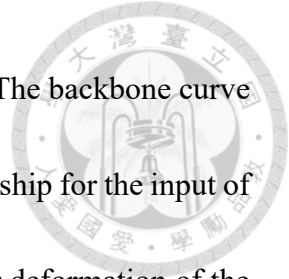
considered twice and the stiffness of the column would be softened. The backbone curve

in **Figure 2-5** must also be transformed into moment-rotation relationship for the input of

flexural hinge. **Figure 6-6** shows the procedure to take out the linear deformation of the

flexural backbone curve and to input the curve into the flexural hinge on the column

model. The linear deformations at points C and D should be taken out and the linear

deformation at point E can be neglected since the linear stiffness does not contribute to

deformations at points without any strength. The calculation equations for deformations

at points C, D, and E are as follows:

$$c = \left(\Delta_{f.mn} - \frac{V_{mn}}{V_y} \Delta_{f,y} \right) / H \tag{6.16}$$

$$d = \left(\Delta_s - \frac{V_{mn}}{V_y} \Delta_{f,y} \right) / H \tag{6.17}$$

$$e = \frac{\Delta_a}{H} \tag{6.18}$$

Section 2.2.2 provides calculation procedure and equations for the parameters in the

above equations.

The shear hinge is defined by the shear backbone curve in **Figure 2-1** as introduced

in **Section 2.2.1**. However, as mentioned previously, the column model focuses the linear

behavior on the column element, and focuses the nonlinear behavior on the hinges. The

backbone curve in **Figure 2-1** includes the linear section, and should be taken out as

discussed previously. **Figure 6-7** shows the procedure to take out the linear deformations

213
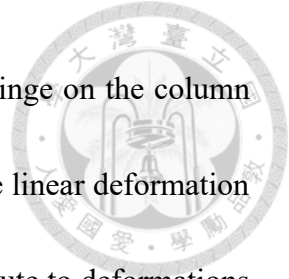
of the shear backbone curve and to input the curve onto the shear hinge on the column

model. The linear deformation at point C should be taken out and the linear deformation

at point D can be neglected since the linear stiffness does not contribute to deformations

at points without any strength. The calculation equations for deformations at points C and

D are as follows:

$$c = \left(\Delta_{s.n} - \frac{V_n}{V_{cr}}\Delta_{s,cr}\right)/H \tag{6.19}$$
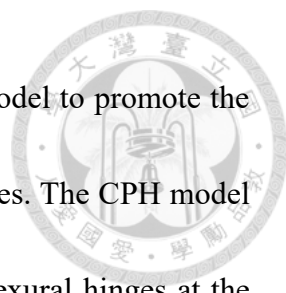
$$d = \frac{\Delta_a}{H} \tag{6.20}$$

Section 2.2.1 provides calculation procedure and equations for the parameters in the

above equations.

The combination of the above-mentioned linear column element and nonlinear

flexural and shear hinges can be indicated by **Figure 6-5 (c)**. To conclude, the ETABS

model can simulate linear flexural deformations, linear slip deformations, linear shear

deformations, nonlinear flexural behaviors, and nonlinear shear behaviors of actual RC

columns.

6.3.2 OpenSees Concentrated Plastic Hinge Model

The concentrated plastic hinge model introduced in this section is constructed in

structural analysis program OpenSees and is developed by this research. The model will

be abbreviated as CPH model for the following contents. As mentioned in the introduction,

the CPH model is developed based on the concept of the ETABS model to promote the column modeling concept of NCREE/TEASDA (2021) into OpenSees. The CPH model follows the modeling concept of ETABS model by applying two flexural hinges at the top and bottom of the column with moment-rotation relationship to consider the change in curvature due to the column boundary conditions, and a shear hinge on the column with force-displacement relationship. The linear behavior of the column is also setup to be focused on the linear element section. **Figure 6-8** provides the layout of the CPH model. The flexural hinges are indicated as flexural-shear rotational springs in the figure, and the shear hinge is indicated as shear lateral springs in the figure. The linear element is indicated as a uniform 3D rectangular section between the nodes. The hinges are setup on the column models through zero-length elements as introduced in **Section 2.3.6**, and the zero-length elements are applied on the top and bottom nodes in **Figure 6-8**. The CPH model is constructed by two end nodes and connected with a beam-column element (**Section 2.3.3**) as shown in **Figure 6-8**. To simplify the model setup, since the shear demand remains constant throughout the column body, setting up the shear hinge at the center or ends of the column provides the same response. As a result, the shear hinge is applied on the zero-length element on the bottom of the column to avoid additional definition of nodes at the center of the column.

The column element is constructed by defining an elastic section onto the beam-

215

column element. The command for the elastic section is as follows:

section Elastic $secTag $E $A $Iz $G $alphaY

To follow the concept of NCREE/TEASDA (2021) on the linear stiffness of the column model, the flexural rigidity and shear rigidity in **Eqs. (6.14)** and **(6.15)** are taken into consideration. *"$E"* is input as the concrete elastic modulus E_c. *"$A"* is input as the gross sectional area of the column. *"$Iz"* is input as the $0.3I_g$ for columns with axial load lower than $0.1 f_c' A_g$. *"$G"* is the shear modulus and is calculated with Poisson's ratio taken as 0.25. *"$alphaY"* is the shear shape factor and can be taken as $\frac{b}{d}$ for RC columns. The command for the beam-column element is as follows:

element nonlinearBeamColumn $eleTag $iNode $jNode $numIntgrPts $secTag $transfTag

"$iNode"* and *"$jNode" input the top and bottom nodes of the column. *"$numIntgrPts"* inputs the number of Gauss-Lobatto integration points along the element. *"$secTag"* inputs the tag of the elastic section defined previously. *"$transfTag"* inputs the global coordinate transformation function tag. The setup of this elastic section can consider the flexural deformations, shear deformations, and reinforcement slips between the column body and the foundations or joints.

The application of the flexural hinges onto the linear column model follows the procedure in **Section 6.3.1**. The linear deformations are taken out of the flexural backbone

216
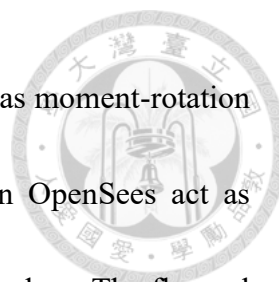
curve as discussed in **Figure 6-6**, and the backbone curves are input as moment-rotation relationship. As introduced previously, the zero-length elements in OpenSees act as hinges and allow for inputs of model behaviors on all degrees of freedom. The flexural hinges are defined through Pinching4 models, and the models are then applied onto the rotational degree of freedom on the top and bottom zero-length elements of the column model. The input command is as follows:

element zeroLength $eleTag $iNode $jNode -mat $FlexuralHinge -dir 3

The input parameters for the flexural hinge onto Pinching4 model are introduced in **Section 6.2.1** and the tag of the defined flexural hinge on Pinching4 model is input onto the zero-length element by command *"-mat $FlexuralHinge"* on the rotational direction by command *"-dir 3"*.The indications of the flexural springs are shown in **Figure 6-8** on the nodes on the column ends, since it is the flexural-shear backbone curves in **Figure 2-5** that is input on the springs, the springs are then defined as flexural-shear springs.

The application of the shear hinge onto the linear column model follows the procedure in **Section 6.3.1**. The linear deformations are taken out of the shear backbone curve as discussed in **Figure 6-7**, and the backbone curves are input as force-displacement relationship. As introduced previously, the zero-length elements in OpenSees act as hinges and allow for inputs of model behaviors on all degrees of freedom. The shear hinges are defined through Pinching4 models, and the models are then applied onto the

217
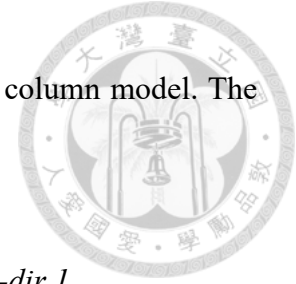
lateral degree of freedom on the bottom zero-length element of the column model. The input command is as follows:

element zeroLength $eleTag $iNode $jNode -mat $ShearHinge -dir 1

The input parameters for the shear hinge onto Pinching4 model are introduced in **Section 6.2.1** and the tag of the defined shear hinge model on Pinchgin4 model is input onto the zero-length element by command *"-mat $ShearlHinge"* on the lateral direction by command *"-dir 1"*. The indication of the shear spring is shown in **Figure 6-8** on the bottom column node, since it is the shear backbone curve in **Figure 2-1** that is input on the spring, the spring is then defined as shear spring.

The combination of the above-mentioned linear column element and nonlinear flexural-shear and shear springs can be indicated by **Figure 6-8**. To conclude, the CPH model can simulate linear flexural deformations, linear slip deformations, linear shear deformations, nonlinear flexural behaviors, and nonlinear shear behaviors of actual RC columns.

6.3.3 OpenSees Fiber Section Model

The fiber section model introduced in this section is constructed in structural analysis program OpenSees based on procedures provided by the OpenSees Official Website (https://opensees.berkeley.edu/). The model will be abbreviated as Fiber model for the

218

following contents. As introduced in **Section 2.3.2**, the analysis procedure in OpenSees

is mainly based on the finite element analysis of fiber sections. The establishment of a

reinforced concrete fiber section consists of steel fibers and concrete fibers to simulate

the moment curvature relationship (i.e. flexure behavior) of the section. **Figure 6-9 (a)**

shows the layout of the Fiber model. The out-most dark grey region is the cover concrete

and is simulated by unconfined concrete fibers. The inner light grey region is the core

concrete and is simulated by confined concrete fibers. Concrete07 constitutive material

model (**Figure 2-8**) is selected for the confined and unconfined concrete materials, which

is introduced in **Section 2.3.4**. OpenSees Official Website (https://opensees.berkeley.edu/)

provides detailed introduction on the input parameters of the Concrete07 model, and will

not be further discussed in this research. The black circles in the figure indicate the

longitudinal reinforcements, and a bilinear relationship with 1.5% of strain hardening is

assumed for the steel material. Since it is the longitudinal reinforcement steel material

that governs the flexural hysteresis behavior of a RC column fiber section, Pinching4

model is used for the input of the steel material, and the flexural hysteresis parameters are

defined on the steel material based on the procedures provided in **Section 6.2.1**. The fiber

section is defined by the following commands:

Section Fiber $secTag

{

219

patch rect $matTag $numSubdivY $numSubdivZ $yI $zI $yJ $zJ

layer straight $matTag $numFiber $areaFiber $yStart $zStart $yEnd $zEnd

}

The command *"patch rect"* defines rectangular fibers for concrete materials, and the tag of specific concrete materials is input in the command *"$matTag"*. The command *"layer straight"* defines a pile of steel fibers on the section, and the tag of the longitudinal reinforcement is input in the command *"$matTag"*. OpenSees Official Website (https://opensees.berkeley.edu/) provides detailed introduction on the rest of the parameters, and will not be further discussed in this section. After the definition of the fiber section, the section is then defined onto a nonlinear beam-column element as introduced in **Section 2.3.2**, forming the overall fiber column element as shown in **Figure 6-9 (a)**.

Based on the definition of the Fiber model, the model can simulate the linear and nonlinear flexural behaviors of a RC column very accurately since the materials on the section are defined with their constitutive stress-strain relationships, and the response is a combination of contributions from concrete materials and steel materials based on plane-remain-plane assumption. As a result, the model can provide accurate simulation from elastic flexural behavior, nonlinear concrete behavior, yielding of longitudinal reinforcements, and to reaching of nominal moment strengths of the section.

220
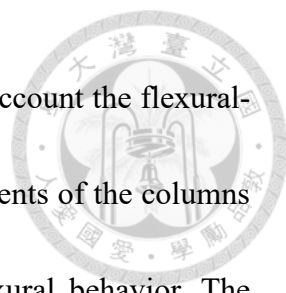
6.3.4 OpenSees Modified Fiber Section Model

The modified fiber section model introduced in this section is constructed in structural analysis program OpenSees and is developed by this research. The model will be abbreviated as Modified Fiber model for this section, but be abbreviated as Fiber model in the rest of the contents. **Section 6.3.3** introduced the original Fiber model, and stated that it can simulate linear and nonlinear flexural behaviors accurately. However, the actual behavior of a RC column is not governed by flexural behavior solely. Bond slip deformations, shear deformations, nonlinear shear behaviors, and flexural-shear behaviors can all contribute to actual response of a RC column, and the original fiber model lacks the consideration of these behaviors. As a result, the Modified Fiber model is then developed by this research.

Figure 6-9 (b) shows the layout of the Modified Fiber model. For the zero-length element at the top of the column, an axial spring, a flexural-shear lateral spring, and a slip rotational spring are added. For the zero-length element at the bottom of the column, a shear lateral spring, and a slip rotational spring are added. These springs are added to the model to provide additional behaviors that are not simulated by the original Fiber model.

Elwood (2004) developed the shear and axial limit state materials inside OpenSees and provide instructions for their corresponding setup. **Section 2.3.5** introduces both materials. Since the fiber section can simulate the flexural behavior up to the point of core

221
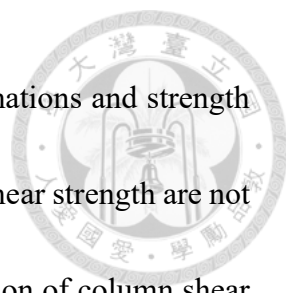
concrete crushing or reinforcement fracturing, it does not take into account the flexural-shear failure behavior, which occurs when the transverse reinforcements of the columns are not sufficient to provide full development of ductility for flexural behavior. The flexural-shear spring (shear limit state material) is implemented to simulate such condition. To allow for the shear limit state material to activate, the concrete and steel constitutive material models are modified following procedures provided by Elwood (2004). The column section may still be able to carry gravity load if collapse is prevented after flexural-shear failure and the lateral strength degrades to zero, thus the axial spring (axial limit state material) is setup to simulate the post-failure gravity load carrying capacity of RC columns. The materials are applied onto the zero-length elements at the top end of the column on the lateral and axial directions respectively.

Since the original Fiber model is perfectly locked on both ends for the column, bond slip effects for columns with low axial loads are not considered. To take into account the flexibility due to slip of the longitudinal bars between the columns and foundations, elastic rotational springs (slip springs) are setup on the zero-length elements on both ends of the column on the rotational degree of freedom. **Section 2.3.6** provides the definition for the flexibility of the spring, and the command is as follows:

uniaxialMaterial Elastic $matTag $E

"$E" inputs the calculated stiffness to consider bond slip effects by **Eq (2.29)**

Lastly, since the original Fiber model simulates flexural deformations and strength assuming plane-remain-plane behavior, the shear deformations and shear strength are not simulated by the model. NCREE/TEASDA (2021) provided simulation of column shear behavior by the shear backbone curve in **Figure 2-1**, following the same procedure with the two previous models using constant initial axial load to estimate the shear strength of the column. **Section 6.3.1** and **Section 6.3.2** provides equations and procedures to transform the shear backbone curve into a shear hinge and to be applied onto the column model. The shear hinge is implemented by the Pinching4 model onto a lateral spring on the zero-length element at the bottom end of the column. Since it is the shear backbone curve that is input on the spring, the spring is then defined as shear spring in **Figure 6-9 (b)**. However, the backbone transformation relationship for the neglection of the linear deformations is not same as the ETABS model and CPH model for the Modified Fiber model. The ETABS model and CPH model must take out the linear deformation on the shear backbone curve fully to prevent repeated consideration of linear deformations since the linear column element has already considered flexural rigidity and shear rigidity. The case for the Modified Fiber model is not the same since the fiber element simulates flexural deformations solely. As a result, only the flexural deformations on the shear backbone are required to be taken out for the Modified Fiber model, and **Eq. (6.19)** can be modified as follows:
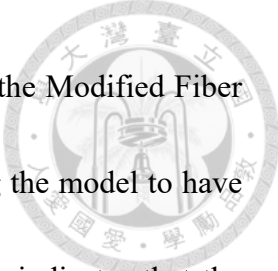
$$c = \left(\Delta_{s.n} - \frac{V_n}{V_{cr}}\Delta_{f,cr}\right)/H \qquad (6.20)$$

Where $\Delta_{f,cr}$ can be calculated as **Eq. (2.5)**. While the deformation at point B should be

calculated as follows:

$$b = \left(\Delta_{s,cr}\right)/H \qquad (6.21)$$

Where $\Delta_{s,cr}$ can be calculated as **Eq. (2.4)**. The modified shear backbone curve can then

be inputted onto Pinching4 model and applied onto the zero-length element on the bottom

of the column model.

The combination of the above-mentioned fiber column element, limit state springs,

slip springs, and shear spring can be indicated by **Figure 6-9 (b)**. To conclude, the

Modified Fiber model can simulate linear flexural deformations by the fiber column

element, linear slip deformations by the slip springs, linear shear deformations by the

linear section of the shear spring, nonlinear flexural behaviors by the fiber element, and

nonlinear shear behaviors by the shear spring. The Modified Fiber model holds its

advantage when simulating behaviors of flexural-dominant RC members by the setup of

constitutive material models on the fiber section, and can simulate the initial stiffness

from elastic behaviors up to the development of nonlinear behaviors accurately, compared

to the simplified linear stiffness of the ETABS model and the CPH model. Moreover, it

is concluded in **Chapter 5** that considering the varying axial load can provide better

accuracy when estimating the flexural strength. The fiber section of the Modified Fiber

model simulates the flexural strength by sectional behavior, allowing the model to have

varied flexural strengths when subjecting to varied axial loads. This indicates that the

fiber section can simulate similar behavior as the ETABS P-M-M flexural hinge, taking

into the consideration of varying axial load phenomena, while providing with a prompter

analysis procedure. The model allows this research to compare the time history analysis

results of a simplified stiffness and constant flexural strength column model and an

accurate stiffness and varied flexural strength column model. Since the original Fiber

model is not a complete model that considers the overall behavior of RC columns well, it

is then replaced by the Modified Fiber model to represent the concept of using fiber

section to simulate flexural behaviors. For the following contents, the mentioned Fiber

model is then referred to the Modified Fiber model

6.4 Comparison of Model Backbone Curves

The monotonic backbone curves of the proposed CPH model and Fiber model are

presented in this section to explain the behavior of different elements and hinges as well

as their combination response in detail. The section takes column T1C1, which is a

flexural-dominant column, and column T1C2, which is a shear-dominant column, for

example to compare the flexural-dominant and shear-dominant responses separately for
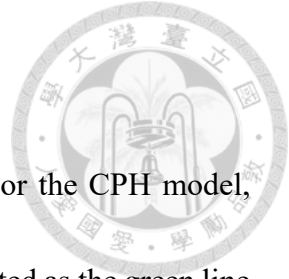
the two models.

The flexural-dominant column responses are discussed first. For the CPH model, without any modification, the original flexural backbone curve is plotted as the green line and the original shear backbone curve is plotted as the red line in **Figure 6-10 (a)**. Both curves are shown to have the same initial stiffness since both backbone curves are simulated with the effective stiffness recommended by ASCE/SEI 41-13 (2014) as proposed in NCREE/TEASDA (2021). To input the two backbone curves as hinges onto the column element and to focus the linear deformation on the column element, the flexural and shear backbone curves are modified as the green and the red lines in **Figure 6-10 (b)**. The lateral load-displacement curve for the linear column element is indicated as the blue line in the figure. Combined, the actual response (black dotted line) follows the linear column element during linear behavior, reaches the shear cracking point on the shear hinge first and results with a stiffness degradation, then reaches the yielding strength on the flexural hinge and results with another stiffness degradation. Finally, the strength is limited by the yielding plateau of the flexural hinge. Flexural-shear failure occurs as strength degradation contributed by the flexural hinge is observed.
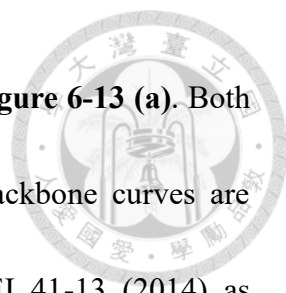
For the Fiber model, without any modification, the original flexural backbone curve is plotted as the green line and the original shear backbone curve is plotted as the red line in **Figure 6-11 (a)**. Slight difference in the initial stiffness can be observed since the shear

226

backbone curve is simulated with the simplified effective stiffness recommended by

ASCE/SEI 41-13 (2014) and the flexural backbone curve is simulated based on the actual

material design layout on the section. To input the shear backbone curve as a hinge onto

the fiber column element and to focus the linear deformation on the fiber column element,

the shear backbone curve is modified as the red line in **Figure 6-11 (b)** and the original

flexural backbone curve of the fiber column element is remained as the green line in the

figure. Combined, the actual response (black dotted line) follows the fiber column

element during linear behavior, reaches the shear cracking point on the shear hinge first

and results with a stiffness degradation, then reaches the yielding strength on the fiber

column element and results with another stiffness degradation. Finally, the strength is

limited by the yielding plateau of the fiber column element. Flexural-shear failure occurs

as strength degradation contributed by the shear limit state material is observed.
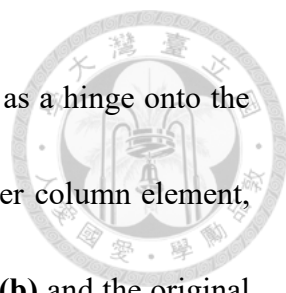
Figure 6-12 plots the response of the CPH model (green line) and the Fiber model

(red line) for a flexural-dominant column together. The lateral load-displacement

behavior and the unloading stiffness is shown to correspond well for the two models,

while the reloading behavior for the Fiber model initiates at a lower displacement. For

the overall behavior, the two models are shown to provide consistent flexural response.

The shear-dominant column responses are then discussed. For the CPH model,

without any modification, the original flexural backbone curve is plotted as the green line
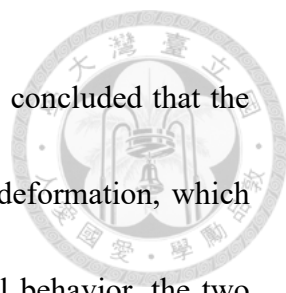
and the original shear backbone curve is plotted as the red line in **Figure 6-13 (a)**. Both

curves are shown to have the same initial stiffness since both backbone curves are

simulated with the effective stiffness recommended by ASCE/SEI 41-13 (2014) as

proposed in NCREE/TEASDA (2021). To input the two backbone curves as hinges onto

the column element and to focus the linear deformation on the column element, the

flexural and shear backbone curves are modified as the green and the red lines in **Figure**

6-13 (b). The lateral load-displacement curve for the linear column element is indicated

as the blue line in the figure. Combined, the actual response (black dotted line) follows

the linear column element during linear behavior, reaches the shear cracking point on the

shear hinge first and results with a stiffness degradation, then reaches the strength point

on the shear hinge and strength degradation initiates. Finally, the strength drops to zero

after the lateral displacement exceeds the collapse point of the shear hinge.

For the Fiber model, without any modification, the original flexural backbone curve

is plotted as the green line and the original shear backbone curve is plotted as the red line

in **Figure 6-14 (a)**. Significant difference in the initial stiffness can be observed since the

shear backbone curve is simulated with the simplified effective stiffness recommended

by ASCE/SEI 41-13 (2014) and the flexural backbone curve is simulated based on the

actual material design layout on the section. The longitudinal reinforcement ratio for this

column is higher, which leads to a higher initial stiffness and a significant difference from

the simplified effective stiffness. To input the shear backbone curve as a hinge onto the

fiber column element and to focus the linear deformation on the fiber column element,

the shear backbone curve is modified as the red line in **Figure 6-14 (b)** and the original

flexural backbone curve of the fiber column element is remained as the green line in the

figure. Combined, the actual response (black dotted line) follows the fiber column

element during linear behavior, reaches the shear cracking point on the shear hinge first

and results with a stiffness degradation, then reaches the strength point on the shear hinge

and strength degradation initiates. Finally, the strength drops to zero after the lateral

displacement exceeds the collapse point of the shear hinge.

Figure 6-15 plots the response of the CPH model (green line) and the Fiber model

(red line) for a shear-dominant column together. The initial stiffness is shown to vary for

the two backbone curves even though the same shear backbone curve is input on both

models. This is because of higher longitudinal reinforcement ratio for this column

example. With higher longitudinal reinforcement ratio, the column is expected to develop

higher initial stiffness due to more contribution from the steel material, which has a higher

modulus of elasticity compared to concrete material. The effective stiffness of the CPH

model is defined based on axial load ratio, as a result, the change in effective stiffness is

not sensitive to the change in longitudinal reinforcement ratio. The difference in linear

deformation also affects the deformation at strength point since the deformation at

229
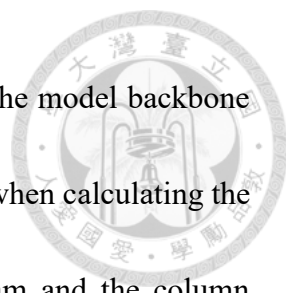
strength point is accumulated from the linear deformation. It can be concluded that the

Fiber model can provide a more accurate estimation for the linear deformation, which

also affects the nonlinear deformation development. For the overall behavior, the two

models are still shown to provide consistent shear response.

6.5 Comparison of Energy Dissipation Capacity

To validate the hysteresis modeling proposed by Ling et al. (2022) with shaking

table-tested column responses, the overall energy dissipation capacity of the test

hysteresis curves and the model hysteresis curves should be calculated and compared. As

introduced in **Section 6.1**, to take out the error from the difference in developed

displacement between the test and the model response, displacement history analysis is

performed on the column models based on actual lateral displacement time history

response from the test results, and only the drifts which contribute to large lateral

deformations and development of energy dissipation capacities would be taken into

consideration.

To compare the hysteresis behavior between test and model responses, only the test

responses without collapse and possess significant unloading and reloading behavior

during developments of larger deformations can provide good comparison indices. For

the nine RC columns in Su (2007), **Chapter 4** presents their hysteresis curves. Among

230

the nine columns, the strength of column T1C2 varies largely with the model backbone

curve as shown in **Figure 5-23**, which may lead to large differences when calculating the

energy dissipation capacity. Due to slip between the top steel beam and the column

foundation, column T2C1 mostly focuses in linear behavior as shown in **Figure 4-41**. The

two columns in frame T3 and T4 collapse without significant nonlinear unloading and

reloading behaviors as shown in **Figure 4-71** and **Figure 4-87**. As a result, only columns

T1C1, T1C3, and T2C3 provide good hysteresis curves for comparison. Column T1C1

and T1C3 can be used for comparison on flexural-dominant columns, and column T2C3

can be used for comparison on shear-dominant columns. To focus on the drifts which

dominant the hysteresis behaviors, the smaller drifts are taken out. **Figure 6-16** plots the

filtered hysteresis curves of the three columns. The filtered lateral displacement history

will then be applied on the ETABS model, the CPH model, and the Fiber model to

generate the corresponding hysteresis curves of the models, and to compare with the test

responses.

6.5.1 Flexural Hysteresis Response

For the flexural-dominant columns, the hysteresis curves for the ETABS model are

shown in **Figure 6-17** as magenta lines. The backbone curve is only shown to capture

well for column T1C3 in the positive direction where longitudinal reinforcement yielding

<center>231</center>

and stiffness degradation up to the yielding plateau is observed. For the rest, such behavior is not observed from the test response and there exists slight difference between the model and the test backbone curve. This is due to the formation of initial cracks on both columns, which may have degraded the initial stiffness of both columns, thus the stiffer stiffness before longitudinal reinforcement yielding is softened. The model pinching points are shown to capture well for both columns. The unloading stiffness degradation is underestimated for column T1C1 in the positive direction, but is simulated well in the negative direction. The unloading stiffness degradation is simulated well for column T1C3 in both directions from small to large lateral drifts. It is to mention that both columns have the same design and same applied axial load, therefore the model outputs the same hysteresis curve. It is the difference in crack patterns, varying axial loads, and even measurement discrepancies for the test specimens that may lead to different unloading and pinching behavior of identical columns. For the comparison on energy dissipation capacity, the ratio of E_{Test}/E_{ETABS} is 0.69 for column T1C1 and 0.82 for column T1C3, both showing good simulation results.

The hysteresis curves for the CPH model are shown in **Figure 6-18** as green lines. The backbone curve is only shown to capture well for column T1C3 in the positive direction where longitudinal reinforcement yielding and stiffness degradation up to the yielding plateau is observed. For the rest, such behavior is not observed and there exists

232

slight difference between the model and the test backbone curve. The reasons are explained previously. The model pinching points are shown to capture well for both columns. The unloading stiffness degradation is underestimated for column T1C1 in the positive direction, but is simulated well in the negative direction. The unloading stiffness degradation is simulated well for column T1C3 in both directions from small to large lateral drifts. For the comparison on energy dissipation capacity, the ratio of E_{Test}/E_{CPH} is 0.77 for column T1C1 and 0.92 for column T1C3, both showing good simulation results.

The hysteresis curves for the Fiber model are shown in **Figure 6-19** as red lines. The backbone curve is only shown to capture well for column T1C3 in the positive direction where longitudinal reinforcement yielding and stiffness degradation up to the yielding plateau is observed. For the rest, such behavior is not observed and there exists slight difference between the model and the test backbone curve. The reasons are explained previously. The model pinching points are shown to be more conservative with more severe pinching behavior simulated for both columns. The unloading stiffness degradation is underestimated for column T1C1 in the positive direction, but is simulated well in the negative direction. The unloading stiffness degradation is simulated well for column T1C3 in both directions from small to large lateral drifts. For the comparison on energy dissipation capacity, the ratio of E_{Test}/E_{Fiber} is 0.87 for column T1C1 and 1.04 for column T1C3, both showing accurate simulation results.

233

6.5.2 Shear Hysteresis Response

For the shear-dominant columns, the hysteresis curve for the ETABS model is shown in **Figure 6-20** as magenta lines. The backbone curve is shown to capture well for column T2C3 in the both directions. The slight difference is in the positive direction when the test response developed a very large lateral displacement without severe strength degradation, while the model simulates the strength degradation down to zero value. Without formation of initial cracks, the model captures the initial stiffness well. The model pinching points are shown to be captured accurately. The unloading stiffness degradation is slightly underestimated for the column in both directions. For the comparison on energy dissipation capacity, the ratio of E_{Test}/E_{ETABS} is 0.72 for the column, showing good simulation results.

The hysteresis curve for the CPH model is shown in **Figure 6-21** as green lines. The backbone curve is shown to capture well for column T2C3 in the both directions. The slight difference is in the positive direction when the test response developed a very large lateral displacement without severe strength degradation, while the model simulates the strength degradation down to zero value. Without formation of initial cracks, the model captures the initial stiffness well. The model pinching points are shown be to captured accurately. The unloading stiffness degradation is underestimated for the column in both

234

directions. For the comparison on energy dissipation capacity, the ratio of E_{Test}/E_{ETABS}

is 0.68 for the column, showing good simulation results.

The hysteresis curve for the Fiber model is shown in **Figure 6-22** as red lines. The

backbone curve is shown to capture well for column T2C3 in the both directions. The

slight difference is in the positive direction when the test response developed a very large

lateral displacement without severe strength degradation, while the model simulates the

strength degradation down to zero value. Without formation of initial cracks, the model

captures the initial stiffness well. The model pinching points are shown to be captured

accurately. The unloading stiffness degradation is underestimated for the column in both

directions. For the comparison on energy dissipation capacity, the ratio of E_{Test}/E_{ETABS}

is 0.65 for the column, showing good simulation results.
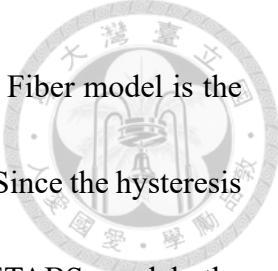
6.5.3 Validation and Comparison of Hysteresis Models

The original hysteresis parameters provided by Ling et al. (2022) on the pivot model

is implemented by the ETABS model, and one objective of this section is to validate the

feasibility for the cyclic loading-based hysteresis parameters to represent actual shaking

table responses. The test to ETABS model cumulative energy dissipation capacity ratio

for the two flexural-dominant columns are 0.69 and 0.82 respectively. The test to model

cumulative energy dissipation capacity ratio for the shear-dominant column is 0.72. The

235

original average test to model cumulative energy dissipation capacity ratio based on a

wide range of column database provided by Ling et al. (2022) is 0.95 and with a COV of

0.14 for flexural-dominant columns, and the AVE is 0.85 with a COV of 0.23 for shear-

dominant columns. The values are summarized in **Table 6-3**. Considering that the initial

stiffness is softened by the formation of initial cracks for the flexural-dominant columns

leading to error between the test and model backbone curve, the ratios of 0.69 and 0.82

have provided well simulated hysteresis behaviors. As for the shear-dominant column,

the ratio of 0.72 is within the acceptable range with the original model, and provides well

simulated hysteresis behavior. It is to mention that when developing analytical models,

the capturing of strength behavior is the first tier and require the most accurate prediction

result. The capturing of displacement behavior is the second tier which is affected by the

accuracy of strength prediction results. The capturing of hysteresis behavior and to the

calculation of overall energy dissipation capacity is the third tier which its accuracy is

affected by the accuracy of strength and displacement models. To conclude, the optimized

hysteresis parameter calculation equations provided by Ling et al. (2022) on the Pivot

model is shown to capture the hysteresis behavior of shaking table-tested column

responses well, and validated to simulated actual ground motion loading responses.
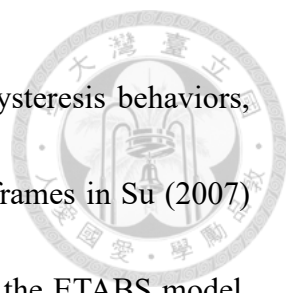
    Table 6-3 provides comparison on values for all the test to model cumulative energy

dissipation capacity ratios. For the flexural-dominant columns, ETABS model provides

the most overestimation on the energy dissipation capacity, while the Fiber model is the

most accurate and even simulates conservative result for one column. Since the hysteresis

parameters are transformed based on the values defined in the ETABS model, the

transformed parameters are also shown to simulate shaking table-tested responses well.

The Fiber model possesses a more pinched hysteresis curve compared to the two other

models due to the difference in the element that governs the pinching behavior in the

Fiber model. For the ETABS and CPH model, the hysteresis behavior is directly defined

on the load-displacement hinges of members and the responses are directly reflected on

the hysteresis curves. However, the hysteresis behavior is defined on the longitudinal

reinforcement stress-strain relationship for the Fiber model. The hysteresis response is

then required to transform from stress-strain behavior into load-displacement behavior to

reflect on the hysteresis curve. Therefore, the pinching behavior of the Fiber model may

vary from the original defined point that is transformed form the ETABS model. With a

more pinched hysteresis curve simulated, the energy dissipation capacity of the Fiber

model will be lesser than the original ETABS model, allowing the Fiber model to always

stand on the conservative side.

6.6 Time History Analysis
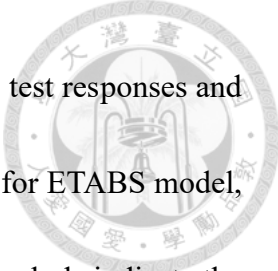
To validate the three column models introduced in this chapter with shaking table-

237

tested column responses by lateral displacement, base shear, and hysteresis behaviors, time history analysis is performed on the column models. All four frames in Su (2007) are taken into consideration, and all four frames are simulated with the ETABS model, CPH model, and Fiber model. The actual ground accelerations measured in the shaking table tests during each run in each test are applied on the column models.

The presented results follow the sequence starting from lateral displacements to base shear responses and to hysteresis curves of individual columns. For each response of individual columns, the presented results follow the sequence of ETABS model, CPH mode, to Fiber model. After presenting the above responses for all columns in the same frame, the hysteresis curves of the frames are then presented. The frames are presented from frame T1 to T4. All the time history responses are enlarged to focus on the time period that is of concern. The natural periods of the test and models at initial stage and after runs are summarized in **Table 6-4**. For the ETABS model, only the natural periods at the initial condition are provided since the program could not measure the natural periods of the models after input of ground accelerations. The test-measured maximum strengths (indicated as Test), calculated strengths that are inputted into the models (indicated as Input), and actual-developed maximum strengths by the column models (indicated as ETABS, CPH, and Fiber) are summarized in **Table 6-5**.

The required information and plotted figures are mentioned prior to the main content

238

in each section. For all the plotted figures, the black lines indicate the test responses and the colored lines indicate the column model responses, with magenta for ETABS model, green for CPH model, and red for Fiber model. The grey triangular symbols indicate the maximum strength point for the test responses and the colored triangular symbols indicate the maximum strength point for the column model responses. For all the figures, solid lines indicate correct responses, and dotted lines indicate broken and un-referenceable responses.

6.6.1 T1 Analysis Result

As shown in **Table 4-7**, there are a total of four runs of ground motions subjected on Frame T1. R2 and R3 have an input PGA of 500 gal to simulate linear behaviors of structures under small-to-medium earthquakes. R4 has an input PGA of 1g to simulate strength developments and collapse behaviors of structures under large earthquakes, and R6 has an input PGA of 800gal. The test terminates with collapse of all columns after R6.

Column C1

Column C1 is located on the north side of frame T1. **Figure 6-23**, **Figure 6-24**, and **Figure 6-25** plot the lateral displacement responses. **Figure 6-26**, **Figure 6-27**, and **Figure 6-28** plot the base shear responses. **Figure 6-29**, **Figure 6-30**, and **Figure 6-31** plot the hysteresis curves. The strength development sequence for the column during R4

is summarized in **Table 6-6**.

The time at development of maximum strength in the positive direction is at 25.135 second for the test result, 25.065 second for ETABS model, 25.045 second for CPH model, and 25.110 second for Fiber model. For the negative direction, 24.525 second, 24.480 second, 24.440 second, and 24.495 second respectively. The results indicate that the Fiber model develops its maximum strengths at the closest time to the test result in both directions.

For the lateral displacement responses, since the responses during R2 and R3 are still under linear behavior and since the initial natural periods are predicted well for the models, all the model responses correspond well to the test response.

During R4, the ETABS model response in **Figure 6-23** corresponds well with the test response up to 24 second as large lateral drifts entering nonlinear behavior is developed afterwards. The large lateral drift in the negative direction is slightly underestimated by the model, and is significantly underestimated in the positive direction. After 25 second, without significant nonlinear lateral displacements developed to cause sufficient stiffness softening, the model is not able to oscillate around the same natural period as the test response, therefore the lateral displacements are not simulated well during the remaining drifts in R4 and throughout R6. The collapse of the frame is due to degradation on a significant shear crack on column C3 which pulls column C1 to collapse,

240

this behavior is not simulated by the model and thus collapse does not occur.

For the CPH model in R4, the model response in **Figure 6-24** corresponds well with the test response up to 24 second as large lateral drifts entering nonlinear behavior is developed afterwards. The large lateral drift in the negative direction is captured accurately by the model, and is slightly underestimated in the positive direction. After 25 second, with significant nonlinear lateral displacements developed to cause sufficient stiffness softening, the model is able to oscillate at a natural period (0.2910 sec) closer to the test response (0.4607 sec) but not accurate enough, therefore the lateral displacements are roughly simulated during the remaining drifts in R4 and throughout R6. Collapse is not simulated by the model, but a residual displacement to the positive direction is generated at the end of R6.

For the Fiber model in R4, the model response in **Figure 6-25** corresponds well with the test response up to 24 second as large lateral drifts entering nonlinear behavior is developed afterwards. The large lateral drift in the negative direction is captured accurately by the model, and is slightly overestimated in the positive direction. After 25 second, with significant nonlinear lateral displacements developed to cause sufficient stiffness softening, the model is able to oscillate at a natural period (0.4115 sec) close to the test response (0.4607 sec), therefore the lateral displacements are well simulated during the remaining drifts in R4 and throughout R6. Collapse is not simulated by the

model.

To conclude, the Fiber model provides the most accurate simulation on the lateral displacement responses due to accurate lateral displacements developed and sufficient softening of stiffness which allows for the model to oscillate more consistently with the test response.

For the base shear responses, since the responses during R2 and R3 are still under linear behavior and since the initial natural periods are predicted well for the models, all the model responses correspond well to the test response. The slight overestimation in base shear during each drift may be caused by the formation of initial cracks on the column which may have softened the initial stiffness, thus lowering the test base shear developed.

During R4, the ETABS model response in **Figure 6-26** corresponds well with the test response up to 24 second as large base shear entering nonlinear behavior is developed and maximum strengths are reached in both directions afterwards. The strength response between 24 to 25 second where large values are developed corresponds well with the test results. The maximum strength developed in both directions are slightly underestimated by the model, with values of 117.96 kN and 117.30 kN for the model comparing to the values of 130.86 kN and 136.12 kN for the test results. After 25 second, the model is not able to oscillate around the same natural period as the test response, therefore the base

242
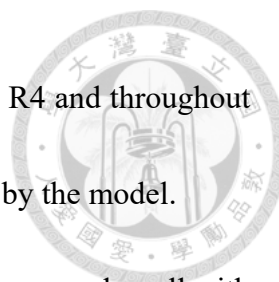
shear responses are not simulated well during the remaining drifts in R4 and throughout R6 with too low of a model natural period. Collapse is not simulated by the model.

For the CPH model in R4, the model response in **Figure 6-27** corresponds well with the test response up to 24 second as large base shear entering nonlinear behavior is developed and maximum strengths are reached in both directions afterwards. The strength response between 24 to 25 second where large values are developed corresponds well with the test results. The maximum strength developed in both directions are slightly underestimated by the model, with values of 117.09 kN and 116.75 kN for the model comparing to the values of 130.86 kN and 136.12 kN for the test results. After 25 second, the model is able to oscillate at a natural period (0.2910 sec) closer to the test response (0.4607 sec) but not accurate enough, therefore the base shear responses are roughly simulated during the remaining drifts in R4 and throughout R6. Collapse is not simulated by the model.

For the Fiber model in R4, the model response in **Figure 6-28** corresponds well with the test response up to 24 second as large base shear entering nonlinear behavior is developed and maximum strengths are reached in both directions afterwards. The strength response between 24 to 25 second where large values are developed corresponds well with the test results. The maximum strength developed in the negative direction is slightly underestimated and accurately captured in the positive direction by the model, with values

243

of 129.94 kN and 124.35 kN for the model comparing to the values of 130.86 kN and

136.12 kN for the test results. After 25 second, the model is able to oscillate at a natural

period (0.4115 sec) close to the test response (0.4607 sec), therefore the base shear

responses are well simulated during the remaining drifts in R4 and throughout R6.

Collapse is not simulated by the model.

To conclude, the Fiber model provides the most accurate simulation on the base

shear responses due to accurate base shear developed and sufficient softening of stiffness

which allows for the model to oscillate more consistently with the test response. While

the two other models provide conservative simulations with lower strengths.

For the hysteresis curves, the responses during R2 and R3 are still under linear

behavior as shown in **Figure 6-29**, **Figure 6-30**, and **Figure 6-31**. The overestimation in

stiffness for all models may be caused by the formation of initial cracks on the column

which may have softened the test initial stiffness.

During R4, the responses of all models are shown to be governed by the flexural

elements, indicating flexural-dominant behavior. The ETABS model response in **Figure

6-29** shows that the lateral displacement is underestimated in both directions but the

pinching behavior is captured well by the model. During R6, the lateral displacements are

underestimated in both directions. The reloading stiffness is accurate in the negative

direction but is too stiff in the positive direction. The pinching behavior is slightly

244

underestimated. Overall, the model is shown to capture the strength behavior well, but underestimates the lateral displacements for post-strength development behaviors, while providing well simulated pinching behavior.

For the CPH model in R4, the model response in **Figure 6-30** shows that the lateral displacement is slightly underestimated in the positive direction but overestimated in the negative direction. The pinching behavior is captured well by the model. During R6, the lateral displacement is slightly underestimated in the positive direction and is captured well in the negative direction. The reloading stiffness is accurate in both directions. The pinching behavior is slightly underestimated. Overall, the model is shown to capture the strength behavior well, but slightly underestimates the lateral displacements for post-strength development behaviors, while providing well simulated pinching behavior.

For the Fiber model in R4, the model response in **Figure 6-31** shows that the lateral displacement is overestimated in the positive direction but accurate in the negative direction. The pinching behavior is more conservative for the model. During R6, the lateral displacements are captured accurately in both directions and the reloading stiffness is accurate in both directions. The pinching behavior is captured well. Overall, the model is shown to capture the strength and lateral displacement behavior well, while providing conservative pinching behavior with lesser energy dissipation capacity.

To conclude, both the ETABS and CPH model provide conservative simulations on

245
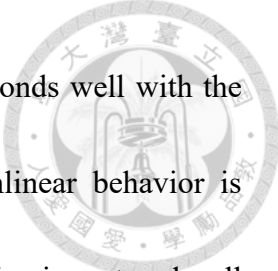
the force-displacement relationships and accurate simulations on the hysteresis behaviors. With material constitutive behaviors defined on the fiber section, it is the Fiber model that can react more accurately with the input ground motion through the fiber section, which can sensitively simulate flexural behaviors. The Fiber model is shown to provide the most accurate simulation result on the overall behavior.

Column C2

Column C2 is located on the center of frame T1. **Figure 6-32**, **Figure 6-33**, and **Figure 6-34** plot the lateral displacement responses. **Figure 6-35**, **Figure 6-36**, and **Figure 6-37** plot the base shear responses. **Figure 6-38**, **Figure 6-39**, and **Figure 6-40** plot the hysteresis curves. The strength development sequence for the column during R4 is summarized in **Table 6-7**.

The time at development of maximum strength in the positive direction is at 24.300 second for the test result, 24.290 second for ETABS model, 24.275 second for CPH model, and 24.280 second for Fiber model. For the negative direction, 24.175 second, 24.430 second, 24.430 second, and 24.405 second respectively. The results indicate that all models develop their maximum strength around the same time as the test response.

For the lateral displacement responses, since the responses during R2 and R3 are still under linear behavior and since the initial natural periods are predicted well for the models, all the model responses correspond well to the test response.

246

During R4, the ETABS model response in **Figure 6-32** corresponds well with the test response up to 24 second as large lateral drifts entering nonlinear behavior is developed afterwards. The first large lateral drift in the negative direction is captured well by the model, and is significantly underestimated in the positive direction in the next drift. Shear failure occurs at the two drifts. The lateral deformations are all underestimated afterwards as the model is not able to oscillate around the same natural period as the test response. Collapse of the column doesn't occur since the two outer ductile columns still holds the structural stability, and the behavior is simulated by the model.

For the CPH model in R4, the model response in **Figure 6-33** corresponds well with the test response up to 24 second as large lateral drifts entering nonlinear behavior is developed afterwards. The first large lateral drift in the negative direction is captured well by the model, and is significantly underestimated in the positive direction in the next drift. Shear failure occurs at the two drifts. The lateral deformations are roughly simulated afterwards as the model is able to oscillate at a natural period (0.2910 sec) closer to the test response (0.4607 sec) but not accurate enough. Collapse of the column doesn't occur since the two outer ductile columns still holds the structural stability, and the behavior is simulated by the model.

For the Fiber model in R4, the model response in **Figure 6-34** corresponds well with the test response up to 24 second as large lateral drifts entering nonlinear behavior is

247
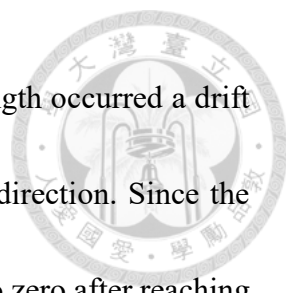
developed afterwards. The first large lateral drift in the negative direction is captured well

by the model, and is significantly underestimated in the positive direction in the next drift.

Shear failure occurs at the two drifts. The lateral deformations are well simulated

afterwards for each drift as the model is able to oscillate at a natural period (0.4115 sec)

close to the test response (0.4607 sec). Collapse of the column doesn't occur since the

two outer ductile columns still holds the structural stability, and the behavior is simulated

by the model.

To conclude, the Fiber model provides the most accurate simulation on the lateral

displacement responses due to accurate lateral displacements developed and sufficient

softening of stiffness of the overall frame which allows for the model to oscillate more

consistently with the test response.

For the base shear responses, since the responses during R2 and R3 are still under

linear behavior and since the initial natural periods are predicted well for the models, all

the model responses correspond well to the test response. The peak values are slightly

underestimated as the stiffness of the test specimen may be higher than the models.
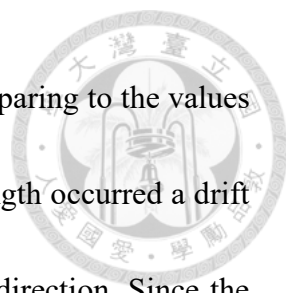
During R4, the ETABS model response in **Figure 6-35** corresponds well with the

test response up to 24 second as large base shear is developed and maximum strengths

are reached in both directions afterwards. The maximum strengths are underestimated by

the model, with values of 91.87 kN and 91.42 kN for the model comparing to the values

248

of 152.68 kN and 163.14 kN for the test results. The maximum strength occurred a drift later in the negative direction and at the same drift in the positive direction. Since the column has low ductility, the lateral strength immediately degrades to zero after reaching the maximum strengths for the test response and is captured by the models, which corresponds well with the test response as no lateral strength can be developed after 25 second.

For the CPH model in R4, the model response in **Figure 6-36** corresponds well with the test response up to 24 second as large base shear is developed and maximum strengths are reached in both directions afterwards. The maximum strengths are underestimated by the model, with values of 89.78 kN and 86.83 kN for the model comparing to the values of 152.68 kN and 163.14 kN for the test results. The maximum strength occurred a drift later in the negative direction and at the same drift in the positive direction. Since the column has low ductility, the lateral strength immediately degrades to zero after reaching the maximum strengths for the test response and is captured by the models, which corresponds well with the test response as no lateral strength can be developed after 25 second.

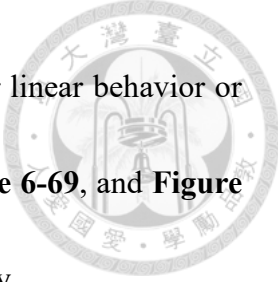For the Fiber model in R4, the model response in **Figure 6-37** corresponds well with the test response up to 24 second as large base shear is developed and maximum strengths are reached in both directions afterwards. The maximum strengths are underestimated by

249

the model, with values of 91.68 kN and 91.84 kN for the model comparing to the values

of 152.68 kN and 163.14 kN for the test results. The maximum strength occurred a drift

later in the negative direction and at the same drift in the positive direction. Since the

column has low ductility, the lateral strength immediately degrades to zero after reaching

the maximum strengths for the test response and is captured by the models, which

corresponds well with the test response as no lateral strength can be developed after 25

second.

To conclude, all models provide the same simulation on the base shear response, and

all models correspond well to the test response. Since the same shear-dominant column

backbone curve is implemented into all three models, it is expected for the models to have

the same strength development behavior.

For the hysteresis curves, the responses during R2 and R3 are still under linear

behavior as shown in **Figure 6-38**, **Figure 6-39**, and **Figure 6-40**. The stiffness for all

models are slightly lower than the test response.

During R4, the responses of all models are shown to be governed by the shear hinges,

indicating shear-dominant behavior. Since the same shear-dominant column backbone

curve is implemented into all three models, all models show the same backbone curve,

and the slight difference is in their initial stiffness as discussed in **Section 6.4**. The models

all underestimate the strength and ductility of the test specimen. The difference in initial
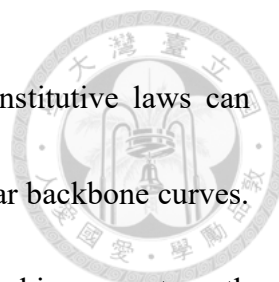
stiffness, linear displacements, algorithm method, and element constitutive laws can affect the actual behaviors for different models even with very similar backbone curves. For example, a drift with unloading and reloading behavior before reaching zero strength in the positive direction is observed for the ETABS and Fiber model. However, the CPH model directly loses its lateral load carrying capacity.
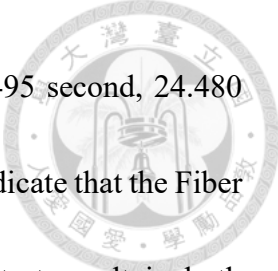
To conclude, all models provide good simulations with conservative strength and lateral displacement behaviors compared with the test response. Since the lateral displacements are governed by the two outer columns after shear failure of the center column, the Fiber model can simulate more accurate flexural behavior for the two outer columns, thus the lateral displacements at post-shear failure condition are more accurate for the Fiber model.

Column C3

Column C3 is located on the south side of frame T1. **Figure 6-41**, **Figure 6-42**, and **Figure 6-43** plot the lateral displacement responses. **Figure 6-44**, **Figure 6-45**, and **Figure 6-46** plot the base shear responses. **Figure 6-47**, **Figure 6-48**, and **Figure 6-49** plot the hysteresis curves. The strength development sequence for the column during R4 is summarized in **Table 6-8**.

The time at development of maximum strength in the positive direction is at 25.105 second for the test result, 25.065 second for ETABS model, 24.295 second for CPH model,

and 25.110 second for Fiber model. For the negative direction, 24.495 second, 24.480 second, 24.440 second, and 24.495 second respectively. The results indicate that the Fiber model develops its maximum strength at the closest time to the test result in both directions.

For the lateral displacement responses, since the responses during R2 and R3 are still under linear behavior and since the initial natural periods are predicted well for the models, all the model responses correspond well to the test response.

During R4, the ETABS model response in **Figure 6-41** corresponds well with the test response up to 24 second as large lateral drifts entering nonlinear behavior is developed afterwards. The large lateral drift in the negative direction is slightly underestimated by the model, and is significantly underestimated in the positive direction. After 25 second, without significant nonlinear lateral displacements developed to cause sufficient stiffness softening, the model is not able to oscillate around the same natural period as the test response, therefore the lateral displacements are not simulated well during the remaining drifts in R4 and throughout R6. The collapse of the frame is due to degradation on a significant shear crack on column C3 which pulls column C1 to collapse, this behavior is not simulated by the model and thus collapse does not occur.

For the CPH model in R4, the model response in **Figure 6-42** corresponds well with the test response up to 24 second as large lateral drifts entering nonlinear behavior is

252

developed afterwards. The large lateral drift in the negative direction is captured accurately by the model, and is slightly underestimated in the positive direction. After 25 second, with significant nonlinear lateral displacements developed to cause sufficient stiffness softening, the model is able to oscillate at a natural period (0.2910 sec) closer to the test response (0.4607 sec) but not accurate enough, therefore the lateral displacements are roughly simulated during the remaining drifts in R4 and throughout R6. Collapse is not simulated by the model, but a residual displacement to the positive direction is generated at the end of R6.

For the Fiber model in R4, the model response in **Figure 6-43** corresponds well with the test response up to 24 second as large lateral drifts entering nonlinear behavior is developed afterwards. The large lateral drift in the negative direction is captured accurately by the model, and is slightly overestimated in the positive direction. After 25 second, with significant nonlinear lateral displacements developed to cause sufficient stiffness softening, the model is able to oscillate at a natural period (0.4115 sec) close to the test response (0.4607 sec), therefore the lateral displacements are well simulated during the remaining drifts in R4 and throughout R6. Collapse is not simulated by the model.

To conclude, the Fiber model provides the most accurate simulation on the lateral displacement responses due to accurate lateral displacements developed and sufficient

softening of stiffness which allows for the model to oscillate more consistently with the test response.

For the base shear responses, since the responses during R2 and R3 are still under linear behavior and since the initial natural periods are predicted well for the models, all the model responses correspond well to the test response. The slight overestimation in base shear during each drift may be caused by the formation of initial cracks on the column which may have softened the initial stiffness, thus lowering the test base shear developed.

During R4, the ETABS model response in **Figure 6-44** corresponds well with the test response up to 24 second as large base shear entering nonlinear behavior is developed and maximum strengths are reached in both directions afterwards. The strength response between 24 to 25 second where large values are developed corresponds well with the test results. The maximum strength developed in the negative direction is slightly underestimated by the model and accurate in the positive direction, with values of 117.04 kN and 116.38 kN for the model comparing to the values of 135.21 kN and 127.21 kN for the test results. After 25 second, the model is not able to oscillate around the same natural period as the test response, therefore the base shear responses are not simulated well during the remaining drifts in R4 and throughout R6 with too low of a model natural period. The base shear in the positive direction is not able to develop to higher values due

254

to degradation on a significant shear crack for the specimen during R6. This behavior is not captured by the model since the model develops consistent strength in both directions. Collapse is not simulated by the model.

For the CPH model in R4, the model response in **Figure 6-45** corresponds well with the test response up to 24 second as large base shear entering nonlinear behavior is developed and maximum strengths are reached in both directions afterwards. The strength response between 24 to 25 second where large values are developed corresponds well with the test results. The maximum strength developed in both directions are slightly underestimated by the model, with values of 118.85 kN and 118.56 kN for the model comparing to the values of 135.21 kN and 127.21 kN for the test results. After 25 second, the model is able to oscillate at a natural period (0.2910 sec) closer to the test response (0.4607 sec) but not accurate enough, therefore the base shear responses are roughly simulated during the remaining drifts in R4 and throughout R6. The base shear in the positive direction is not able to develop to higher values due to degradation on a significant shear crack for the specimen during R6. This behavior is not captured by the model since the model develops consistent strength in both directions. Collapse is not simulated by the model.

For the Fiber model in R4, the model response in **Figure 6-46** corresponds well with the test response up to 24 second as large base shear entering nonlinear behavior is

255

developed and maximum strengths are reached in both directions afterwards. The strength

response between 24 to 25 second where large values are developed corresponds well

with the test results. The maximum strength developed in the negative direction is slightly

underestimated and accurately captured in the positive direction by the model, with values

of 129.97 kN and 124.40 kN for the model comparing to the values of 135.21 kN and

127.21 kN for the test results. After 25 second, the model is able to oscillate at a natural

period (0.4115 sec) close to the test response (0.4607 sec), therefore the base shear

responses are well simulated during the remaining drifts in R4 and throughout R6. The

base shear in the positive direction is not able to develop to higher values due to

degradation on a significant shear crack for the specimen during R6. This behavior is not

captured by the model since the model develops consistent strength in both directions.

Collapse is not simulated by the model.

To conclude, the Fiber model provides the most accurate simulation on the base

shear responses due to accurate base shear developed and sufficient softening of stiffness

which allows for the model to oscillate more consistently with the test response. While

the two other models provide conservative simulations with lower strength values.

For the hysteresis curves, the responses during R2 and R3 are still under linear

behavior as shown in **Figure 6-47**, **Figure 6-48**, and **Figure 6-49**. The overestimation in

stiffness for all models may be caused by the formation of initial cracks on the column

which may have softened the test initial stiffness.

During R4, the responses of all models are shown to be governed by the flexural elements, indicating flexural-dominant behavior. The ETABS model response in **Figure 6-47** shows that the lateral displacement is underestimated in both directions but the pinching behavior is captured well by the model. During R6, the lateral displacements are underestimated in both directions. The reloading stiffness is accurate in the negative direction but the severe stiffness degradation due to shear crack degradation in the positive direction is not simulated. Overall, the model is shown to capture the strength behavior well, but underestimates the lateral displacements for post-strength development behaviors, while providing well simulated pinching behavior.

For the CPH model in R4, the model response in **Figure 6-48** shows that the lateral displacement is slightly underestimated in the positive direction but overestimated in the negative direction. The pinching behavior is captured well by the model. During R6, the lateral displacement is slightly underestimated in the positive direction and is captured well in the negative direction. The reloading stiffness is accurate in the negative direction but the severe stiffness degradation due to shear crack degradation in the positive direction is not simulated. Overall, the model is shown to capture the strength behavior well, but slightly underestimates the lateral displacements for post-strength development behaviors, while providing well simulated pinching behavior.

257

For the Fiber model in R4, the model response in **Figure 6-49** shows that the lateral displacement is overestimated in the positive direction but accurate in the negative direction. The pinching behavior is more conservative for the model. During R6, the lateral displacements are captured accurately in both directions. The reloading stiffness is accurate in the negative direction but the severe stiffness degradation due to shear crack degradation in the positive direction is not simulated. Overall, the model is shown to capture the strength and lateral displacement behavior well, while providing conservative pinching behavior with lesser energy dissipation capacity.

To conclude, both the ETABS and CPH model provide conservative simulations on the force-displacement relationships and accurate simulations on the hysteresis behaviors. With material constitutive behaviors defined on the fiber section, it is the Fiber model that can react more accurately with the input ground motion through the fiber section, which can sensitively simulate flexural behaviors. The Fiber model is shown to provide the most accurate simulation result on the overall behavior.

Frame T1

Figure 6-50, **Figure 6-51**, and **Figure 6-52** plot the hysteresis curves of the overall frame for the three models.

The initial natural period of the overall frame for the test is 0.1281 s, 0.1510 s for ETABS model, 0.1474 s for CPH model, and 0.1329 s for Fiber model. The Fiber model

258

has the closest simulation value to the test, while the ETABS and CPH model provide more conservative estimations with softer stiffness and larger natural period. Since the same concept on column modeling is used to construct the ETABS and CPH model, the two models share their natural periods around the same value. After three runs, the test natural period is 0.4607 s, 0.2910 s for the CPH model, and 0.4115 s for the Fiber model. The test values show that the stiffness is softened after three runs due to formation of cracks and nonlinearity of materials, and it is the Fiber model that simulates the value closest test natural period.

For the hysteresis curves, all the responses during R2 and R3 are still under linear behavior. As introduced previously, all models overestimate the initial stiffness for outer columns and underestimate the initial stiffness for the center column, the cumulated stiffness for the frame is shown to be estimated accurately for all three models.
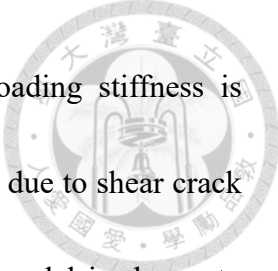
During R4, the ETABS model response in **Figure 6-50** shows that the lateral displacement is underestimated in both directions but the pinching behavior is captured well by the model. The test result shows a trend of peak strength during lower displacement and followed up by a yielding plateau in both directions. This behavior is simulated by the model. During R6, the lateral displacements are underestimated in both directions. The reloading stiffness is accurate in the negative direction but the severe stiffness degradation due to shear crack degradation in the positive direction is not

259

simulated. Overall, the model is shown to capture the strength behavior well, but underestimates the lateral displacements for post-strength development behaviors, while providing well simulated pinching behavior.

For the CPH model in R4, the model response in **Figure 6-51** shows that the lateral displacement is slightly underestimated in the positive direction but overestimated in the negative direction. The pinching behavior is captured well by the model. The test result shows a trend of peak strength during lower displacement and followed up by a yielding plateau in both directions. This behavior is simulated by the model. During R6, the lateral displacement is slightly underestimated in the positive direction and is captured well in the negative direction. The reloading stiffness is underestimated in the negative direction and the severe stiffness degradation due to shear crack degradation in the positive direction is not simulated. Overall, the model is shown to capture the strength behavior well, but slightly underestimates the lateral displacements for post-strength development behaviors, while providing well simulated pinching behavior.

For the Fiber model in R4, the model response in **Figure 6-52** shows that the lateral displacement is overestimated in the positive direction but accurate in the negative direction. The pinching behavior is more conservative for the model. The test result shows a trend of peak strength during lower displacement and followed up by a yielding plateau in both directions. This behavior is simulated by the model. During R6, the lateral

260

displacements are captured accurately in both directions. The reloading stiffness is accurate in the negative direction but the severe stiffness degradation due to shear crack degradation in the positive direction is not simulated. Overall, the model is shown to capture the strength and lateral displacement behavior well, while providing conservative pinching behavior with lesser energy dissipation capacity.

To conclude, both the ETABS and CPH model provide good simulations on the force-displacement relationships and hysteresis behaviors. With accurate material constitutive behaviors defined on the fiber section, it is the Fiber model that can react more accurately with the input ground motion through the fiber section, which can sensitively simulate flexural behaviors. The Fiber model is shown to provide the most accurate simulation result on the overall behavior.

6.6.2 T2 Analysis Result

As shown in **Table 4-7**, there are a total of two runs of ground motions subjected on Frame T2. R2 has an input PGA of 500 gal to simulate linear behaviors of structures under small-to-medium earthquakes. R4 has an input PGA of 1g to simulate strength development and collapse behaviors of structures under large earthquakes. The test terminates after R4.
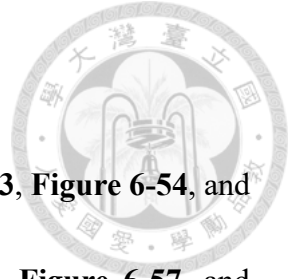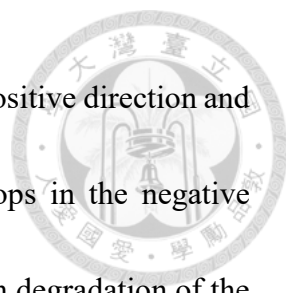
Column C1

Column C1 is located on the north side of frame T2. **Figure 6-53**, **Figure 6-54**, and **Figure 6-55** plot the lateral displacement responses. **Figure 6-56**, **Figure 6-57**, and **Figure 6-58** plot the base shear responses. **Figure 6-59**, **Figure 6-60**, and **Figure 6-61** plot the hysteresis curves. The strength development sequence for the column during R4 is summarized in **Table 6-9**.

The time at development of maximum strength in the positive direction is at 35.220 second for the test result, 24.765 second for ETABS model, 24.275 second for CPH model, and 24.280 second for Fiber model. For the negative direction, 24.510 second, 24.435 second, 24.435 second, and 24.430 second respectively. The results indicate that all models develop their maximum strength in the negative direction around the same time as the test response, but much earlier in the positive direction. It is to mention that the strength development sequence of the test response is affected by slip between the top steel beam and the top foundation of the column specimen, and the maximum strength for the test response may not occur at the time of maximum ground acceleration.

For the lateral displacement responses, since the responses during R2 are still under linear behavior and since the initial natural periods are predicted well for the models, all the model responses correspond well to the test response.

During R4, the ETABS model response in **Figure 6-53** corresponds well with the

test response up to 24 second. Increased lateral drifts develop in the positive direction and are captured by the model. Afterwards, a large lateral drift develops in the negative direction exceeding the test response due to shear failure and strength degradation of the model. The model then oscillates back to reach maximum strength in the positive direction, and directly collapses to the negative direction. Collapse does not occur and lateral displacements are still able to develop after 25 second for the test specimen.

The CPH model and Fiber model have similar responses in R4, the model responses in **Figure 6-54** and **Figure 6-55** correspond well with the test response up to 24 second. Increased lateral drifts develop in the positive direction and are captured by both models as maximum strength is reached. Afterwards, a larger lateral drift develops in the negative direction exceeding the test response due to shear failure and strength degradation of the models. The responses then continue to collapse to the negative direction. Collapse does not occur and lateral displacements are still able to develop after 25 second for the test specimen.

To conclude, all models provide around the same simulation results on the lateral displacement response, and all models predict collapse which is different from the test response. Since the same shear-dominant column backbone curve is implemented into all three models, it is expected for the models to have the same behavior.

For the base shear responses, since the responses during R2 are still under linear
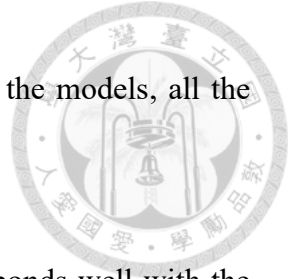
behavior and since the initial natural periods are predicted well for the models, all the model responses correspond well to the test response.

During R4, the ETABS model response in **Figure 6-56** corresponds well with the test response up to 24 second as larger base shear is developed and maximum strengths are reached in both directions afterwards. The strengths are captured by the model accurately, with values of 203.83 kN and 198.57 kN for the model comparing to the values of 187.87 kN and 225.85 kN for the test results. The maximum strength occurs at the same drift in the negative direction but much earlier in the positive direction. The model collapses after reaching shear failure in the positive direction and the lateral load carrying capacity is completely lost. Zero values of base shear are shown for the model while collapse does not occur and base shear are still able to develop after 25 second for the test specimen.

The CPH model and Fiber model have similar responses in R4, the model responses in **Figure 6-57** and **Figure 6-58** correspond well with the test response up to 24 second as larger base shear is developed and maximum strengths are reached in both directions afterwards. The strengths are captured by the models accurately, with values of 194.73 kN and 198.10 kN for the CPH model and values of 192.20 kN and 194.58 kN for the Fiber model comparing to the values of 187.87 kN and 225.85 kN for the test results. The maximum strength occurs at the same drift in the negative direction but much earlier in

264
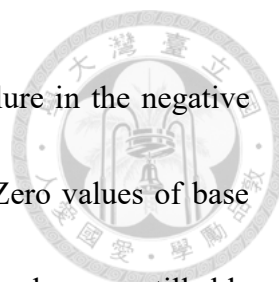
the positive direction. The models collapse after reaching shear failure in the negative

direction and the lateral load carrying capacity is completely lost. Zero values of base

shear are shown for the models while collapse does not occur and base shear are still able

to develop after 25 second for the test specimen.

To conclude, all models provide around the same simulation results on the base shear

responses, and all models predict collapse which is different from the test response. Since

the same shear-dominant column backbone curve is implemented into all three models, it

is expected for the models to have the same behavior.

For the hysteresis curves, the responses during R2 is still under linear behavior or

just reached shear cracking strength as shown in **Figure 6-59**, **Figure 6-60**, and **Figure

6-61**. The stiffness for all models are shown to be estimated accurately.

During R4, the responses of all models are shown to be governed by the shear hinges,

indicating shear-dominant behavior. Since the same shear-dominant column backbone

curve is implemented into all three models, all models show the same backbone curve as

they all collapse to the negative direction, and the slight difference is in their initial

stiffness as discussed in **Section 6.4**. The models capture the strength and pre-shear failure

displacement well, while simulating collapse behavior which doesn't occur for the actual

test response. As explained previously, the actual behaviors for different models can vary

even with very similar backbone curves. For example, the ETABS model simulates
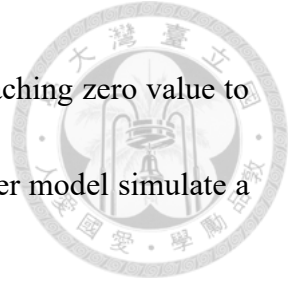
265

strength degradation in the negative direction and unloads before reaching zero value to reach maximum strength in the positive direction. The CPH and Fiber model simulate a more direct collapse to the negative direction.

To conclude, all models provide good simulations with accurate strength and lateral displacement behaviors compared with the test response, while all models simulate collapse behavior, which is conservative since the actual test response does not collapse.

Column C3

Column C3 is located on the south side of frame T2. **Figure 6-62**, **Figure 6-63**, and **Figure 6-64** plot the lateral displacement responses. **Figure 6-65**, **Figure 6-66**, and **Figure 6-67** plot the base shear responses. **Figure 6-68**, **Figure 6-69**, and **Figure 6-70** plot the hysteresis curves. The strength development sequence for the column during R4 is summarized in **Table 6-10**.

The time at development of maximum strength in the positive direction is at 24.295 second for the test result, 24.765 second for ETABS model, 24.275 second for CPH model, and 24.280 second for Fiber model. For the negative direction, 24.445 second, 24.435 second, 24.435 second, and 24.430 second respectively. The results indicate that all models develop their maximum strength around the same time as the test response in both directions. It is to mention that the strength development sequence of the test response is affected by slip between the top steel beam and the top foundation of the column specimen,
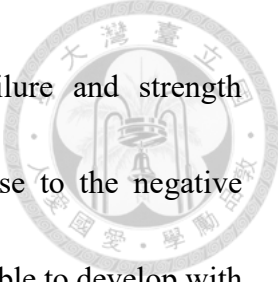
and the maximum strength may not occur at the time of maximum ground acceleration. Column C3 has lesser slip occurrence, allowing it to develop larger lateral displacements and the time of development of test maximum strengths may correspond better with the maximum ground accelerations.

For the lateral displacement responses, since the responses during R2 are still under linear behavior and since the initial natural periods are predicted well for the models, all the model responses correspond well to the test response.

During R4, the ETABS model response in **Figure 6-62** corresponds well with the test response up to 24 second. Increased lateral drifts develop in the positive direction and is underestimated by the model. Afterwards, a large lateral drift develops in the negative direction exceeding the test response due to shear failure and strength degradation of the model. The model then oscillates back to reach maximum strength in the positive direction, and directly collapses to the negative direction. Collapse does not occur and lateral displacements are still able to develop with increasing values after 25 second for the test specimen.

The CPH model and Fiber model have similar responses in R4, the model responses in **Figure 6-63** and **Figure 6-64** correspond well with the test response up to 24 second. Increased lateral drifts develop in the positive direction and is underestimated by both models as maximum strength is reached. Afterwards, a larger lateral drift develops in the

267

negative direction exceeding the test response due to shear failure and strength degradation of the models. The response then continues to collapse to the negative direction. Collapse does not occur and lateral displacements are still able to develop with increasing values after 25 second for the test specimen.

To conclude, all models provide around the same simulation results on the lateral displacement responses, and all models predict collapse which is different from the test response. Since the same shear-dominant column backbone curve is implemented into all three models, it is expected for the models to have the same behavior.

For the base shear responses, since the responses during R2 are still under linear behavior and since the initial natural periods are predicted well for the models, all the model responses correspond well to the test response.

During R4, the ETABS model response in **Figure 6-65** corresponds well with the test response up to 24 second as larger base shear is developed and maximum strengths are reached in both directions afterwards. The strength is captured by the model accurately, with values of 202.36 kN and 198.31 kN for the model comparing to the values of 211.21 kN and 185.28 kN for the test results. The maximum strength occurs at the same drift in the negative direction but one drift later in the positive direction. The model collapses after reaching shear failure in the positive direction and the lateral load carrying capacity is completely lost. Zero values of base shear are shown for the model after 25 second

268

while the base shear for the test specimen gradually degrades due to development of larger lateral displacements. Collapse does not occur for the test specimen.

The CPH model and Fiber model have similar responses in R4, the model responses in **Figure 6-66** and **Figure 6-67** correspond well with the test response up to 24 second as larger base shear is developed and maximum strengths are reached in both directions afterwards. The strengths are captured by the models accurately, with values of 194.80 kN and 198.16 kN for the CPH model and values of 191.99 kN and 195.22 kN for the Fiber model comparing to the values of 211.21 kN and 185.28 kN for the test results. The maximum strengths occur at exact same drifts with the test response in both directions. The models collapse after reaching shear failure in the negative direction and the lateral load carrying capacity is completely lost. Zero values of base shear are shown for the models after 25 second while the base shear for the test specimen gradually degrades due to development of larger lateral displacements. Collapse does not occur for the test specimen.

To conclude, all models provide around the same simulation results on the base shear response, while the CPH and Fiber model predict maximum strength development at the same drifts as the test response. All models predict collapse which is different from the test response. Since the same shear-dominant column backbone curve is implemented into all three models, it is expected for the models to have the same behavior.

269

For the hysteresis curves, the responses during R2 is still under linear behavior or just reached shear cracking strength as shown in **Figure 6-68**, **Figure 6-69**, and **Figure 6-70**. The stiffness for all models are shown to be estimated accurately.

During R4, the responses of all models are shown to be governed by the shear hinges, indicating shear-dominant behavior. Since the same shear-dominant column backbone curve is implemented into all three models, all models show the same backbone curve as they all collapse to the negative direction, and the slight difference is in their initial stiffness as discussed in **Section 6.4**. The models capture the strength and pre-shear failure displacement well, while simulating collapse behavior which doesn't occur for the actual test response. The lateral displacements developed during collapse show the same trend with the strength degradation backbone curve of the test response. Same as column C1, the ETABS model simulated strength degradation in the negative direction and unloads before reaching zero value to reach maximum strength in the positive direction. The CPH and Fiber model simulated a more direct collapse to the negative direction.

To conclude, all models provide good simulations with accurate strength and lateral displacement behaviors compared with the test response, while all models simulated collapse behavior, which is conservative since the actual test response does not collapse.

Frame T2

With slip problems occurring for columns C1 and C3, they behave with different

lateral deformations at the same time period. As a result, it is unable to plot the test

hysteresis curve of the frame for comparison with the models.

The initial natural period of the overall frame for the test is 0.1023 s, 0.1185 s for

ETABS model, 0.1161 s for CPH model, and 0.0918 s for Fiber model. The Fiber model

has the closest simulation value to the test, while the ETABS and CPH model provide

more conservative estimations with softer stiffness and larger natural period. Since the

same concept on column modeling is used to construct the ETABS and CPH model, the

two models share their natural periods around the same value. After R2, the test natural

period is 0.1144 s, 0.1160 s for the CPH model, and 0.1312 s for the Fiber model. After

R4, the test natural period is 0.2997 s, and collapse is simulated by all three models. The

test values show that the stiffness is slightly softened after R2, and degrades more after

R4. The CPH model shows very slight change between the initial condition and after R2,

while the Fiber model shows more degradation.

6.6.3 T3 Analysis Result

As shown in **Table 4-7**, there are a total of two runs of ground motions subjected on

Frame T3. R2 has an input PGA of 500 gal to simulate linear behaviors of structures under

small-to-medium earthquakes. R4 has an input PGA of 1g to simulate strength

development and collapse behaviors of structures under large earthquakes. The test

271

terminates with collapse of all columns after R4.
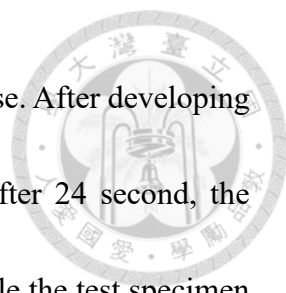
Column C1

Column C1 is located on the north side of frame T3. **Figure 6-71**, **Figure 6-72**, and **Figure 6-73** plot the lateral displacement responses. **Figure 6-74**, **Figure 6-75**, and **Figure 6-76** plot the base shear responses. **Figure 6-77**, **Figure 6-78**, and **Figure 6-79** plot the hysteresis curves. The strength development sequence for the column during R4 is summarized in **Table 6-11**.

The time at development of maximum strength in the positive direction is at 24.295 second for the test result, 23.480 second for ETABS model, 23.080 second for CPH model, and 23.475 second for Fiber model. For the negative direction, 24.430 second, 24.140 second, 23.190 second, and 24.145 second respectively. The results indicate that all models develop their maximum strength earlier than the test response in both directions.

For the lateral displacement responses, since the responses during R2 are still under linear behavior and since the initial natural periods are predicted well for the models, all the model responses correspond well to the test response. The slight overestimation in peak values for the ETABS and CPH model show that the models underestimate the initial stiffness, while the Fiber model predicts the stiffness more accurately.

The ETABS model and Fiber model have similar responses in R4, the model responses in **Figure 6-71** and **Figure 6-73** correspond well with the test response up to

21 second. The models then develop larger drifts than the test response. After developing maximum strength in the negative direction during a large drift after 24 second, the models then drift to the positive direction and directly collapses, while the test specimen collapses to the negative direction in the next drift.

The CPH model response in **Figure 6-72** corresponds well with the test response up to 21 second. The model then develops much larger drifts than the test response. Difference between lateral displacement behaviors of the CPH model and the two other models between 22 to 24 second can be observed. The CPH model predicts a slight larger displacement during one drift, which leads to higher base shear developed and more nonlinearity, indicating more severe stiffness softening. For the following drifts, the reloading stiffness would be softened, leading to larger displacement developed and earlier strength points reached for the CPH model. Just before 24 second, the model develops larger lateral displacement than the displacement at maximum strength in the negative direction (green triangular symbol), thus strength degradation behavior can be expected. After 24 second, the model drifts to the negative direction and directly collapses, while the test specimen collapses to the negative direction afterwards.

To conclude, the ETABS and Fiber model simulate the lateral displacement behaviors and the drift at collapse point well, while the CPH model provides a more conservative simulation with larger displacements developed. Since the same shear-

273

dominant column backbone curve is implemented into all three models, it is expected for the models to have around the same behavior.

For the base shear responses, since the responses during R2 are still under linear behavior and since the initial natural periods are predicted well for the models, all the model responses correspond well to the test response.

The ETABS model and Fiber model have similar responses in R4, the model responses in **Figure 6-74** and **Figure 6-76** correspond well with the test response up to 24 second as the developed strength in the positive direction suddenly degrades to zero. The strengths are more conservative for the models, with values of 115.98 kN and 121.13 kN for the ETABS model and values of 120.88 kN and 120.94 kN for the Fiber model comparing to the values of 204.14 kN and 156.96 kN for the test results. The maximum strength occurs a few drifts earlier in the positive direction and one drift earlier in the negative direction. Since the column has low ductility, the lateral strength immediately degrades to zero after reaching the maximum strengths for the test response and is captured by the models, which correspond well with the test response as no lateral strength can be developed after 25 second.

The CPH model response in **Figure 6-75** slightly overestimates the test response up to 24 second as the developed strength in the positive direction suddenly degrades to zero. The strengths are more conservative for the model, with values of 120.85 kN and 121.00
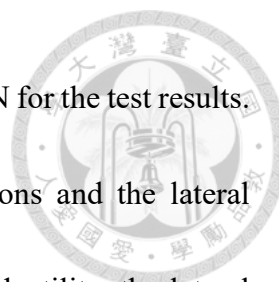
274

kN for the model comparing to the values of 204.14 kN and 156.96 kN for the test results. The maximum strengths occur a few drifts earlier in both directions and the lateral strength gradually degrades afterwards. Since the column has low ductility, the lateral strength immediately degrades to zero after reaching the maximum strengths for the test response. Although the model predicts earlier collapse, it still corresponds to the test response as no lateral strength can be developed after 25 second.

To conclude, the ETABS and Fiber model provide a more accurate simulation, and predict maximum strength development at drifts closer to the test response. The CPH model provides a more conservative simulation with earlier collapse behavior. All models predict collapse corresponding to the test response. Since the same shear-dominant column backbone curve is implemented into all three models, it is expected for the models to have the same behavior.

For the hysteresis curves, the responses during R2 is still under linear behavior or just reached shear cracking strength as shown in **Figure 6-77**, **Figure 6-78**, and **Figure 6-79**. The initial stiffness for the Fiber model is slightly higher than the two other models.

During R4, the responses of all models are shown to be governed by the shear hinges, indicating shear-dominant behavior. Since the same shear-dominant column backbone curve is implemented into all three models, all models show the same backbone curve as the ETABS and Fiber model collapse to the negative direction and the CPH model

collapses to the positive direction. The slight difference is in their initial stiffness as discussed in **Section 6.4**. The models capture the strength conservatively with lower values and underestimate lateral displacements after strength degradation. As explained previously, the actual behaviors for different models can vary even with very similar backbone curves. For example, the ETABS and Fiber model simulate a direct collapse to the positive direction, while the CPH model simulate unloading behavior before collapse.

To conclude, all models provide conservative simulations on the strength and lateral displacement behaviors compared with the test response, since the models predict loss of lateral load carrying capacity at a much lower lateral displacement.

Column C3

Column C3 is located on the south side of frame T3. **Figure 6-80**, **Figure 6-81**, and **Figure 6-82** plot the lateral displacement responses. **Figure 6-83**, **Figure 6-84**, and **Figure 6-85** plot the base shear responses. **Figure 6-86**, **Figure 6-87**, and **Figure 6-88** plot the hysteresis curves. The strength development sequence for the column during R4 is summarized in **Table 6-12**.

The time at development of maximum strength in the positive direction is at 24.240 second for the test result, 23.480 second for ETABS model, 23.080 second for CPH model, and 23.480 second for Fiber model. For the negative direction, during R2, 24.140 second, 23.190 second, and 24.145 second respectively. The results indicate that all models

develop their maximum strength earlier than the test response in both directions.

For the lateral displacement responses, since the responses during R2 are still under linear behavior and since the initial natural periods are predicted well for the models, all the model responses correspond well to the test response. The slight overestimation in peak values for the ETABS and CPH model show that the models underestimate the initial stiffness, while the Fiber model predicts the stiffness more accurately.

The ETABS model and Fiber model have similar responses in R4, the model responses in **Figure 6-80** and **Figure 6-82** correspond well with the test response up to 21 second. The models then develop larger drifts than the test response. After developing maximum strength in the negative direction during a large drift after 24 second, the models then drift to the positive direction and directly collapses, while the test specimen collapses to the negative direction in the next drift.

The CPH model response in **Figure 6-81** corresponds well with the test response up to 21 second. The model then develops much larger drifts than the test response. Difference between lateral displacement behaviors of the CPH model and the two other models between 22 to 24 second can be observed. The CPH model predicts a slight larger displacement during one drift, which leads to higher base shear developed and more nonlinearity, indicating more severe stiffness softening. For the following drifts, the reloading stiffness would be softened, leading to larger displacement developed and

277

earlier strength points reached for the CPH model. Just before 24 second, the model develops larger lateral displacement than the displacement at maximum strength in the negative direction (green triangular symbol), thus strength degradation behavior can be expected. After 24 second, the model drifts to the negative direction and directly collapses, while the test specimen collapses to the negative direction afterwards.

To conclude, the ETABS and Fiber model simulate the lateral displacement behaviors and the drift at collapse point well, while the CPH model provides a more conservative simulation with larger displacements developed. Since the same shear-dominant column backbone curve is implemented into all three models, it is expected for the models to have around the same behavior.

For the base shear responses, since the responses during R2 are still under linear behavior and since the initial natural periods are predicted well for the models, all the model responses correspond well to the test response.

The ETABS model and Fiber model have similar responses in R4, the model responses in **Figure 6-83** and **Figure 6-85** correspond well with the test response up to 24 second as the developed strength in the positive direction suddenly degrades to zero. The strengths are predicted accurately for the models, with values of 118.00 kN and 123.17 kN for the ETABS model and values of 124.01 kN and 123.78 kN for the Fiber model comparing to the values of 122.92 kN and 122.81 kN for the test results. The

278

maximum strength occurs a few drifts earlier in the positive direction and much later in the negative direction since the test maximum strength occurs during R2. Since the column has low ductility, the lateral strength immediately degrades to zero after reaching the maximum strengths for the test response and is captured by the models, which corresponds well with the test response as no lateral strength can be developed after 25 second.

The CPH model response in **Figure 6-84** slightly overestimates the test response up to 24 second as the developed strength in the positive direction suddenly degrades to zero. The strengths are predicted accurately for the models, with values of 123.23 kN and 123.62 kN for the model comparing to the values of 122.92 kN and 122.81 kN for the test results. The maximum strength occurs a few drifts earlier in the positive direction and much later in the negative direction since the test maximum strength occurs during R2. The lateral strength gradually degrades after 23 second. Since the column has low ductility, the lateral strength immediately degrades to zero after reaching the maximum strengths for the test response, although the model predicts earlier collapse, it still corresponds to the test response as no lateral strength can be developed after 25 second.

To conclude, the ETABS and Fiber model provide a more accurate simulation, and predict maximum strength development at drifts closer to the test response. The CPH model provides a more conservative simulation with earlier collapse behavior. All models

279

predict collapse corresponding to the test response. Since the same shear-dominant column backbone curve is implemented into all three models, it is expected for the models to have the same behavior.

For the hysteresis curves, the responses during R2 is still under linear behavior or just reached shear cracking strength as shown in **Figure 6-86**, **Figure 6-87**, and **Figure 6-88**. The initial stiffness for the Fiber model is slightly higher than the two other models.

During R4, the responses of all models are shown to be governed by the shear hinges, indicating shear-dominant behavior. Since the same shear-dominant column backbone curve is implemented into all three models, all models show the same backbone curve as the ETABS and Fiber model collapse to the negative direction and the CPH model collapses to the positive direction. The slight difference is in their initial stiffness as discussed in **Section 6.4**. The models capture the strength accurately and overestimate the lateral displacement at strength point but underestimate the lateral displacement after strength degradation. As explained previously, the actual behaviors for different models can vary even with very similar backbone curves. For example, the ETABS and Fiber model simulate a direct collapse to the positive direction, while the CPH model simulate unloading behavior before collapse.

To conclude, all models provide conservative simulations on the strength and lateral displacement behaviors compared with the test response, since the models predict loss of

lateral load carrying capacity at a much lower lateral displacement.

Frame T3
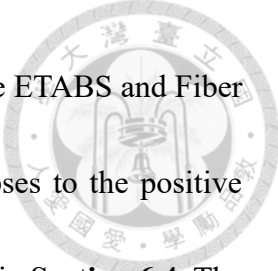
Figure 6-89, **Figure 6-90**, and **Figure 6-91** plot the hysteresis curves of the overall

frame for the three models.

The initial natural period of the overall frame for the test is 0.0958 s, 0.1190 s for

ETABS model, 0.1161 s for CPH model, and 0.0919 s for Fiber model. The Fiber model

has the closest simulation value to the test, while the ETABS and CPH model provide

more conservative estimations with softer stiffness and larger natural period. Since the

same concept on column modeling is used to construct the ETABS and CPH model, the

two models share their natural periods around the same value. After R2, the test natural

period is 0.1043 s, 0.1698 s for the CPH model, and 0.1923 s for the Fiber model. Collapse

occurs for the test and the models after R4 as no natural periods can be measured. The

test values show that the stiffness is slightly softened after R2. Both the CPH and Fiber

model show significant increase in their natural periods. The models may have exceeded

their cracking strength and enter nonlinear behavior after R2.

For the hysteresis curves, all the responses during R2 are still under linear behavior

or just reached shear cracking strength. The initial stiffness for the Fiber model is slightly

higher than the two other models.

During R4, since the same shear-dominant column backbone curve is implemented

281

into all three models, all models show the same backbone curve as the ETABS and Fiber

model collapse to the negative direction and the CPH model collapses to the positive

direction. The slight difference is in their initial stiffness as discussed in **Section 6.4**. The

models capture the strengths conservatively with lower strength values and underestimate

lateral displacements after strength degradation. A yielding plateau is developed by the

test specimen in the positive direction, which is caused by a combination of increasing

strength development for column C1 and strength degradation of column C3. This is not

an indication for flexural behavior, and is not simulated by the models since all columns

are shear-dominant. As explained previously, the actual behaviors for different models

can vary even with very similar backbone curves. For example, the ETABS and Fiber

model simulate a direct collapse to the positive direction, while the CPH model simulates

unloading behavior before collapse.

To conclude, all models provide conservative simulations on the strength and lateral

displacement behaviors compared with the test response, since the models predict loss of

lateral load carrying capacity at a much lower lateral displacement.

6.6.4 T4 Analysis Result

As shown in **Table 4-7**, there are a total of two runs of ground motions subjected on

Frame T4. R2 has an input PGA of 600 gal to simulate linear behaviors of structures under

small-to-medium earthquakes. R4 has an input PGA of 900 gal to simulate strength

development and collapse behaviors of structures under large earthquakes. The test

terminates with collapse of all columns after R4.

Column C1

Column C1 is located on the north side of frame T4. **Figure 6-92**, **Figure 6-93**, and

Figure 6-94 plot the lateral displacement responses. **Figure 6-95**, **Figure 6-96**, and

Figure 6-97 plot the base shear responses. **Figure 6-98**, **Figure 6-99**, and **Figure 6-100**

plot the hysteresis curves. The strength development sequences for the column during R2

and R4 are summarized in **Table 6-13** and **Table 6-14**.

The models develop maximum strengths in both R2 and R4, since the test develops

maximum strengths in R4, the comparison on failure sequence will be focused in R4. For

R4, the time at development of maximum strength in the positive direction is at 24.270

second for the test result, 24.255 second for ETABS model, 24.250 second for CPH model,

and 24.270 second for Fiber model. For the negative direction, 24.425 second, 24.145

second, 24.420 second, and 24.420 second respectively. The results indicate that the Fiber

model develops its maximum strength at the closest time to the test result in both

directions.

For the lateral displacement responses during R2, the ETABS model response in

Figure 6-92 slightly overestimates but corresponds well with the test response up to 24

second. The model then develops a large drift to the positive direction first reaching maximum strength, then to the negative direction and continues to collapse. Collapse does not occur for the test response.

The CPH and Fiber model have similar responses during R2, the model responses in **Figure 6-93** and **Figure 6-94** corresponds well with the test response up to 24 second. The lateral drifts start to increase for both models exceeding the test response afterwards. The models then reach maximum strength in the positive direction and continues to collapse. The Fiber model is able to oscillate for a few drifts before collapsing to the positive direction. Collapse does not occur for the test response.

Since all models collapse after R2, the ground motion during R4 is reapplied on the initial state of each model to continue analysis in R4. For the ETABS model during R4, the response in **Figure 6-92** corresponds well with the test response up to 24 second. The model then develops a large drift to the negative direction first reaching maximum strength, then to the positive direction and continues to collapse. The test specimen is able to oscillate for a few drifts after reaching maximum strengths and follows to collapse in the negative direction. The oscillation is not simulated by the model.

The CPH and Fiber model have similar responses during R4, the model responses in **Figure 6-93** and **Figure 6-94** corresponds well with the test response up to 24 second. The models then develop a large drift to the positive direction first reaching maximum

284

strength, then to the negative direction and continues to collapse. The test specimen is able to oscillate for a few drifts after reaching maximum strengths and follows to collapse in the negative direction. The oscillation is not simulated by the models.

To conclude, limited by the input maximum strength, all models develop their maximum strength in R2 and simulate collapse behavior. The maximum strength of test specimen is higher than the models. As a result, after subjecting to the same ground motion, the test specimen does not reach maximum strength and does not collapse in R2. During R4, all models and the test response develop their maximum strengths and collapse behavior. All models simulate the lateral displacement behaviors and the drift at collapse point well, with more conservative simulations as they collapse earlier than the test response. Since the same shear-dominant column backbone curve is implemented into all three models, it is expected for the models to have around the same behavior.

For the base shear responses during R2, the ETABS model response in **Figure 6-95** corresponds well with the test response up to 24 second as the base shear start to increase and maximum strengths are reached in both directions with the lateral strength suddenly degrading to zero. The test maximum strength has not been developed yet and is still able to provide lateral load carrying capacity.

The CPH and Fiber model have similar responses during R2, the model responses in **Figure 6-96** and **Figure 6-97** correspond well with the test response up to 24 second as

285

the base shear start to increase and maximum strengths are reached in both directions within a few drifts. The lateral strength suddenly degrades to zero afterwards. The test maximum strength has not been developed yet and is still able to provide lateral load carrying capacity.

During R4, the ETABS model response in **Figure 6-95** corresponds well with the test response up to 24 second as the base shear start to increase and maximum strengths are reached in both directions with the lateral strength suddenly degrading to zero. The strengths are more conservative for the model, with values of 98.88 kN and 84.69 kN for the ETABS model comparing to the values of 145.54 kN and 139.71 kN for the test results. The maximum strength occurs a drift earlier in the negative direction and at the same time in the positive direction. Since the column has low ductility, the lateral strength degrades significantly and down to zero within a few drifts after reaching the maximum strengths for the test response and is captured by the model, which corresponds well with the test response as no lateral strength can be developed after 25 second.

The CPH and Fiber model have similar responses during R4, the model responses in **Figure 6-96** and **Figure 6-97** correspond well with the test response up to 24 second as the base shear starts to increase and maximum strengths are reached in both directions with the lateral strength suddenly degrading to zero. The strengths are more conservative for the models, with values of 98.85 kN and 99.57 kN for the CPH model and values of

286

100.38 kN and 96.76 kN for the Fiber model comparing to the values of 145.54 kN and 139.71 kN for the test results. The maximum strengths occur at the exact same drift as the test response in both directions for both models. Since the column has low ductility, the lateral strength degrades significantly and down to zero within a few drifts after reaching the maximum strengths for the test response and is captured by the models, which correspond well with the test response as no lateral strength can be developed after 25 second.

To conclude, limited by the input maximum strength, all models develop their maximum strength in R2 and simulated collapse behavior while the test specimen is still intact. During R4, all models and the test response develop their maximum strength and collapse behavior. All models simulate the base shear behaviors and occurrence of collapse well, with more conservative simulations as they collapse earlier than the test response. Since the same shear-dominant column backbone curve is implemented into all three models, it is expected for the models to have around the same behavior.

For the hysteresis curves in R2, **Figure 6-98**, **Figure 6-99**, and **Figure 6-100** indicate that the responses of all models are shown to be governed by the shear hinges, indicating shear-dominant behavior. Since the same shear-dominant column backbone curve is implemented into all three models, all models show the same backbone curve as the ETABS model collapses to the negative direction and the CPH and Fiber model collapse

287

to the positive direction. The slight difference is in their initial stiffness as discussed in

Section 6.4. The test specimen is shown to still responding in linear behavior, while all

models exceed their maximum strength and simulate collapse. As explained previously,

the actual behaviors for different models can vary even with very similar backbone curves.

For example, the ETABS model simulated a direct collapse, while the CPH and Fiber

model simulate a few unloading behaviors before collapse.

During R4, the ETABS model predicts collapse to the positive direction and the CPH

and Fiber model predict collapse to the negative direction, corresponding well to the test

response. The Fiber model is shown to concentrate mostly under linear condition in the

positive direction and the CPH model is shown to enter strength degradation condition.

The models capture the strength conservatively with lower values and underestimate the

lateral displacement after strength degradation.

To conclude, all models provide conservative simulations on the strength and lateral

displacement behaviors compared with the test response, since the models predict loss of

lateral load carrying capacity at a much lower lateral displacement.

Column C3

Column C3 is located on the south side of frame T4. **Figure 6-101**, **Figure 6-102**,

and **Figure 6-103** plot the lateral displacement responses. **Figure 6-104**, **Figure 6-105**,

and **Figure 6-106** plot the base shear responses. **Figure 6-107**, **Figure 6-108**, and **Figure**

288

6-109 plot the hysteresis curves. The strength development sequences for the column during R2 and R4 are summarized in **Table 6-15** and **Table 6-16**.

The models develop maximum strengths in both R2 and R4, since the test develops maximum strengths in R4, the comparison on failure sequence will be focused in R4. For R4, the time at development of maximum strength in the positive direction is at 24.270 second for the test result, 24.255 second for ETABS model, 24.255 second for CPH model, and 24.270 second for Fiber model. For the negative direction, 24.435 second, 24.145 second, 24.420 second, and 24.420 second respectively. The results indicate that the Fiber model develops its maximum strength at the closest time to the test result in both directions.

For the lateral displacement responses during R2, the ETABS model response in **Figure 6-101** slightly overestimates but corresponds well with the test response up to 24 second. The model then develops a large drift to the positive direction first reaching maximum strength, then to the negative direction and continues to collapse. Collapse does not occur for the test response.

The CPH and Fiber model have similar responses during R2, the model responses in **Figure 6-102** and **Figure 6-103** correspond well with the test response up to 24 second. The lateral drifts start to increase for both models exceeding the test response afterwards. The models then reach maximum strength in the positive direction and continues to

289

collapse. The Fiber model is able to oscillate for a few drifts before collapsing to the positive direction. Collapse does not occur for the test response.

Since all models collapse after R2, the ground motion during R4 is reapplied on the initial state of each model to continue analysis in R4. For the ETABS model during R4, the response in **Figure 6-101** corresponds well with the test response up to 24 second. The model then develops a large drift to the negative direction first reaching maximum strength, then to the positive direction and continues to collapse. The test specimen is able to oscillate for a few drifts after reaching maximum strengths and follows to collapse in the negative direction. The oscillation is not simulated by the model.

The CPH and Fiber model have similar responses during R4, the model responses in **Figure 6-102** and **Figure 6-103** correspond well with the test response up to 24 second. The models then develop a large drift to the positive direction first reaching maximum strength, then to the negative direction and continues to collapse. The test specimen is able to oscillate for a few drifts after reaching maximum strengths and follows to collapse in the negative direction. The oscillation is not simulated by the models.

To conclude, limited by the input maximum strength, all models develop their maximum strength in R2 and simulate collapse behavior. Since the maximum strength of test specimen is higher than the models, the specimen is still intact after R2. During R4, all models and the test response develop their maximum strengths and collapse behavior.

290

All models simulate the lateral displacement behaviors and the drift at collapse point well, with more conservative simulations as they collapse earlier than the test response. Since the same shear-dominant column backbone curve is implemented into all three models, it is expected for the models to have around the same behavior.

For the base shear responses during R2, the ETABS model response in **Figure 6-104** corresponds well with the test response up to 24 second as the base shear start to increase and maximum strengths are reached in both directions with the lateral strength suddenly degrading to zero. The test maximum strength has not been developed yet and is still able to provide lateral load carrying capacity.

The CPH and Fiber model have similar responses during R2, the model responses in **Figure 6-105** and **Figure 6-106** correspond well with the test response up to 24 second as the base shear start to increase and maximum strengths are reached in both directions within a few drifts. The lateral strength suddenly degrades to zero afterwards. The test maximum strength has not been developed yet and is still able to provide lateral load carrying capacity.

During R4, the ETABS model response in **Figure 6-104** corresponds well with the test response up to 24 second as the base shear start to increase and maximum strengths are reached in both directions with the lateral strength suddenly degrading to zero. The strengths are more conservative for the model, with values of 102.94 kN and 88.56 kN

291

for the ETABS model comparing to the values of 124.28 kN and 159.46 kN for the test results. The maximum strength occurs a drift earlier in the negative direction and at the same time in the positive direction. Since the column has low ductility, the lateral strength degrades significantly and down to zero within a few drifts after reaching the maximum strengths for the test response and is captured by the model, which corresponds well with the test response as no lateral strength can be developed after 25 second.

The CPH and Fiber model have similar responses during R4, the model responses in **Figure 6-105** and **Figure 6-106** correspond well with the test response up to 24 second as the base shear start to increase and maximum strengths are reached in both directions with the lateral strength suddenly degrading to zero. The strengths are more conservative for the models, with values of 106.46 kN and 105.05 kN for the CPH model and values of 106.29 kN and 101.04 kN for the Fiber model comparing to the values of 124.28 kN and 159.46 kN for the test results. The maximum strengths occur at the exact same drift as the test response in both directions for both models. Since the column has low ductility, the lateral strength degrades significantly and down to zero within a few drifts after reaching the maximum strengths for the test response and is captured by the models, which correspond well with the test response as no lateral strength can be developed after 25 second.

To conclude, limited by the input maximum strength, all models develop their

maximum strength in R2 and simulated collapse behavior while the test specimen is still intact. During R4, all models and the test response develop their maximum strength and collapse behavior. All models simulate the base shear behaviors and the occurrence of collapse well, with more conservative simulations as they collapse earlier than the test response. Since the same shear-dominant column backbone curve is implemented into all three models, it is expected for the models to have around the same behavior.

For the hysteresis curves in R2, **Figure 6-107**, **Figure 6-108**, and **Figure 6-109** indicate that the responses of all models are shown to be governed by the shear hinges, indicating shear-dominant behavior. Since the same shear-dominant column backbone curve is implemented into all three models, all models show the same backbone curve as the ETABS model collapses to the negative direction and the CPH and Fiber model collapse to the positive direction. The slight difference is in their initial stiffness as discussed in **Section 6.4**. The test specimen is shown to still responding in linear behavior, while all models exceed their maximum strength and simulate collapse. As explained previously, the actual behaviors for different models can vary even with very similar backbone curves. For example, the ETABS model simulated a direct collapse, while the CPH and Fiber model simulate a few unloading behaviors before collapse.

During R4, the ETABS model predict collapse to the positive direction and the CPH and Fiber model predict collapse to the negative direction, corresponding well to the test

response. The Fiber model is shown to concentrate mostly under linear condition in the positive direction and the CPH model is shown to enter strength degradation condition. The models capture the strength conservatively with lower values and underestimate the lateral displacement after strength degradation.

To conclude, all models provide conservative simulations on the strength and lateral displacement behaviors compared with the test response, since the models predict loss of lateral load carrying capacity at a much lower lateral displacement.

Frame T4

Figure 6-110, **Figure 6-111**, and **Figure 6-112** plot the hysteresis curves of the overall frame for the three models.

The initial natural period of the overall frame for the test is 0.1001 s, 0.1495 s for ETABS model, 0.1473 s for CPH model, and 0.1029 s for Fiber model. The Fiber model has the closest simulation value to the test, while the ETABS and CPH model provide more conservative estimations with softer stiffness and larger natural period. Since the same concept on column modeling is used to construct the ETABS and CPH model, the two models share their natural periods around the same value. After R2, the test natural period is 0.1154 s, collapse occur for the models after R2 as no natural periods can be measured. Collapse also occur for the test and the models after R4 so no natural periods can be measured. The test values show that the stiffness is slightly softened after R2,

294
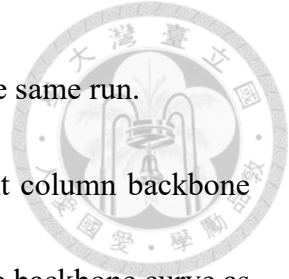
while all models simulate significant collapse damage behavior in the same run.

For the hysteresis curves in R2, since the same shear-dominant column backbone curve is implemented into all three models, all models show the same backbone curve as the ETABS model collapses to the negative direction and the CPH and Fiber model collapse to the positive direction. The slight difference is in their initial stiffness as discussed in **Section 6.4**. The test specimen is shown to still responding in linear behavior, while all models exceed their maximum strength and simulated collapse. As explained previously, the actual behaviors for different models can vary even with very similar backbone curves. For example, the ETABS model simulated a direct collapse, while the CPH and Fiber model simulate a few unloading behaviors before collapse.

During R4, the ETABS model predict collapse to the positive direction and the CPH and Fiber model predict collapse to the negative direction, corresponding well to the test response. Since the two columns in Frame T4 have identical responses, the cumulated frame hysteresis curve is shown to possess the same behavior as individual columns, but with higher strength values. The Fiber model is shown to concentrate mostly under linear condition in the positive direction and the CPH model is shown to enter strength degradation condition. The models capture the strength conservatively with lower values and underestimate the lateral displacement after strength degradation.

To conclude, all models provide conservative simulations on the strength and lateral

displacement behaviors compared with the test response, since the models predict loss of

lateral load carrying capacity at a much lower lateral displacement.

6.7 Discussion on Time History Analysis Result

As the overall lateral displacements and base shear responses are introduced, this

section discusses the further processed stiffness time history responses of all three column

models of all nine column specimens frame by frame. The test stiffness time history

responses are introduced in **Section 4.4.2**. This section also concludes the pros and cons

of the ETABS model, CPH model, and Fiber model based on their model setup and time

history analysis results.

6.7.1 Stiffness Behavior

The simulated stiffness time history responses for all nine columns are presented in

this section. The measured stiffness are plotted as grey circular symbols on the figures,

and the ETABS model, CPH model, and Fiber model responses are plotted as magenta,

green, and red circular symbols respectively. The data points are the secant stiffness

values, which is the slope of the line connecting the data point and the zero point. As

discussed in **Section 4.4.2**, numerous small lateral forces are subjected on the columns

before and after the large forces that induce the development of strength for shaking table

tests, which leads to numerous small lateral displacements. For the processing of data

points, drifts smaller than 1 mm are neglected since they may lead to error readings, and those larger than 1 mm are calculated to compare the stiffness time history response of the three models with the shaking table test responses.

The strength development sequences of flexure-dominated and shear-dominated RC columns with increasing lateral deformations are introduced in **Section 4.4.2**, and this section will focus on comparing the model responses with the test responses, which will be presented frame by frame. **Section 4.4.2** have presented discussions on the test responses of each column in detail, and the test behaviors will not be re-discussed as the conclusions provided will be directly implemented in this section.

Frame T1
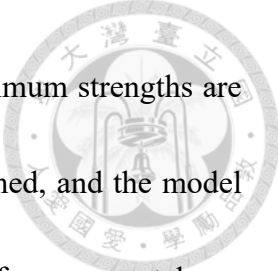
The test stiffness responses for columns C1 and C3 are similar and their modeling results are also identical, therefore, the responses of the two columns will be discussed together, and the response for column C2 will be discussed separately.

Figure 6-113 and **Figure 6-119** show the ETABS model responses for both columns. The model develops its linear stiffness before 24 second in R2. The elastic stiffness in this time period, which is the stiffness in the negative direction for column C1 and in the positive direction for column C3, is underestimated by the models. Since the input initial stiffness for the model is the effective stiffness, which simulates the behavior from material elasticity to reinforcement yielding by a linear stiffness, it is expected for the

297

model to underestimate the test elastic stiffness. The model stiffness is slightly degraded after 24 second as shear cracking strength is exceeded and the column enters nonlinear behavior. After 24 second in R2 up to 24 second in R4, the model stiffness remains around the same value as no larger earthquake force is subjected to soften the stiffness, the test stiffness is overestimated in this region. After 24 second in R4, maximum strengths are developed as the yielding plateaus on the flexural elements are reached, and the model stiffness significantly degrades. The values are closer to the test stiffness but still slightly overestimates. The model stiffness remains around the same value up to the end of R6 maintaining the same difference with the test stiffness.

Figure 6-114 and **Figure 6-120** show the CPH model responses for both columns. The model develops its linear stiffness before 24 second in R2. The elastic stiffness in this time period, which is the stiffness in the negative direction for column C1 and in the positive direction for column C3, is underestimated by the model. Since the input initial stiffness for the model is the effective stiffness, which simulates the behavior from material elasticity to reinforcement yielding by a linear stiffness, it is expected for the model to underestimate the test elastic stiffness. The model stiffness is slightly degraded after 24 second as shear cracking strength is exceeded and the column enters nonlinear behavior. After 24 second in R2 up to 24 second in R4, the model stiffness remains around the same value as no larger earthquake force is subjected to soften the stiffness, the test

stiffness is overestimated in this region. After 24 second in R4, maximum strengths are

developed as the yielding plateaus on the flexural elements are reached, and the model

stiffness significantly degrades. The values correspond to the test stiffness accurately up

to the end of R6.

Figure 6-115 and **Figure 6-121** show the Fiber model responses for both columns.

The model captures the elastic stiffness, which is the stiffness in the negative direction

for column C1 and in the positive direction for column C3, accurately to the test response.

The model stiffness is slightly degraded after 24 second as the materials enter nonlinearity.

After 24 second in R2 up to 24 second in R4, the model stiffness remains around the same

value as no larger earthquake force is subjected to soften the stiffness, the test stiffness is

overestimated in this region. After 24 second in R4, maximum strengths are developed as

the yielding plateaus on the flexural elements are reached, and the model stiffness

significantly degrades. The values correspond to the test stiffness accurately up to the end

of R6.

Figure 6-116 shows the ETABS model response for column C2. The model develops

its linear stiffness before 24 second in R2. No test stiffness is processed in this time period

for comparison. The model stiffness is slightly degraded after 24 second as shear cracking

strength is exceeded and the column enters nonlinear behavior. After 24 second in R2 up

to 24 second in R4, the model stiffness remains around the same value as no larger

earthquake force is subjected to soften the stiffness, the test stiffness is underestimated in this region. Since the column has higher longitudinal reinforcement ratio, it is expected for the column to develop higher stiffness. The contribution of higher reinforcement ratio to stiffness is not captured by the initial effective stiffness of the model, thus the model stiffness is lower than the actual test response even at its initial state. After 24 second in R4, maximum strengths are developed as the shear strengths on the shear hinges are reached, and the model stiffness degrades significantly down to zero. The model and test responses correspond well after the maximum strength development.

Figure 6-117 shows the CPH model response for column C2. The model develops its linear stiffness before 24 second in R2. No test stiffness is processed in this time period for comparison. The model stiffness is slightly degraded after 24 second as shear cracking strength is exceeded and the column enters nonlinear behavior. After 24 second in R2 up to 24 second in R4, the model stiffness remains around the same value as no larger earthquake force is subjected to soften the stiffness, the test stiffness is underestimated in this region. Since the column has higher longitudinal reinforcement ratio, it is expected for the column to develop higher stiffness. The contribution of higher reinforcement ratio to stiffness is not captured by the initial effective stiffness of the model, thus the model stiffness is lower than the actual test response even at its initial state. After 24 second in R4, maximum strengths are developed as the shear strengths on the shear hinges are

300

reached, and the model stiffness degrades significantly down to zero. The model and test responses correspond well after the maximum strength development.

Figure 6-118 shows the Fiber model responses for column C2. The model develops its linear stiffness before 24 second in R2. No test stiffness is processed in this time period for comparison. The model stiffness is degraded in the positive direction and slightly degraded in the negative direction after 24 second as shear cracking strength is exceeded and the column enters nonlinear behavior. After 24 second in R2 up to 24 second in R4, the model stiffness remains around the same value as no larger earthquake force is subjected to soften the stiffness, the test stiffness is only slightly underestimated in this region. Since the column has higher longitudinal reinforcement ratio, it is expected for the column to develop higher stiffness. The contribution of higher reinforcement ratio to stiffness is captured by the initial stiffness of the Fiber model during elastic condition. As a result, even when the model stiffness is softened after 24 second in R2, it can still simulate stiffness close to the actual test response. After 24 second in R4, maximum strengths are developed as the shear strengths on the shear hinges are reached, and the model stiffness degrades significantly down to zero. The model and test responses correspond well after the maximum strength development.

Frame T2

The test stiffness responses for both columns are similar during R2 but vary in R4

due to slip between the top steel beam and column foundation. Slip does not occur for the models, thus, the modeling results are identical for both columns, and the responses for both columns will be discussed together.
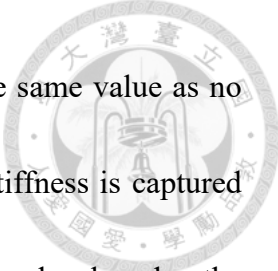
Figure 6-122 and **Figure 6-125** show the ETABS model responses for both columns. The model develops its linear stiffness before 24 second in R2. The elastic stiffness in this time period, which is the stiffness in both directions for both columns, is underestimated by the model. Since the input initial stiffness for the model is the effective stiffness, which simulates the behavior from material elasticity to shear cracking by a linear stiffness, it is expected for the model to underestimate the test elastic stiffness. The model stiffness is degraded after 24 second as shear cracking strength is exceeded and the column enters nonlinear behavior. After 24 second in R2 up to the end of the run, the model stiffness remains around the same value as no larger earthquake force is subjected to soften the stiffness, the test stiffness is slightly underestimated in this region. Before 24 second during R4, the model stiffness remains around the same value and estimates the test stiffness accurately. After 24 second in R4, maximum strengths are developed as the shear strengths on the shear hinges are reached, and the model stiffness degrades significantly down to zero and collapses. Collapse does not occur for the test specimens.

Figure 6-123 and **Figure 6-126** show the CPH model responses for both columns. The model develops its linear stiffness before 24 second in R2. The elastic stiffness in

302

this time period, which is the stiffness in both directions for both columns, is

underestimated by the model. Since the input initial stiffness for the model is the effective

stiffness, which simulates the behavior from material elasticity to shear cracking by a

linear stiffness, it is expected for the model to underestimate the test elastic stiffness. The

model stiffness is degraded after 24 second as shear cracking strength is exceeded and the

column enters nonlinear behavior. After 24 second in R2 up to the end of the run, the

model stiffness remains around the same value as no larger earthquake force is subjected

to soften the stiffness, the test stiffness is slightly underestimated in this region. Before

24 second during R4, the model stiffness remains around the same value and estimates

the test stiffness accurately. After 24 second in R4, maximum strengths are developed as

the shear strengths on the shear hinges are reached, and the model stiffness degrades

significantly down to zero and collapses. Collapse does not occur for the test specimens.

Figure 6-124 and **Figure 6-127** show the Fiber model responses for both columns.

The model develops its linear stiffness before 24 second in R2. The elastic stiffness in

this time period, which is the stiffness in both directions for both columns, is simulated

but slightly overestimated by the model. The Fiber model simulates the elastic behavior

of the column based on constitutive laws of the materials, thus can capture a higher

stiffness at the initial condition. The model stiffness is degraded after 24 second as shear

cracking strength is exceeded and the column enters nonlinear behavior. After 24 second

303

in R2 up to 24 second in R4, the model stiffness remains around the same value as no larger earthquake force is subjected to soften the stiffness, the test stiffness is captured accurately in this region. After 24 second in R4, maximum strengths are developed as the shear strengths on the shear hinges are reached, and the model stiffness degrades significantly down to zero and collapses. Collapse does not occur for the test specimens.

Frame T3

The test stiffness responses for both columns are similar during both runs and the modeling results are identical for both columns, thus, the responses for both columns will be discussed together.
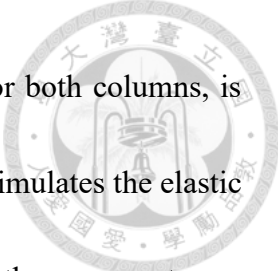
Figure 6-128 and **Figure 6-131** show the ETABS model responses for both columns. The model develops its linear stiffness before 24 second in R2. The elastic stiffness in this time period, which is the stiffness in the positive direction for both columns, is slightly underestimated by the model. Since the input initial stiffness for the model is the effective stiffness, which simulates the behavior from material elasticity to shear cracking by a linear stiffness, it is expected for the model to underestimate the test elastic stiffness. The model stiffness is degraded after 24 second as shear cracking strength is exceeded and the column enters nonlinear behavior. After 24 second in R2 up to 24 second in R4, the model stiffness remains around the same value as no larger earthquake force is subjected to soften the stiffness, the test stiffness is significantly underestimated in this

304

region. After 24 second in R4, maximum strengths are developed as the shear strengths on the shear hinges are reached, and the model stiffness degrades significantly down to zero and collapses, corresponding to the test response.

Figure 6-129 and **Figure 6-132** show the CPH model responses for both columns. The model develops its linear stiffness before 24 second in R2. The elastic stiffness in this time period, which is the stiffness in the positive direction for both columns, is slightly underestimated by the model. Since the input initial stiffness for the model is the effective stiffness, which simulates the behavior from material elasticity to shear cracking by a linear stiffness, it is expected for the model to underestimate the test elastic stiffness. The model stiffness is degraded after 24 second as shear cracking strength is exceeded and the column enters nonlinear behavior. After 24 second in R2 up to 21 second in R4, the model stiffness remains around the same value as no larger earthquake force is subjected to soften the stiffness, the test stiffness is significantly underestimated in this region. After 21 second in R4, maximum strengths are developed as the shear strengths on the shear hinges are reached, and the model stiffness degrades gradually within a few drifts. The model stiffness then degrades significantly down to zero and collapses after 23 second, which is earlier than the test response.

Figure 6-130 and **Figure 6-133** show the Fiber model responses for both columns. The model develops its linear stiffness before 24 second in R2. The elastic stiffness in

305

this time period, which is the stiffness in in the positive direction for both columns, is simulated but slightly overestimated by the model. The Fiber model simulates the elastic behavior of the column based on constitutive laws of the materials, thus can capture a higher stiffness at the initial condition. The model stiffness is degraded after 24 second as shear cracking strength is exceeded and the column enters nonlinear behavior. After 24 second in R2 up to 24 second in R4, the model stiffness remains around the same value as no larger earthquake force is subjected to soften the stiffness, the test stiffness is underestimated in this region. After 24 second in R4, maximum strengths are developed as the shear strengths on the shear hinges are reached, and the model stiffness degrades significantly down to zero and collapses, corresponding to the test response.

Frame T4
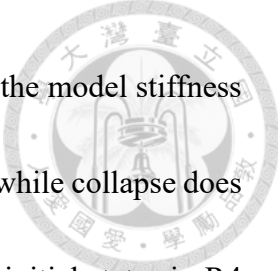
The test stiffness responses for both columns are similar during both runs and the modeling results are identical for both columns, thus, the responses for both columns will be discussed together.

Figure 6-134 and **Figure 6-137** show the ETABS model responses for both columns. The model develops its linear stiffness before 24 second in R2. The elastic stiffness in this time period, which is the stiffness in the negative direction for column C1 and in both directions for column C3, is underestimated by the model. Since the input initial stiffness for the model is the effective stiffness, which simulates the behavior from material

306

elasticity to shear cracking by a linear stiffness, it is expected for the model to

underestimate the test elastic stiffness. After 24 second in R2, maximum strengths are

developed as the shear strengths on the shear hinges are reached, and the model stiffness

degrades significantly down to zero and collapses, while collapse does not occur for the

test specimens. The model is re-simulated from its initial states in R4 since it collapses in

R2. With larger earthquake force, the model stiffness is degraded after 20 second in R4

as shear cracking strength is exceeded and the column enters nonlinear behavior. Up to

24 second in R4, the model stiffness remains around the same value with slight

degradation, the test stiffness is slightly underestimated in this region. After 24 second in

R4, maximum strengths are developed as the shear strengths on the shear hinges are

reached, and the model stiffness degrades significantly down to zero and collapses,

corresponding to the test response.

Figure 6-135 and Figure 6-138 show the CPH model responses for both columns.

The model develops its linear stiffness before 24 second in R2. The elastic stiffness in

this time period, which is the stiffness in the negative direction for column C1 and in both

directions for column C3, is underestimated by the model. Since the input initial stiffness

for the model is the effective stiffness, which simulates the behavior from material

elasticity to shear cracking by a linear stiffness, it is expected for the model to

underestimate the test elastic stiffness. After 24 second in R2, maximum strengths are

developed as the shear strengths on the shear hinges are reached, and the model stiffness degrades significantly down to zero within a few drifts and collapses, while collapse does not occur for the test specimens. The model is re-simulated from its initial states in R4 since it collapses in R2. With larger earthquake force, the model stiffness is degraded after 20 second in R4 as shear cracking strength is exceeded and the column enters nonlinear behavior. Up to 24 second in R4, the model stiffness remains around the same value with slight degradation, the test stiffness is slightly underestimated in this region. After 24 second in R4, maximum strengths are developed as the shear strengths on the shear hinges are reached, and the model stiffness degrades significantly down to zero and collapses, corresponding to the test response.

Figure 6-136 and **Figure 6-139** show the Fiber model responses for both columns. The model develops its linear stiffness before 24 second in R2. The elastic stiffness in this time period, which is the stiffness in the negative direction for column C1 and in both directions for column C3, is captured accurately by the model. The Fiber model simulates the elastic behavior of the column based on constitutive laws of the materials, thus can capture a higher stiffness at the initial condition. After 24 second in R2, maximum strengths are developed as the shear strengths on the shear hinges are reached, and the model stiffness degrades significantly down to zero within a few drifts and collapses, while collapse does not occur for the test specimens. The model is re-simulated from its

initial states in R4 since it collapses in R2. With larger earthquake force, the model

stiffness is degraded after 20 second in R4 as shear cracking strength is exceeded and the

column enters nonlinear behavior. Up to 24 second in R4, the model stiffness remains

around the same value with slight degradation, the test stiffness is accurately captured by

the model in this region. After 24 second in R4, maximum strengths are developed as the

shear strengths on the shear hinges are reached, and the model stiffness degrades

significantly down to zero and collapses, corresponding to the test response.

6.7.2 Overall Behavior

This chapter introduces the ETABS model recommended by NCREE/TEASDA

(2021), the CPH model developed by this research following the column modeling

concept of ETABS model, and the Fiber model developed by this research based on fiber

section modeling.

Displacement history analysis based on actual lateral displacements of test

specimens are conducted on the models to validate the energy dissipation capacities of

the models with shaking table test responses. Time history analysis are conducted on the

models to compare the time history and hysteresis responses of different models under

subjection of ground motions with shaking table test responses, and to validate the

feasibility of the cyclic loading-developed column models to simulate actual ground

motion situations.

For the construction of the ETABS and CPH model in their corresponding structural analysis software, the linear behavior is simulated by a linear column element with the input of simple flexural and shear rigidity parameters which only varies with the subjected axial load. The nonlinear flexural behavior is simulated by a flexural hinge with an input of quadrilinear force-displacement relationship. The nonlinear shear behavior is simulated by a shear hinge with an input of trilinear force-displacement relationship. For the construction of the Fiber model in OpenSees, the linear behavior is simulated by a fiber section column element, which requires the definition of confined and unconfined concrete material and steel material constitutive properties, and the definition of the concrete fibers and steel fibers on correct positions on the column section. The fiber section is sensitive to all design parameters of a column specimen since its behavior is developed based on the constitutive materials. The nonlinear flexural behavior can also be simulated by the fiber section column element. The nonlinear shear behavior is simulated by the same hinge as the two other models. To conclude, the ETABS and CPH models simulate linear behaviors based on simplified effective stiffness models, and the Fiber model simulates linear behavior based on material constitutive properties, which can vary sensitively with change in specimen design parameters. The ETABS and CPH models simulate flexural behaviors based on simplified flexural hinges, and the Fiber

310
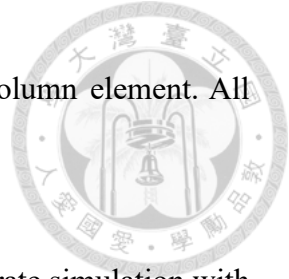
model is more complex due to its definition of the fiber section column element. All

models simulate shear behaviors with the same shear hinge.

For the natural periods, the Fiber model provides the most accurate simulation with

the test value, while the ETABS and CPH model provide conservative simulations with

softer stiffness and larger natural period. For flexural behaviors, the time history analysis

results indicate that the Fiber model, which simulates flexural strength considering the

change in axial load, provides the most accurate simulation results on the lateral

displacement and base shear responses, providing with conservative hysteresis behavior

as the energy dissipation capacity is lower. The ETABS and CPH model, which simulates

flexural strength neglecting the change in axial load, provide conservative simulation

results on the base shear responses with lower strength values, and underestimate the

lateral displacements, while providing with accurate hysteresis behavior. For shear

behaviors, the time history analysis results indicate that all models provide around the

same result, with conservative base shear responses as the strength values are lower, and

conservative lateral displacements since the models predict earlier collapse than the test

result, while providing with accurate hysteresis behavior. For stiffness behaviors, since

the Fiber model can simulate accurate linear displacements, which is accumulated to the

nonlinear displacements affecting the overall stiffness development and degradation, it

provides the most accurate simulation on the stiffness responses. The ETABS and CPH

model provide conservative simulation on the stiffness responses by estimating lower stiffness than the actual test response, leading to larger developed lateral displacements and accumulated damages.
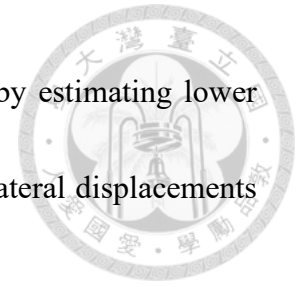
To summarize, the Fiber model is more complex to construct, but provides with a more accurate simulation result. The ETABS and CPH model are simpler to construct, while providing conservative simulation results. The analysis results correspond with the concept of complex models with accurate analysis result and simplified models with conservative analysis result. The column modeling techniques introduced in **Chapter 5**, including the flexural and shear force-displacement relationships and simplified effective stiffness models, the hysteresis modeling proposed by Ling et al. (2022), and the ETABS model developed by NCREE/TEASDA (2021) as well as the CPH and Fiber model developed by this research, are shown to simulate the shaking table-tested column responses in Su (2007) well, and are validated for the nonlinear and hysteresis modeling of RC columns during performance of nonlinear time domain analysis on RC structures.

CHAPTER 7: CONCLUSIONS AND FUTURE WORK

7.1 Summary

The main objectives of this research are as follows:

1. To study shaking table test responses of flexural and shear-dominant intermediate-short reinforced concrete columns on their strength, stiffness, and collapse behaviors.

2. To validate the feasibility for cyclic loading test responses to represent shaking table test responses on shear-dominant reinforced concrete columns for simpler and more economic test setup.

3. To compare the shaking table test responses with current analytical models to propose modeling techniques on column strength and lateral load-displacement behavior.

4. To develop both simplified and detailed column models inside structural analysis program OpenSees on column modeling for nonlinear time domain analysis.

5. To compare the responses of column model proposed by NCREE/TEASDA (2021) and the responses of column models proposed by this research with shaking table-tested column responses by performing nonlinear time history analysis to validate the feasibilities of the models.

This research separates the contents into four chapters to perform study on the above

objectives. **Chapter 3** briefly introduces the cyclic loading tests on reinforced concrete intermediate-short columns conducted by Weng (2007). **Chapter 4** introduces the shaking table tests on reinforced concrete intermediate-short columns conducted by Su (2007) in detail by presenting the lateral displacement, base shear, and axial load time history responses as well as hysteresis responses of each column, and discusses observed behaviors. **Chapter 5** compares the cyclic loading-tested column responses with shaking table-tested column responses on their strength, stiffness, and collapse behaviors. **Chapter 5** then continues to discuss observed behaviors on the strength of shaking table-tested columns governed by flexural and shear behavior, and performs research on the strength modeling of the columns with or without the consideration of varying axial load. The last part of **Chapter 5** compares current effective stiffness models and column backbone curve models with the shaking table-tested column responses introduced in **Chapter 4**. **Chapter 6** first introduces the column model proposed by NCREE/TEASDA (2021) which is capable of simulating column behaviors when performing nonlinear time domain analysis, and continues to introduce the CPH simplified column model (CPH model) and the Fiber detailed column model (Fiber model) proposed by this research. Displacement history analysis on the column models is then performed based on actual lateral displacement response of the shaking table-tested columns to validate the feasibility for the cyclic loading-developed hysteresis modeling proposed by Ling et al.

314

(2022) to simulate actual shaking table test responses. Time history analysis is performed

on the column models at the last part of **Chapter 6** to compare the responses of different

models and validate their feasibility to simulate shaking table-tested responses by

comparing with the results introduced in **Chapter 4**.

7.2 Conclusions

Several research objectives are introduced in the last section, and all the objectives

can be summarized into one core research purpose, which is to validate the feasibility of

the cyclic loading-based responses and cyclic loading-developed analytical models to

represent and simulate actual shaking table-tested responses, and to promote the

implementation of nonlinear time domain analysis. The conclusions of this research can

be discussed by each objective, and concluded together at last. The conclusions of this

research are as follows:

1. This research processed the flexural and shear strengths, axial load values at

    maximum strengths, and effective stiffness values of the shaking table-tested column

    results conducted by Su (2007) for further research purpose. The Varying axial loads

    of shaking table tests due to overturning moments are identified, and this research

    concludes that the flexural strengths of individual flexural-dominant reinforced

    concrete columns are governed by their initial sustained axial load, and are affected

315
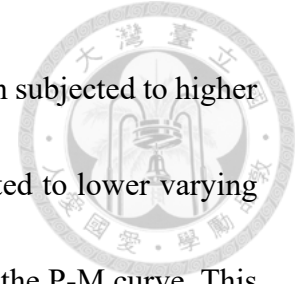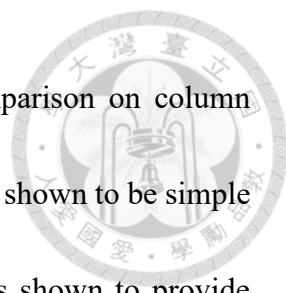
by the varying axial loads, with enhanced flexural strength when subjected to higher varying axial loads and lowered flexural strength when subjected to lower varying axial loads for columns responding below the balance point on the P-M curve. This research further concludes that the shear strengths of individual shear-dominant reinforced concrete columns are governed by their initial sustained axial load, and are affected by failure sequence instead of varying axial loads, with the first developed shear strength on one direction larger than the second developed shear strength on the other direction due to better integrity of concrete material on the column body during the first developed shear strength.

2. The comparison results of cyclic loading-tested columns and shaking table-tested columns indicate that the cyclic loading test results are shown to be capable to represent shaking table test results. On the one hand, the cyclic loading test results provide good consistency and accuracy with shaking table test stiffness, collapse deformation, and displacement behavior. On the other hand, the shear strength values are lower for the cyclic loading test results due to lower loading rate. This indicates that the shear strength is enhanced when subjecting to actual ground motions, and the tested strengths from cyclic loading tests will always be more conservative with values lower than the actual strength of shaking table test responses under actual ground motions. By single material-wise, higher loading rate can directly enhance

316
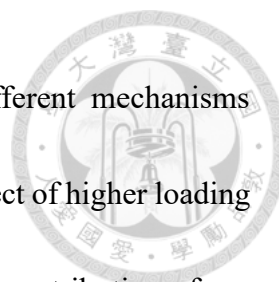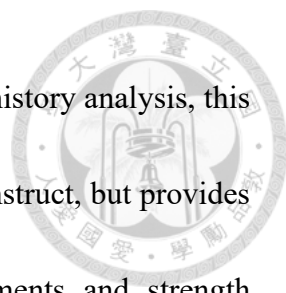
the compressive or tensile strength of the material, with different mechanisms governing different types of materials. By member-wise, the effect of higher loading rate on strength enhancement may not be that direct due to contributions from different materials and effect of larger sizes, but still holds its benefit. By structural-wise, the redundancy of the structure, the load distribution on members with different stiffness, and additional dynamic effects can also affect or enhance the strength development in addition to higher loading rates. For example, singly-tested reinforced concrete shear walls can have strength enhancement up to 11 %, and frame-tested (structure) reinforced concrete columns can have strength enhancement up to 16 %. The conclusion sums up that it is allowed for the utilization of cyclic loading tests on earthquake engineering research due to its simpler test setups and consistent behavior with shaking table-tested responses.

3. The comparison results on the shaking table test responses with column strength models in NCREE/TEASDA (2021) indicate that for both flexural and shear strength of columns, the sustained axial load should be considered when estimating column strengths due to its enhancement on strength development. The flexural strength development is concluded to be more accurate with the consideration of varying axial load, but conservative enough if fixed initial axial load (sustained axial load) is considered, and the shear strength development is concluded to be more accurate

317
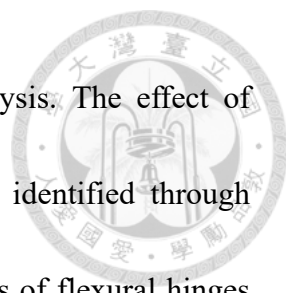
without the consideration of varying axial load. For the comparison on column effective stiffness models, the ASCE/SEI 41-17 (2017) model is shown to be simple and accurate, while the Elwood and Eberhard (2009) model is shown to provide elaborate estimations for low axial load conditions, and the Elwood and Eberhard (2006) model is shown to be conservative with lower values. NCREE/TEASDA (2021) takes into account the effective stiffness model recommended by ASCE/SEI 41-17 (2017) for the development of shear and flexural backbone curves for RC columns. For the comparison on lateral load-displacement relationships provided by NCREE/TEASDA (2021), the flexural-dominant and shear-dominant lateral load-displacement curves of RC columns are shown to be capable of simulating actual shaking table-tested responses.

4. The proposed CPH and Fiber models are shown to be capable of simulating linear flexural deformations, linear slip deformations, linear shear deformations, nonlinear flexural behaviors, and nonlinear shear behaviors of actual RC columns. The CPH model estimates the flexural strength by the initially sustained axial load on the column section, and the Fiber model is able to estimate the flexural strength sensitively to the varying axial load due to overturning moment when subjected to ground motions. The transformed hysteresis behaviors of the proposed models are consistent with the original Pivot model.

318

5. Based on the results of displacement history analysis and time history analysis, this research concludes that the Fiber model is more complex to construct, but provides with a more accurate simulation result on lateral displacements and strength development responses, and conservative estimation with lower energy dissipation capacity. The ETABS and CPH model are simpler to construct, while providing conservative simulation results with larger lateral displacements and lower strength developments, and accurate estimation on the energy dissipation capacity. The overall comparison on the hysteresis curves indicate that the strength degradation behavior is mostly governed by the backbone curve strength degradation with increasing lateral deformation instead of in-cycle strength degradation, allowing for the hysteresis models to concentrate on the pinching and unloading stiffness behavior. The column modeling techniques introduced in **Chapter 5**, including the flexural and shear force-displacement relationships and simplified effective stiffness models, the hysteresis modeling proposed by Ling et al. (2022), and the ETABS model developed by NCREE/TEASDA (2021) as well as the CPH and Fiber model developed by this research, are shown to simulate the shaking table-tested column responses in Su (2007) well, and are validated for the modeling of RC columns during nonlinear time domain analysis.

6. This research discusses the concept of reinforced concrete column modeling for

nonlinear pushover analysis and nonlinear time domain analysis. The effect of varying axial load on column flexural and shear strength is identified through shaking table test responses in this research, and different types of flexural hinges with or without the consideration of varying axial load is recommended for the two types of analyses respectively, while the fixed initial axial load shear hinge is recommended for both. For nonlinear pushover analysis which the analysis procedure is simple and straightforward, to consider the effect of varying axial load on the flexural strength through the varying axial load flexural hinge is recommended to be implemented on the column model for more accurate member behavior and force distribution. Yeh and Chou (2017) performed pushover analysis on a high-rise building with large varying axial loads and showed the difference on column flexural strength by the two types of flexural hinges. The overall capacity curves of the structure indicate that the responses with or without the consideration of varying axial load on flexural strength provides just around the same result. For nonlinear time domain analysis which the analysis procedure is more complicated and cumbersome, to neglect the varying axial load by using the fixed axial load flexural hinge is recommended to be implemented on the column model to provide conservative and efficient simulation results. If the varying axial load is to be considered for more accurate member behavior and force distribution, the flexural

320

fiber section is recommended to be implemented on the column model to provide more accurate and efficient simulation results than the varying axial load flexural hinge column model.
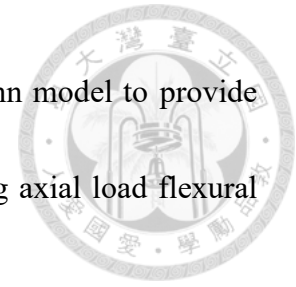
In conclusion, this research performs validation on the feasibility of the cyclic loading-based responses and cyclic loading-developed analytical models to represent and simulate actual shaking table-tested responses step by step. First, the shaking table test responses are studied in detail, and the cyclic loading test responses are validated for representation. Then, the strength, stiffness, and displacement column models that are developed based on cyclic loading responses are compared and validated with the shaking test responses and observed axial load behaviors. Following up, the cyclic loading-developed hysteresis modeling parameters are validated by displacement history analysis with inputs of actual lateral displacement responses. Lastly, to sum up, the comparison on time history analysis results indicate that the models can simulate lateral displacements, base shear, and hysteresis responses well, and the column models introduced in this research are validated for the nonlinear and hysteresis modeling of RC columns during performance of nonlinear time domain analysis on RC structures.

7.3 Future Work

Several topics are identified during the process of this research and are

321
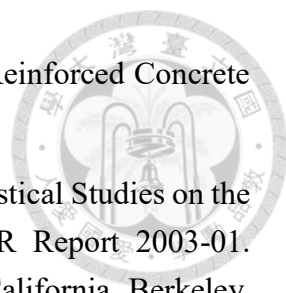
recommended for future study:
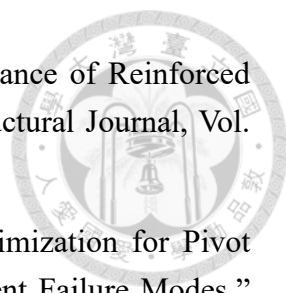
1. Due to the difficulty on collecting shaking table-tested hysteresis curves for shear-dominant columns without collapse, and on processing of the actual lateral displacement time history response of hysteresis curves to perform displacement history analysis, this research only compares two hysteresis curves for flexural-dominant columns and one for shear-dominant columns. More shaking table tested hysteresis curves should be collected and compared with the modeled energy dissipation capacities for better validation on the hysteresis behaviors of proposed models.

2. The proposed Fiber model holds its advantage when simulating flexural behaviors for more accurate lateral displacement and base shear responses. This research validates its accuracy on the simulation of flexural-dominant reinforced concrete column responses. The Fiber model, which considers both flexural and shear behavior, can also be applied on various reinforced concrete members such as beams, walls, and slabs, or even SRC members based on the same concept of fiber model with shear hinge, but requires varied definition on shear behaviors.

REFERENCES

ABRI (Architecture and Building Research Institute) (2021) "Assessment of Seismic Performance of Buildings Subjected to Fire (2/3) – Research on Post-Fire Seismic Performance of Reinforced Concrete Building Structures." Technical Report GRB 11015G0005, 400 pp. (in Chinese).

ACI Committee 374 (2006) "Acceptance Criteria for Moment Frames Based on Structural Testing (ACI 374.1-05) and Commentary." American Concrete Institute, Farmington Hills, MI, 2006, 9 pp.

ACI (American Concrete Institute) (2014) "Building Code Requirements for Structural Concrete (ACI 318-14) and Commentary (ACI 318R-14)." ACI Committee 318, Farmington Hills, MI, 519 pp.

ACI (American Concrete Institute) (2019) "Building Code Requirements for Structural Concrete (ACI 318-19) and Commentary (ACI 318R-19)." ACI Committee 318, Farmington Hills, MI, 623 pp.

ASCE/SEI 41-13 (2014) "Seismic Evaluation and Retrofit of Existing Buildings (41-13)." American Society of Civil Engineers, ASCE/SEI 41-13, Reston, VA, 518 pp.

ASCE/SEI 41-17 (2017) "Seismic Evaluation and Retrofit of Existing Buildings (41-17)." American Society of Civil Engineers (ASCE), Reston, VA, 170 pp.

Chang, G. A., and Mander, J. B. (1994) "Seismic Energy Based Fatigue Damage Ananlysis of Bridge Columns: Part 1 - Evaluation of Seismic Capacity." NCEER Technical Report No. NCEER-94-0006, State University of New York, Buffalo, N.Y.

ETABS/CSI (2016) "ETABS：Extended 3D Analysis of Building Systems, Nonlinear Version 2016." Computer and Structures, Inc., Berkeley, California.

Dowell, R. K., Seible, F., and Wilson, E. L. (1998) "Pivot Hysteresis Model for Reinforced Concrete Members." ACI Structural Journal, Vol. 95(5), pp. 607-617.

Elwood, K. J. (2004) "Modeling Failures in Existing Reinforced Concrete Columns." Canadian Journal of Civil Engineering, 31(5): pp. 846-859.

Elwood, K. J., and Eberhard, M. O. (2006) "Effective Stiffness of Reinforced Concrete Columns." PEER Research Digest 2006-1. Pacific Earthquake Engineering Research Center, University of California, Berkeley, CA.

Elwood, K. J., and Eberhard, M. O. (2009) "Effective Stiffness of Reinforced Concrete Columns." ACI Structural Journal, Vol. 106(S45), pp. 476-484.

Elwood, K. J., and Moehle, J. P. (2003) "Shake Table Tests and Analystical Studies on the Gravity Load Collapse of Reinforced Concrete Frames." PEER Report 2003-01. Pacific Earthquake Engineering Research Center, University of California, Berkeley, CA, 346 pp.

Elwood, K. J., and Moehle, J. P., (2005a) "Drift Capacity of Reinforced Concrete Columns with Light Transverse Reinforcement." Earthquake Spectra, Vol. 21(1), pp. 71-89.

Elwood, K. J., and Moehle, J. P., (2005b) "Axial Capacity Model for Shear Damaged Columns." ACI Structural Journal, Vol. 102(4), pp. 578-587.

Guo, W. W. (2008) "Study on the collapse behavior of Nonductile Reinforced Concrete Frames Subjected to Earthquake Loadings." PhD dissertation, Department of Construction Engineering, National Taiwan University of Science and Technology, Taipei, Taiwan. (in Chinese).

Hsu, Y. C., Mogili, S., Tsai, R. J., and Hwang, S. J. (2023) "Shear Strength Prediction of Reinforced Concrete Walls with Opening and Boundary Elements." Journal of Structural Engineering, ASCE, Vol. 149(7), 04023084.

Hwang, S. J., and Lee, H. J. (2002) "Strength Prediction for Discontinuity Regions by Softened Strut-and-Tie Model." Journal of Structural Engineering, ASCE, Vol. 128(12), pp.1519-1526.

Hwang, S. J., Tsai, R. J., Lam, W. K., and Moehle, J. P. (2017) "Simplification of Softened Strut-and-Tie Model for Strength Prediction of Discontinuity Regions." ACI Structural Journal, Vol. 114(5), pp. 1239-1248.

Kakavand, M. A. (2012) "Limit State Material Manual v14." available on https://opensees.berkeley.edu/

Li, Y. A., Huang, Y. T., and Hwang, S. J. (2014) "Seismic Response of Reinforced Concrete Short Columns Failed in Shear." ACI Structural Journal, Vol. 111(4), pp. 945-954.

Li, Y. A., and Hwang, S. J. (2017) "Prediction of the Lateral Load Displacement Curves for Reinforced Concrete Short Columns Failed in Shear." Journal of Structural Engineering, ASCE, Vol. 143(2), 04016164.

Li, Y. A., Weng, P. W., and Hwang, S. J. (2019) "Seismic Performance of Reinforced Concrete Intermediate Short Columns Failed in Shear." ACI Structural Journal, Vol. 116(3), pp. 195-206.

Ling, Y. C., Mogili, S., and Hwang, S. J. (2022) "Parameter Optimization for Pivot Hysteresis Model for Reinforced Concrete Columns with Different Failure Modes." Earthquake Engineering & Structural Dynamics, Vol. 51, pp. 2167-2187.

MacGregor, J. G. (1997) "Reinforced Concrete: Mechanics and Design." 3rd Edition, Englewood Cliffs, NJ: Prentice Hall Inc. 1997, 939 pp.

McKenna, F., Fenves, G. L., and Scott, M. H. (2000) "Open System for Earthquake Engineering Simulation." University of California, Berkeley, http://opensees.berkeley.edu

NCREE (1999) "Preliminary Reconnaissance Report on Chi-Chi Earthquake." National Center for Research on Earthquake Engineering, Technical Report NCREE-99-027, 152 pp. (in Chinese).

NCREE (2008) "Technology Handbook for Seismic Evaluation and Retrofit of School Buildings." National Center for Research on Earthquake Engineering, Technical Report NCREE-08-023, 218 pp. (in Chinese).

NCREE (2009) "Technology Handbook for Seismic Evaluation and Retrofit of School Buildings Second Edition." National Center for Research on Earthquake Engineering, Technical Report NCREE-09-023, 299 pp. (in Chinese).

NCREE (2013) "Technology Handbook for Seismic Evaluation and Retrofit of School Buildings Third Edition." National Center for Research on Earthquake Engineering, Technical Report NCREE-13-023, 325 pp. (in Chinese).

NCREE/TEASPA (2018) "Taiwan Earthquake Assessment for Structures by Pushover Analysis (TEASPA V3.1)." National Center for Research on Earthquake Engineering, Technical Report NCREE-18-015, 153 pp. (in Chinese).

NCREE/TEASPA (2020) "Technical Handbook for Taiwan Earthquake Assessment and Strengthening of Structures by Pushover Analysis (TEASPA V4.0)." National Center for Research on Earthquake Engineering, Technical Report NCREE-20-005, 445 pp. (in Chinese).

NCREE/TEASDA (2021) "Taiwan Earthquake Assessment for RC Structures by Dynamic Analysis (TEASDA 1.0)." National Center for Research on Earthquake Engineering, Technical Report NCREE-21-001, 176 pp. (in Chinese).

Pacific Earthquake Engineering Research Center (PEER) "OpenSees Wiki."
    https://opensees.berkeley.edu/wiki/index.php/Main_Page

Paulay, T., and Priestley, M. J. N. (1992) "Seismic Design of Reinforced Concrete and
    Masonry Buildings." John Wiley & Sons, Inc., New York, 274 pp.

Sharma, A., Eligehausen, R., and Reddy, GR. (2013) "Pivot Hysteresis Model Parameters
    for Reinforced Concrete Columns, Joints, and Structures." ACI Structural Journal, Vol.
    110(2), pp. 217-228.

Shen, W.-C., Hwang, S.-J., Li, Y.-A., Weng, P.-W., and Moehle, J. P. (2021) "Force-
    Displacement Model for Shear-Critical Reinforced Concrete Columns." ACI Structural
    Journal, Vol. 118(1), pp. 241-249.

Su, R. H. (2007) "Shake Table Tests on Reinforced Concrete Column Failed in Shear."
    Master thesis, Department of Construction Engineering, National Taiwan University of
    Science and Technology, Taipei, Taiwan, 191 pp. (in Chinese).

Thürlimann, B. (1979) "Shear Strength of Reinforced and Prestressed Concrete - CEB
    Approach." ACI Special Publication, SP 59, pp. 93-116.

Weng, P. W. (2007) "Study on the Seismic Performance Curves of Reinforced Concrete
    Columns Failed in Shear." Master thesis, Department of Construction Engineering,
    National Taiwan University of Science and Technology, Taipei, Taiwan, 212 pp. (in
    Chinese).

Yeh, Y. K., and Chou, D. G. (2017) "Effects of M3 or PMM Nonlinear Hinges in Pushover
    Analysis of Reinforced Concrete Buildings." Technical Report NCREE-17-016, 65 pp.
    (in Chinese).

Zhang, L. X. B., and Hsu, T. T. C. (1998) "Behavior and Analysis of 100 MPa Concrete
    Membrane Elements." Journal of Structural Engineering, ASCE, Vol. 124(1), pp. 24-
    34.
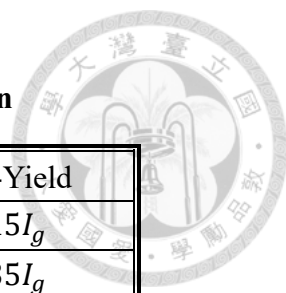
Table 2-1. Effective moment of inertia of column

Axial Load Ratio	Pre-Yield	Post-Yield
$P \leq 0.1 \times f'_c \times A_g$	$0.3I_g$	$0.15I_g$
$P \geq 0.5 \times f'_c \times A_g$	$0.7I_g$	$0.35I_g$

Table 2-2. Coefficient r at axial collapse point of shear failure columns

$\dfrac{P}{A_g f'_c}$	$\dfrac{A_{st}}{bs}$	r
≤ 0.1	≥ 0.006	0.06
≥ 0.6	≥ 0.006	0.008
≤ 0.1	≤ 0.0005	0.006
≥ 0.6	≤ 0.0005	0.0

Table 3-1. Cyclic loading test - material strength

Steel Size		D10	D25
Steel Strength	f_y (MPa)	457.0	481.2
	f_u (MPa)	670.7	700.4
Concrete Strength	f_c' (MPa)	33.1	

Table 3-2. Cyclic loading test - specimen design parameters

Specimen	4DL,4DH	4NL,4NH	3DL,3DH	3NL,3NH
Design	Ductile Intermediate Column	Non-Ductile Intermediate Column	Ductile Short Column	Non-Ductile Short Column
Icon				
Stirrup	D10@10cm	D10@30cm	D10@10cm	D10@30cm
	135° Hook	90° Hook	135° Hook	90° Hook
Longitudinal Bars	16-D25	16-D25	16-D25	16-D25
Steel Ratio	ρ_l = 3.24 % ρ_t = 0.43 %	ρ_l = 3.24 % ρ_t = 0.10 %	ρ_l = 3.24 % ρ_t = 0.43 %	ρ_l = 3.24 % ρ_t = 0.10 %
Section	50*50cm	50*50cm	50*50cm	50*50cm
Axial Load	Low Axial Load 0.1 $f_c'A_g$, High Axial Load 0.3 $f_c'A_g$			
Steel	D10 420 MPa, D25 420 MPa			
Concrete	Foundation 28 MPa；Column and Top Beam 21 MPa			

328

Table 4-1. Shaking table test - material strength

Steel Size		D4	D10	D25
Steel Strength	f_y (MPa)	643.8	457.0	481.2
	f_u (MPa)		670.7	700.4
Concrete Strength	f_c' (MPa)	33.1		

Table 4-2. Shaking table test - specimen design parameters
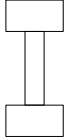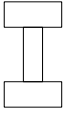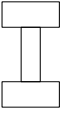
Specimen	4DL	4NL	3DL	3NL
Design	Ductile Intermediate Column	Non-Ductile Intermediate Column	Ductile Short Column	Non-Ductile Short Column
Icon				
Stirrup	D4@5cm	D4@15cm	D4@5cm	D4@15cm
	135° Hook	90° Hook	135° Hook	90° Hook
Longitudinal Bars	8-D13	16-D13	16-D13	16-D13
Steel Ratio	$\rho_l = 1.62\,\%$ $\rho_t = 0.30\,\%$	$\rho_l = 3.24\,\%$ $\rho_t = 0.07\,\%$	$\rho_l = 3.24\,\%$ $\rho_t = 0.30\,\%$	$\rho_l = 3.24\,\%$ $\rho_t = 0.07\,\%$
Section	25*25cm	25*25cm	25*25cm	25*25cm
Axial Load	Low Axial Load 0.1 $f_c'A_g$			
Steel	D4 600 MPa, D13 420 MPa			
Concrete	Foundation 28 MPa；Column and Top Beam 21 MPa			

Table 4-3. T1 column design parameters

	Test1-C1	Test1-C2	Test1-C3
Category	4DL	4NL	4DL
Initial AL (kN)	157	53	167
ALR (%)	8.40	2.84	8.94
ρ_l (%)	1.62	3.24	1.62
ρ_h (%)	0.30	0.07	0.30
Span (cm)	135		

Table 4-4. T2 column design parameters

	Test2-C1	Test2-C3
Category	3DL	3DL
Initial AL (kN)	177	178
ALR (%)	9.47	9.53
ρ_l (%)	3.24	3.24
ρ_h (%)	0.30	0.30
Span (cm)	270	

Table 4-5. T3 column design parameters

	Test3-C1	Test3-C3
Category	3NL	3NL
Initial AL (kN)	170	191
ALR (%)	9.10	10.22
ρ_l (%)	3.24	3.24
ρ_h (%)	0.07	0.07
Span (cm)	270	

Table 4-6. T4 column design parameters

	Test4-C1	Test4-C3
Category	4NL	4NL
Initial AL (kN)	103	152
ALR (%)	5.51	8.14
ρ_l (%)	3.24	3.24
ρ_h (%)	0.07	0.07
Span (cm)	270	

Table 4-7. Shaking table test input ground motions

Test	Run	Type of Motion	Command PGA (gal)	Achieved PGA (gal)
T1	1	White Noise	30	48
	2	TCU082ew	500	394
	3	TCU082ew	500	-483
	4	TCU082ew	1000	951
	5	White Noise	30	37
	6	TCU082ew	800	575
T2	1	White Noise	30	35
	2	TCU082ew	500	-417
	3	White Noise	30	-39
	4	TCU082ew	1000	-1483
	5	White Noise	30	36
T3	1	White Noise	30	37
	2	TCU082ew	500	-488
	3	White Noise	30	40
	4	TCU082ew	1000	-1204
T4	1	White Noise	30	-36
	2	TCU082ew	600	-601
	3	White Noise	30	-36
	4	TCU082ew	900	-1150

Table 4-8. Shaking table test column maximum measured strength

Test	Col.	Developed Strength (kN)		Corresponding Axial Load (kN)	
		Max (+)	Max (-)	Strength (+)	Strength (-)
1	C1	130.86	136.12	-403.71	-614.74
	C2	152.68	163.14	+87.41	+86.17
	C3	135.21	127.21	-607.69	-407.39
2	C1	187.87	225.85	-186.63	-371.36
	C3	211.21	185.28	-210.98	-166.64
3	C1	204.14	156.96	-105.69	-276.19
	C3	119.97	122.81	-249.01	-110.97
4	C1	145.54	139.71	-24.58	-169.91
	C3	124.28	159.46	-220.46	-59.55
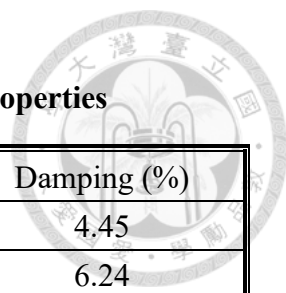
Table 4-9. Shaking table test specimen fundamental properties

Test	Run	Nat. period (sec)	Nat. freq. (Hz)	Damping (%)
T1	1	0.1281	7.8040	4.45
	5	0.4607	2.1708	6.24
T2	1	0.1023	9.7759	4.18
	3	0.1144	8.7391	3.87
	5	0.2997	3.3382	8.29
T3	1	0.0958	10.4395	4.32
	3	0.1043	9.5897	4.73
T4	1	0.1001	9.9929	3.57
	3	0.1154	8.6668	3.71

Table 4-10. T1 failure sequence

R4 (1 g)			
Time (sec)	C1	C2	C3
24.155			Lon. Bar Yield (-)
24.160	Lon. Bar Yield (-)		
24.175		Shear Failure (-)	
24.180		Lon. Bar Yield (-)	
24.290		Lon. Bar Yield (+)	Lon. Bar Yield (+)
24.295	Lon. Bar Yield (+)		
24.300		Shear Failure (+)	
24.305		Axial Failure	
24.495			Max Strength (-)
24.525	Max Strength (-)		
25.105			Max Strength (+)
25.135	Max Strength (+)		
R6 (800 gal)			
Time (sec)	C1	C2	C3
35.195			Axial Failure
35.485			Collapse
37.530	Axial Failure		
38.180	Collapse	Collapse	

332
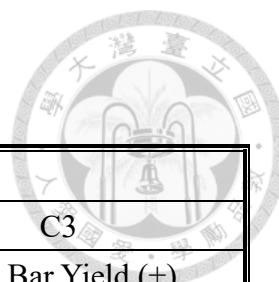
Table 4-11. T2 failure sequence

R4 (1 g)		
Time (sec)	C1	C3
24.265		Lon. Bar Yield (+)
24.295		Max Strength (+)
24.440		Lon. Bar Yield (-)
24.445		Max Strength (-)
24.460	Lon. Bar Yield (-)	
24.510	Max Strength (-)	
35.210	Lon. Bar Yield (+)	
35.220	Max Strength (+)	

Table 4-12. T3 failure sequence

R2 (500 gal)		
Time (sec)	C1	C3
24.425		Max Strength (-)
R4 (1 g)		
Time (sec)	C1	C3
24.240		Max Strength (+)
24.280	Lon. Bar Yield (+)	
24.295	Max Strength (+)	
24.430	Max Strength (-) Axial Failure	
24.440		Axial Failure
24.935		Collapse
24.995	Collapse	

333
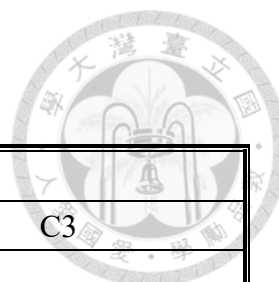
Table 4-13. T4 failure sequence

Time (sec)	C1	C3
R4 (1 g)		
24.265	Lon. Bar Yield (+)	
24.270	Shear Failure (+)	Shear Failure (+)
24.425	Shear Failure (-)	
24.435		Lon. Bar Yield (-) Shear Failure (-)
25.475	Axial Failure	
25.490		Axial Failure
26.040	Collapse	
26.095		Collapse

Table 4-14. Sustained axial loads and corresponding shear strengths

Category	Column	Sustained Axial Load (%)	Shear Strength (kN)
4NL	T1C2	2.84	163.14
	T4C1	5.51	145.54
	T4C3	8.14	159.46
3DL	T2C1	9.47	225.85
	T2C3	9.57	211.21
3NL	T3C1	9.10	204.14
	T3C3	10.22	122.81

Table 4-15. T1 Measured stiffness

T1	Condition	Average Stiffness (kN/cm)					
		C1		C2		C3	
		+	-	+	-	+	-
R2	Elastic	113.69	276.85			254.57	154.47
	Cracked	118.26	143.71	349.26	339.35	135.55	138.77
R3	Cracked	89.36	121.91	311.09	313.47	108.70	87.53
R4	Cracked	83.01	99.98	269.66	287.65	89.66	84.17
Cracked (AVE)		101.83	123.42	314.49	304.27	117.10	107.90

334
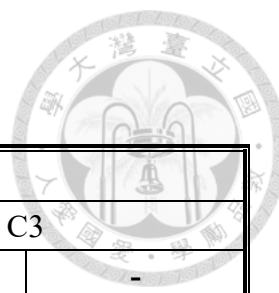
Table 4-16. T2 Measured stiffness

T2	Condition	Average Stiffness (kN/cm)			
		C1		C3	
		+	-	+	-
R2	Elastic	629.17	658.87	624.12	640.75
	Cracked	407.74	461.85	443.77	324.73
R3	Cracked	349.94	333.35	349.40	352.29
Cracked (AVE)		399.31	434.59	422.20	330.58

Table 4-17. T3 Measured stiffness

T3	Condition	Average Stiffness (kN/cm)			
		C1		C3	
		+	-	+	-
R2	Elastic	620.93		745.50	
	Cracked	552.56	484.66	547.14	528.96
R3	Cracked	547.48	455.25	500.01	481.59
Cracked (AVE)		550.30	472.63	529.19	510.42

Table 4-18. T4 Measured stiffness

T4	Condition	Average Stiffness (kN/cm)			
		C1		C3	
		+	-	+	-
R2	Elastic	286.18	419.42	376.07	443.05
	Cracked	256.53	233.22	290.76	283.70
R3	Cracked	254.92	224.49	275.60	252.44
Cracked (AVE)		256.01	230.90	286.15	275.41
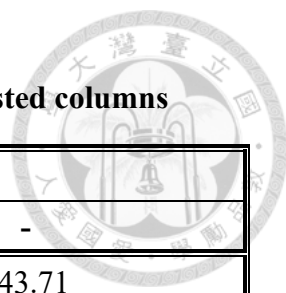
Table 4-19. Measured effective stiffness of shaking table-tested columns

Test	Column	Effective Stiffness (kN/cm)	
		+	-
T1	C1	118.26	143.71
	C2	349.26	339.35
	C3	135.55	138.77
T2	C1	407.74	461.85
	C3	443.77	324.73
T3	C1	552.56	484.66
	C3	547.14	528.96
T4	C1	256.53	233.22
	C3	290.76	283.70

Table 4-20. Collapse points of shaking table-tested columns

Behavior	Columns	Drift Ratio (%)
Flexural-shear	T1C1	11.49
	T1C3	4.93
Shear	T3C1	6.44
	T3C3	6.51
	T4C1	4.97
	T4C3	7.05

Table 5-1. Different loading rates on strength of RC shear wall with openings

Specimen	Loading Rate	Test Strength (kN)	Ratio
S1W5-0.28-0.01	0.01 cm/s	299	1.09
S1W5-0.28-1.0	1.0 cm/s	325	
S1W5-0.28-0.014	0.014 DR/s	278	1.19
S1W5-0.28-1.4	1.4 DR/s	330	
FS1W5-0.28C-2.5-0.014	0.014 DR/s	292	1.11
FS1W5-0.28C-2.5-1.4	1.4 DR/s	324	
S1W5-0.28C-4.5-0.014	0.014 DR/s	298	1.06
S1W5-0.28C-4.5-1.4	1.4 DR/s	317	
AVE			1.11
COV			0.05

Table 5-2. Strength comparison for shaking table and cyclic loading tests

Columns	Strength Ratio	Modified Strength Ratio
T1C2	1.44	
	1.41	
T2C1	1.22	1.22
	1.04	1.04
T2C3	1.14	1.14
	1.03	1.03
T3C1	1.77	
	1.37	
T3C3	1.06	1.06
	1.05	1.05
T4C1	1.29	1.29
	1.29	1.29
T4C3	1.10	1.10
	1.48	1.48
AVE	1.25	1.16
COV	0.17	0.13
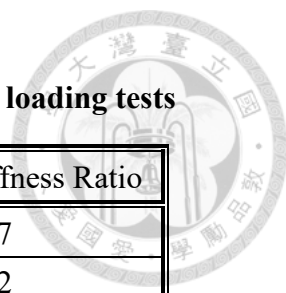
Table 5-3. Stiffness comparison for shaking table and cyclic loading tests

Columns	Stiffness Ratio	Modified Stiffness Ratio
T1C2	0.97	0.97
	0.92	0.92
T2C1	0.98	0.98
	0.81	0.81
T2C3	0.69	
	0.88	
T3C1	0.89	0.89
	1.00	1.00
T3C3	0.97	0.97
	0.99	0.99
T4C1	0.67	
	0.68	
T4C3	0.81	
	0.77	
AVE	0.86	0.94
COV	0.14	0.07

Table 5-4. Collapse point comparison for shaking table and cyclic loading tests

Columns	Collapse Displacement Ratio
T3C1	1.07
T3C3	1.08
T4C1	0.99
T4C3	1.41
AVE	1.14
COV	0.16

338

Table 5-5. Axial load values during sustained, high, and low conditions

Test	Col.	Axial Load (%)		
		High	Sustained	Low
1	C1	32.90	8.40	21.60
	C2	-4.61	2.84	-4.68
	C3	32.52	8.94	21.80
2	C1	19.87	9.47	9.99
	C3	11.29	9.53	8.92
3	C1	14.78	9.10	5.66
	C3	13.32	10.22	5.94
4	C1	9.09	5.51	1.32
	C3	11.80	8.14	3.19

Table 5-6. Strength estimation for column flexural strength

Considerations	Total		High AL	Low AL
	AVE	COV	AVE	AVE
Zero Axial Load	1.34	0.17	1.52	1.17
Initial Axial Load	1.16	0.16	1.32	1.00
Varying Axial Load	1.09	0.14	1.15	1.02

Table 5-7. Modified strength estimation for column flexural strength

Considerations	Total		High AL	Low AL
	AVE	COV	AVE	AVE
Zero Axial Load	1.32	0.18	1.53	1.12
Initial Axial Load	1.17	0.18	1.35	0.99
Varying Axial Load	1.14	0.10	1.22	1.05

Table 5-8. Strength estimation for column shear strength

Considerations	Total		First	Second
	AVE	COV	AVE	AVE
Zero Axial Load	1.54	0.23	1.59	1.49
Initial Axial Load	1.27	0.24	1.36	1.19
Varying Axial Load	1.40	0.38	1.53	1.24
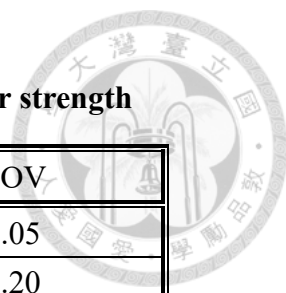
Table 5-9. Modified strength estimation for column shear strength

Reinforcement Design	AVE	COV
Ductile	1.07	0.05
Non-Ductile	1.43	0.20

Table 5-10. Effective stiffness estimation for flexural-dominant columns

Effective Stiffness Model	AVE	COV
ASCE/SEI 41-17 (2017)	0.58	0.08
Elwood and Eberhard (2006)	0.83	0.08
Elwood and Eberhard (2009)	0.59	0.08

Table 5-11. Effective stiffness estimation for shear-dominant columns

Effective Stiffness Model	AVE	COV
ASCE/SEI 41-17 (2017)	1.05	0.24
Elwood and Eberhard (2006)	1.47	0.26
Elwood and Eberhard (2009)	1.22	0.29

Table 5-12. Modified effective stiffness estimation for shear-dominant columns

Effective Stiffness Model	AVE	COV
ASCE/SEI 41-17 (2017)	1.16	0.17
Elwood and Eberhard (2006)	1.63	0.19
Elwood and Eberhard (2009)	1.35	0.24
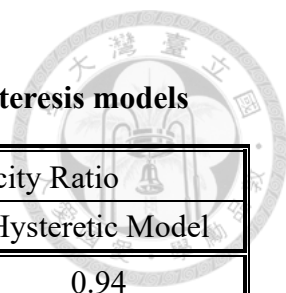
Table 6-1. Energy dissipation capacity ratio for different hysteresis models

Category	Test to Model Energy Dissipation Capacity Ratio		
	Pivot Model	Pinching4 Model	Hysteretic Model
Flexure	1.11	0.91	0.94
Flexural-Shear	1.05	0.94	1.11
Shear	0.76	0.72	0.84

Table 6-2. Energy dissipation capacity ratio for converted hysteresis models

Category	Pivot Model to Model Energy Dissipation Capacity Ratio	
	Pinching4 Model	Hysteretic Model
Flexure	0.82	0.85
Flexural-Shear	0.90	1.06
Shear	0.96	1.11

Table 6-3. Energy dissipation capacity ratio for different column models

Test	Column	Energy Dissipation Capacity Ratio			Ling et al. (2022)	
		ETABS	CPH	Fiber	AVE	COV
T1	C1	0.69	0.77	0.87	0.95	0.14
	C3	0.82	0.92	1.04		
T2	C3	0.72	0.68	0.65	0.85	0.23

Table 6-4. Natural period comparison between test and models

Test	Run	Natural Period (sec)			
		Test	ETABS	CPH	Fiber
T1	1	0.1281	0.1510	0.1474	0.1329
	5	0.4607		0.2910	0.4115
T2	1	0.1023	0.1185	0.1161	0.0918
	3	0.1144		0.1160	0.1312
	5	0.2997		Collapse	Collapse
T3	1	0.0958	0.1190	0.1161	0.0919
	3	0.1043		0.1698	0.1932
T4	1	0.1001	0.1495	0.1473	0.1029
	3	0.1154		Collapse	Collapse
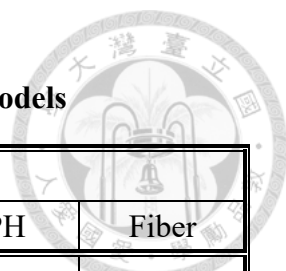
Table 6-5. Strength comparison between test and models

		Strength (kN)				
Column	Direction	Test	Input	ETABS	CPH	Fiber
T1C1	(+)	130.86	118.18	117.96	117.09	129.94
T1C1	(-)	136.12	118.18	117.30	116.75	124.35
T1C2	(+)	152.68	93.11	91.87	89.78	91.68
T1C2	(-)	163.14	93.11	91.42	86.83	91.84
T1C3	(+)	135.21	119.81	117.04	118.85	129.97
T1C3	(-)	127.21	119.81	116.38	118.56	124.40
T2C1	(+)	187.87	204.97	202.83	194.73	192.20
T2C1	(-)	225.85	204.97	198.57	198.10	194.58
T2C3	(+)	211.21	205.19	202.36	194.80	191.99
T2C3	(-)	185.28	205.19	198.31	198.16	195.22
T3C1	(+)	204.14	121.13	115.98	120.85	120.88
T3C1	(-)	156.96	121.13	121.13	121.00	120.94
T3C3	(+)	122.92	124.09	118.00	123.23	124.01
T3C3	(-)	122.81	124.09	123.17	123.62	123.78
T4C1	(+)	145.54	100.44	98.88	98.85	100.38
T4C1	(-)	139.71	100.44	84.69	99.57	96.76
T4C3	(+)	124.28	106.96	102.94	106.46	106.29
T4C3	(-)	159.46	106.96	88.56	105.05	101.04

Table 6-6. T1 C1 model failure sequence

Frame T1 - Column C1 - Run R4				
Time (sec)	Test	ETABS	CPH	Fiber
24.440			Strength (-)	
24.480		Strength (-)		
24.495				Strength (-)
24.525	Strength (-)			
25.045			Strength (+)	
25.065		Strength (+)		
25.110				Strength (+)
25.135	Strength (+)			

342
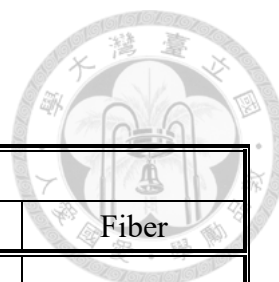
Table 6-7. T1 C2 model failure sequence
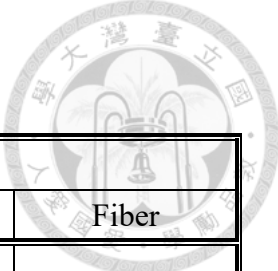
Frame T1 - Column C2 - Run R4				
Time (sec)	Test	ETABS	CPH	Fiber
24.175	Strength (-)			
24.275			Strength (+)	
24.280				Strength (+)
24.290		Strength (+)		
24.300	Strength (+)			
24.405				Strength (-)
24.430		Strength (-)	Strength (-)	

Table 6-8. T1 C3 model failure sequence

Frame T1 - Column C3 - Run R4				
Time (sec)	Test	ETABS	CPH	Fiber
24.295			Strength (+)	
24.440			Strength (-)	
24.480		Strength (-)		
24.495	Strength (-)			Strength (-)
25.065		Strength (+)		
25.105	Strength (+)			
25.110				Strength (+)

Table 6-9. T2 C1 model failure sequence

Frame T2 - Column C1 - Run R4				
Time (sec)	Test	ETABS	CPH	Fiber
24.275			Strength (+)	
24.280				Strength (+)
24.430				Strength (-)
24.435		Strength (-)	Strength (-)	
24.510	Strength (-)			
24.765		Strength (+)		
35.220	Strength (+)			

Table 6-10. T2 C3 model failure sequence

Frame T2 - Column C3 - Run R4				
Time (sec)	Test	ETABS	CPH	Fiber
24.275			Strength (+)	
24.280				Strength (+)
24.295	Strength (+)			
24.430				Strength (-)
24.435		Strength (-)	Strength (-)	
24.445	Strength (-)			
24.765		Strength (+)		

Table 6-11. T3 C1 model failure sequence

Frame T3 - Column C1 - Run R4				
Time (sec)	Test	ETABS	CPH	Fiber
23.080			Strength (+)	
23.190			Strength (-)	
23.475				Strength (+)
23.480		Strength (+)		
24.140		Strength (-)		
24.145				Strength (-)
24.295	Strength (+)			
24.430	Strength (-)			

344
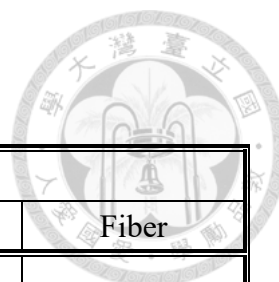
Table 6-12. T3 C3 model failure sequence

Frame T3 - Column C3 - Run R4				
Time (sec)	Test	ETABS	CPH	Fiber
R2	Strength (-)			
23.080			Strength (+)	
23.190			Strength (-)	
23.480		Strength (+)		Strength (+)
24.140		Strength (-)		
24.145				Strength (-)
24.240	Strength (+)			

Table 6-13. T4 C1 R2 model failure sequence

Frame T4 - Column C1 - Run R2				
Time (sec)	Test	ETABS	CPH	Fiber
24.295		Strength (+)		
24.415		Strength (-)		
24.425			Strength (-)	Strength (-)
25.020			Strength (+)	
25.025				Strength (+)

Table 6-14. T4 C1 R4 model failure sequence

Frame T4 - Column C1 - Run R4				
Time (sec)	Test	ETABS	CPH	Fiber
24.145		Strength (-)		
24.250			Strength (+)	
24.255		Strength (+)		
24.270	Strength (+)			Strength (+)
24.420			Strength (-)	Strength (-)
24.425	Strength (-)			

Table 6-15. T4 C3 R2 model failure sequence

Frame T4 - Column C3 - Run R2				
Time (sec)	Test	ETABS	CPH	Fiber
24.295		Strength (+)		
24.415		Strength (-)		
24.425			Strength (-)	Strength (-)
25.020			Strength (+)	
25.025				Strength (+)

Table 6-16. T4 C3 R4 model failure sequence

Frame T4 - Column C3 - Run R4				
Time (sec)	Test	ETABS	CPH	Fiber
24.145		Strength (-)		
24.255		Strength (+)	Strength (+)	
24.270	Strength (+)			Strength (+)
24.420			Strength (-)	Strength (-)
24.435	Strength (-)			

346
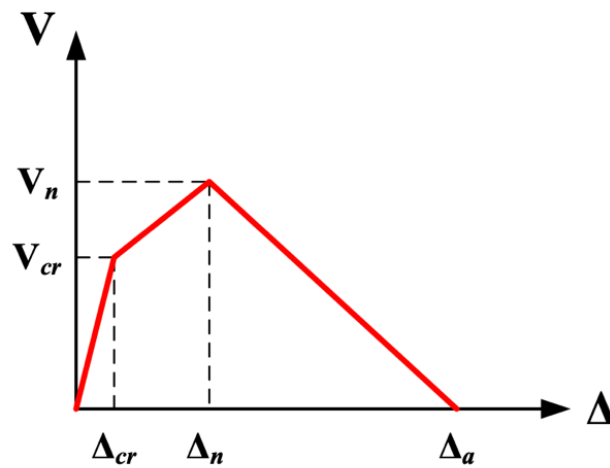
Figure 2-1. Shear failure backbone curve of column (NCREE/TEASDA 2021)

(a) Intermediated column   (b) short column
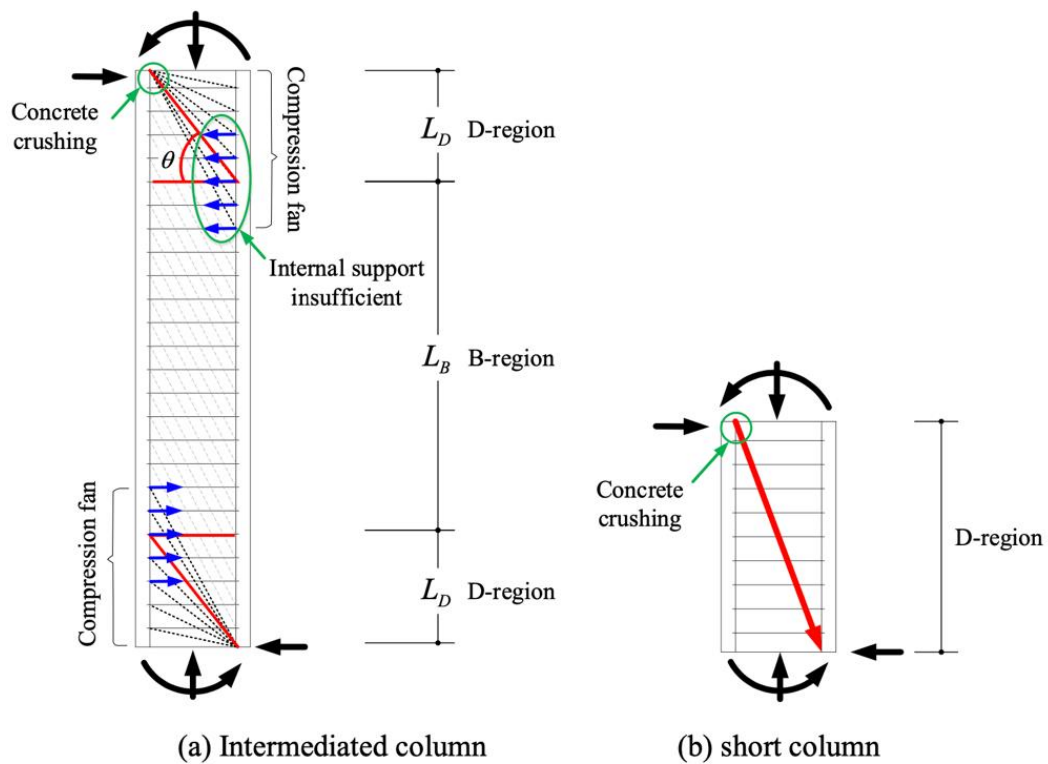
Figure 2-2. Column force transfer mechanism (NCREE/TEASDA 2021)

$$\theta_{\text{initial}} = 63.4°$$

$$V_{n,c} = K \zeta f_c' A_{str} \cos \theta$$

$$V_{n,t} = Eq(3.6)$$

$$V_{n,c} > V_{n,t}$$

Yes

No

$$\theta = 63.4°$$

$$\theta = 63.4° - \Delta\theta$$

$$Cal. \quad V_{n,c}$$

$$V_n = V_{n,t}$$

Yes

$$V_{n,c} = V_{n,t}$$

No

$$\theta \leq 45°$$

No

END

Yes

$$V_n = V_{n,c}$$
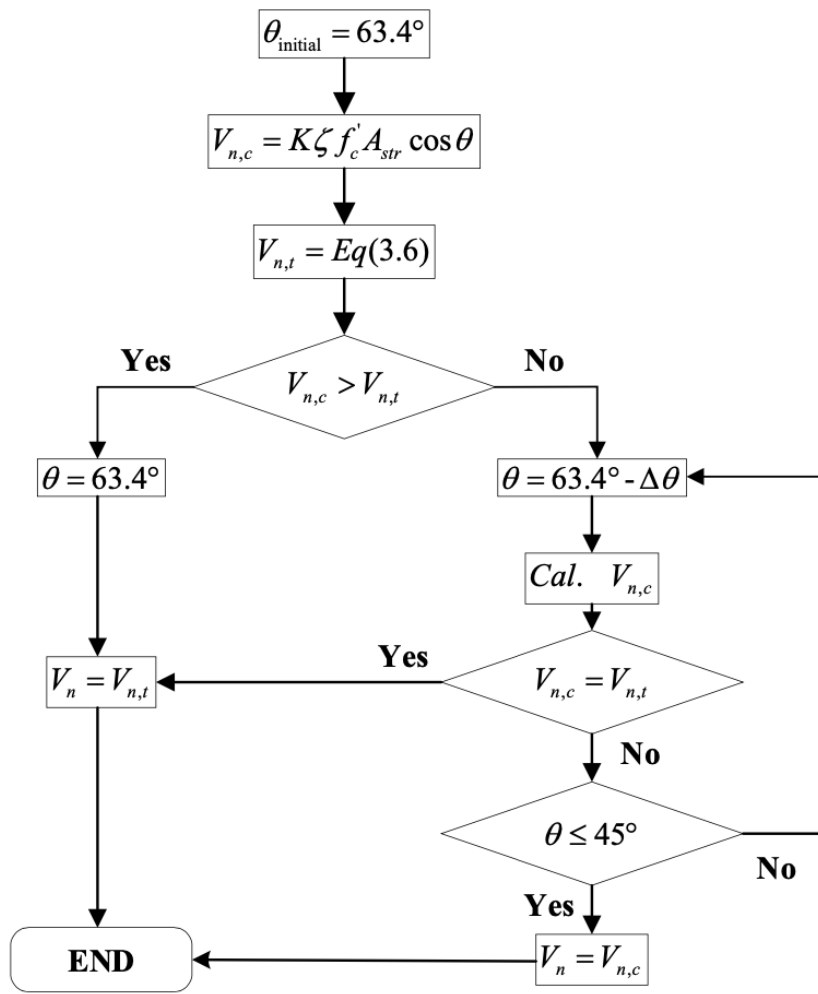
Figure 2-3. Iteration procedure for column shear strength calculation (NCREE/TEASDA 2021)
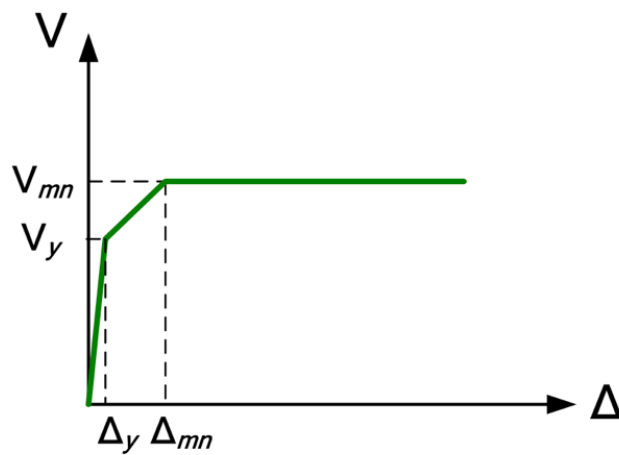
Figure 2-4. Flexure failure backbone curve of column (NCREE/TEASDA 2021)

348
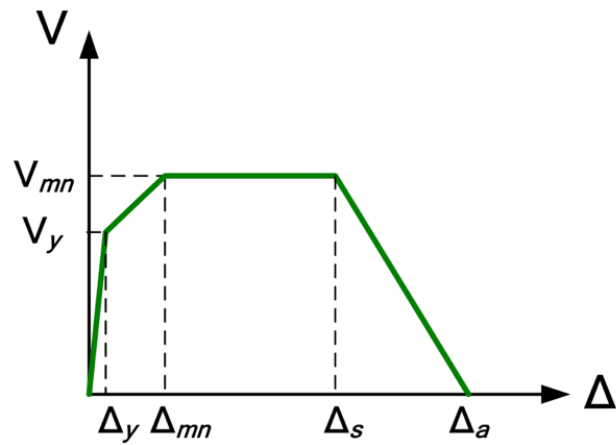
Figure 2-5. Flexural-Shear failure backbone curve of column (NCREE/TEASDA 2021)
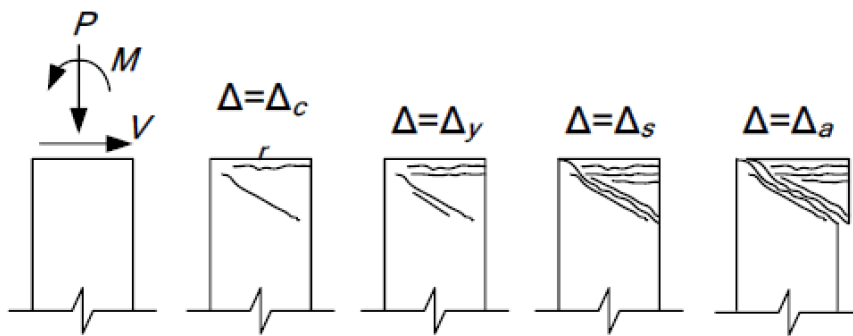
Figure 2-6. Development of column flexural-shear failure behavior (NCREE/TEASDA 2021)

349
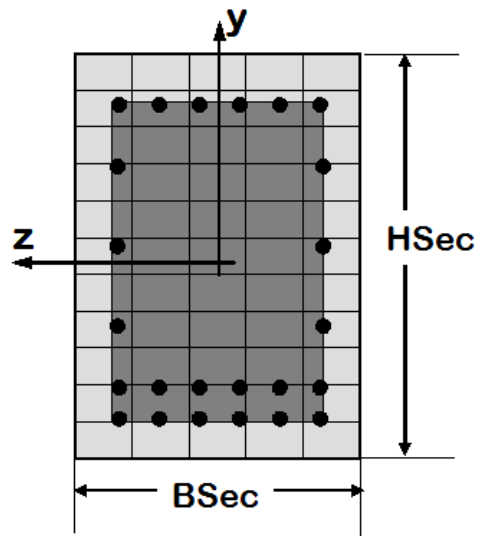
Figure 2-7. Reinforced concrete fiber section

(https://opensees.berkeley.edu/)
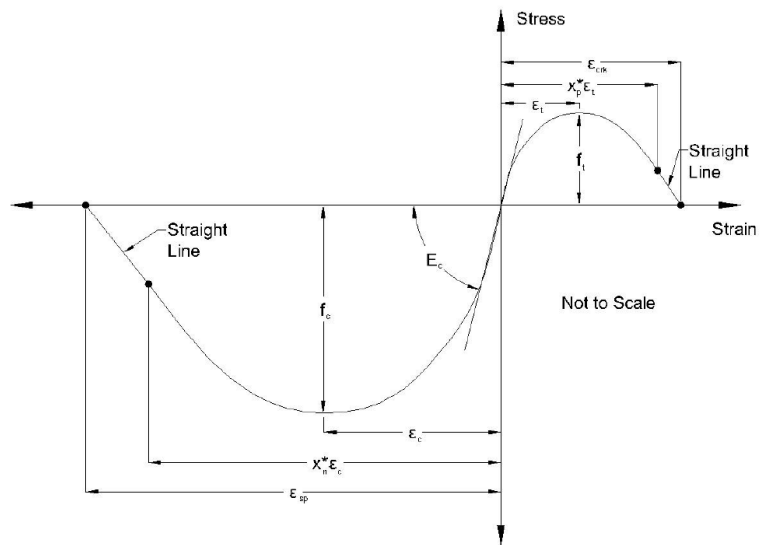
Figure 2-8. Concrete07 material model stress-strain relationship

(https://opensees.berkeley.edu/)
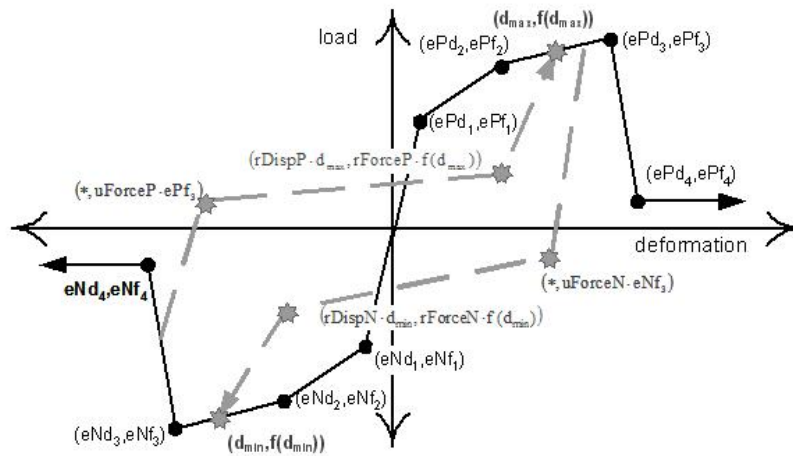
Figure 2-9. Pinching4 material model force-displacement relationship

(https://opensees.berkeley.edu/)

Figure 2-10. Hysteretic material model stress-strain relationship

(https://opensees.berkeley.edu/)
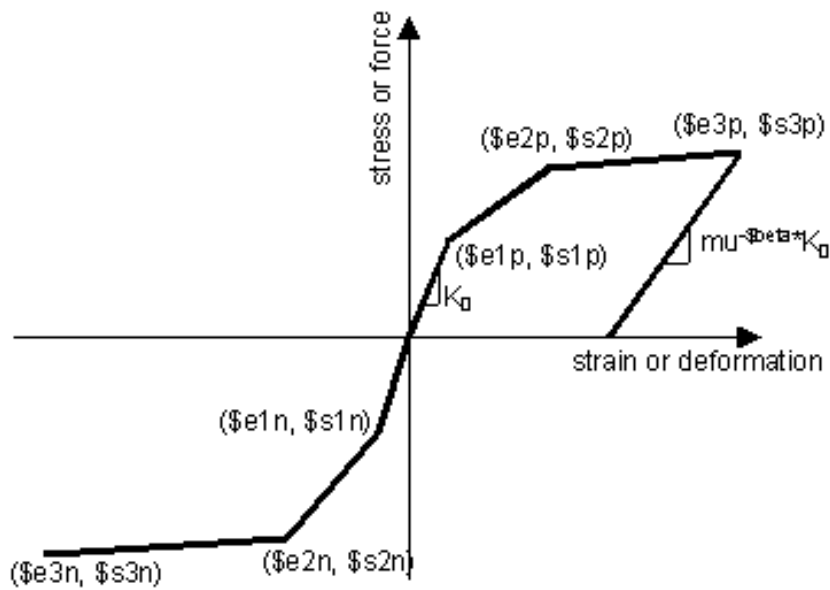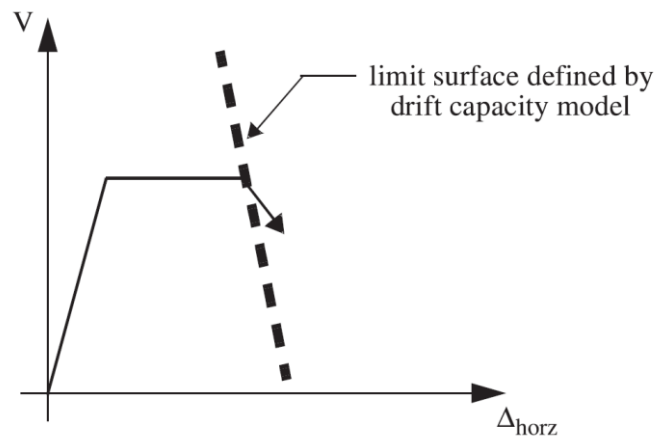
Figure 2-11. Shear failure model (Elwood 2004)
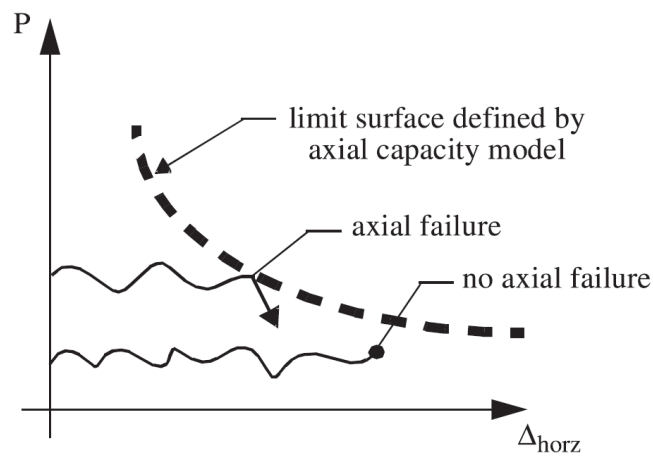
Figure 2-12. Axial failure model (Elwood 2004)
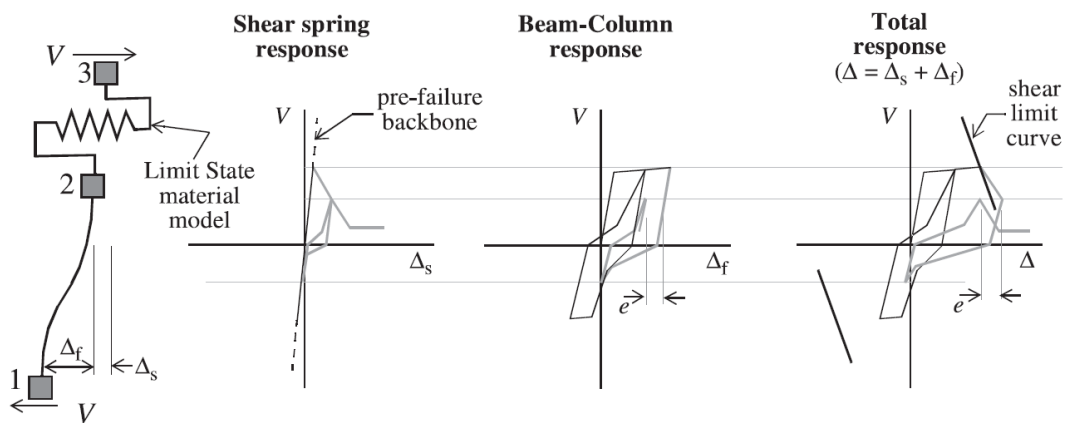
Figure 2-13. Shear spring in series model using shear limit state material model (Elwood 2004)

352
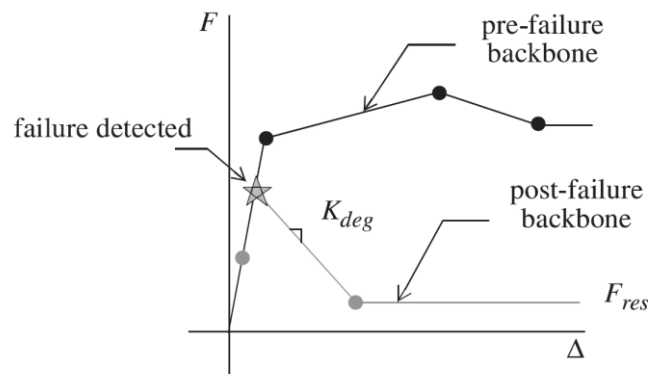
Figure 2-14. Redefinition of backbone curve after failure is detected (Elwood 2004)
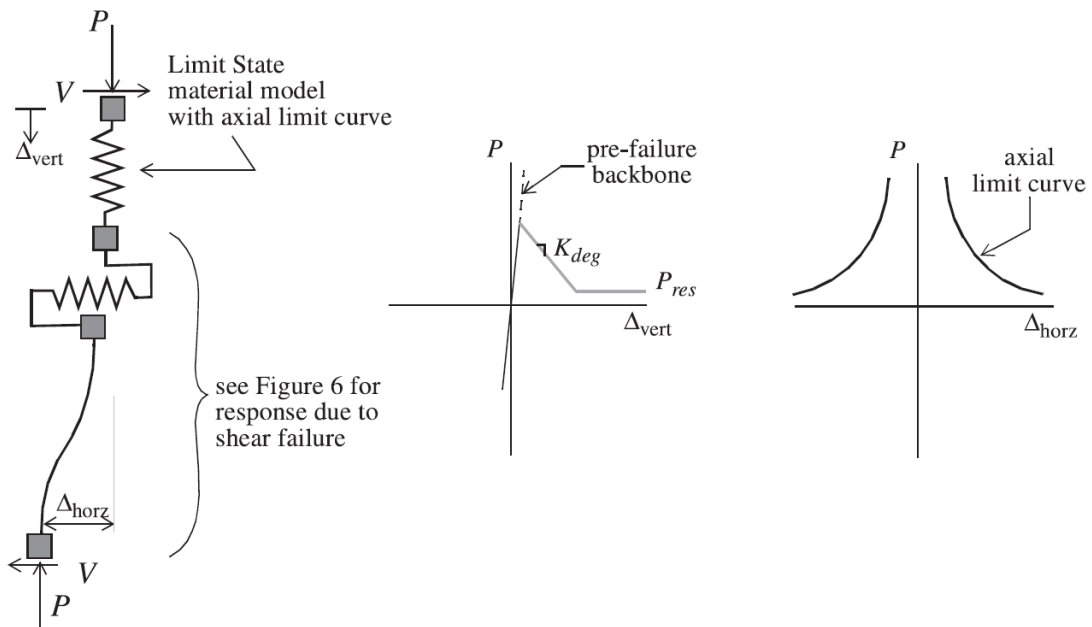
Figure 2-15. Axial spring in series model using axial limit state material model (Elwood 2004)

Shear spring response

V

V_u

K_{deg}

Δ_s

Beam-Column response

V

K_{unload}

Δ_f

Total response ($\Delta = \Delta_s + \Delta_f$)

V

shear limit curve

K^t_{deg}

Δ

P

P_s

axial limit curve

displacement at shear failure

displacement at axial failure for $P = P_s$

Δ_s Δ_a Δ
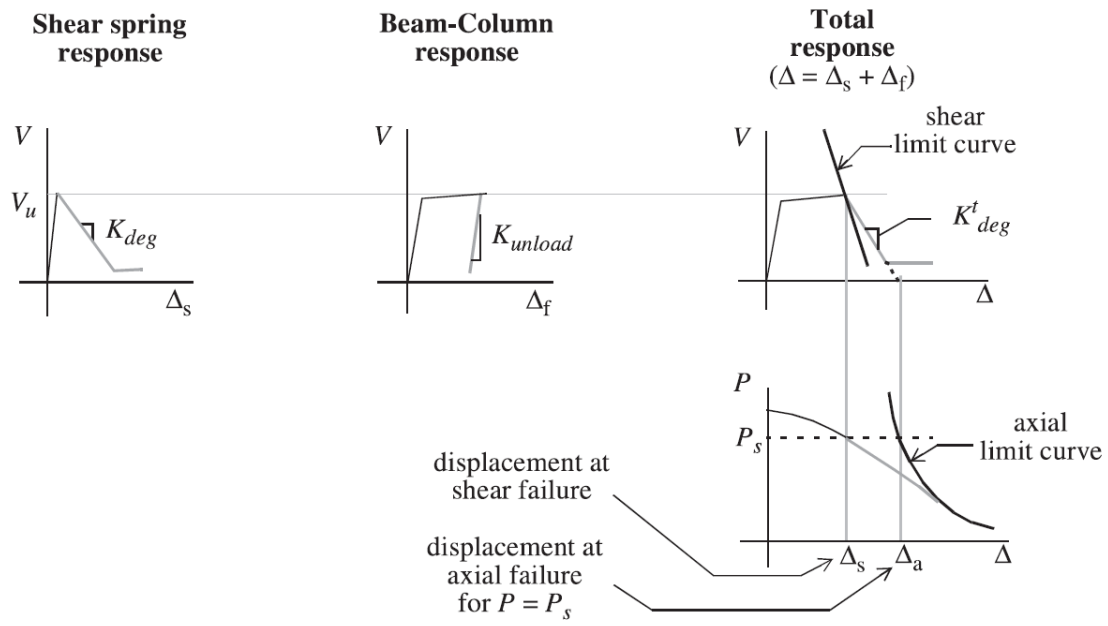
Figure 2-16. Determination of degrading slope K_{deg} (Elwood 2004)

354
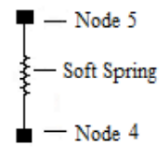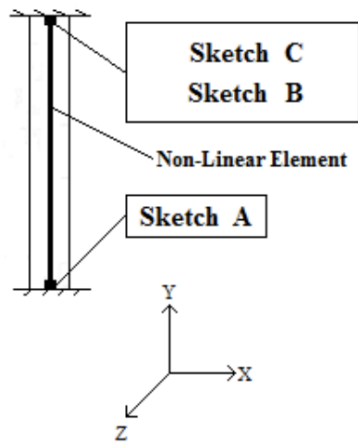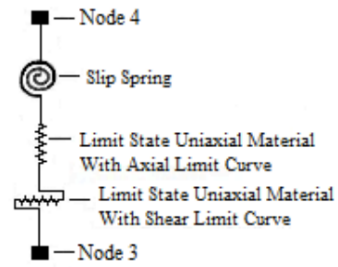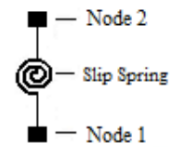
Figure 2-17. Schematic presentation of the column model (Kakavand 2012)
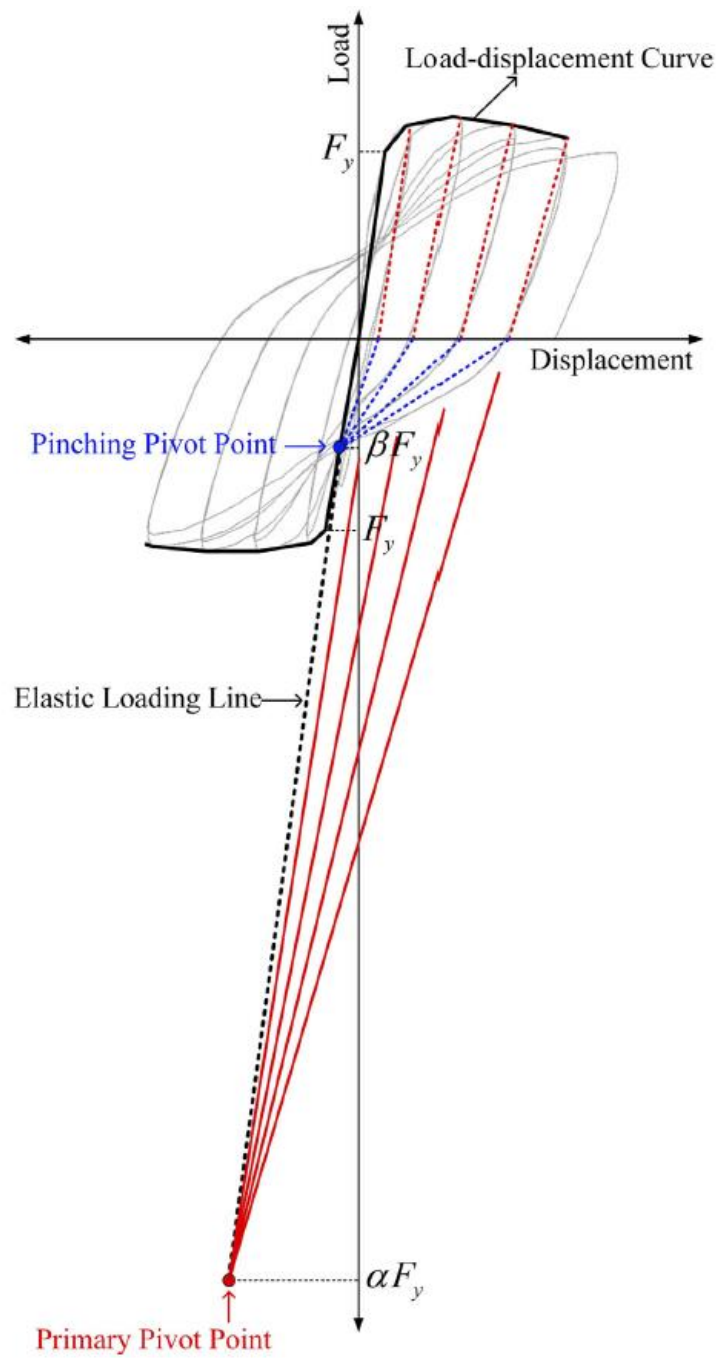
Figure 2-18. Pivot Model parameter relationship (Ling et al. 2022)

356
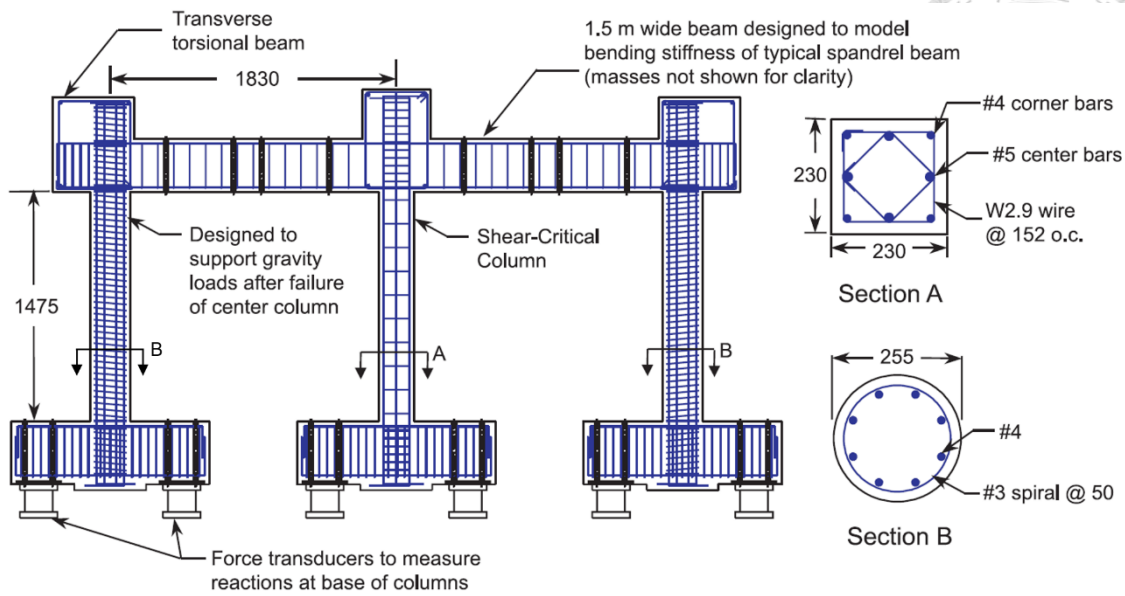
**Figure 2-19. Three-column frame test specimen design layout
(Elwood and Moehle 2003)**
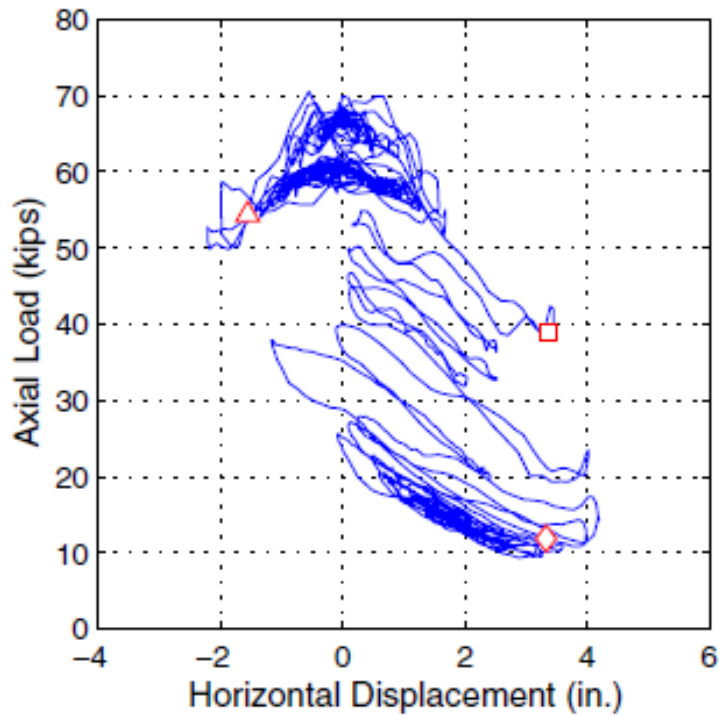
**Figure 2-20. S2 center column axial load – horizontal displacement response
(Elwood and Moehle 2003)**

357
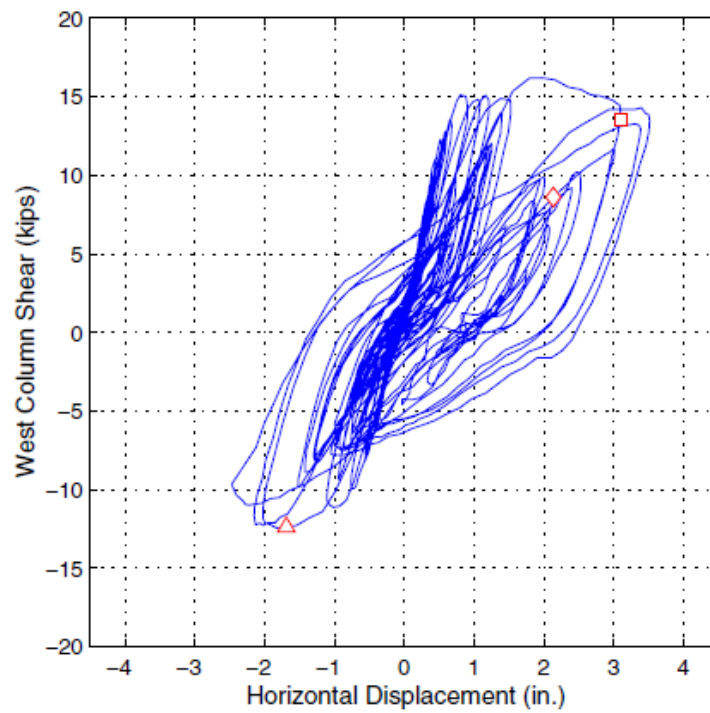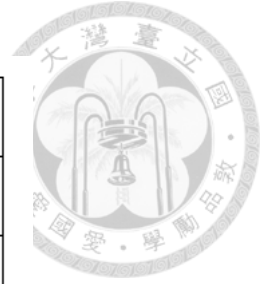
Figure 2-21. S1 west column hysteresis response (Elwood and Moehle 2003)
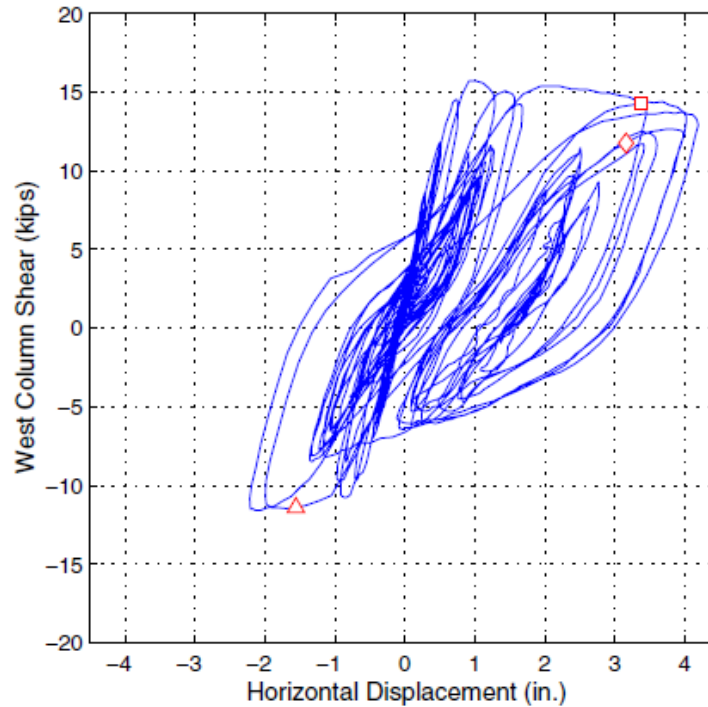
Figure 2-22. S2 west column hysteresis response (Elwood and Moehle 2003)
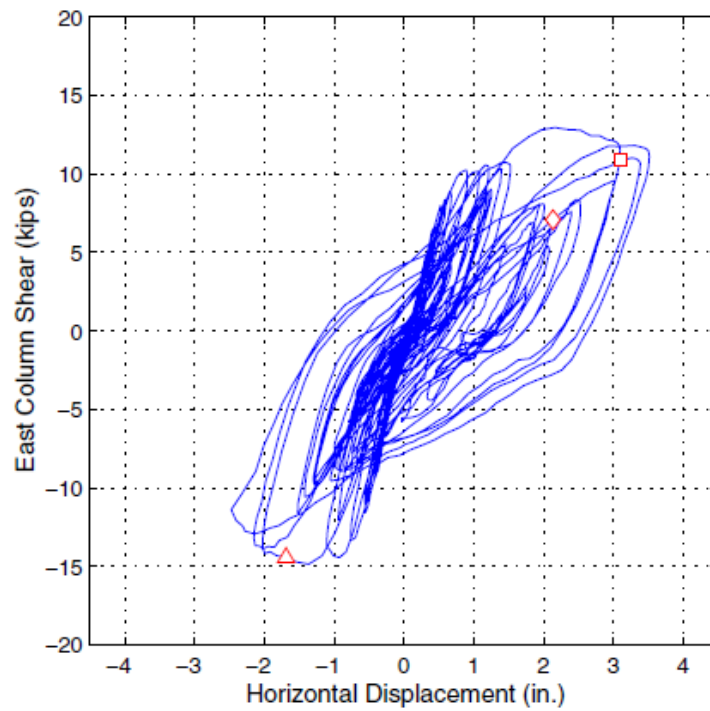
Figure 2-23. S1 east column hysteresis response (Elwood and Moehle 2003)
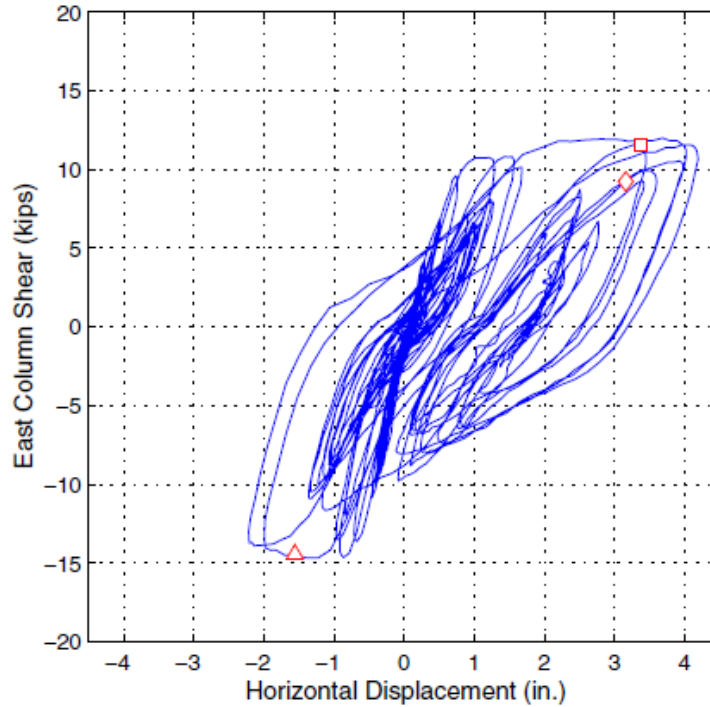
Figure 2-24. S2 east column hysteresis response (Elwood and Moehle 2003)

359
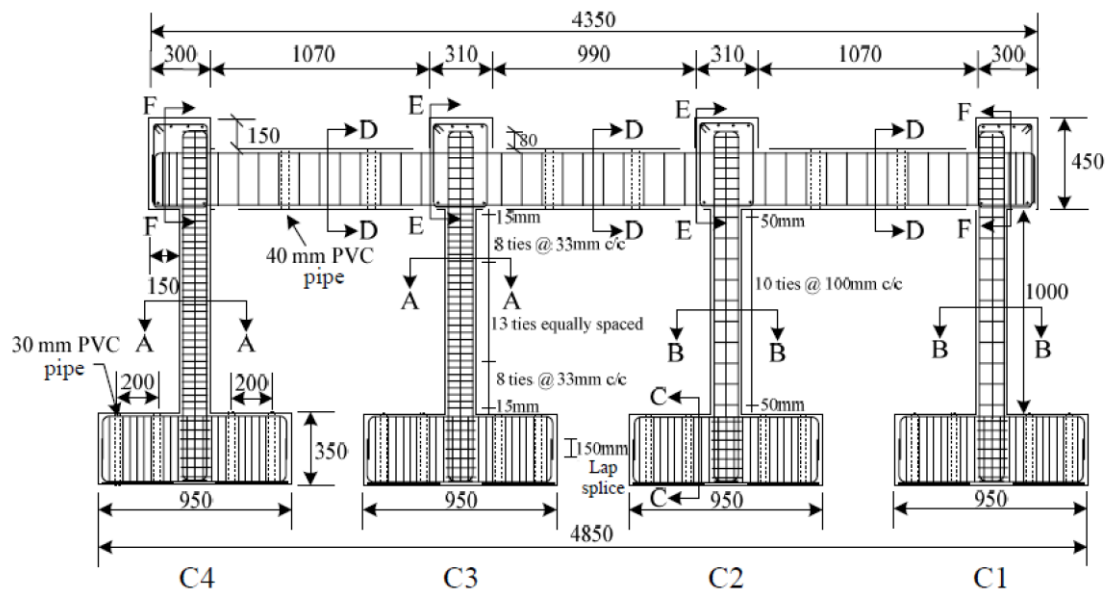
Figure 2-25. Specimen P1/P2 design layout (Guo 2008)
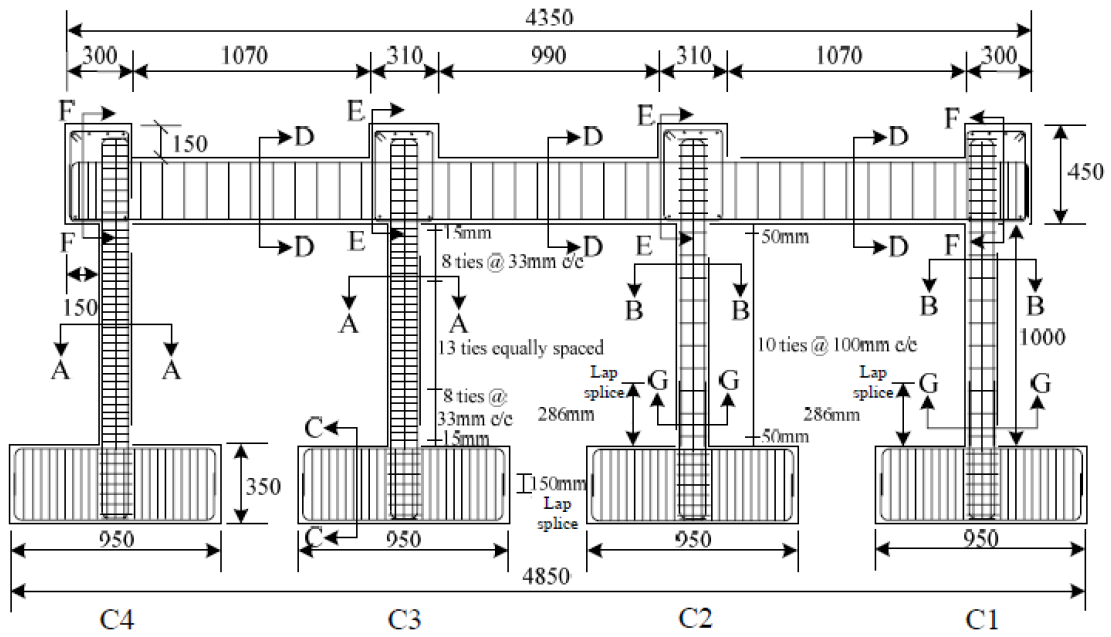
Figure 2-26. Specimen L design layout (Guo 2008)

360
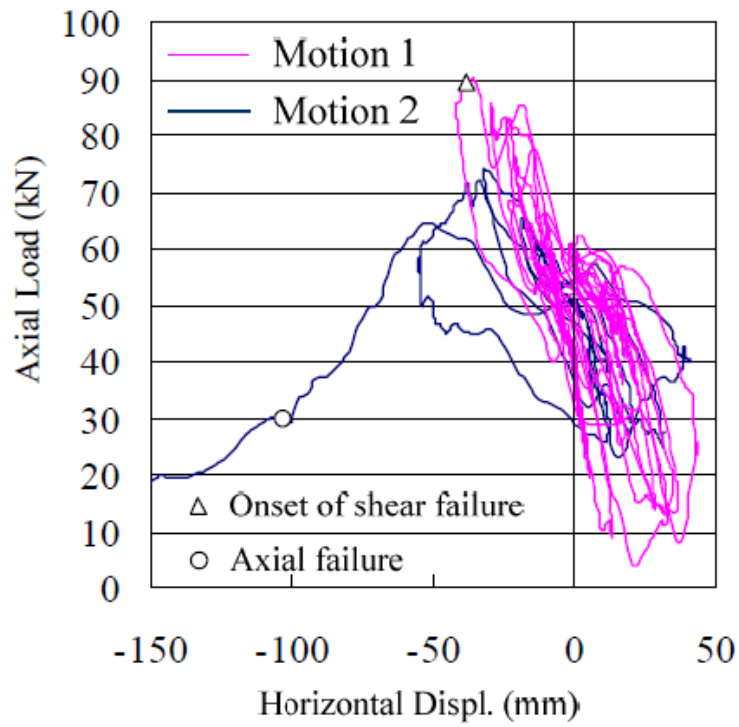
Figure 2-27. Specimen P1 Column C1 axial load – horizontal displacement response (Guo 2008)
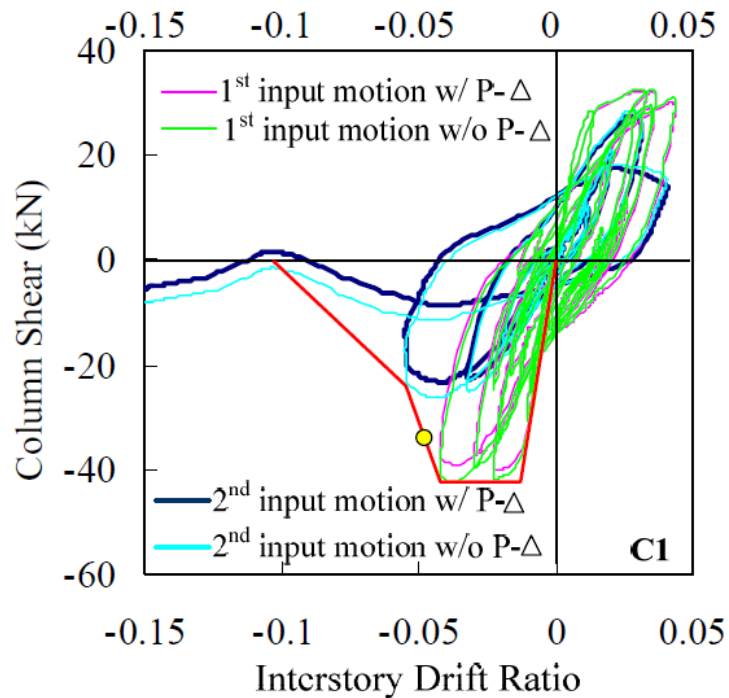
Figure 2-28. Specimen P1 Column C1 hysteresis response (Guo 2008)

361
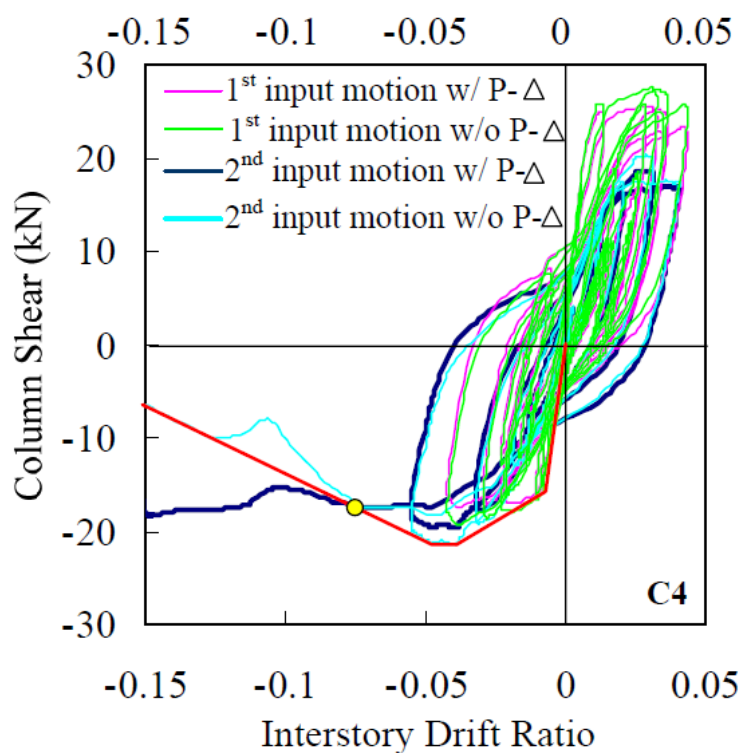
Figure 2-29. Specimen P1 Column C4 hysteresis response (Guo 2008)
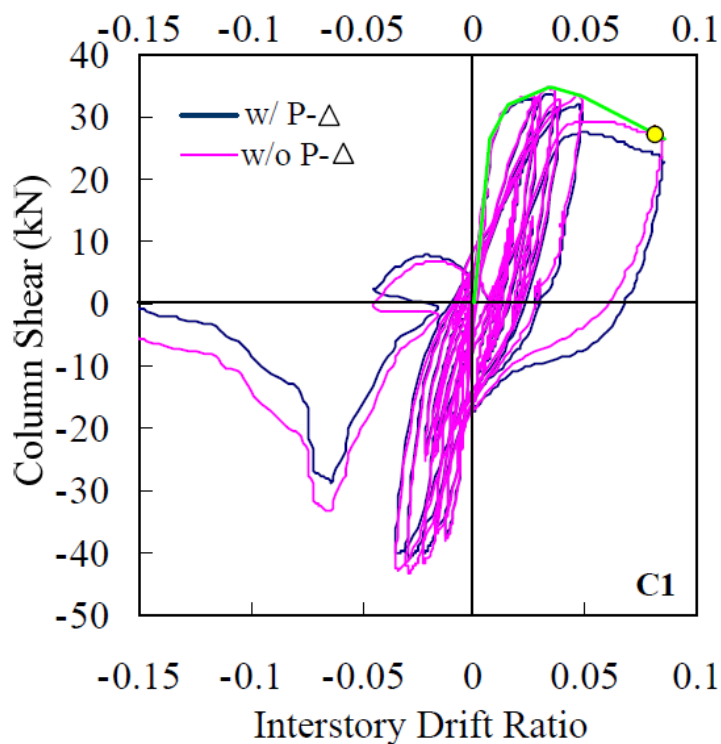
Figure 2-30. Specimen L Column C1 hysteresis response (Guo 2008)

362
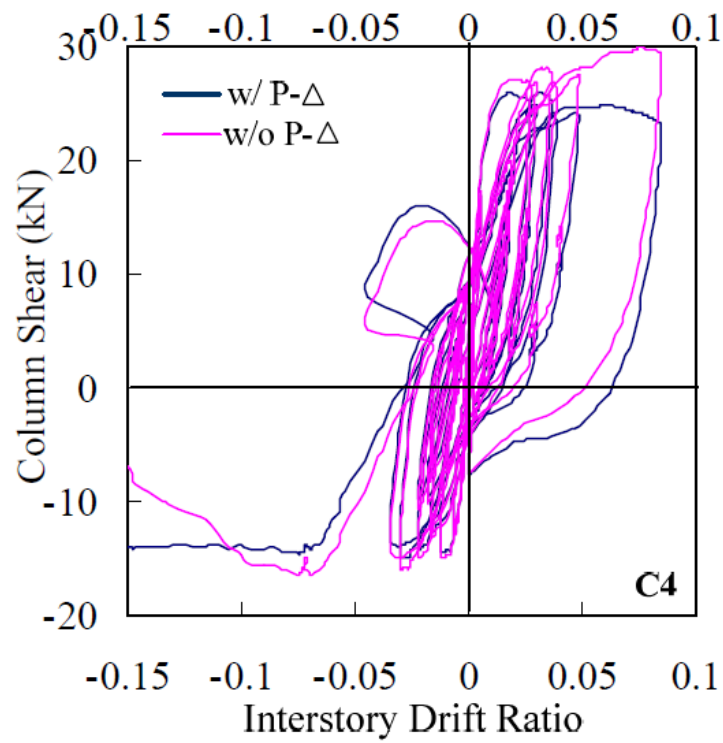
Figure 2-31. Specimen L Column C4 hysteresis response (Guo 2008)
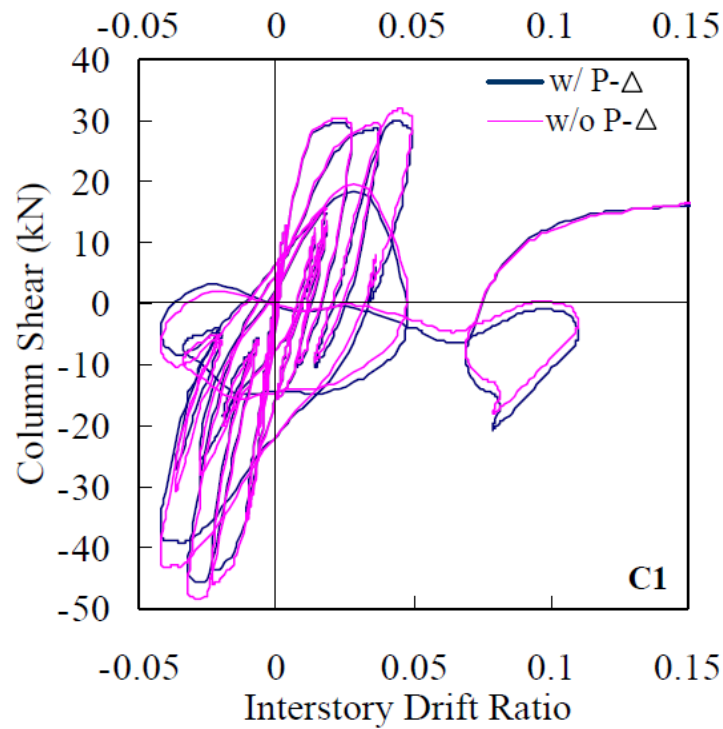
Figure 2-32. Specimen P2 Column C1 hysteresis response (Guo 2008)
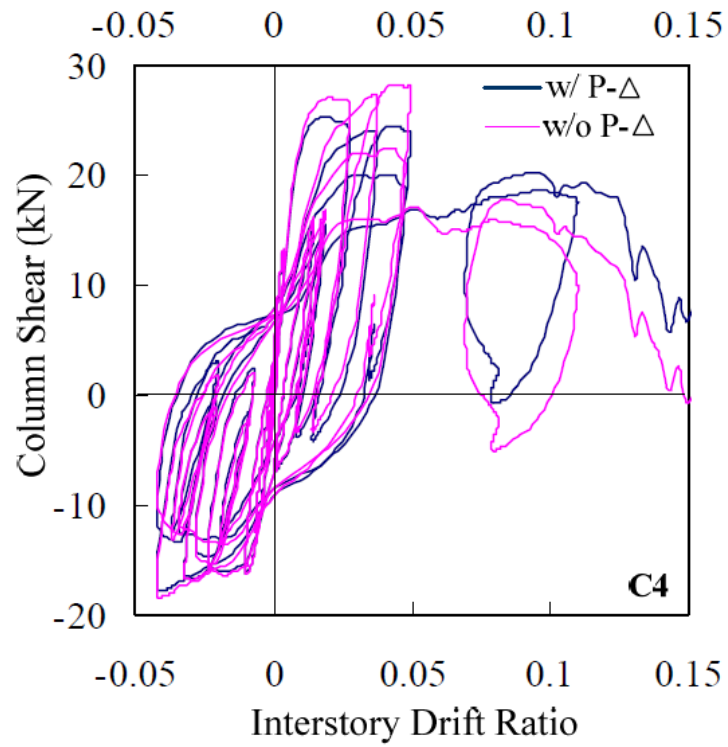
Figure 2-33. Specimen P2 Column C4 hysteresis response (Guo 2008)
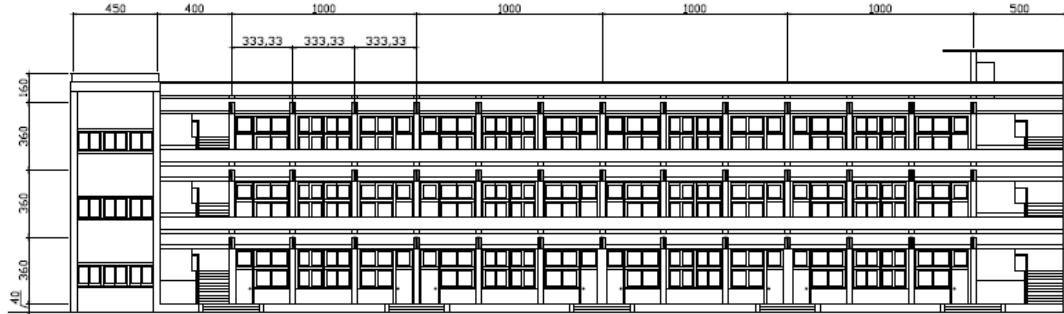
Figure 2-34. Three-story conventional school building elevation layout (Yeh and Chou 2017)

364
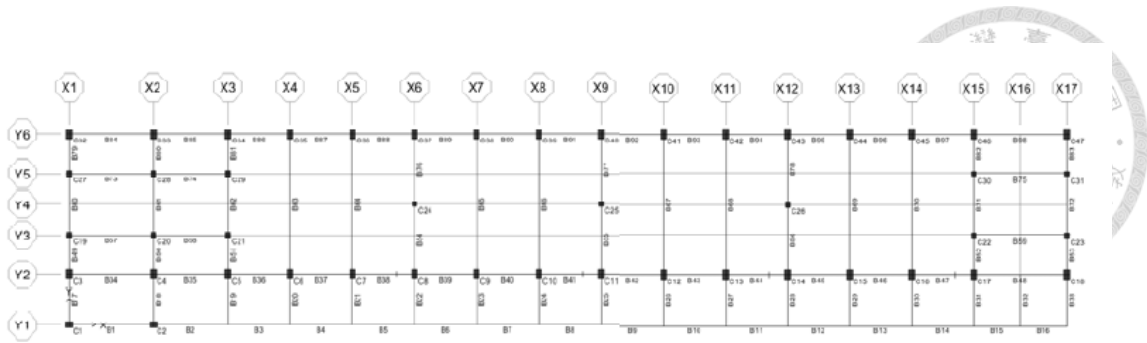
Figure 2-35. Three-story conventional school building floor plan layout (Yeh and Chou 2017)
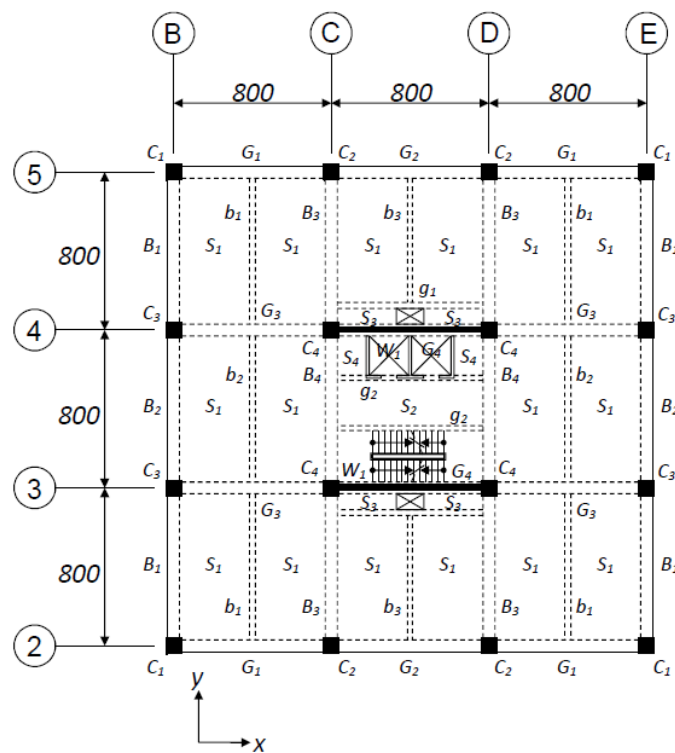
Figure 2-36. Ten-story residential building floor plan layout (Yeh and Chou 2017)

365
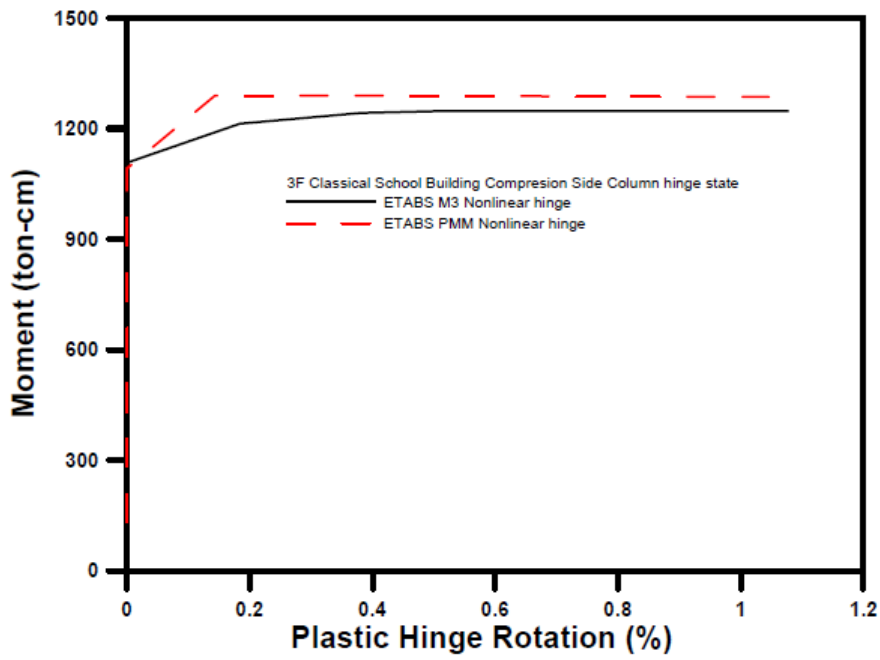
Figure 2-37. School building column moment-rotation response (compression) (Yeh and Chou 2017)
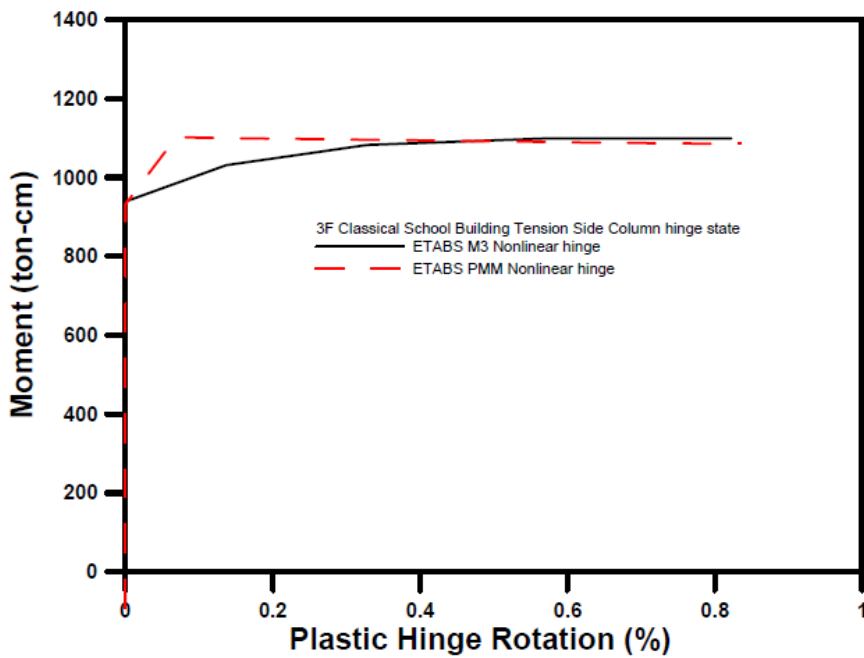
Figure 2-38. School building column moment-rotation response (tension)   (Yeh and Chou 2017)

366
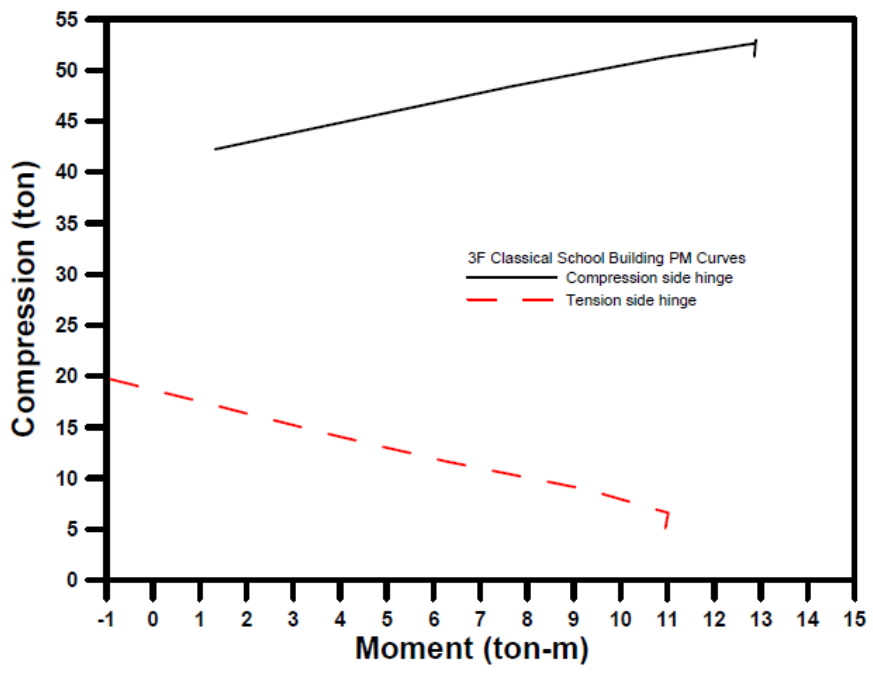
Figure 2-39. School building column axial load-moment response (PMM hinge)
(Yeh and Chou 2017)
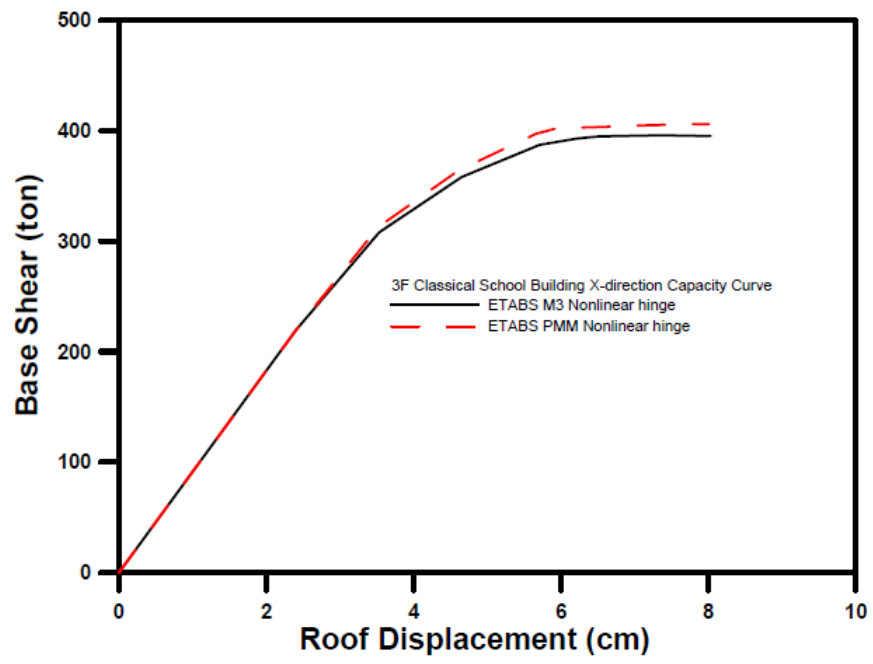
Figure 2-40. School building total capacity curve comparison for two models
(Yeh and Chou 2017)

367
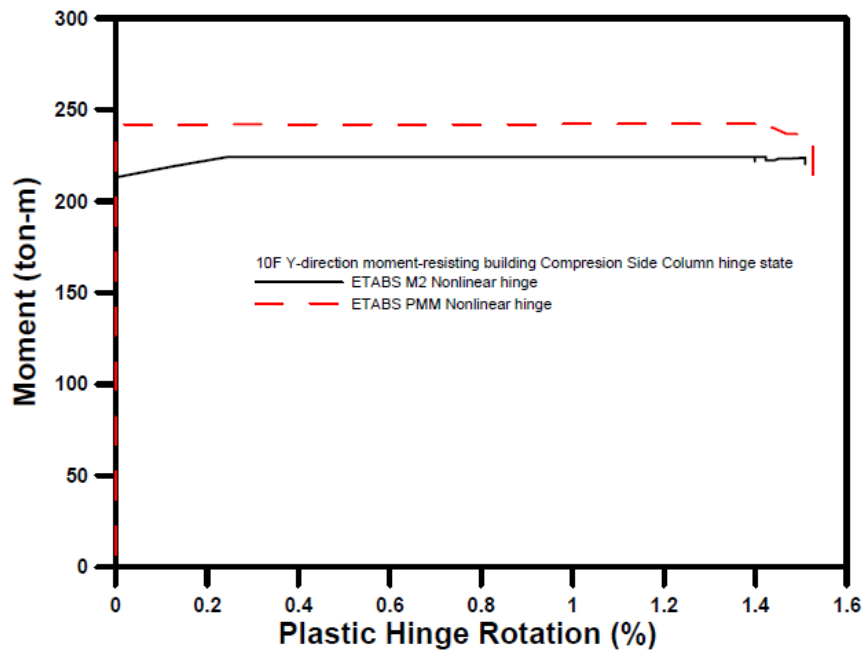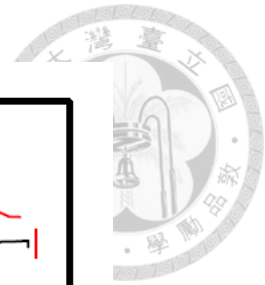
Figure 2-41. Residential building column moment-rotation response (compression)
(Yeh and Chou 2017)
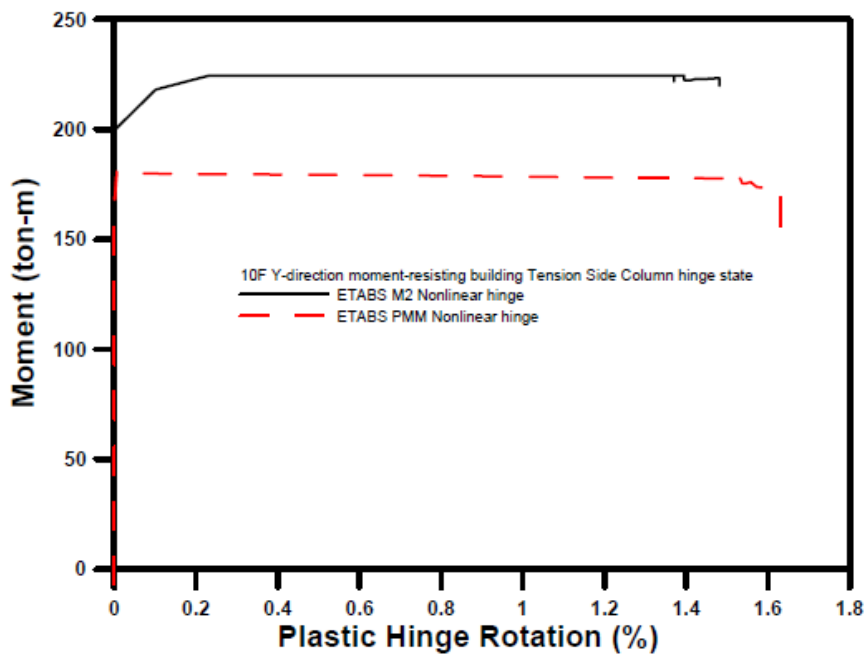
Figure 2-42. Residential building column moment-rotation response (tension)
(Yeh and Chou 2017)
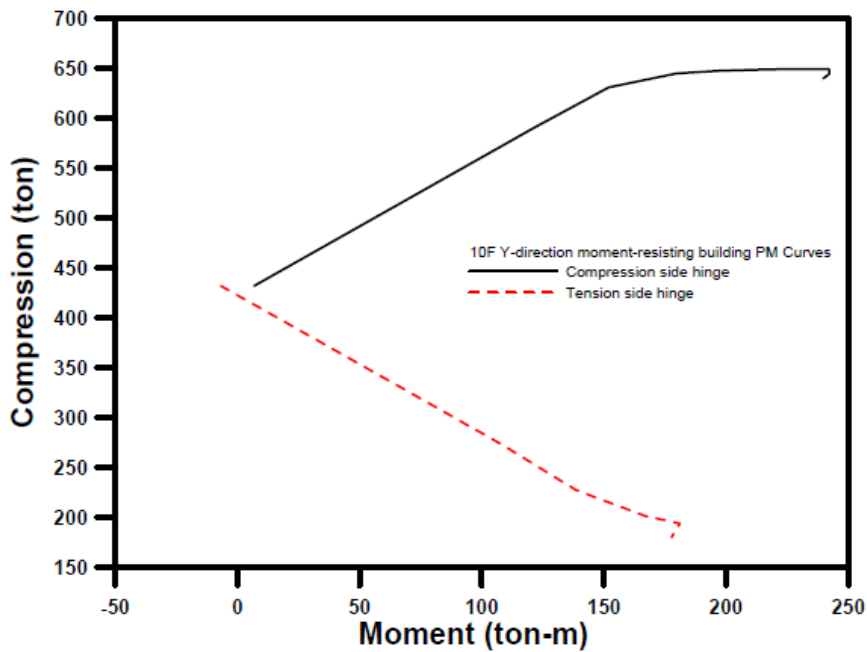
Figure 2-43. Residential building column axial load-moment response (PMM hinge) (Yeh and Chou 2017)
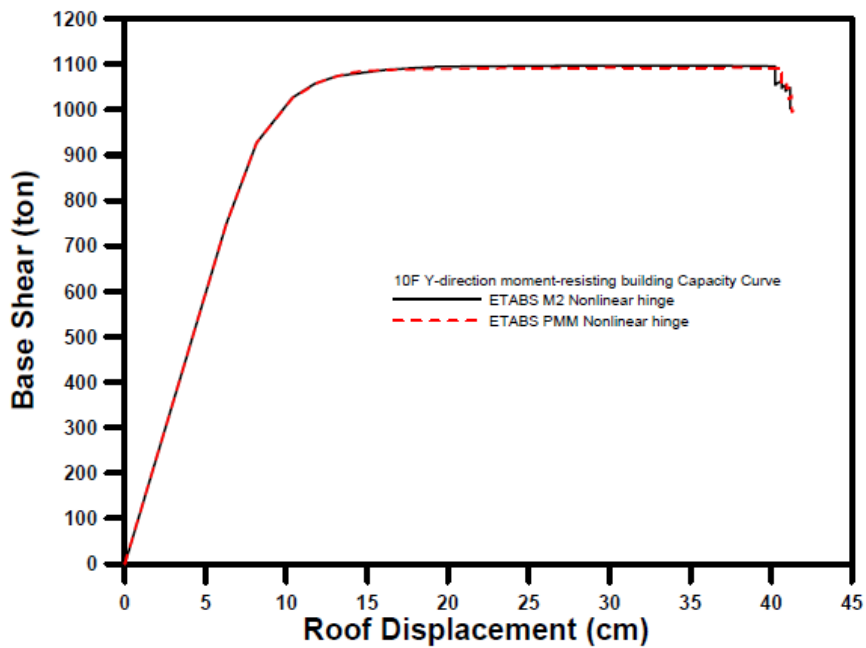
Figure 2-44. Residential building total capacity curve comparison for two models (Yeh and Chou 2017)

369

Section A-A
Column Section

50cm

16-#8 Longitudinal Bars
#3@30cm Stirrup
90° Hook
4cm Clear Cover

50cm

Section B-B
Joint Section

100cm

#8@15cm Joint Stirrup
4cm Clear Cover

70cm

Section C-C
Foundation Section

150cm

#8@15cm Foundation Stirrup
4cm Clear Cover

70cm
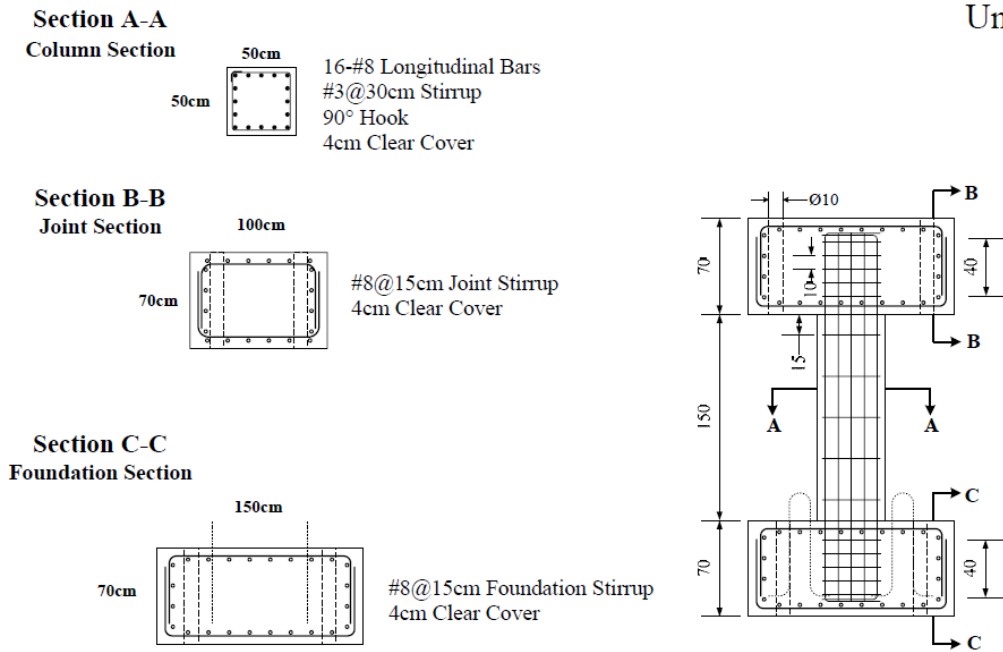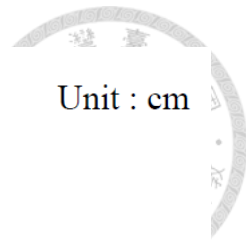
Figure 3-1. Cyclic loading test 3NL specimen design layout (Weng 2007)

Section A-A
Column Section

50cm

16-#8 Longitudinal Bars
#3@10cm Stirrup
135° Hook
4cm Clear Cover

50cm

Section B-B
Joint Section

100cm

#8@15cm Joint Stirrup
4cm Clear Cover

70cm

Section C-C
Foundation Section

150cm

#8@15cm Foundation Stirrup
4cm Clear Cover

70cm
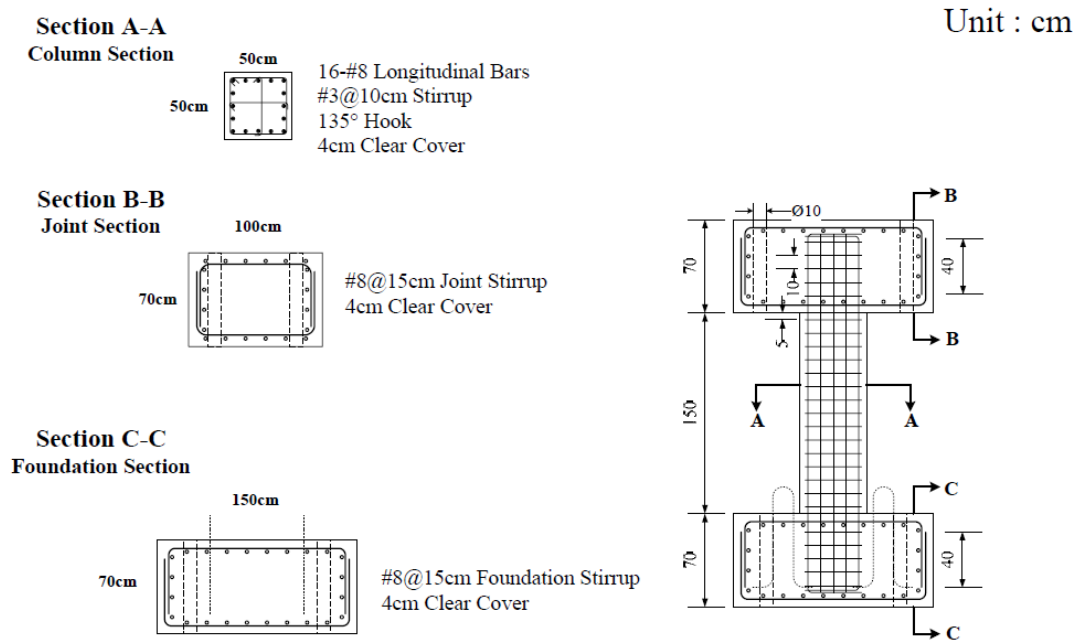
Figure 3-2. Cyclic loading test 3DL specimen design layout (Weng 2007)

370
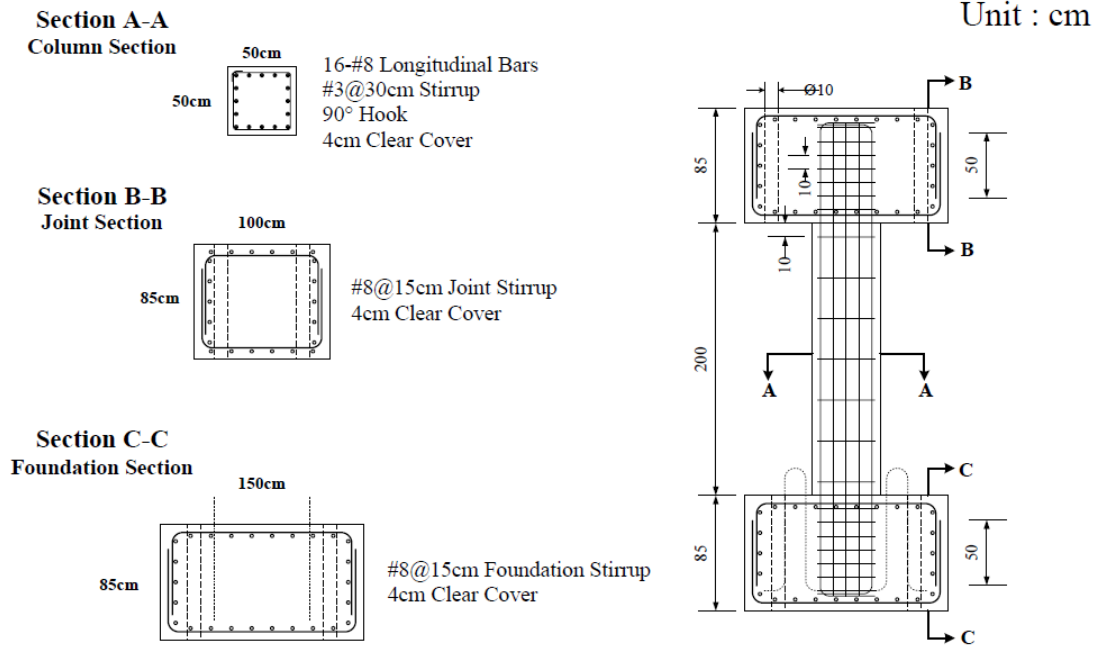
Figure 3-3. Cyclic loading test 4NL specimen design layout (Weng 2007)
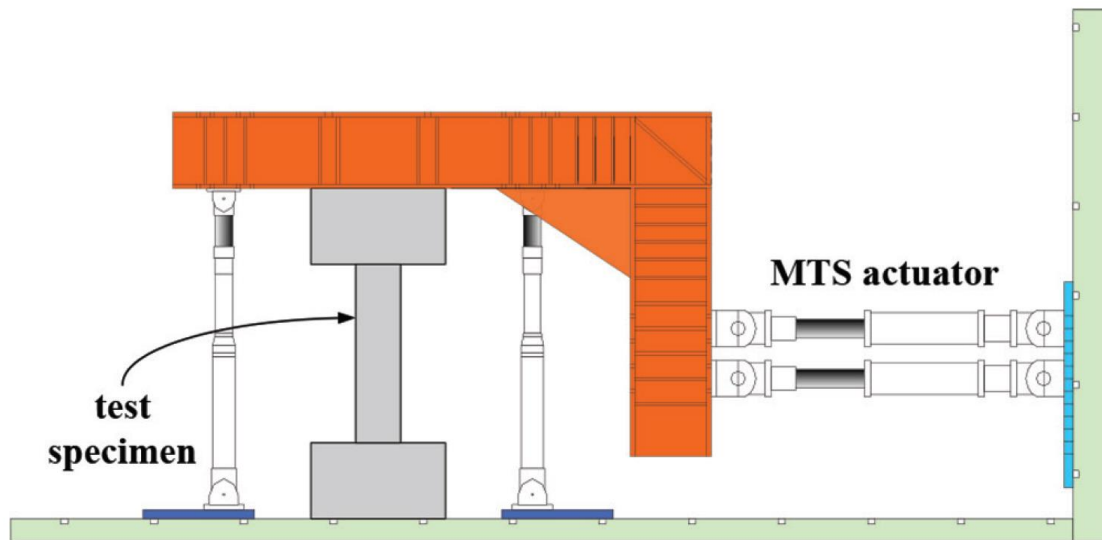
Figure 3-4. Cyclic loading test setup (Weng 2007)
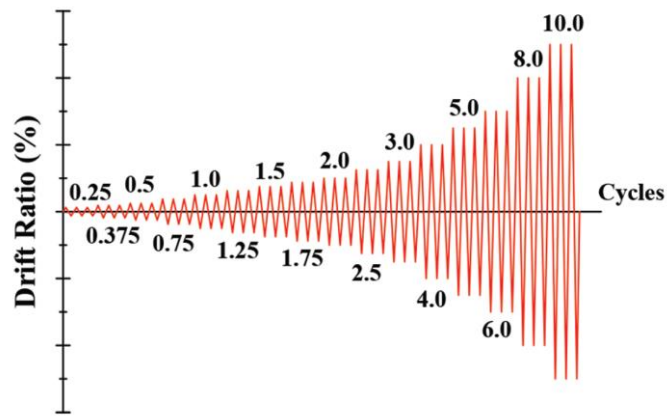
Figure 3-5. Cyclic loading test displacement cycles (Weng 2007)
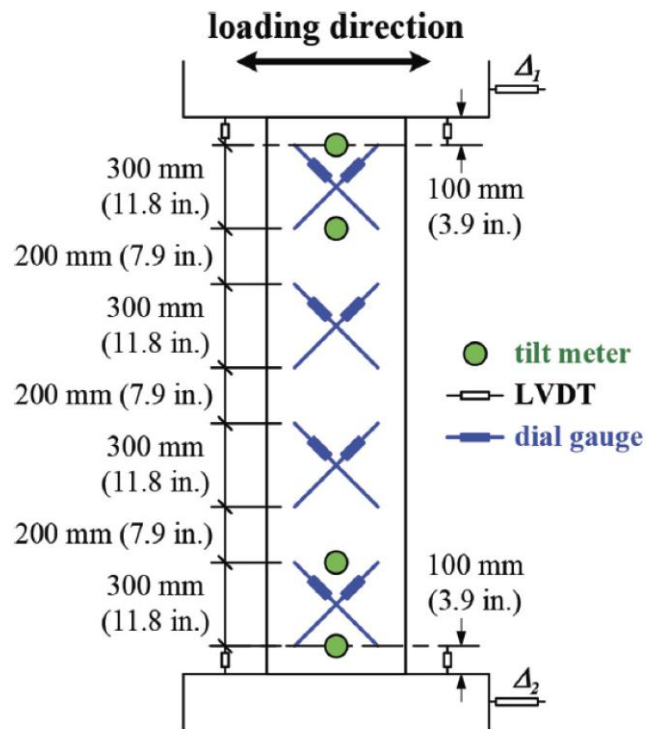
Figure 3-6. Cyclic loading test instrumentation setup (Weng 2007)

372

4NL
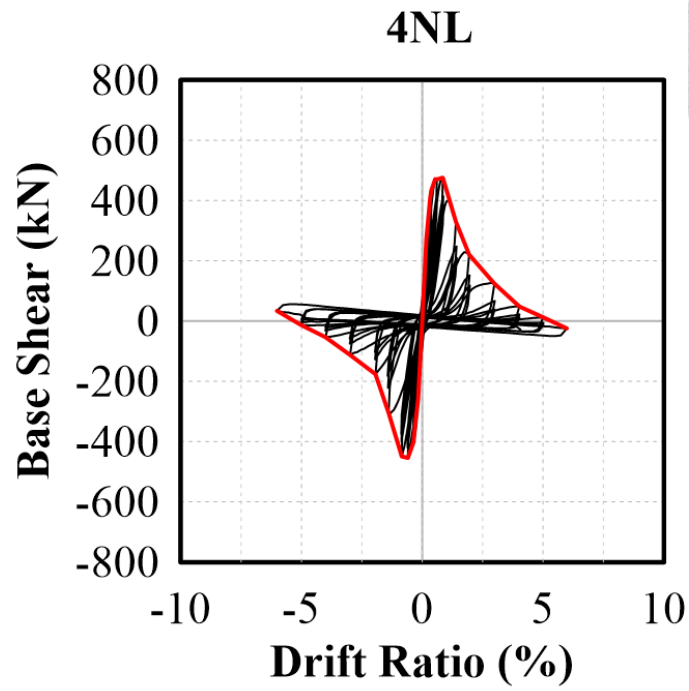
Figure 3-7. Specimen 4NL hysteresis response

3DL
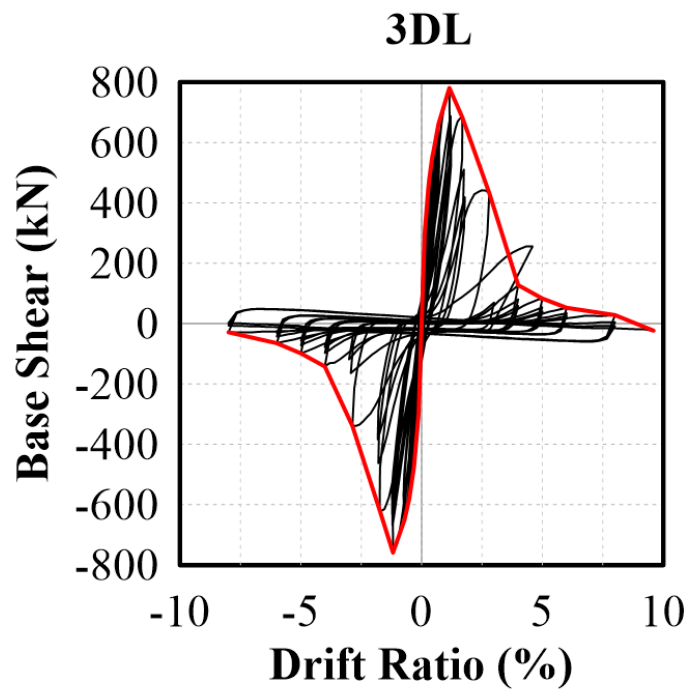
Figure 3-8. Specimen 3DL hysteresis response
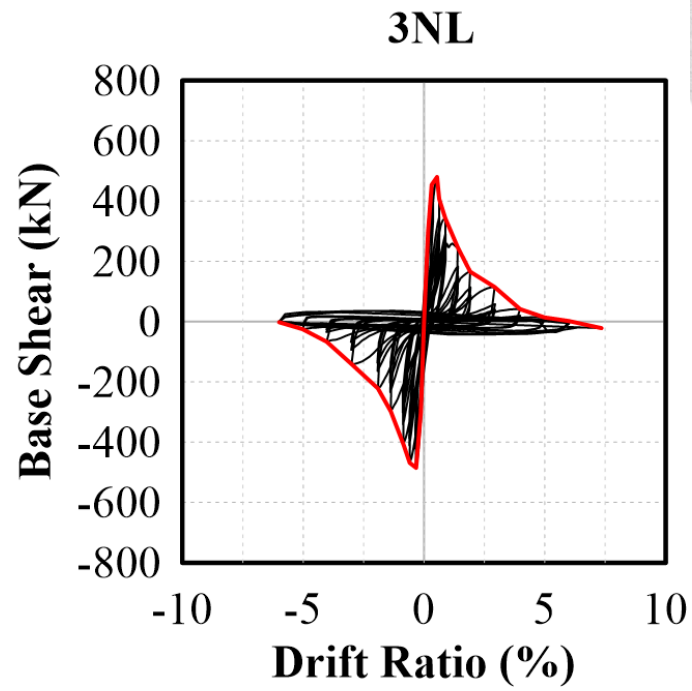
Figure 3-9. Specimen 3NL hysteresis response
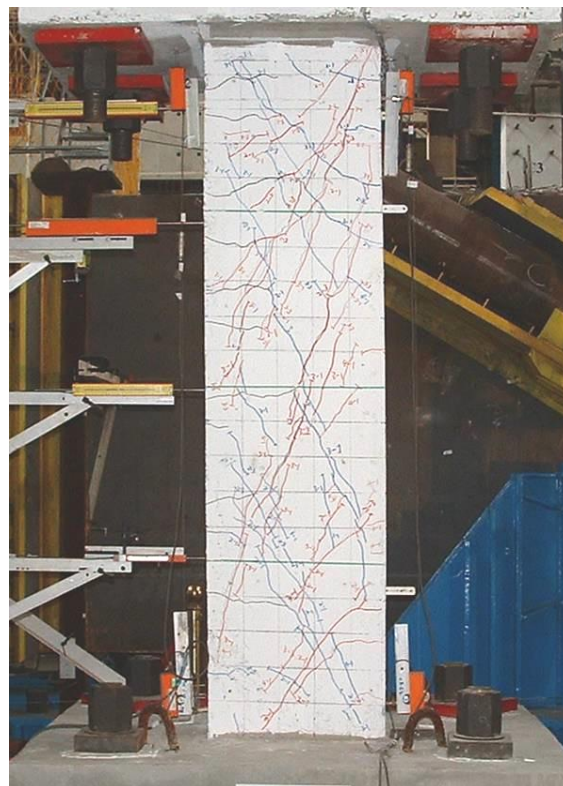
Figure 3-10. Specimen 4NL crack pattern at strength point (0.85%) (Weng 2007)

Figure 3-11. Specimen 4NL crack pattern before collapse (6%) (Weng 2007)
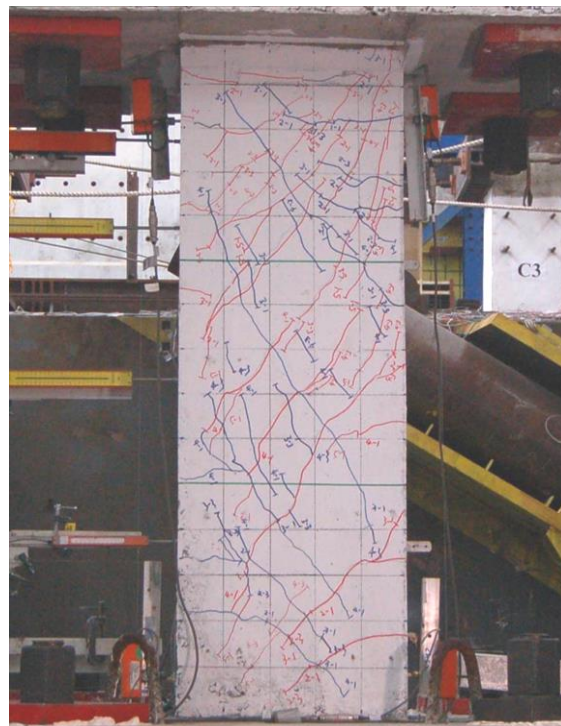
Figure 3-12. Specimen 3DL crack pattern at strength point (1.15%) (Weng 2007)

375

Figure 3-13. Specimen 3DL crack pattern before collapse (8%) (Weng 2007)
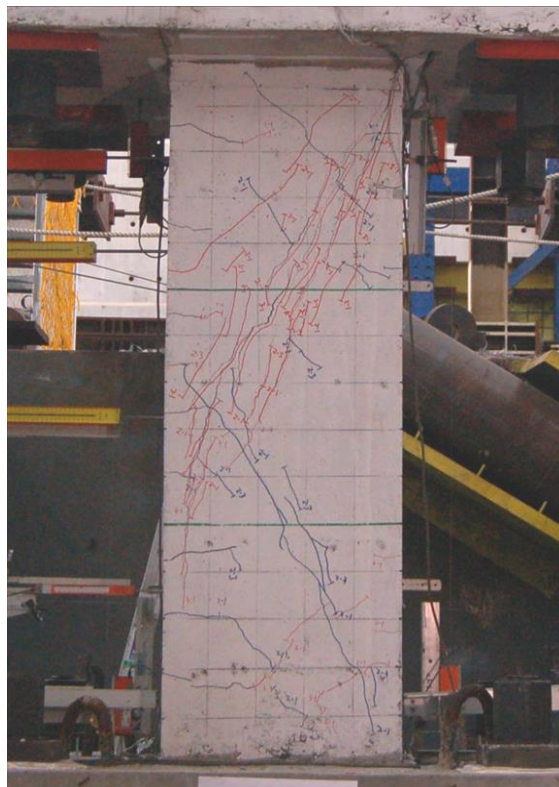
Figure 3-14. Specimen 3NL crack pattern at strength point (0.628%) (Weng 2007)

Figure 3-15. Specimen 3NL crack pattern before collapse (5%) (Weng 2007)
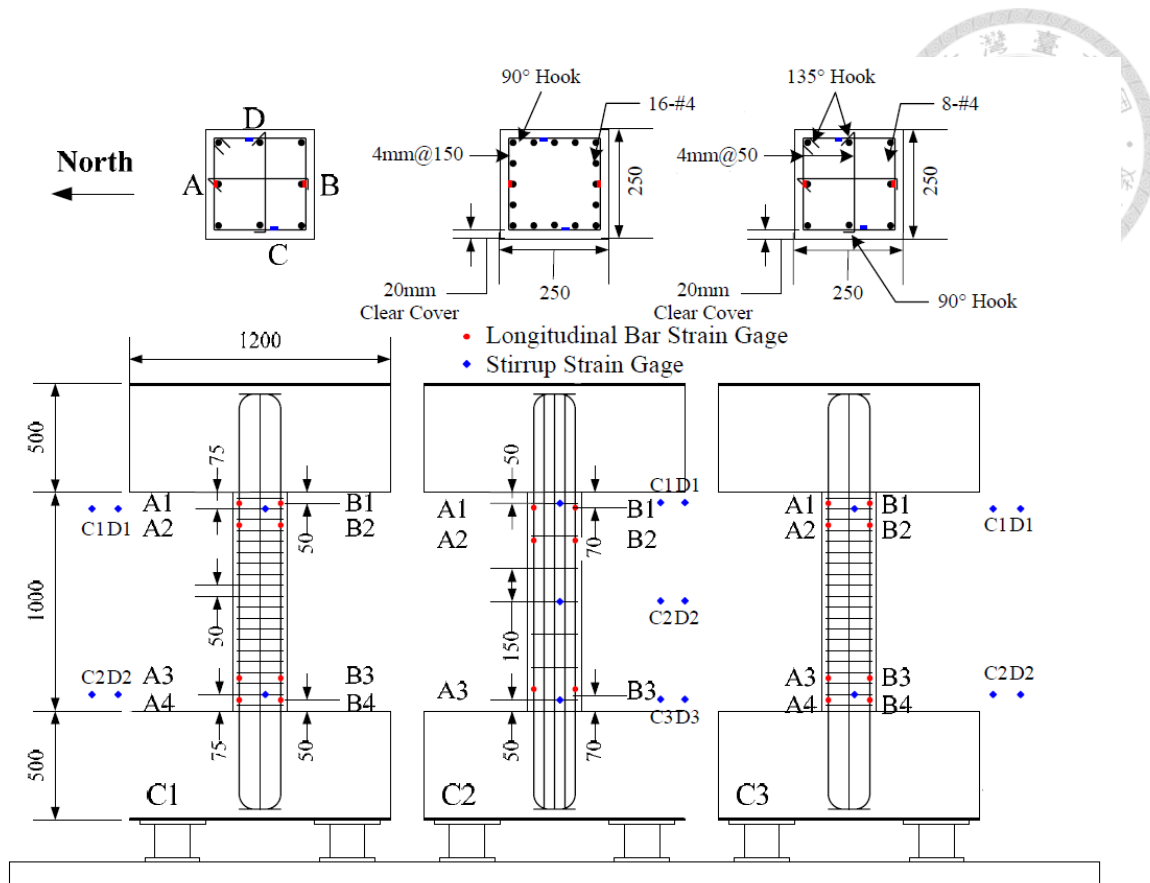
Figure 4-1. Shaking table test T1 specimen design layout (Su 2007)
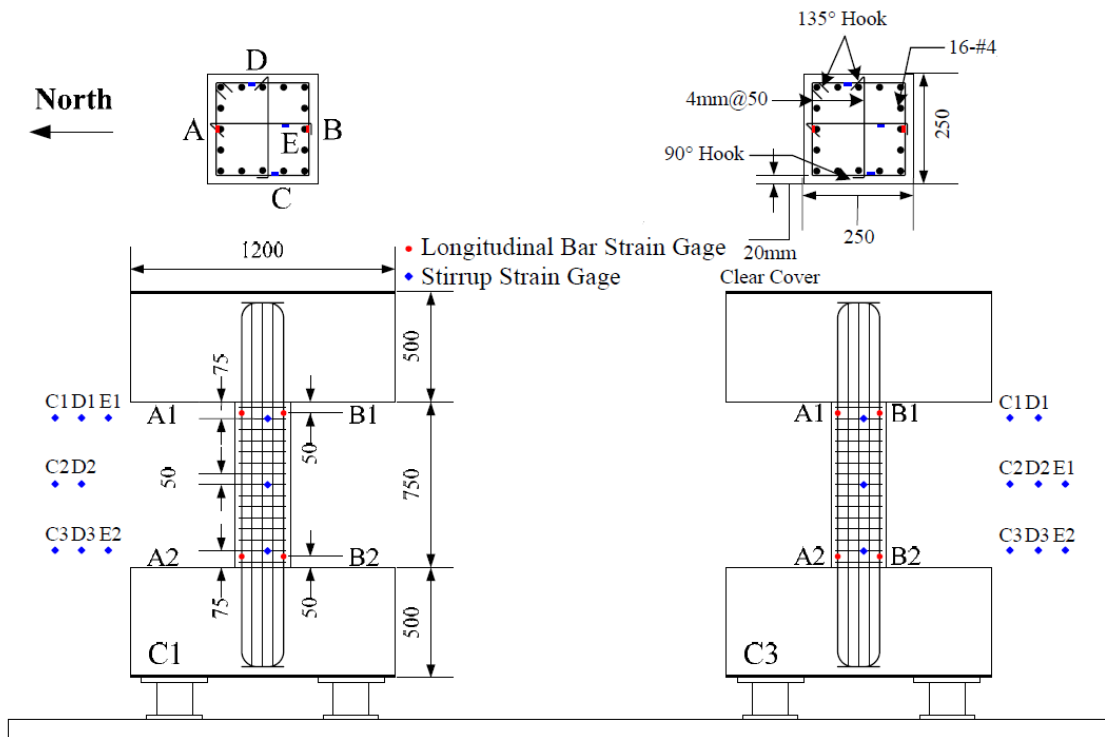
Figure 4-2. Shaking table test T2 specimen design layout (Su 2007)

378
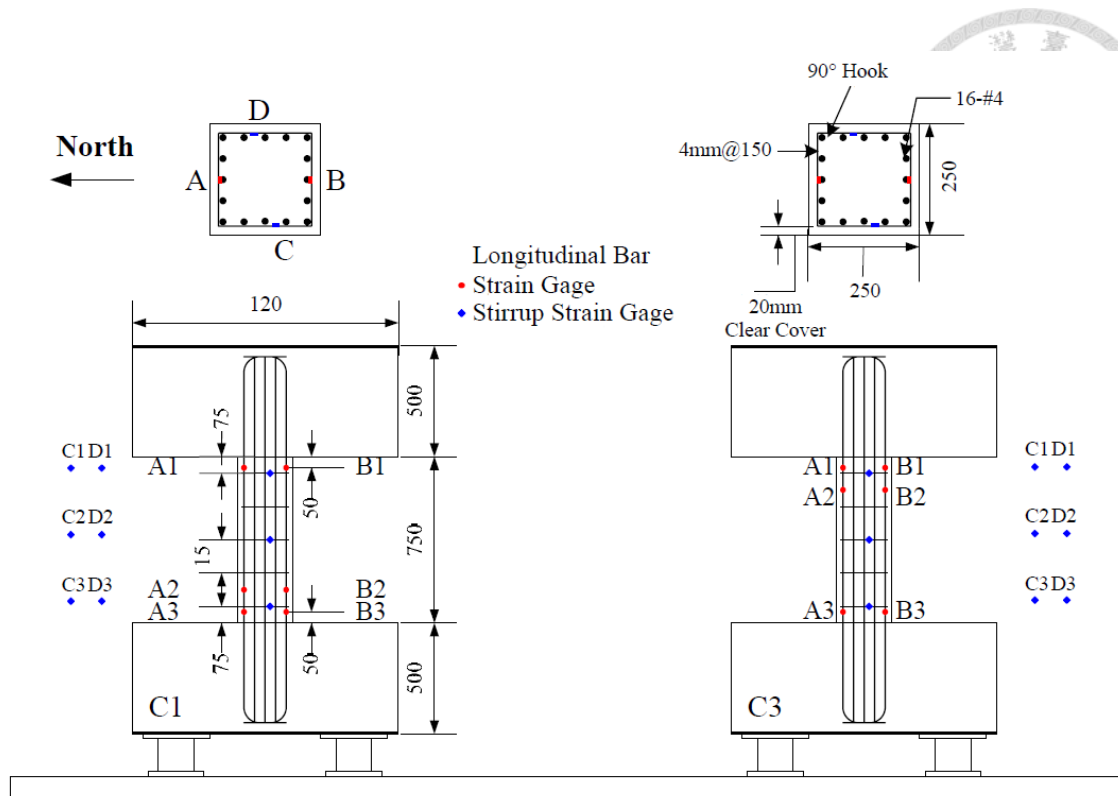
Figure 4-3. Shaking table test T3 specimen design layout (Su 2007)
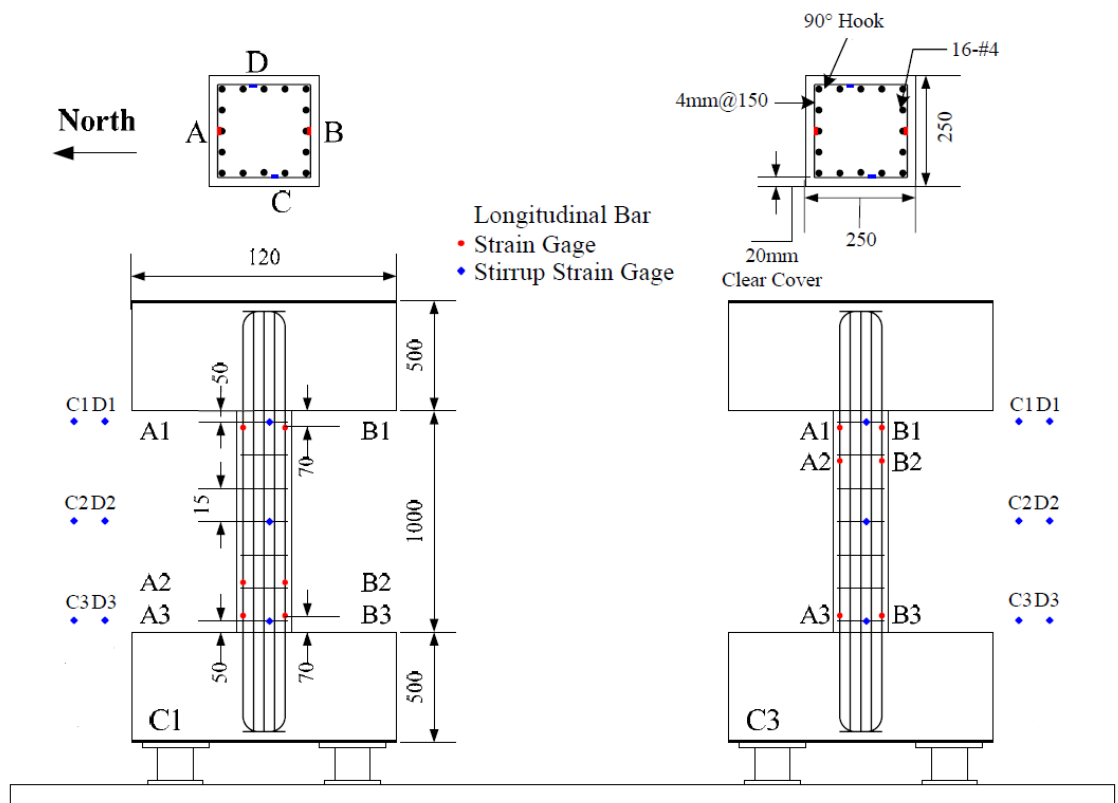
Figure 4-4. Shaking table test T4 specimen design layout (Su 2007)
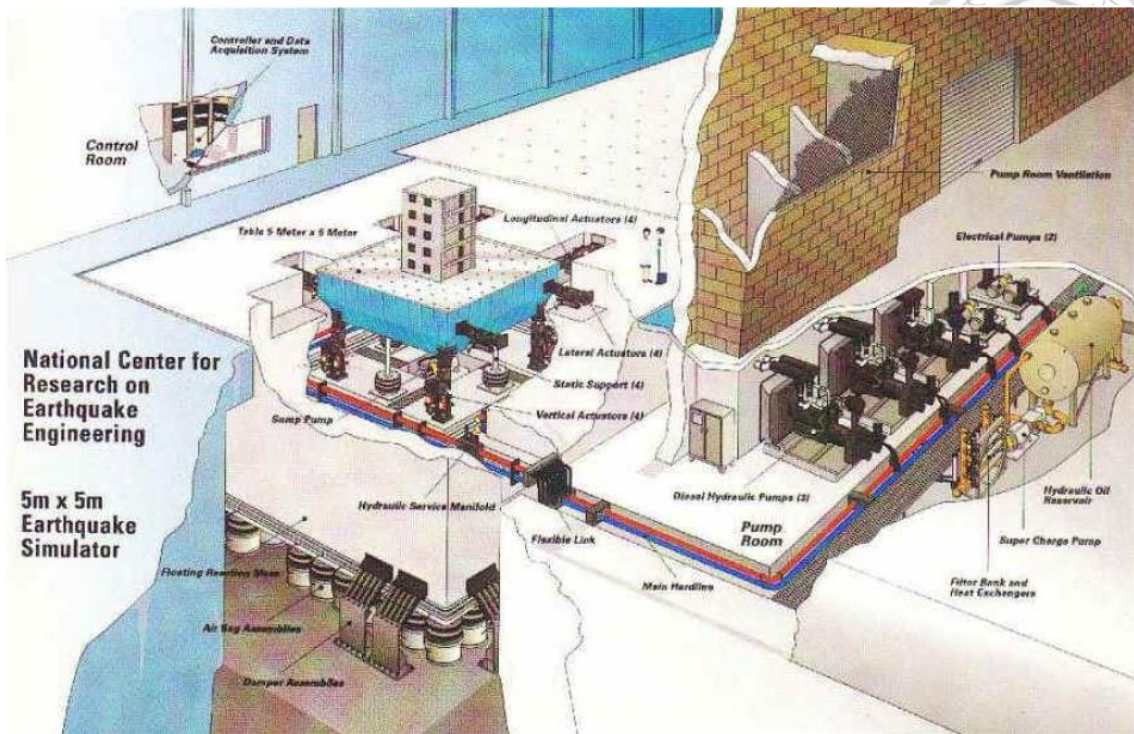
Figure 4-5. NCREE Taipei lab shaking table setup (Su 2007)

Figure 4-6. Casted shaking table test column specimens (Su 2007)

Figure 4-7. Shaking table test overall setup (Su 2007)
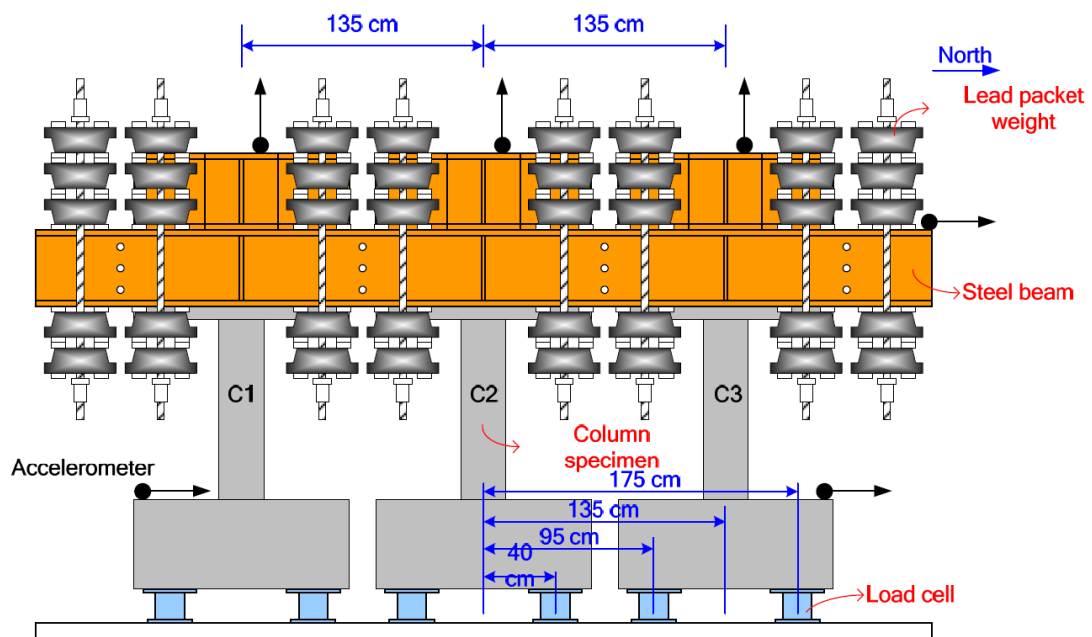
Figure 4-8. Shaking table test instrumental setup (Su 2007)

381
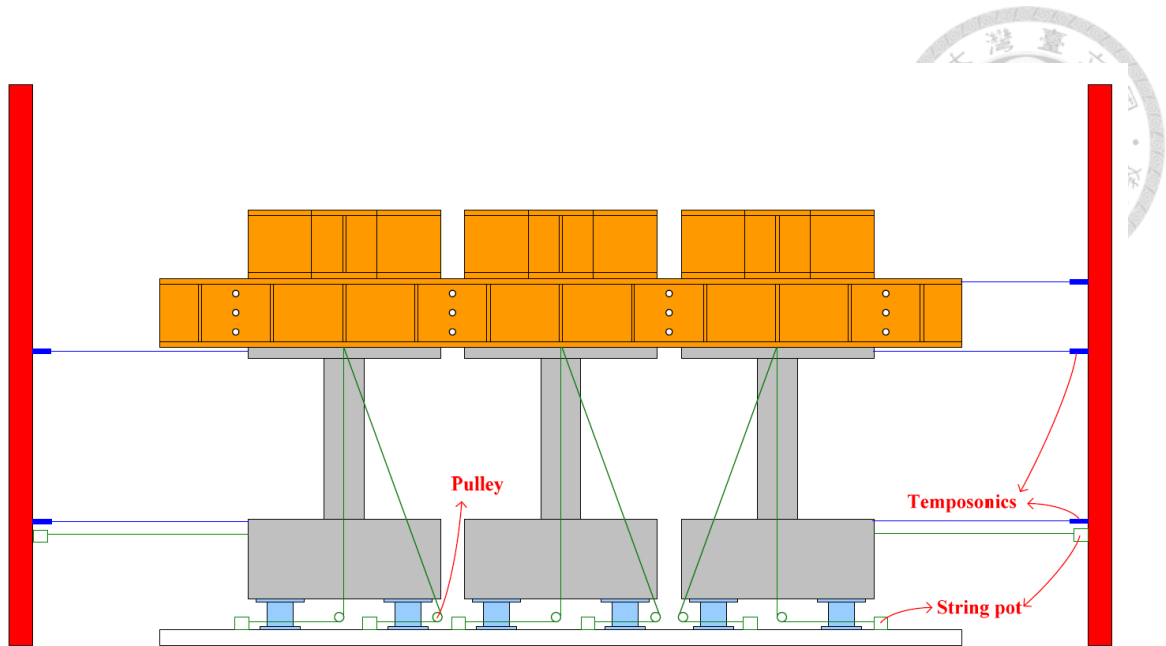
Figure 4-9. Shaking table test measurement setup (Su 2007)
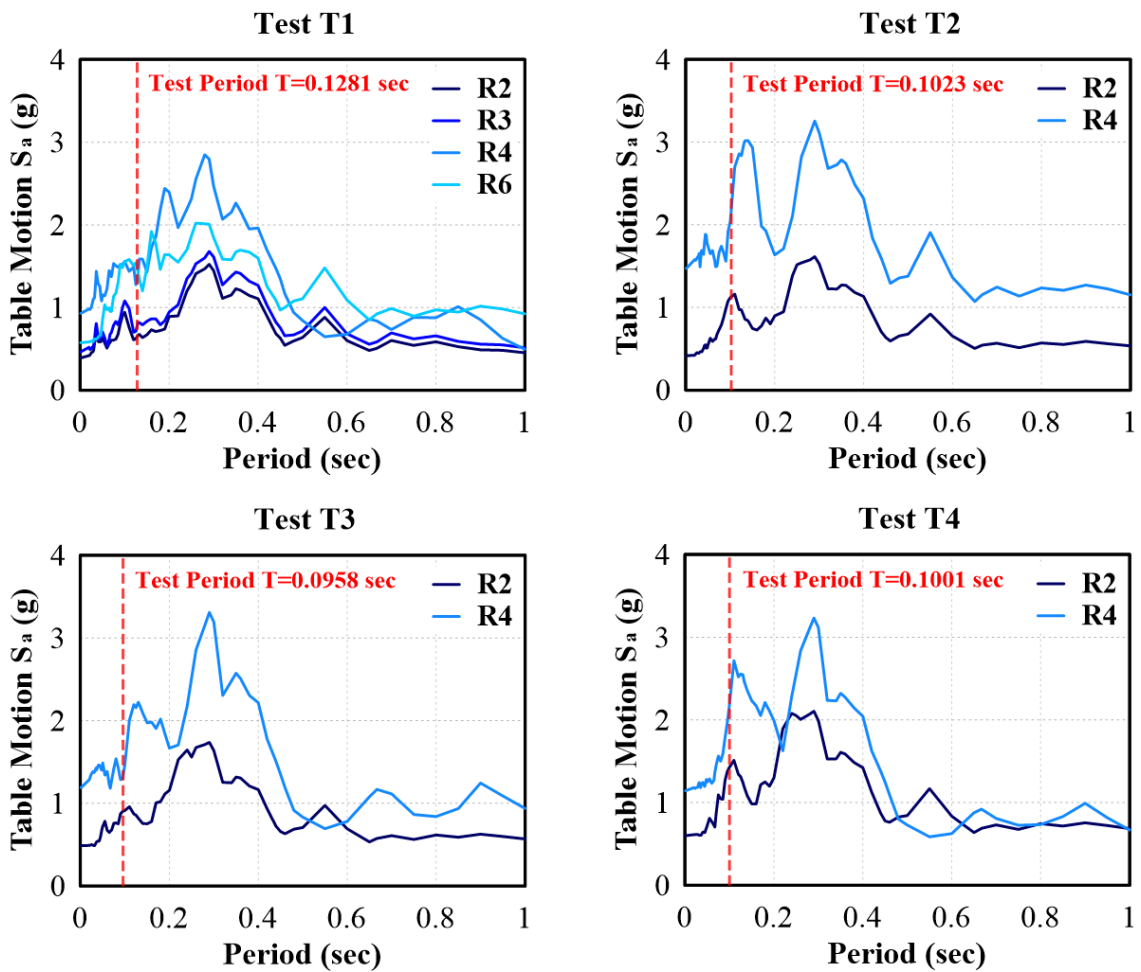
Figure 4-10. Shaking table test ground motion response spectra

382
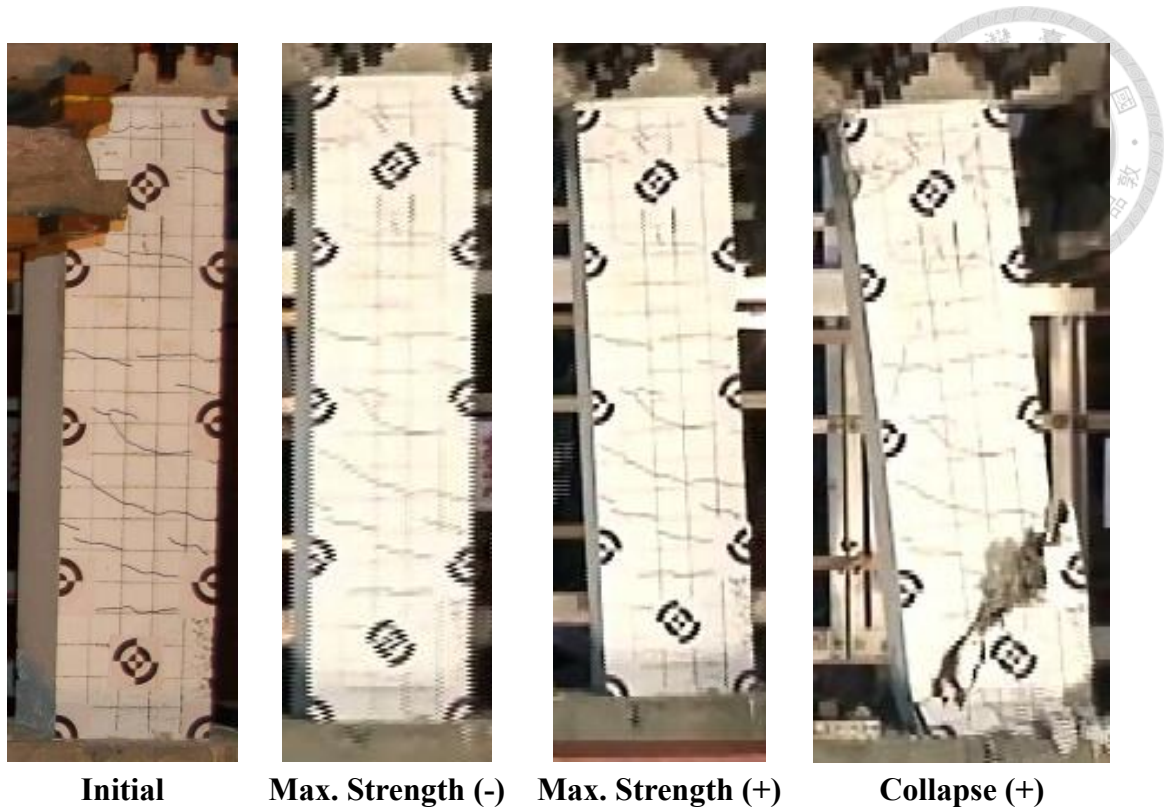
Initial   **Max. Strength (-)**   **Max. Strength (+)**   **Collapse (+)**

Figure 4-11. T1 C1 Crack pattern development
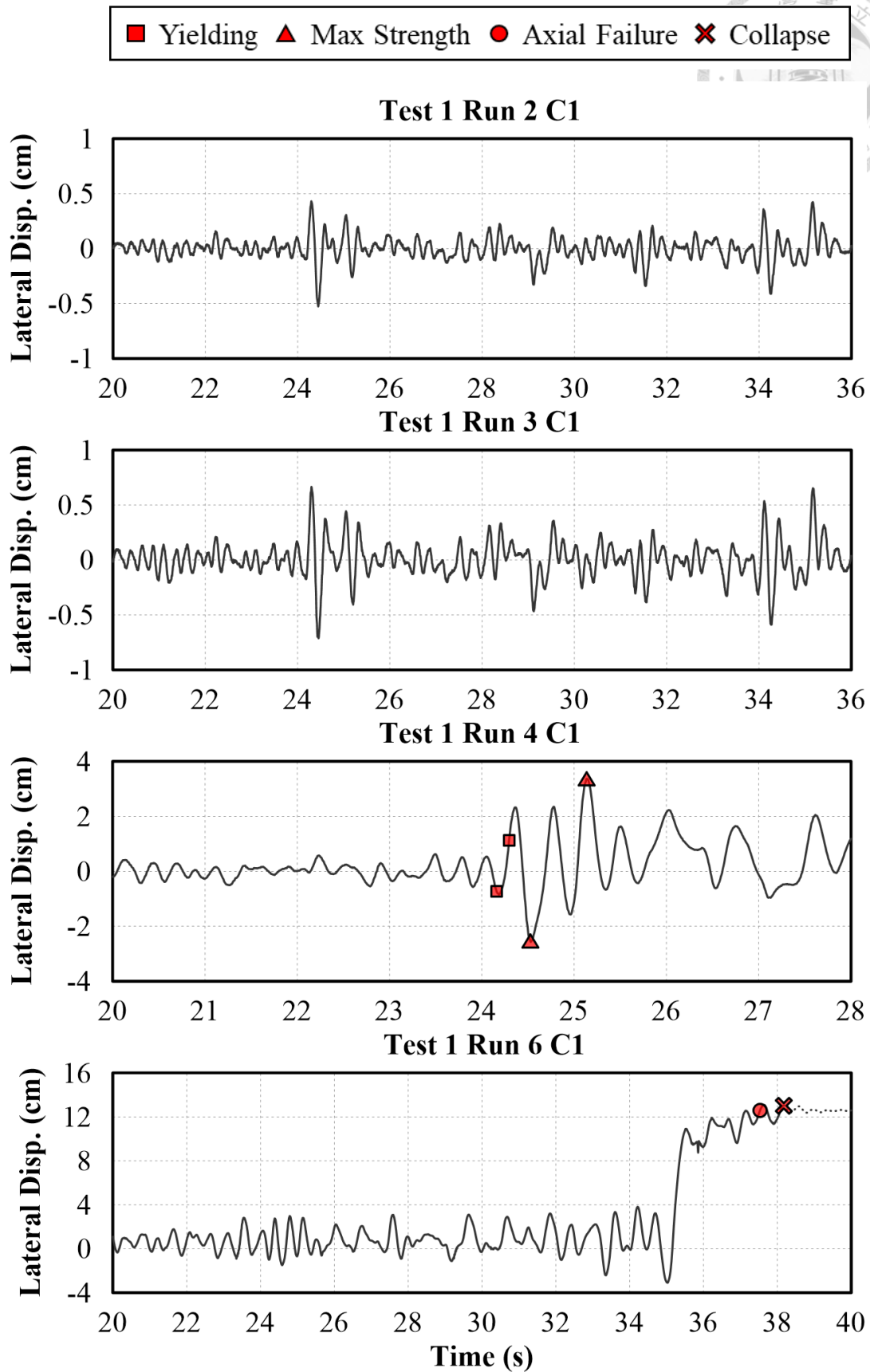
Figure 4-12. T1 C1 Lateral displacement time history response
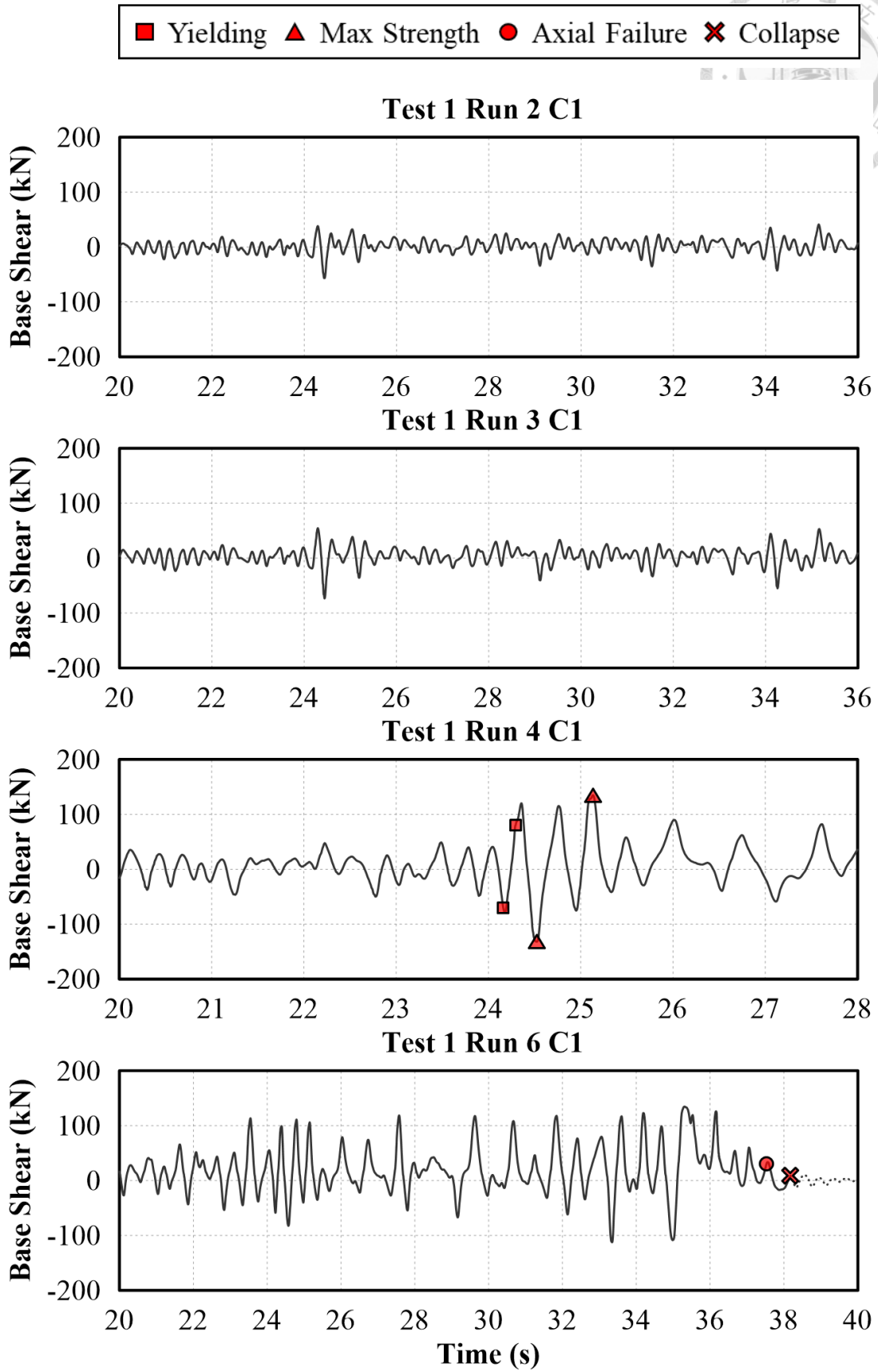
Figure 4-13. T1 C1 Base shear time history response
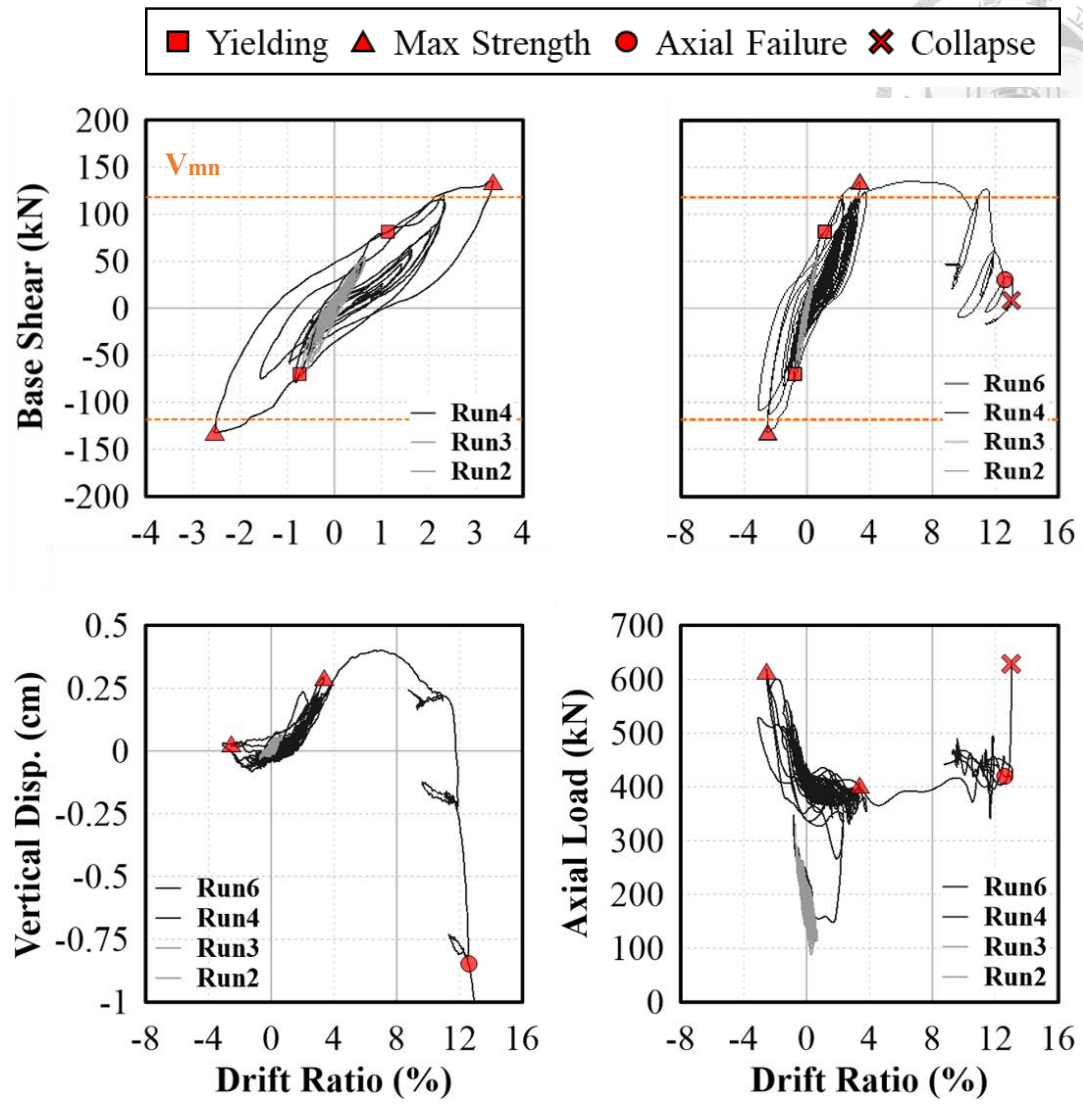
Figure 4-14. T1 C1 Hysteresis response
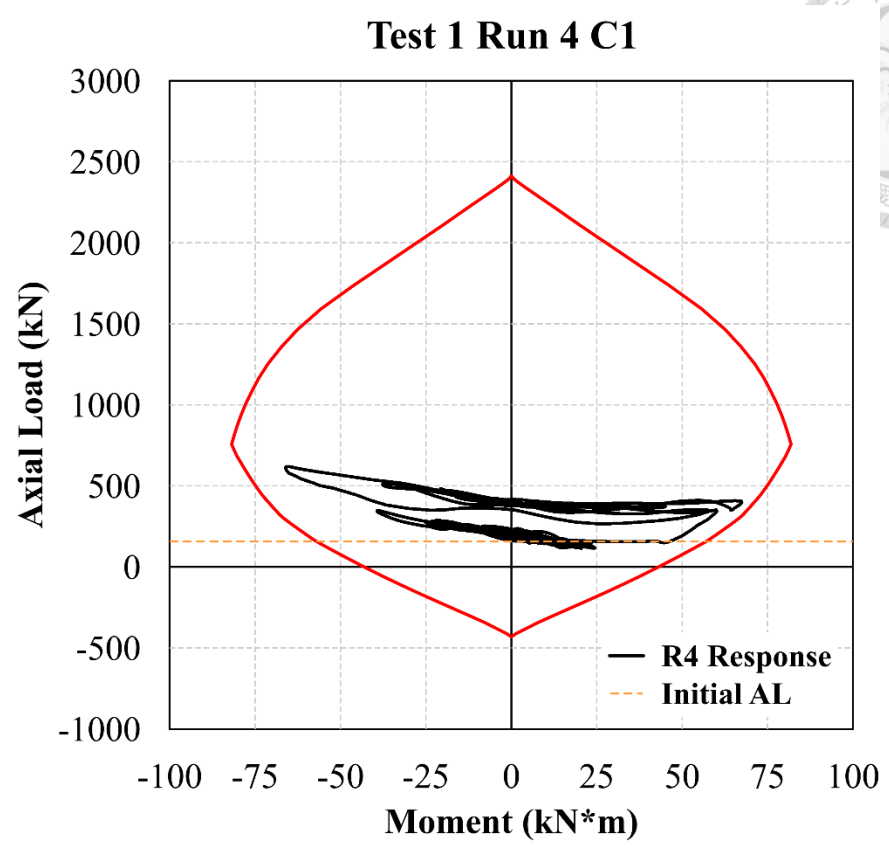
Figure 4-15. T1 C1 Moment-Axial Load Response
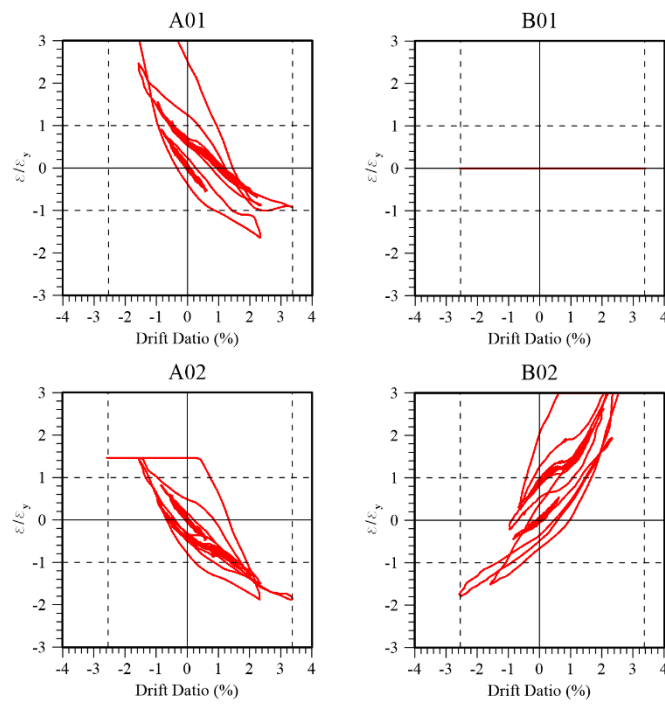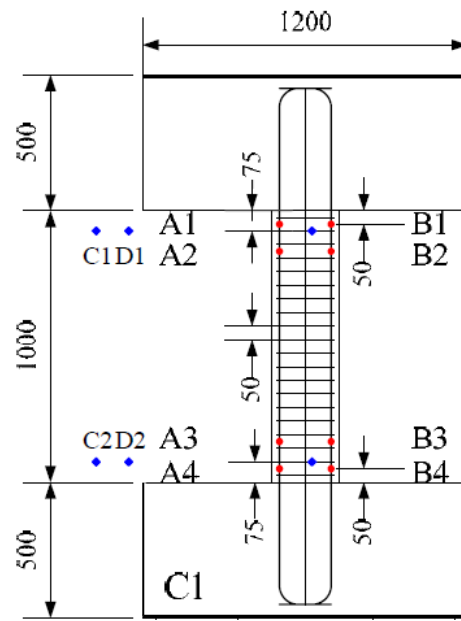
Figure 4-16. T1 C1 Top longitudinal reinforcement strain gage readings
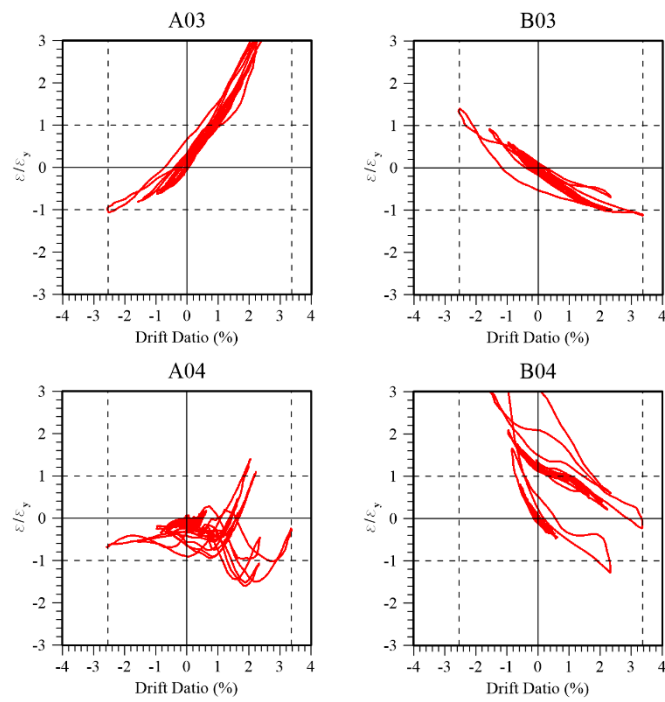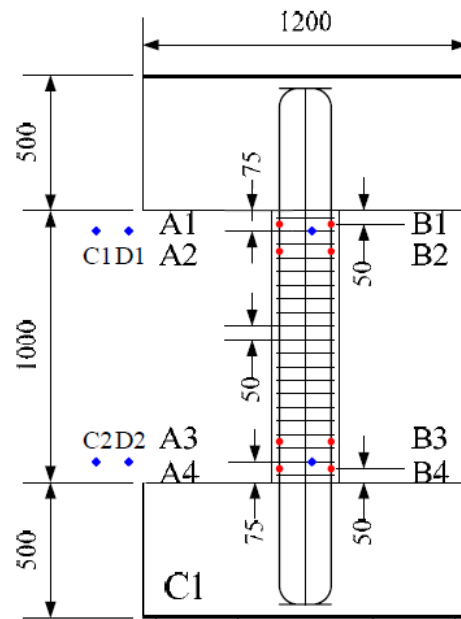
Figure 4-17. T1 C1 Bottom longitudinal reinforcement strain gage readings

389
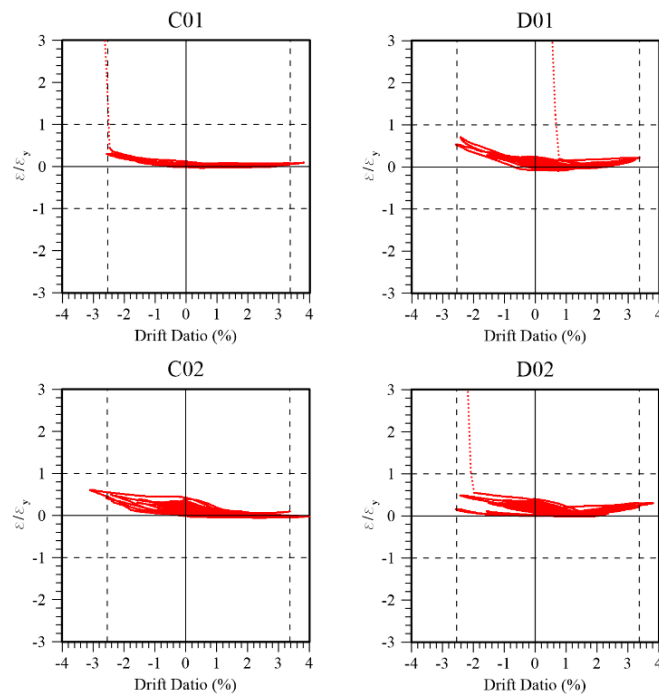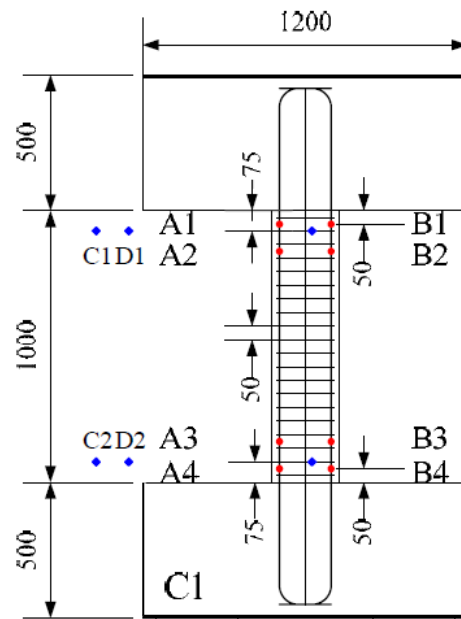
Figure 4-18. T1 C1 Stirrup strain gage readings

390

| Initial | Shear Failure (+) | Shear Failure (-) | End of Run4 |
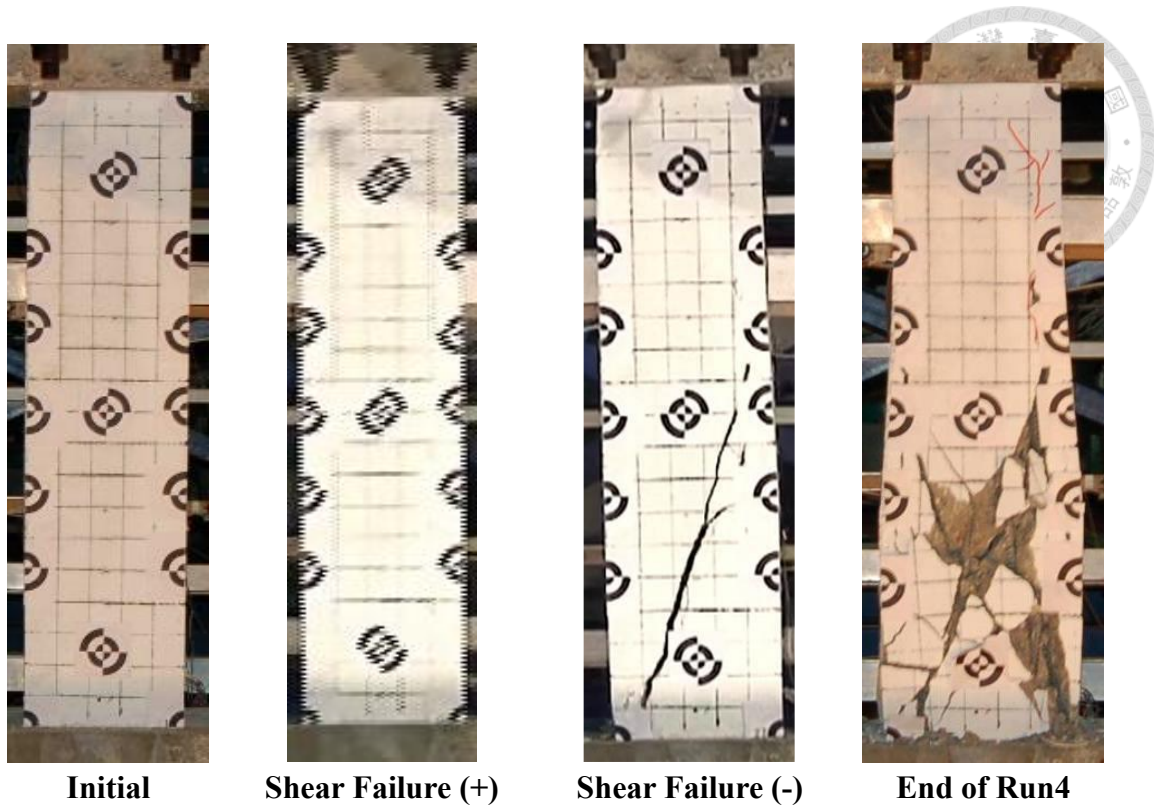
Figure 4-19. T1 C2 Crack pattern development
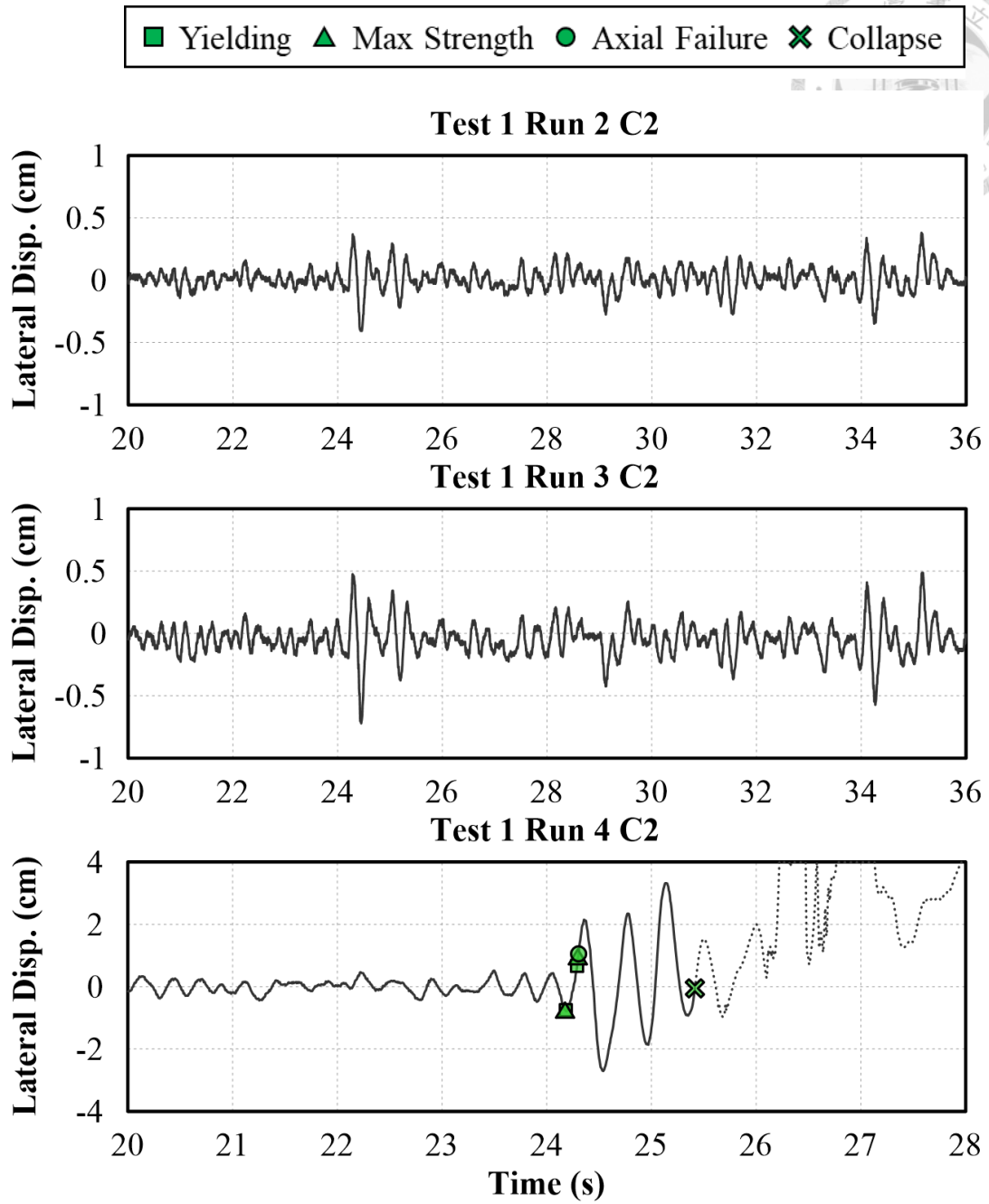
Figure 4-20. T1 C2 Lateral displacement time history response
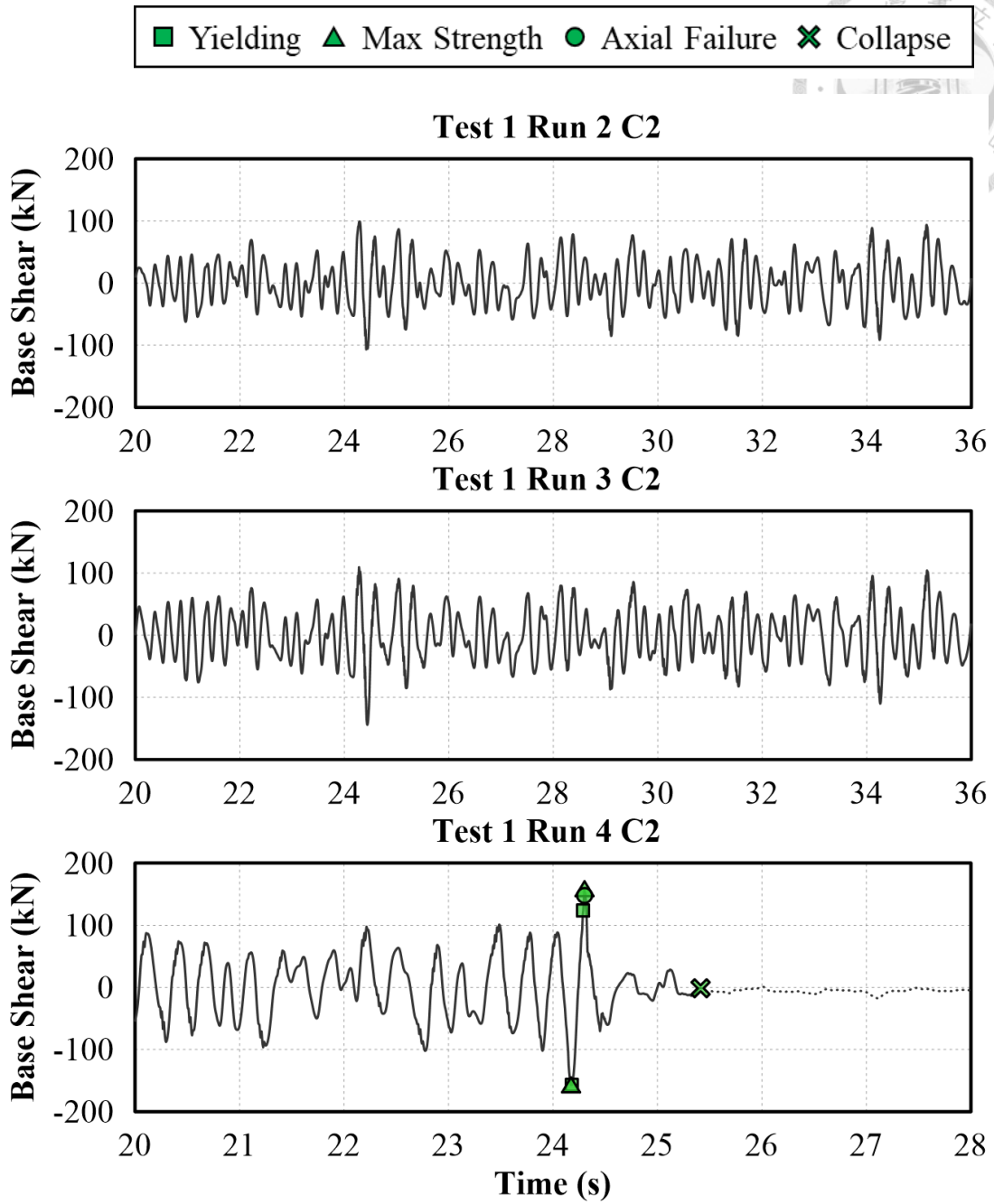
Figure 4-21. T1 C2 Base shear time history response
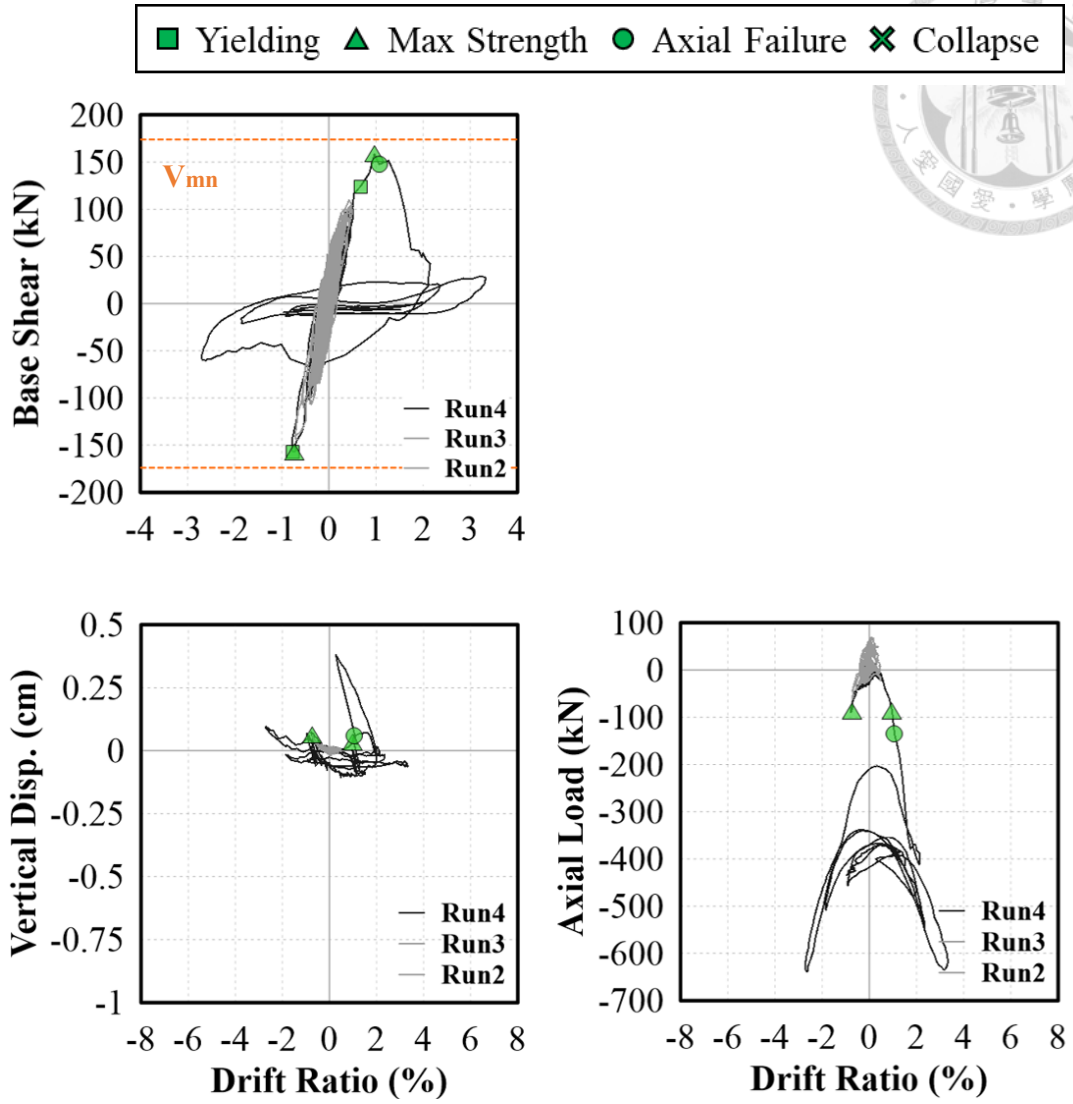
Figure 4-22. T1 C2 Hysteresis response
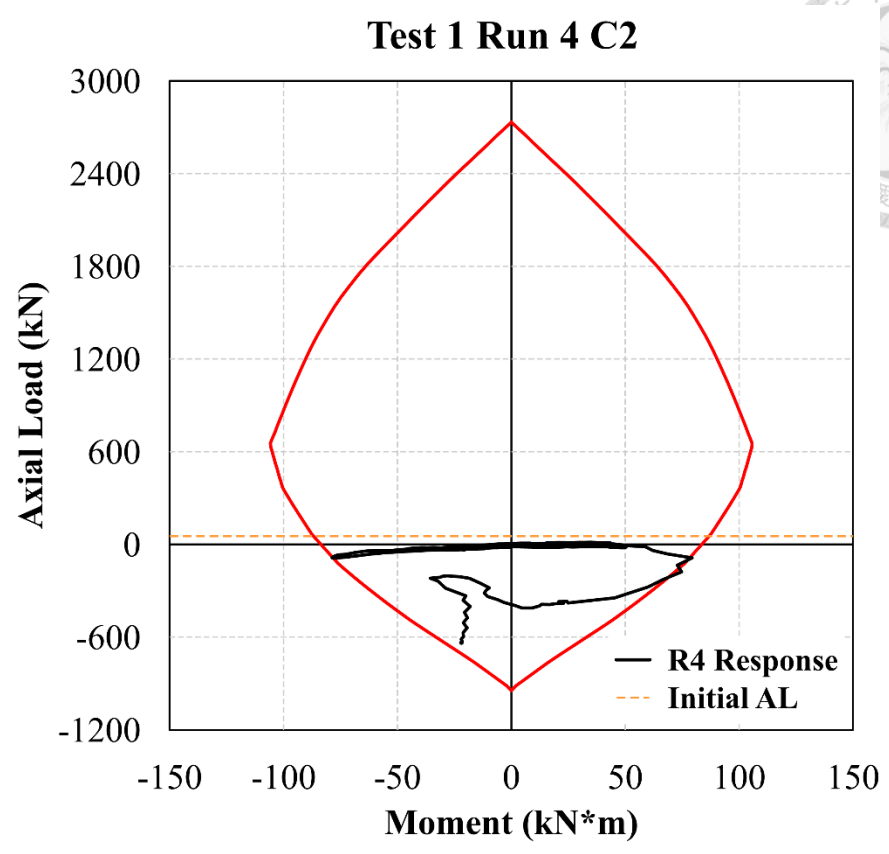
Figure 4-23. T1 C2 Moment-Axial Load Response
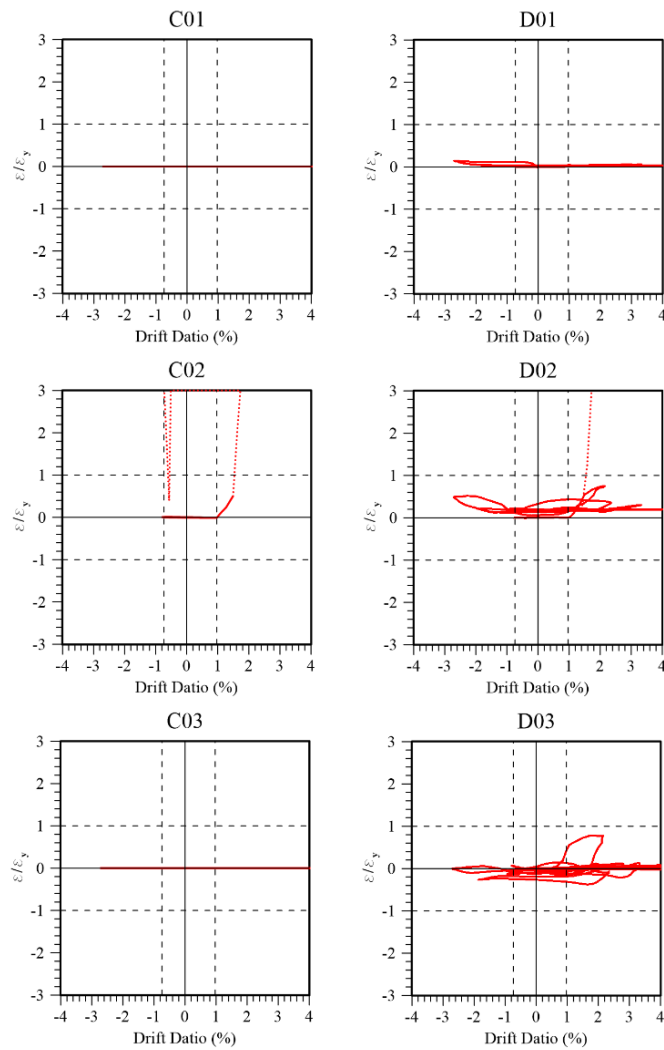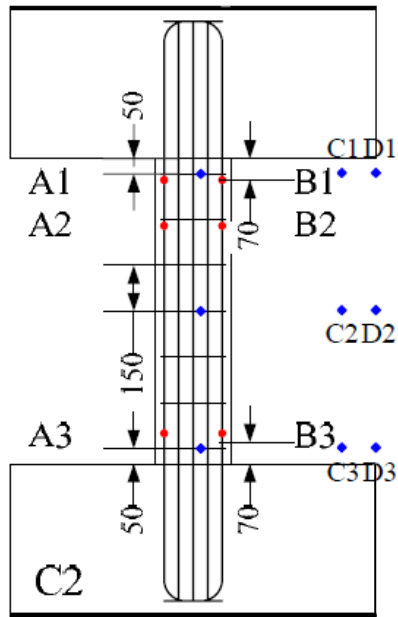
Figure 4-24. T1 C2 Stirrup strain gage readings

396
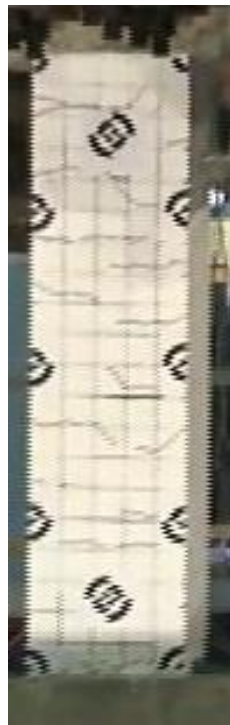
| Initial | Max. Strength (-) | Max. Strength (+) | Collapse (+) |

Figure 4-25. T1 C3 Crack pattern development
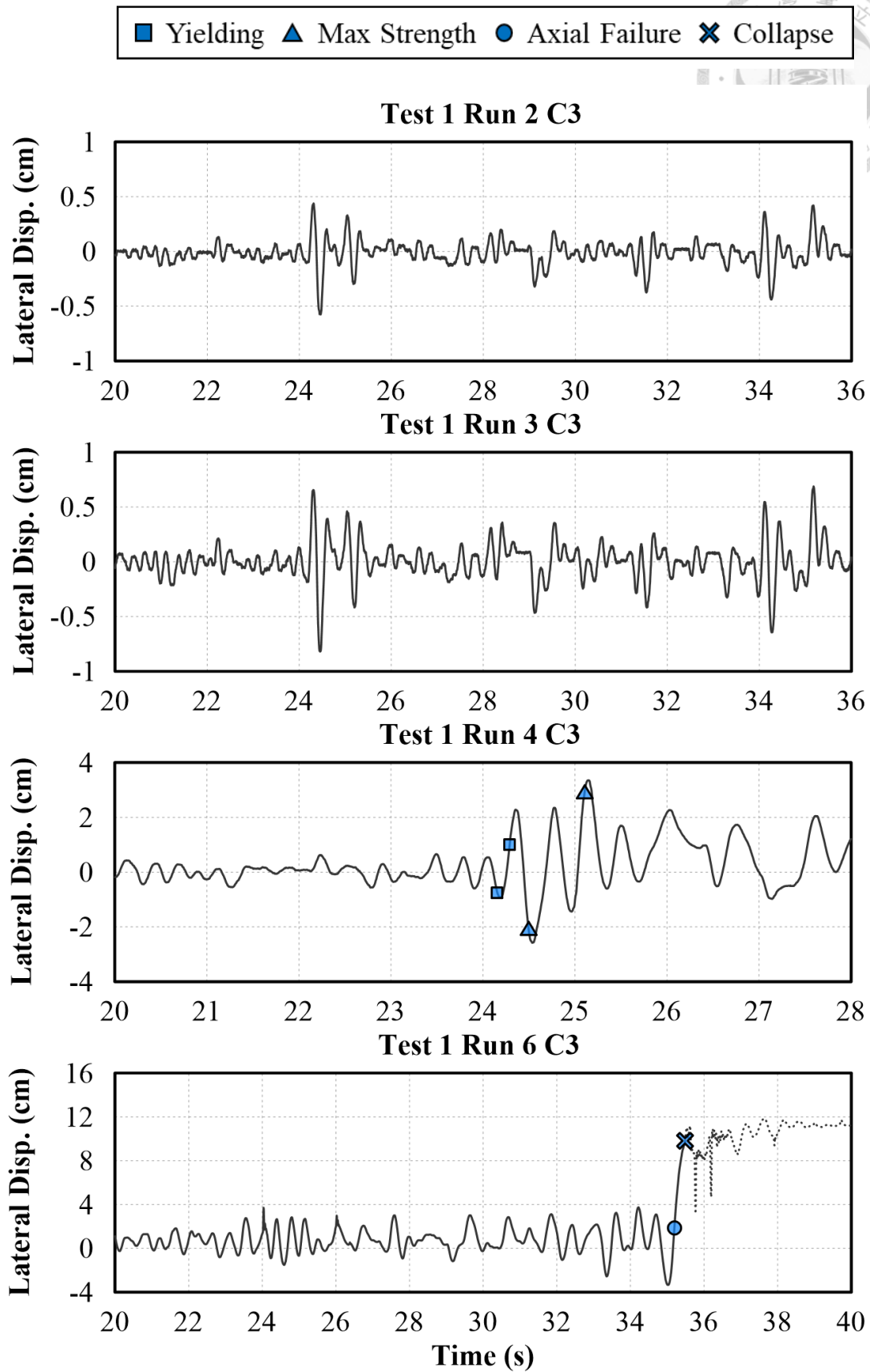
Figure 4-26. T1 C3 Lateral displacement time history response
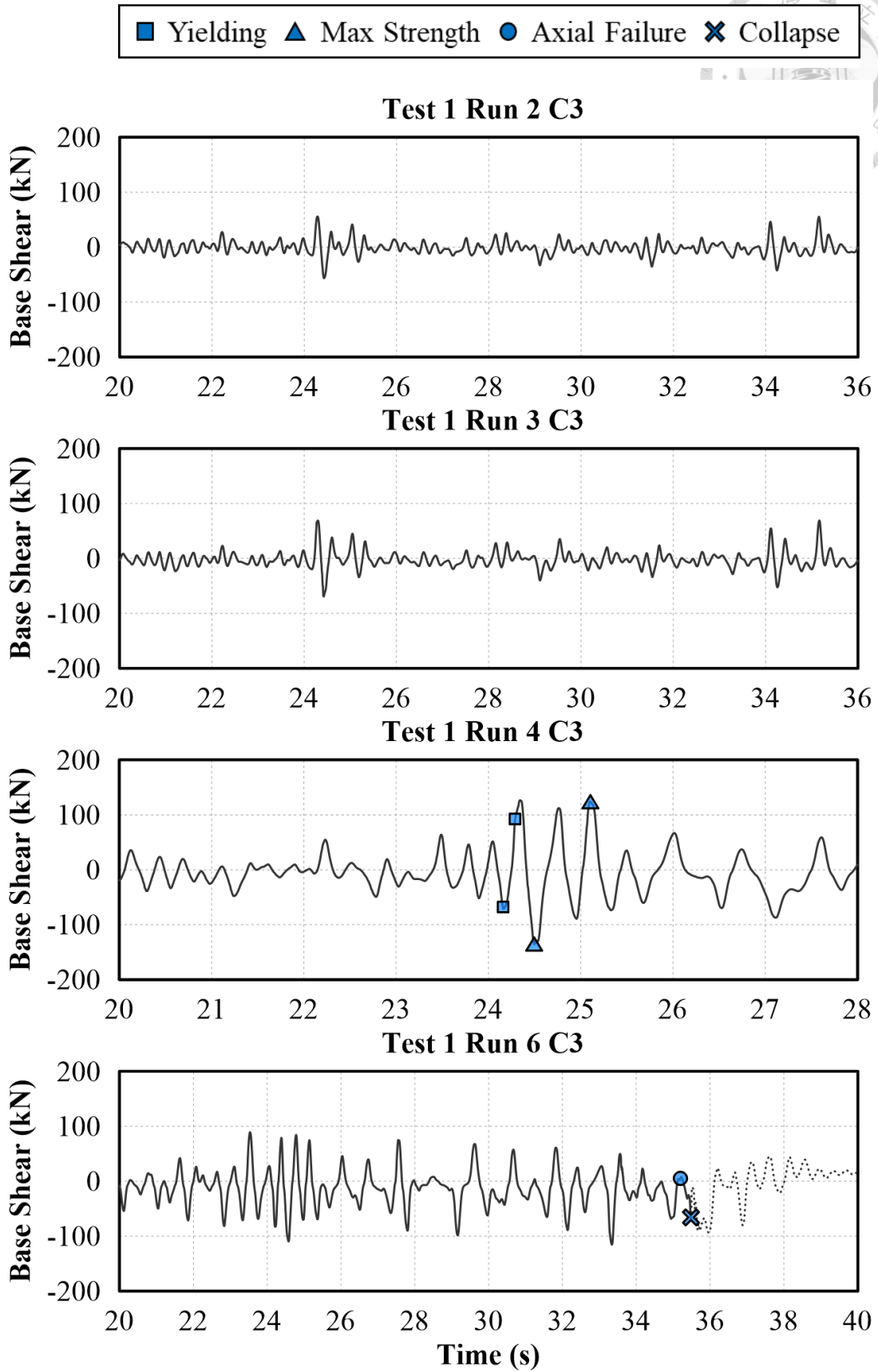
Figure 4-27. T1 C3 Base shear time history response
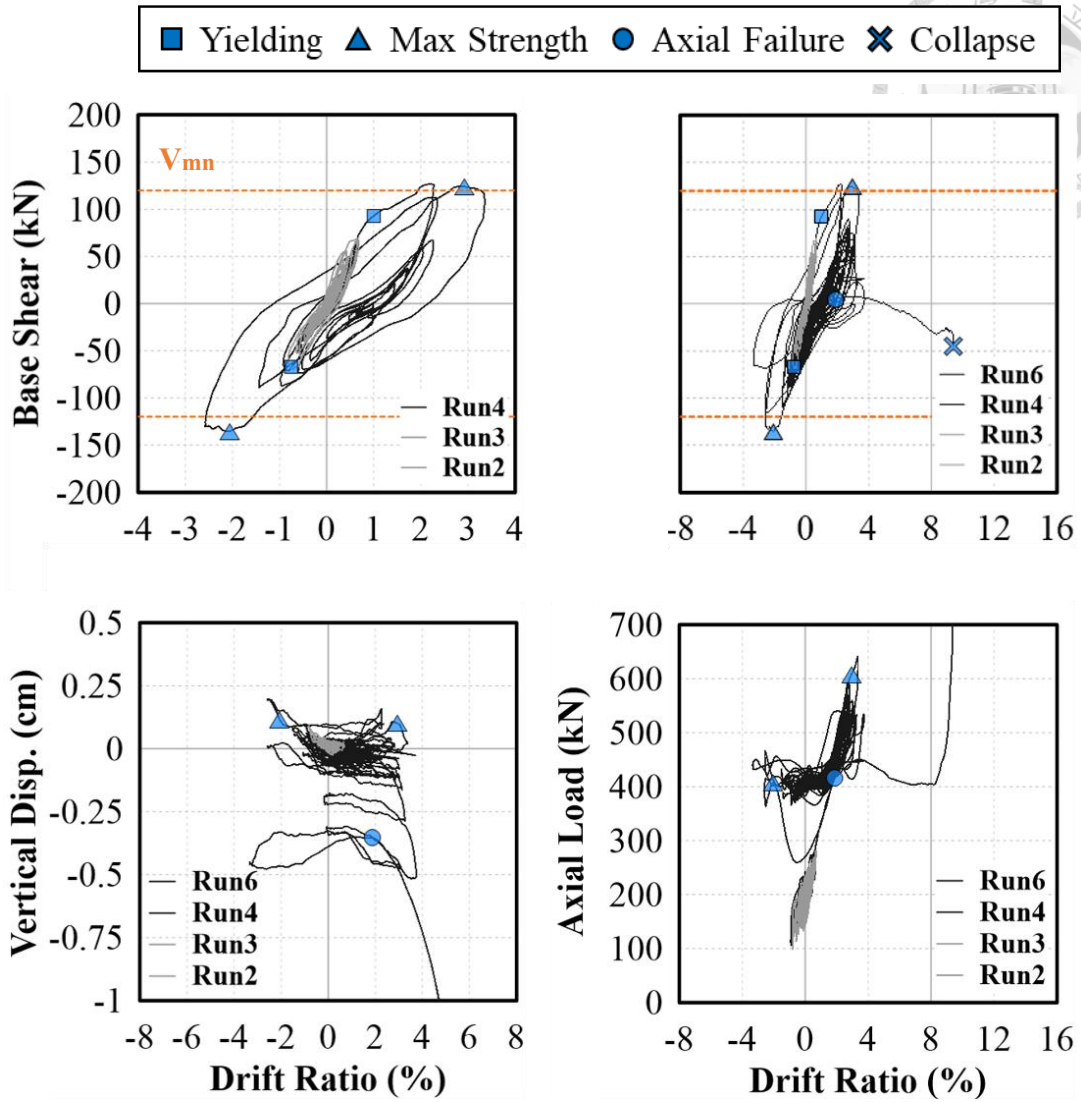
Figure 4-28. T1 C3 Hysteresis response
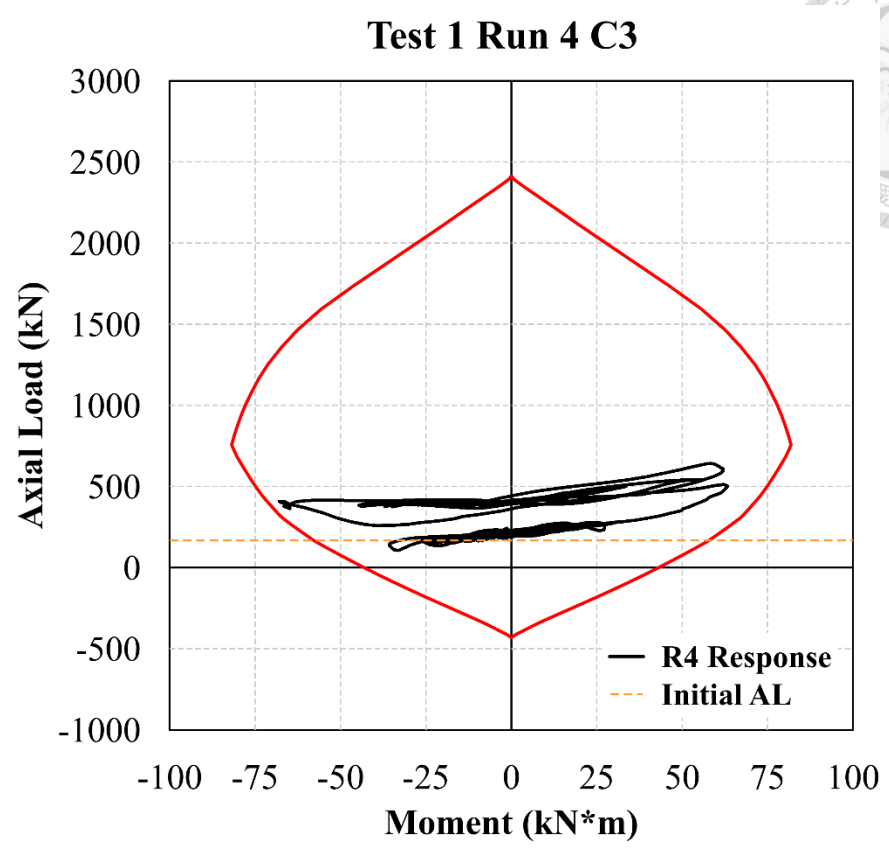
Figure 4-29. T1 C3 Moment-Axial Load Response
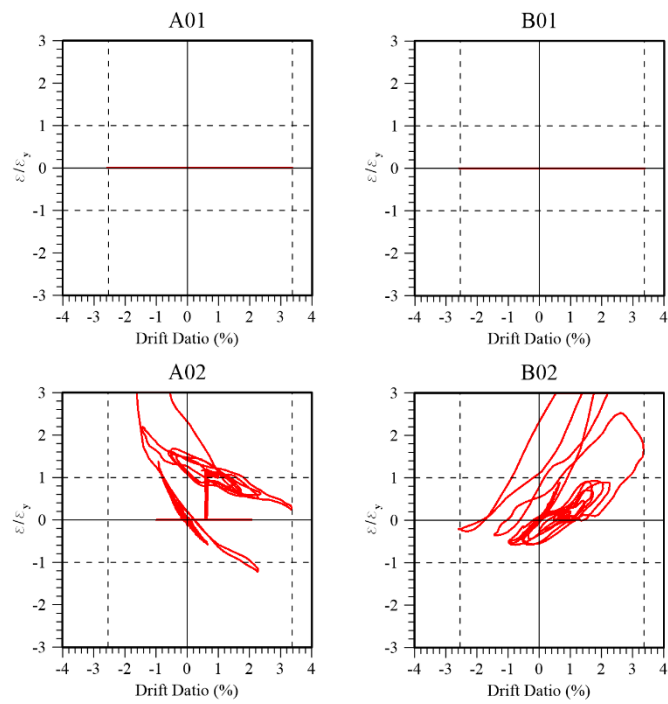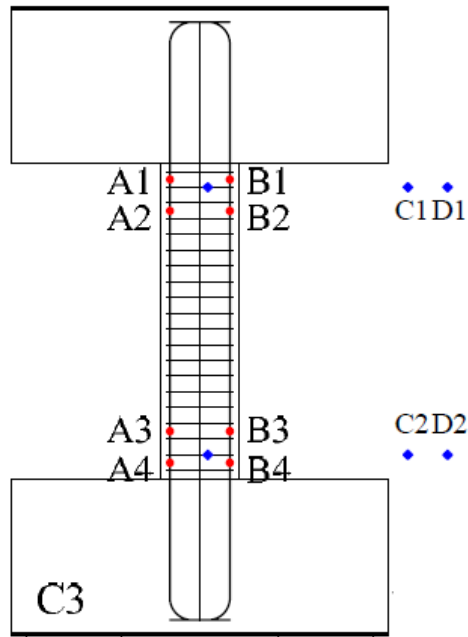
Figure 4-30. T1 C3 Top longitudinal reinforcement strain gage readings
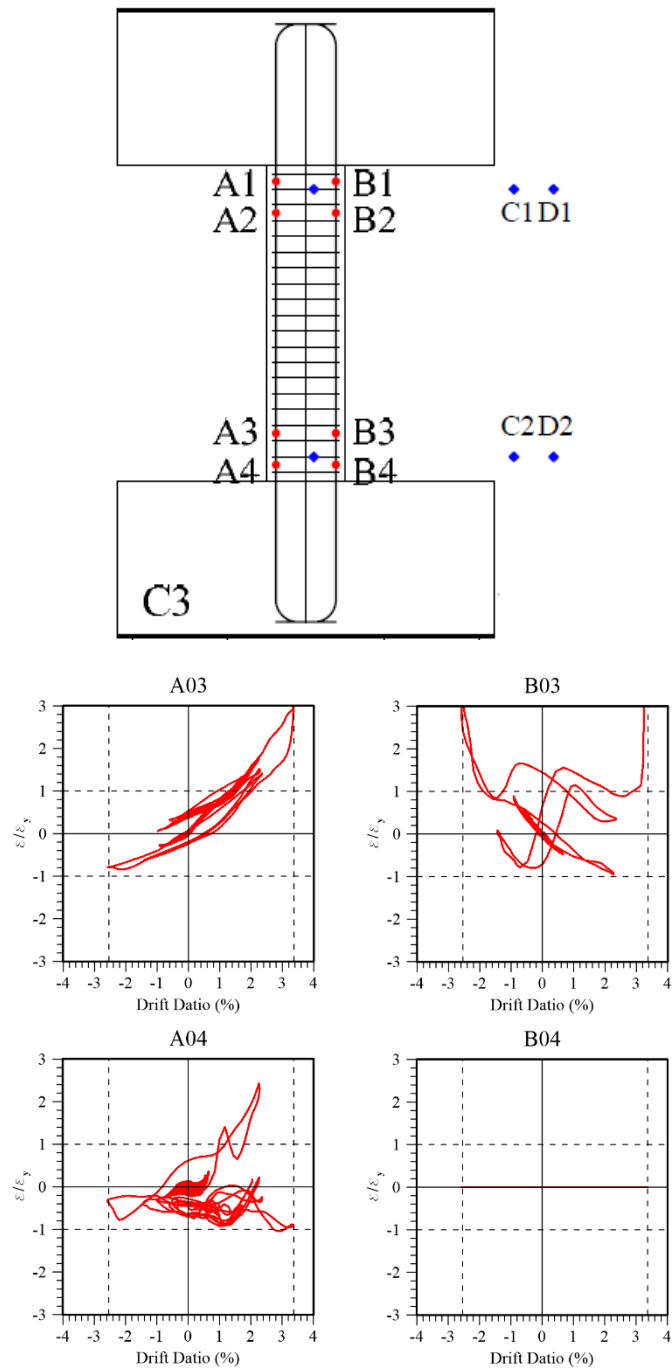
Figure 4-31. T1 C3 Bottom longitudinal reinforcement strain gage readings

403
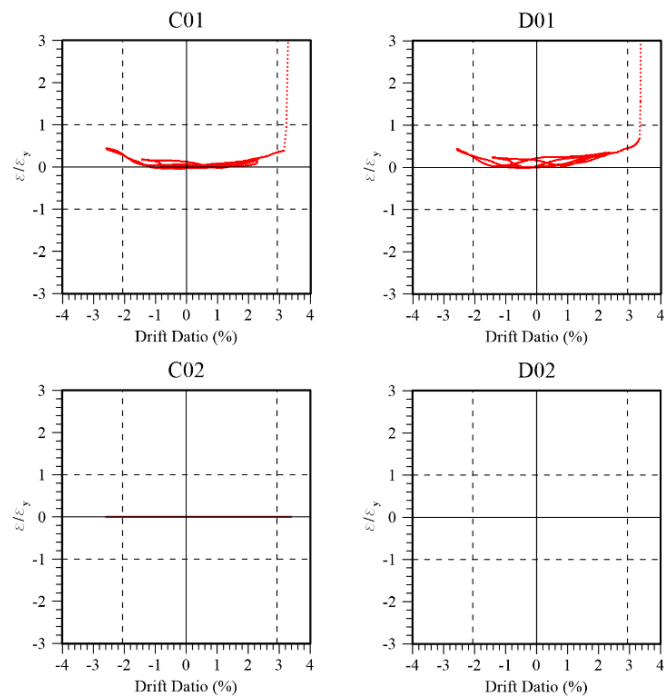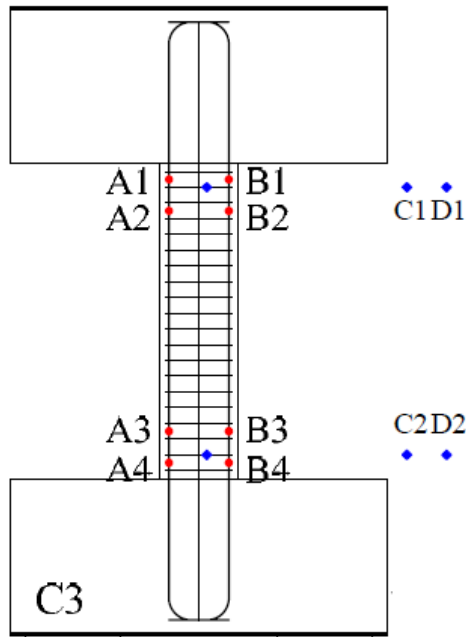
Figure 4-32. T1 C3 Stirrup strain gage readings

Figure 4-33. T1 Frame crack pattern after each run

405
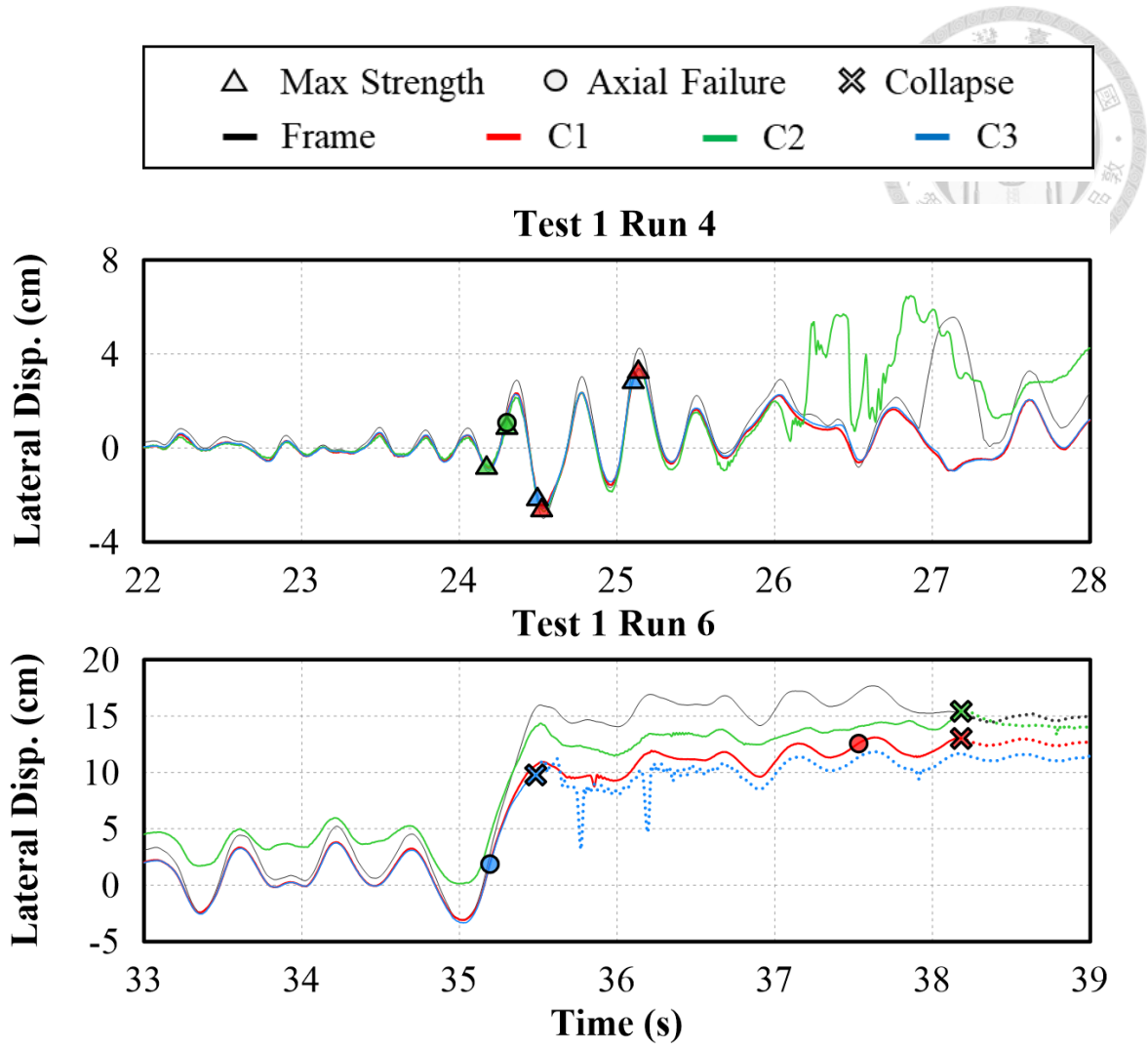
Figure 4-34. T1 Overall lateral displacement comparison
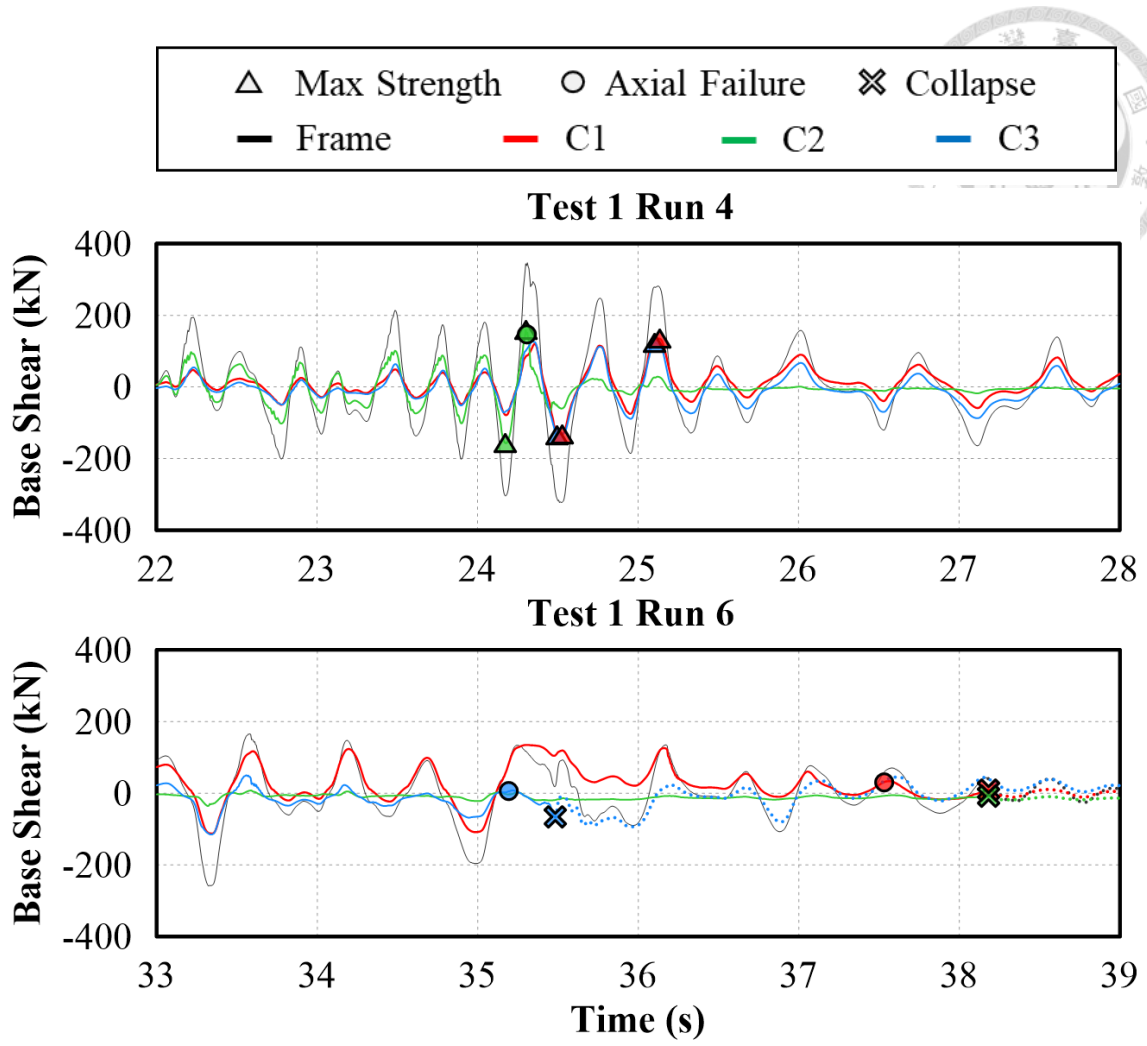
Figure 4-35. T1 Overall base shear comparison

407
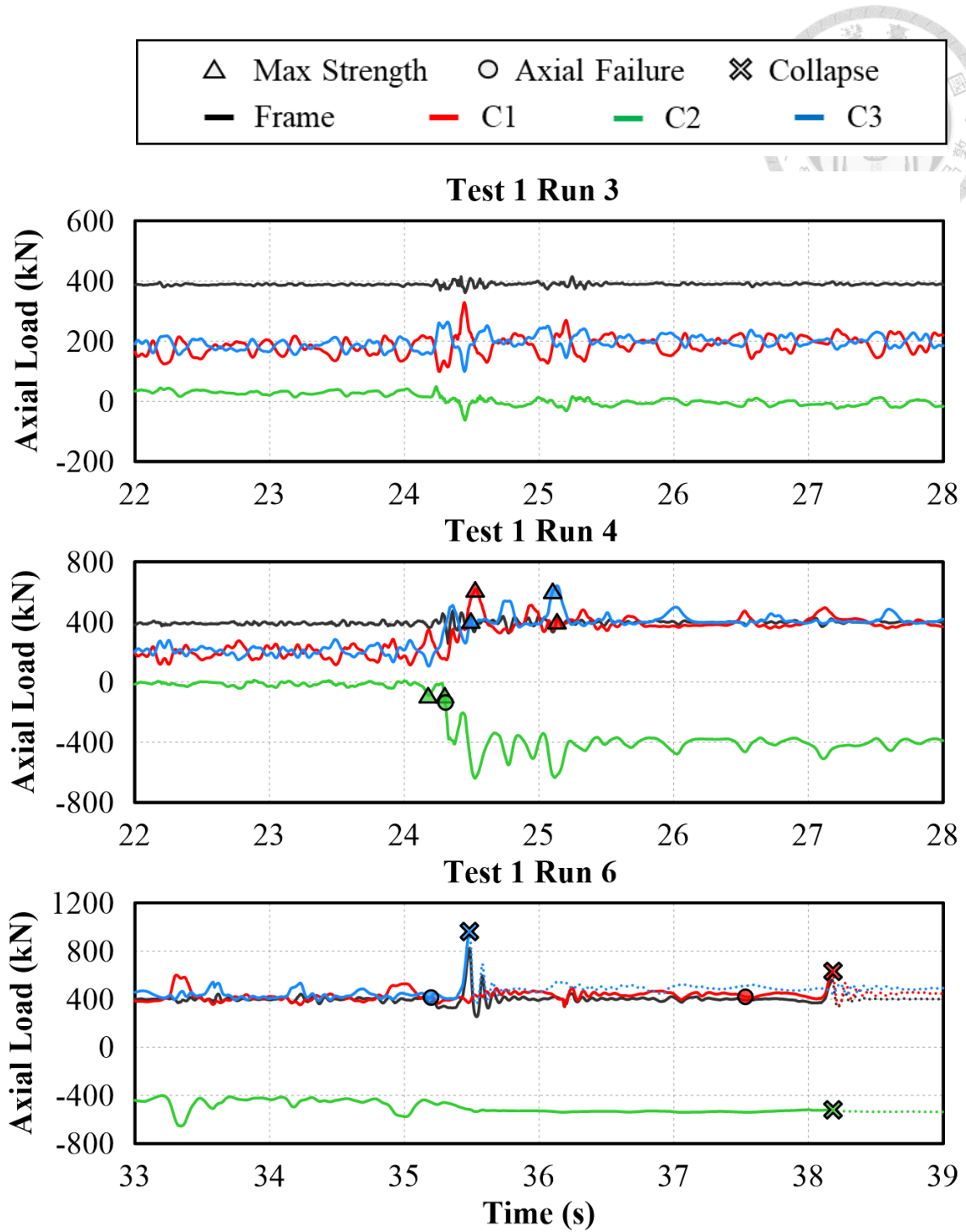
Figure 4-36. T1 Overall axial load comparison

408
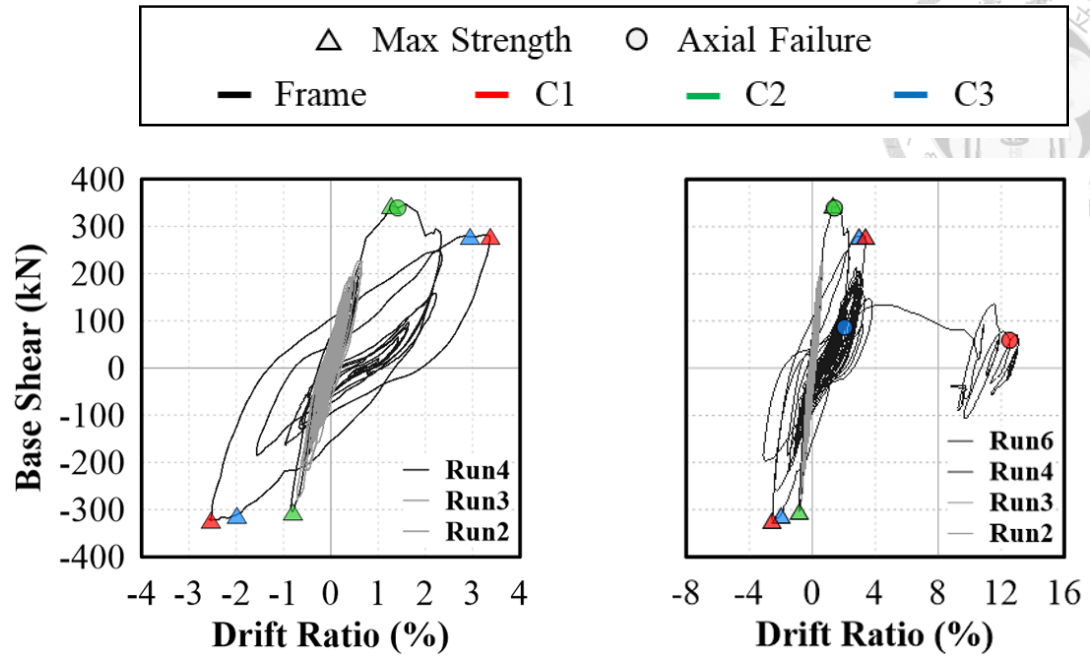
Figure 4-37. T1 Frame hysteresis response
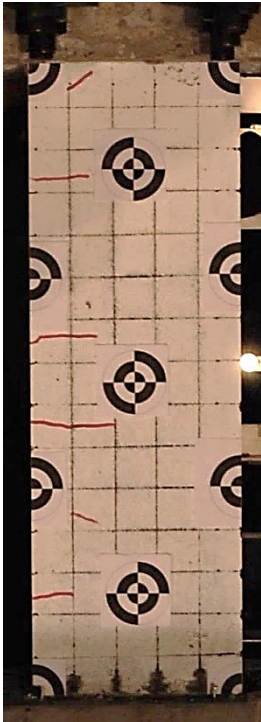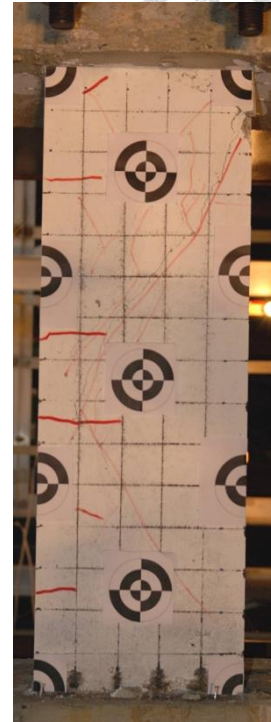
End of Run2　　　　**Shear Failure (+)**　　　　**End of Run4**

Figure 4-38. T2 C1 Crack pattern development
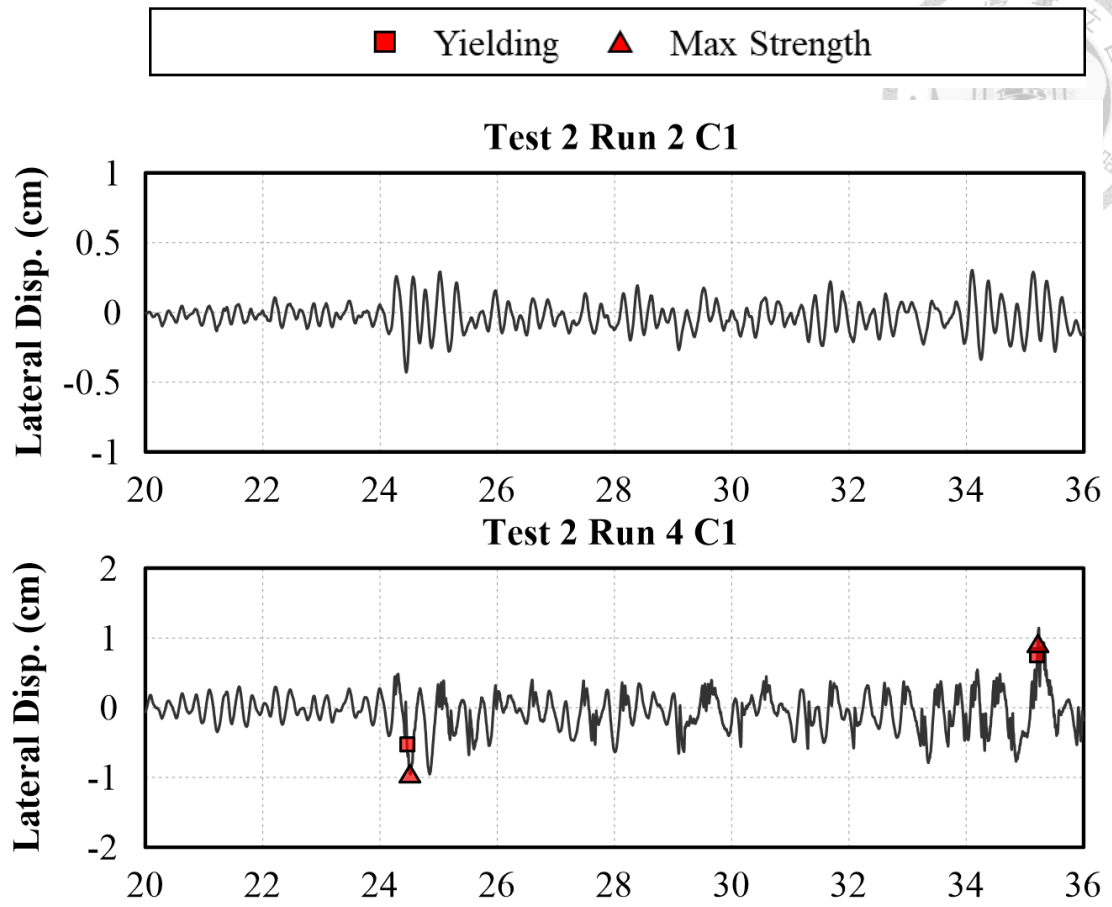
Figure 4-39. T2 C1 Lateral displacement time history response
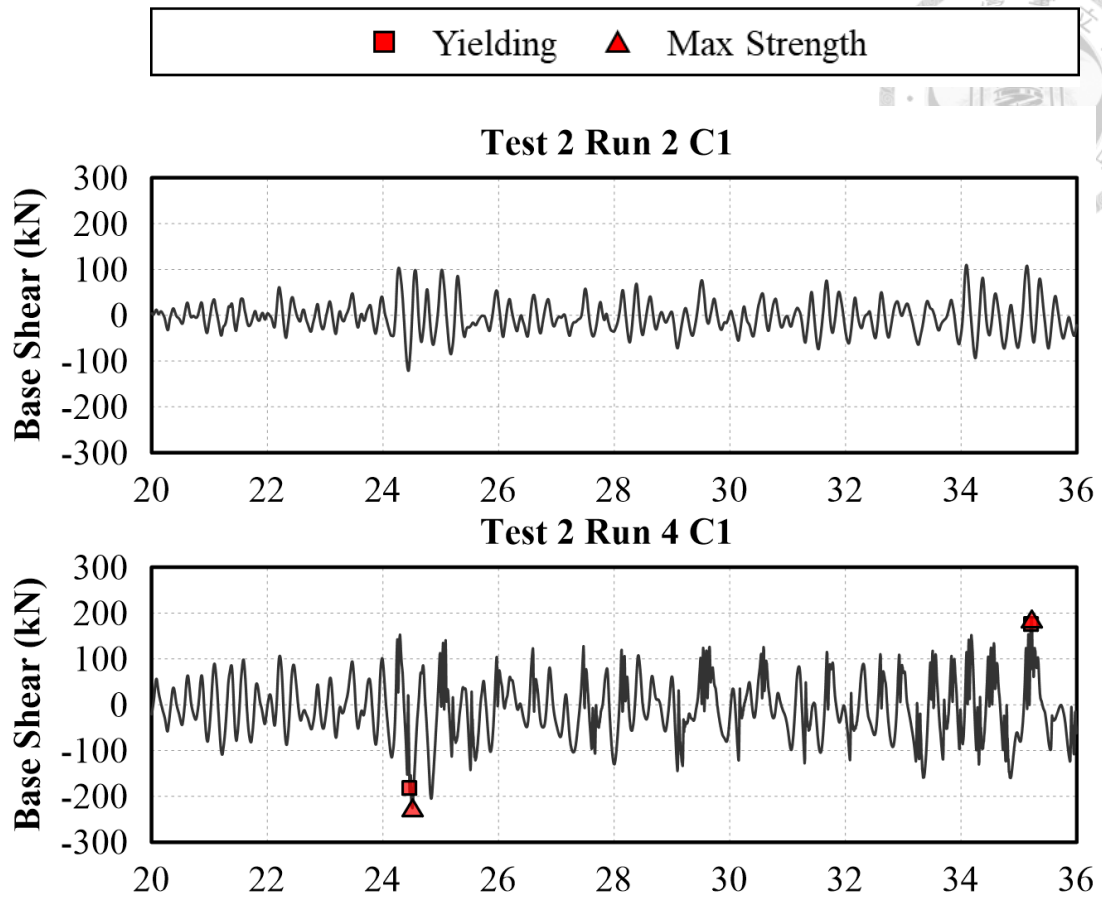
Figure 4-40. T2 C1 Base shear time history response
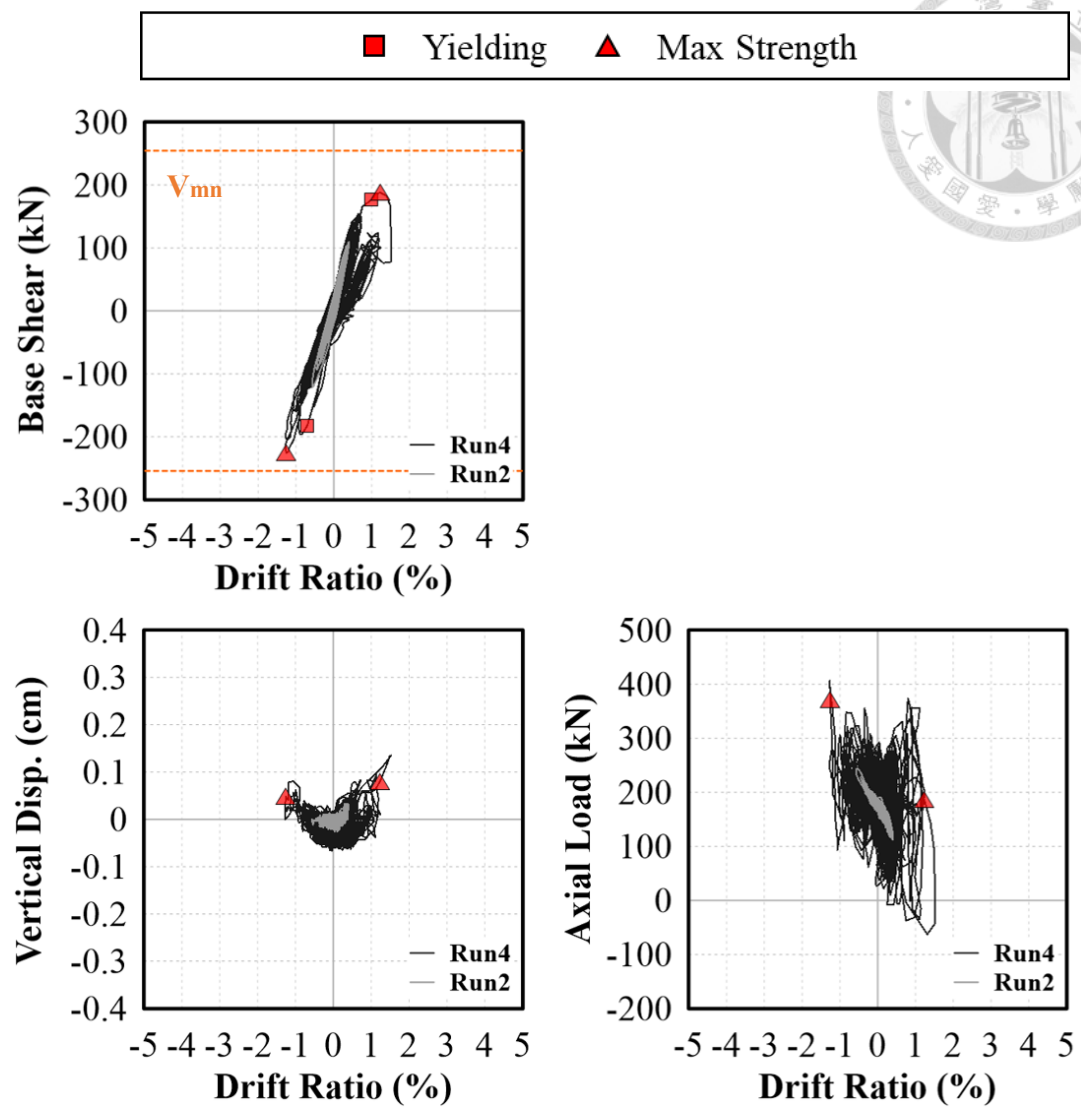
Figure 4-41. T2 C1 Hysteresis response
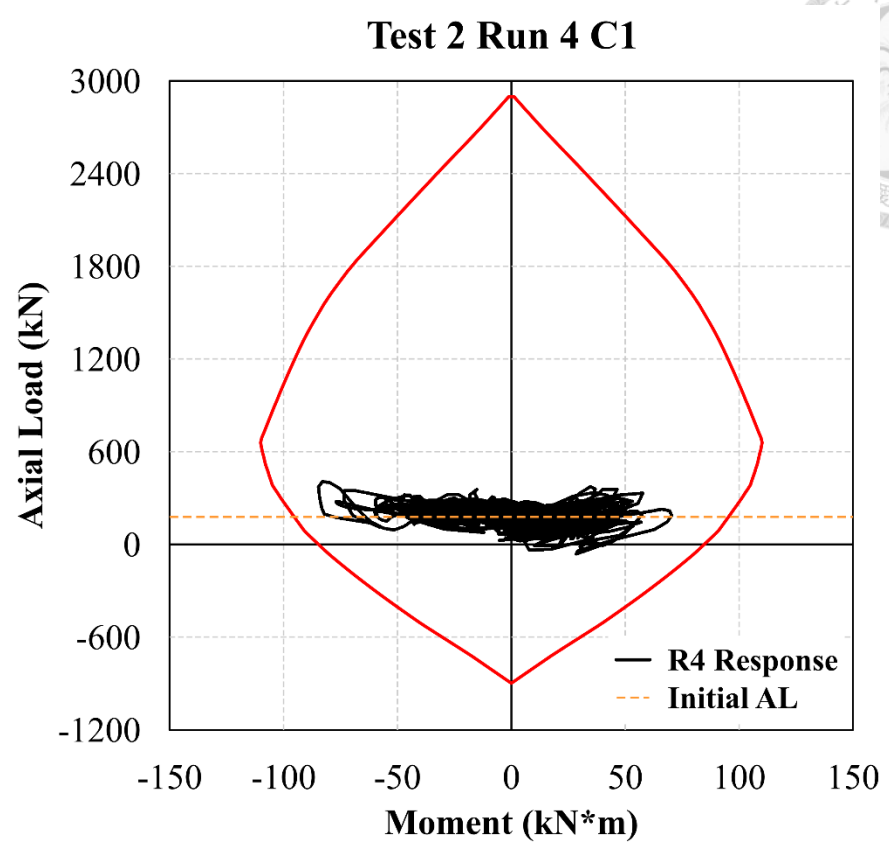
Figure 4-42. T2 C1 Moment-Axial Load Response
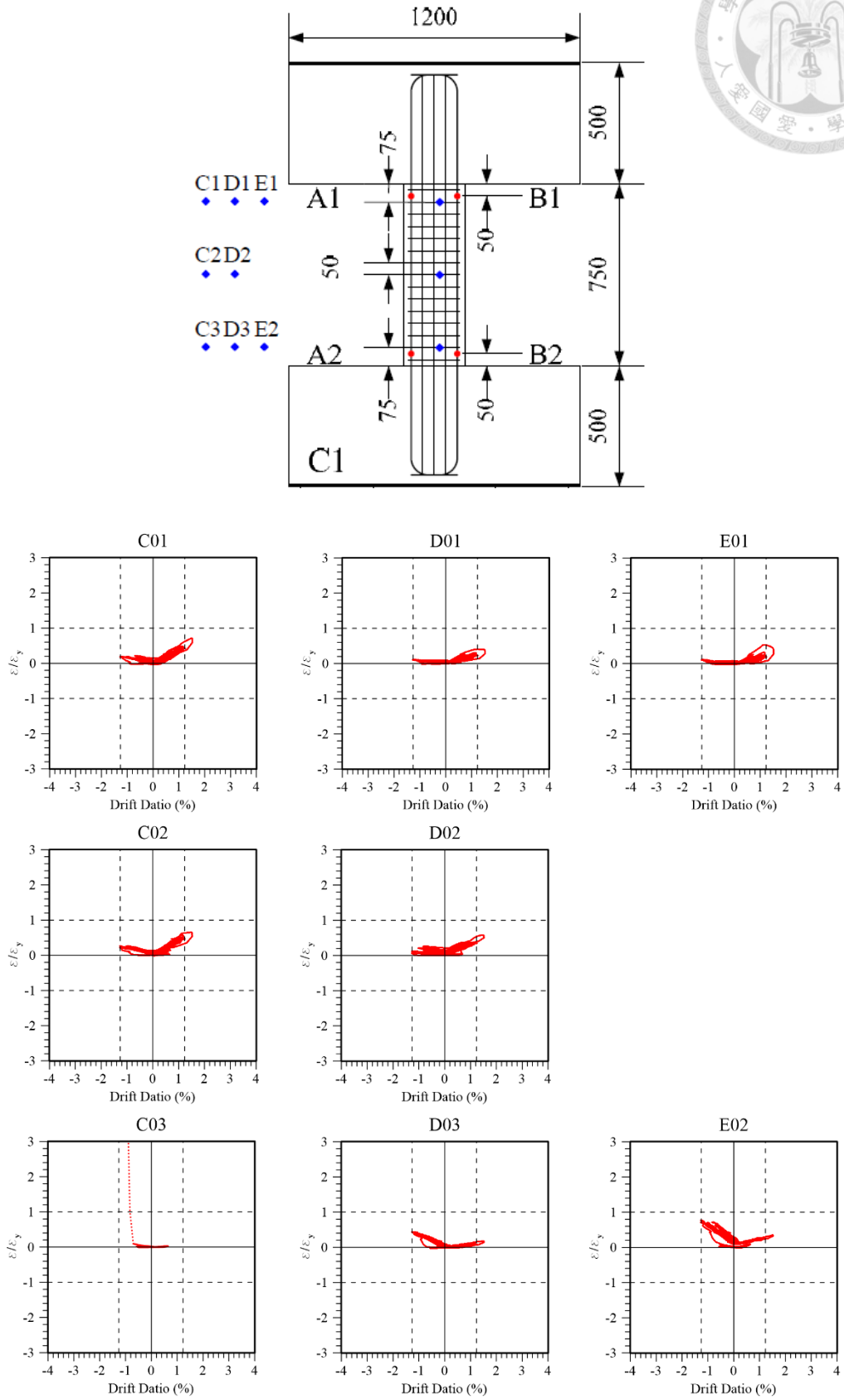
Figure 4-43. T2 C1 Stirrup strain gage readings

415
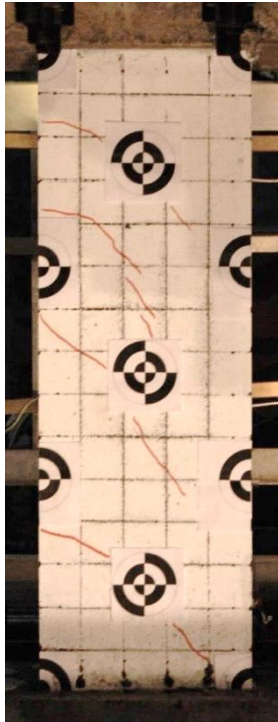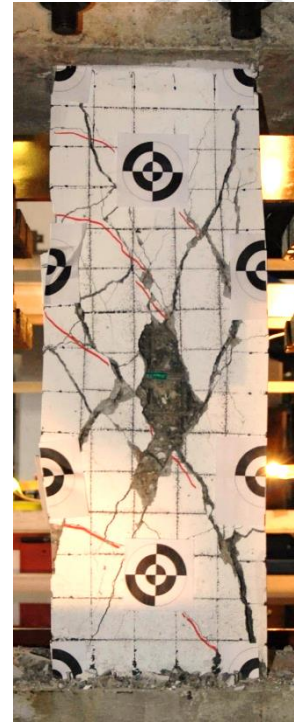
| End of Run2 | Shear Failure (+) | End of Run4 |

Figure 4-44. T2 C3 Crack pattern development
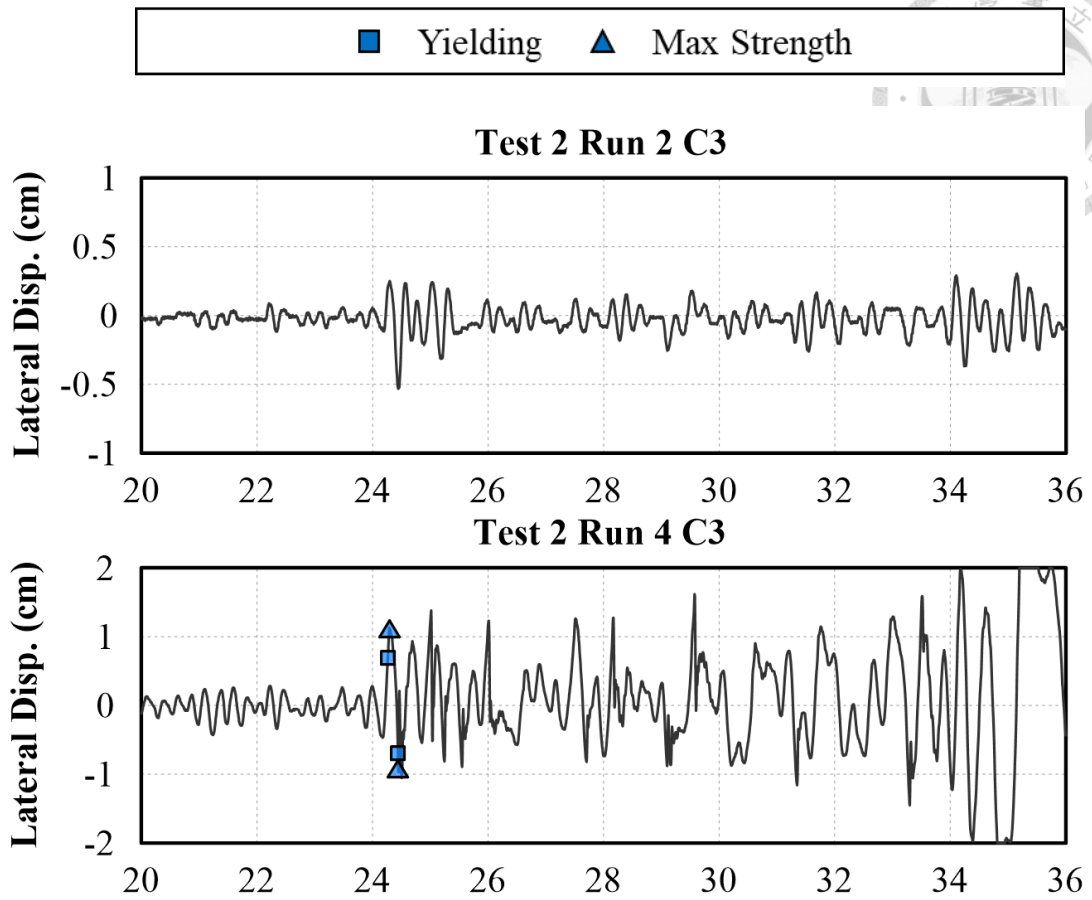
Figure 4-45. T2 C3 Lateral displacement time history response
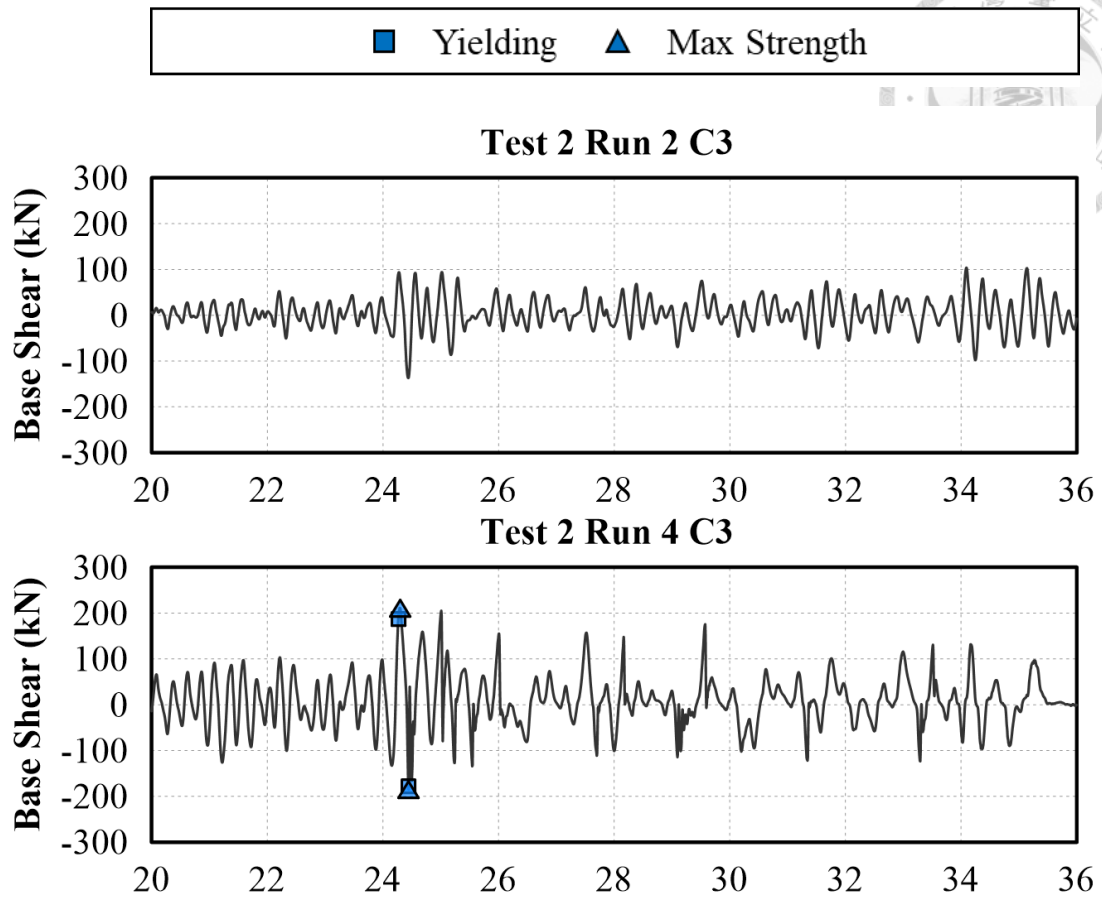
Figure 4-46. T2 C3 Base shear time history response
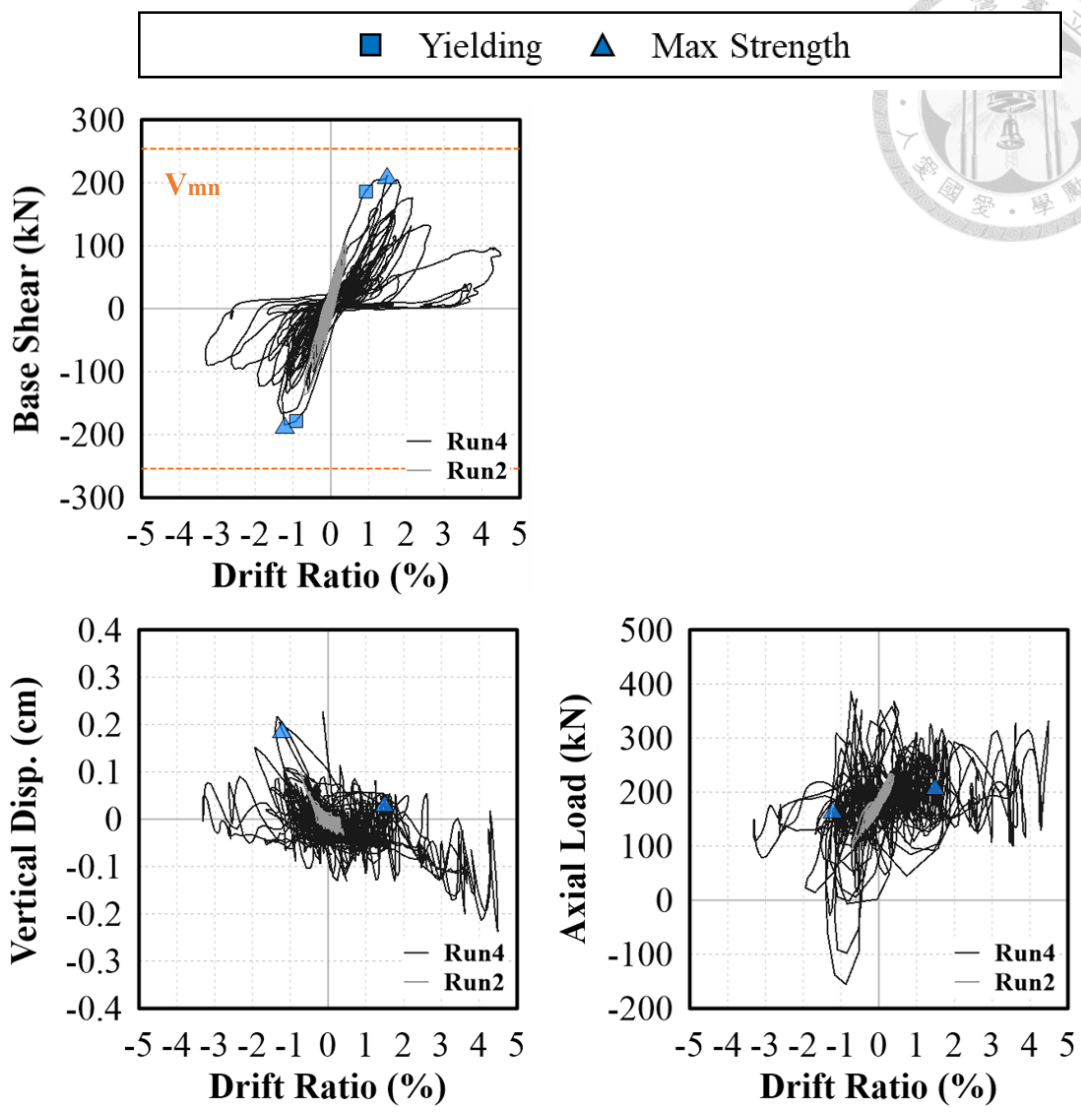
Figure 4-47. T2 C3 Hysteresis response
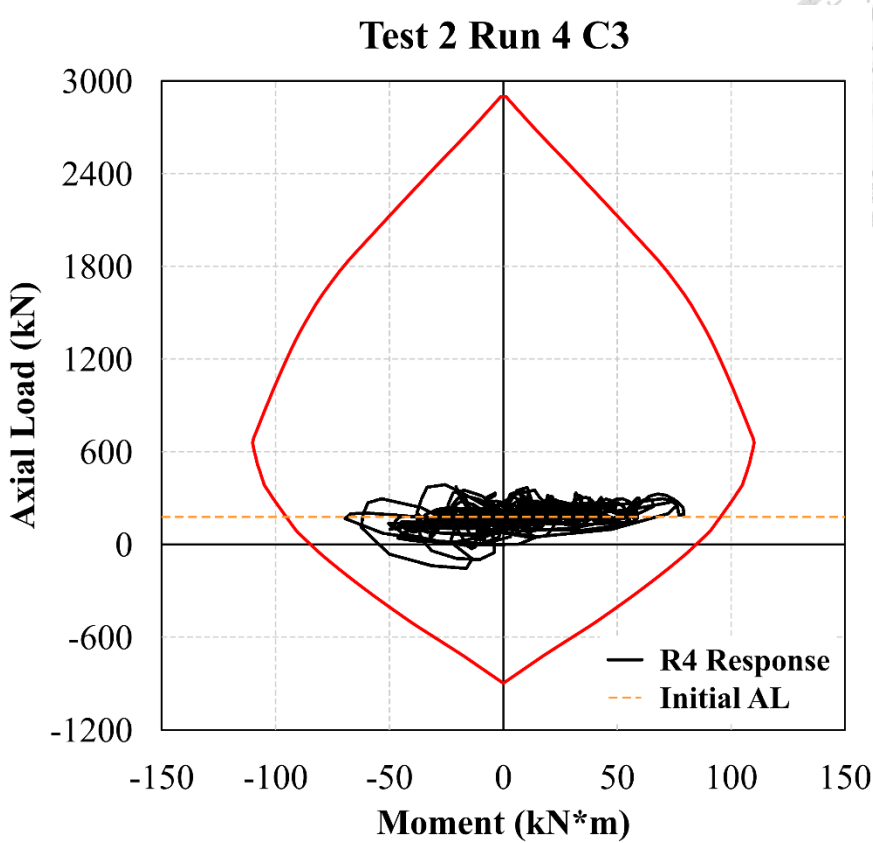
Figure 4-48. T2 C3 Moment-Axial Load Response
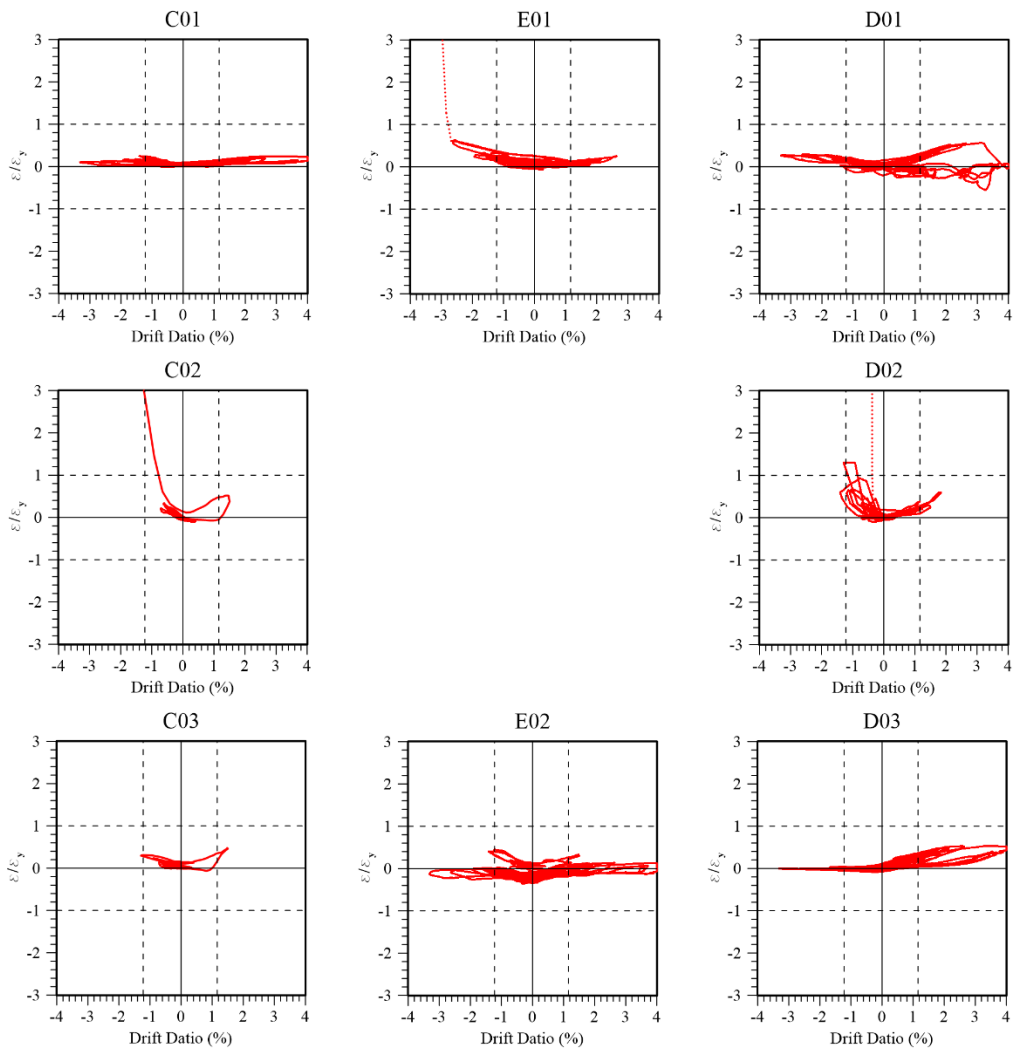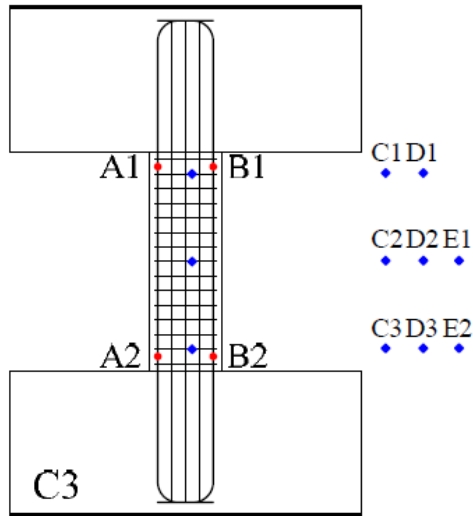
Figure 4-49. T2 C3 Stirrup strain gage readings

421
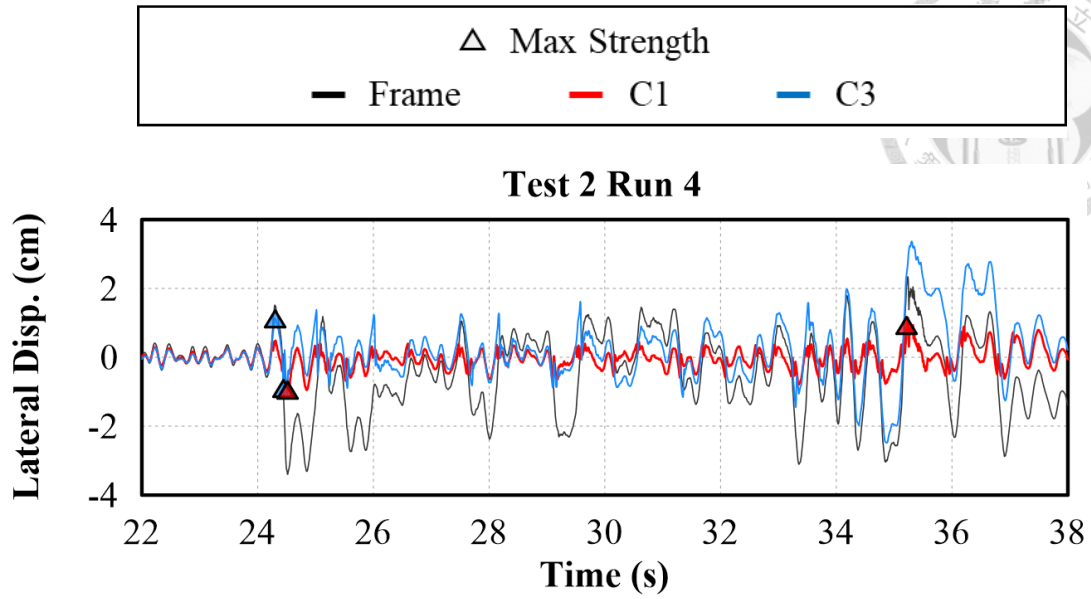
Figure 4-50. T2 Overall lateral displacement comparison
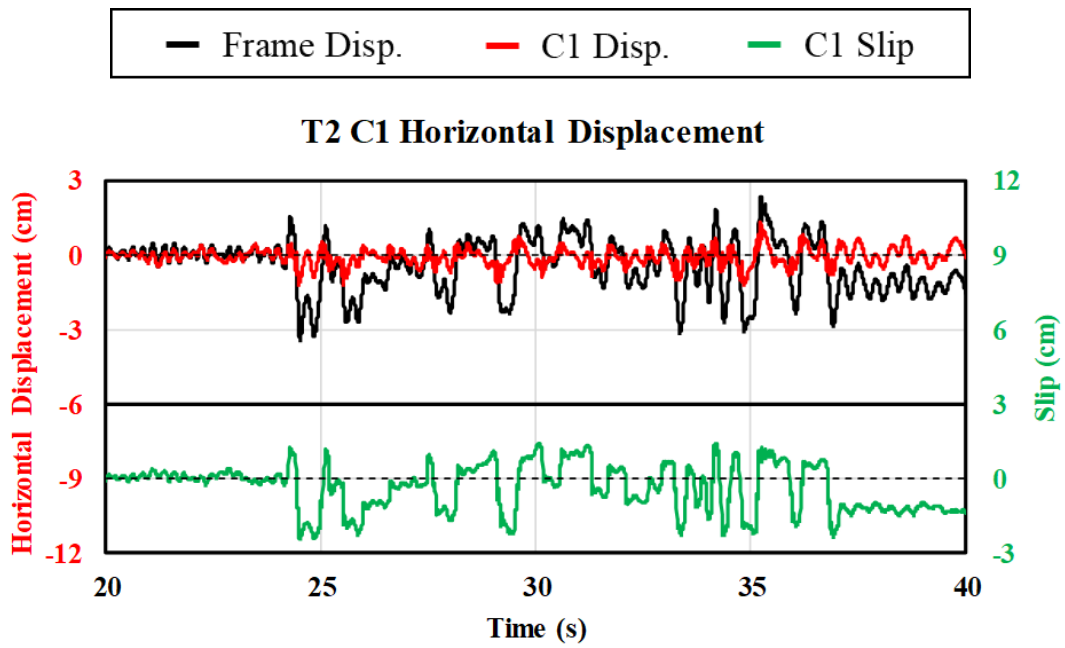
Figure 4-51. T2 C1 Top steel beam slip

422
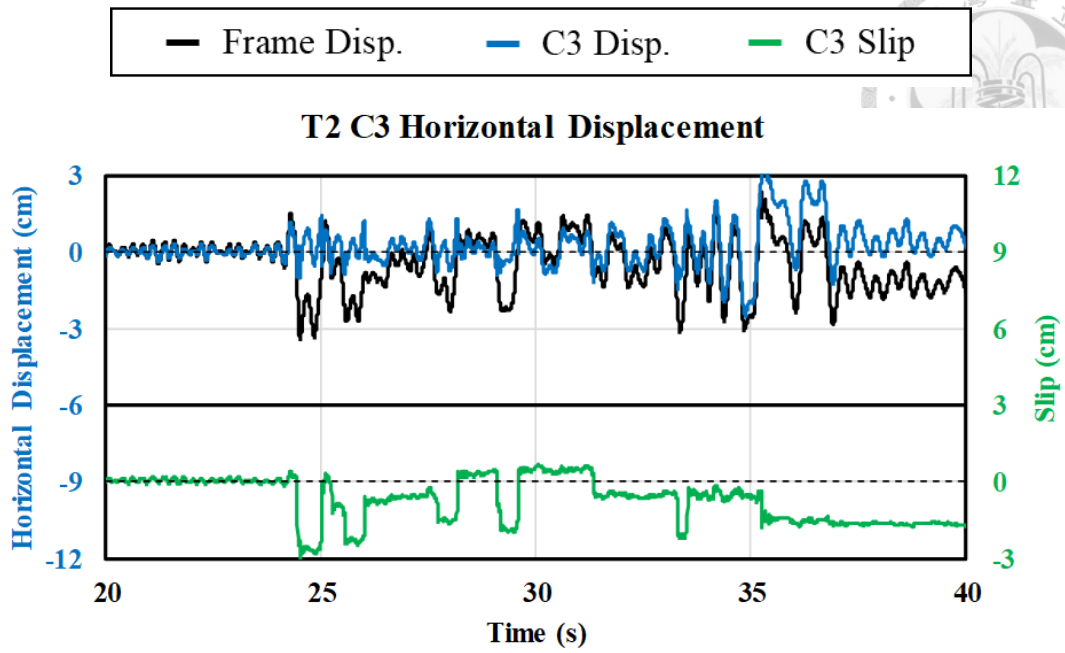
Figure 4-52. T2 C3 Top steel beam slip
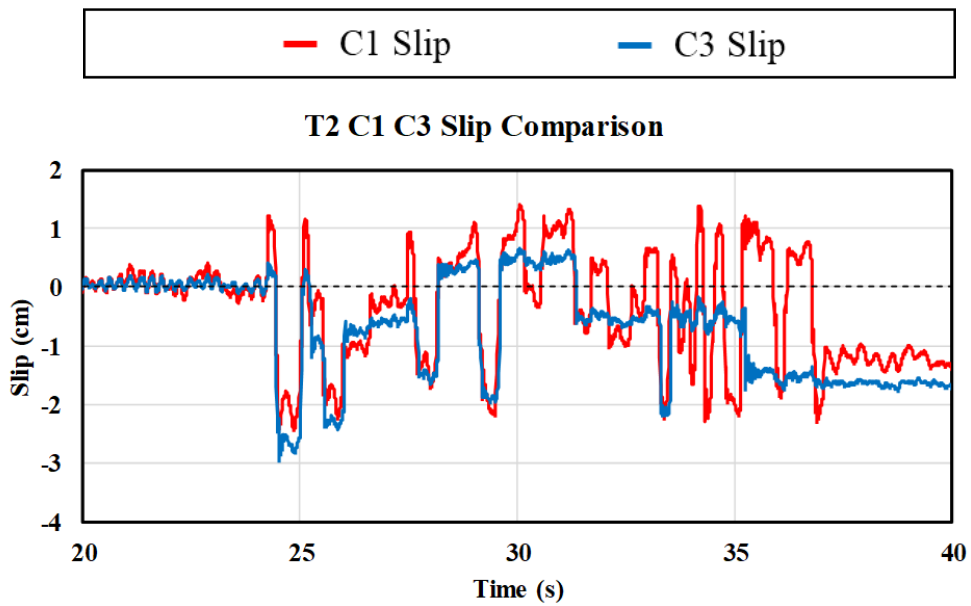
Figure 4-53. T2 C1 C3 Slip comparison
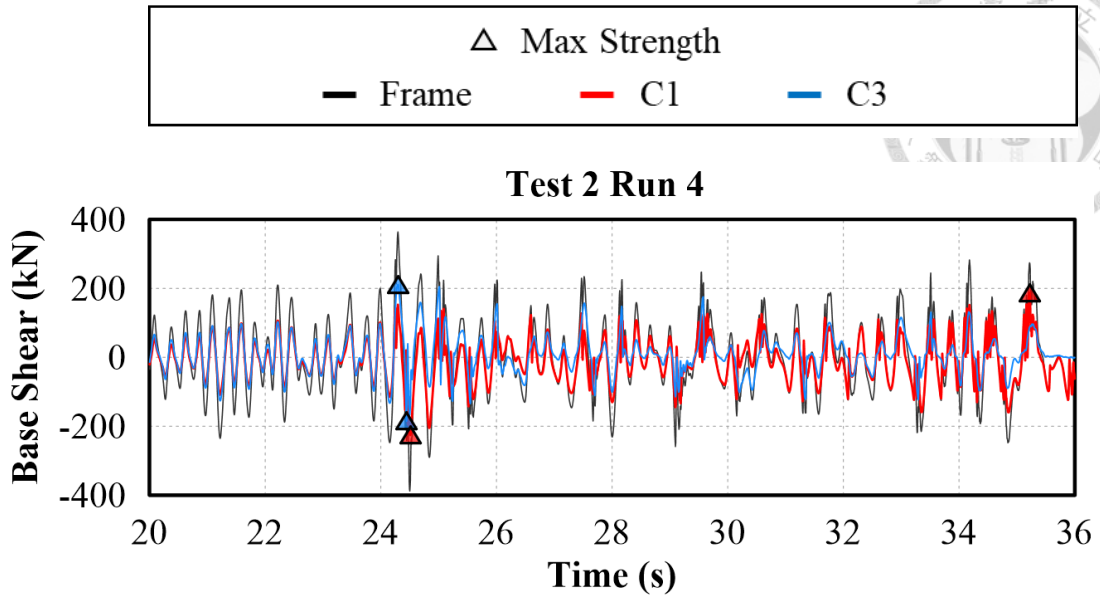
Figure 4-54. T2 Overall base shear comparison
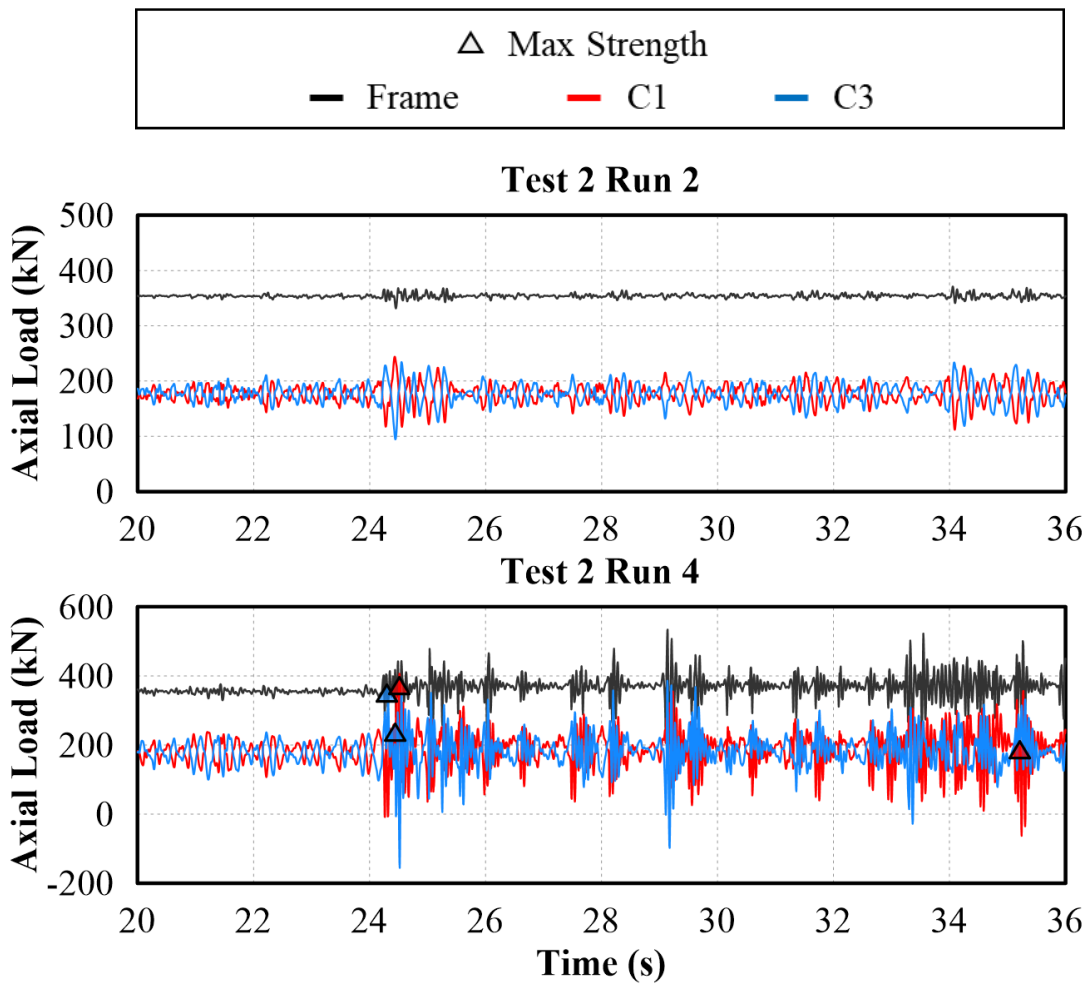
Figure 4-55. T2 Overall axial load comparison

424

Initial   **End of Run2**   **Shear Failure (+)**   **Collapse (-)**
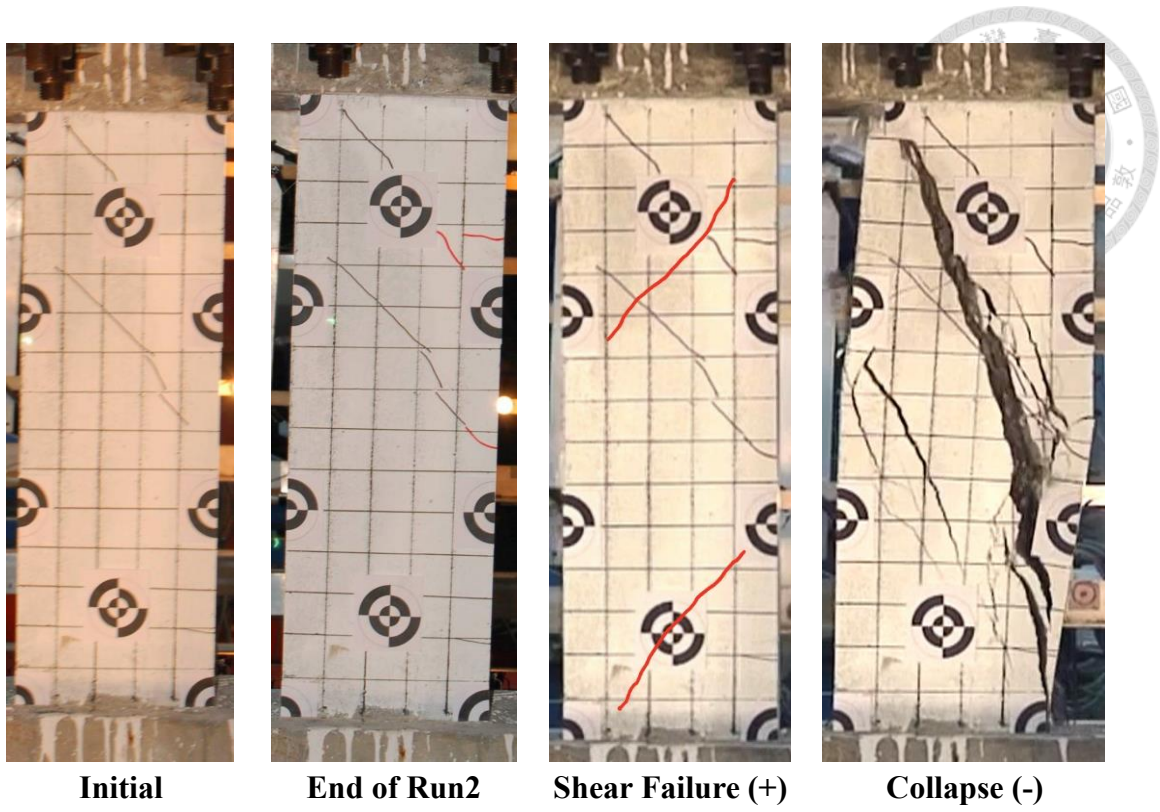
Figure 4-56. T3 C1 Crack pattern development
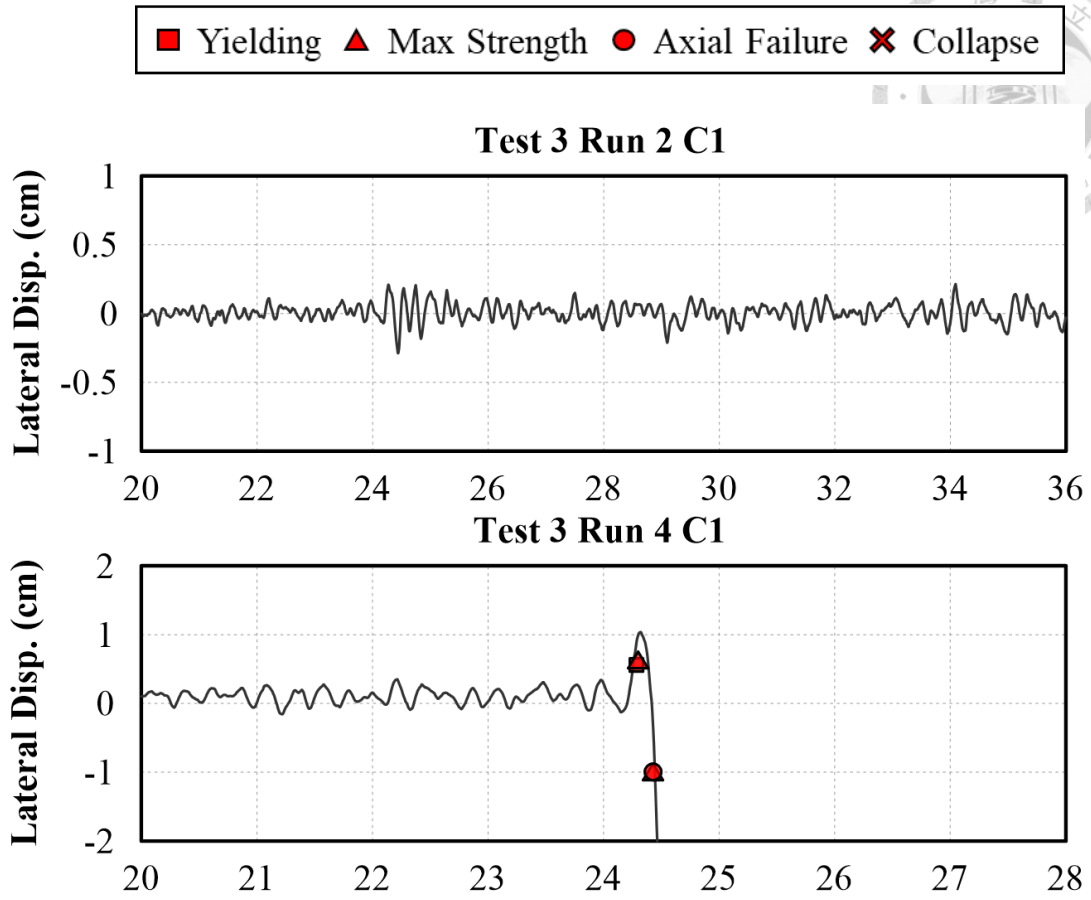
Figure 4-57. T3 C1 Lateral displacement time history response
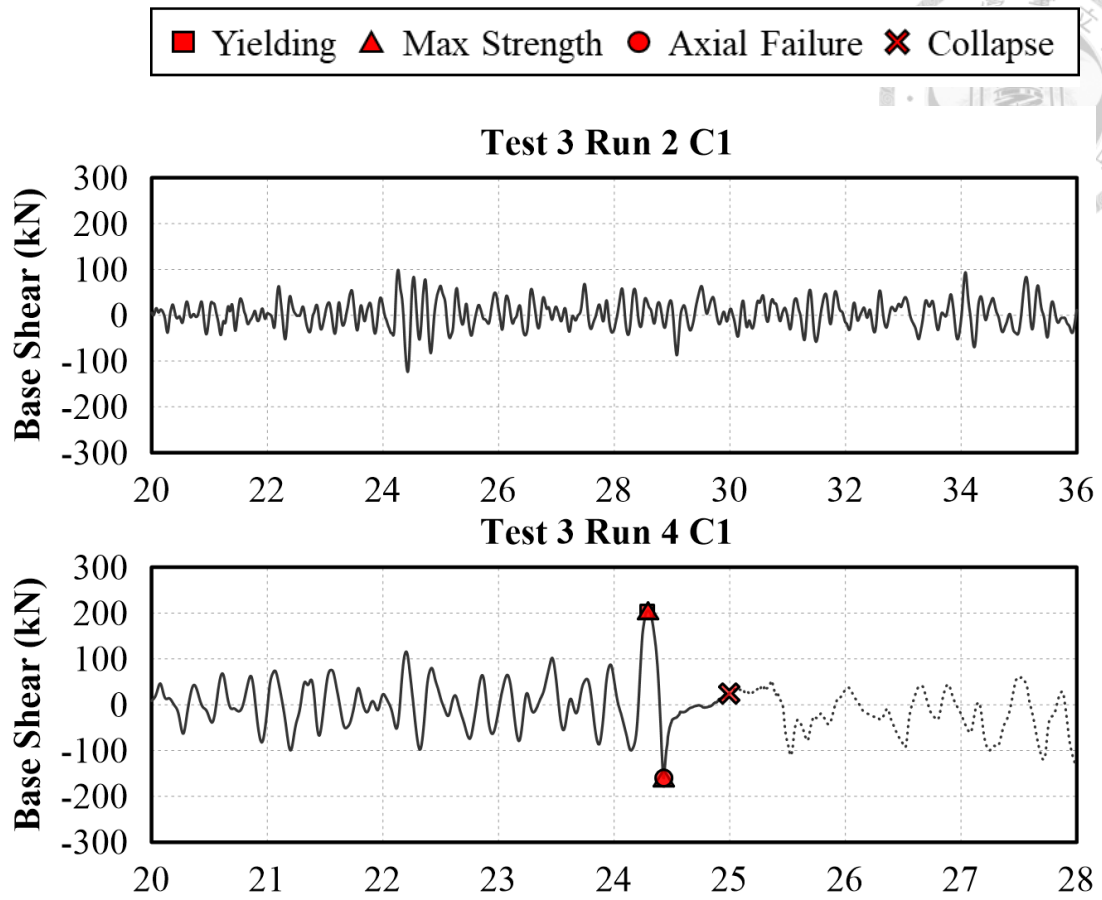
Figure 4-58. T3 C1 Base shear time history response

427
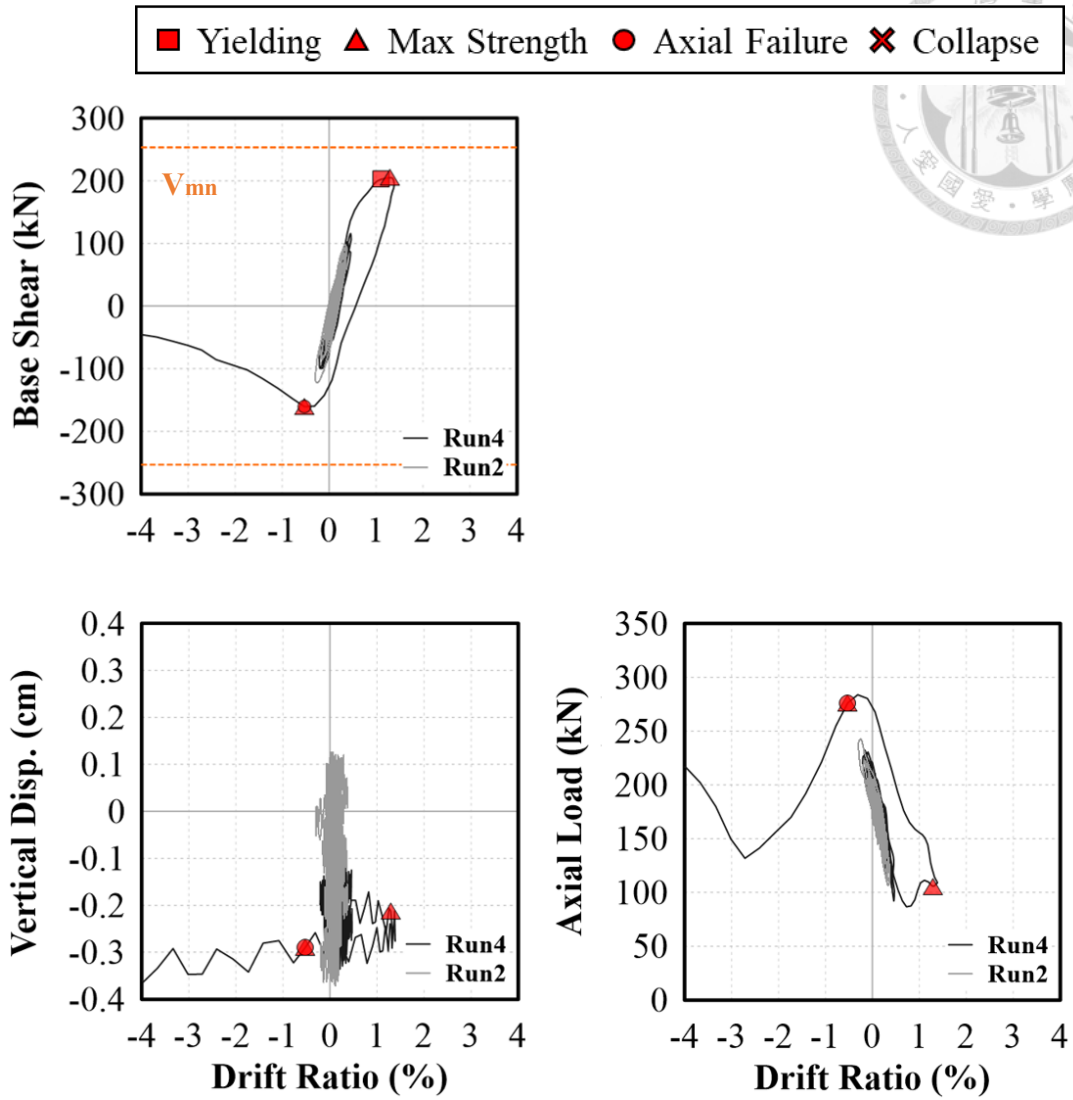
Figure 4-59. T3 C1 Hysteresis response

428
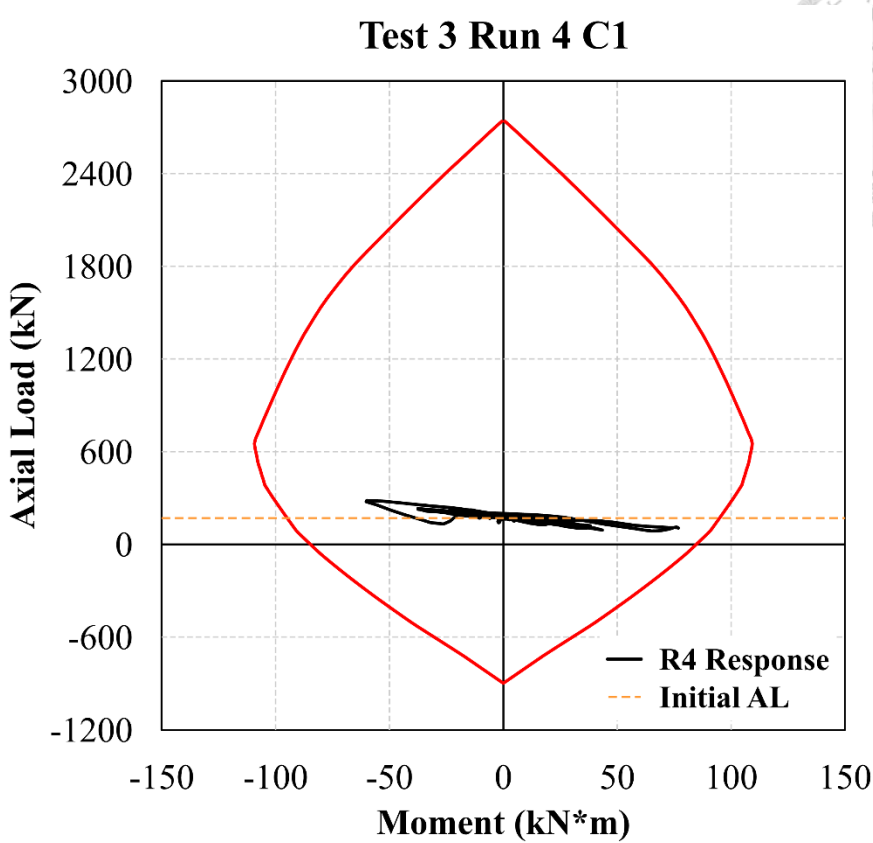
Figure 4-60. T3 C1 Moment-Axial Load Response
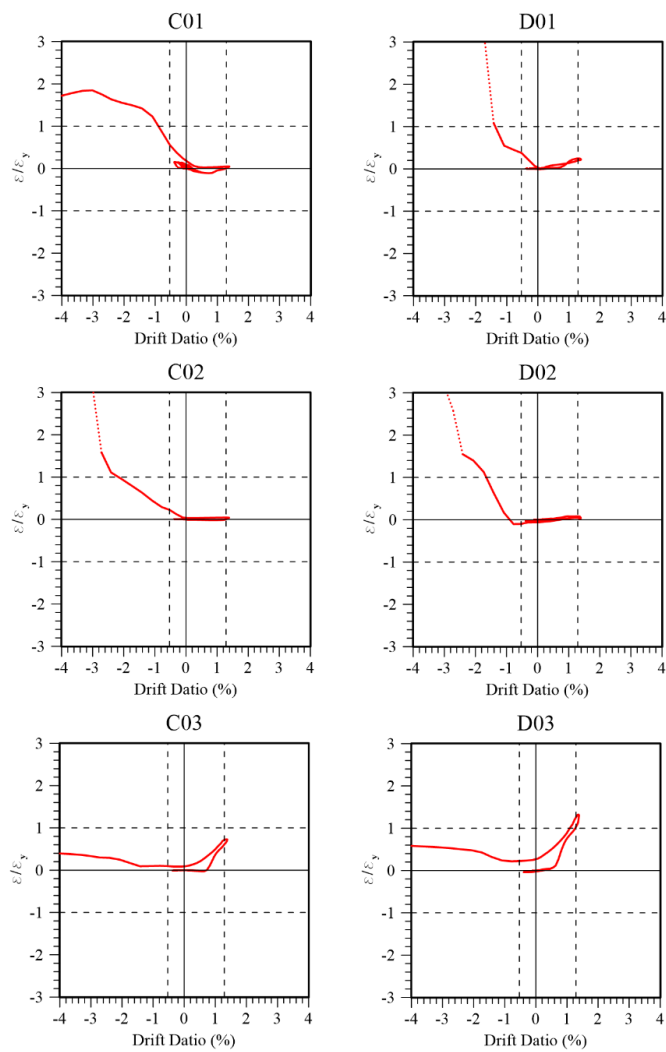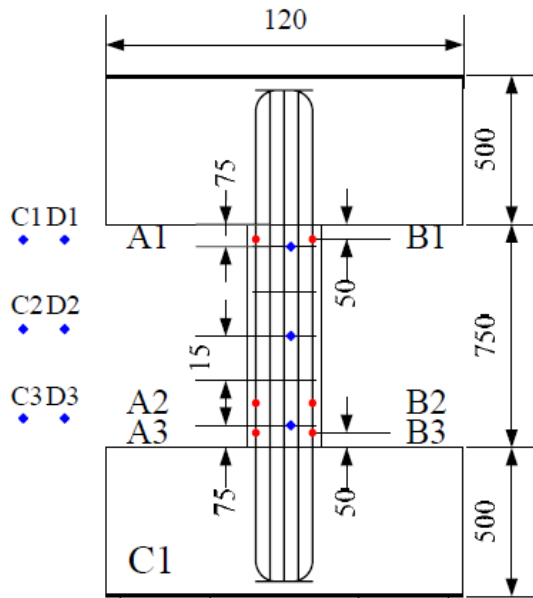
Figure 4-61. T3 C1 Stirrup strain gage readings

430

| Initial | End of Run2 | Shear Crack (+) | Collapse (-) |
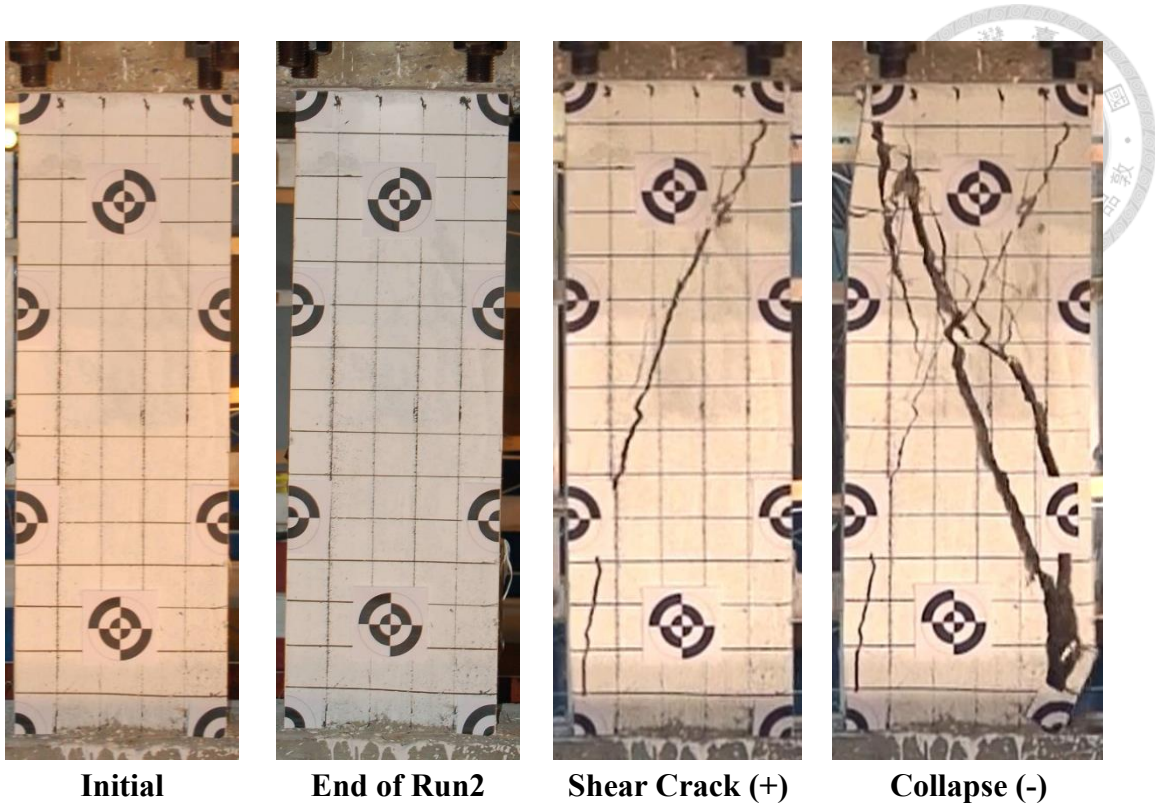
Figure 4-62. T3 C3 Crack pattern development

431
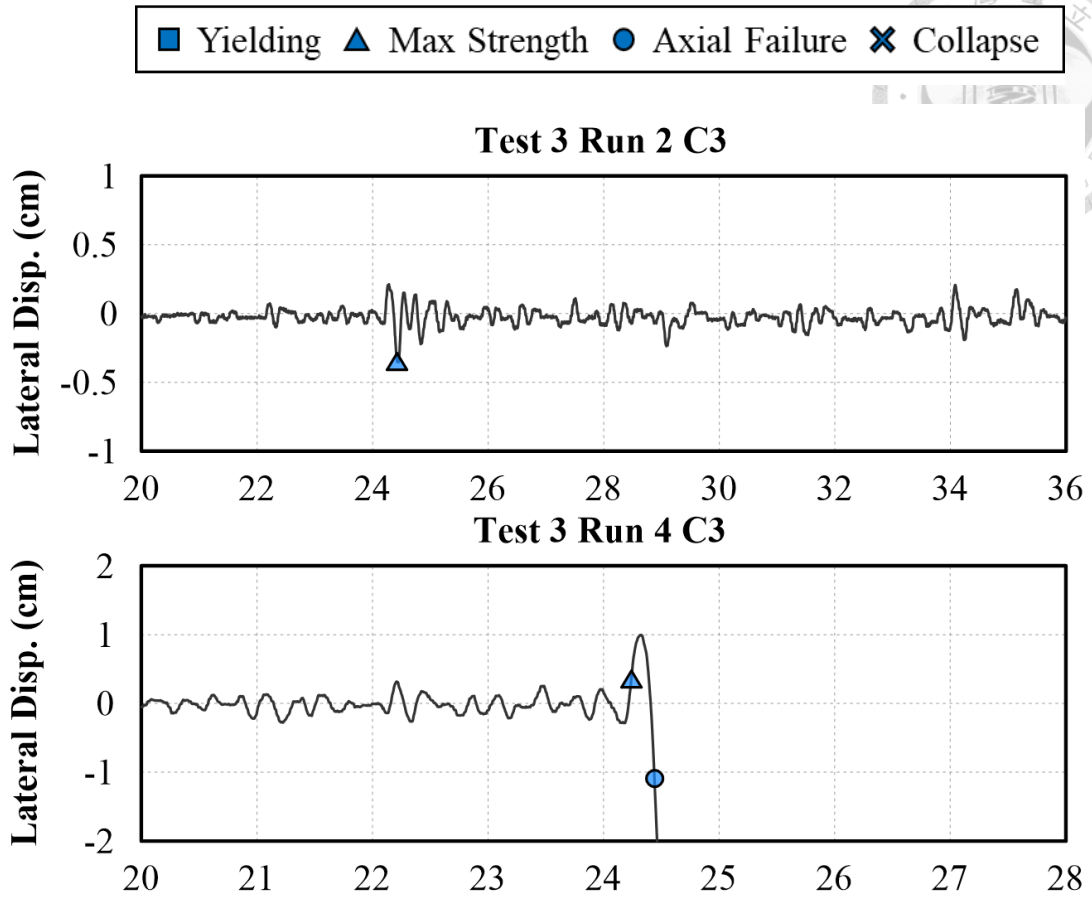
Figure 4-63. T3 C3 Lateral displacement time history response
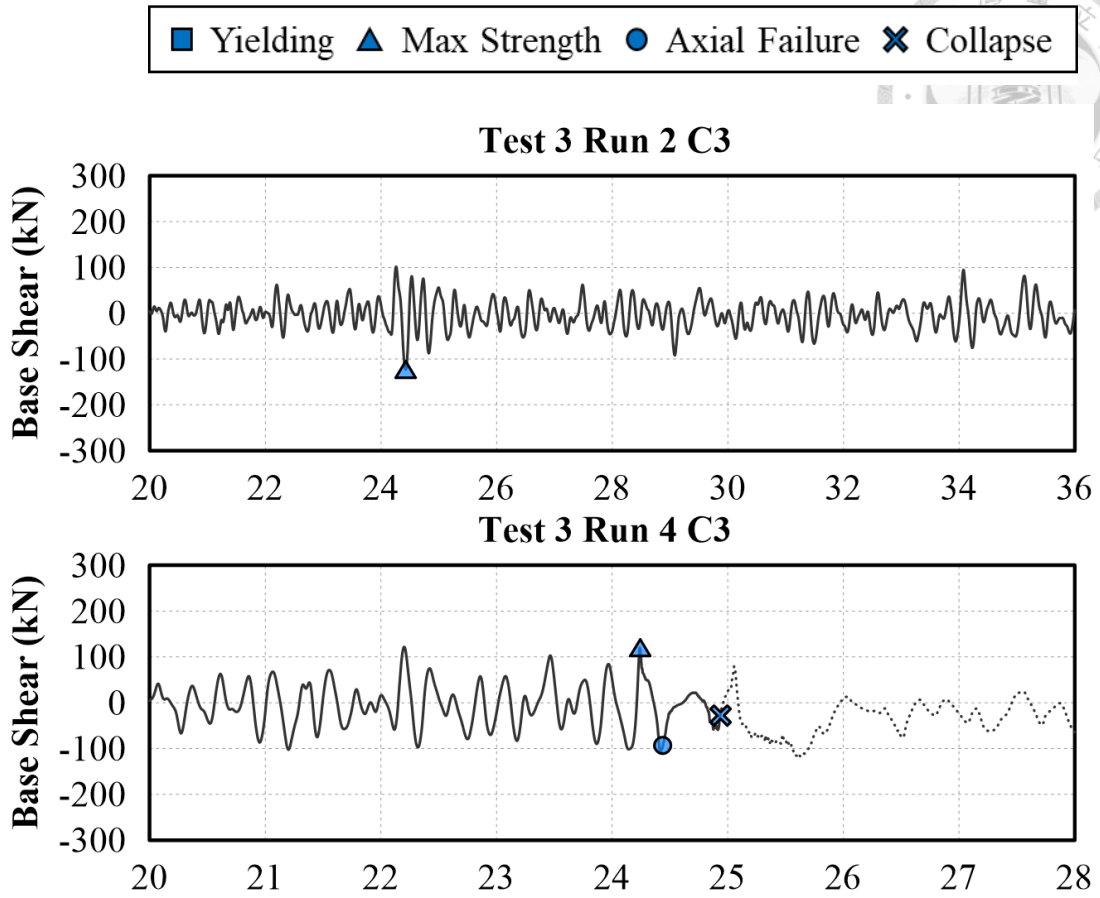
Figure 4-64. T3 C3 Base shear time history response
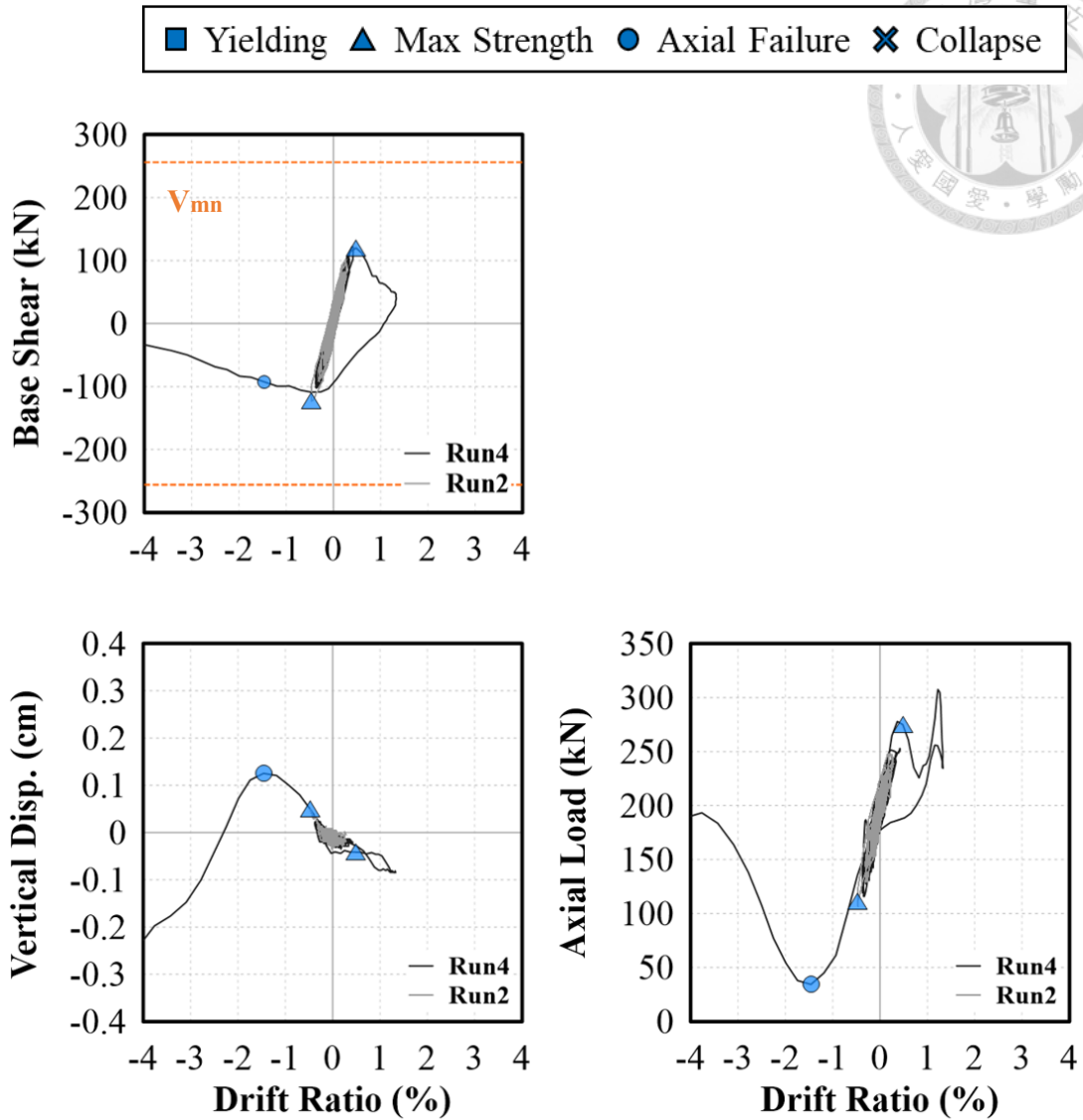
Figure 4-65. T3 C3 Hysteresis response
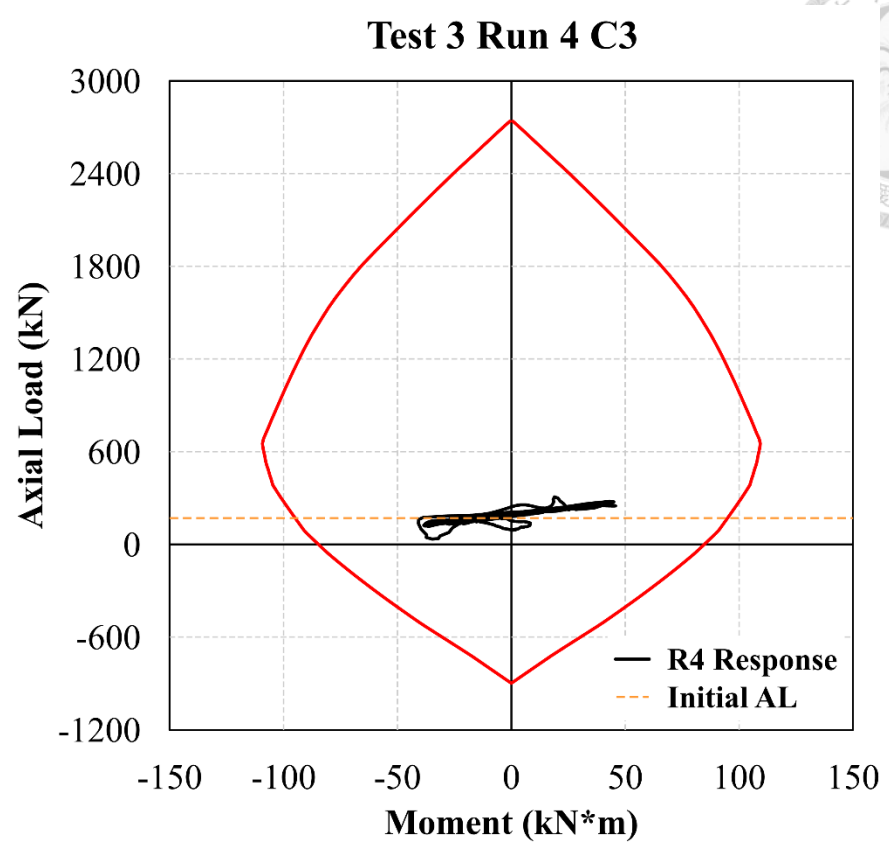
Figure 4-66. T3 C3 Moment-Axial Load Response
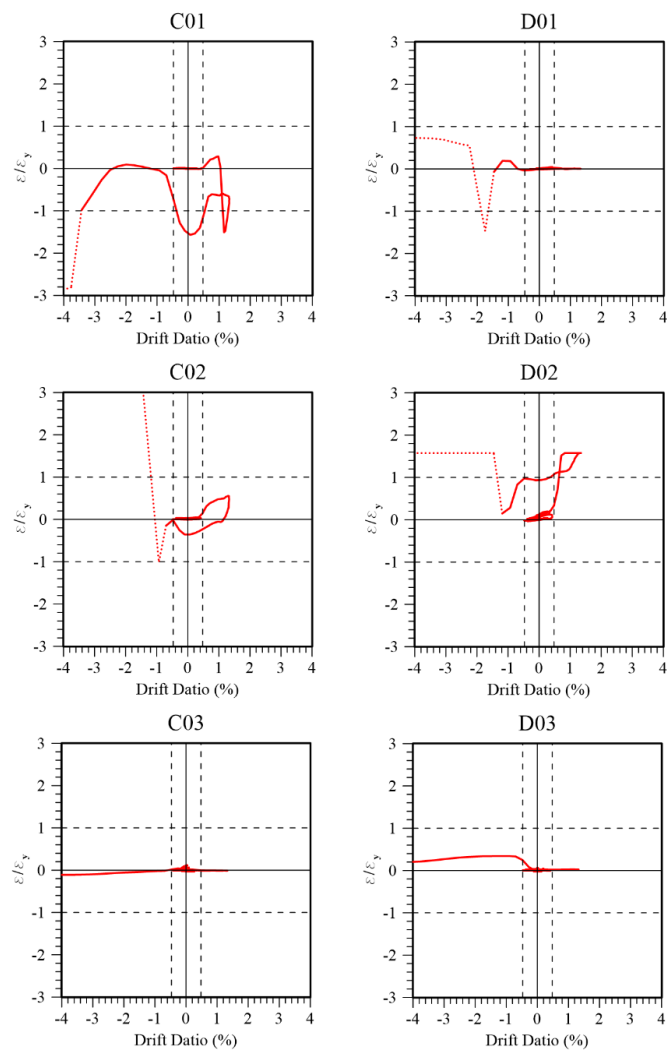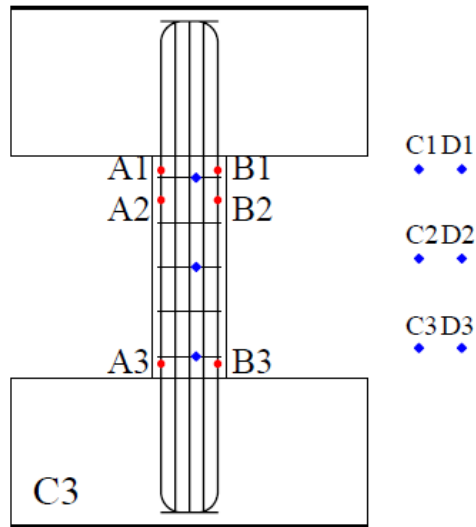
Figure 4-67. T3 C3 Stirrup strain gage readings

436
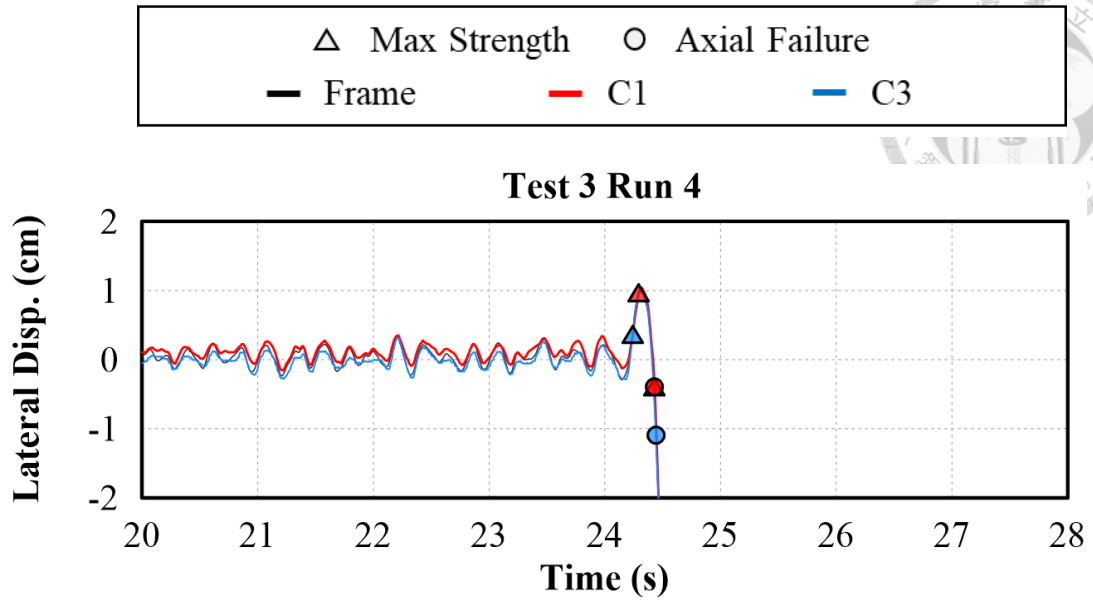
Figure 4-68. T3 Overall lateral displacement comparison
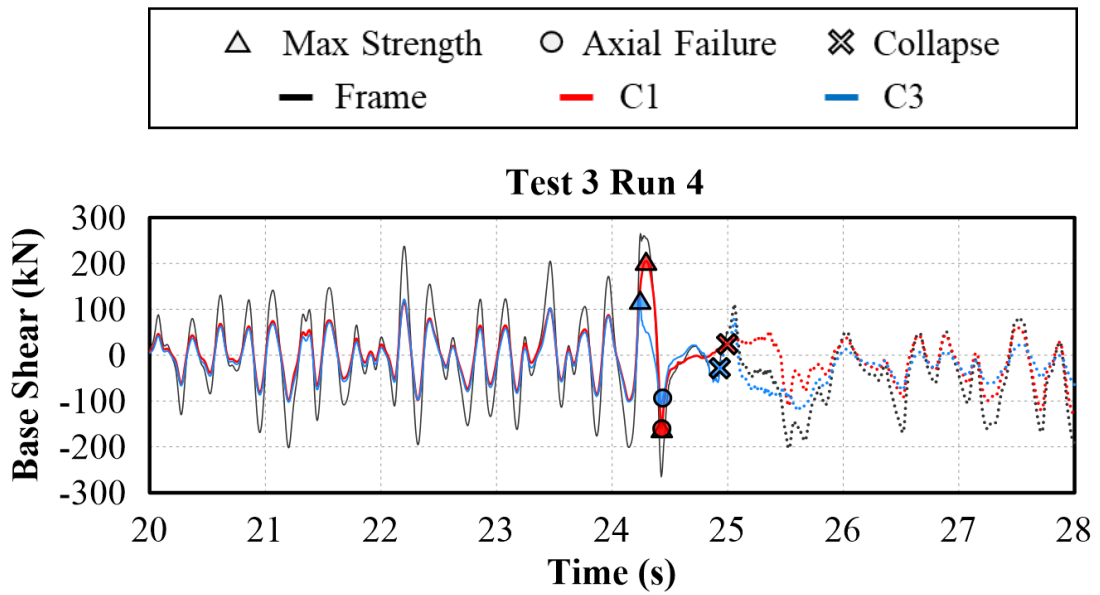
Figure 4-69. T3 Overall base shear comparison

437
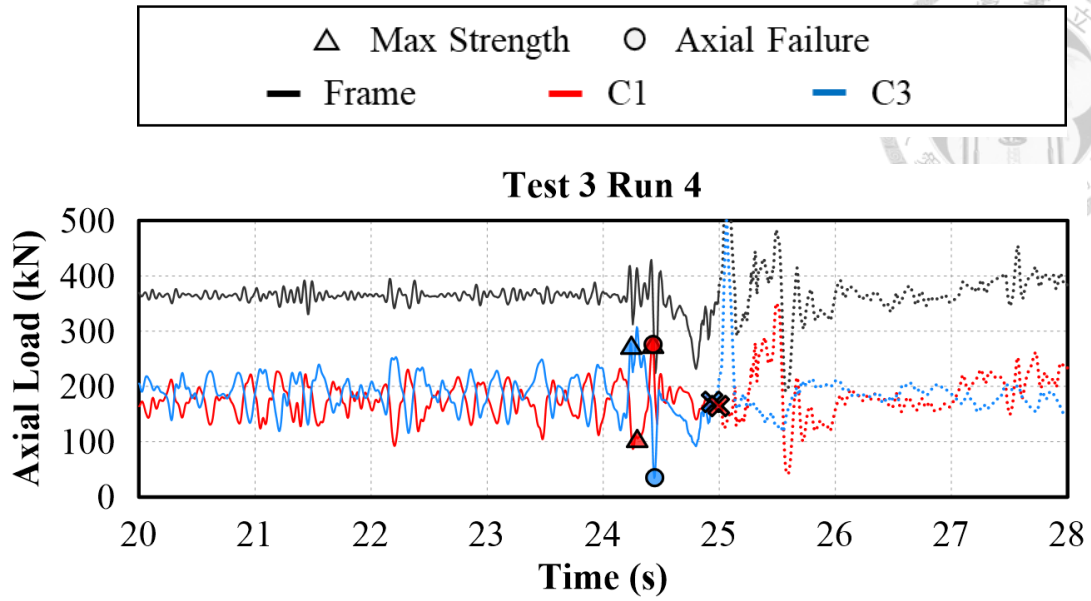
Figure 4-70. T3 Overall axial load comparison
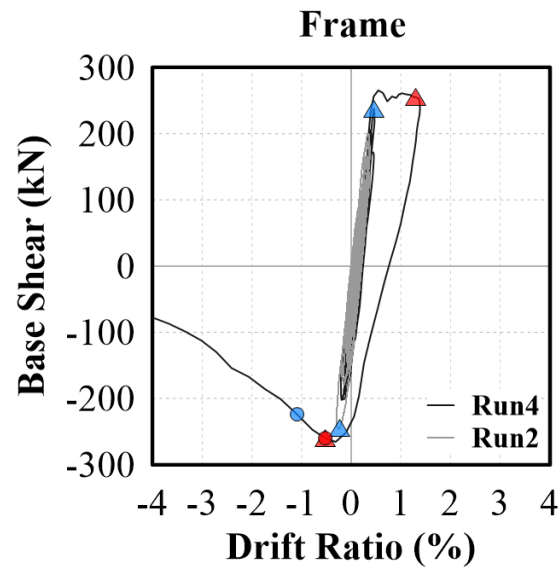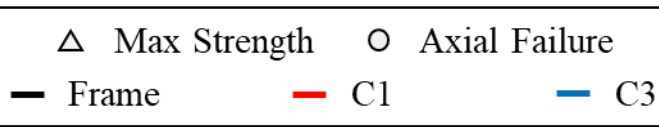
Figure 4-71. T3 Frame hysteresis response

438

| Initial | End of Run2 | Shear Failure (-) | Collapse (-) |
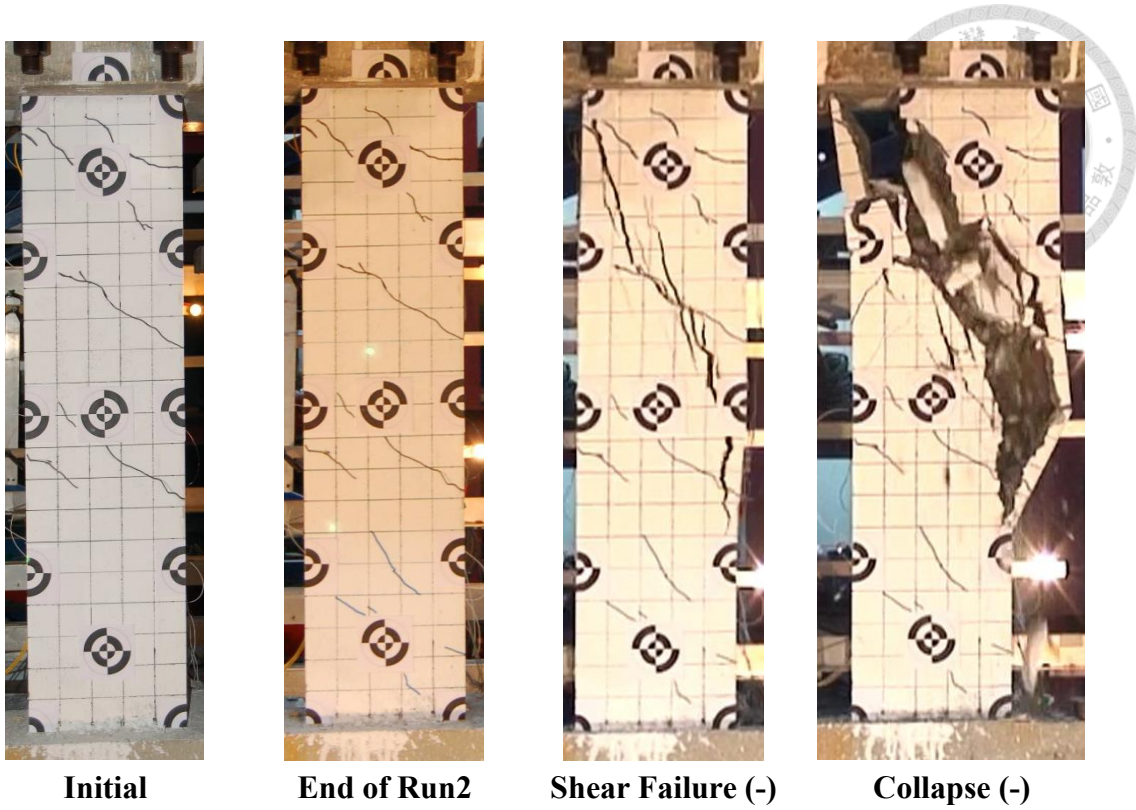
Figure 4-72. T4 C1 Crack pattern development

439
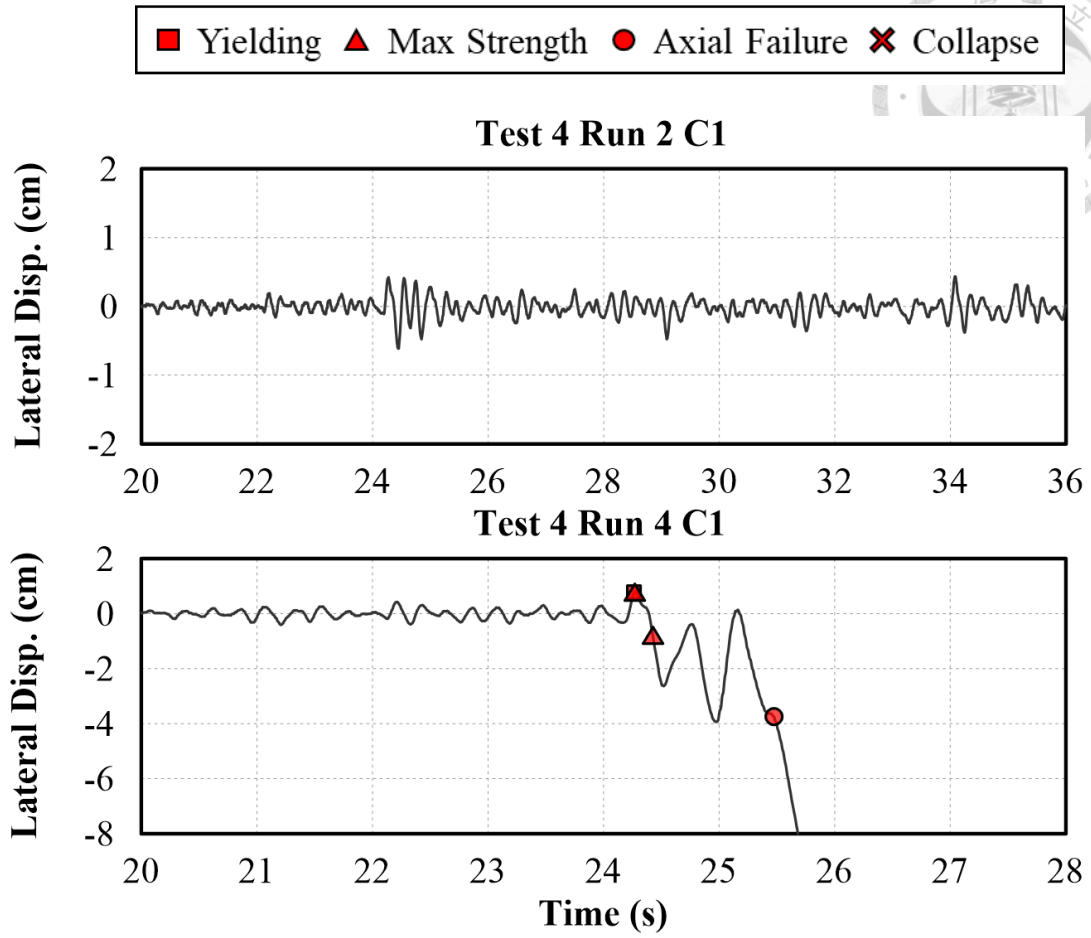
Figure 4-73. T4 C1 Lateral displacement time history response
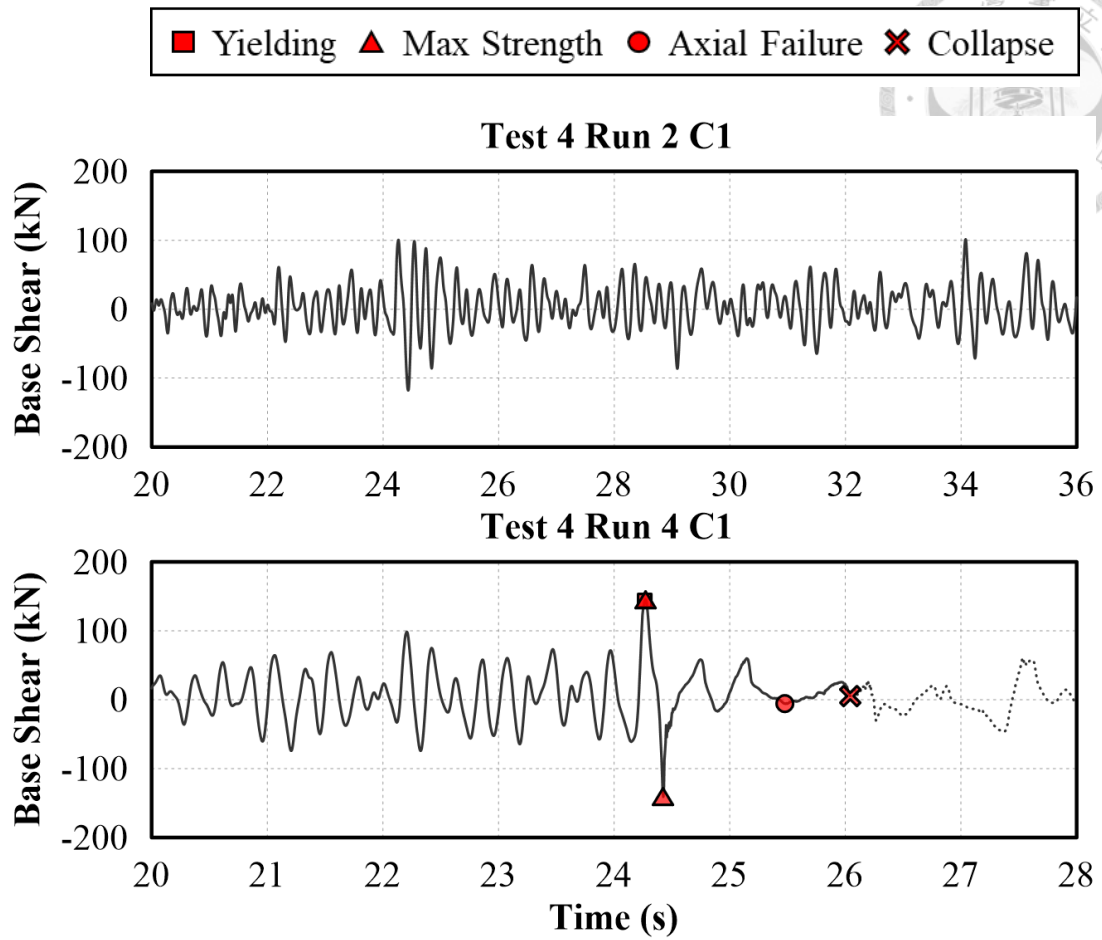
Figure 4-74. T4 C1 Base shear time history response
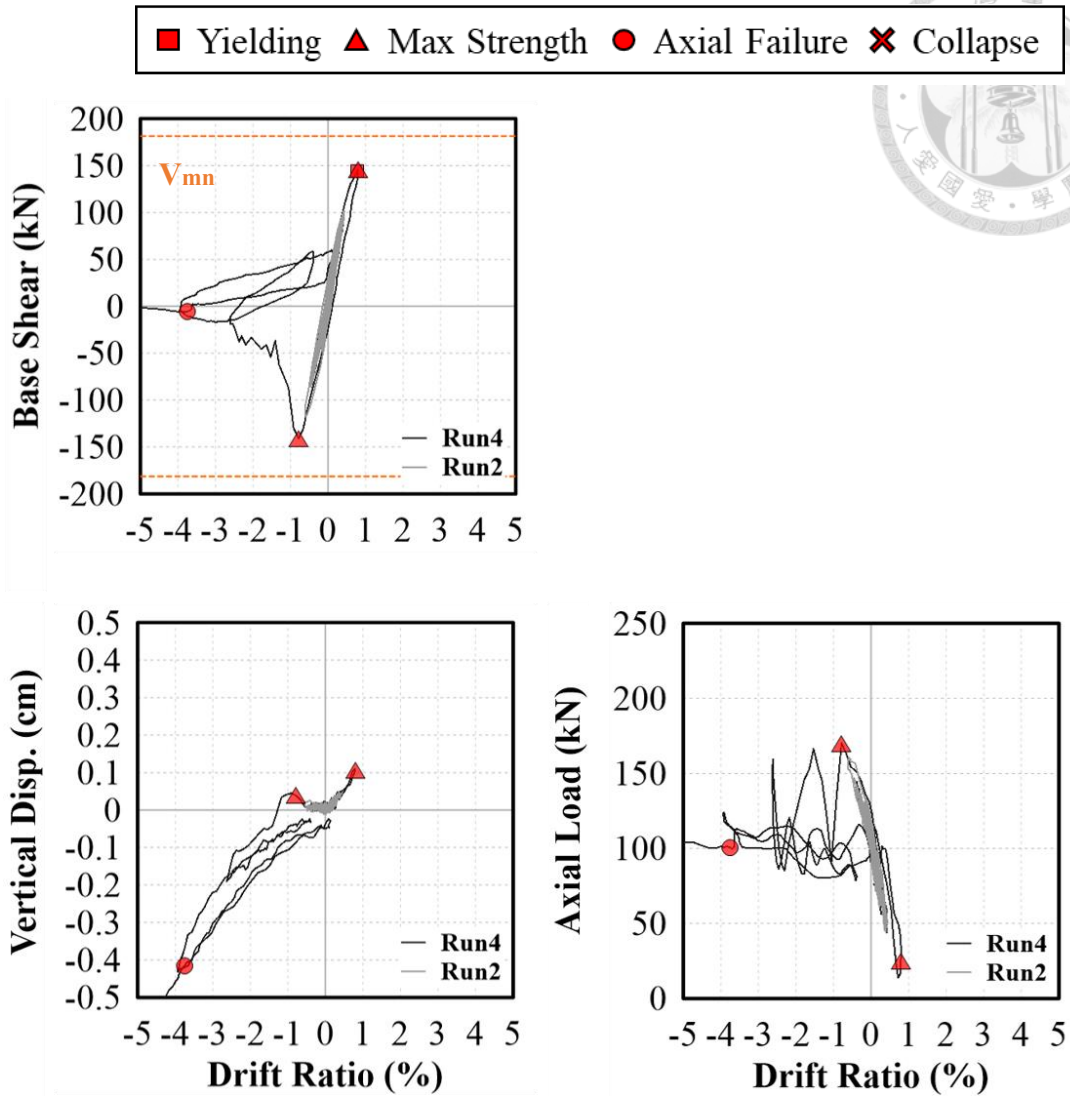
Figure 4-75. T4 C1 Hysteresis response
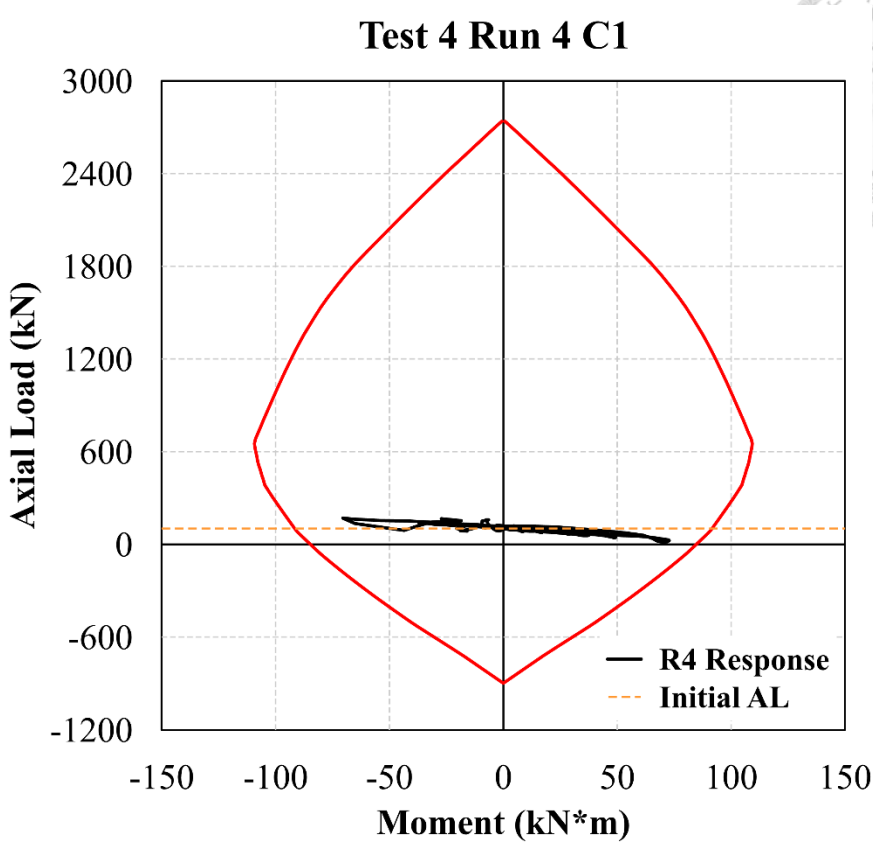
Figure 4-76. T4 C1 Moment-Axial Load Response
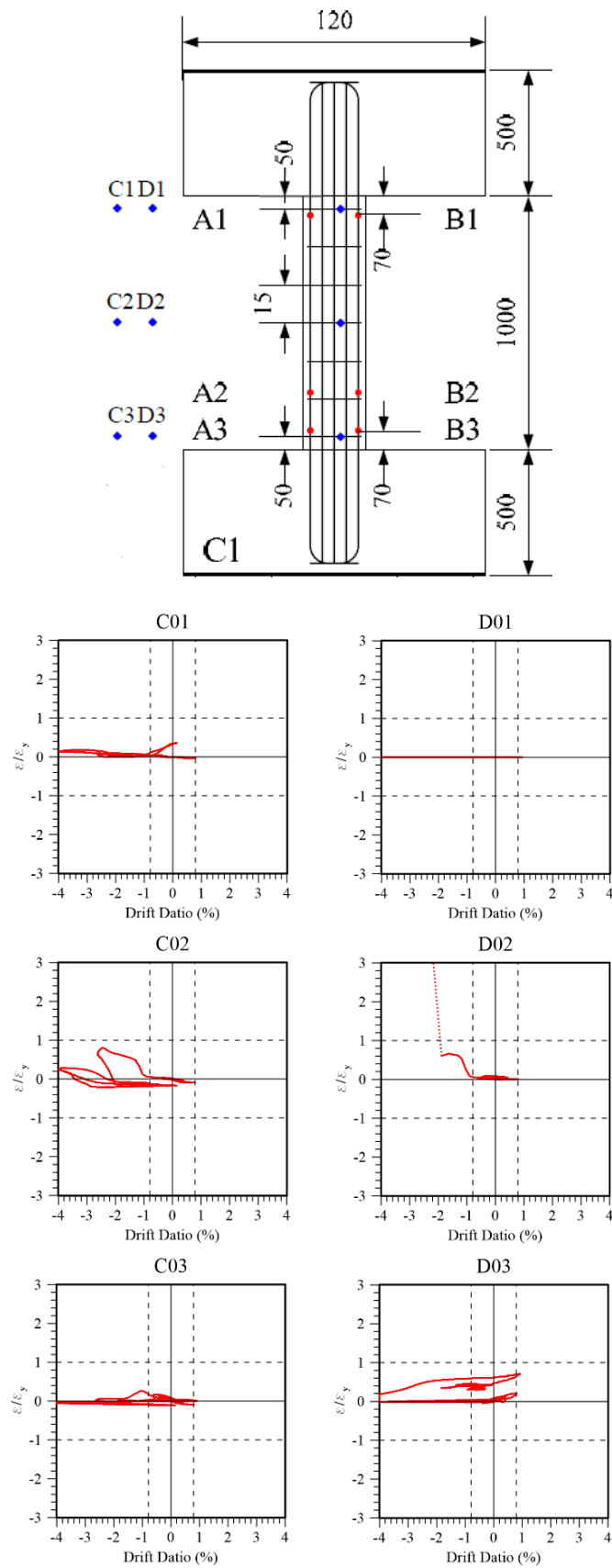
Figure 4-77. T4 C1 Stirrup strain gage readings

444

| Initial | End of Run2 | Shear Failure (-) | Collapse (-) |
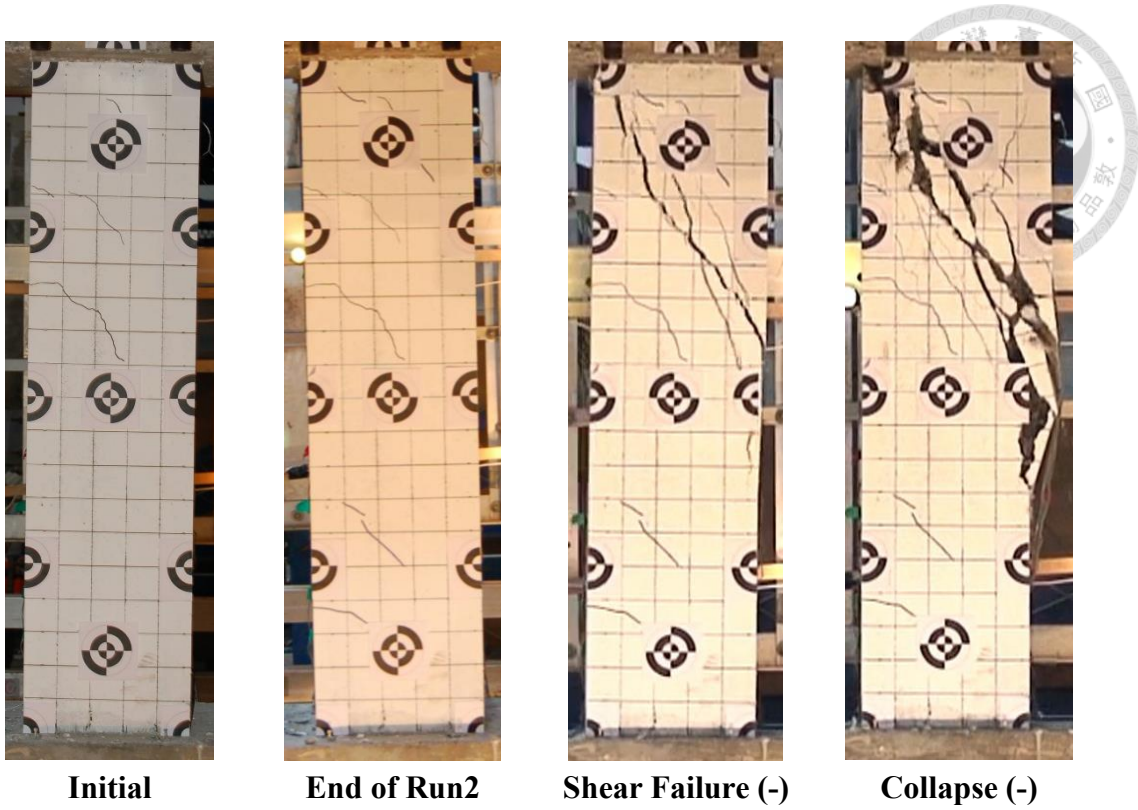
Figure 4-78. T4 C3 Crack pattern development
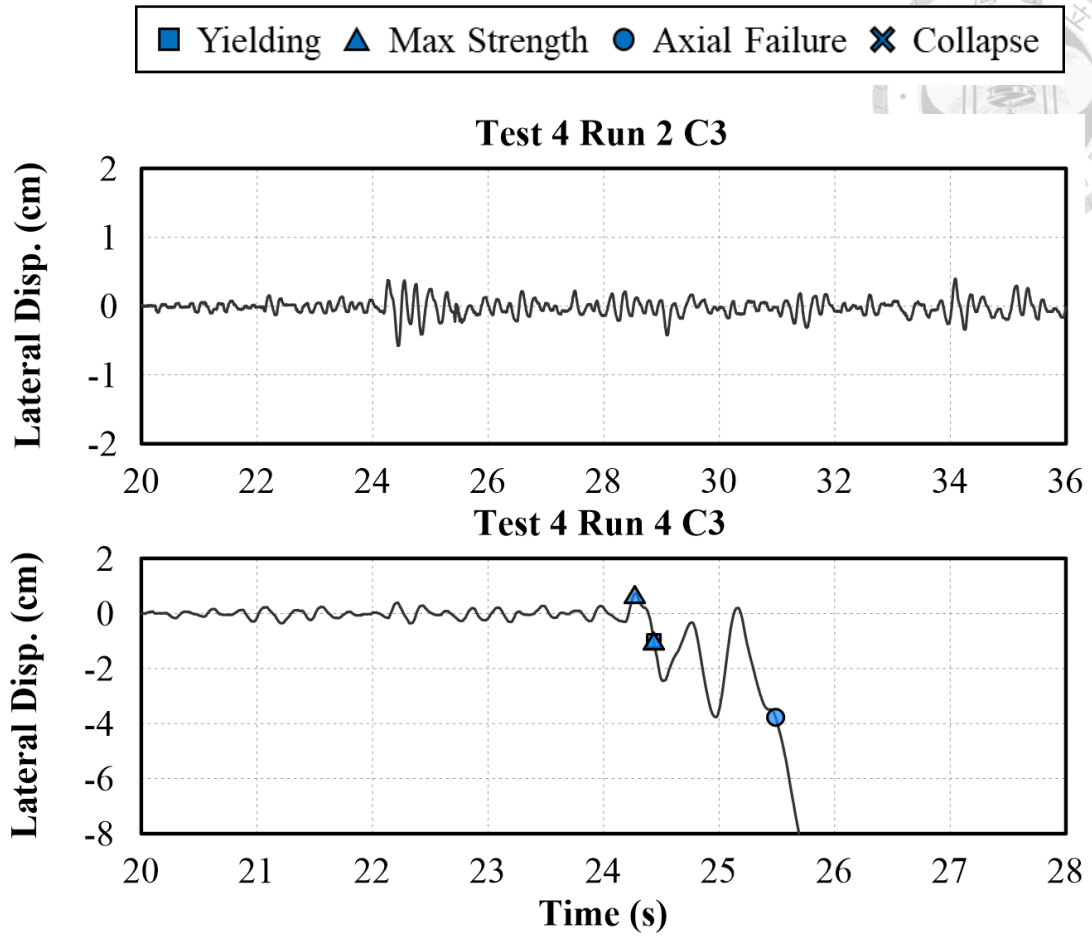
Figure 4-79. T4 C3 Lateral displacement
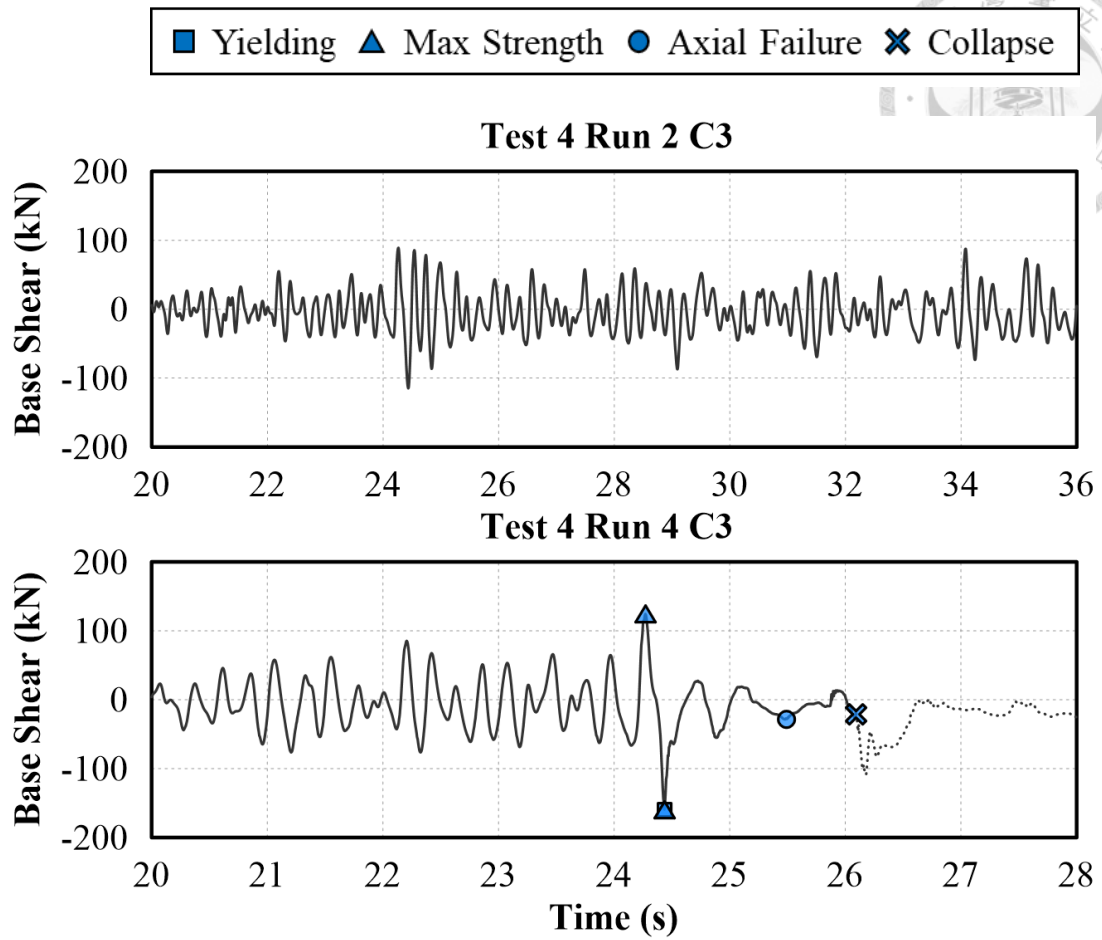
Figure 4-80. T4 C3 Base shear time history response
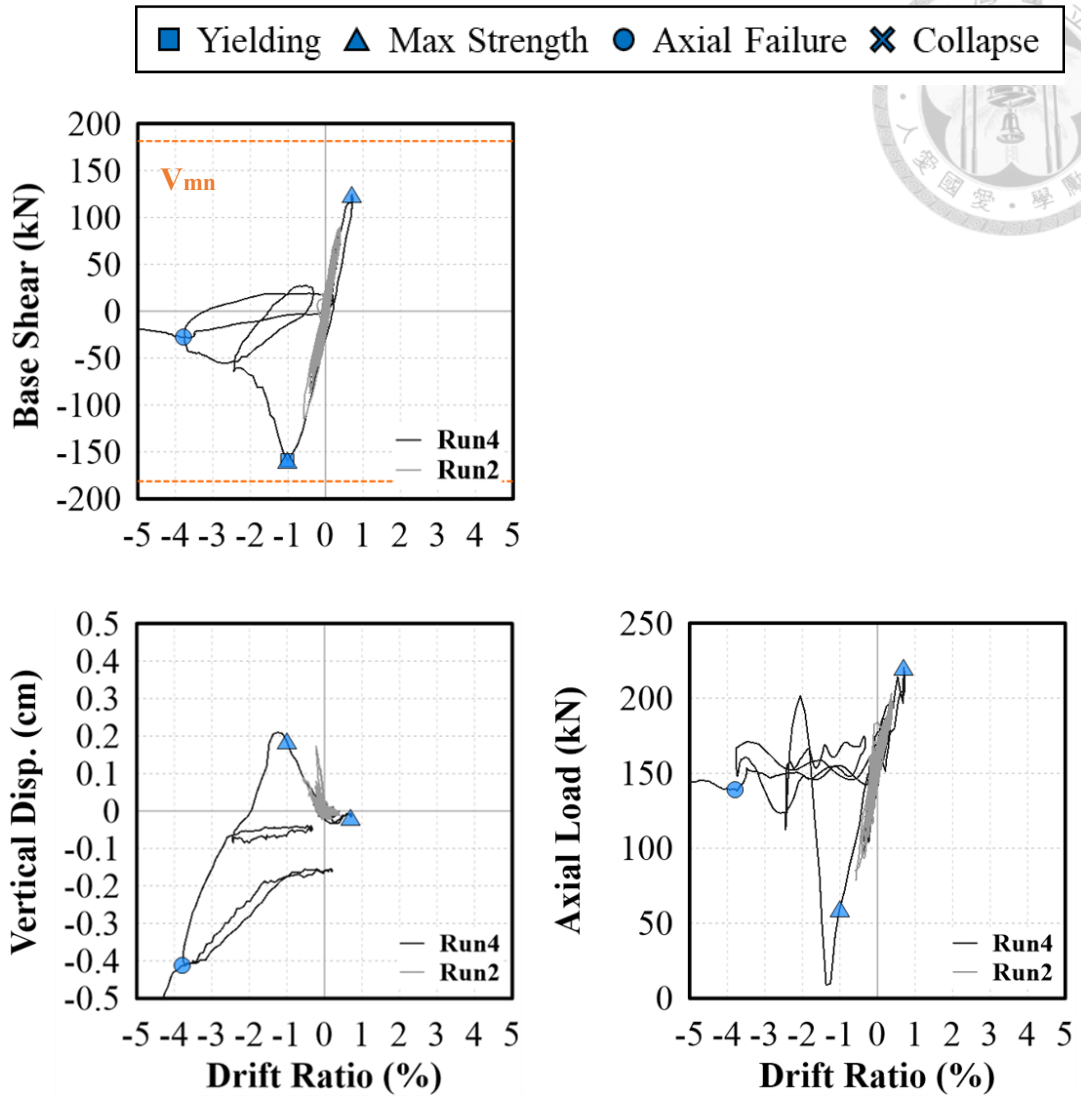
Figure 4-81. T4 C3 Hysteresis response

448
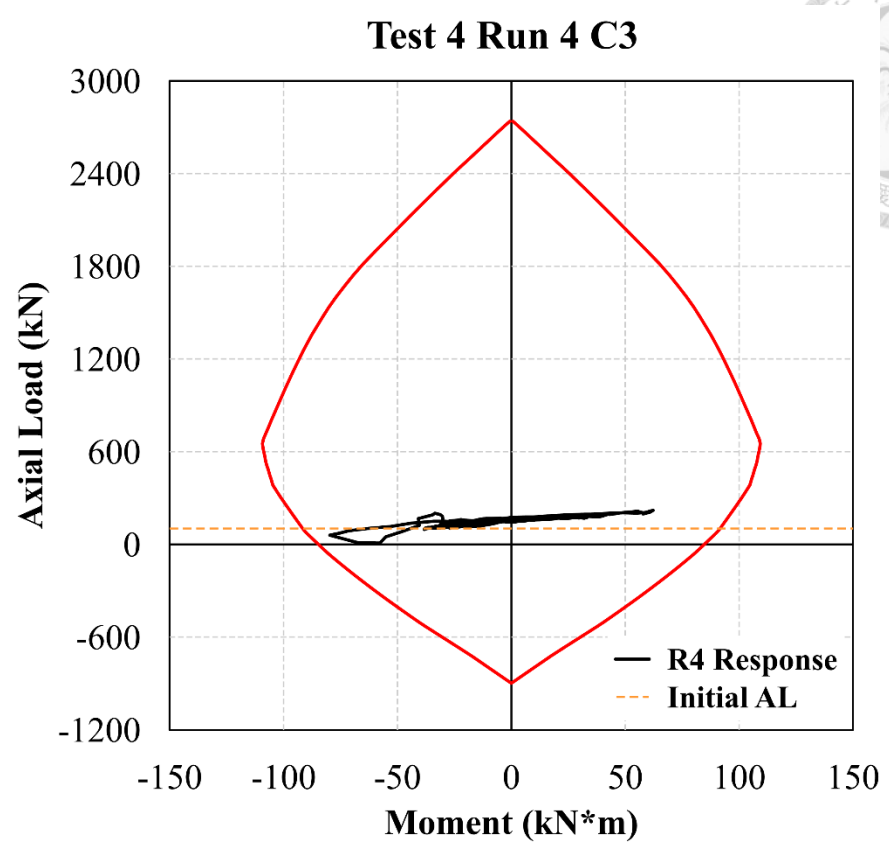
Figure 4-82. T4 C3 Moment-Axial Load Response

449
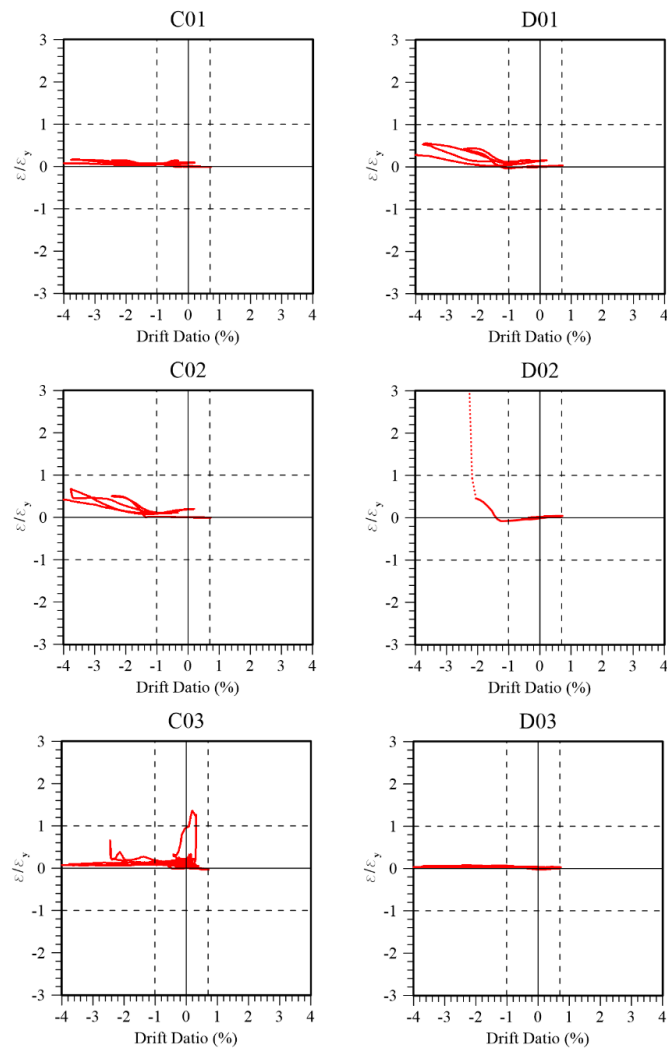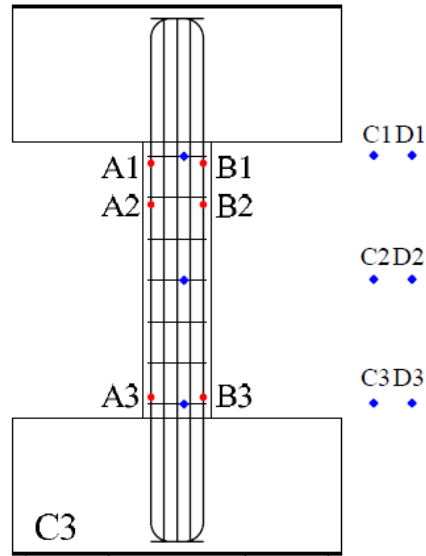
Figure 4-83. T4 C3 Stirrup strain gage readings

450
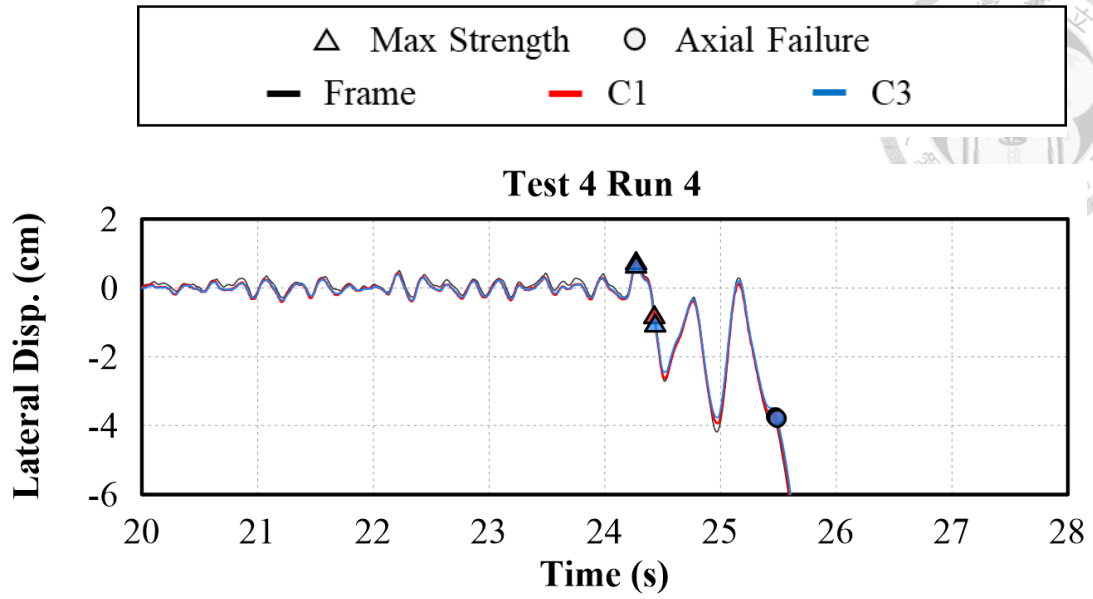
Figure 4-84. T4 Overall lateral displacement comparison
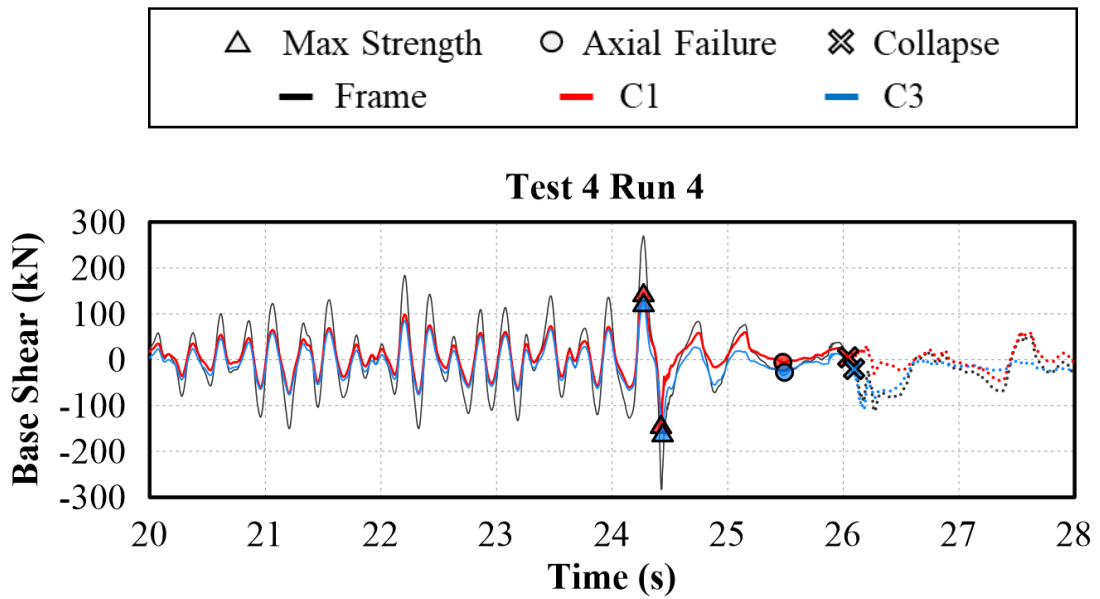
Figure 4-85. T4 Overall base shear comparison

451
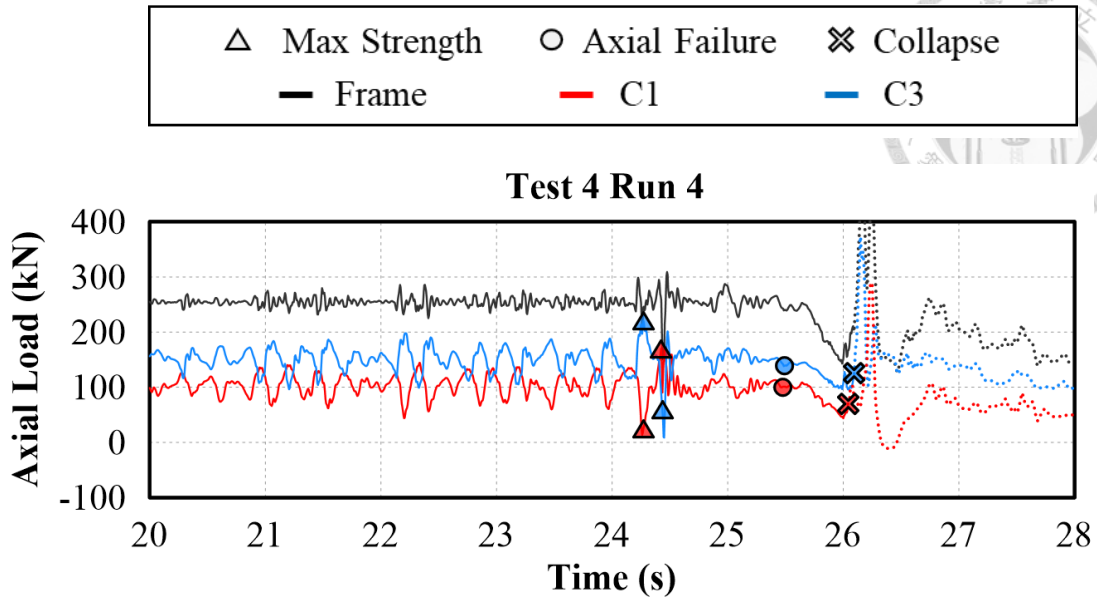
Figure 4-86. T4 Overall axial load comparison
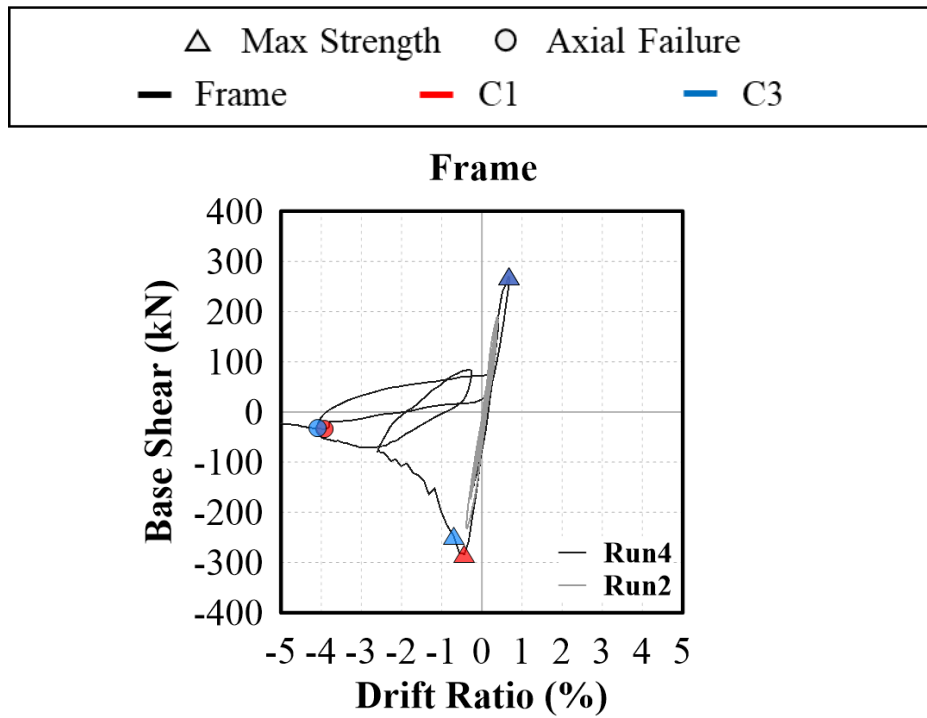
Figure 4-87. T4 Frame hysteresis response

452
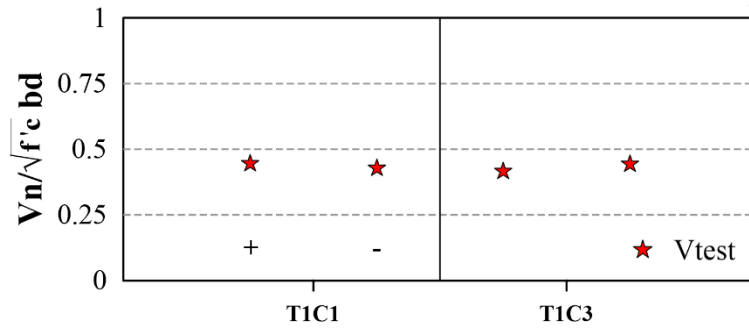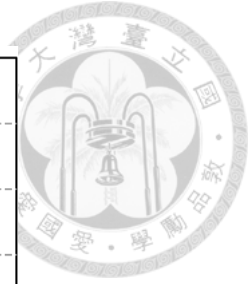
Figure 4-88. Test flexural strengths (arranged in direction)
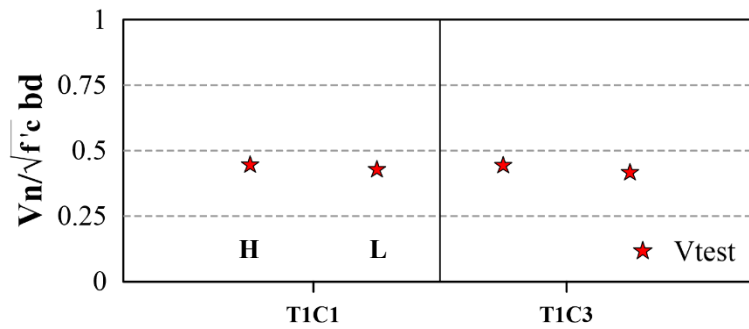
Figure 4-89. Test flexural strengths (arranged in high/low axial load)
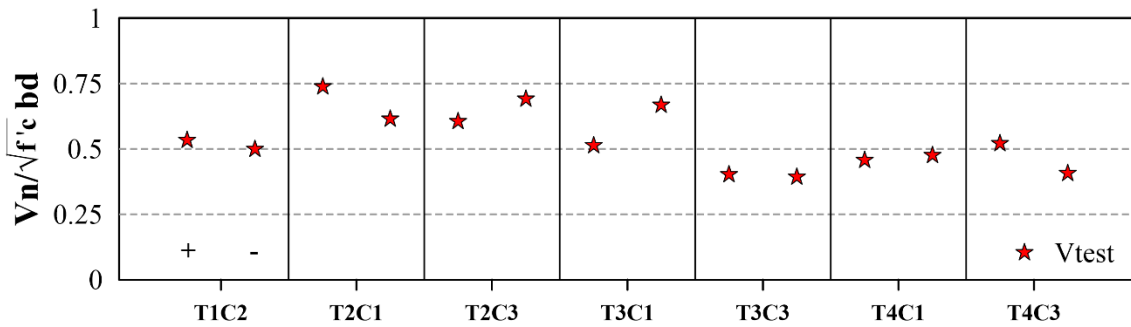
Figure 4-90. Test shear strengths (arranged in direction)
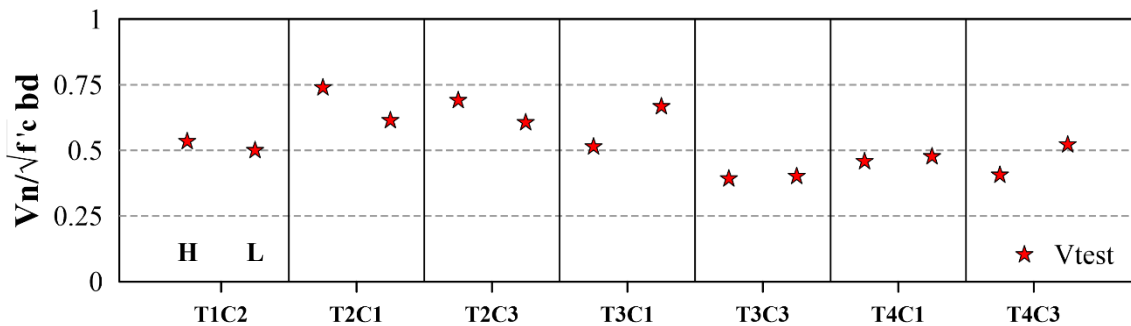
Figure 4-91. Test shear strengths (arranged in high/low axial load)

453
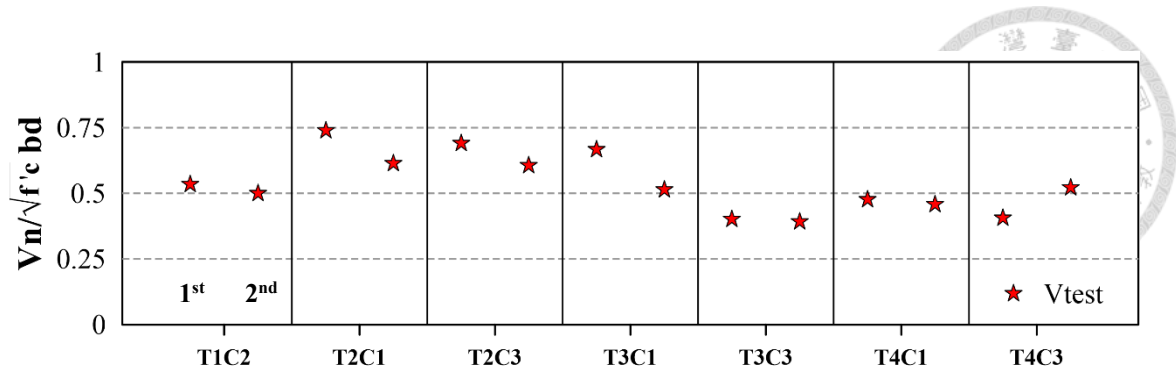
Figure 4-92. Test shear strengths (arranged in sequence)
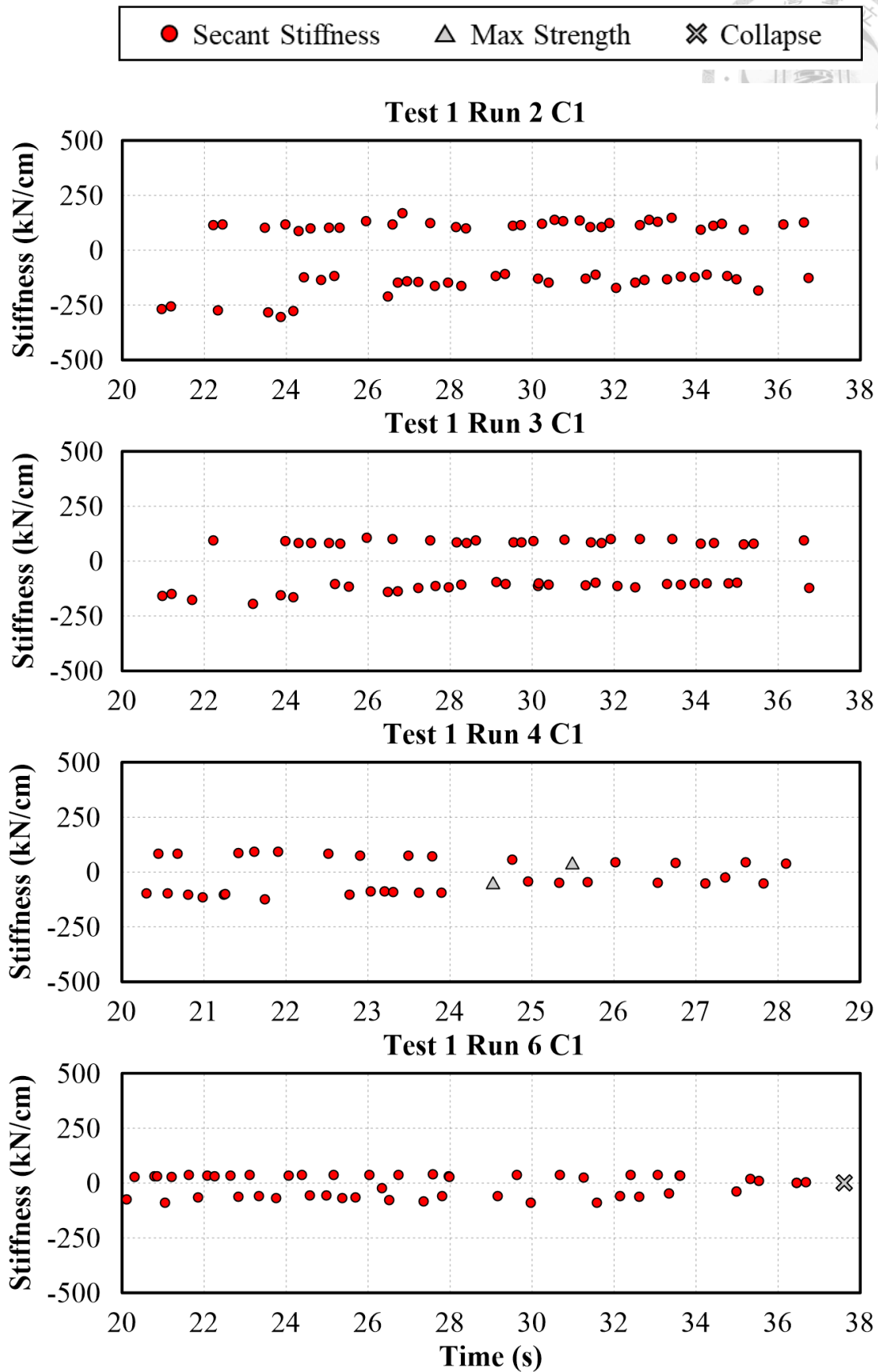
Figure 4-93. T1 C1 Stiffness time history response

455
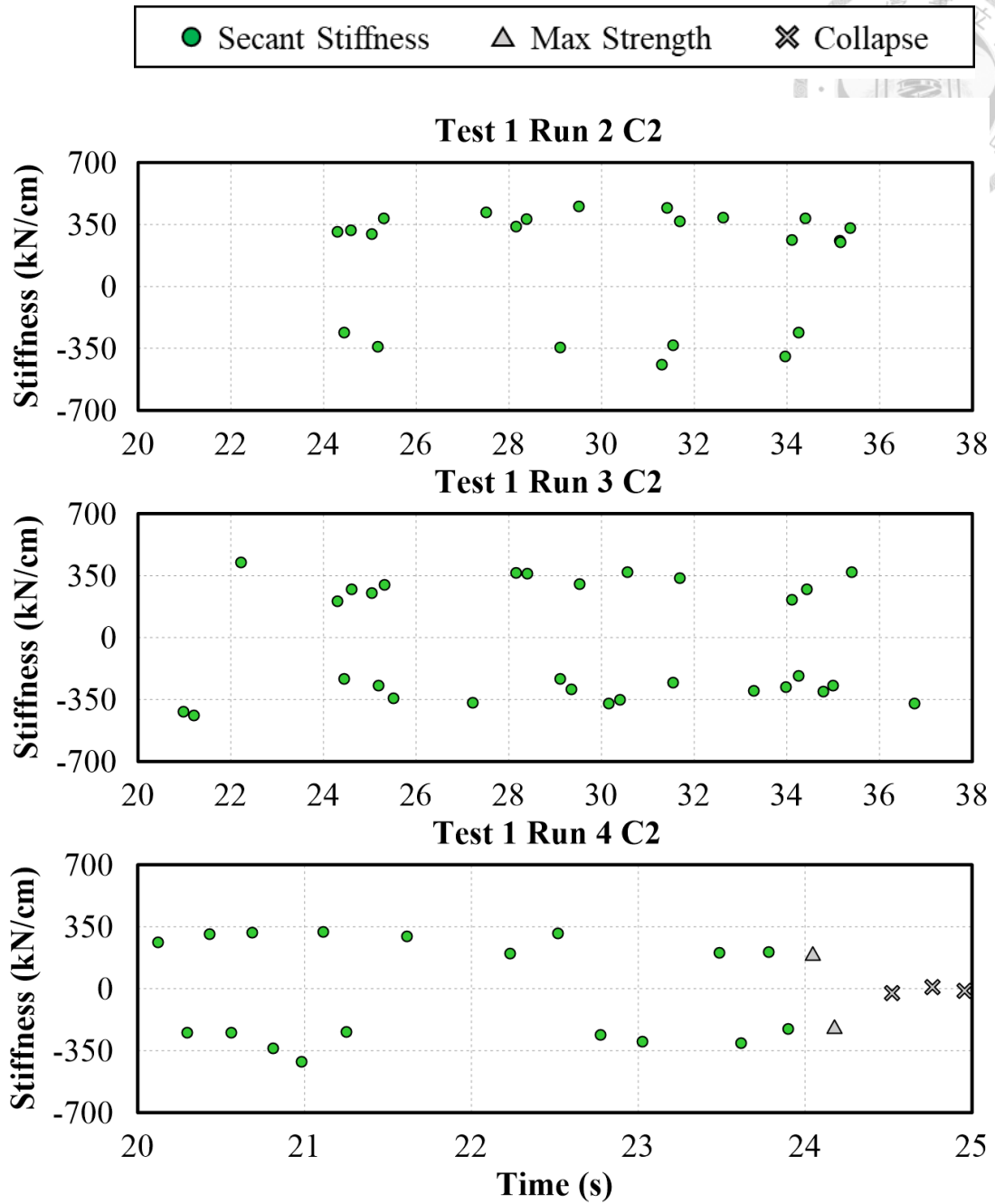
Figure 4-94. T1 C2 Stiffness time history response

456
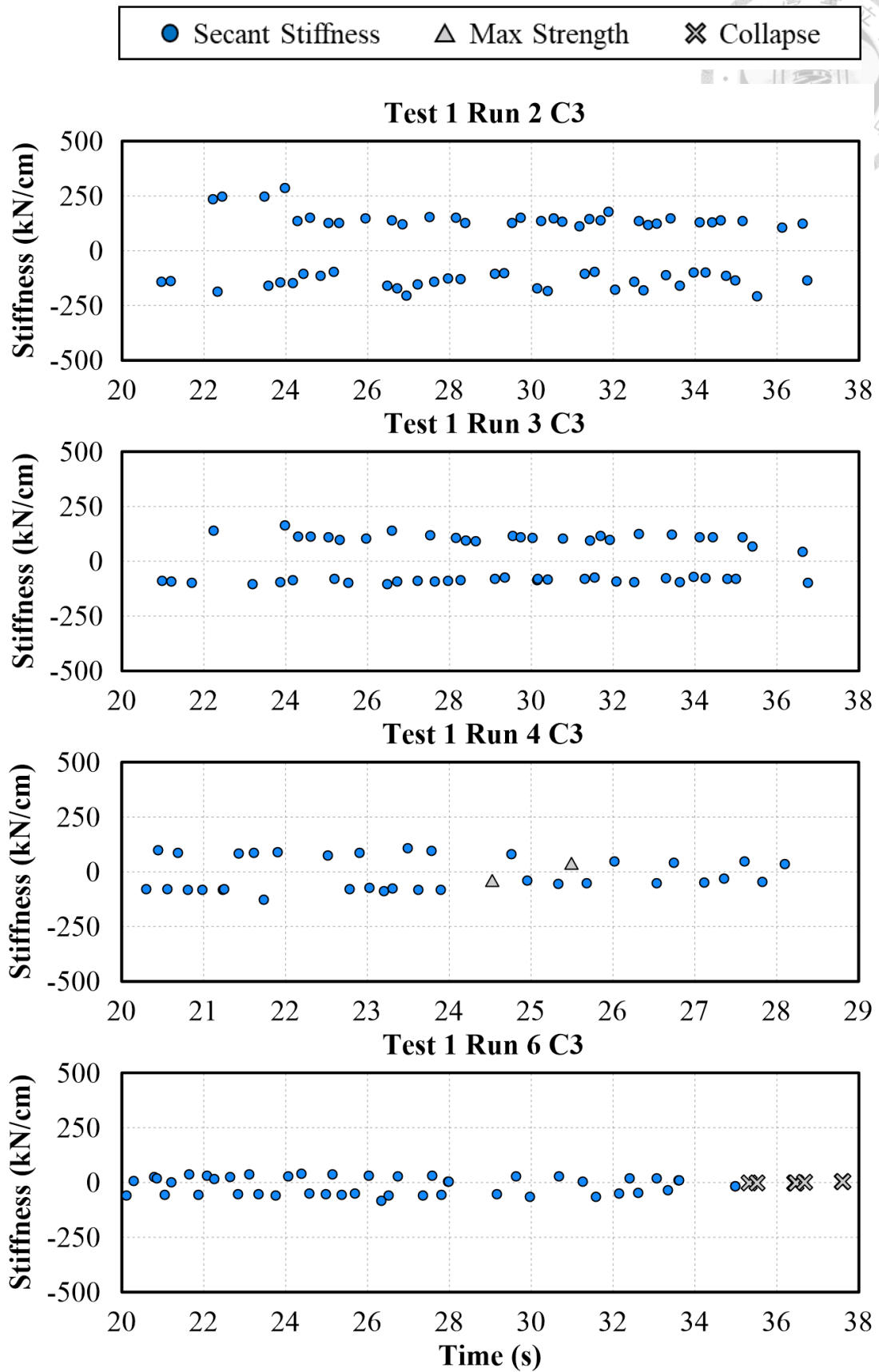
Figure 4-95. T1 C3 Stiffness time history response

457
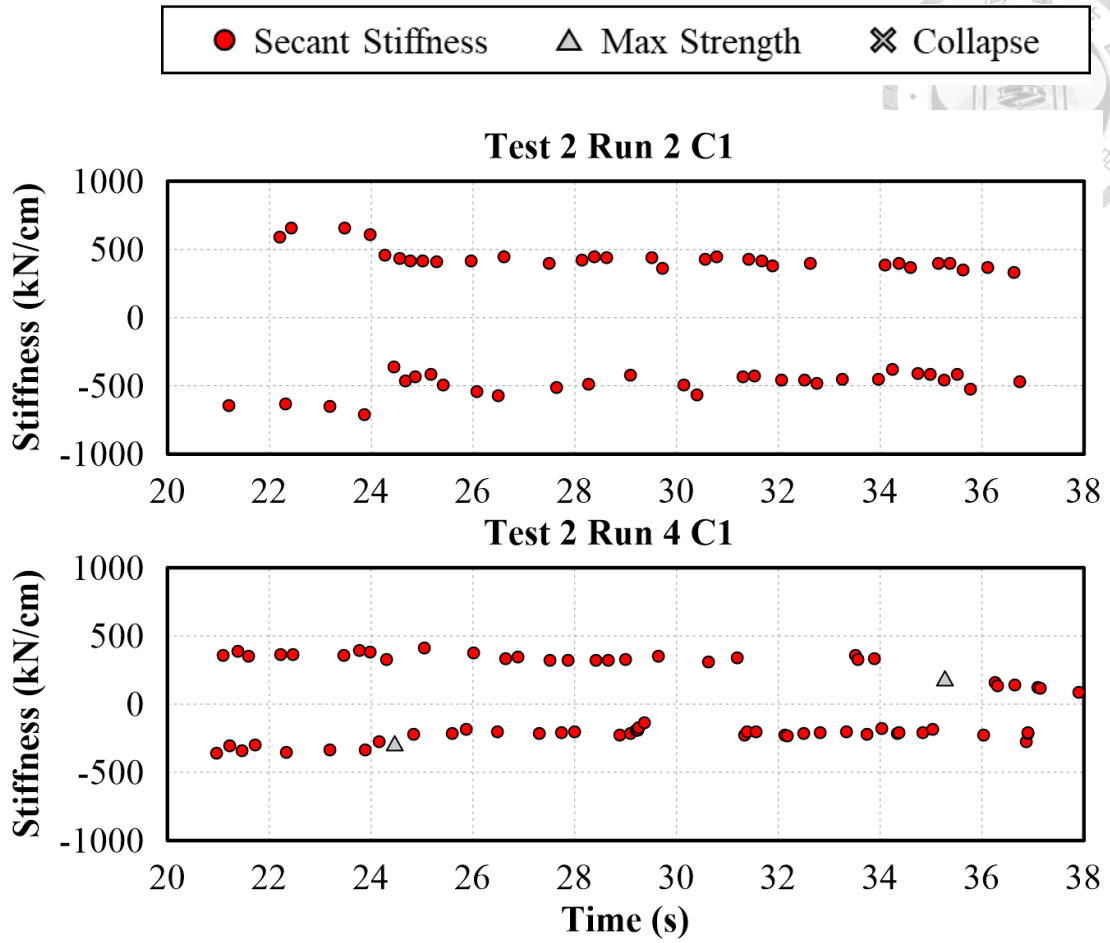
Figure 4-96. T2 C1 Stiffness time history response
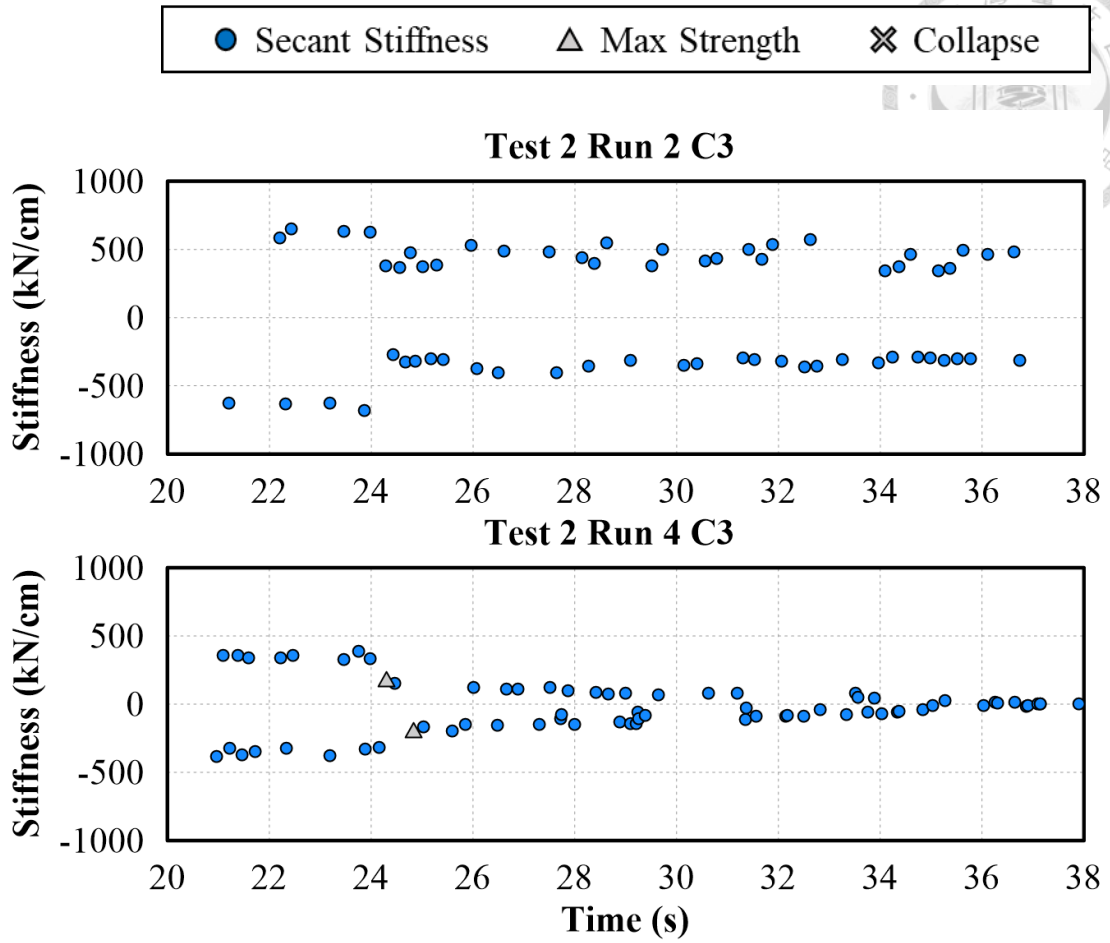
Figure 4-97. T2 C3 Stiffness time history response
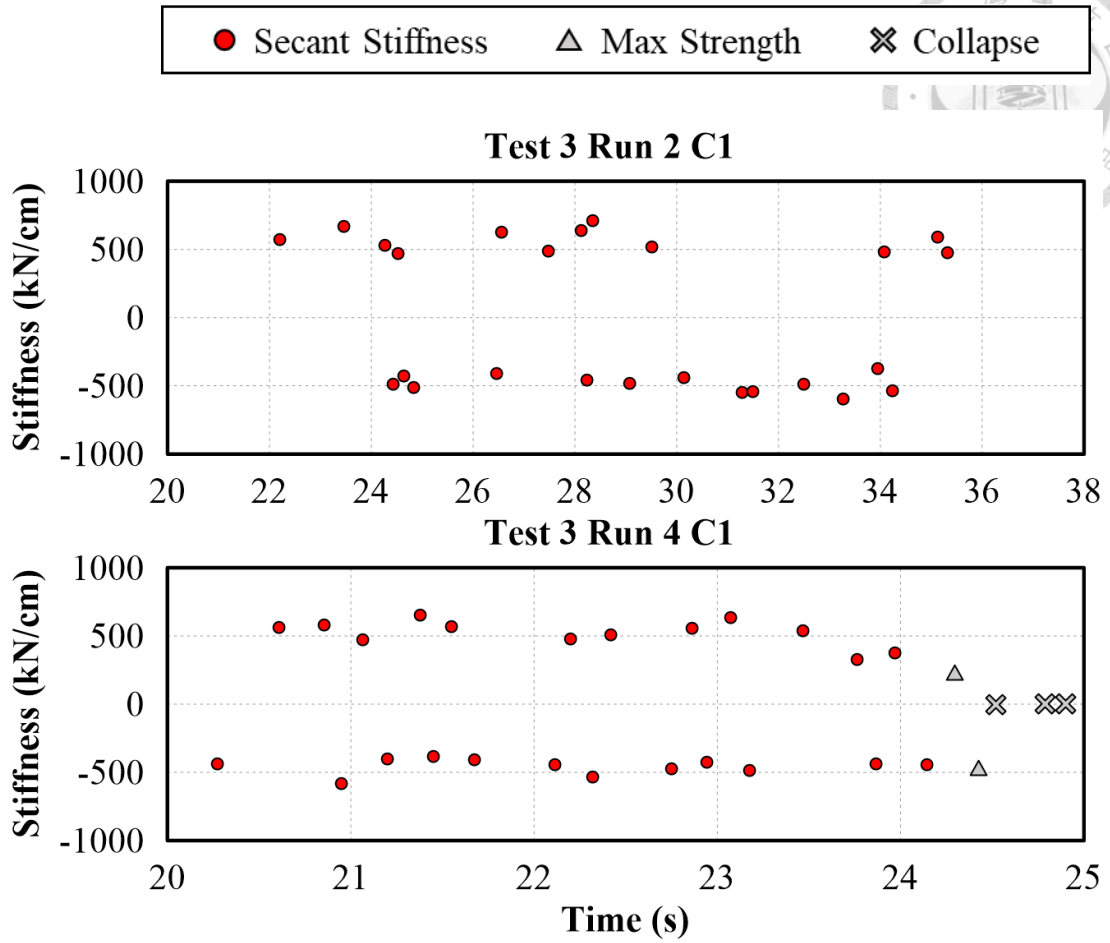
Figure 4-98. T3 C1 Stiffness time history response
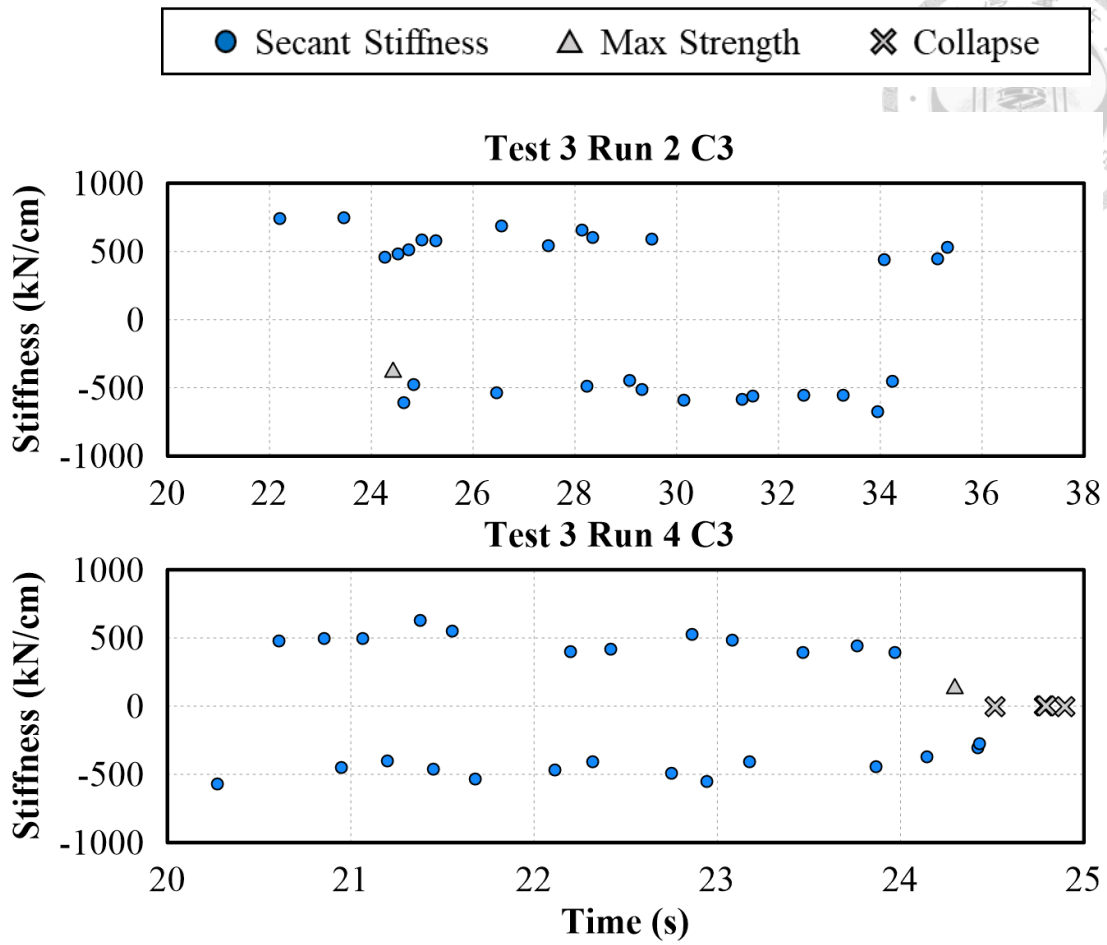
Figure 4-99. T3 C3 Stiffness time history response
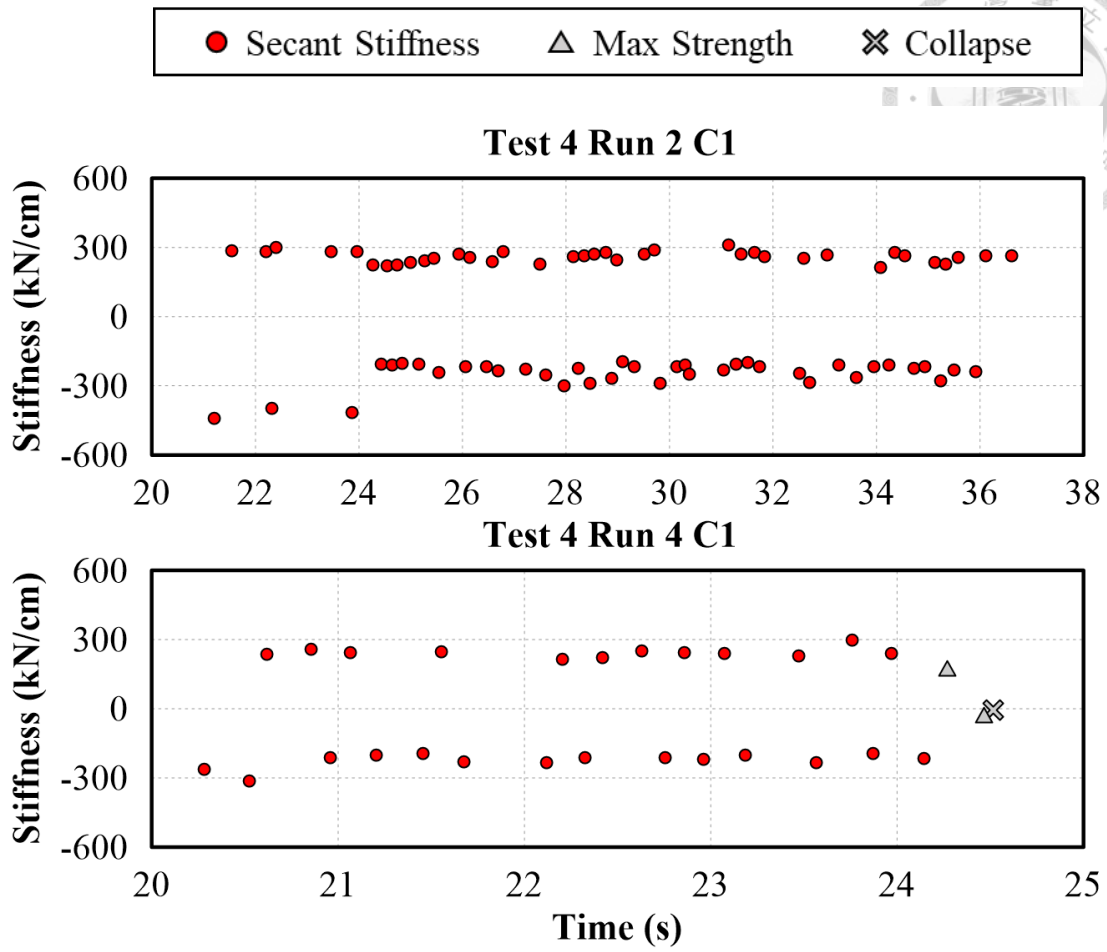
Figure 4-100. T4 C1 Stiffness time history response
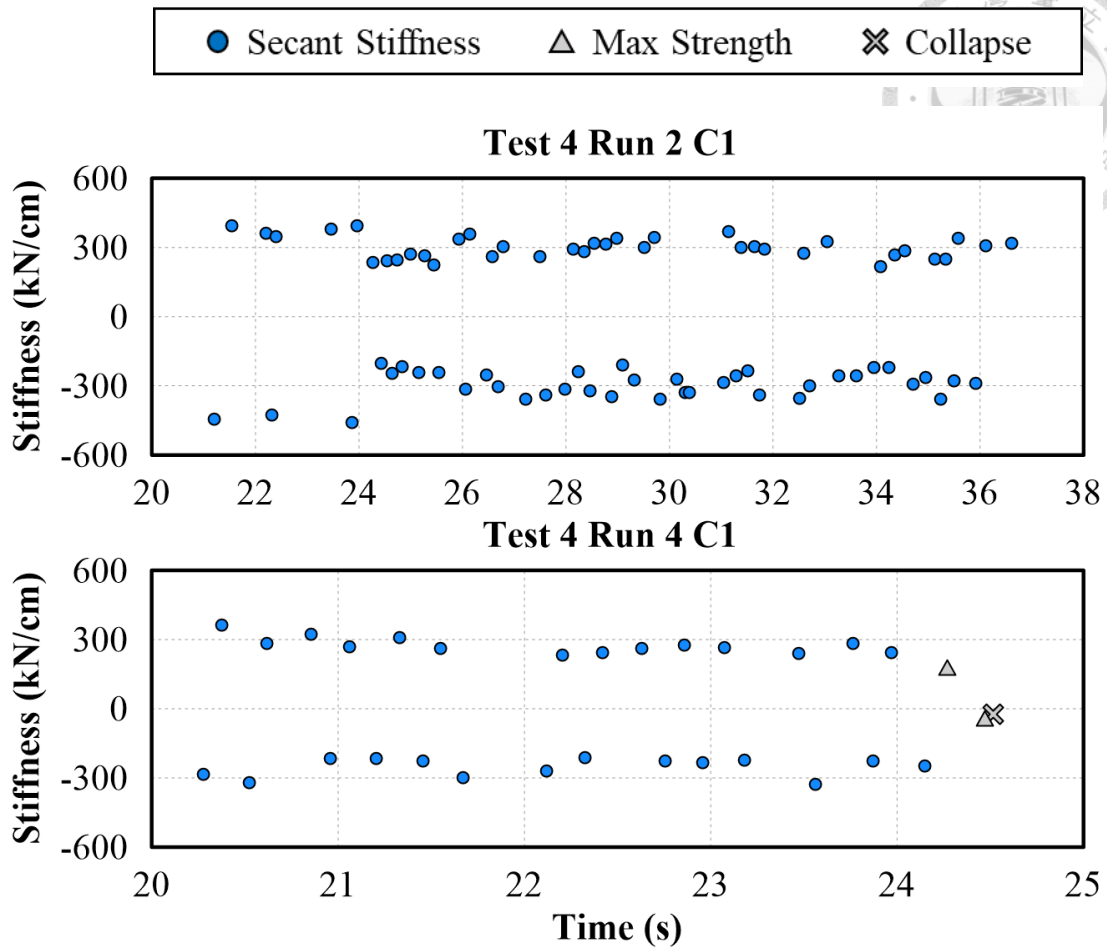
Figure 4-101. T4 C3 Stiffness time history response
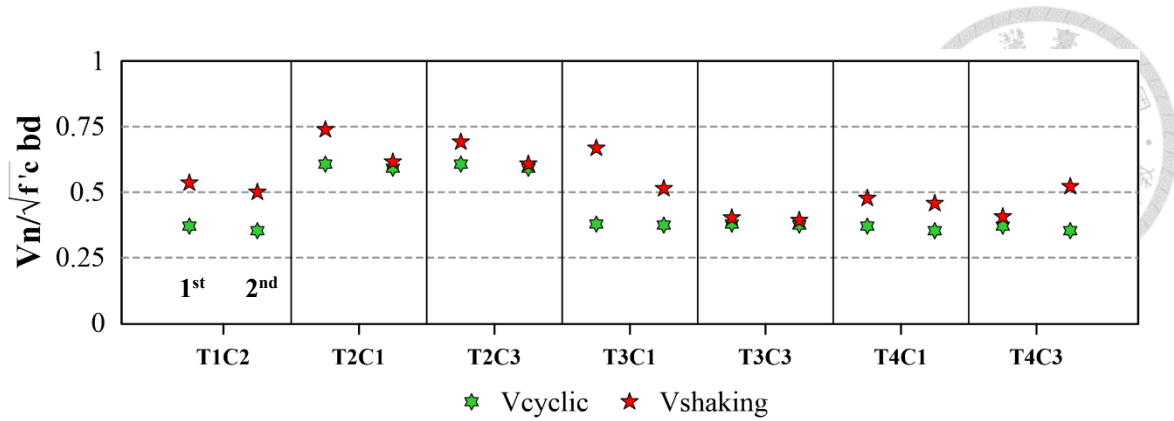
Figure 5-1. Cyclic loading and shaking table test column strength comparison
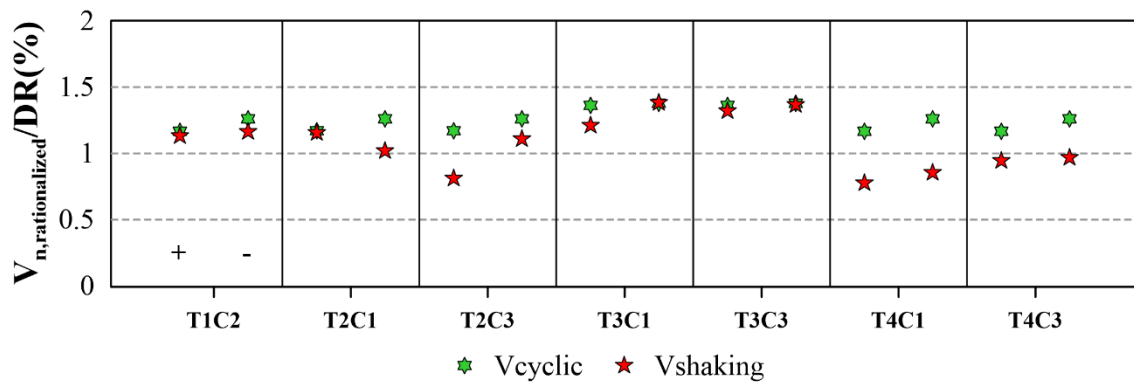
Figure 5-2. Cyclic loading and shaking table test column stiffness comparison
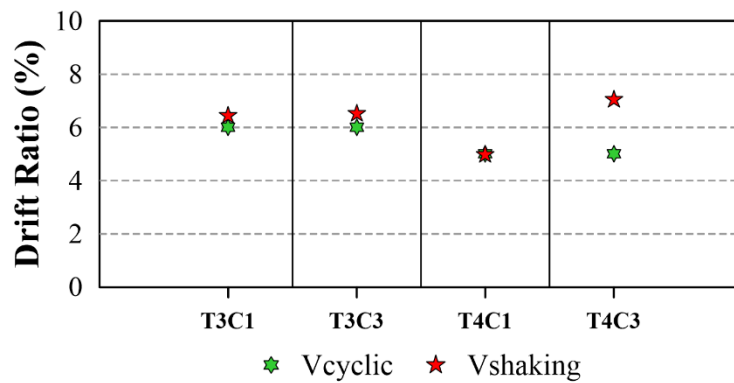
Figure 5-3. Cyclic loading and shaking table test column collapse point comparison

464
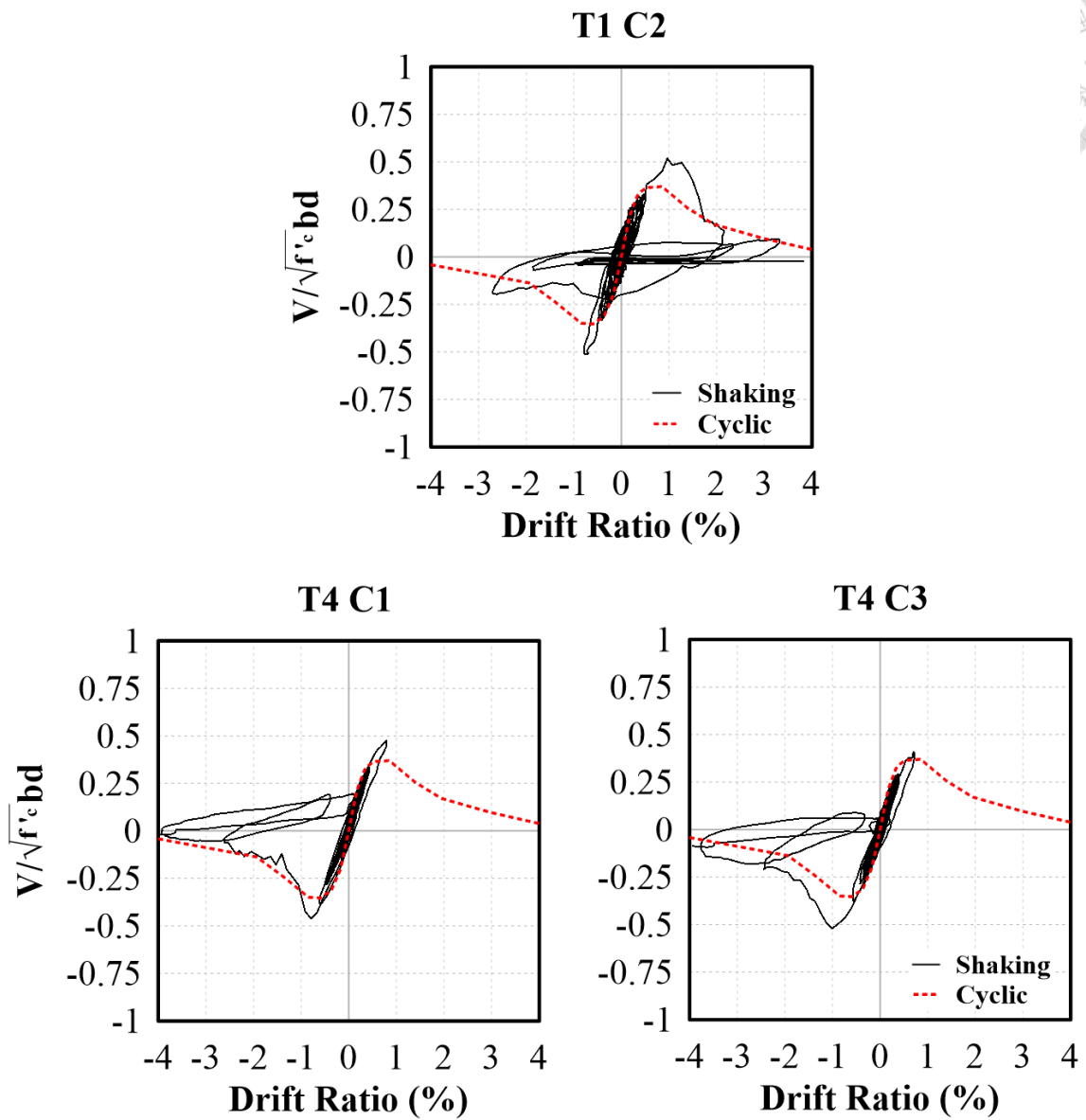
Figure 5-4. Specimen 4NL load-displacement relationship comparison
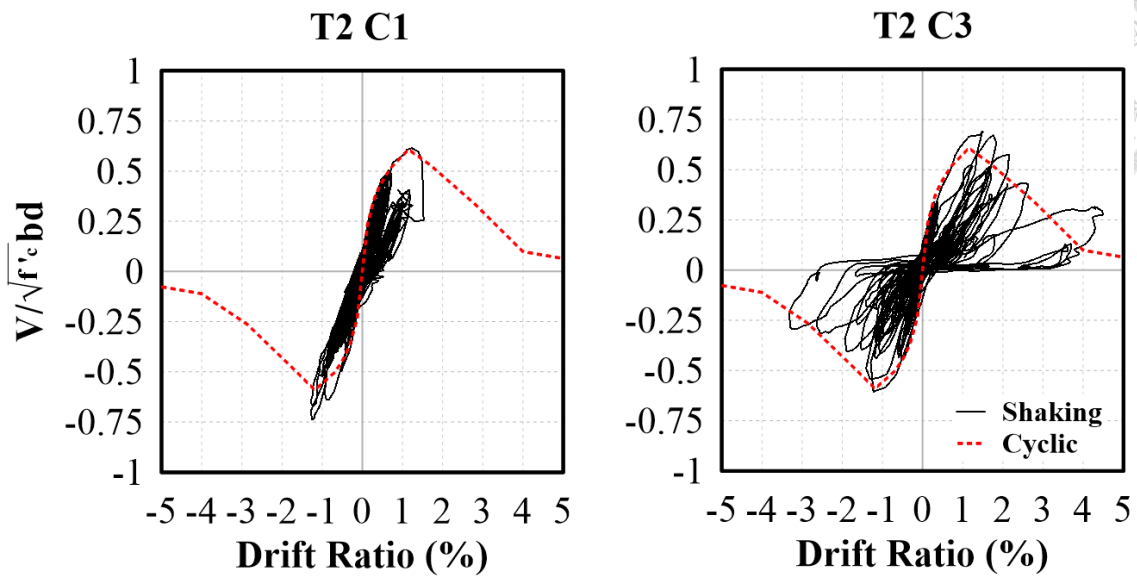
Figure 5-5. Specimen 3DL load-displacement relationship comparison
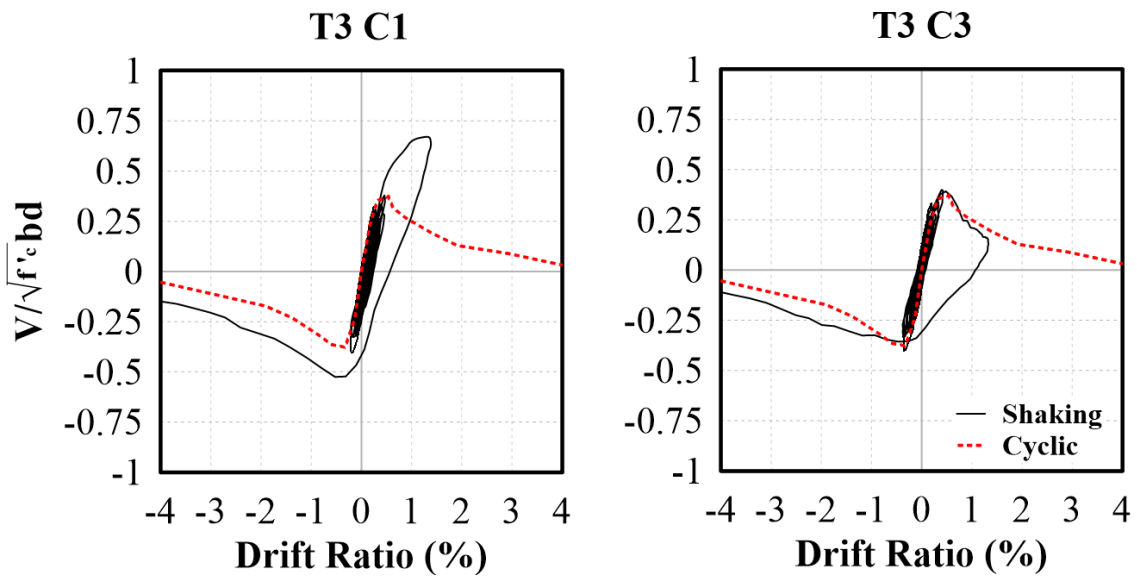
Figure 5-6. Specimen 3NL load-displacement relationship comparison

466
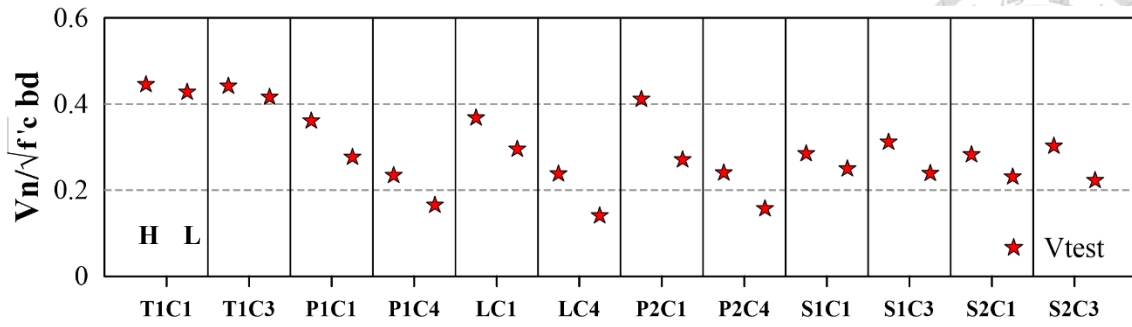
Figure 5-7. Flexural strength of column due to varying axial load
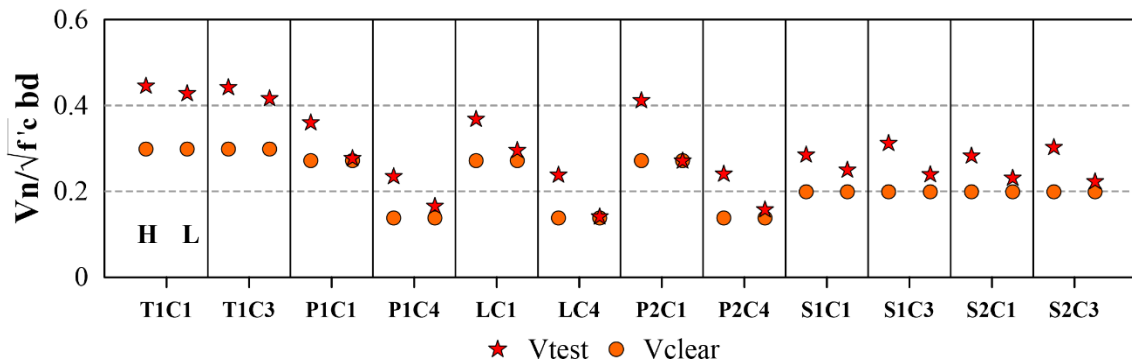
Figure 5-8. Modeling of column flexural strength without axial load
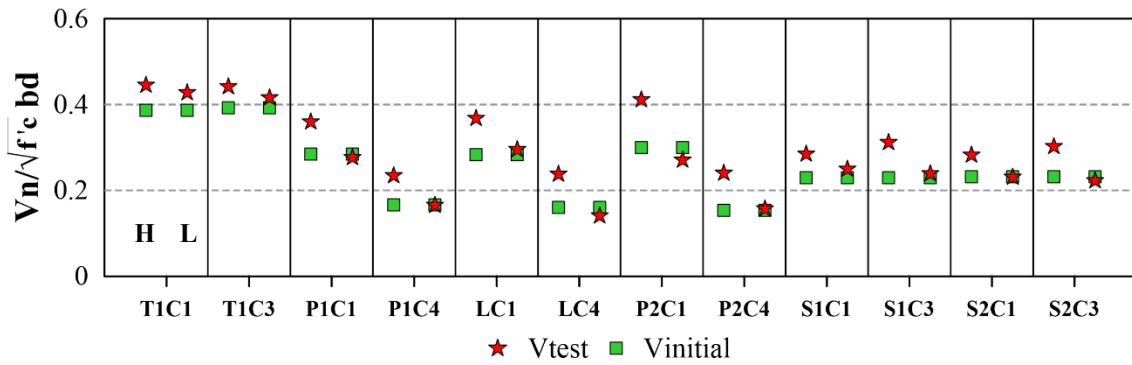
Figure 5-9. Modeling of column flexural strength with initial axial load

467
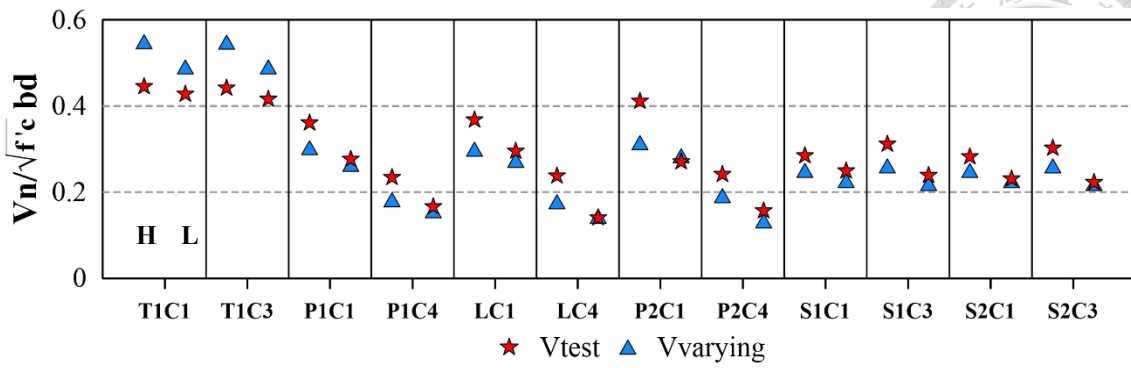
Figure 5-10. Modeling of column flexural strength considering varying axial load
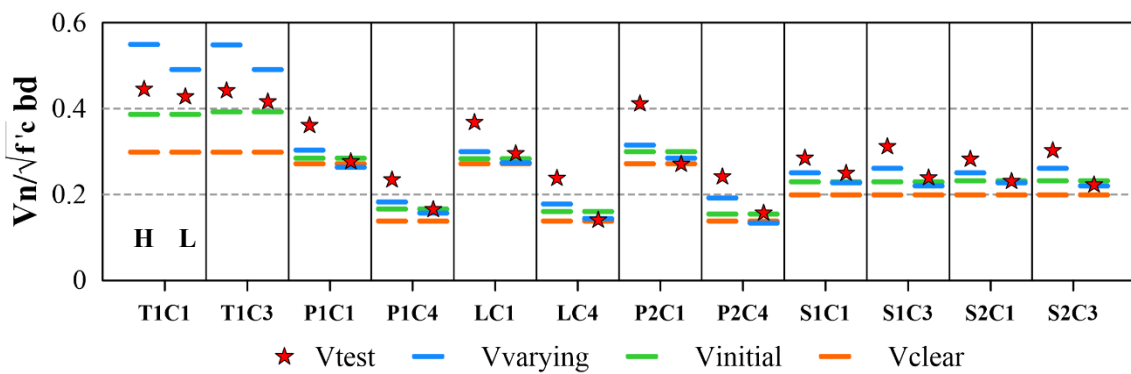
Figure 5-11. Comparison on modeling of column flexural strength
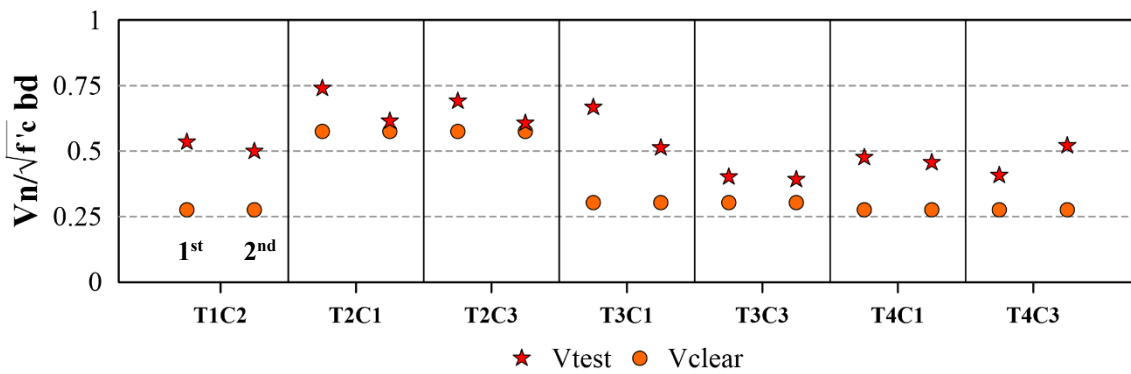
Figure 5-12. Modeling of column shear strength without axial load

468
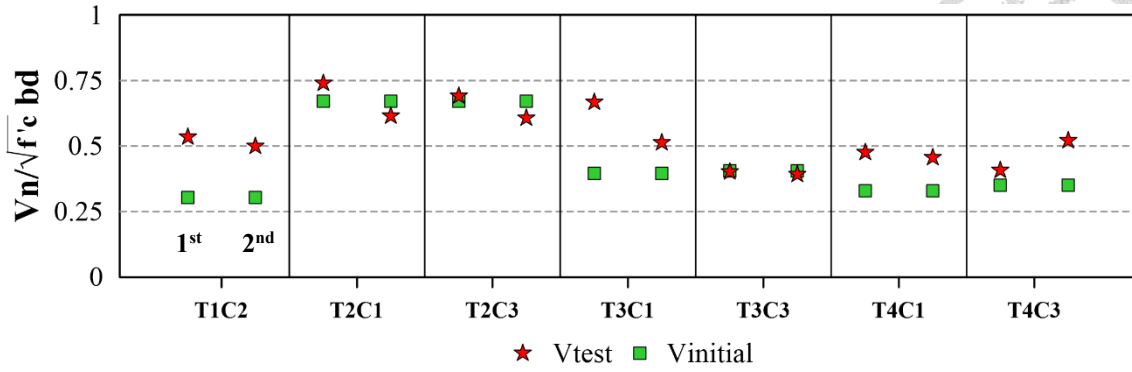
Figure 5-13. Modeling of column shear strength with initial axial load
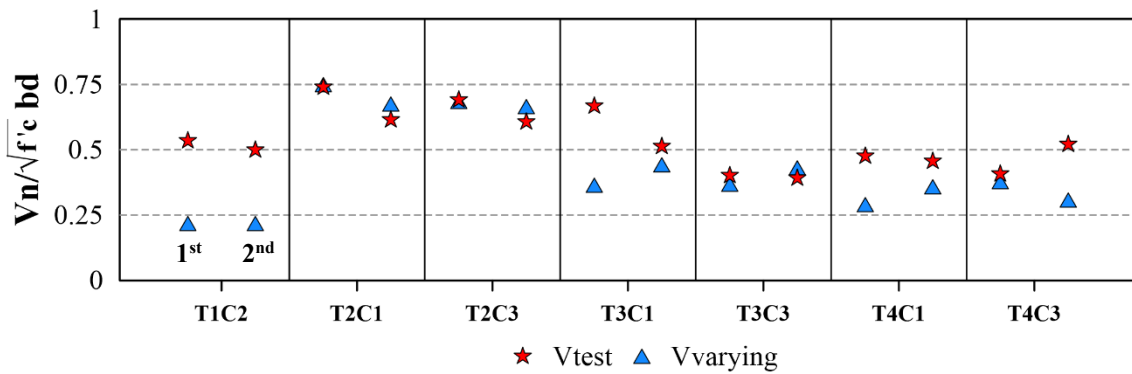
Figure 5-14. Modeling of column shear strength considering varying axial load
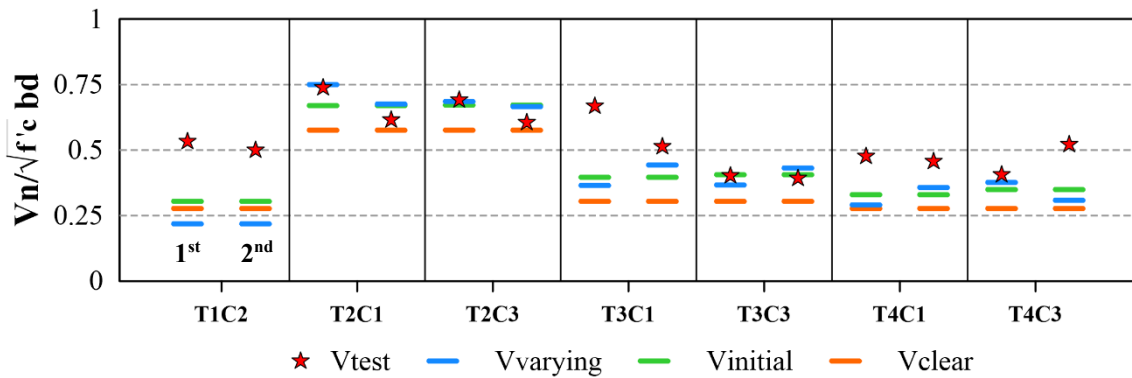
Figure 5-15. Comparison on modeling of column shear strength

469
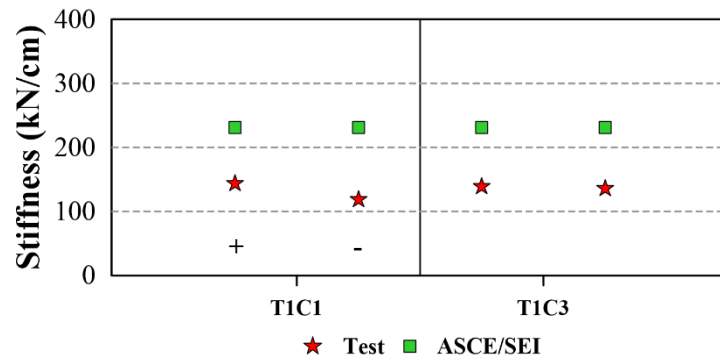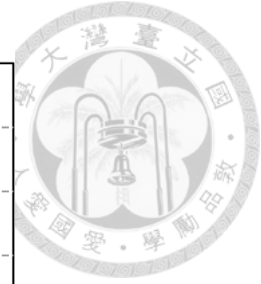
Figure 5-16. Modeling of flexural-column effective stiffness by ASCE/SEI 41-17 (2017)
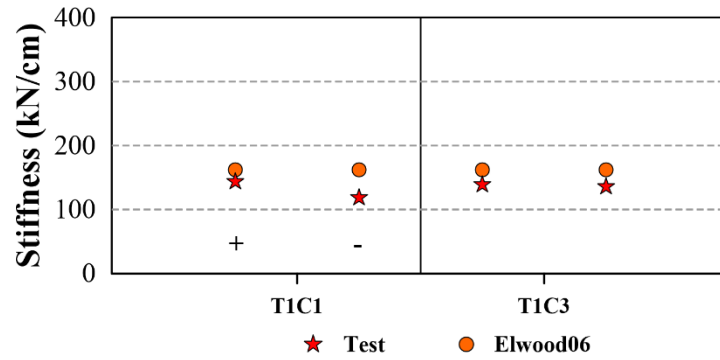
Figure 5-17. Modeling of flexural-column effective stiffness by Elwood and Eberhard (2006)
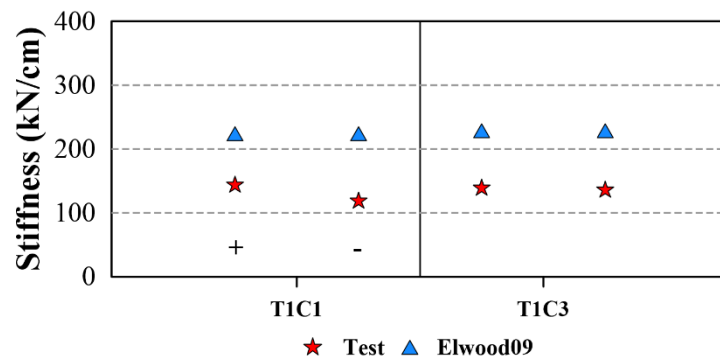
Figure 5-18. Modeling of flexural-column effective stiffness by Elwood and Eberhard (2009)

470
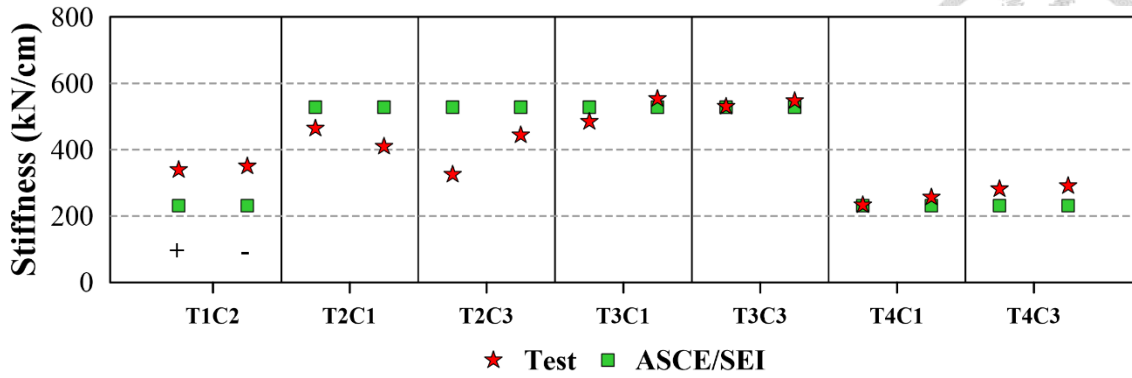
**Figure 5-19. Modeling of shear-column effective stiffness
by ASCE/SEI 41-17 (2017)**
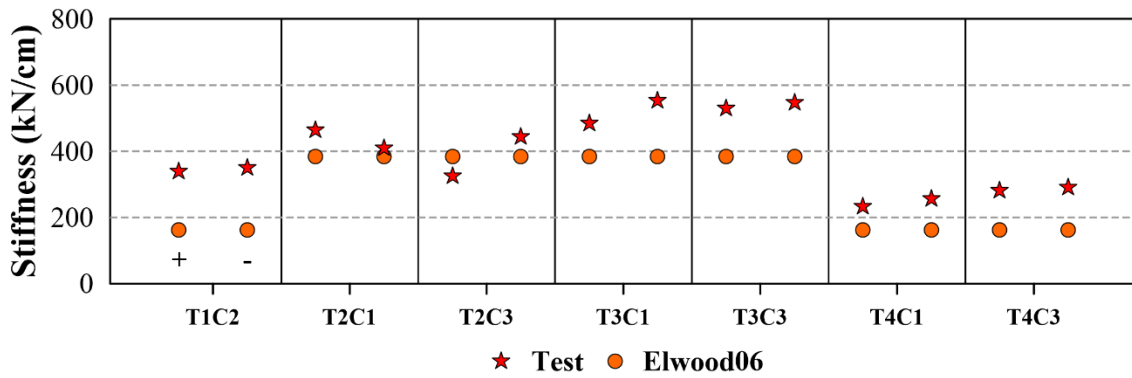
**Figure 5-20. Modeling of shear-column effective stiffness
by Elwood and Eberhard (2006)**
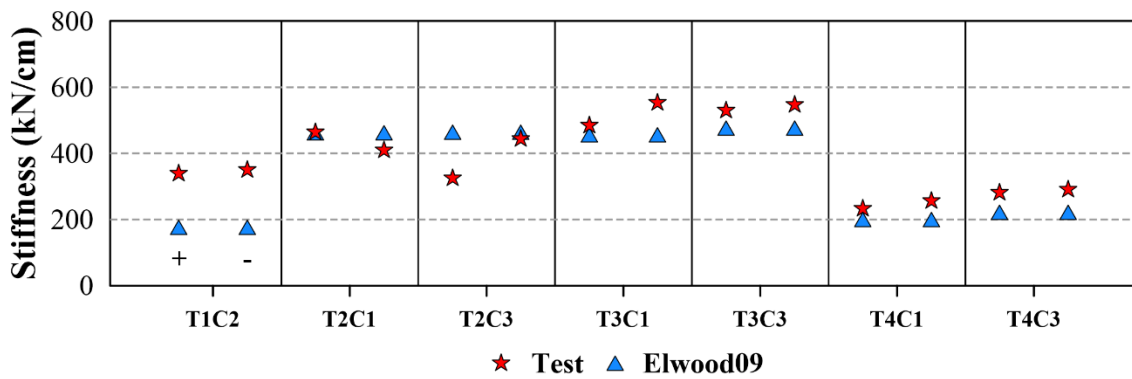
**Figure 5-21. Modeling of shear-column effective stiffness
by Elwood and Eberhard (2009)**

471
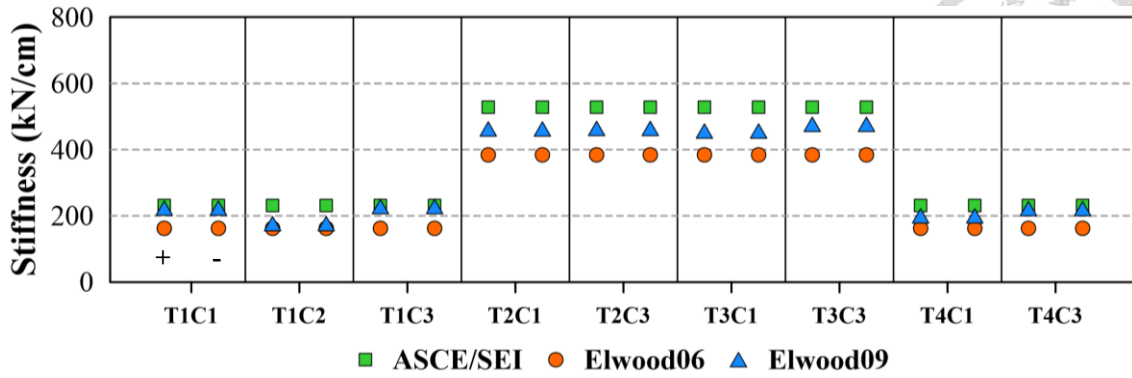
Figure 5-22. Comparison on different effective stiffness models
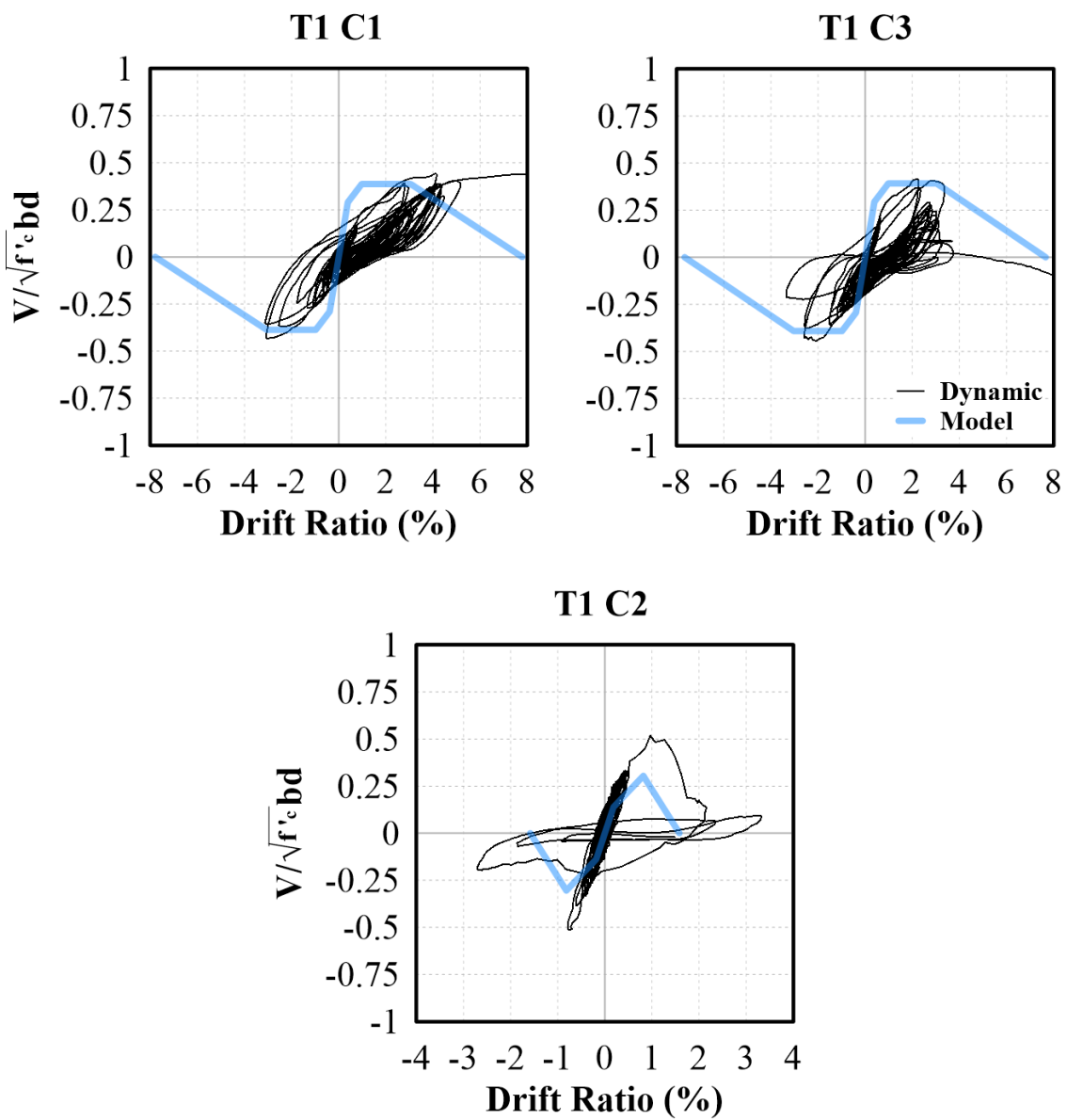
Figure 5-23. Comparison on backbone curves for frame T1 columns

472

T2 C1

T2 C3
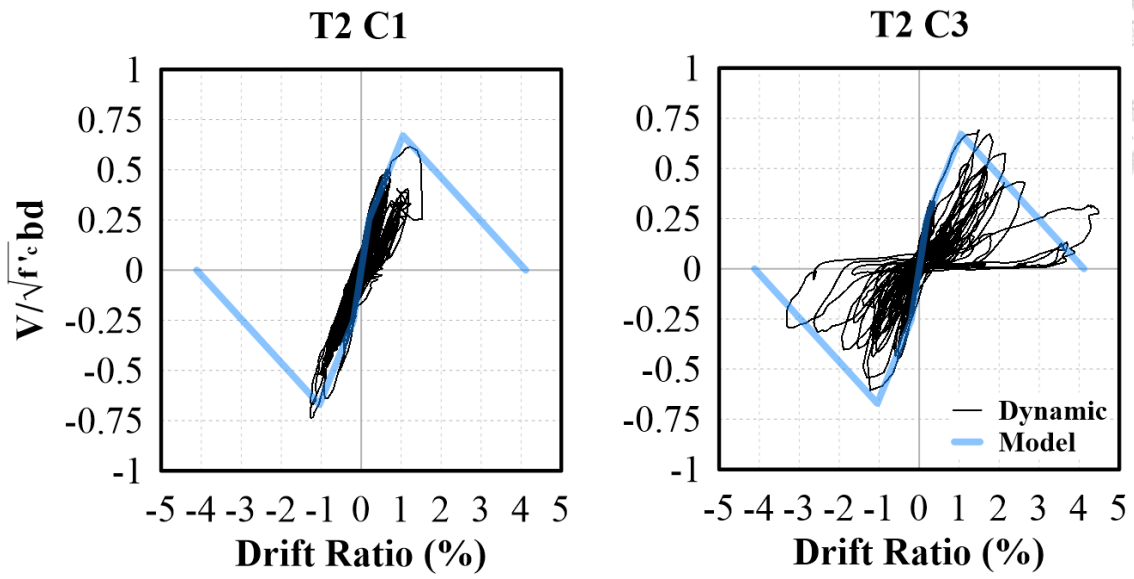
Figure 5-24. Comparison on backbone curves for frame T2 columns

T3 C1

T3 C3
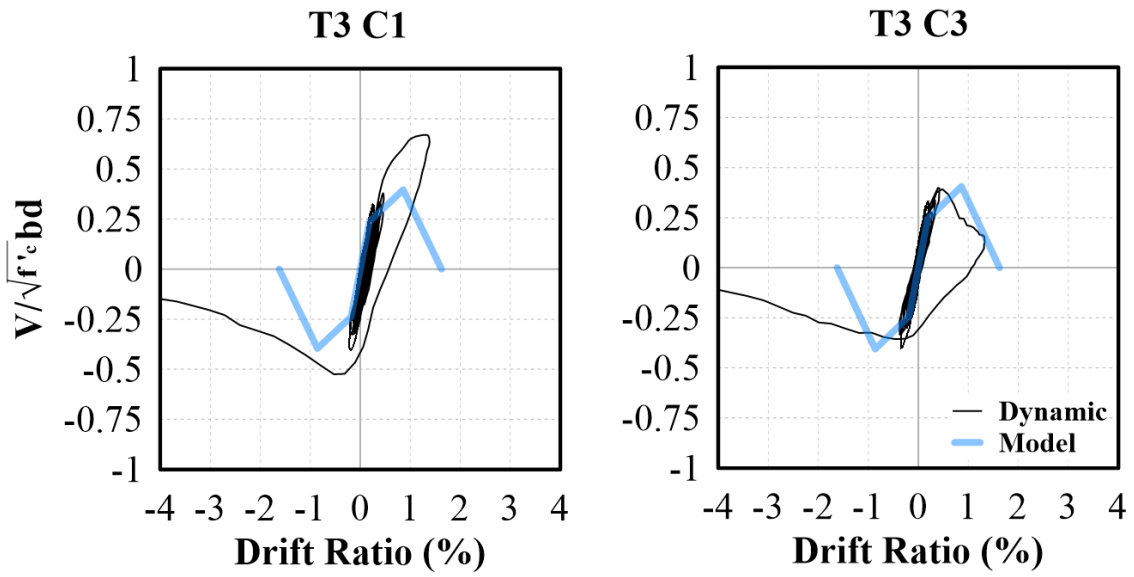
Figure 5-25. Comparison on backbone curves for frame T3 columns

473

T4 C1

T4 C3
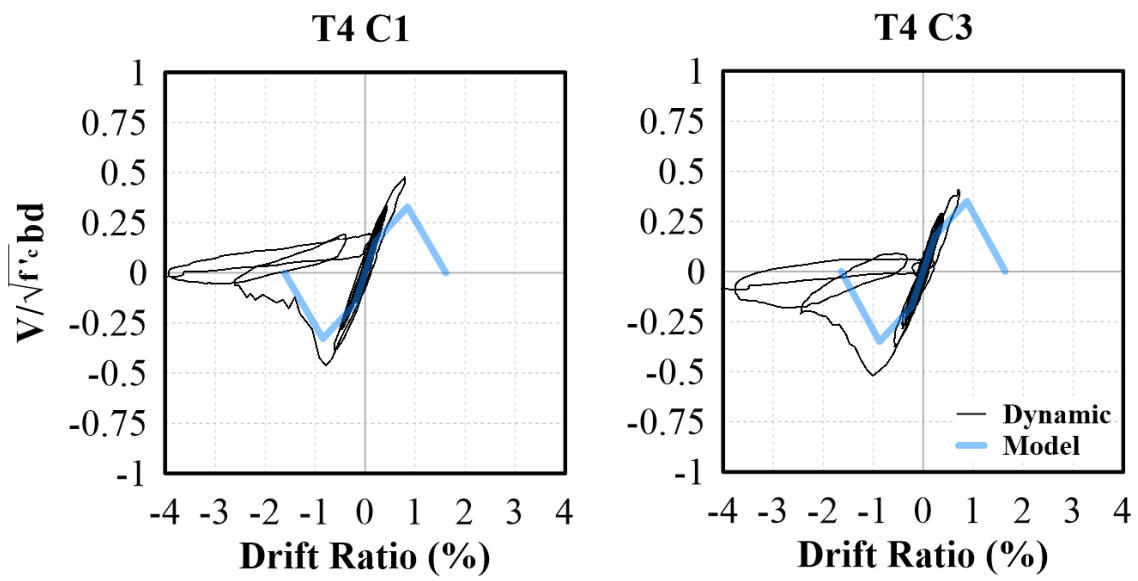
Figure 5-26. Comparison on backbone curves for frame T4 columns

474

Flexure Failure

Flexural-Shear Failure

Shear Failure
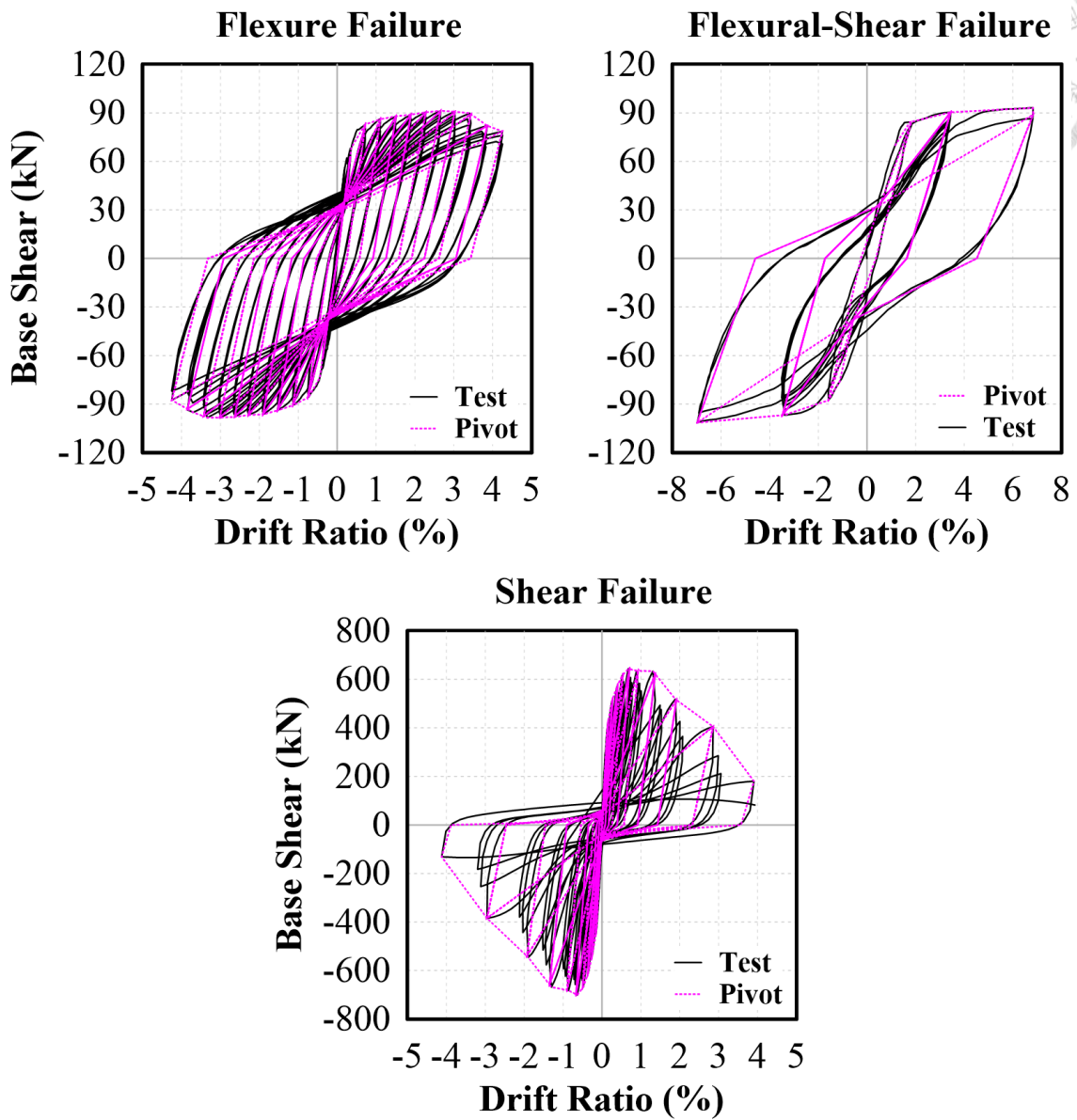
Figure 6-1. Pivot Model simulation result
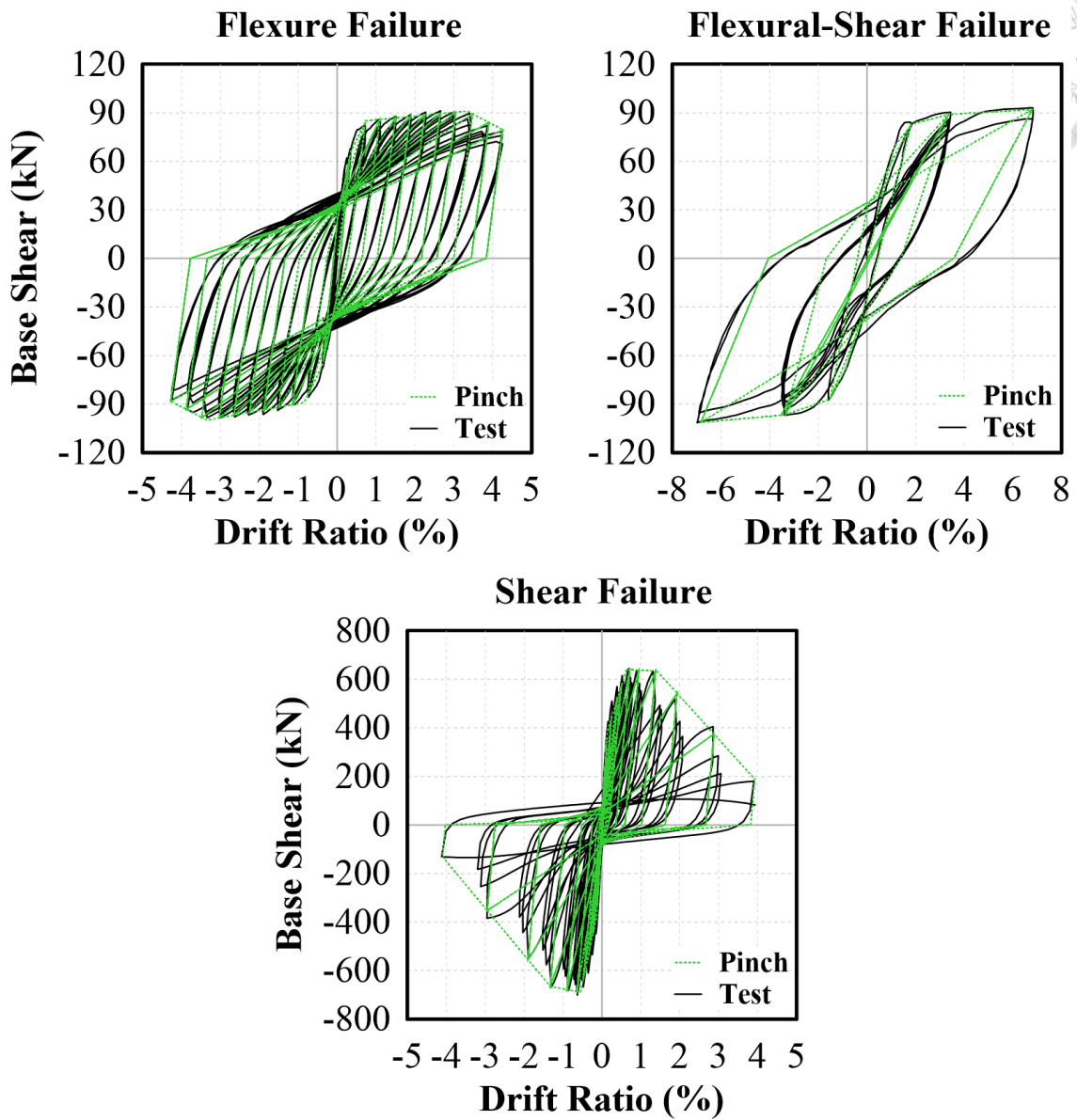
Figure 6-2. Pinching4 Material Model simulation result

476
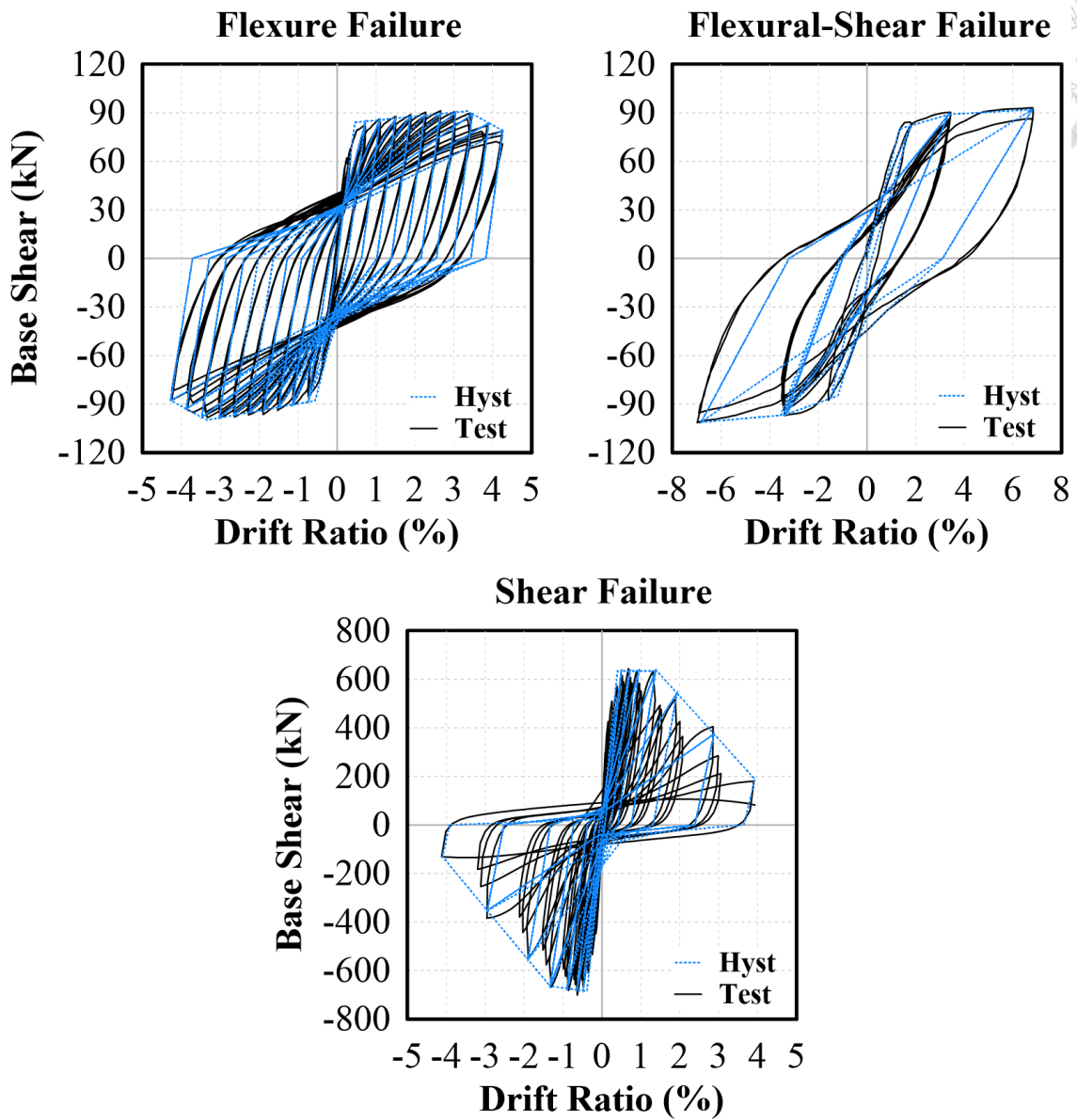
Figure 6-3. Hysteretic Material Model simulation result

477
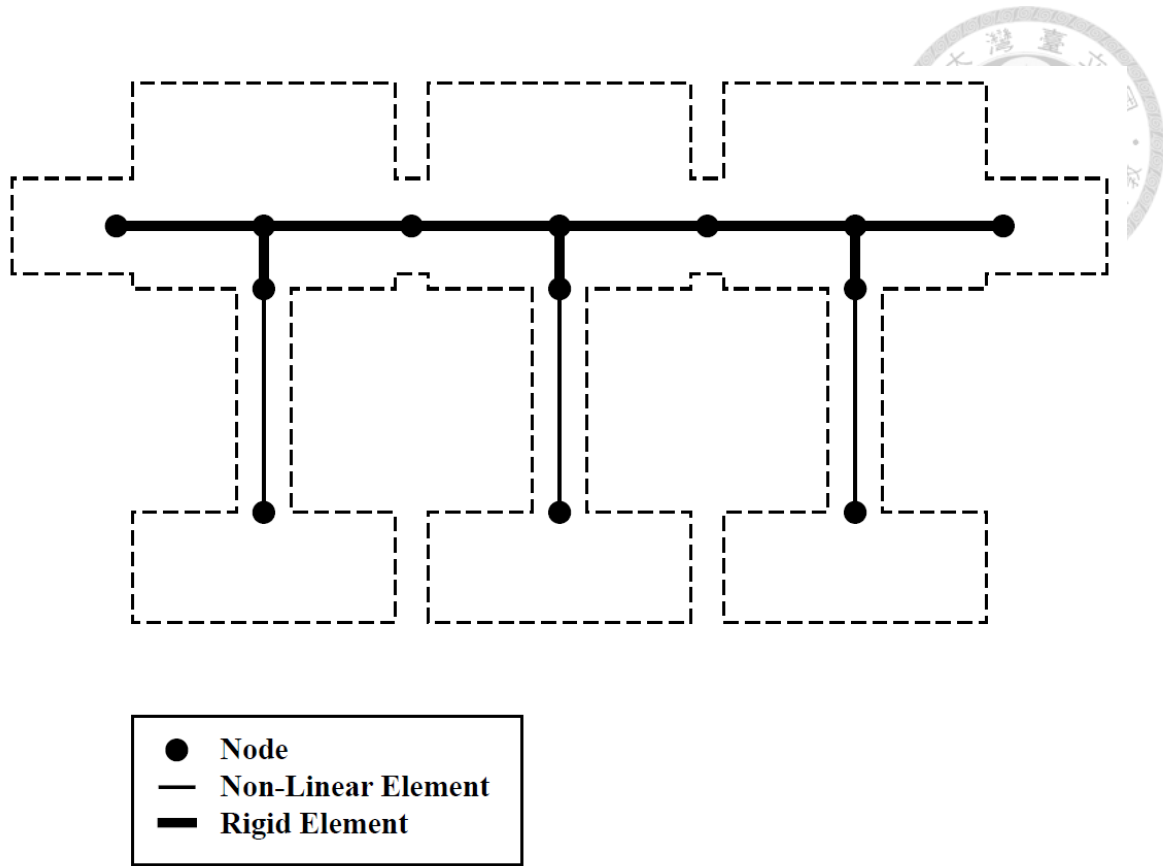
Figure 6-4. Numerical model layout (Frame)

(a) Fiber Model   (b) CPH Model   (c) ETABS Model
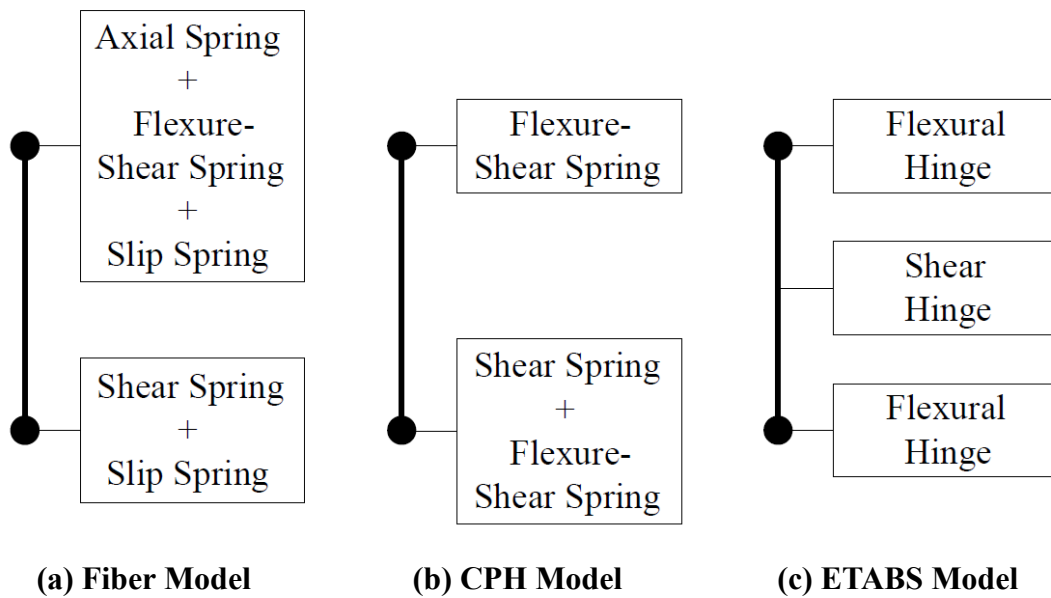
Figure 6-5. Numerical model layout (Member)

478
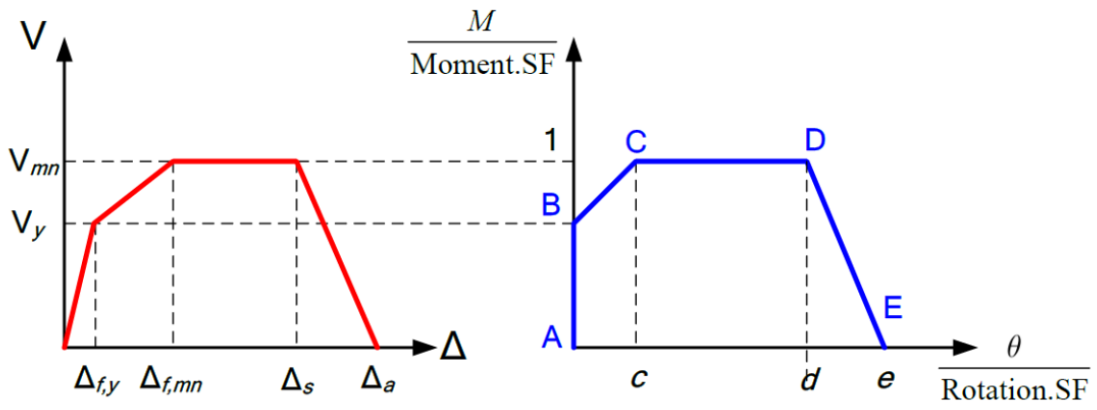
Figure 6-6. Input backbone curve for flexural hinge
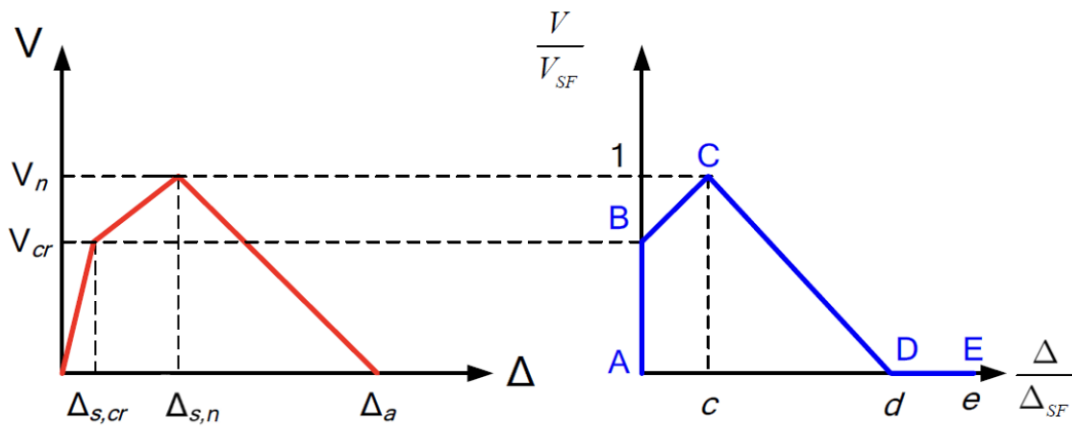
Figure 6-7. Input backbone curve for shear hinge
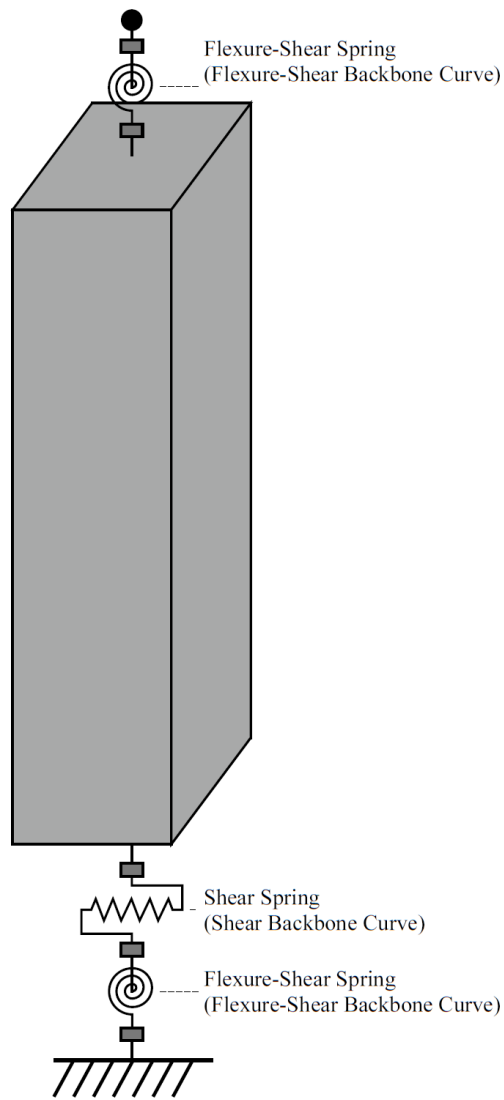
Figure 6-8. CPH model layout
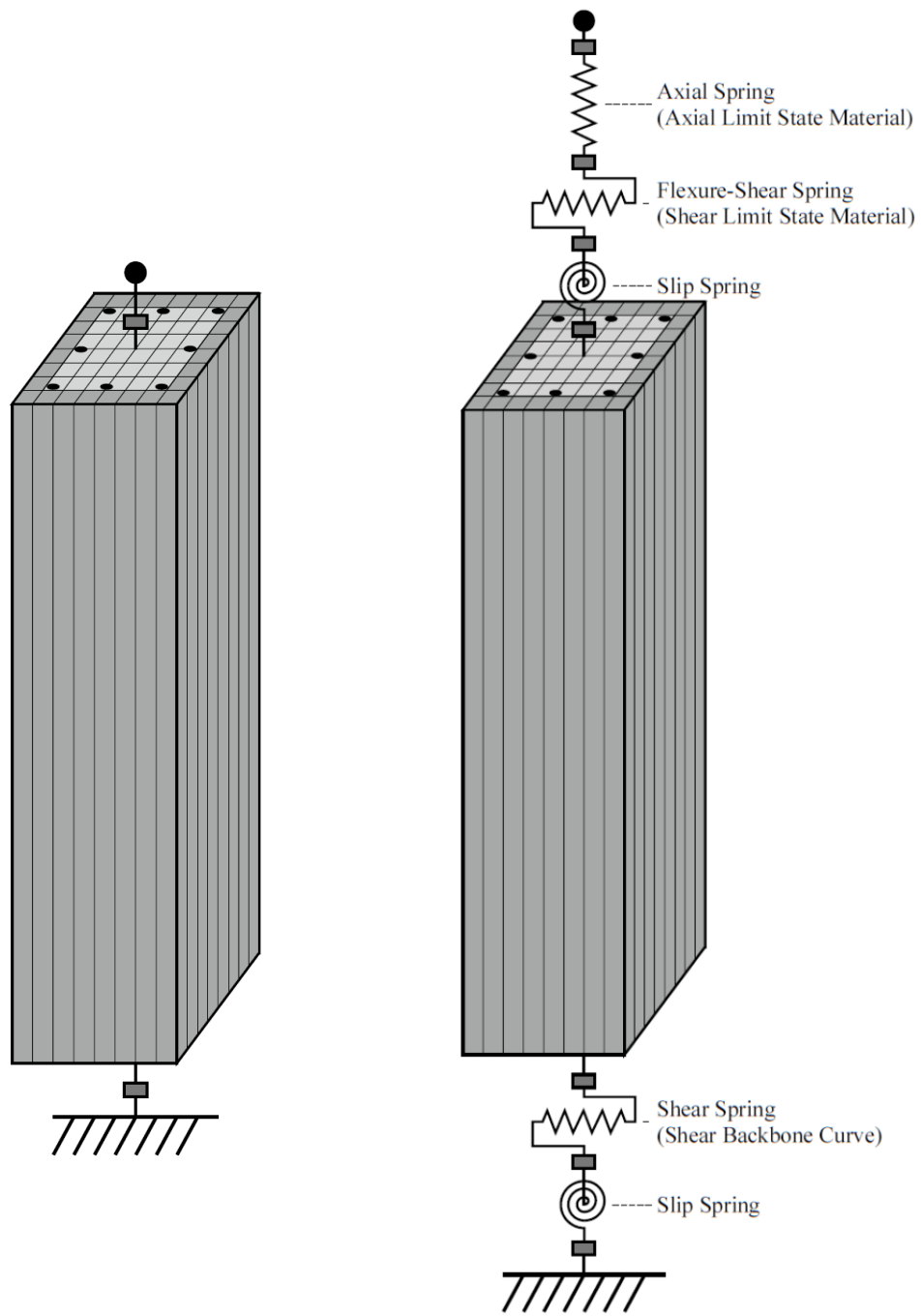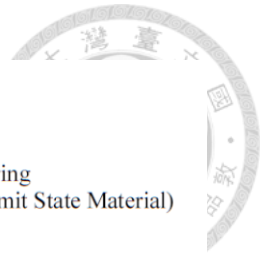
(a) Fiber Model   **(b) Modified Fiber Model**

Figure 6-9. Fiber model layout
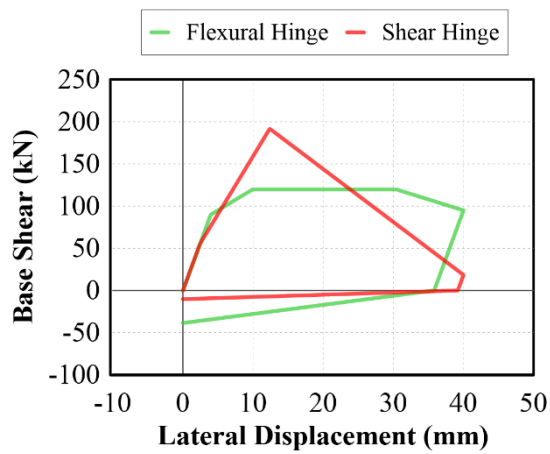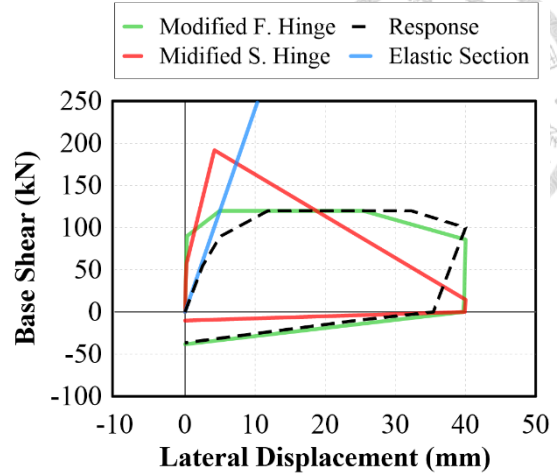
Figure 6-10. CPH model backbone curve for column T1C1 (flexural-dominant)
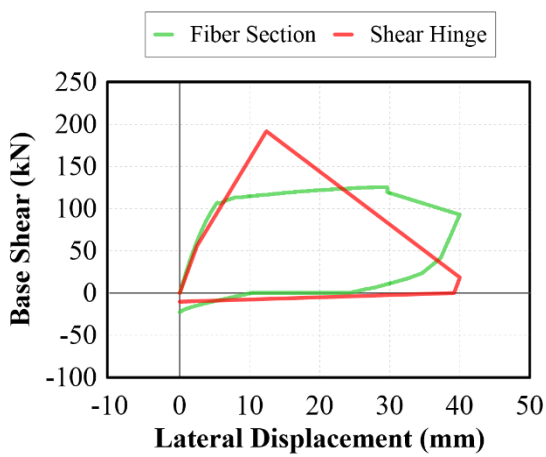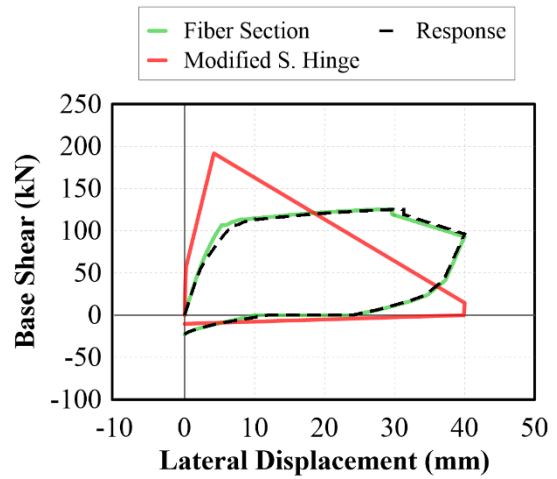
Figure 6-11. Fiber model backbone curve for column T1C1 (flexural-dominant)

482
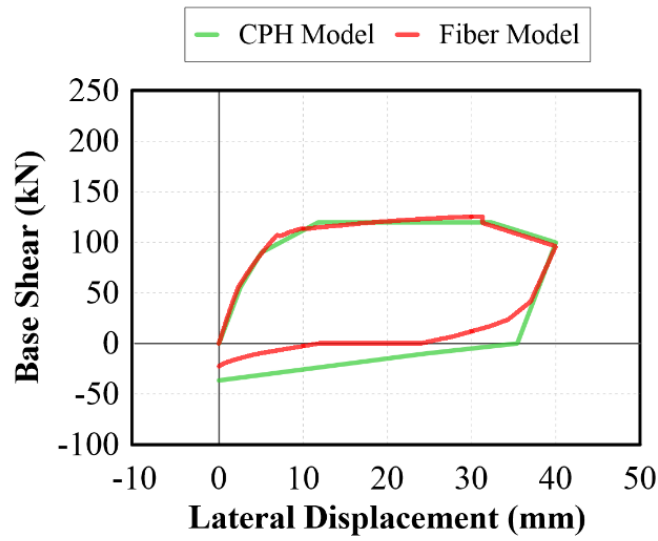
Figure 6-12. Response comparison for column T1C1 (flexural-dominant)

(a)

(b)
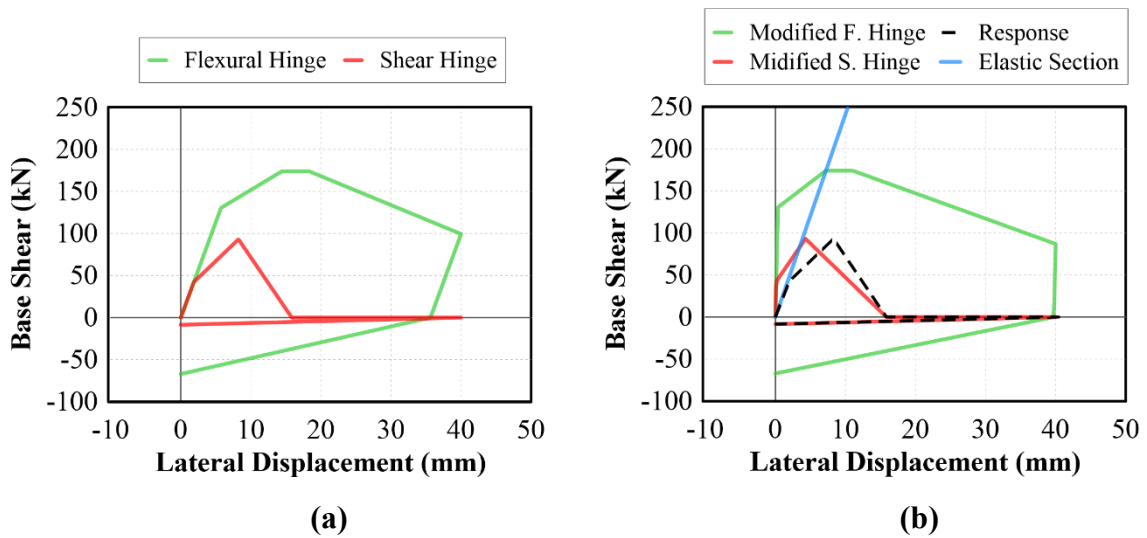
Figure 6-13. CPH model backbone curve for column T1C2 (shear-dominant)

483
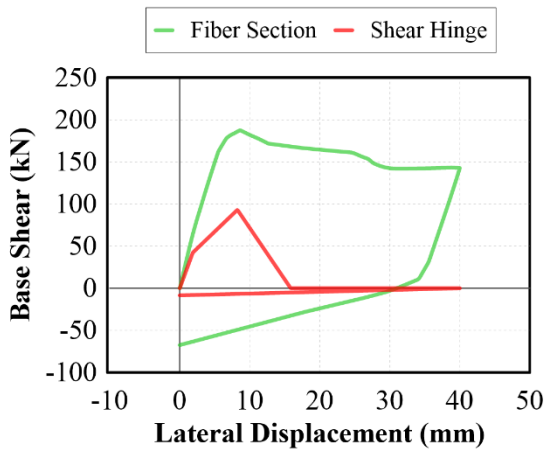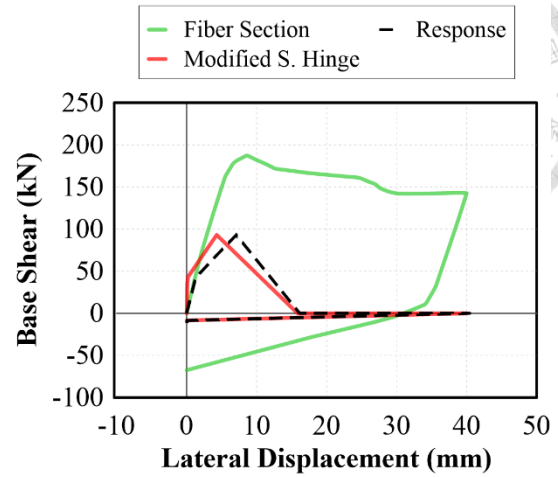
Figure 6-14. Fiber model backbone curve for column T1C2 (shear-dominant)
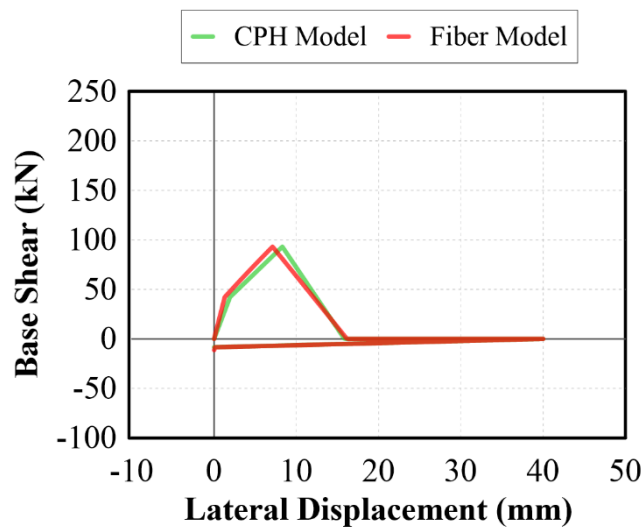
Figure 6-15. Response comparison for column T1C2 (shear-dominant)

484
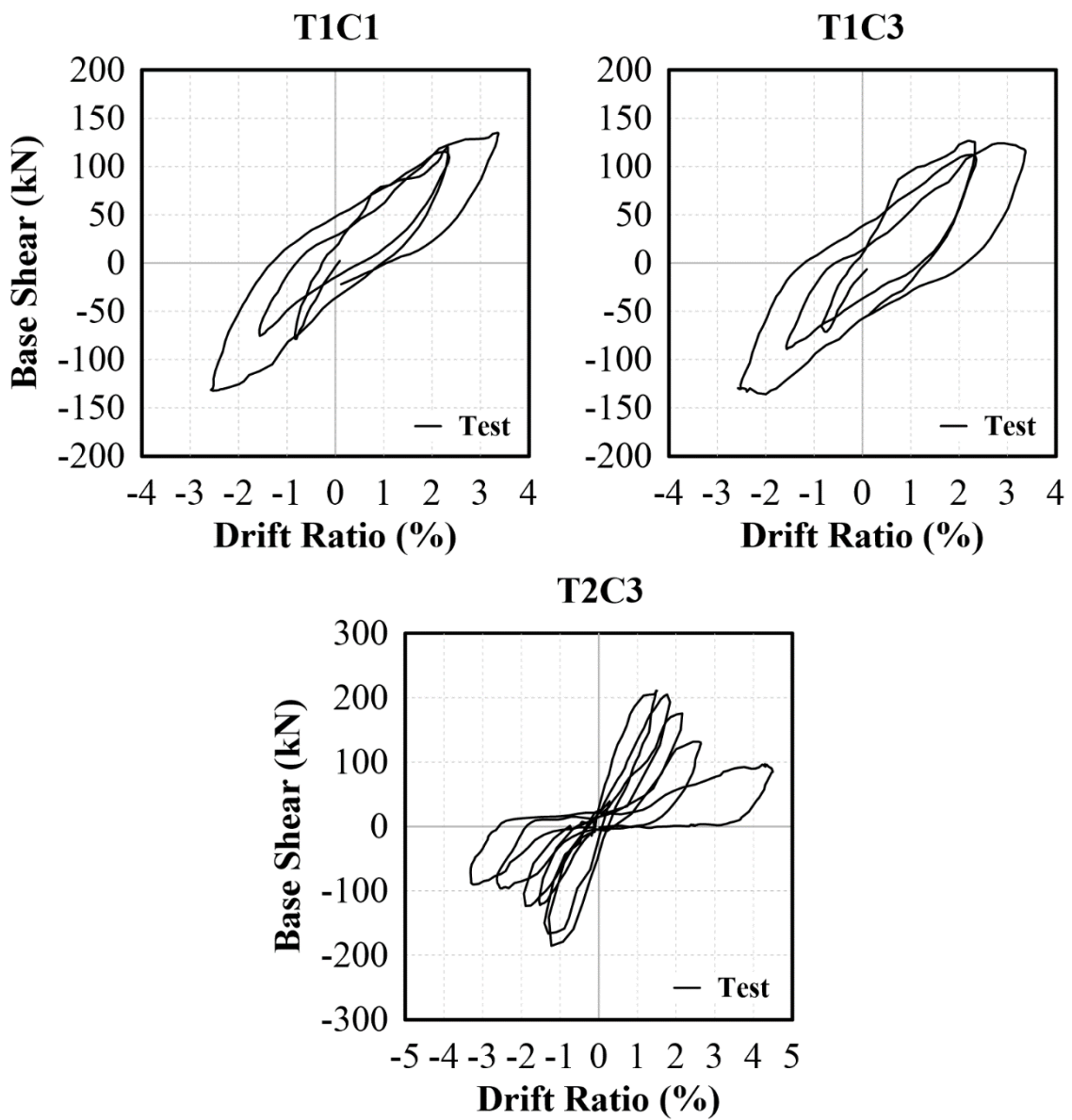
Figure 6-16. Shaking table test response for displacement history analysis
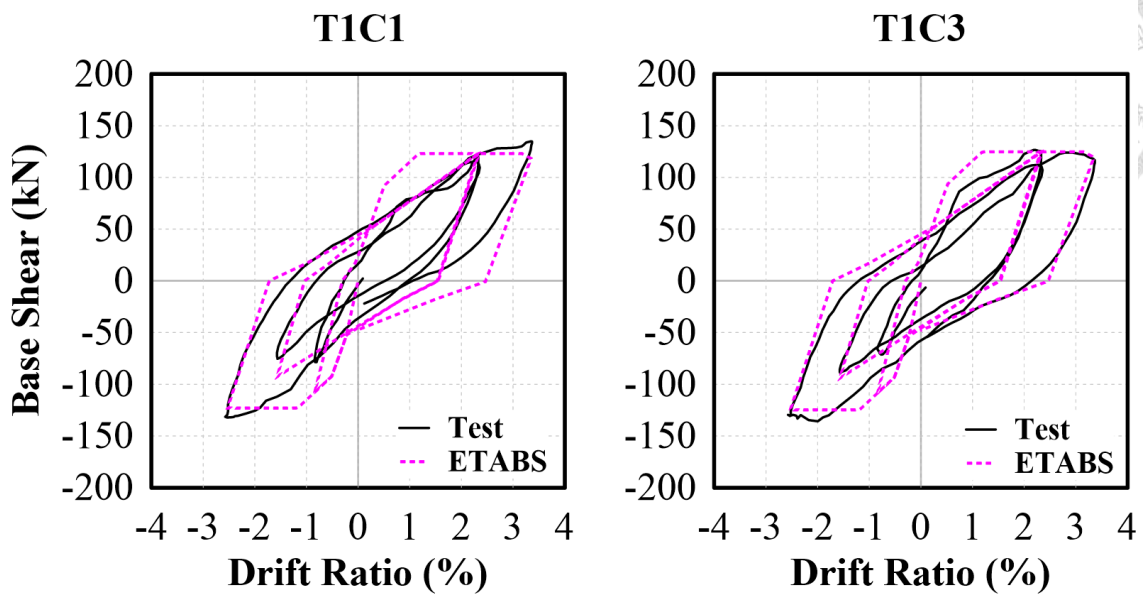
Figure 6-17. ETABS model flexural response for displacement history analysis
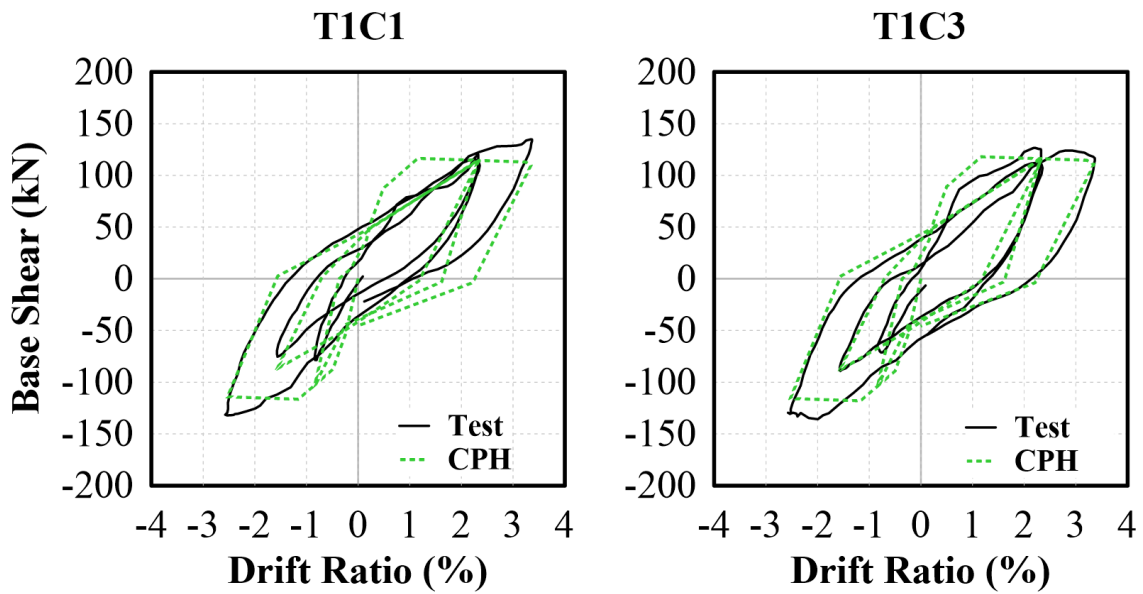
Figure 6-18. CPH model flexural response for displacement history analysis

486
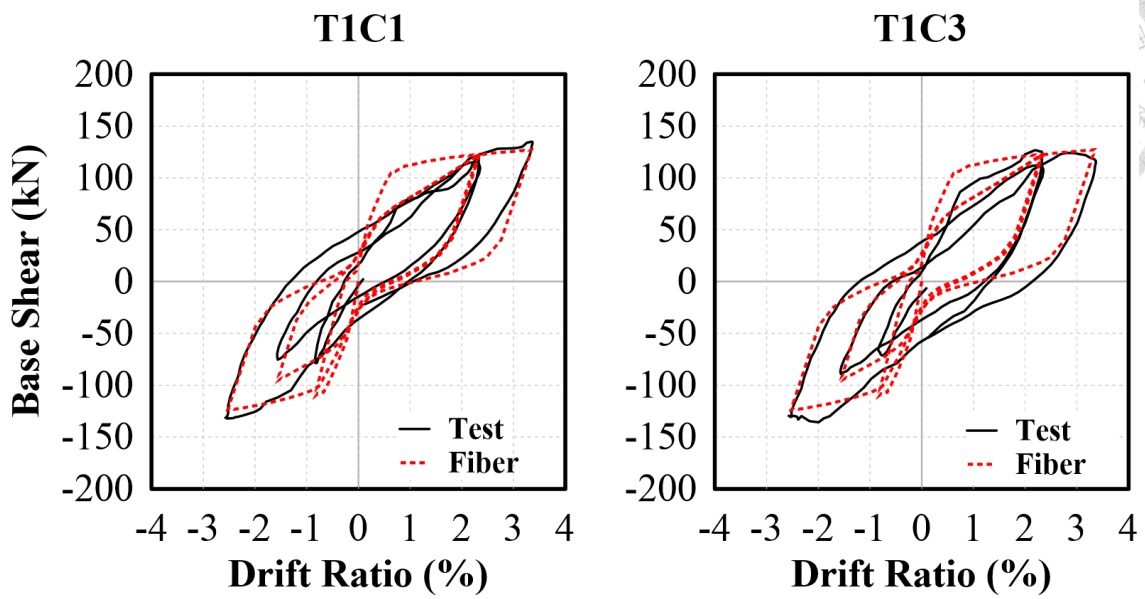
Figure 6-19. Fiber model flexural response for displacement history analysis
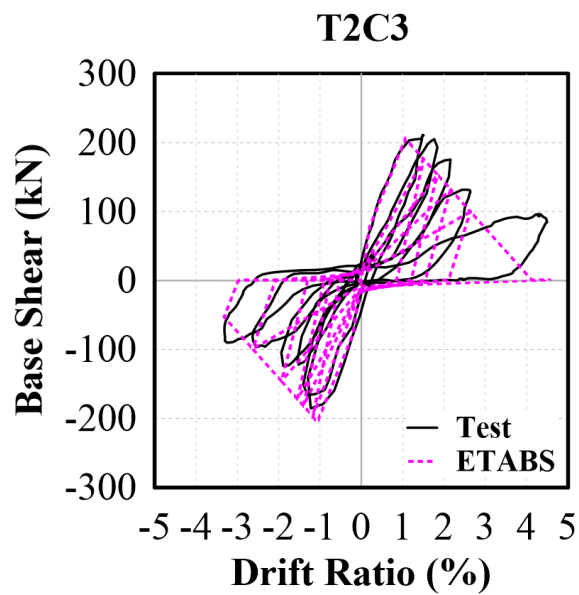
Figure 6-20. ETABS model shear response for displacement history analysis

487

T2C3
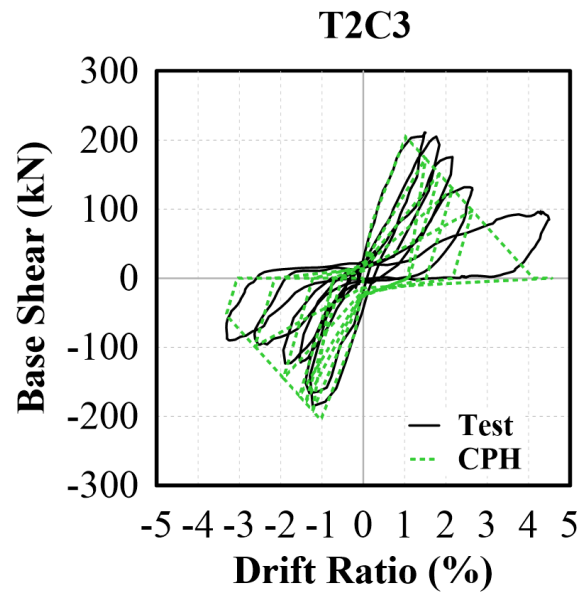
Figure 6-21. CPH model shear response for displacement history analysis

T2C3
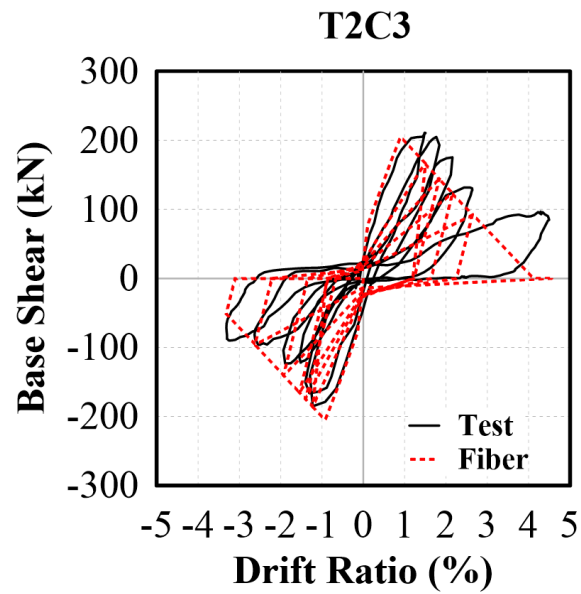
**Figure 6-22. Fiber model shearresponse for displacement history analysis**

488
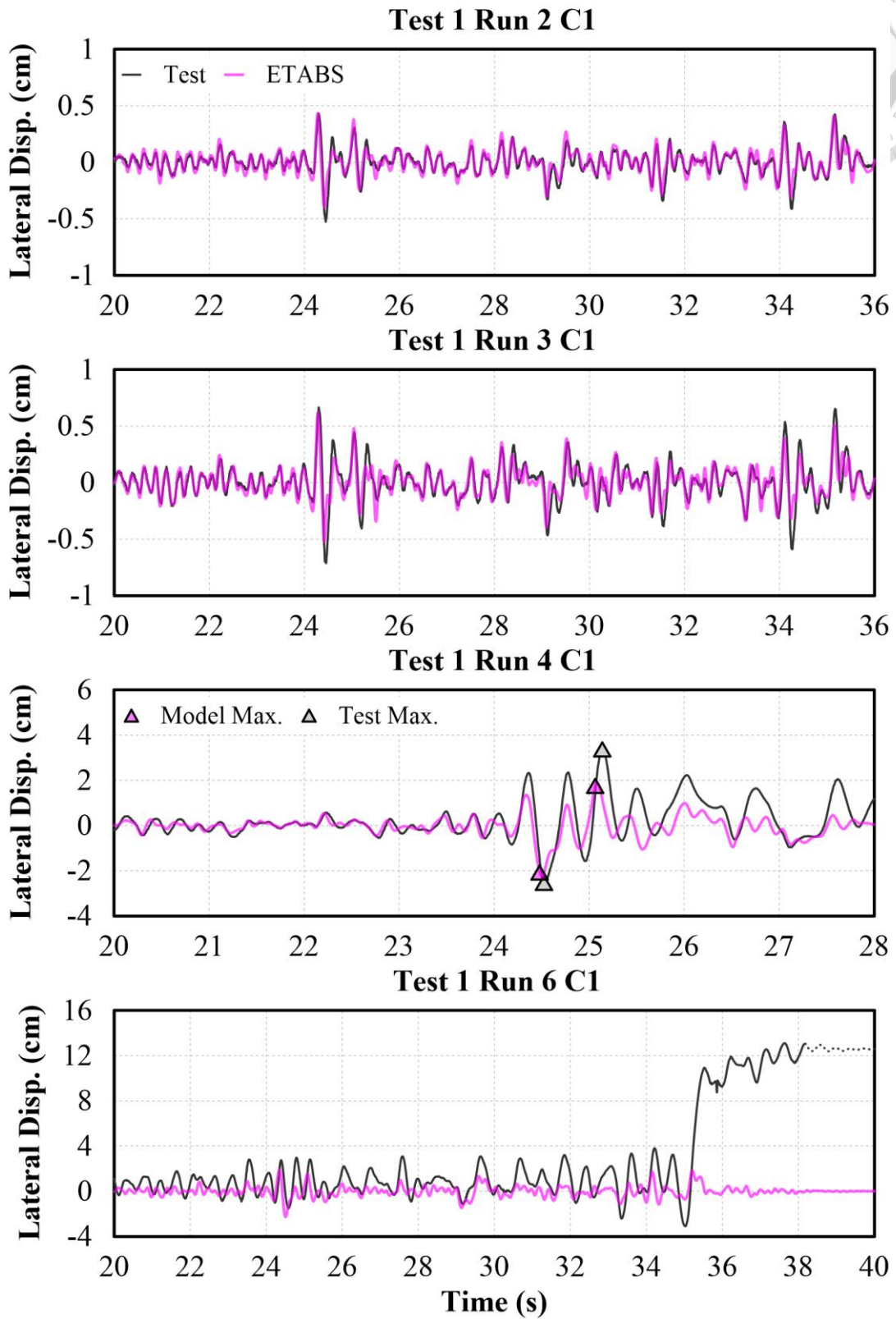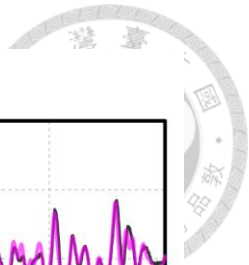
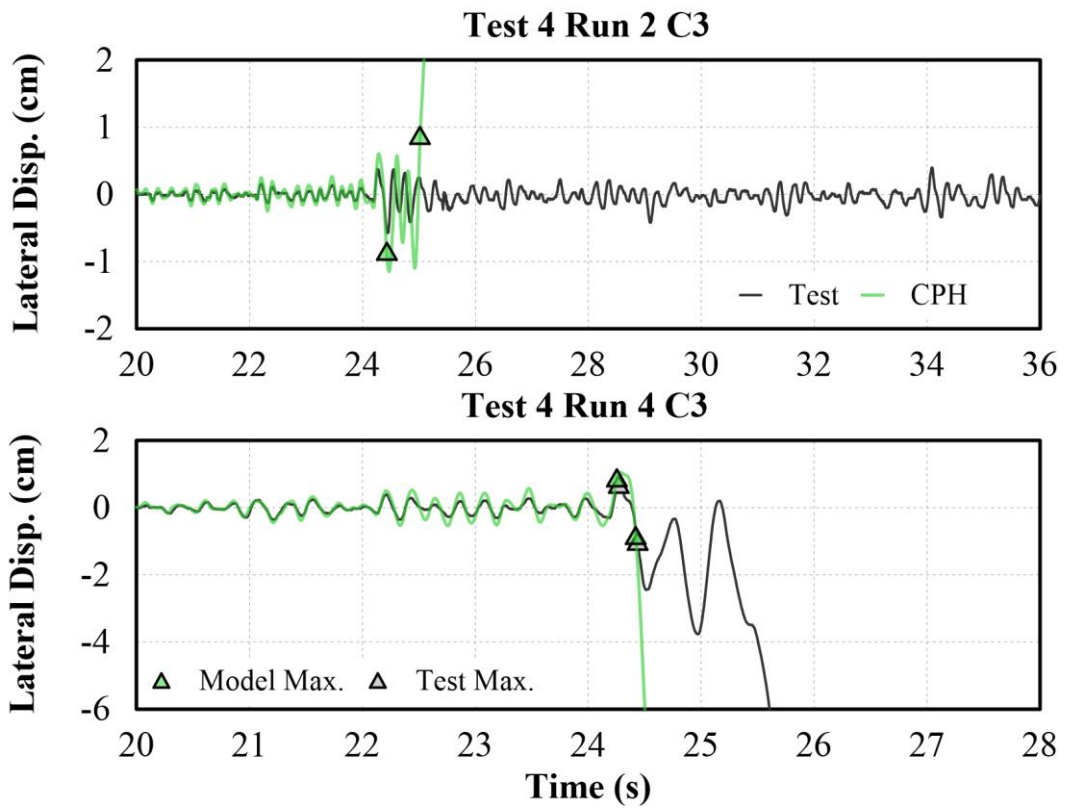**Figure 6-23. Comparison on T1 C1 lateral displacement for ETABS model**
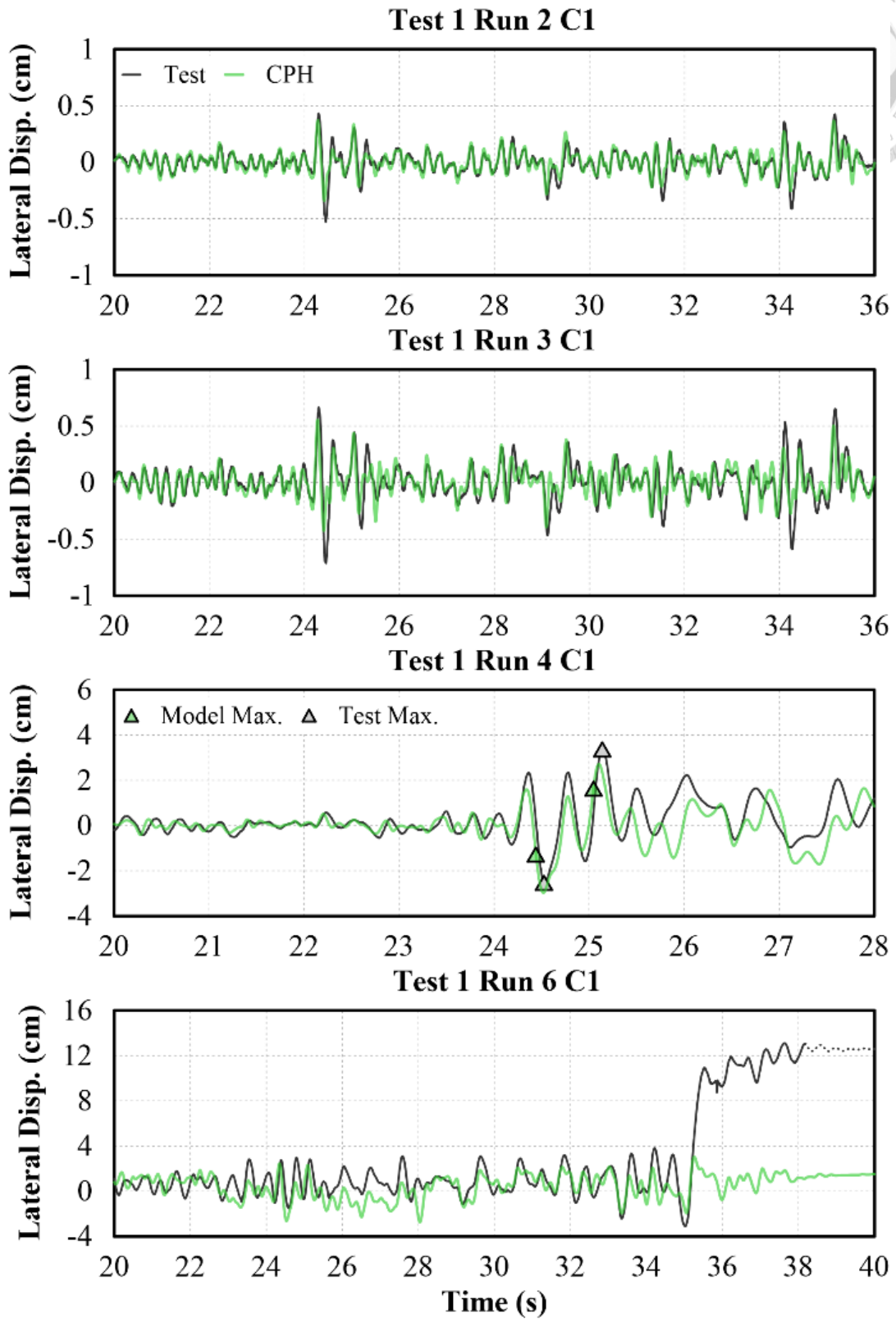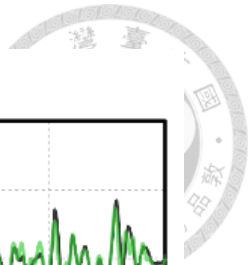
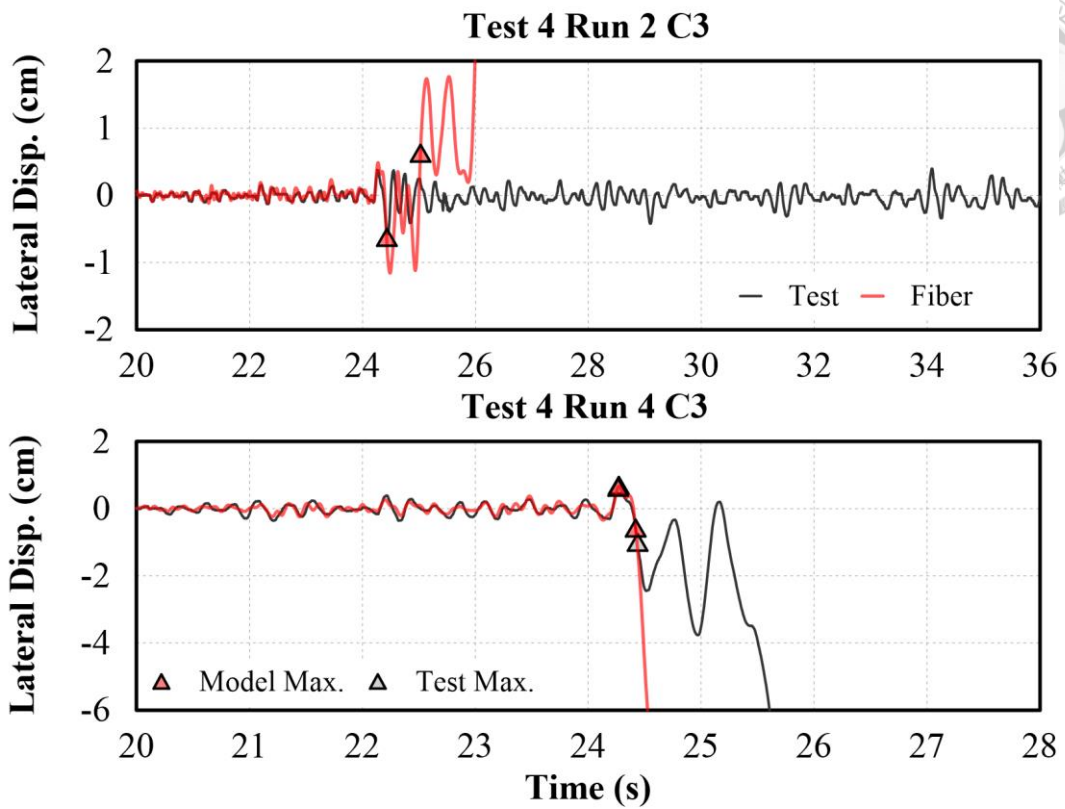**Figure 6-24. Comparison on T1 C1 lateral displacement for CPH model**

490
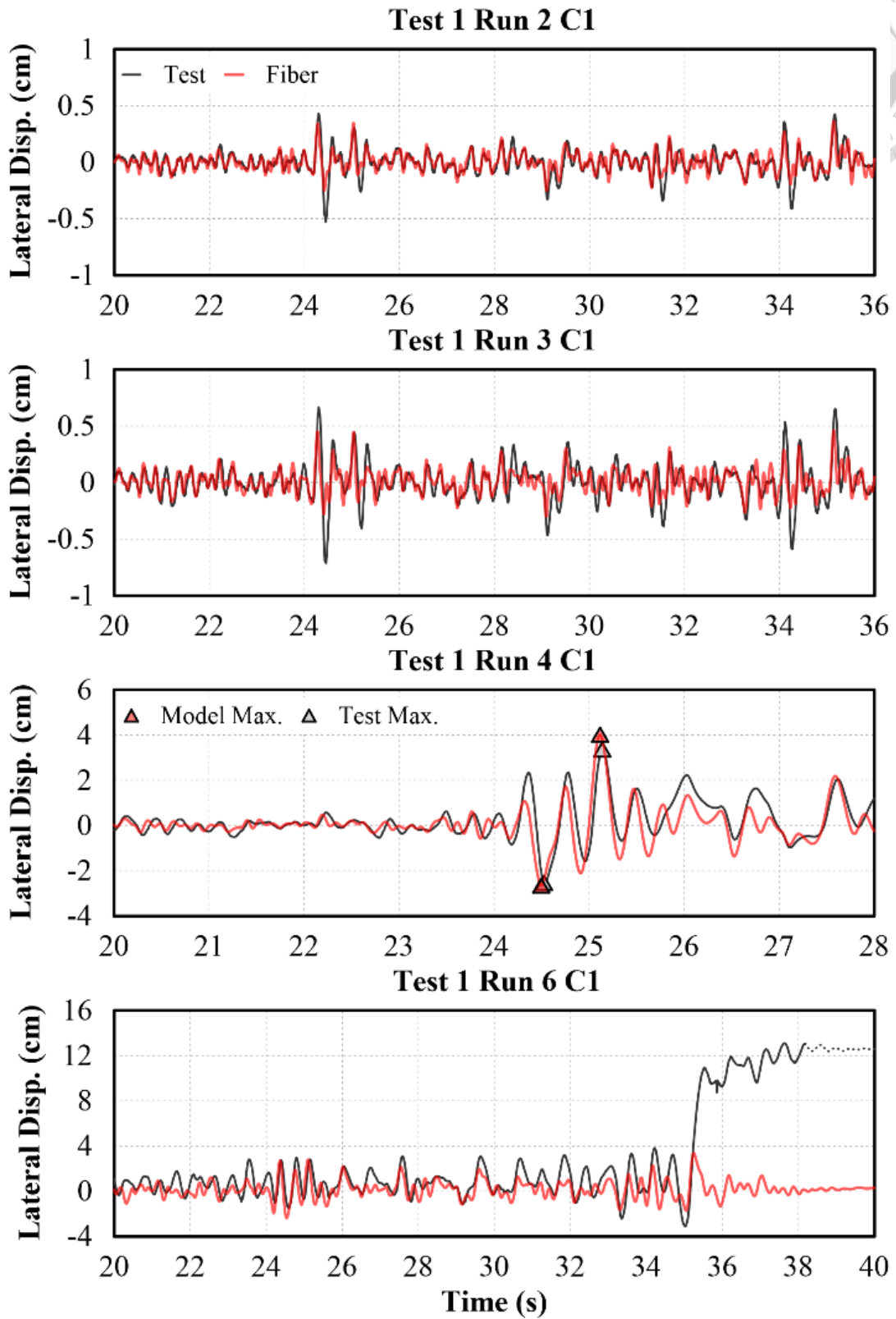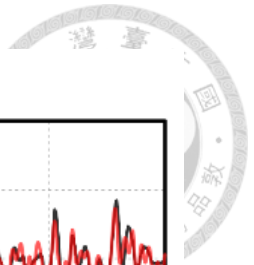
Figure 6-25. Comparison on T1 C1 lateral displacement for Fiber model
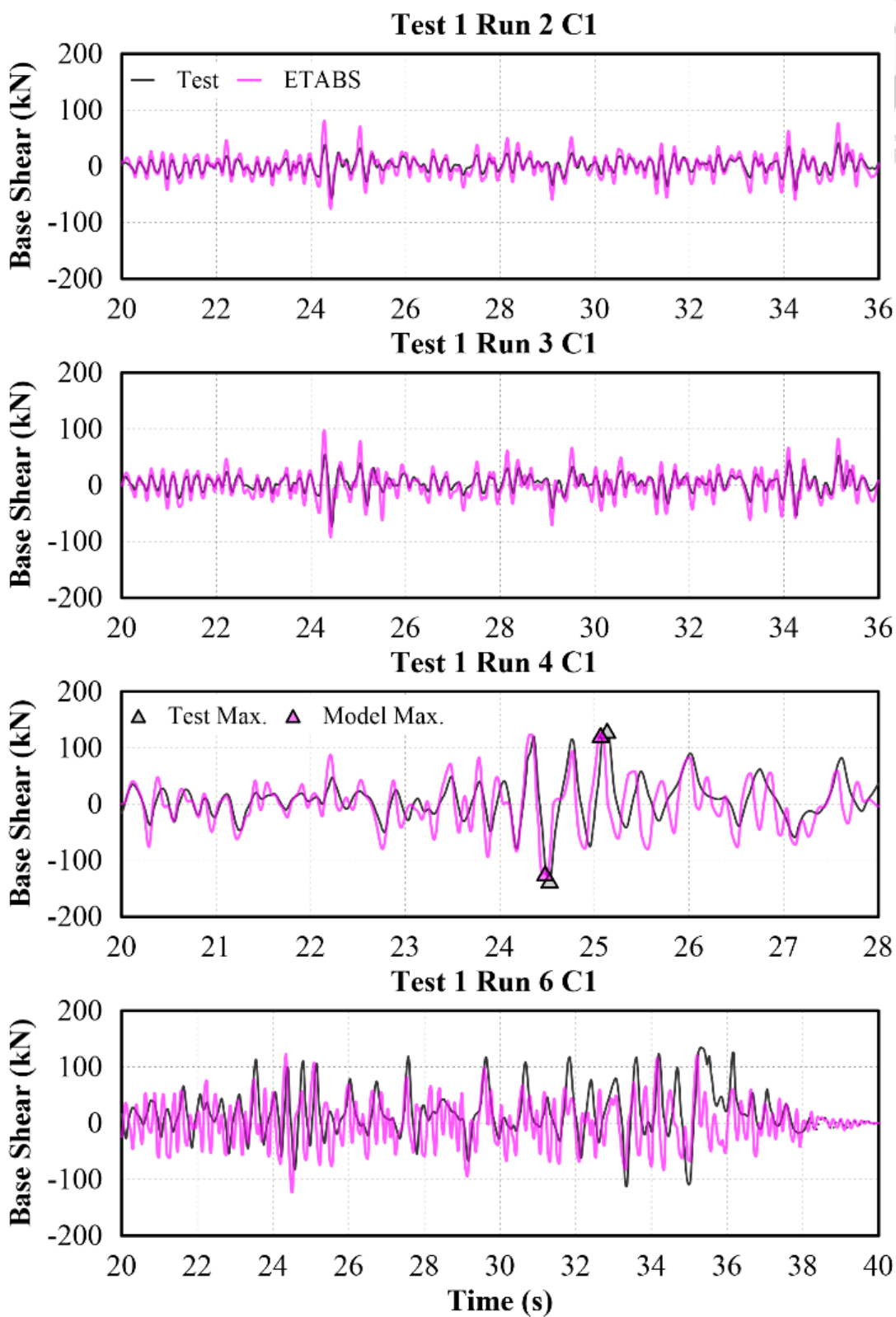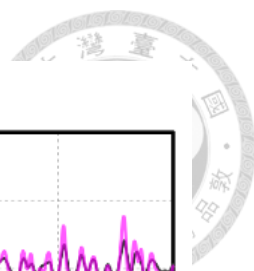
Figure 6-26. Comparison on T1 C1 base shear for ETABS model
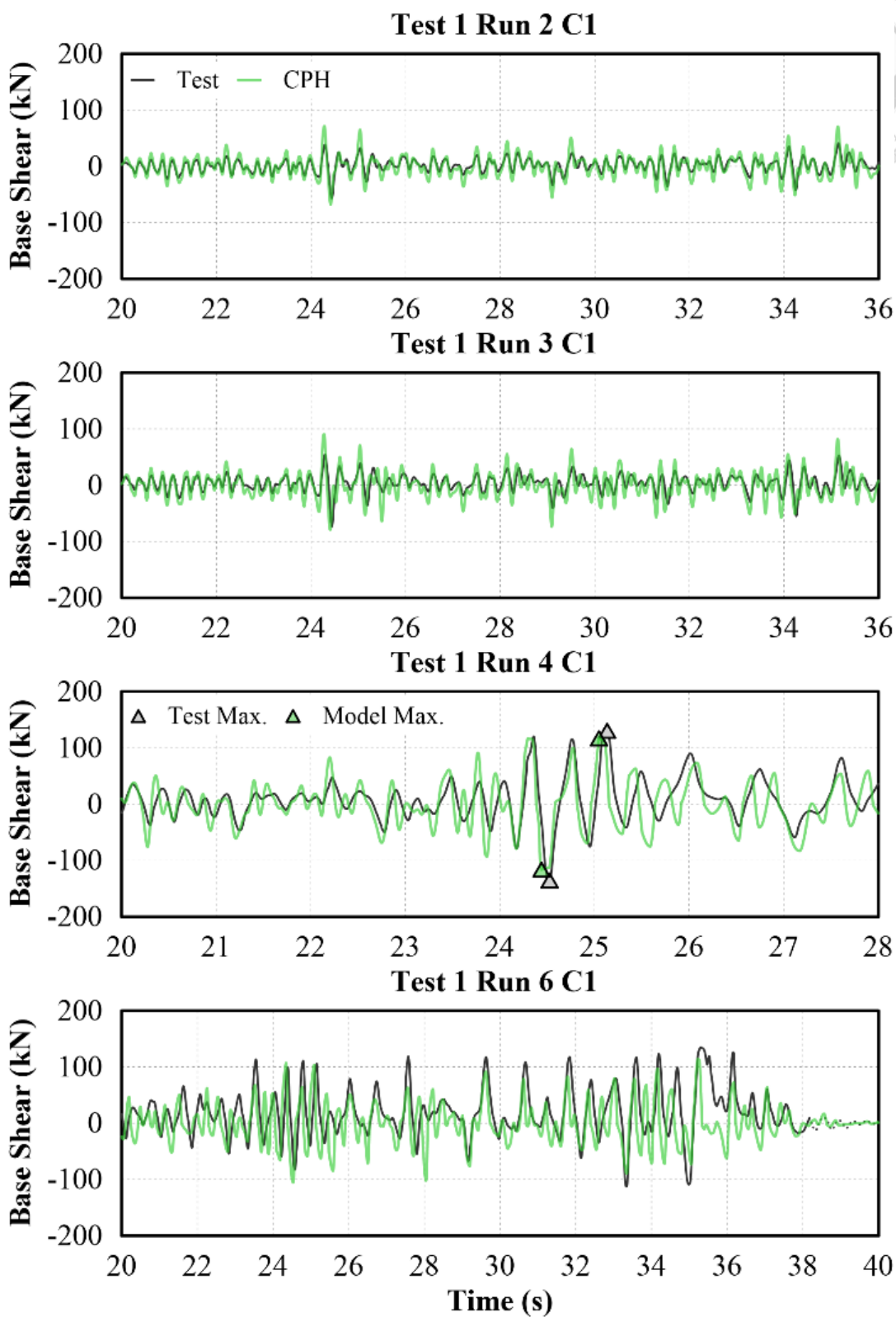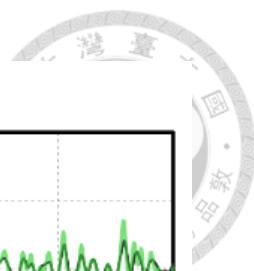
Figure 6-27. Comparison on T1 C1 base shear for CPH model
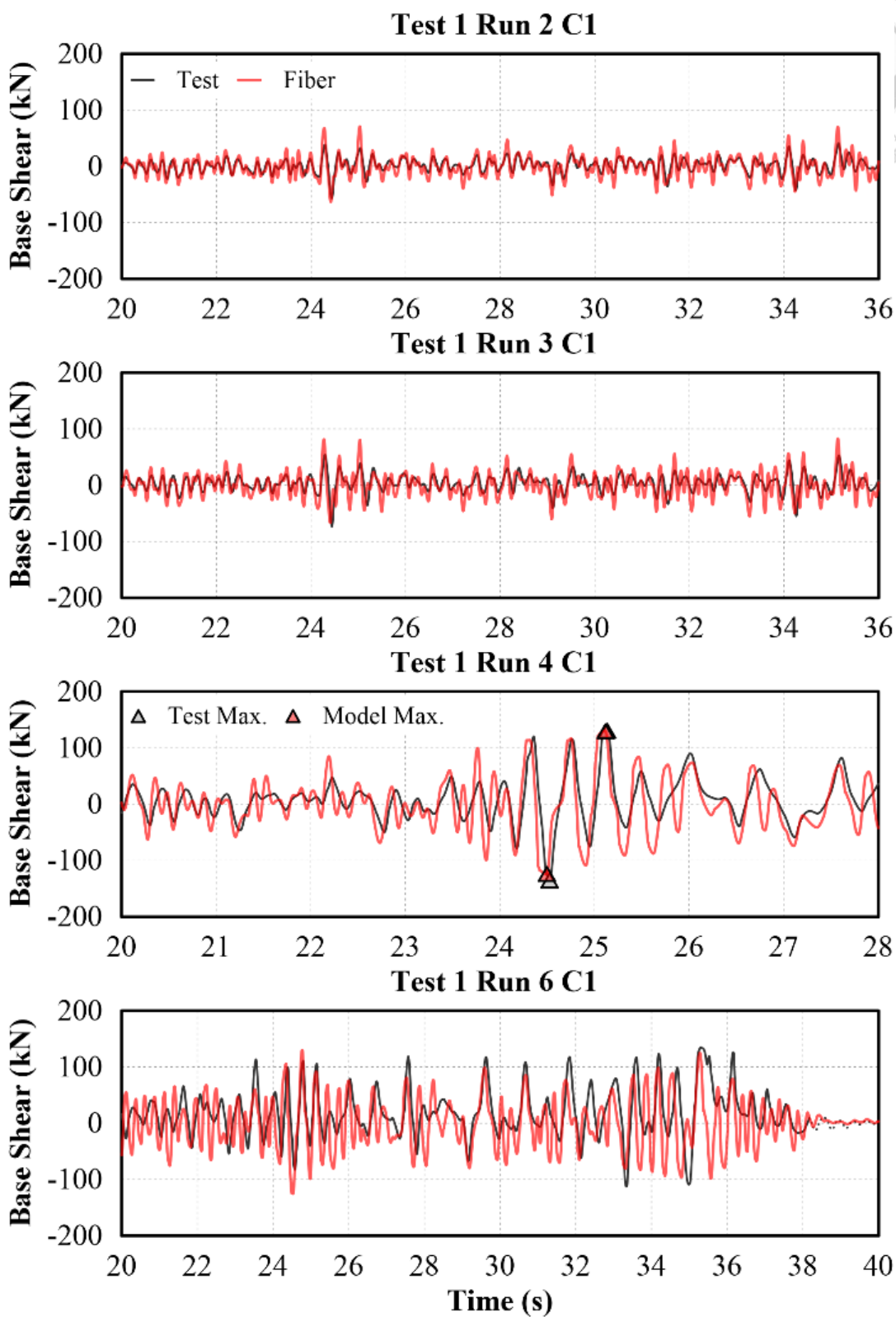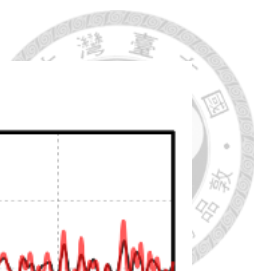
Figure 6-28. Comparison on T1 C1 base shear for Fiber model
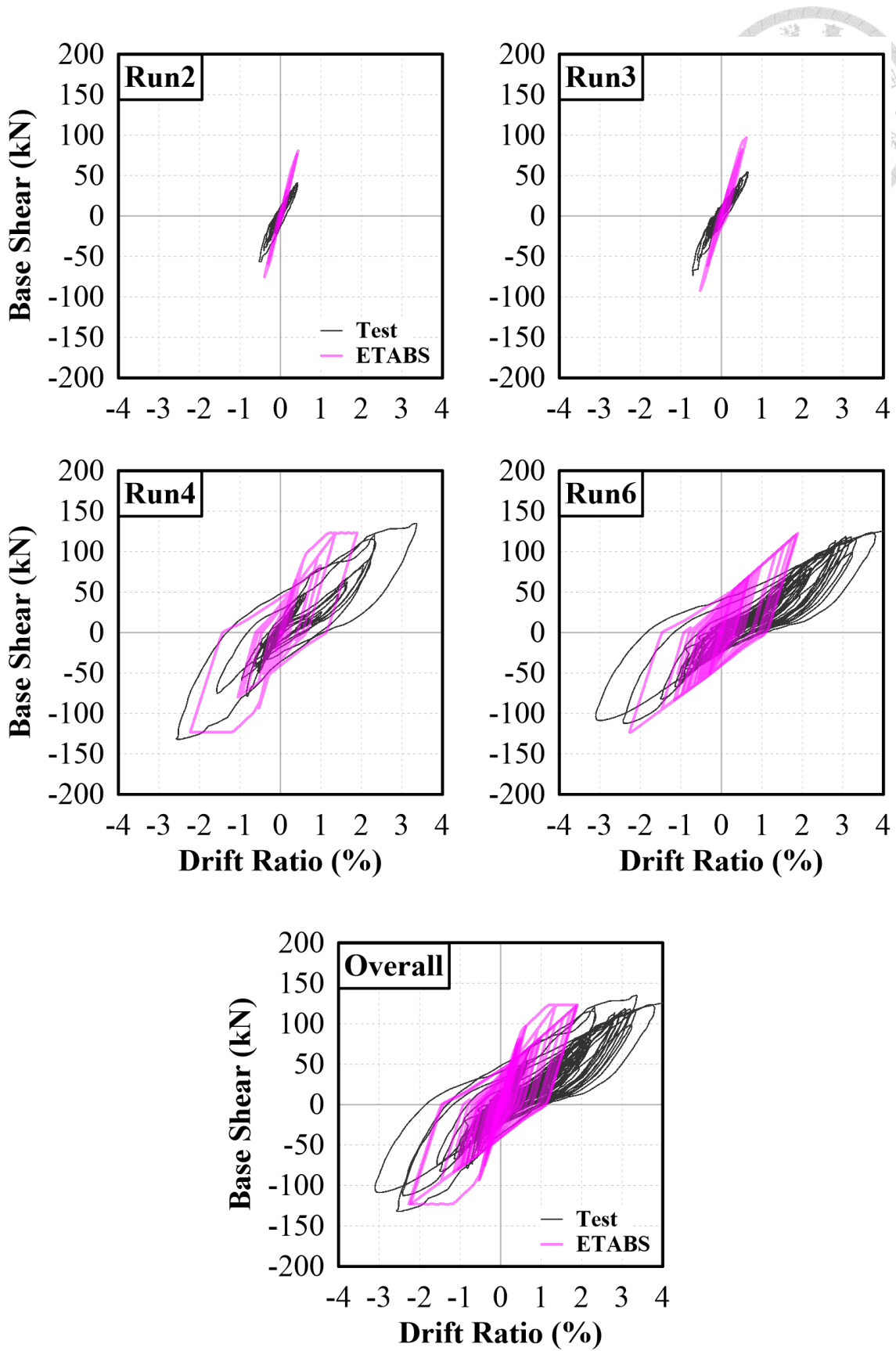
Figure 6-29. Comparison on T1 C1 hysteresis curve for ETABS model

495
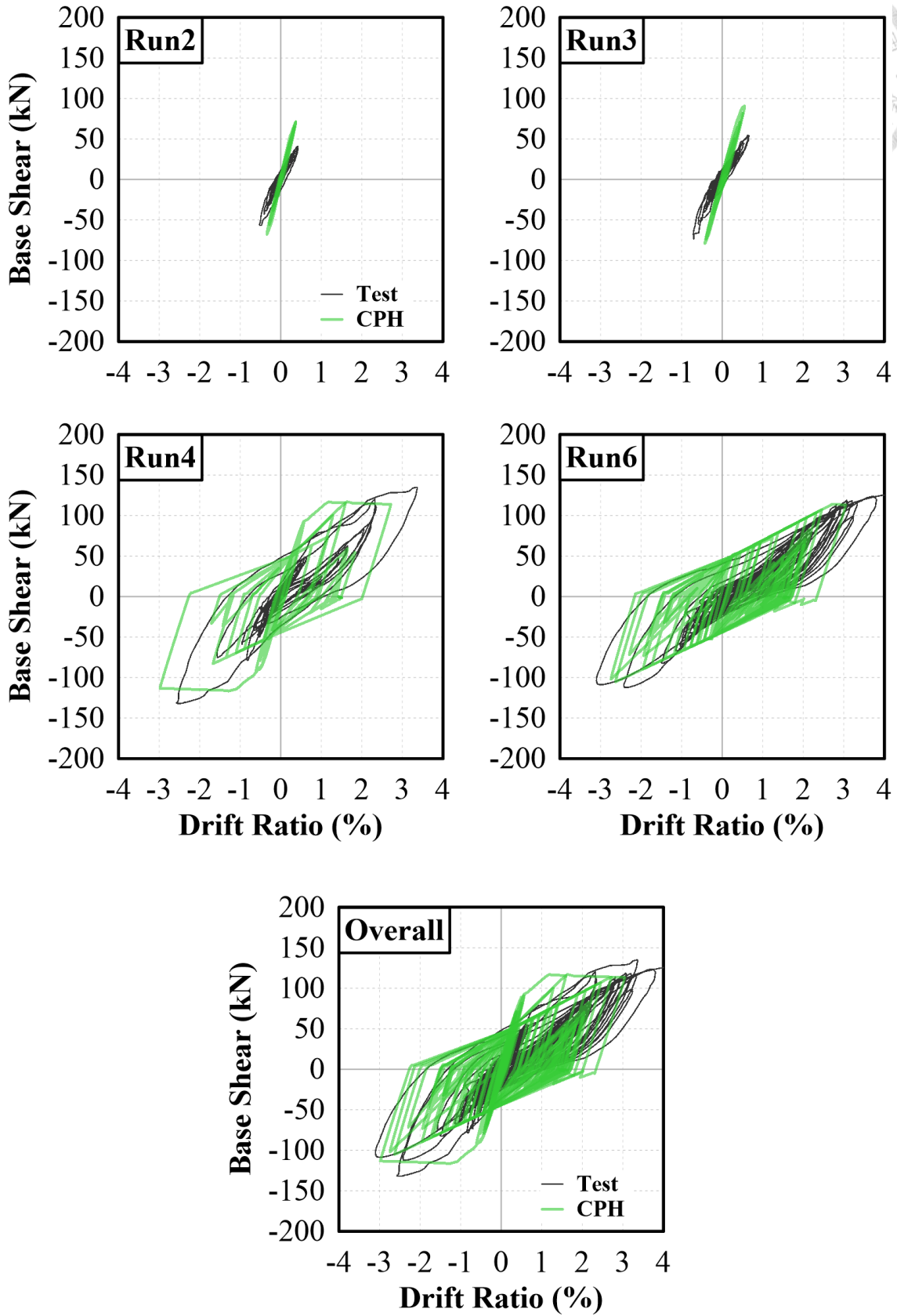
Figure 6-30. Comparison on T1 C1 hysteresis curve for CPH model

496
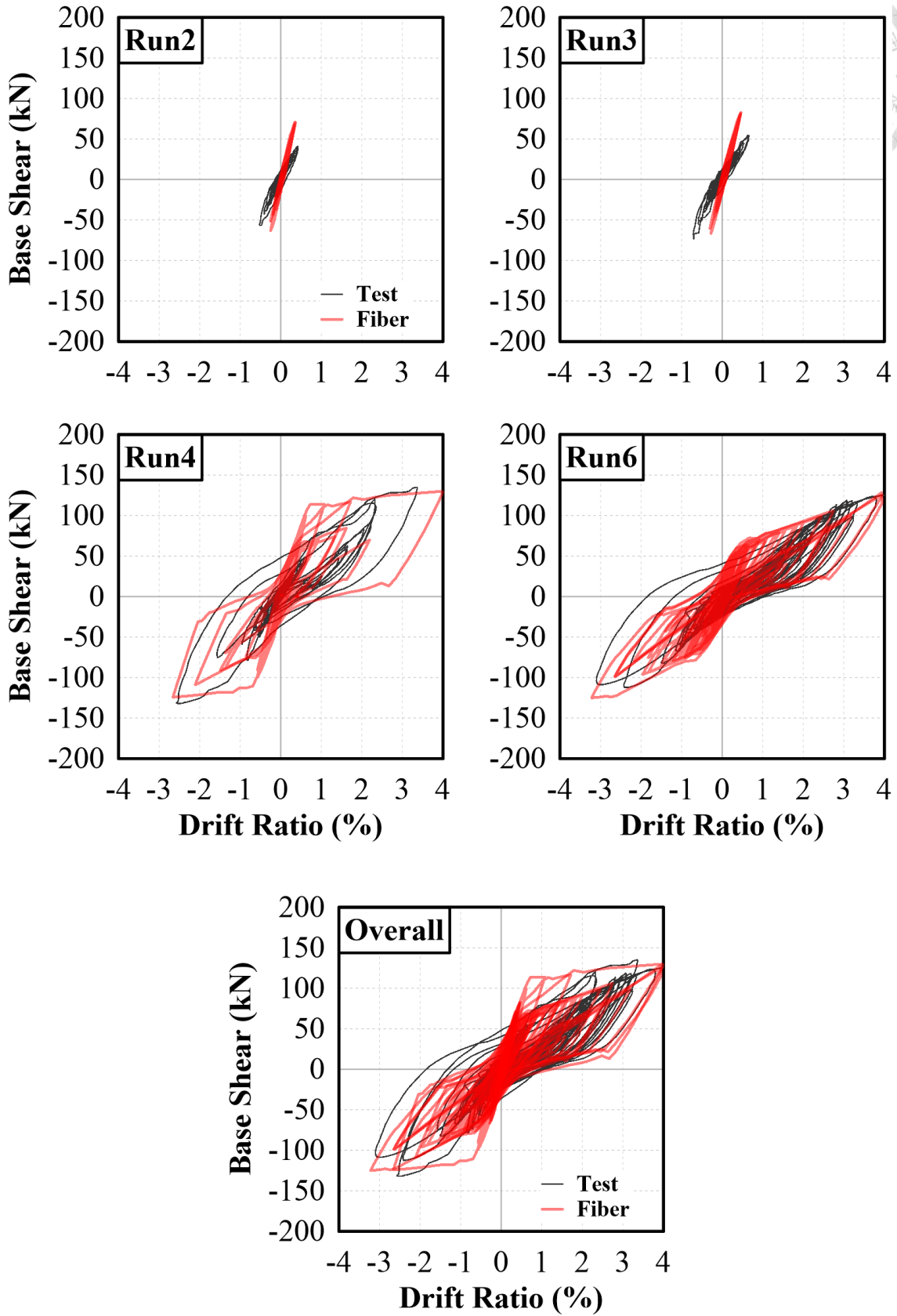
Figure 6-31. Comparison on T1 C1 hysteresis curve for Fiber model

497
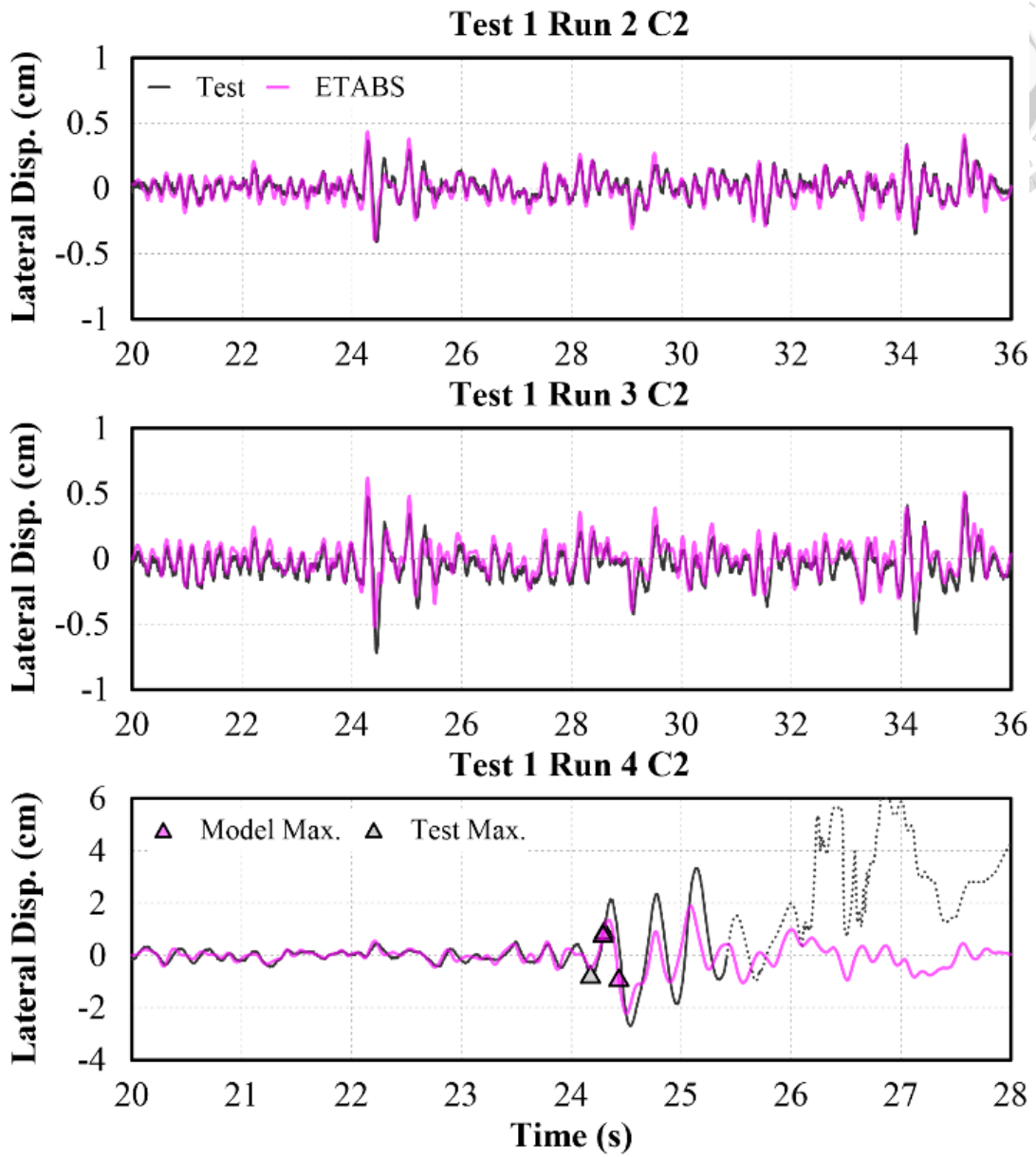
Figure 6-32. Comparison on T1 C2 lateral displacement for ETABS model
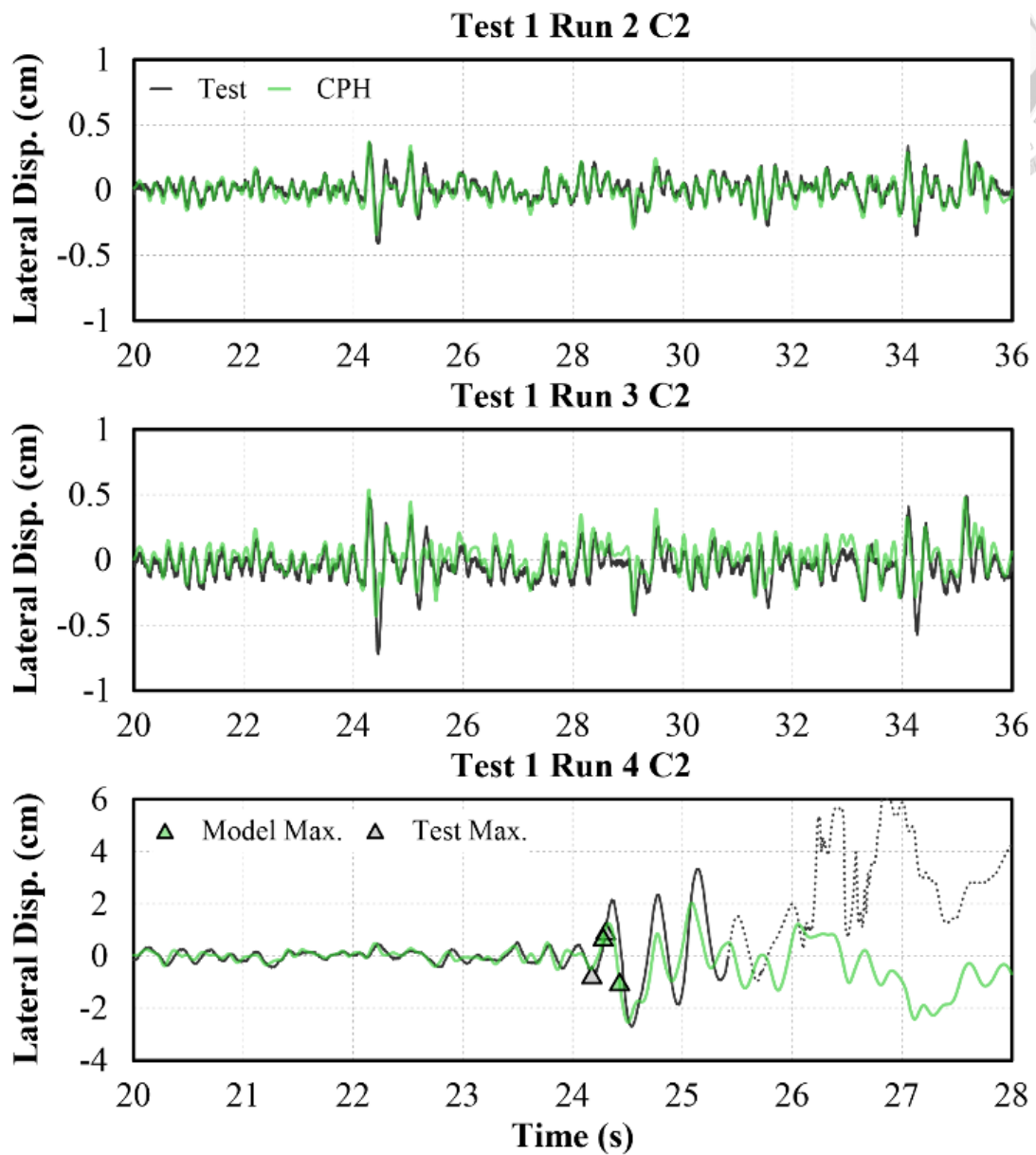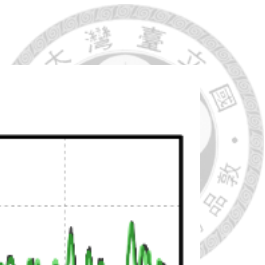
Figure 6-33. Comparison on T1 C2 lateral displacement for CPH model
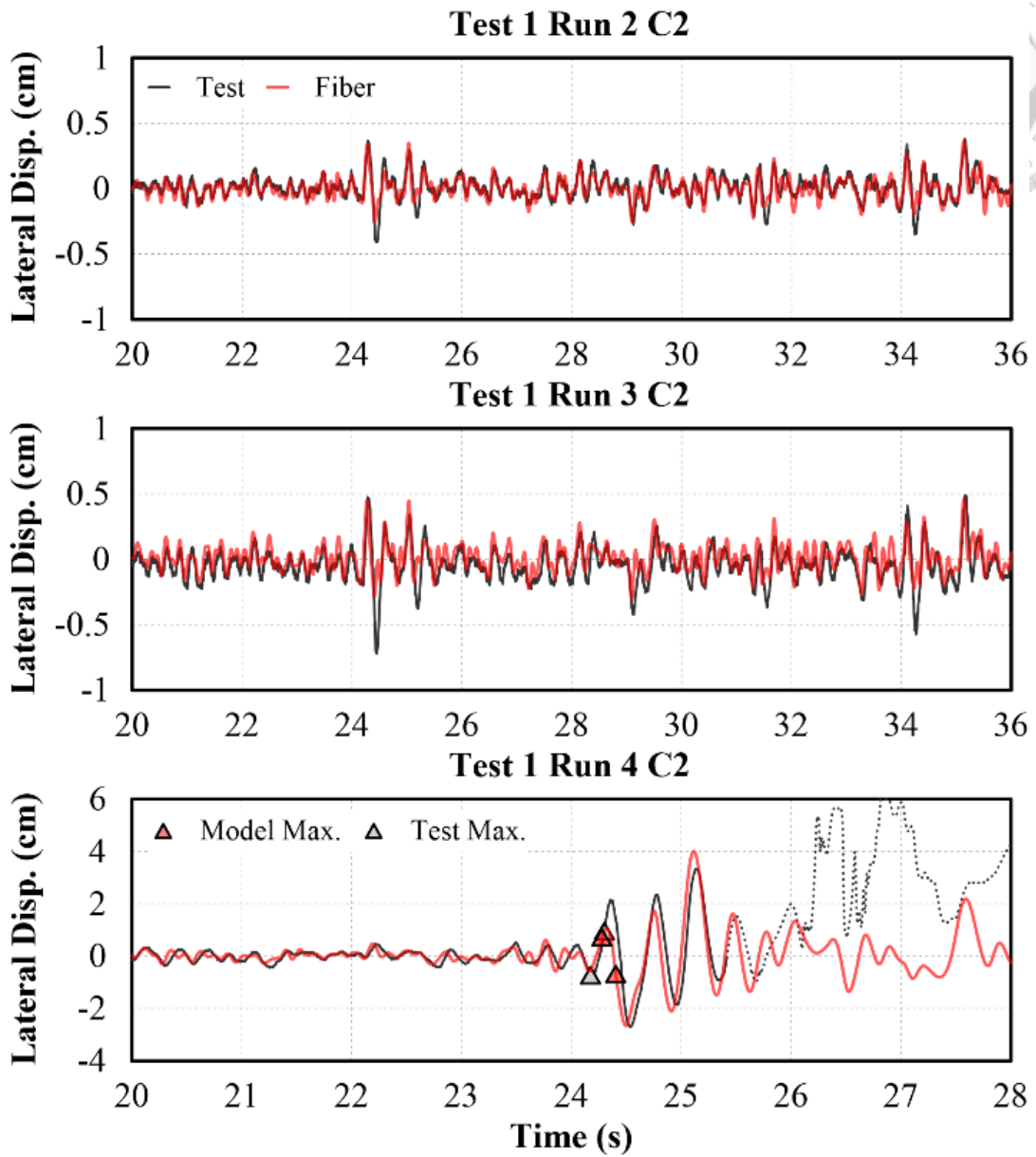
**Figure 6-34. Comparison on T1 C2 lateral displacement for Fiber model**
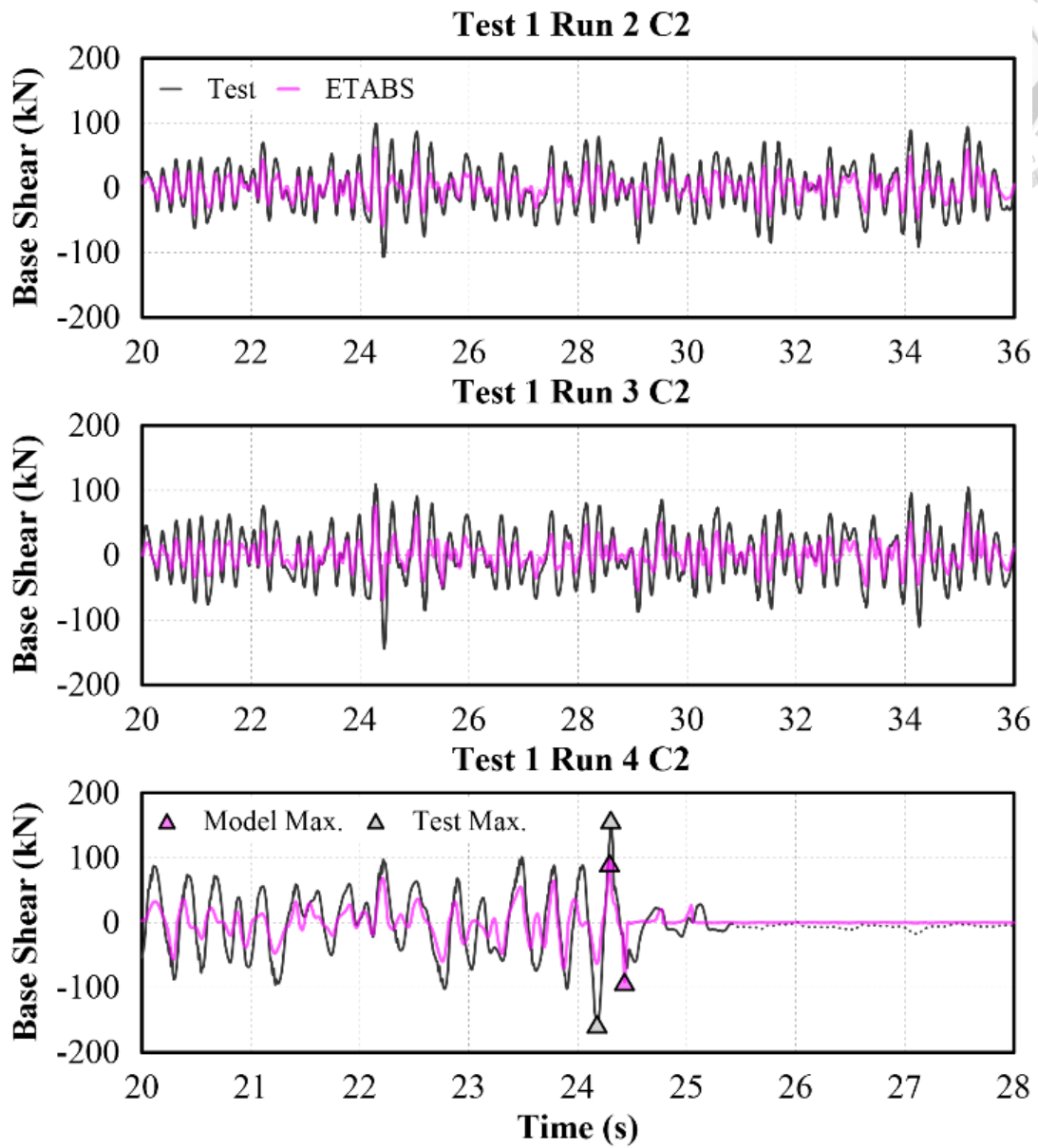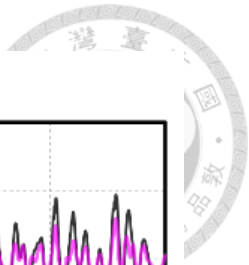
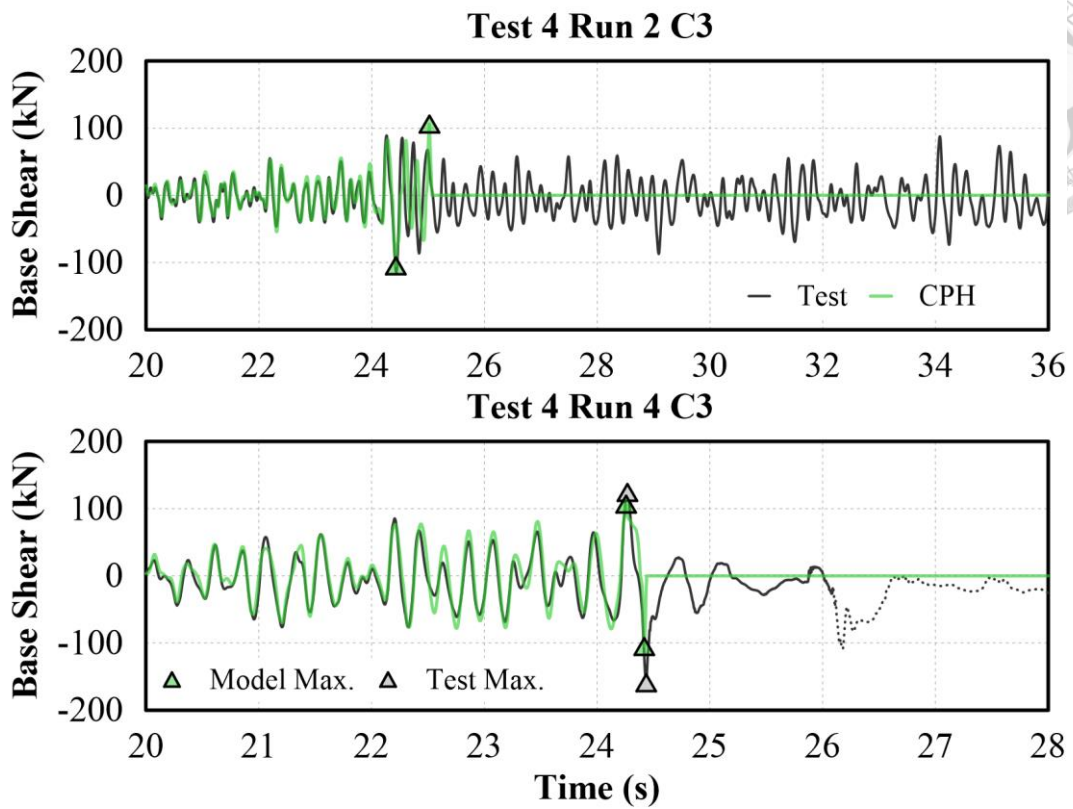**Figure 6-35. Comparison on T1 C2 base shear for ETABS model**

501
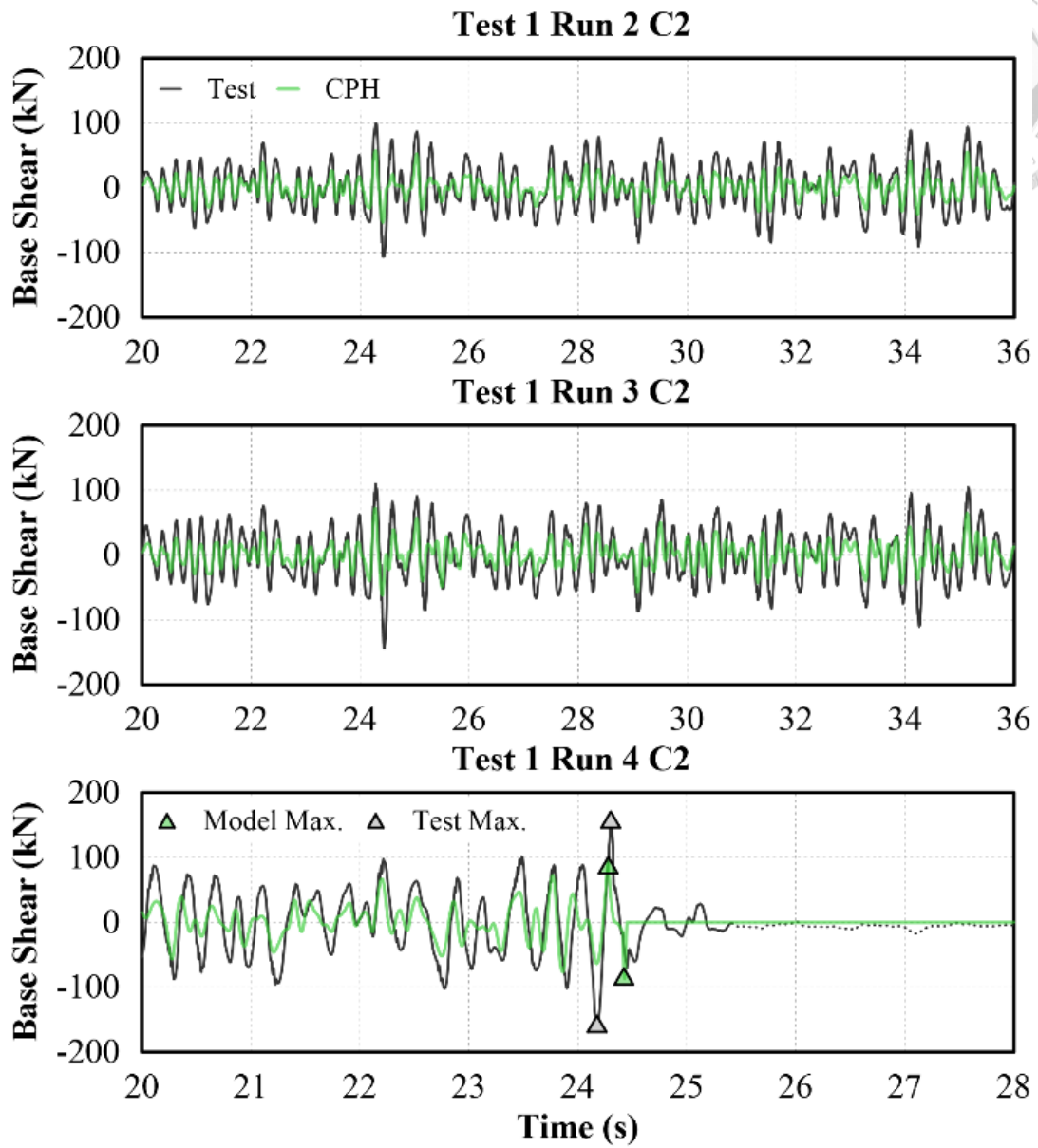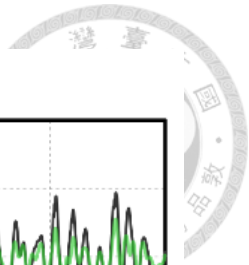
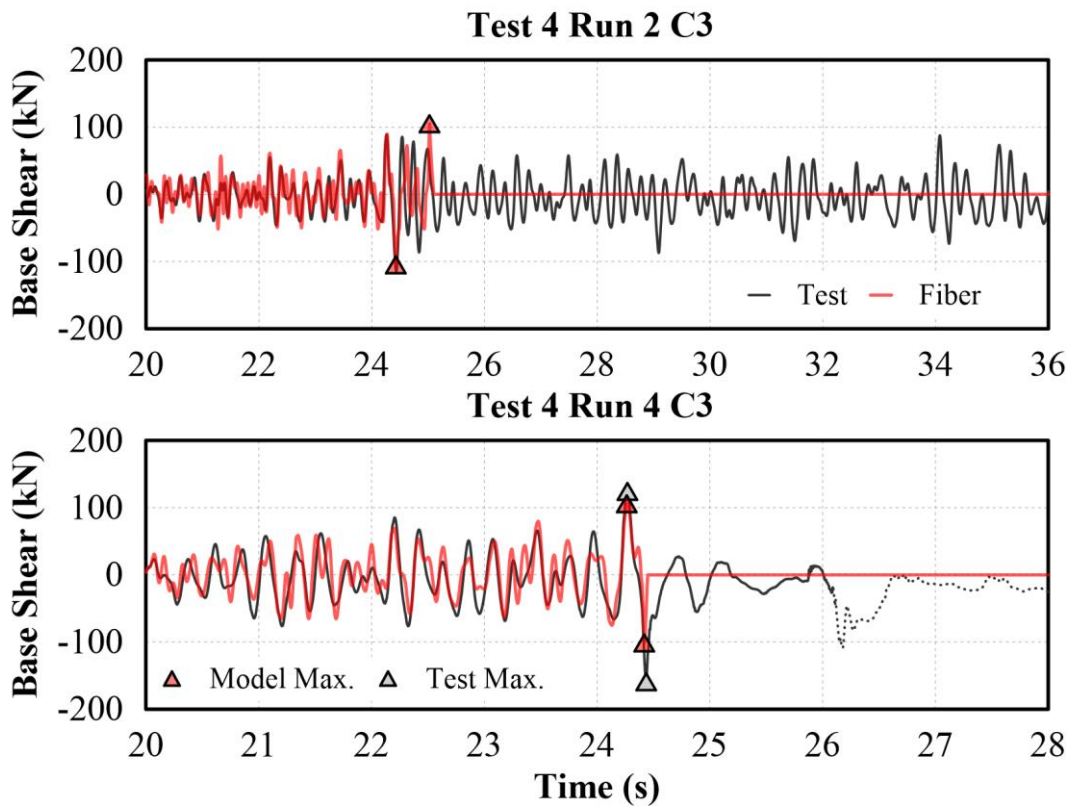**Figure 6-36. Comparison on T1 C2 base shear for CPH model**
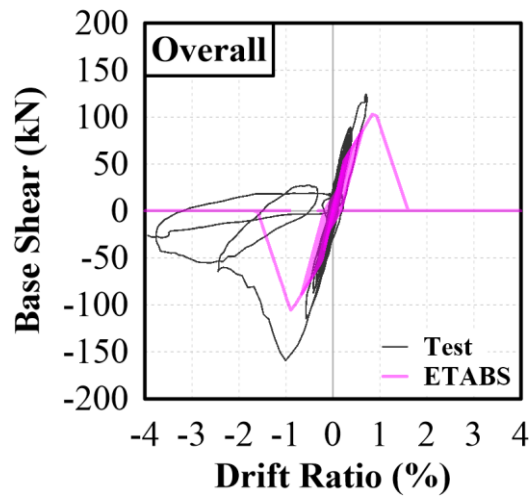
502
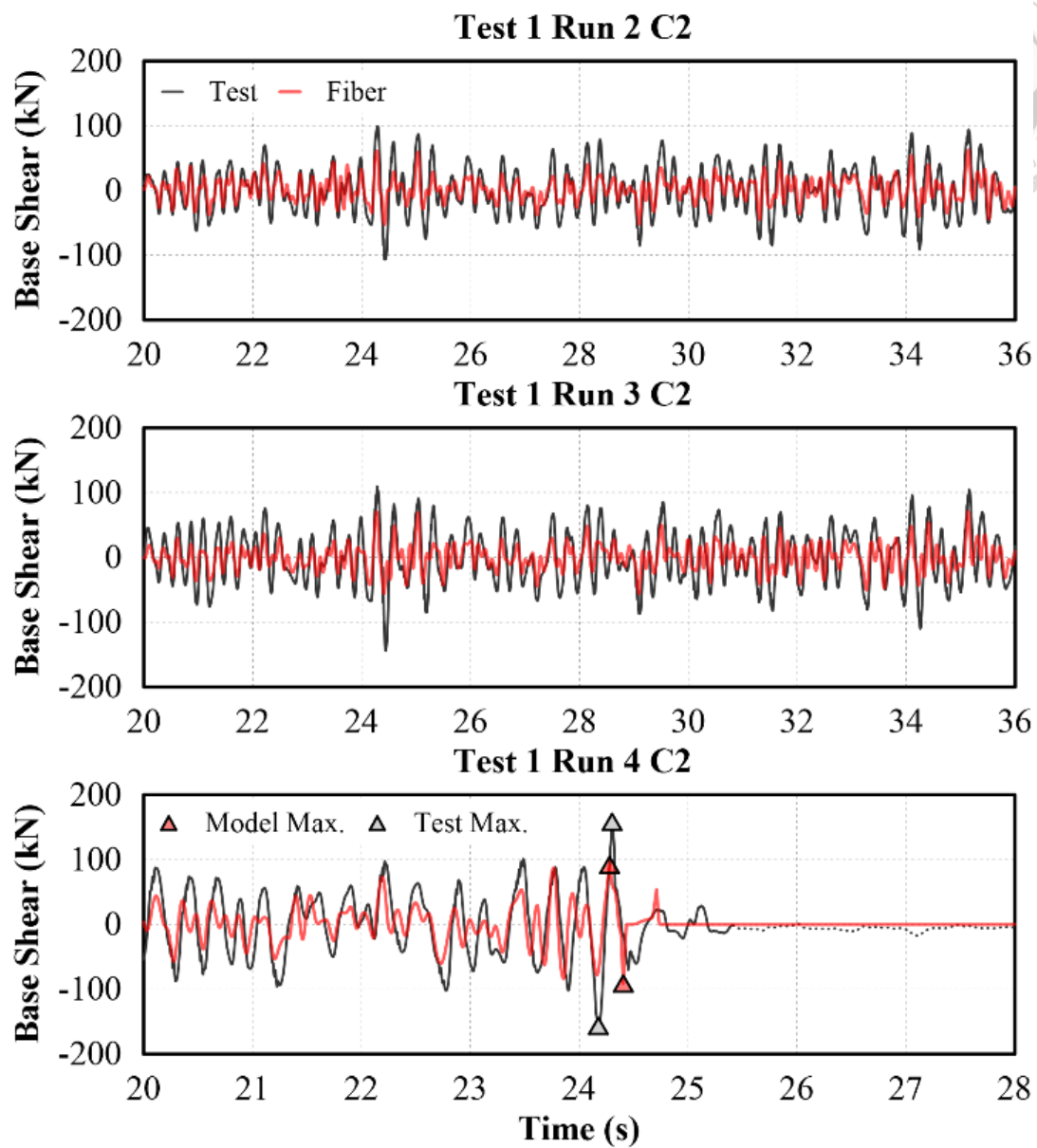
Figure 6-37. Comparison on T1 C2 base shear for Fiber model
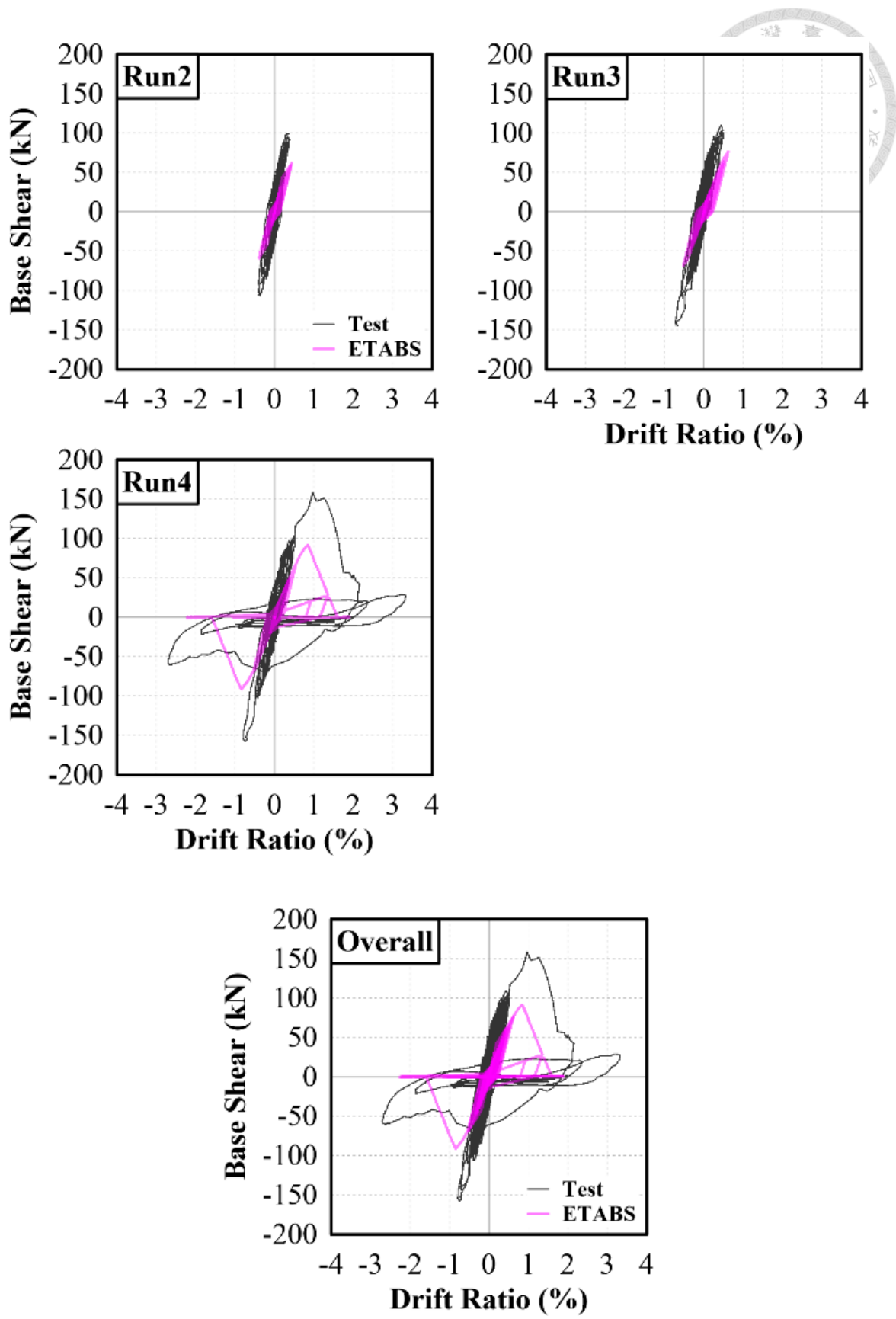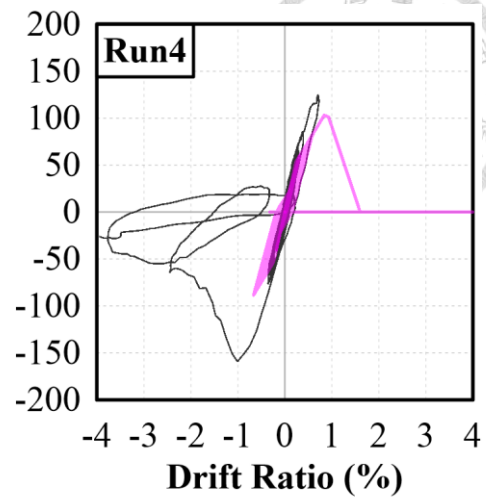
Figure 6-38. Comparison on T1 C2 hysteresis curve for ETABS model
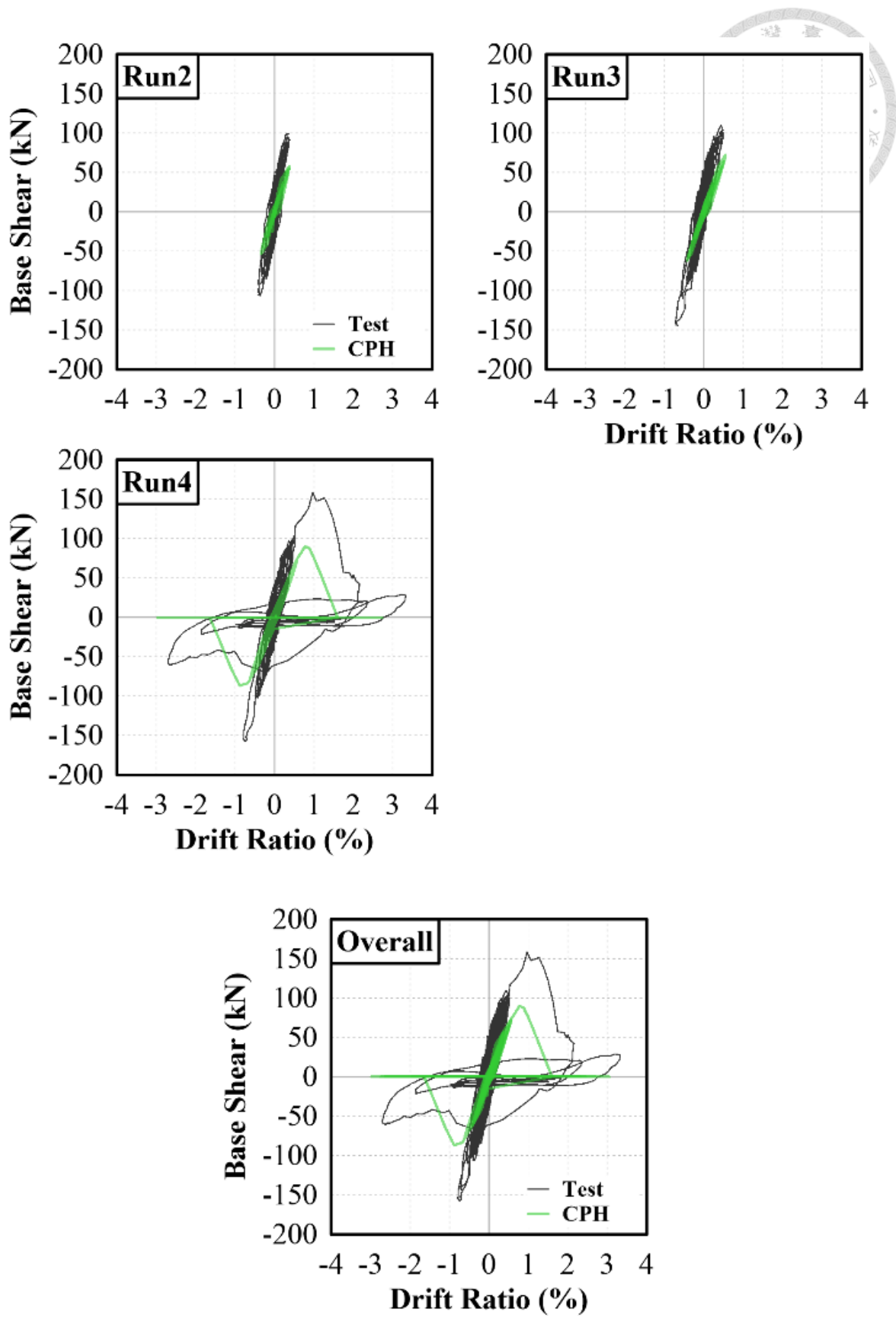
Figure 6-39. Comparison on T1 C2 hysteresis curve for CPH model

505
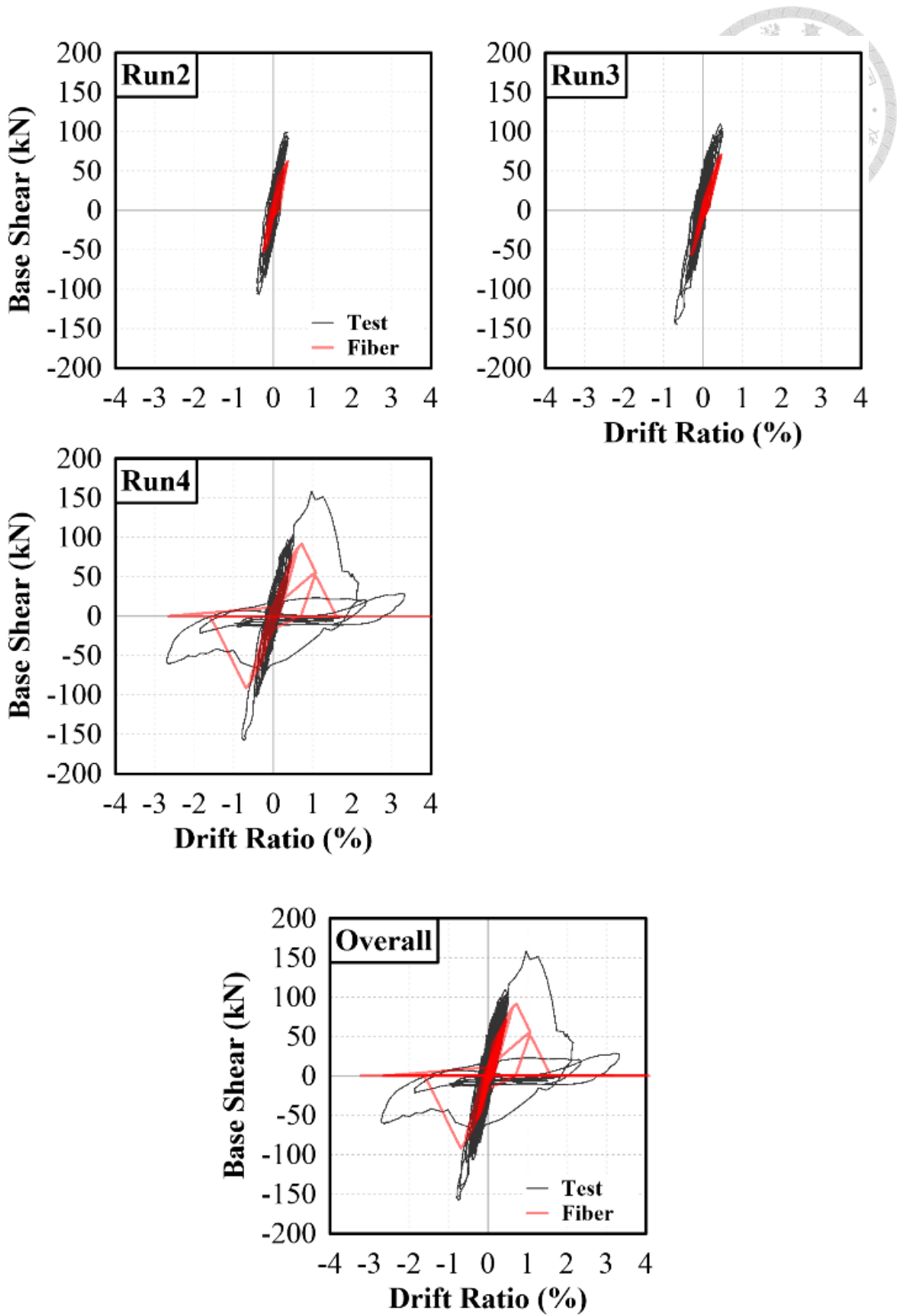
Figure 6-40. Comparison on T1 C2 hysteresis curve for Fiber model
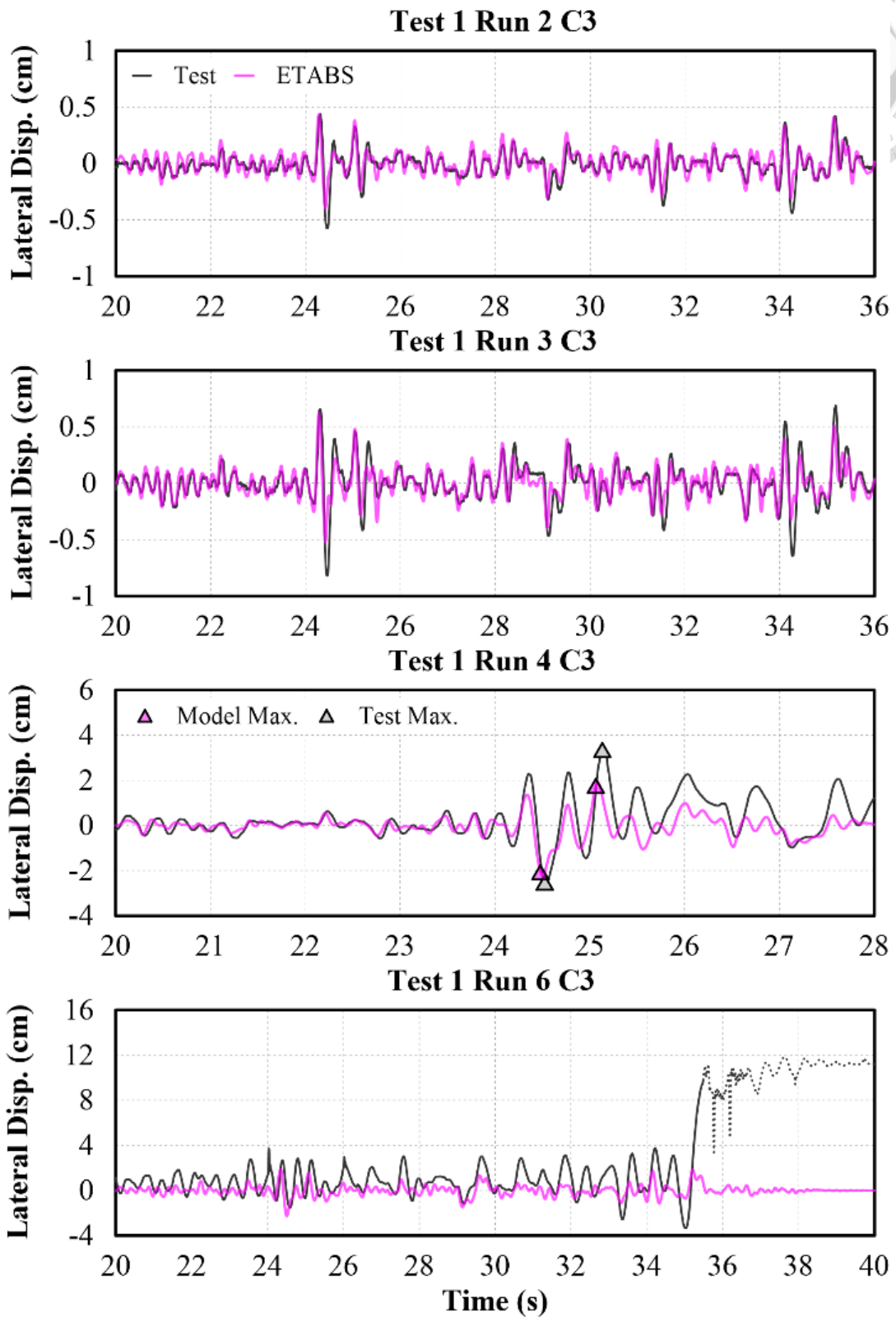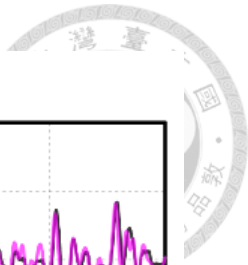
Figure 6-41. Comparison on T1 C3 lateral displacement for ETABS model
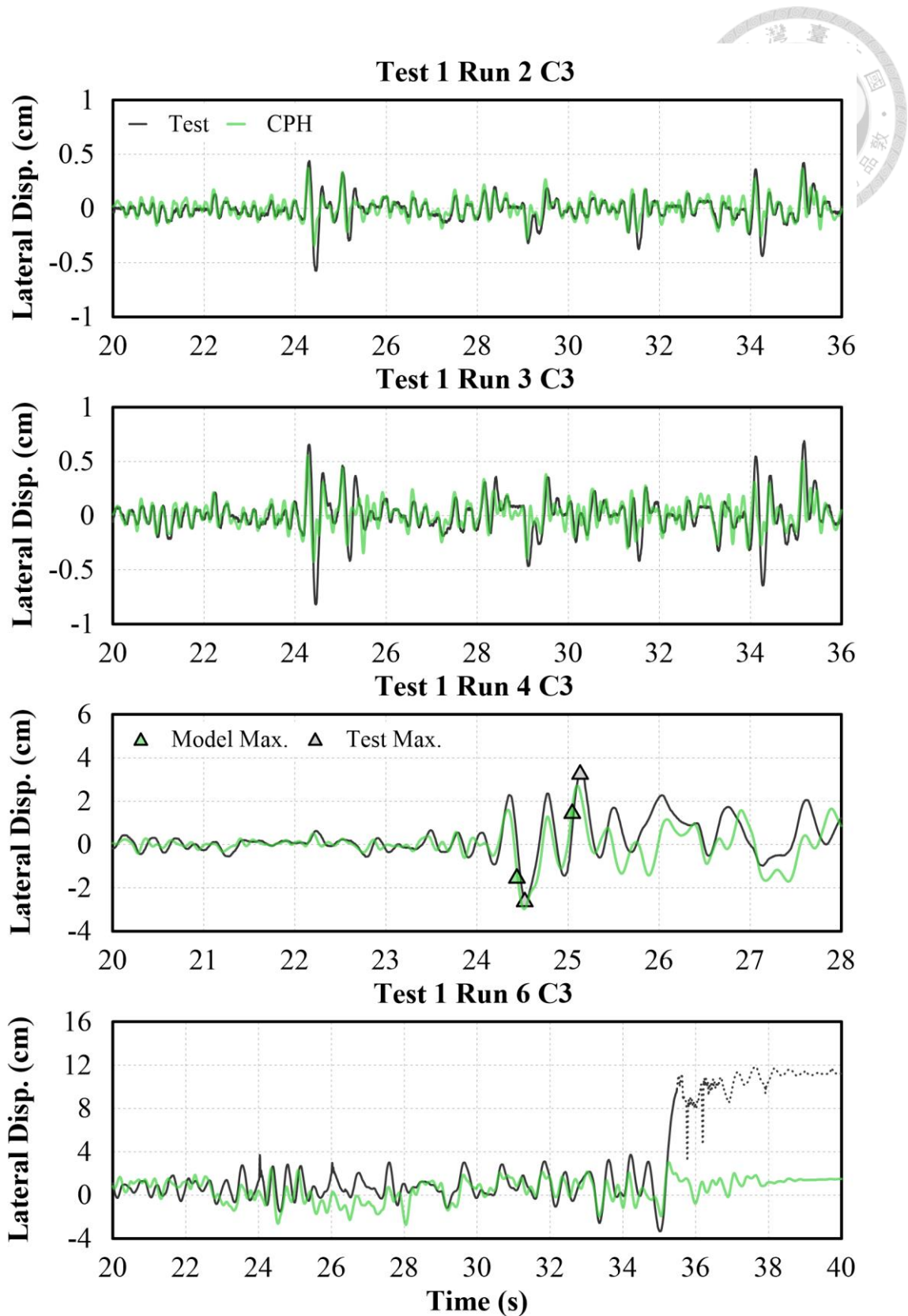
Figure 6-42. Comparison on T1 C3 lateral displacement for CPH model
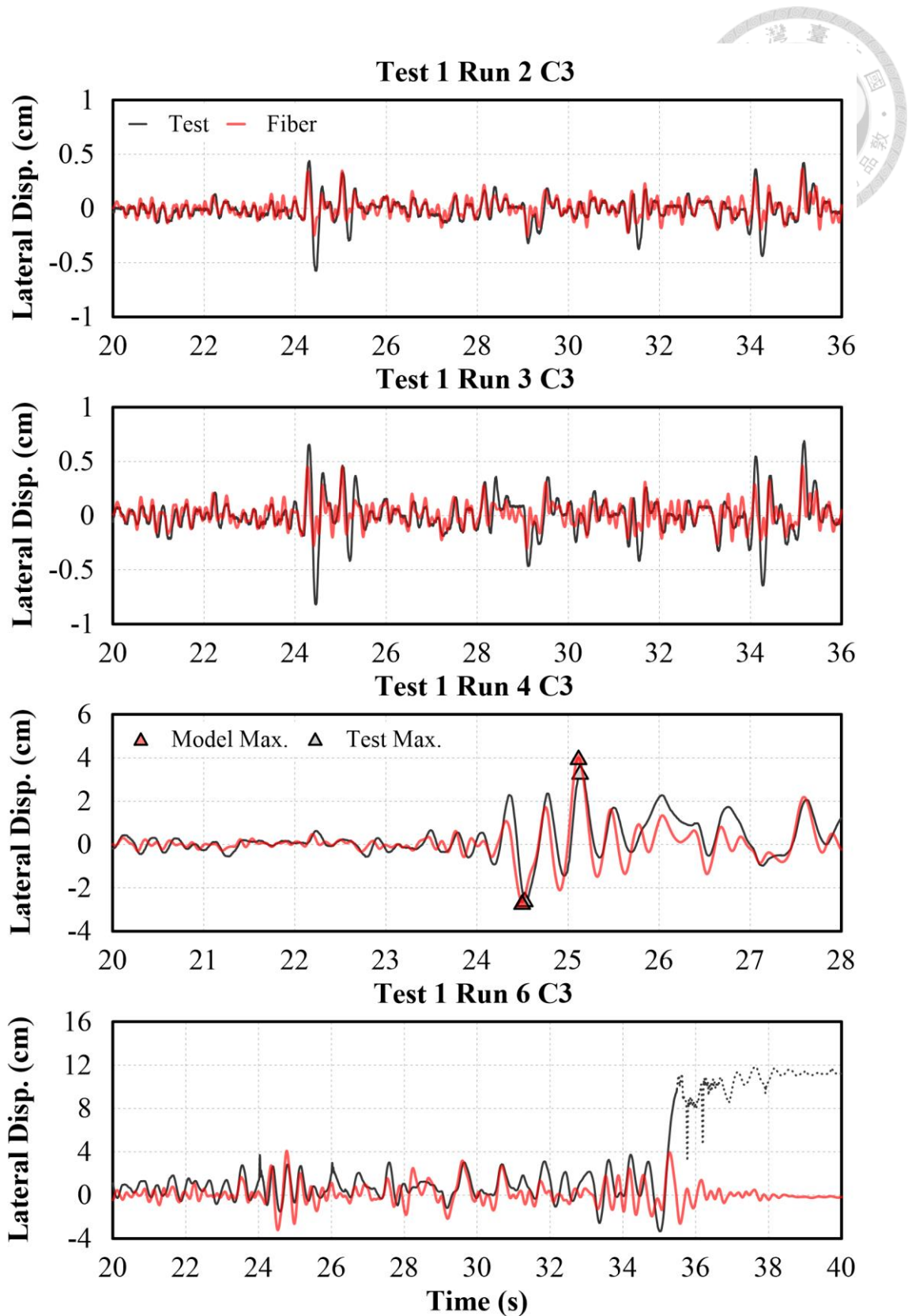
Figure 6-43. Comparison on T1 C3 lateral displacement for Fiber model
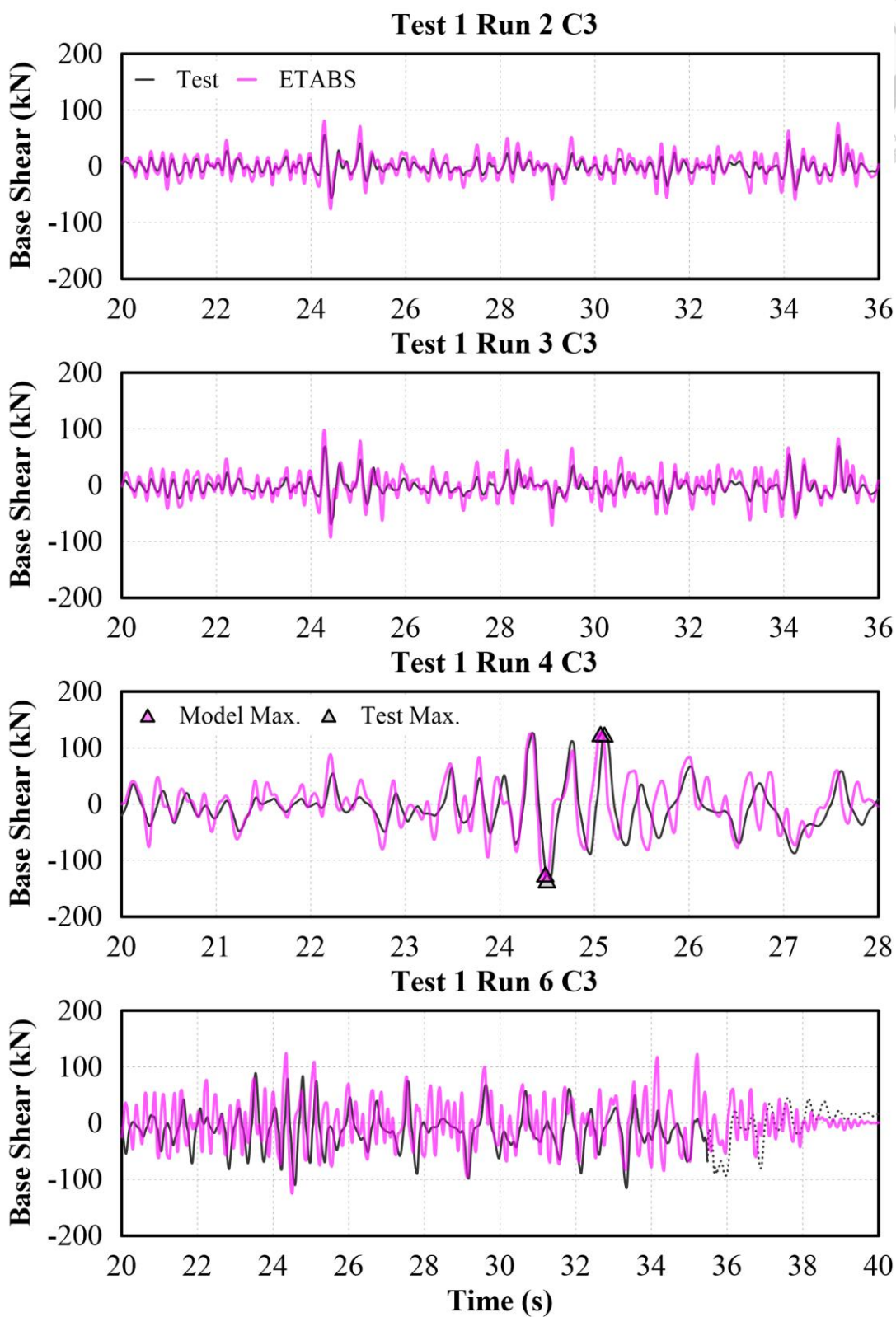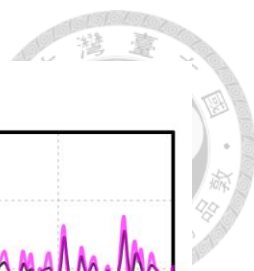
Figure 6-44. Comparison on T1 C3 base shear for ETABS model

510
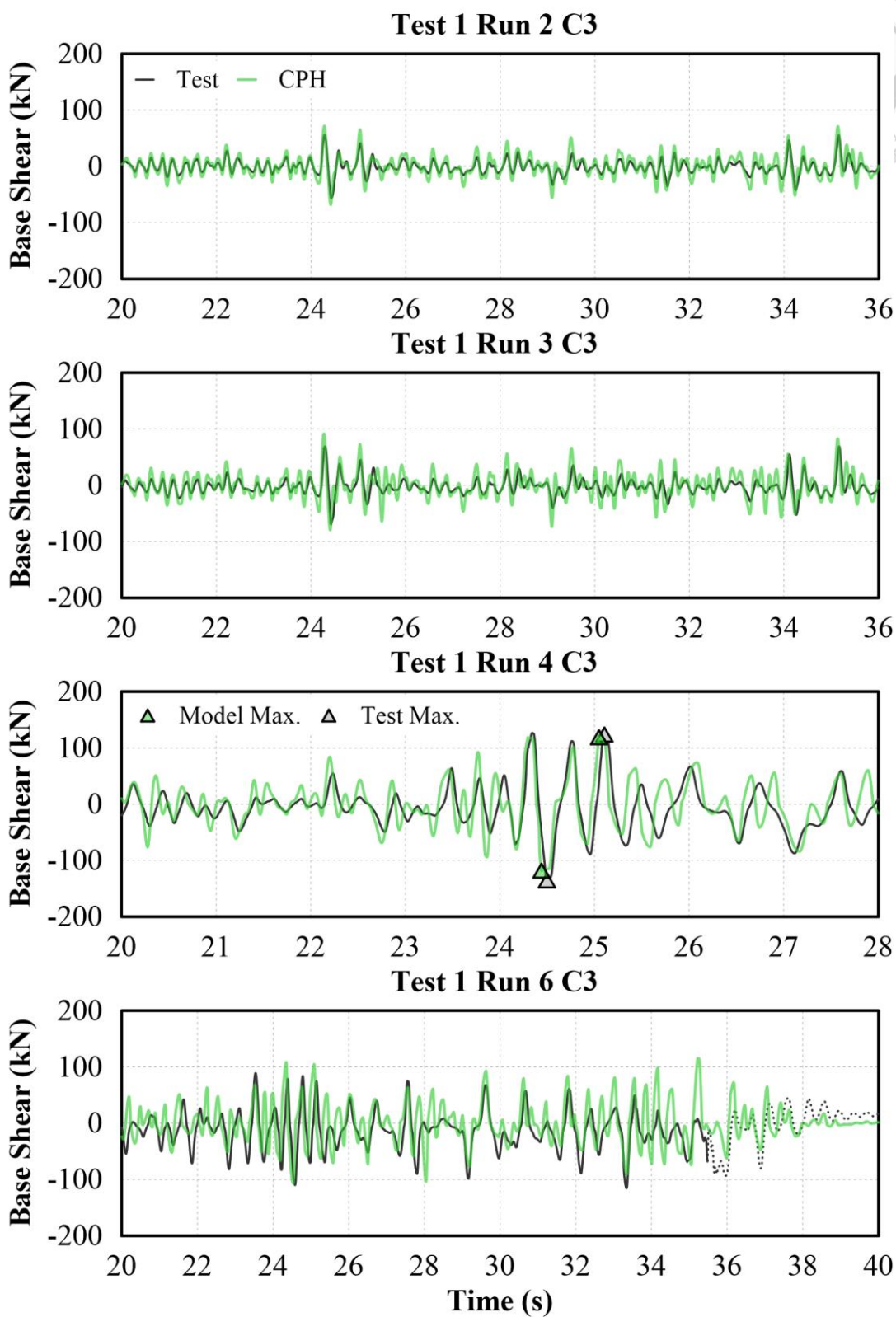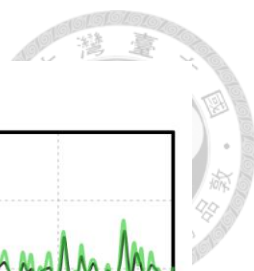
Figure 6-45. Comparison on T1 C3 base shear for CPH model
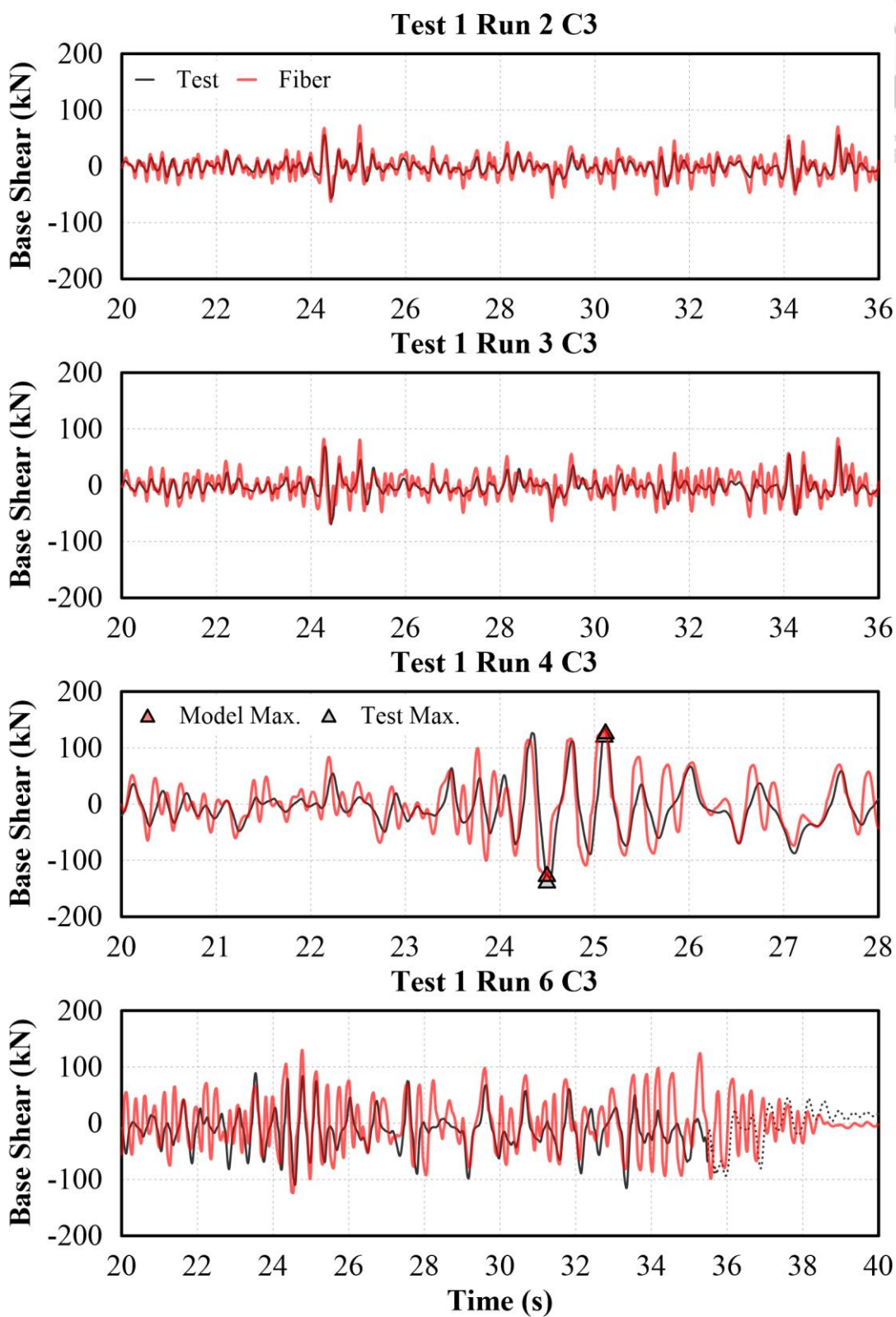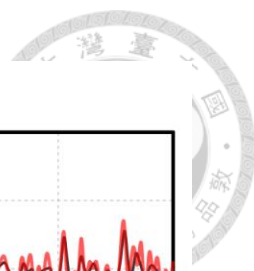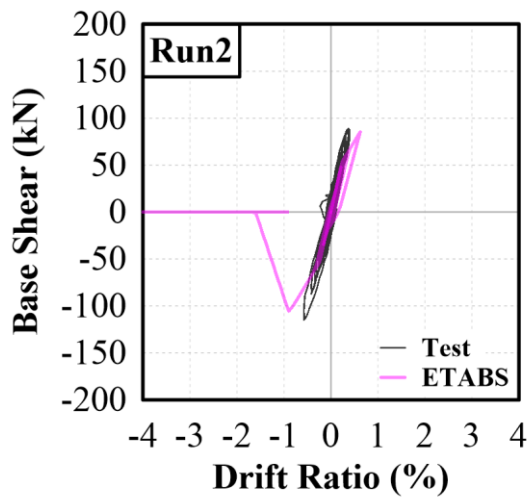
Figure 6-46. Comparison on T1 C3 base shear for Fiber model
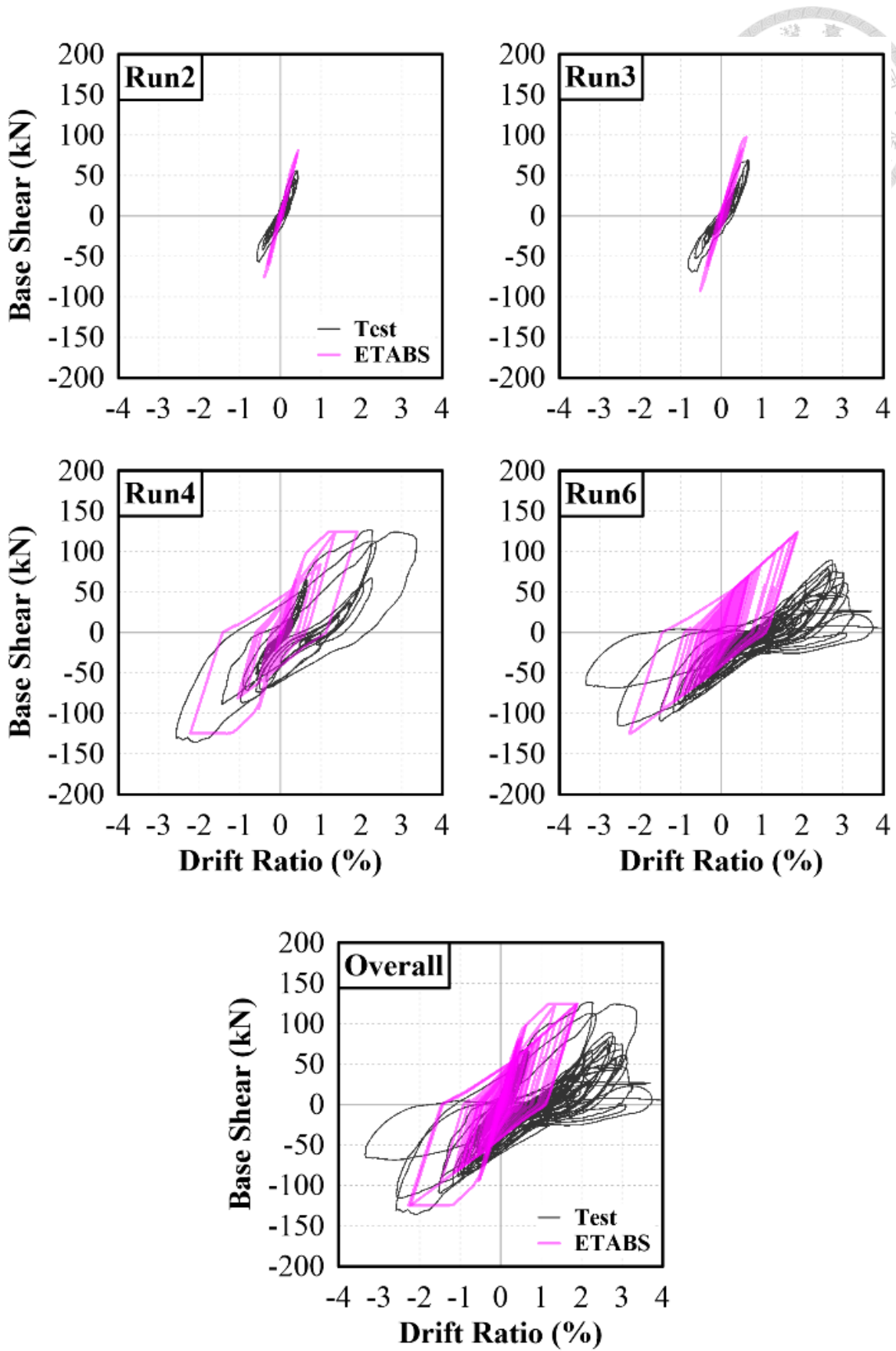
Figure 6-47. Comparison on T1 C3 hysteresis curve for ETABS model
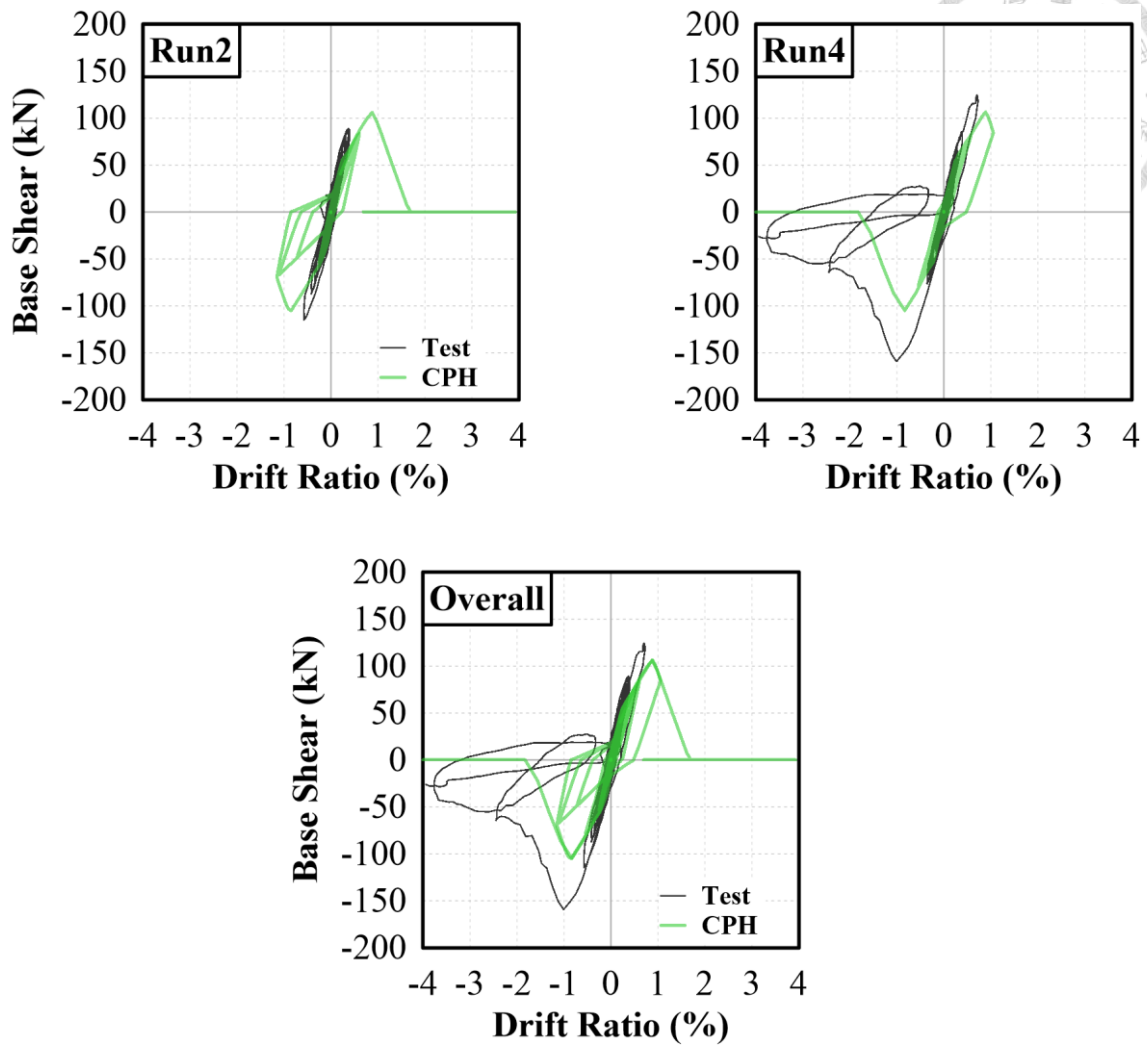
513
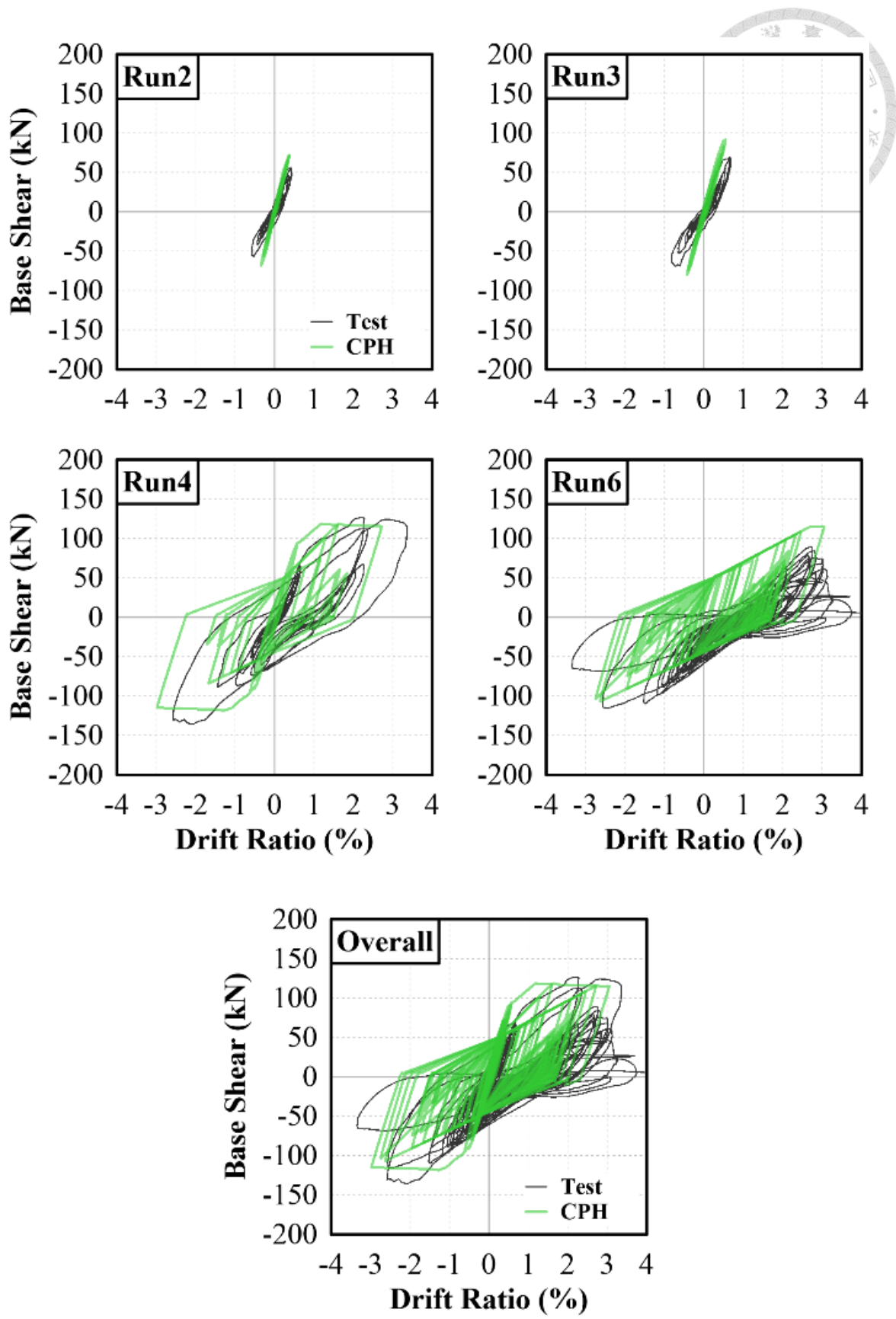
Figure 6-48. Comparison on T1 C3 hysteresis curve for CPH model
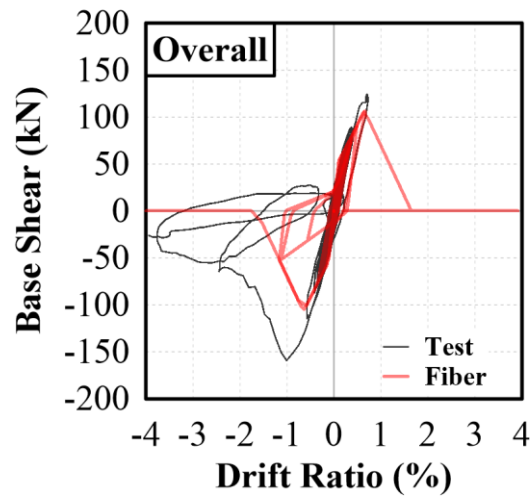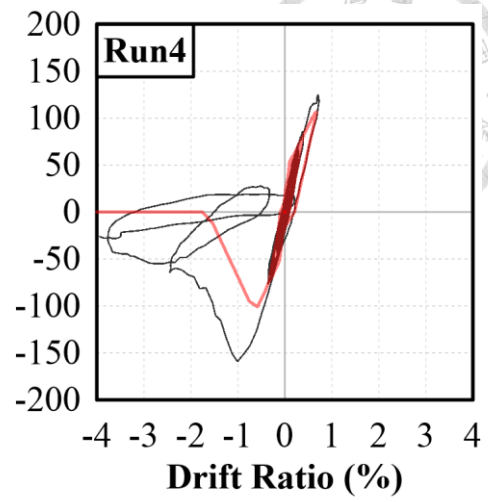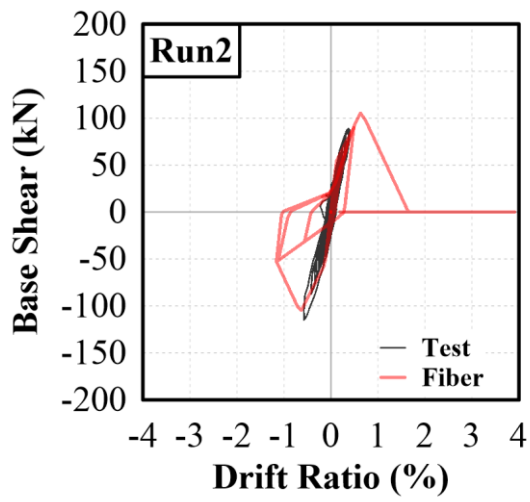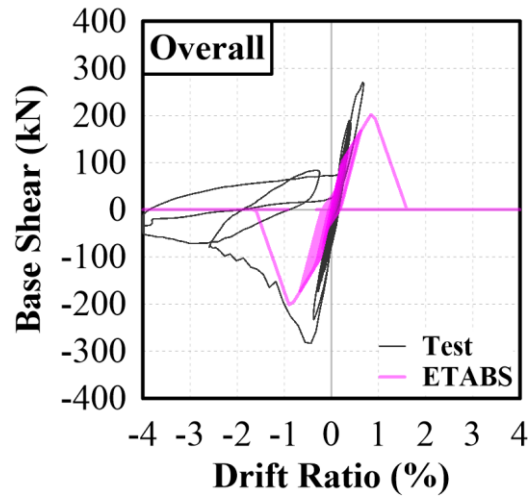
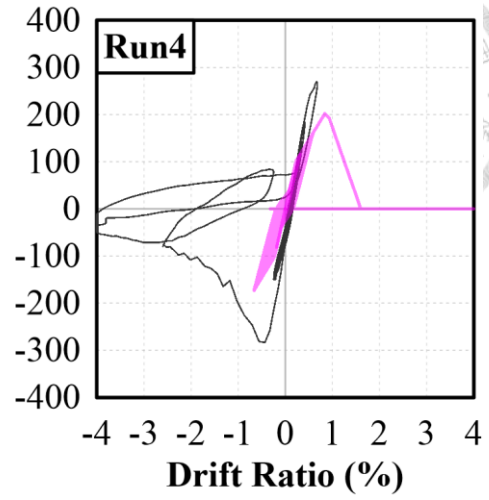514
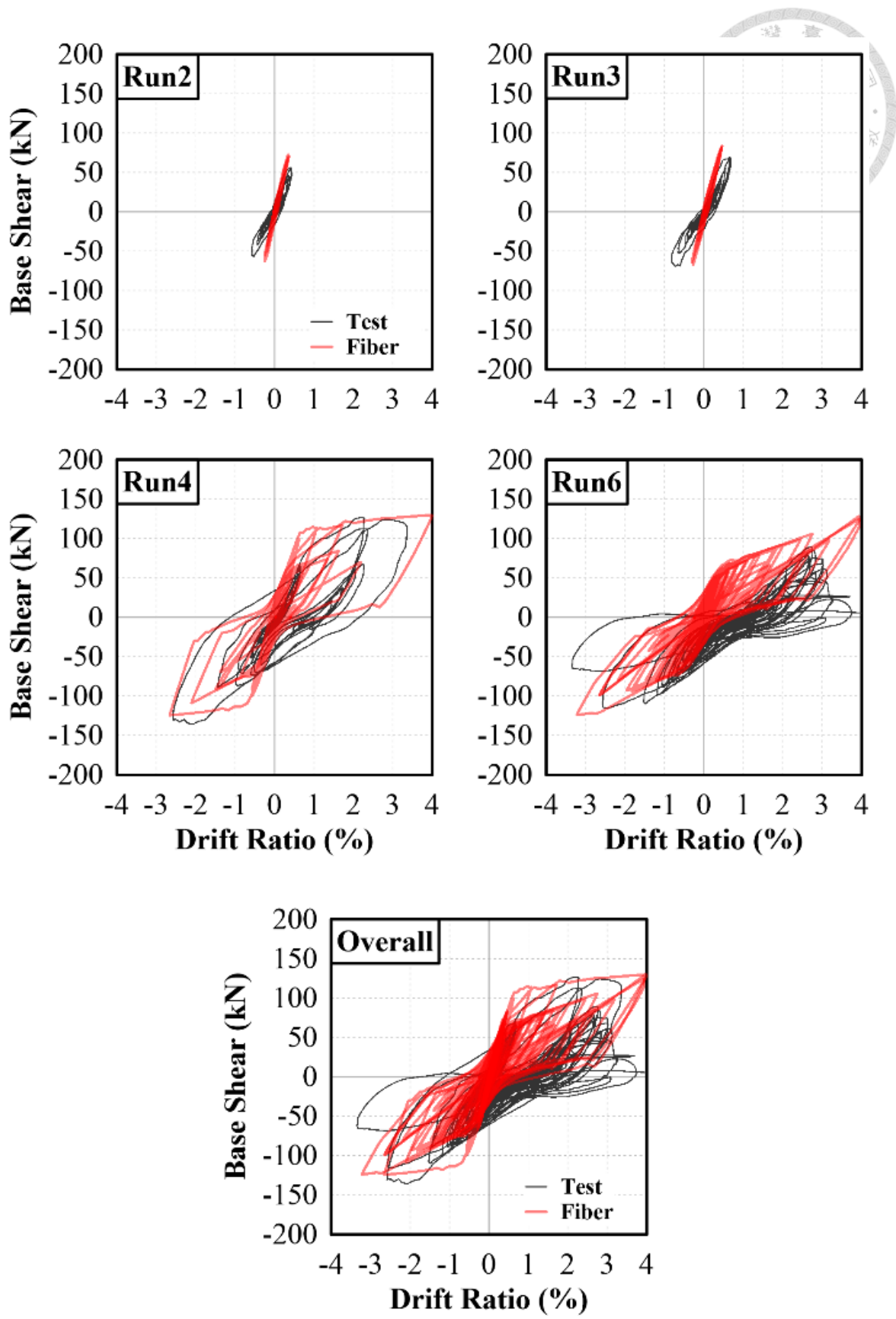
Figure 6-49. Comparison on T1 C3 hysteresis curve for Fiber model

515
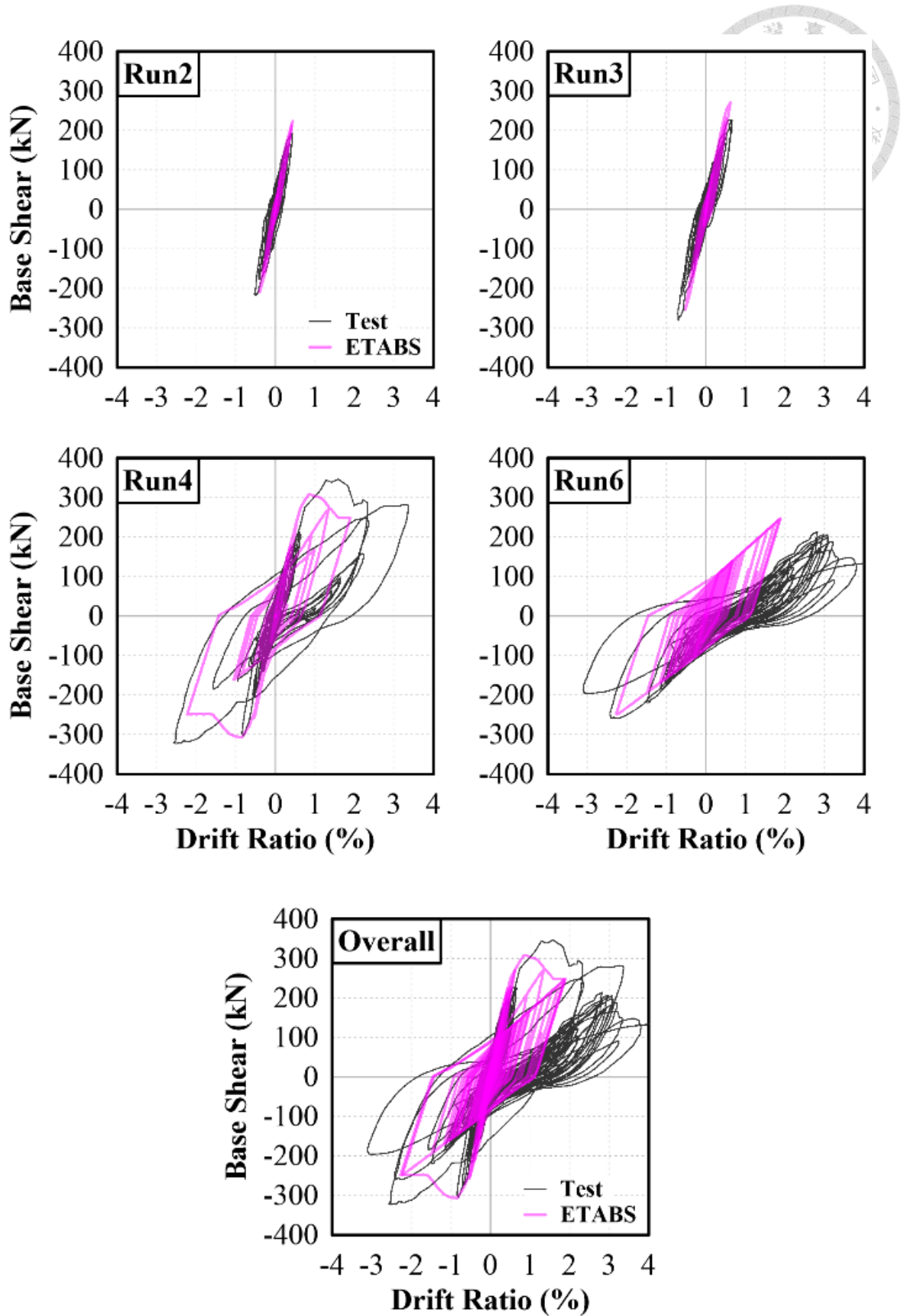
Figure 6-50. Comparison on T1 Frame hysteresis curve for ETABS model

516
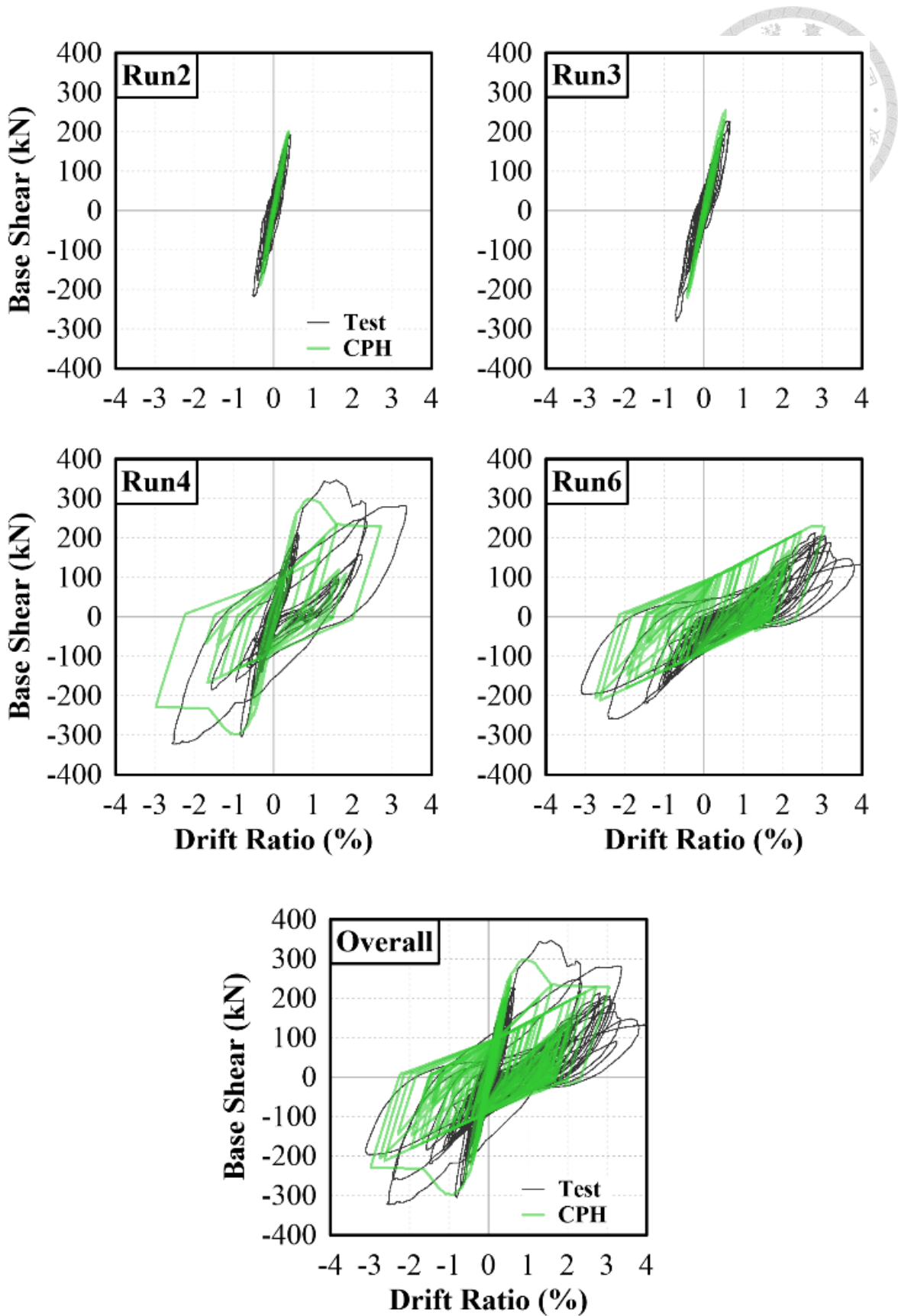
Figure 6-51. Comparison on T1 Frame hysteresis curve for CPH model

517
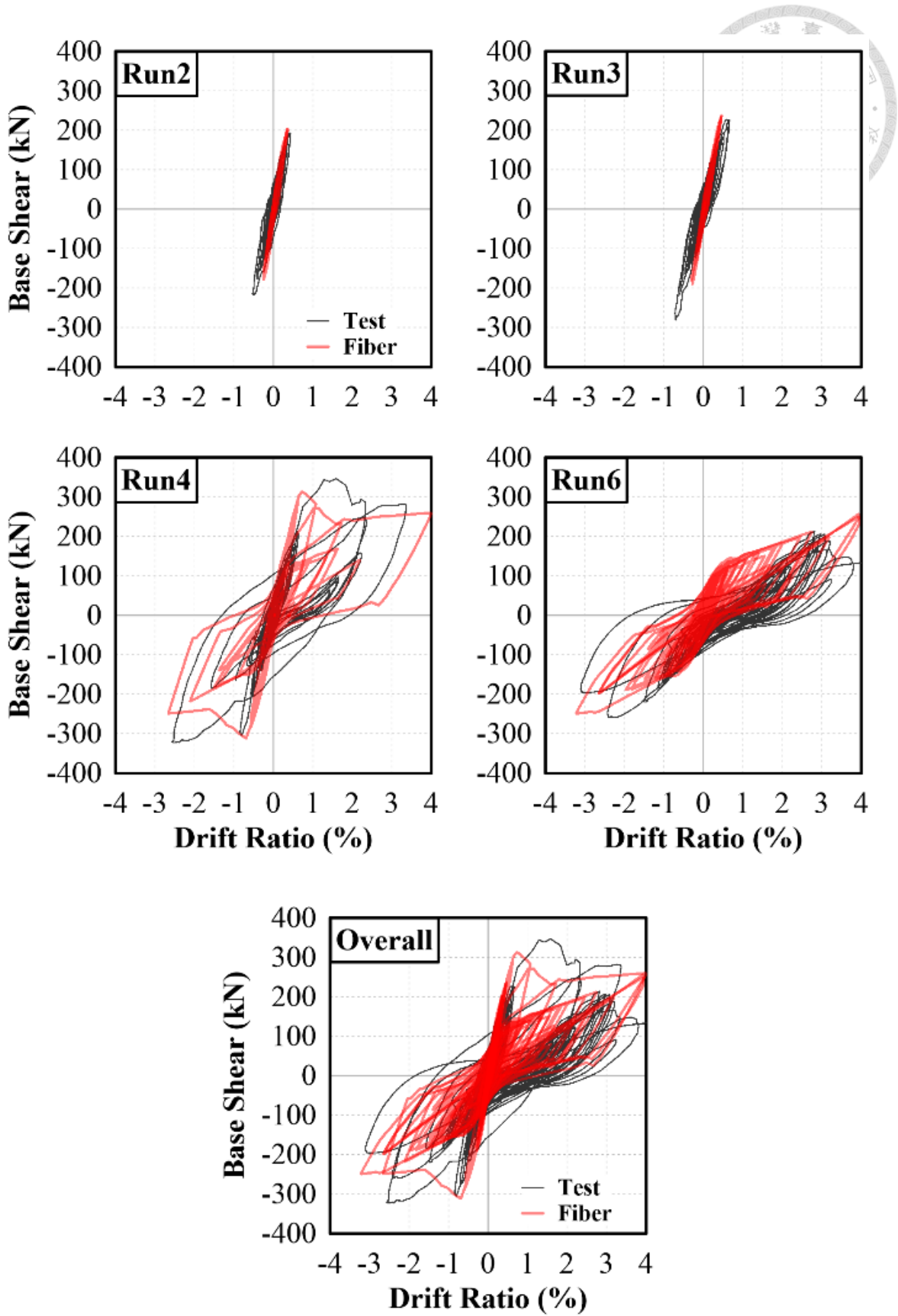
Figure 6-52. Comparison on T1 Frame hysteresis curve for Fiber model

518

Test 2 Run 2 C1

Test 2 Run 4 C1
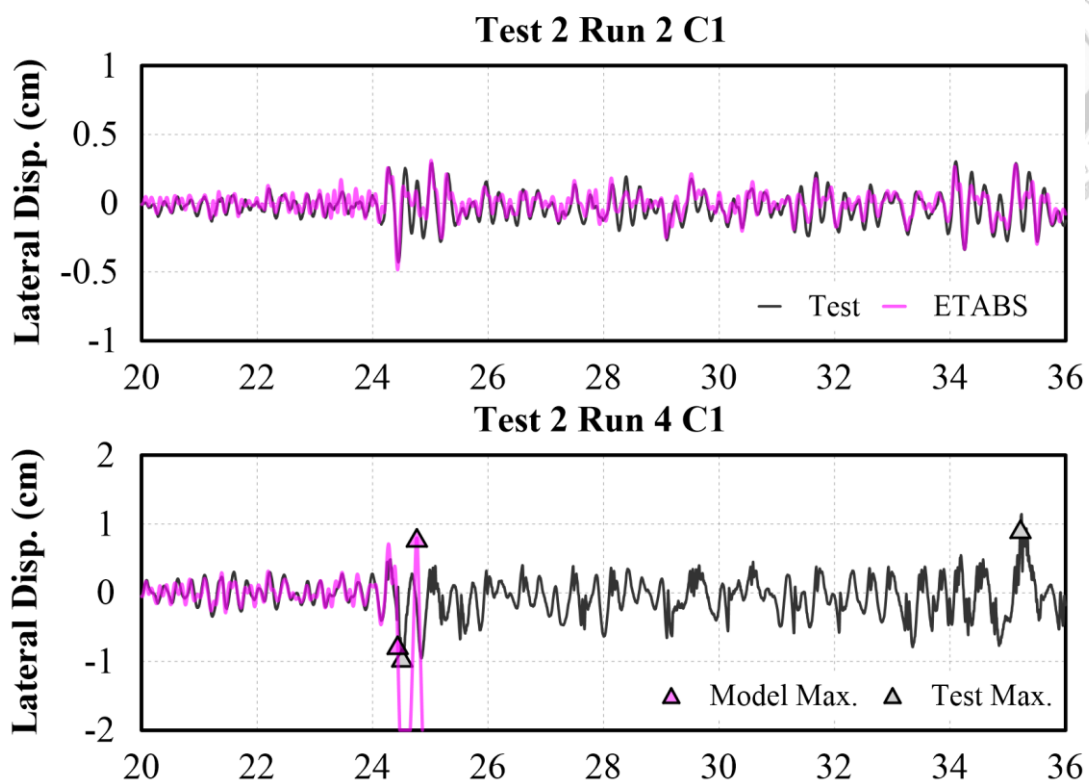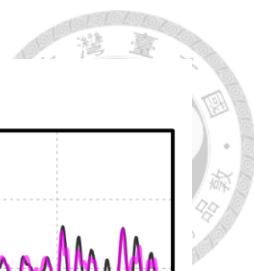
Figure 6-53. Comparison on T2 C1 lateral displacement for ETABS model

Test 2 Run 2 C1

Test 2 Run 4 C1
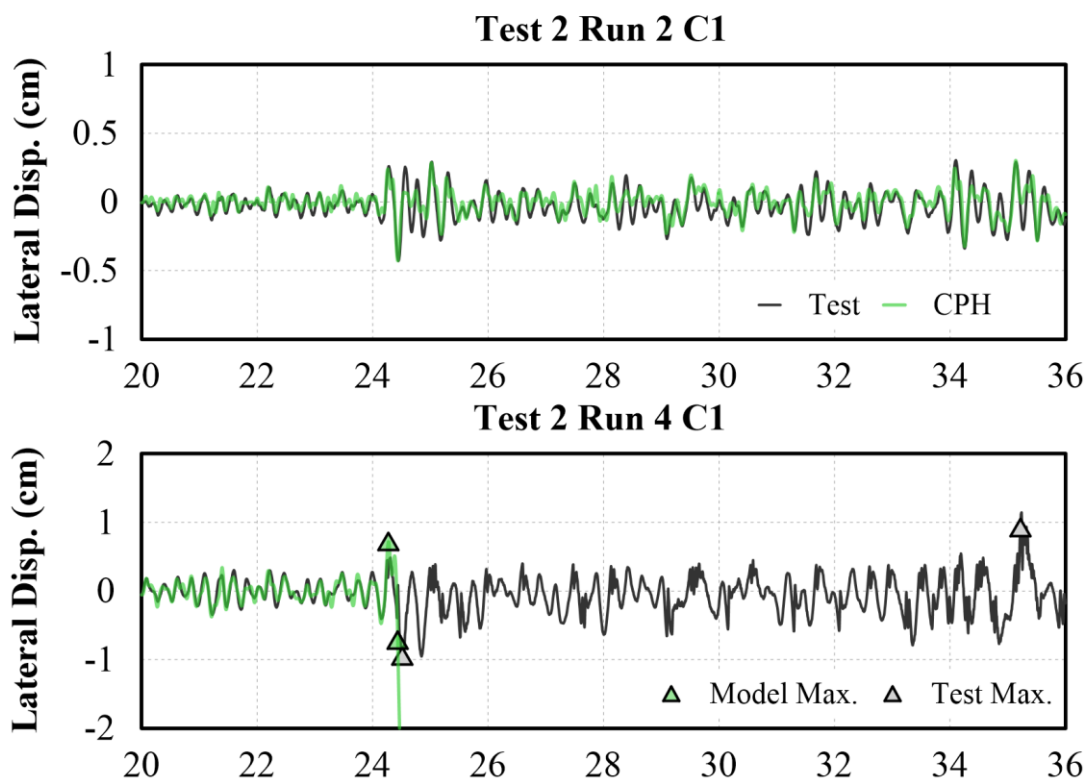
Figure 6-54. Comparison on T2 C1 lateral displacement for CPH model

Test 2 Run 2 C1

Test 2 Run 4 C1
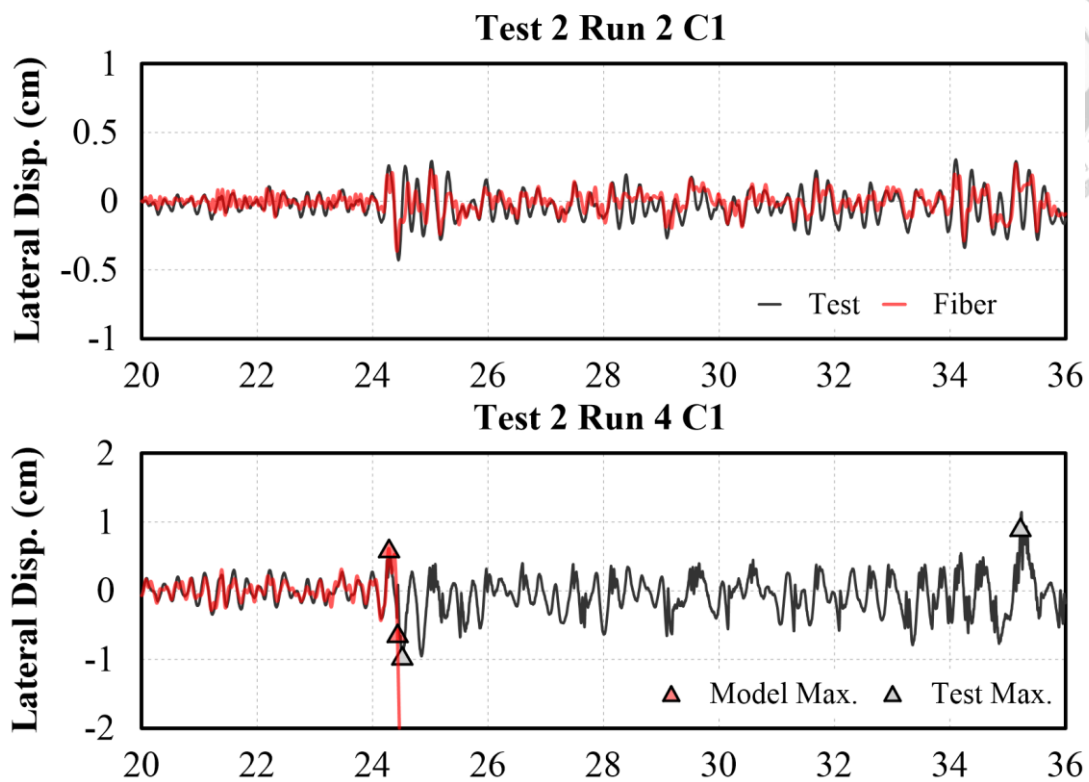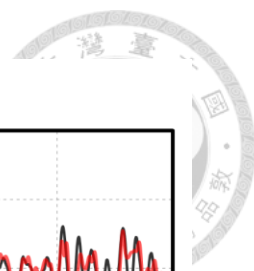
Figure 6-55. Comparison on T2 C1 lateral displacement for Fiber model

Test 2 Run 2 C1

Test 2 Run 4 C1
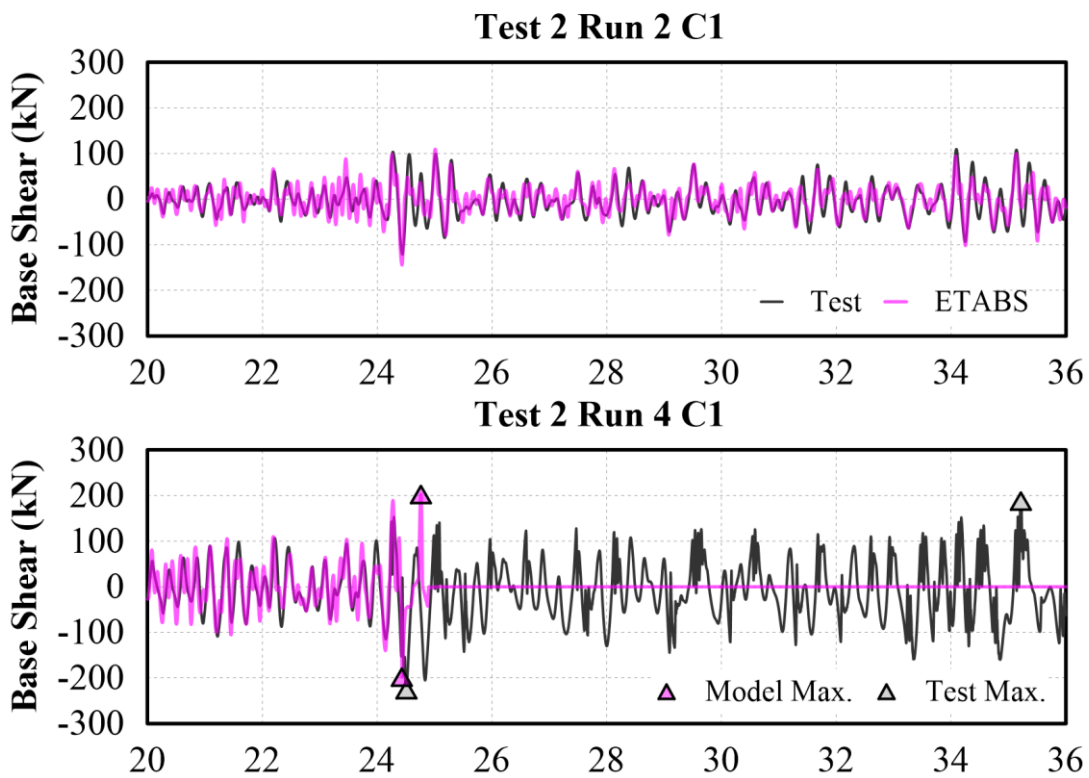
Figure 6-56. Comparison on T2 C1 base shear for ETABS model

520

Test 2 Run 2 C1

Test 2 Run 4 C1
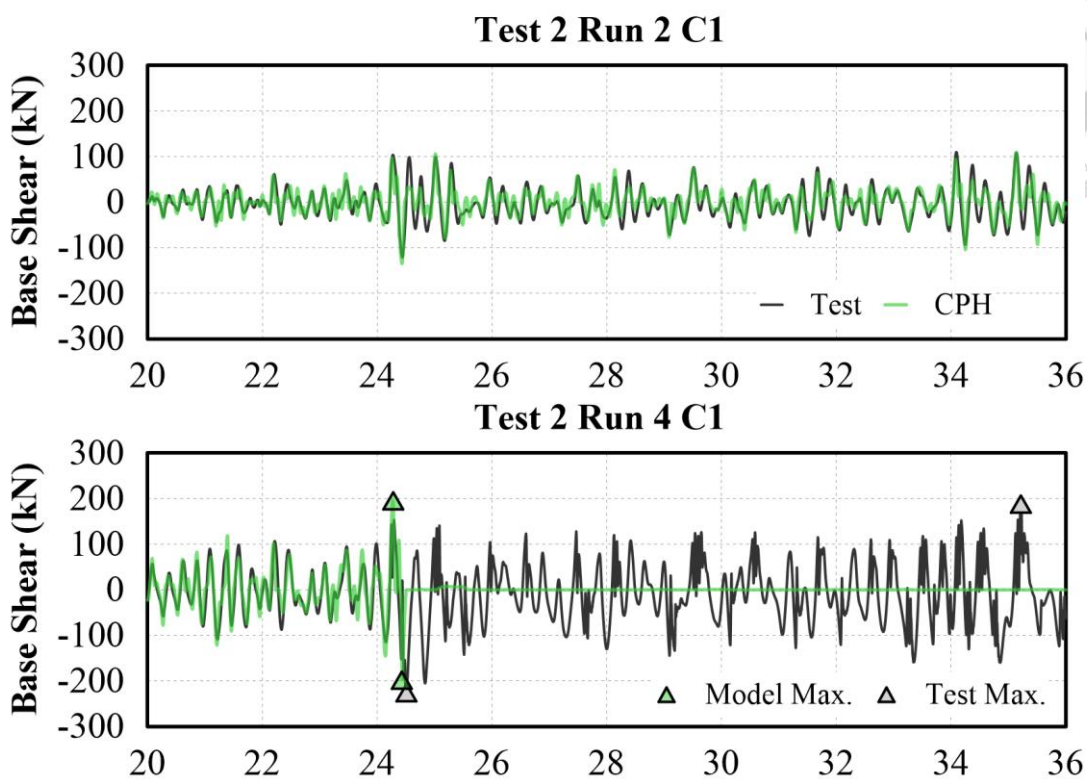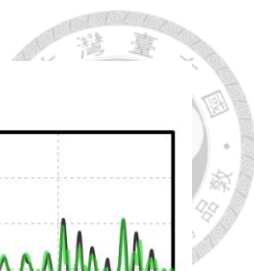
Figure 6-57. Comparison on T2 C1 base shear for CPH model

Test 2 Run 2 C1

Test 2 Run 4 C1
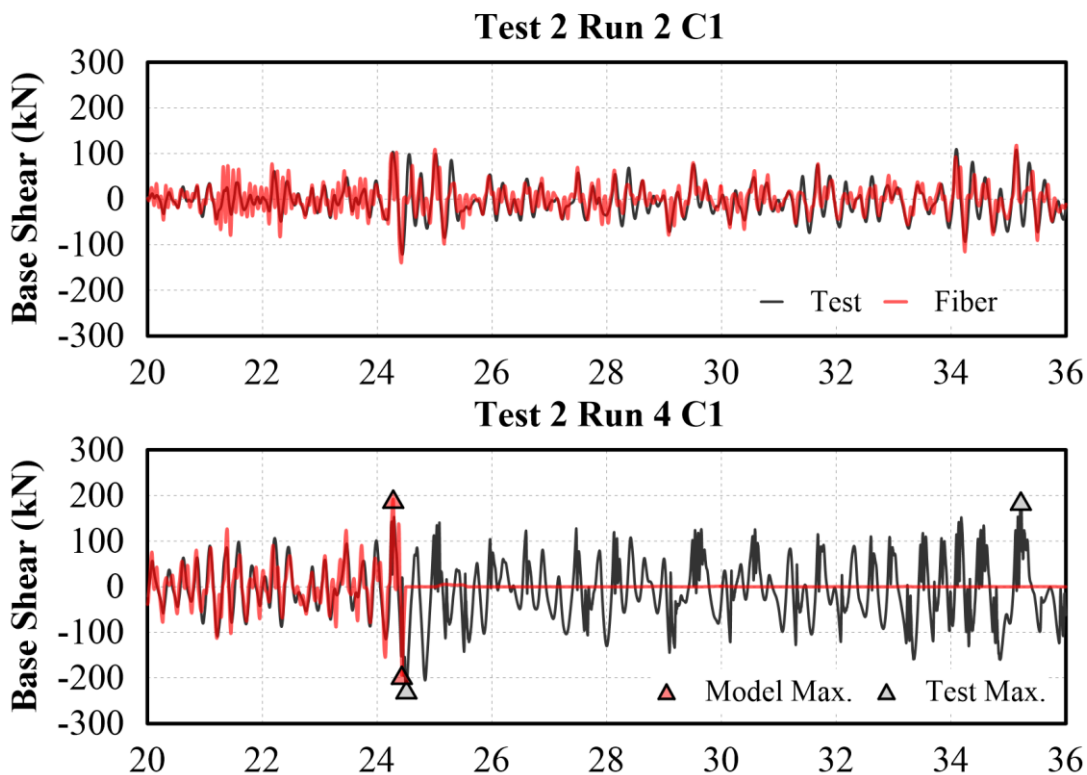
Figure 6-58. Comparison on T2 C1 base shear for Fiber model

521
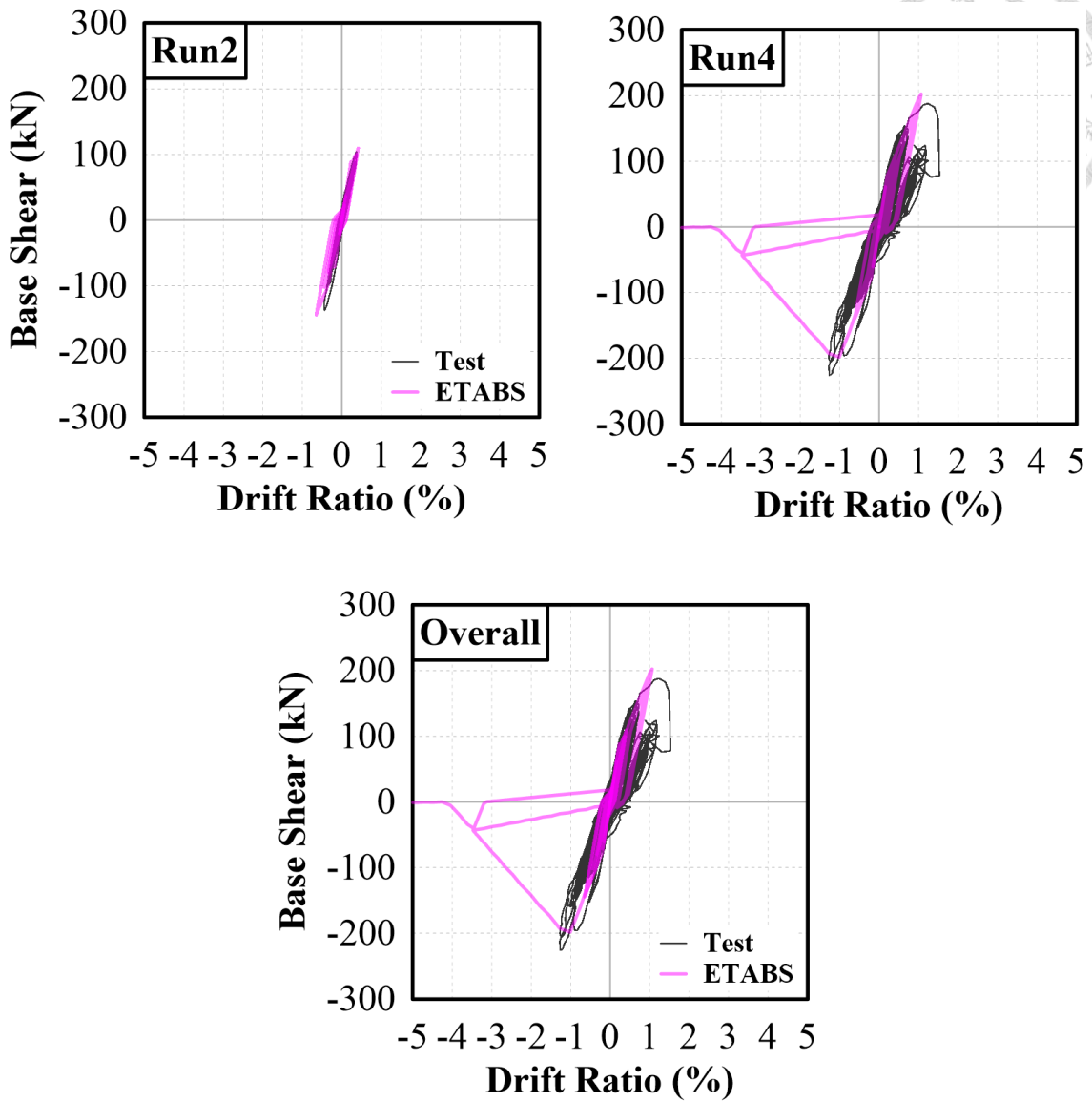
Figure 6-59. Comparison on T2 C1 hysteresis curve for ETABS model

522
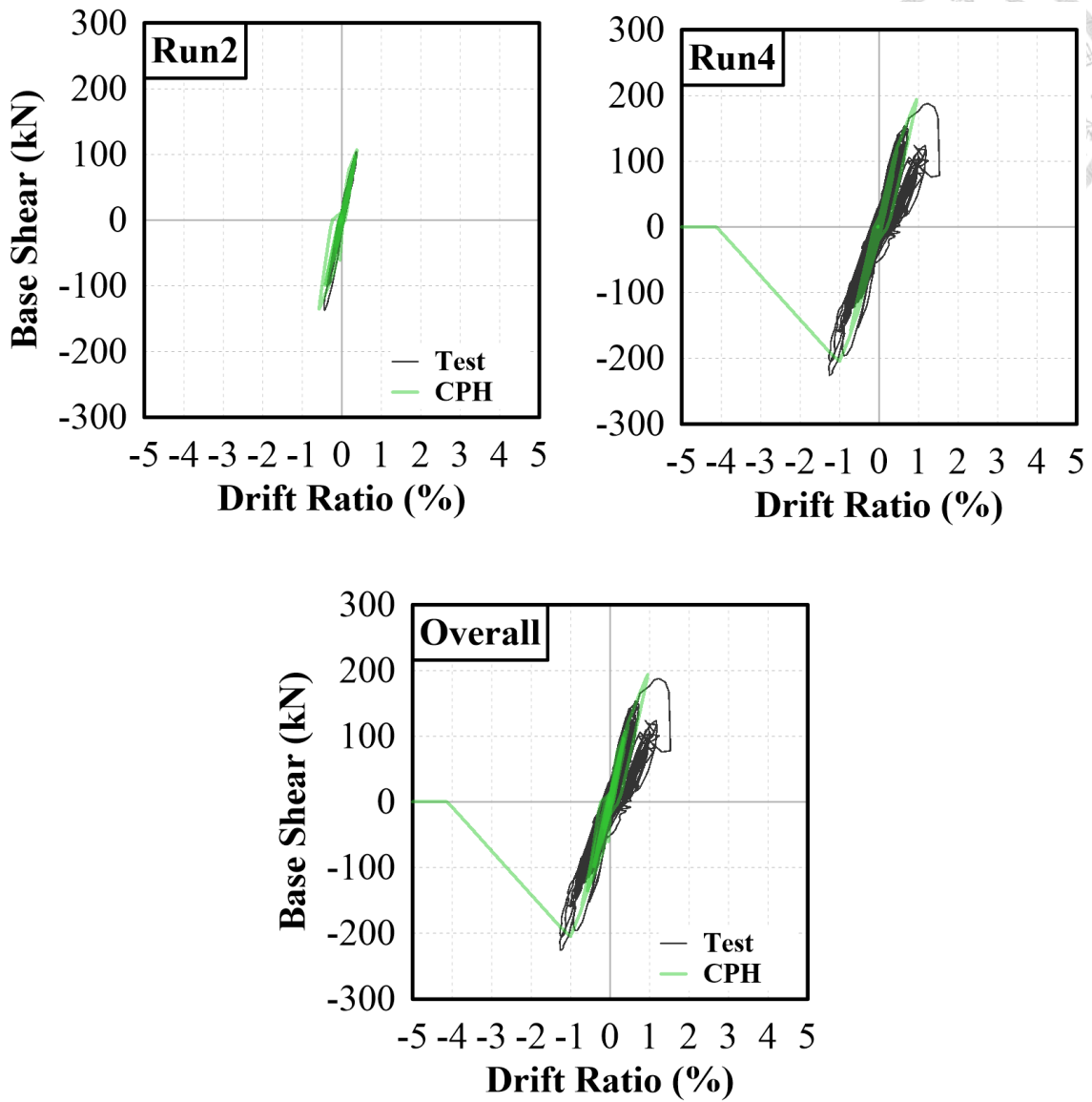
Figure 6-60. Comparison on T2 C1 hysteresis curve for CPH model
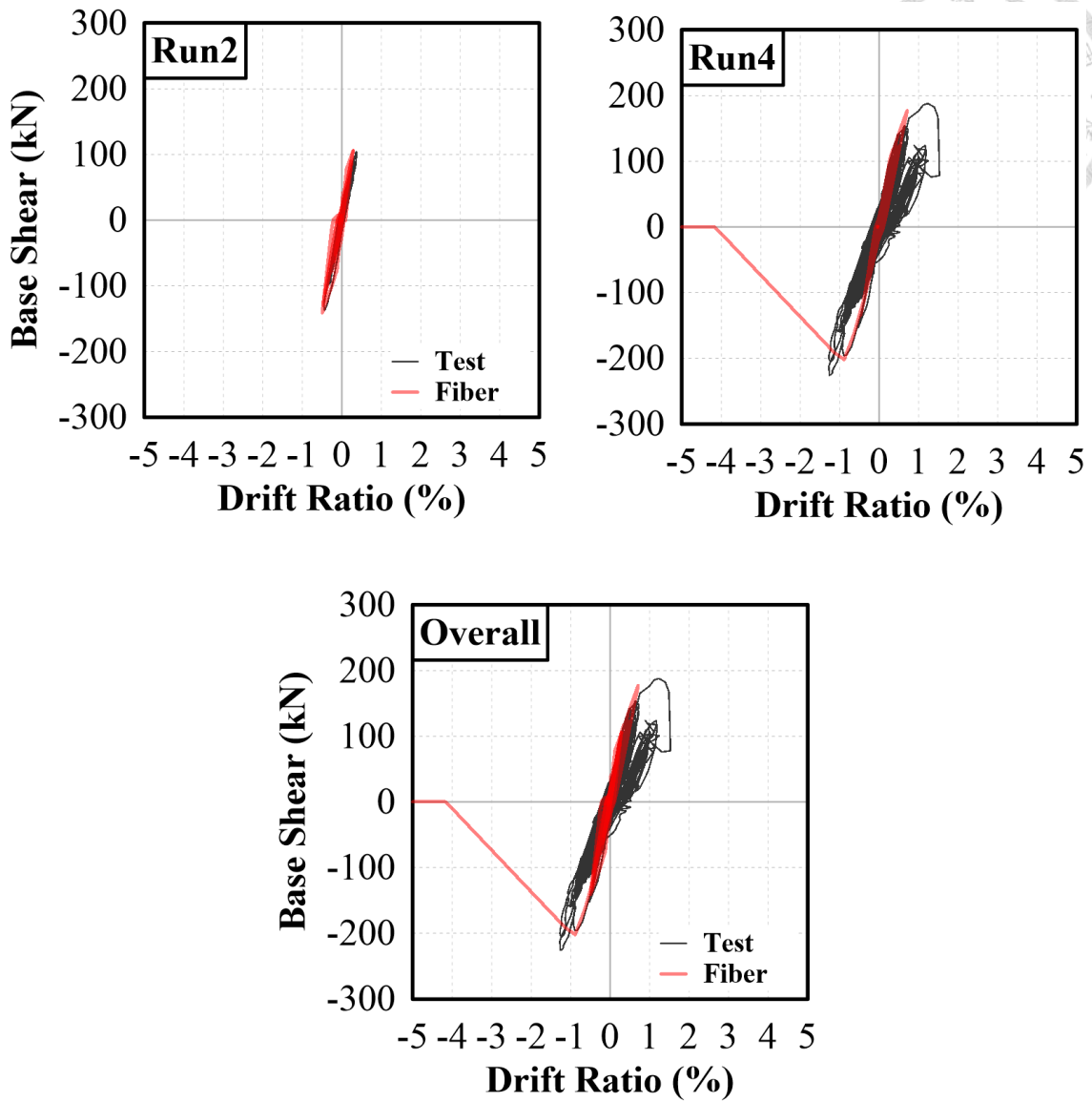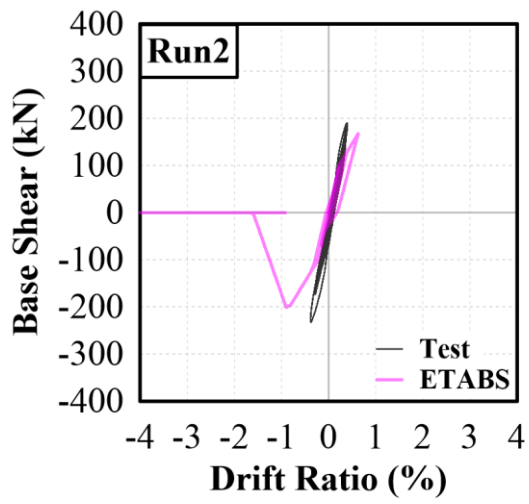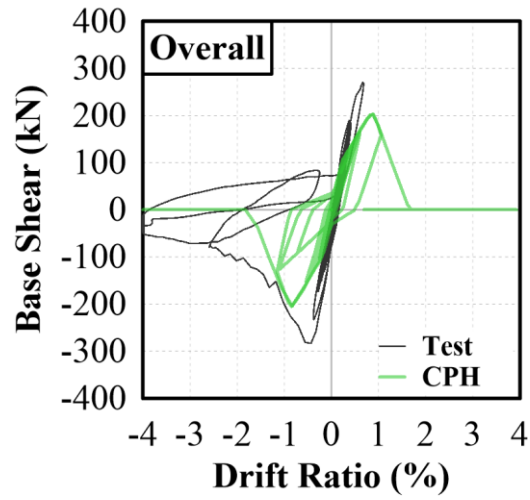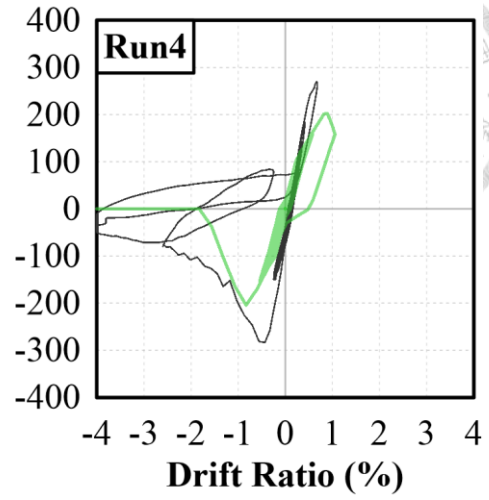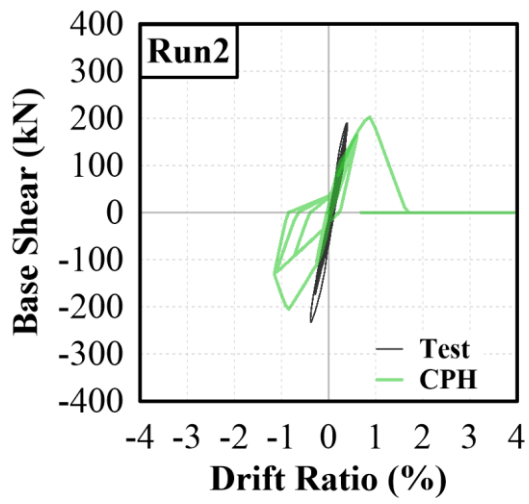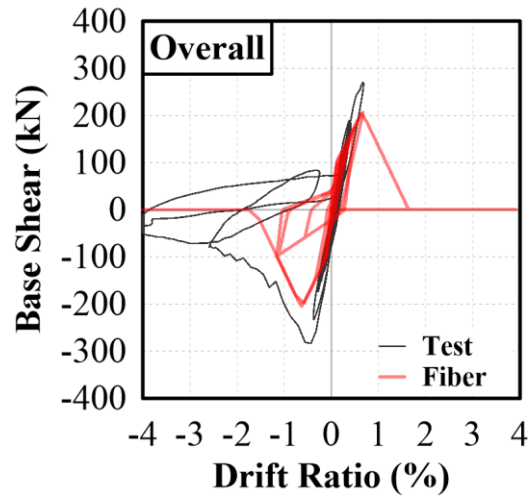
Figure 6-61. Comparison on T2 C1 hysteresis curve for Fiber model

524
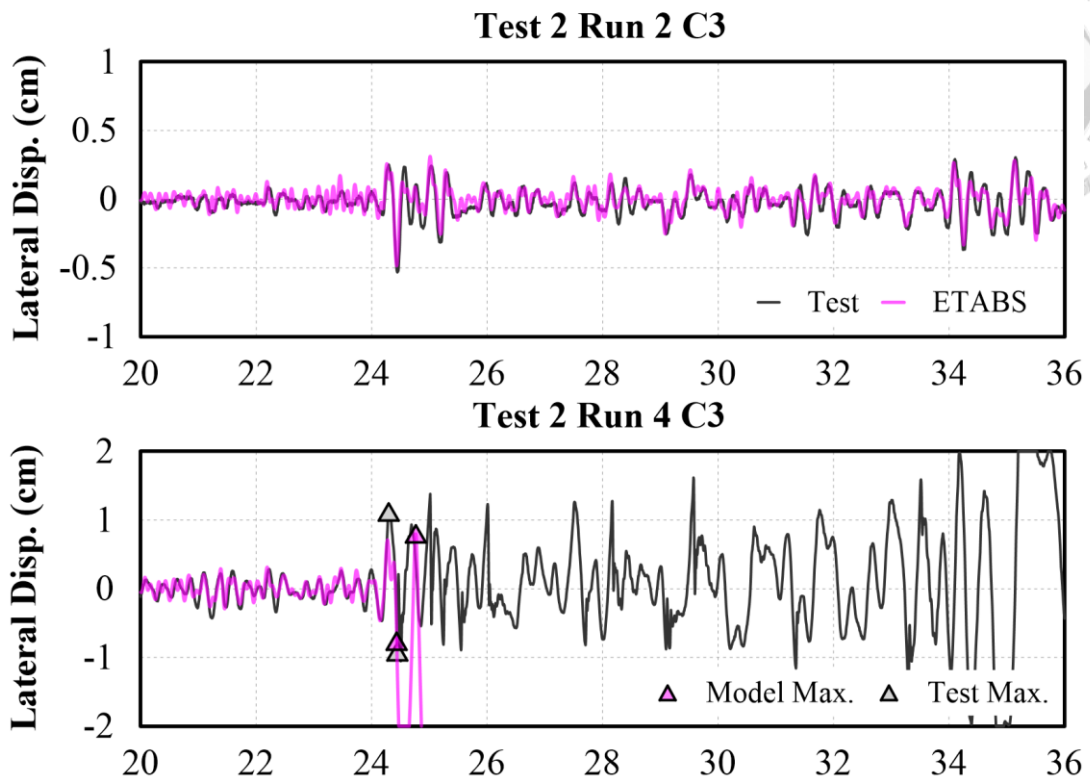
Figure 6-62. Comparison on T2 C3 lateral displacement for ETABS model
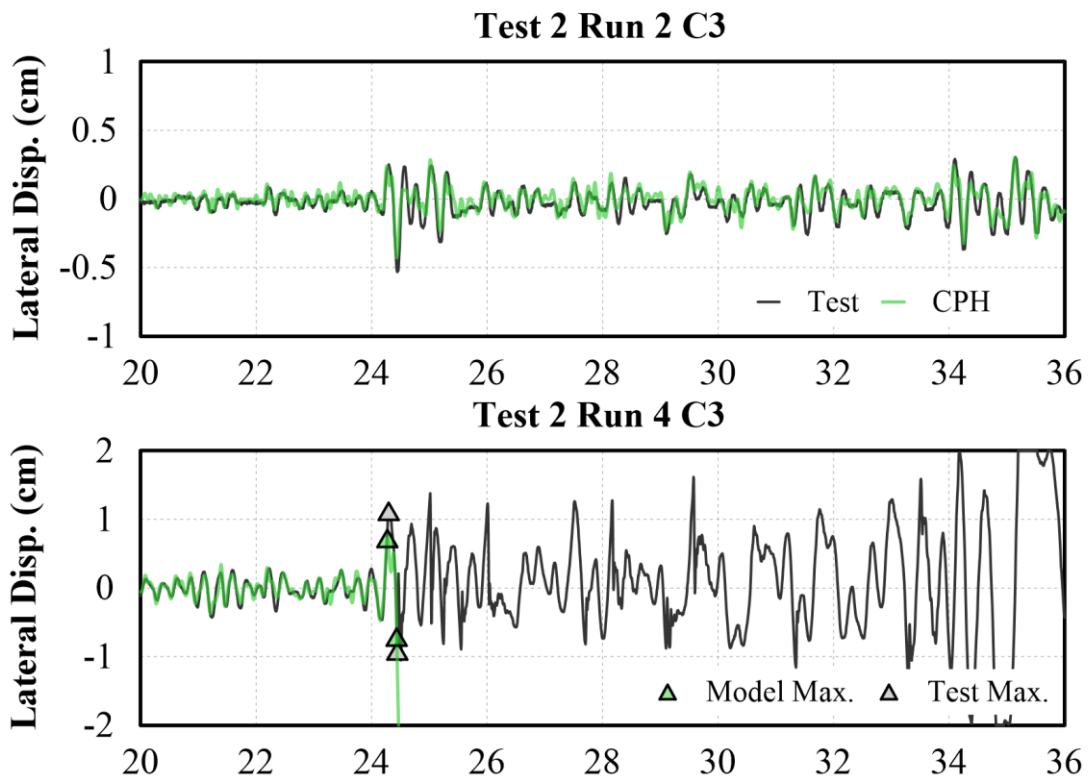
Figure 6-63. Comparison on T2 C3 lateral displacement for CPH model

525
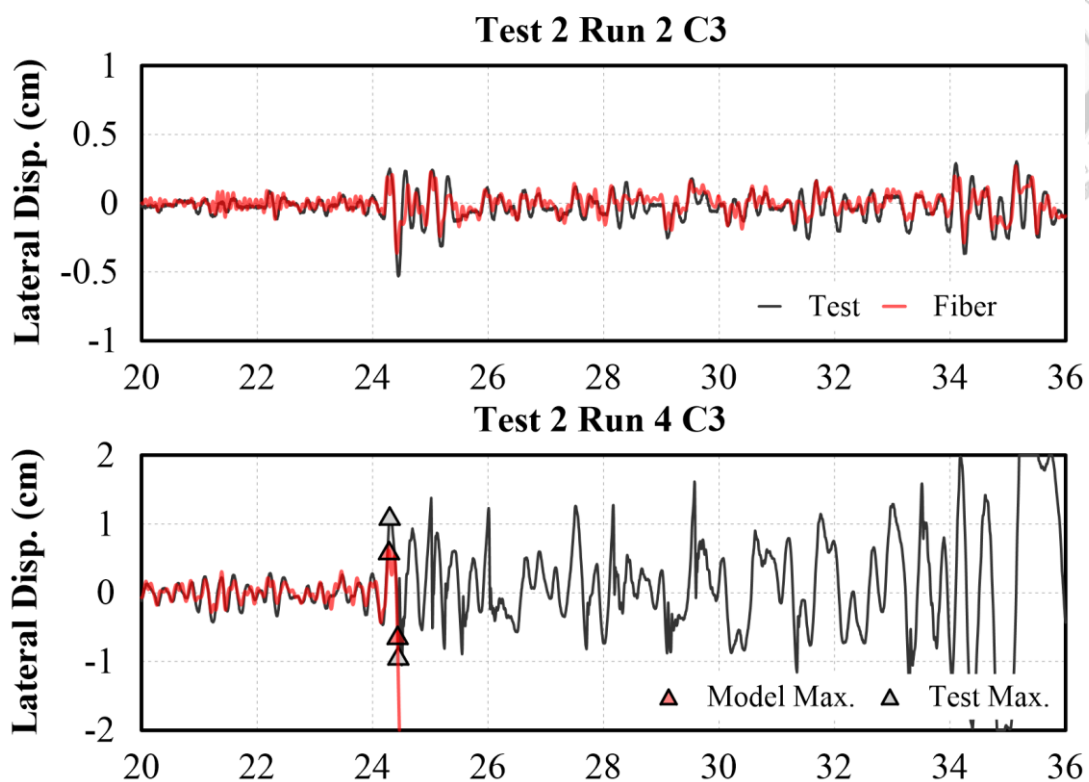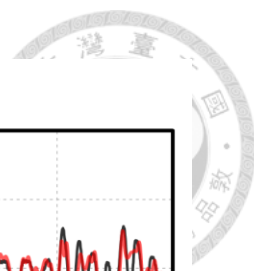
Figure 6-64. Comparison on T2 C3 lateral displacement for Fiber model
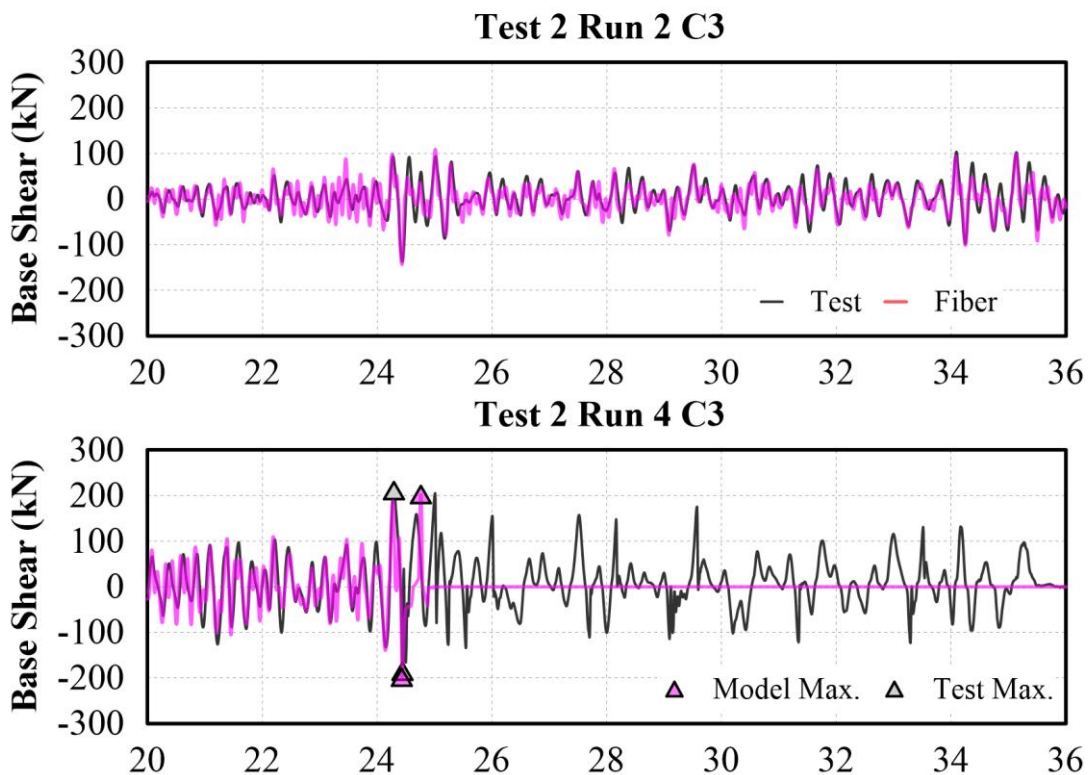
Figure 6-65. Comparison on T2 C3 base shear for ETABS model

526

Test 2 Run 2 C3

Test 2 Run 4 C3
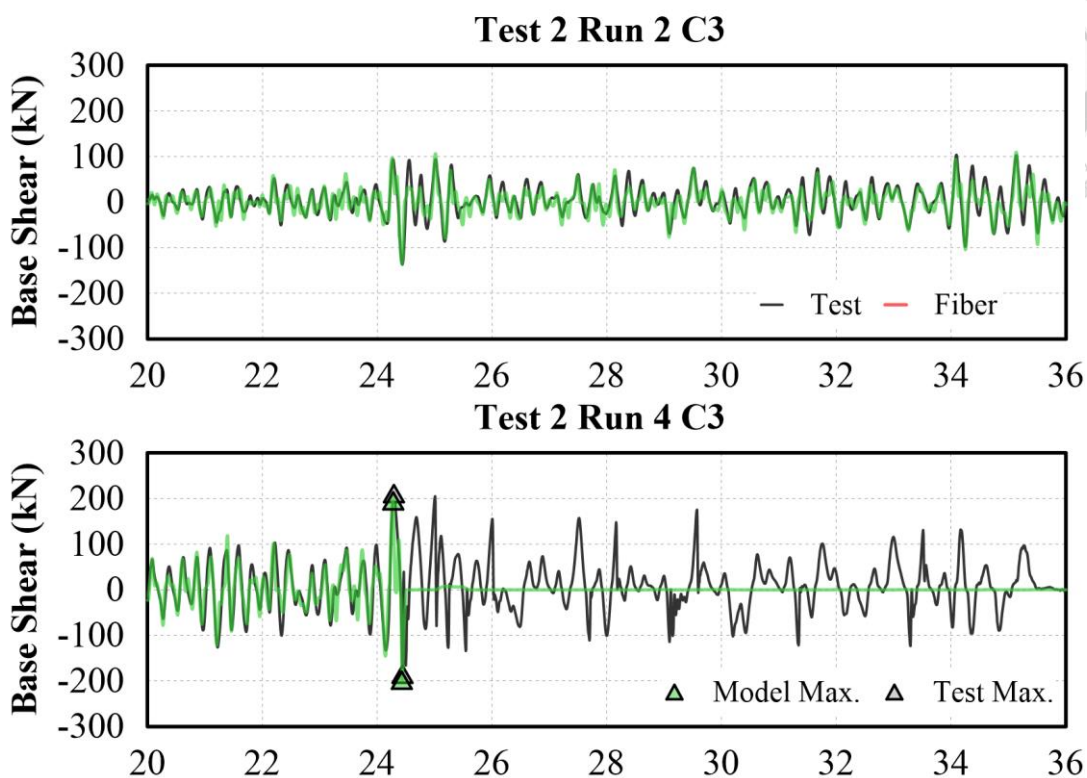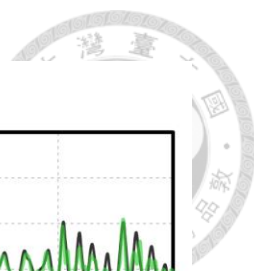
Figure 6-66. Comparison on T2 C3 base shear for CPH model

Test 2 Run 2 C3

Test 2 Run 4 C3
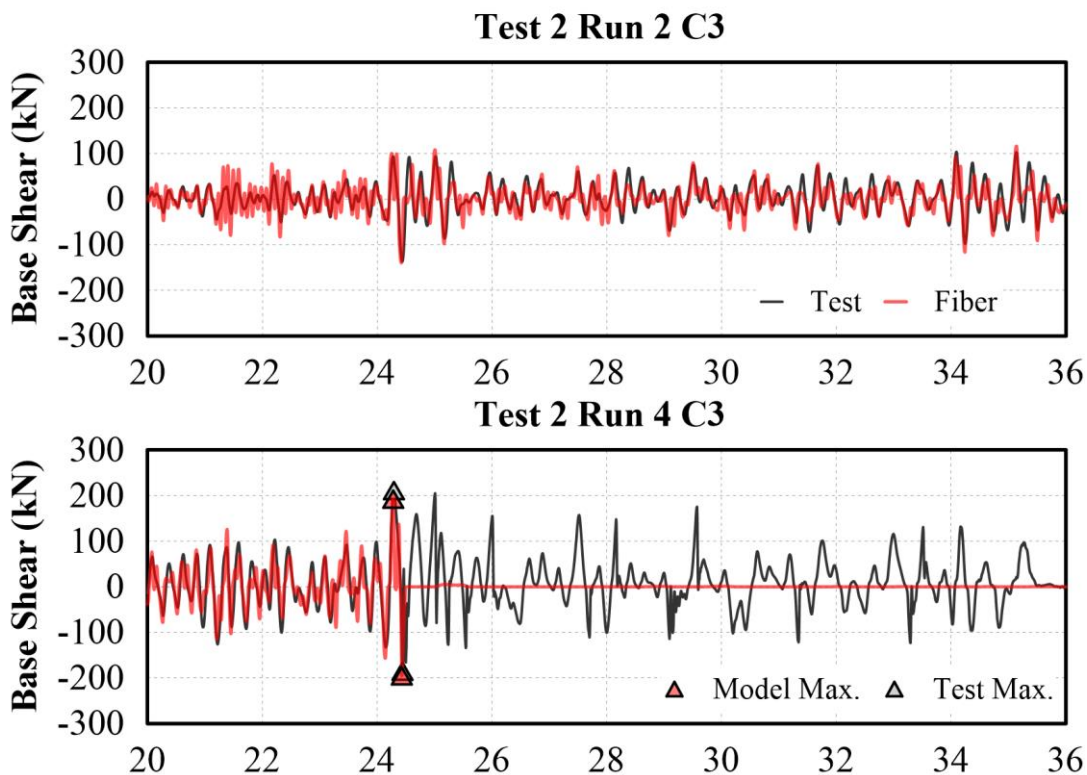
Figure 6-67. Comparison on T2 C3 base shear for Fiber model

527
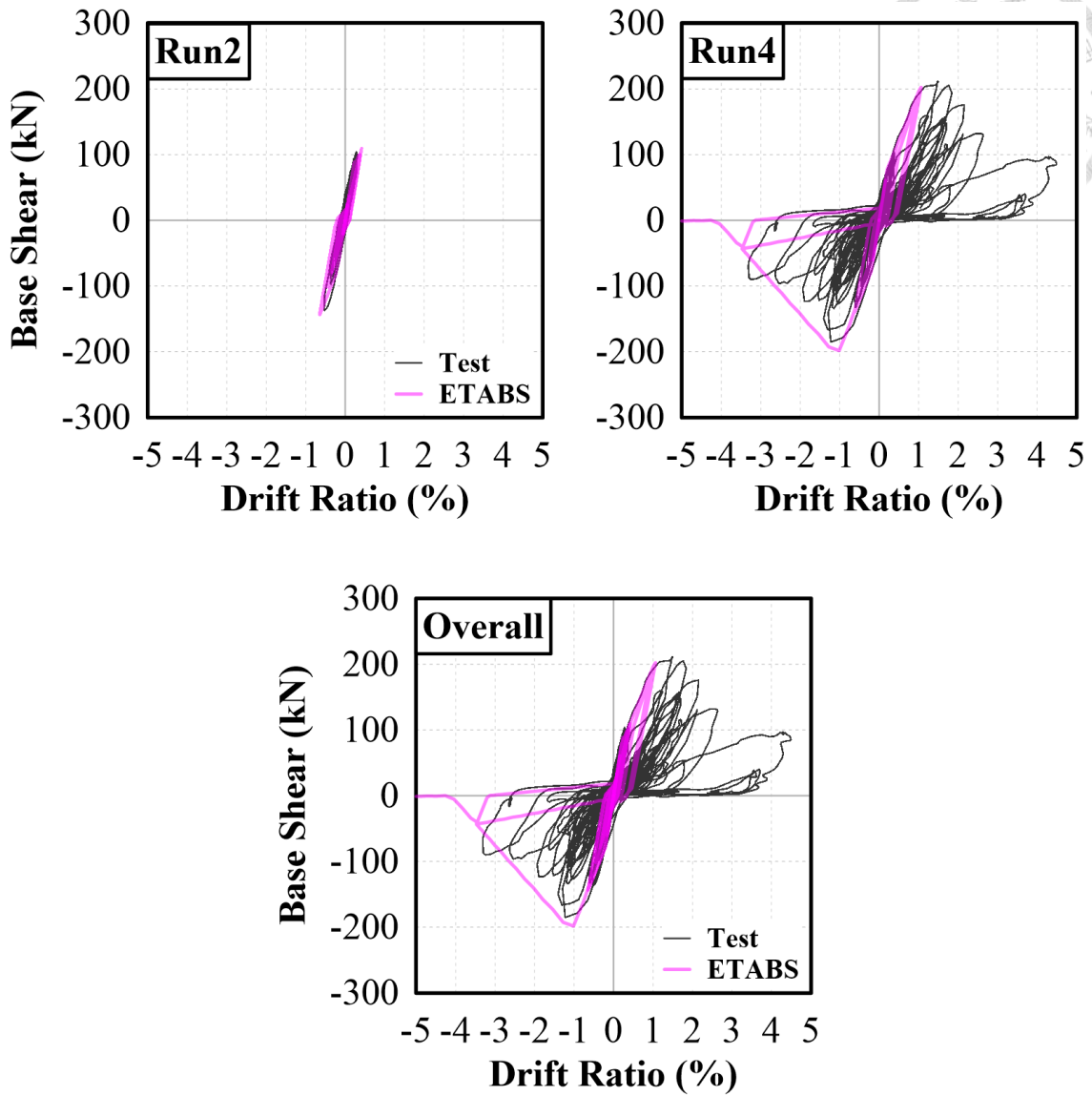
Figure 6-68. Comparison on T2 C3 hysteresis curve for ETABS model

528
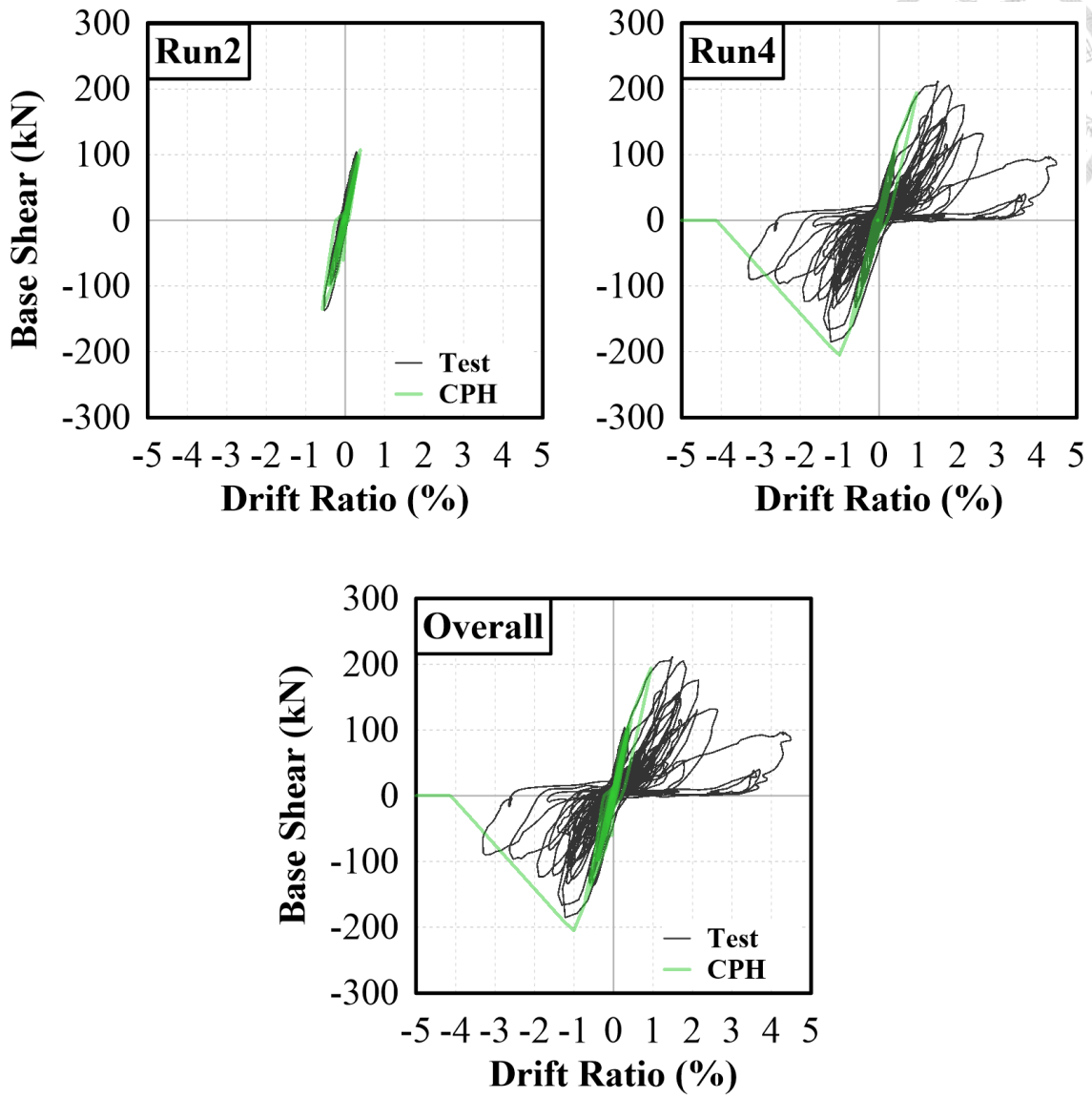
Figure 6-69. Comparison on T2 C3 hysteresis curve for CPH model

529
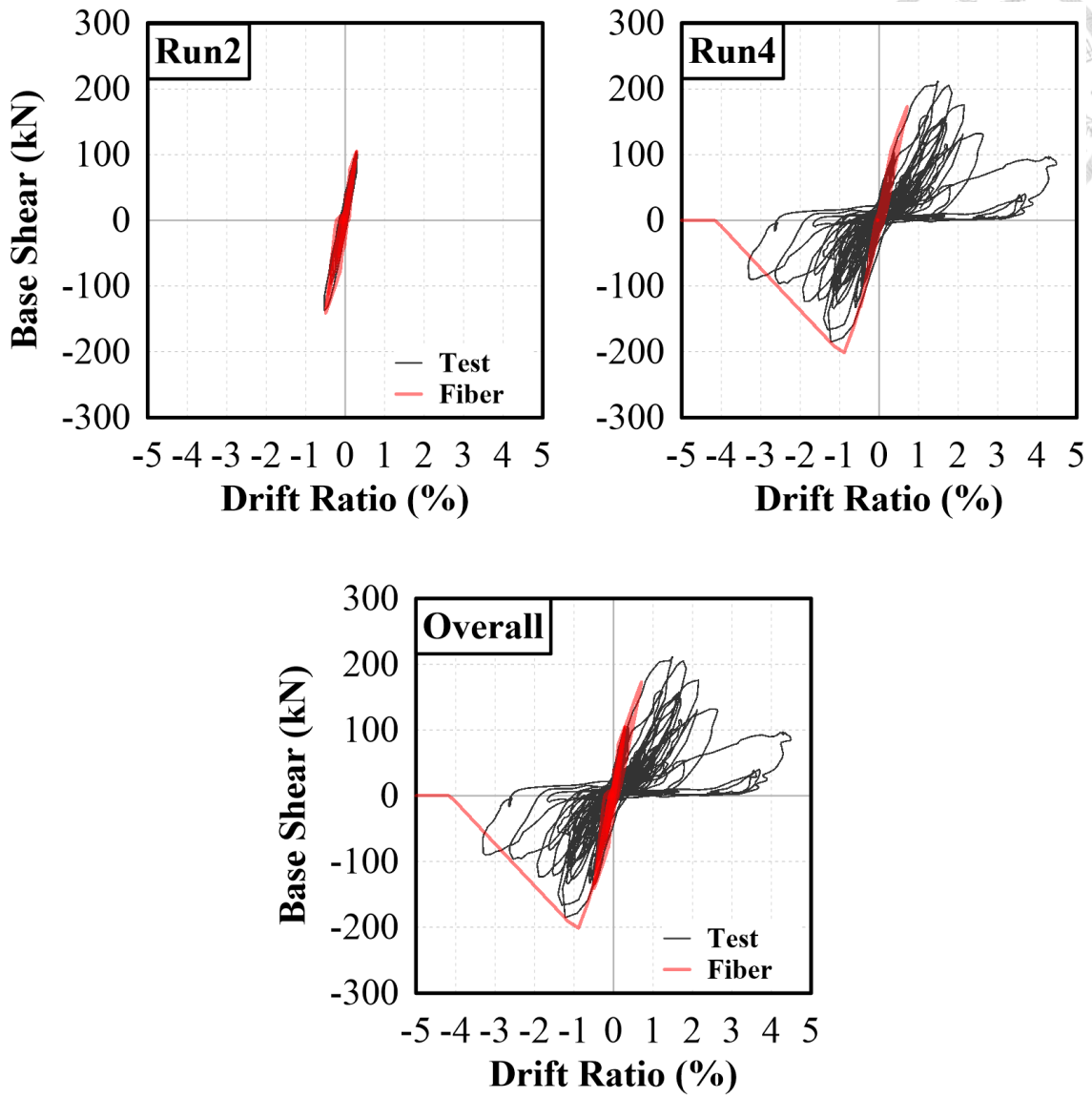
Figure 6-70. Comparison on T2 C3 hysteresis curve for Fiber model
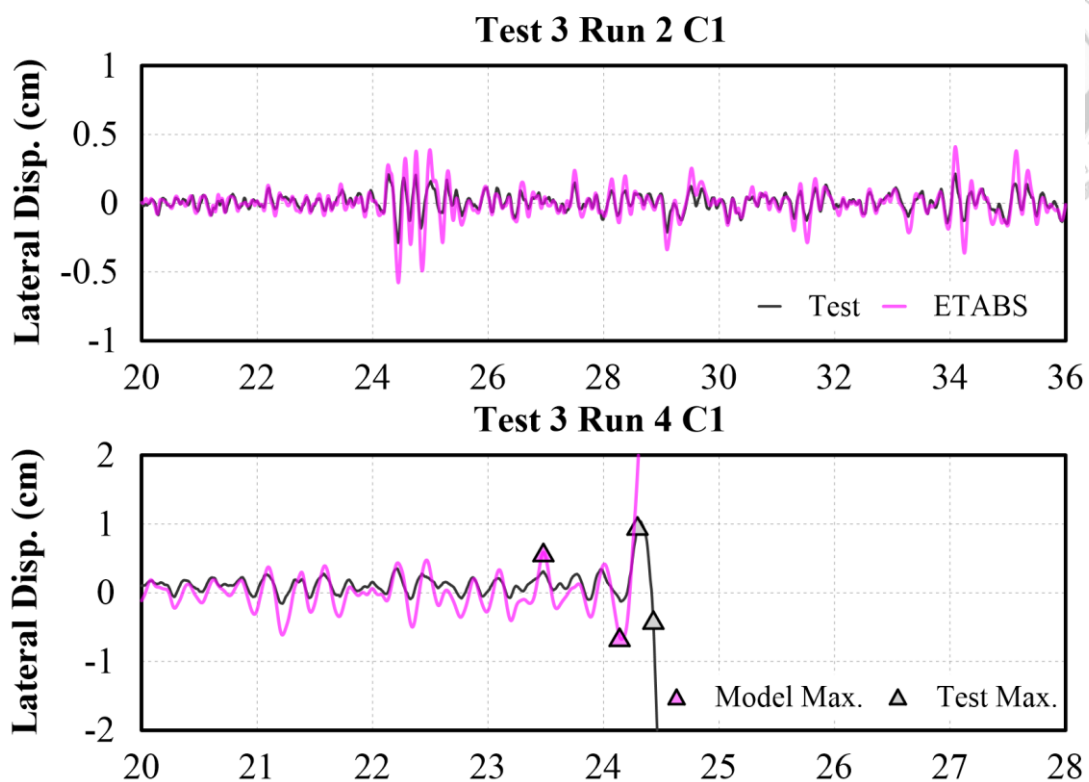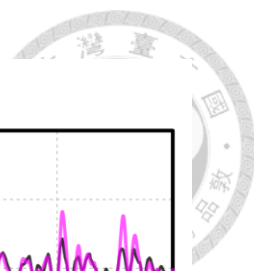
Figure 6-71. Comparison on T3 C1 lateral displacement for ETABS model
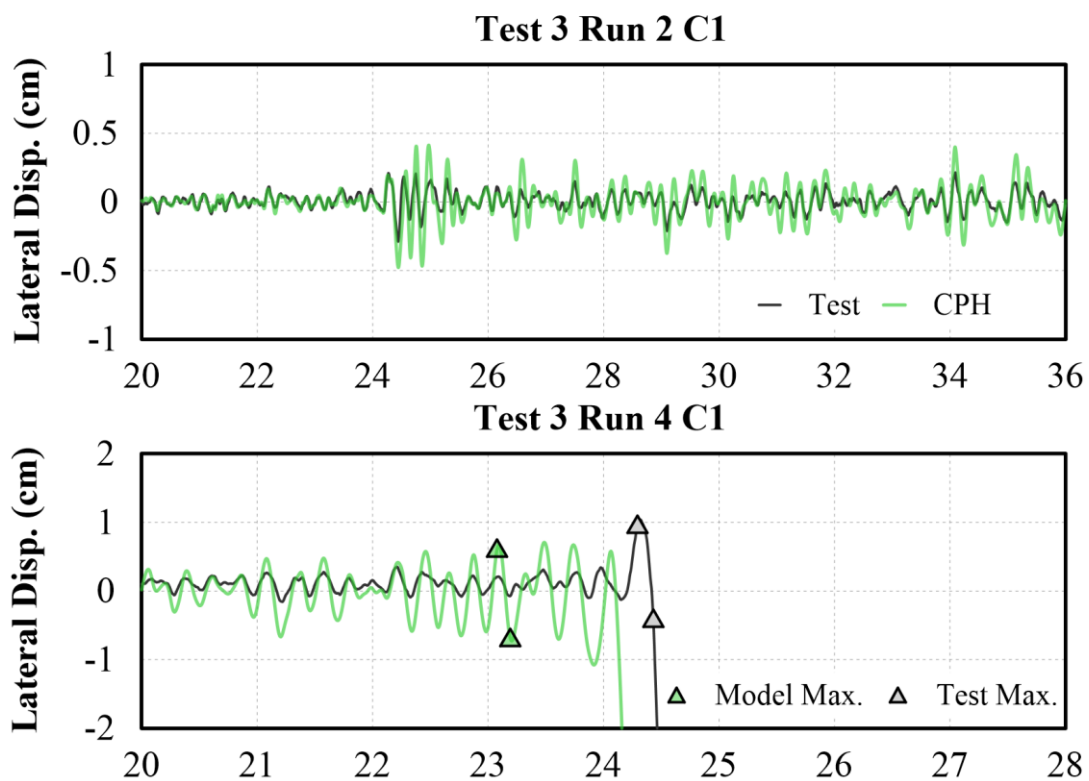
Figure 6-72. Comparison on T3 C1 lateral displacement for CPH model

531
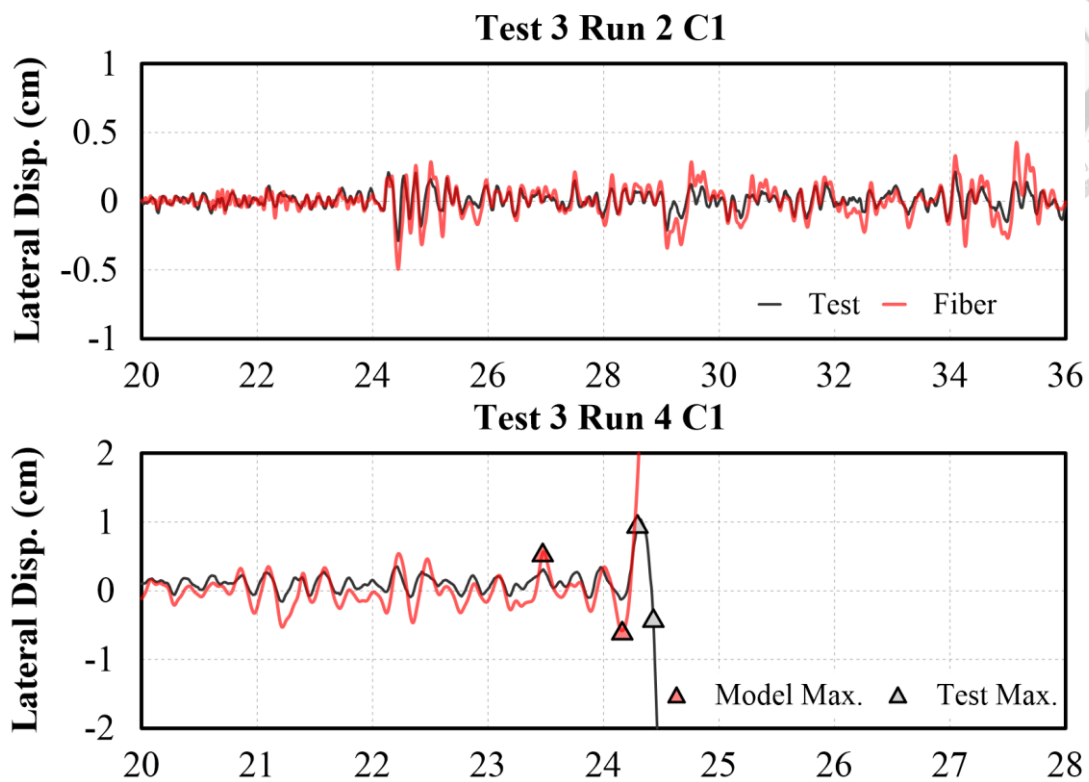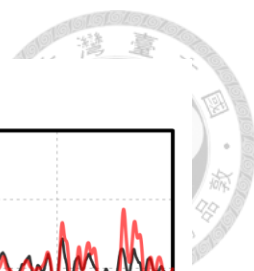
Figure 6-73. Comparison on T3 C1 lateral displacement for Fiber model
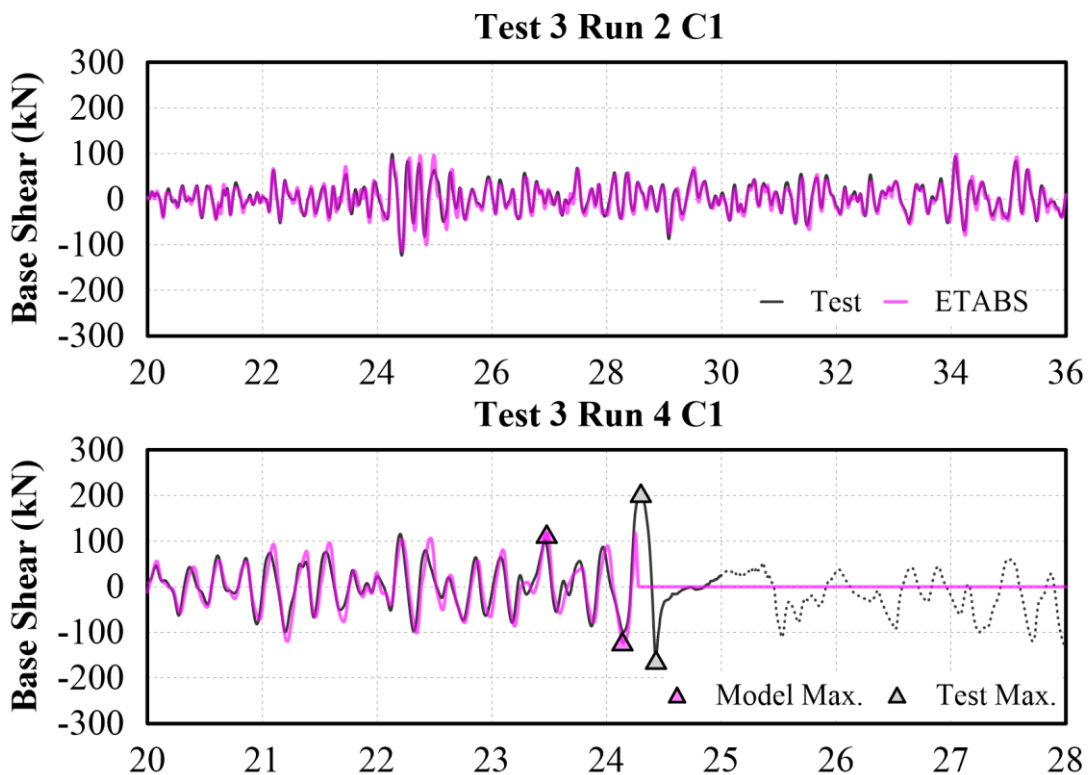
Figure 6-74. Comparison on T3 C1 base shear for ETABS model

532
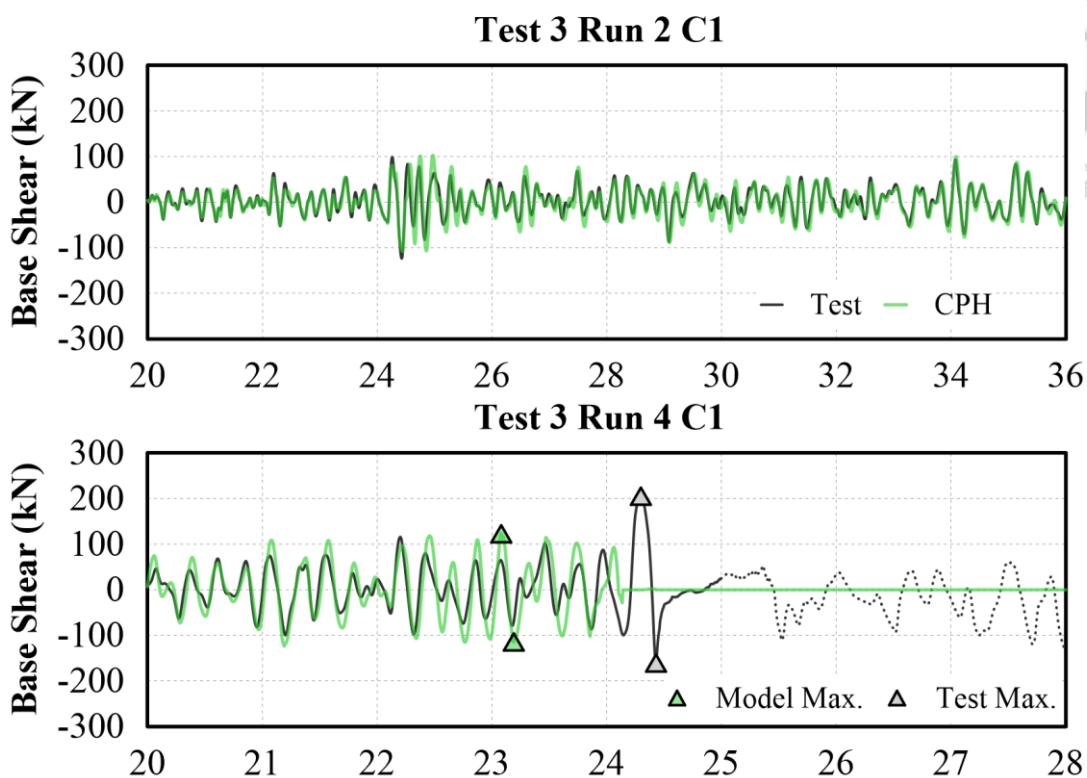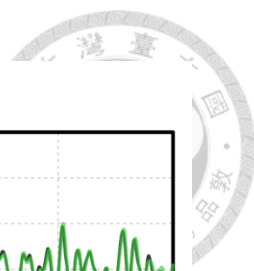
Figure 6-75. Comparison on T3 C1 base shear for CPH model
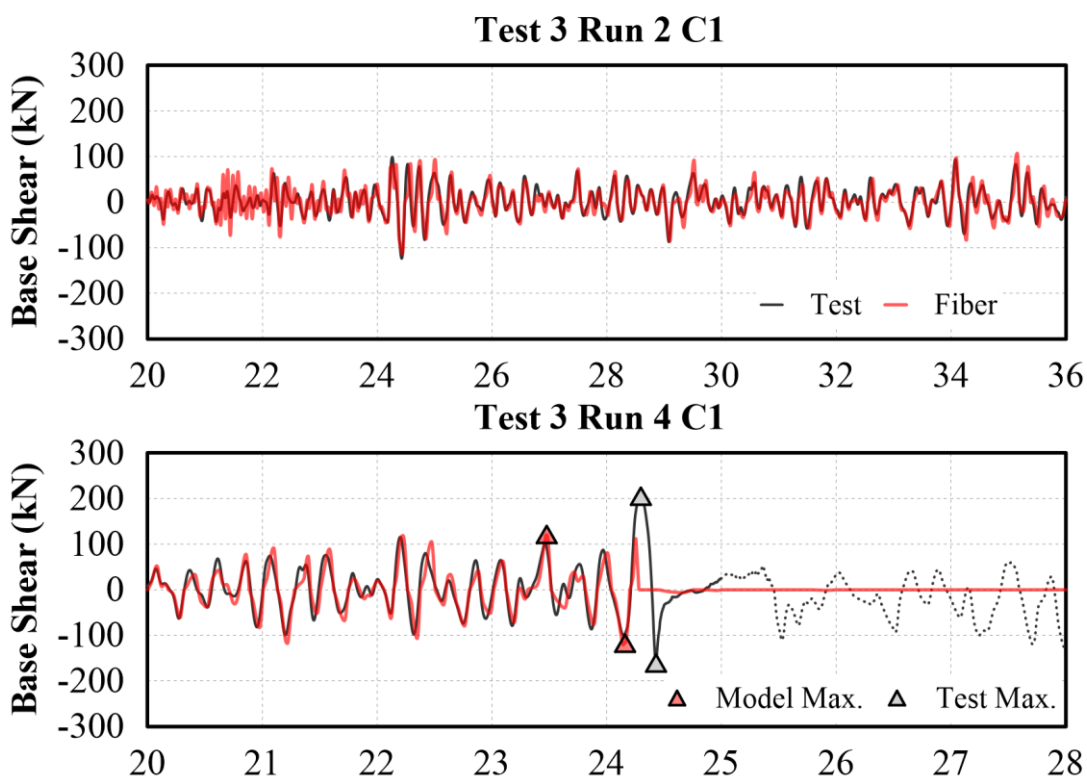
Figure 6-76. Comparison on T3 C1 base shear for Fiber model

533
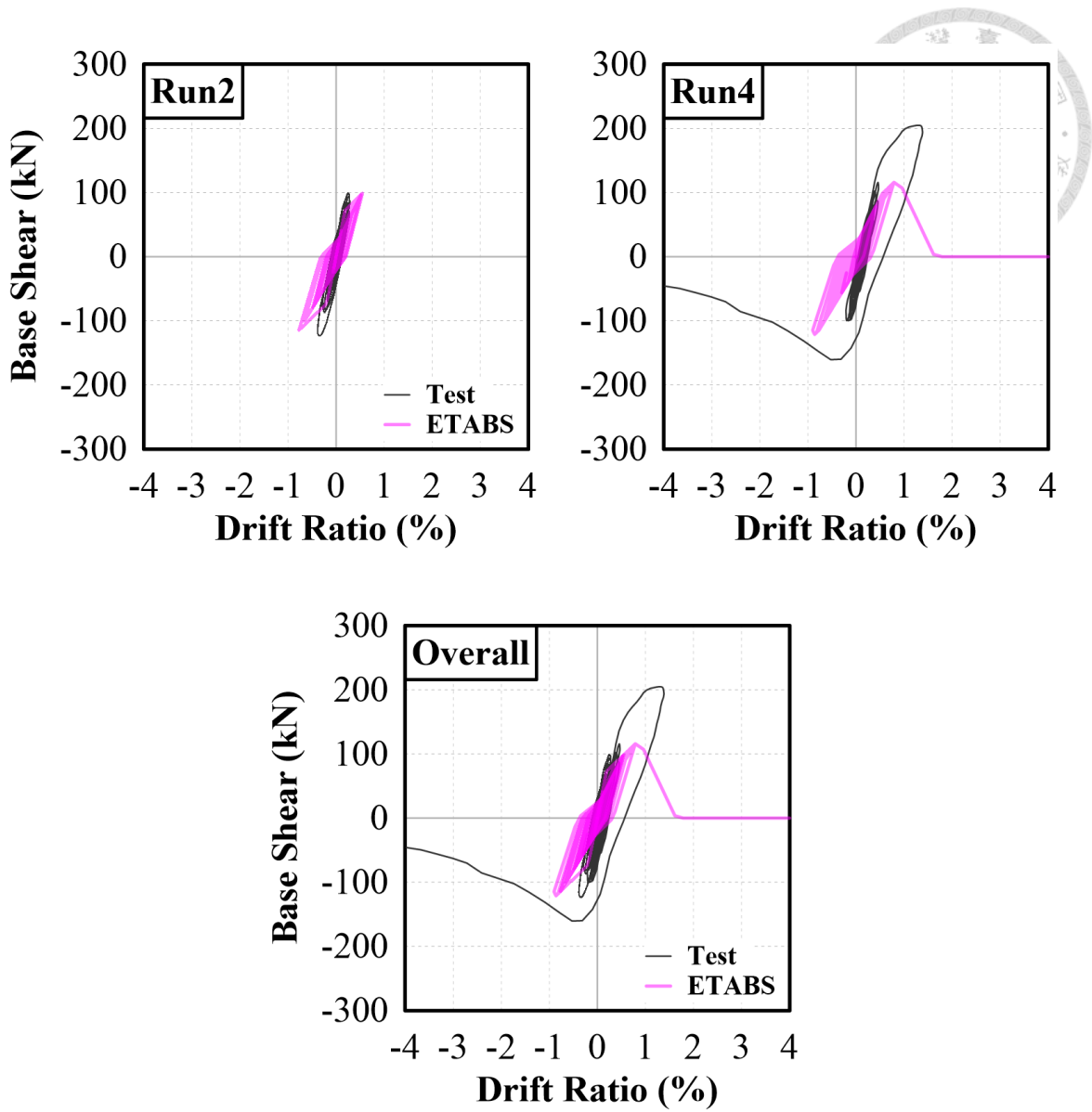
Figure 6-77. Comparison on T3 C1 hysteresis curve for ETABS model
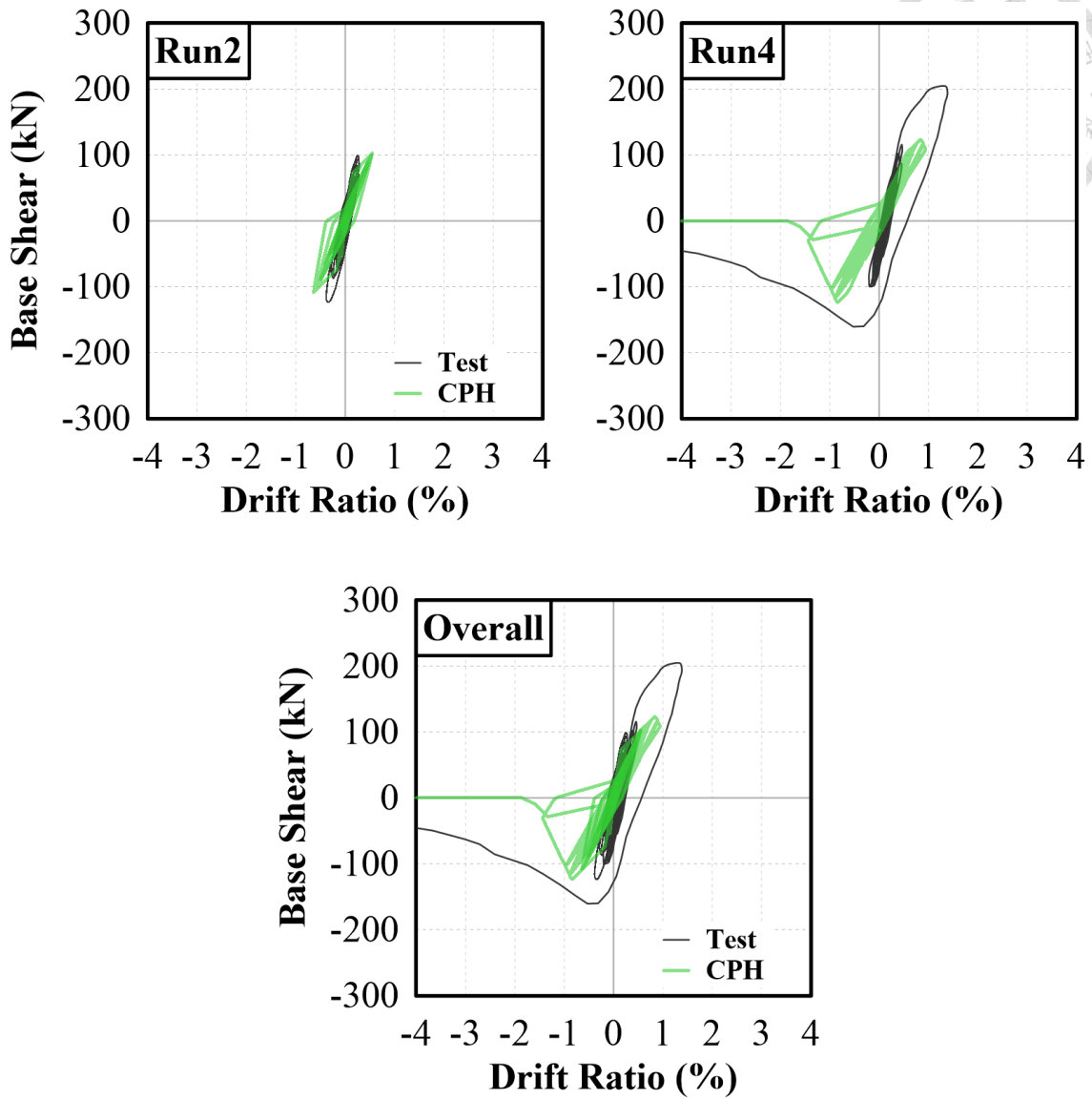
Figure 6-78. Comparison on T3 C1 hysteresis curve for CPH model
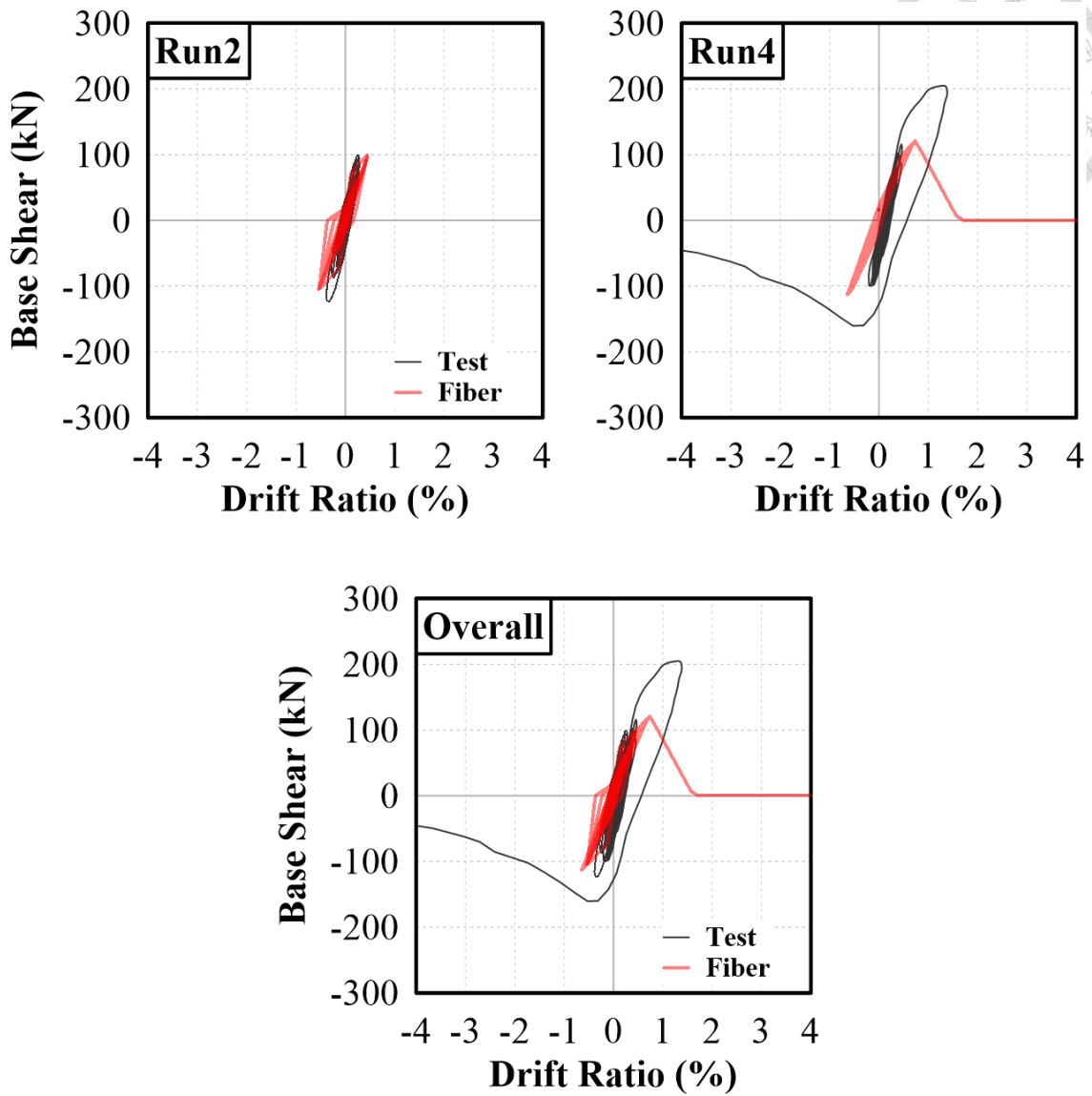
Figure 6-79. Comparison on T3 C1 hysteresis curve for Fiber model

536

Test 3 Run 2 C3

Test 3 Run 4 C3
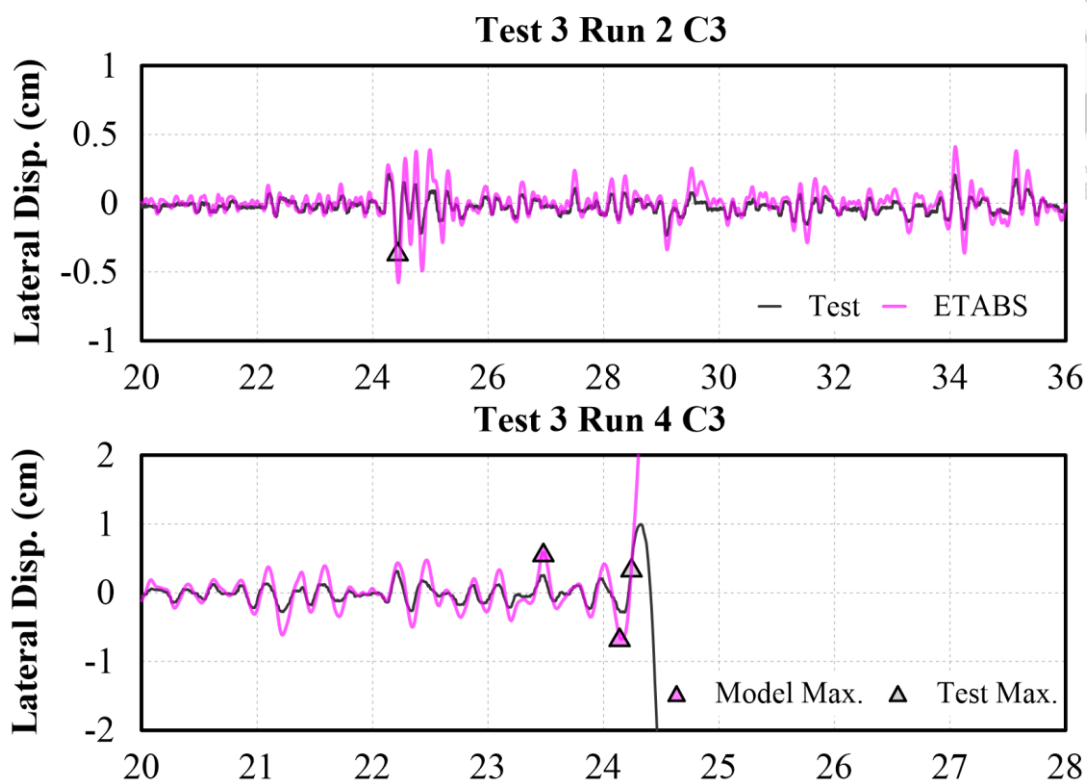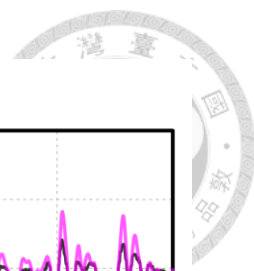
Figure 6-80. Comparison on T3 C3 lateral displacement for ETABS model

Test 3 Run 2 C3

Test 3 Run 4 C3
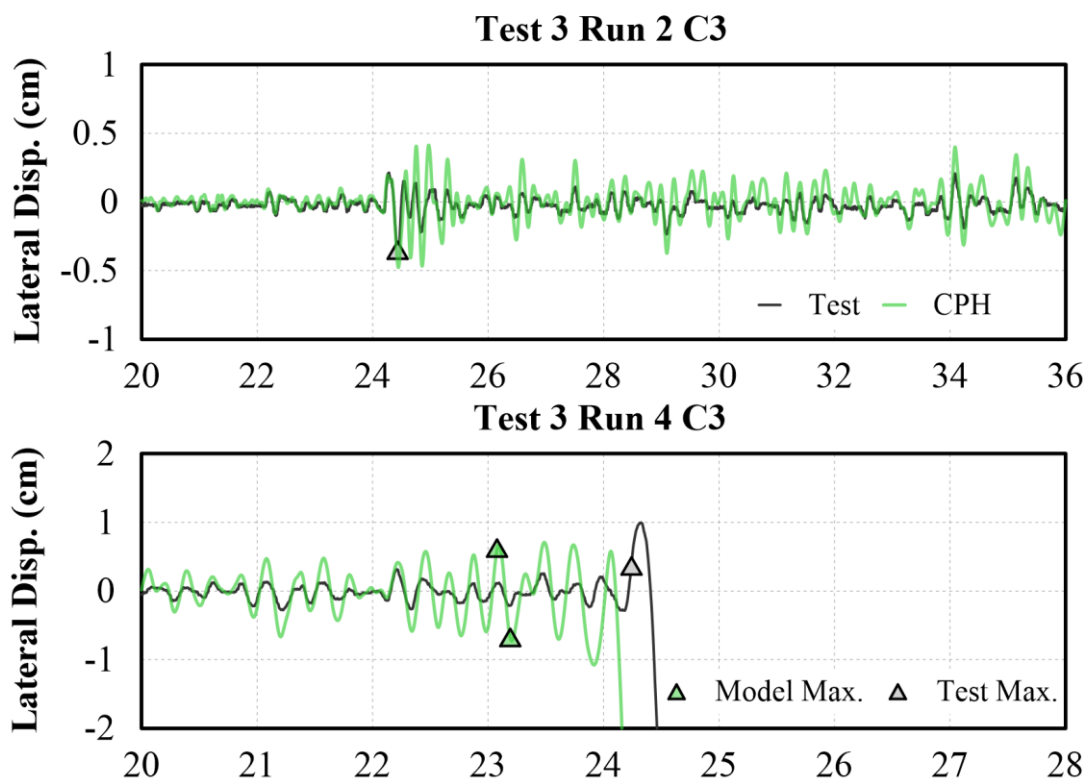
Figure 6-81. Comparison on T3 C3 lateral displacement for CPH model
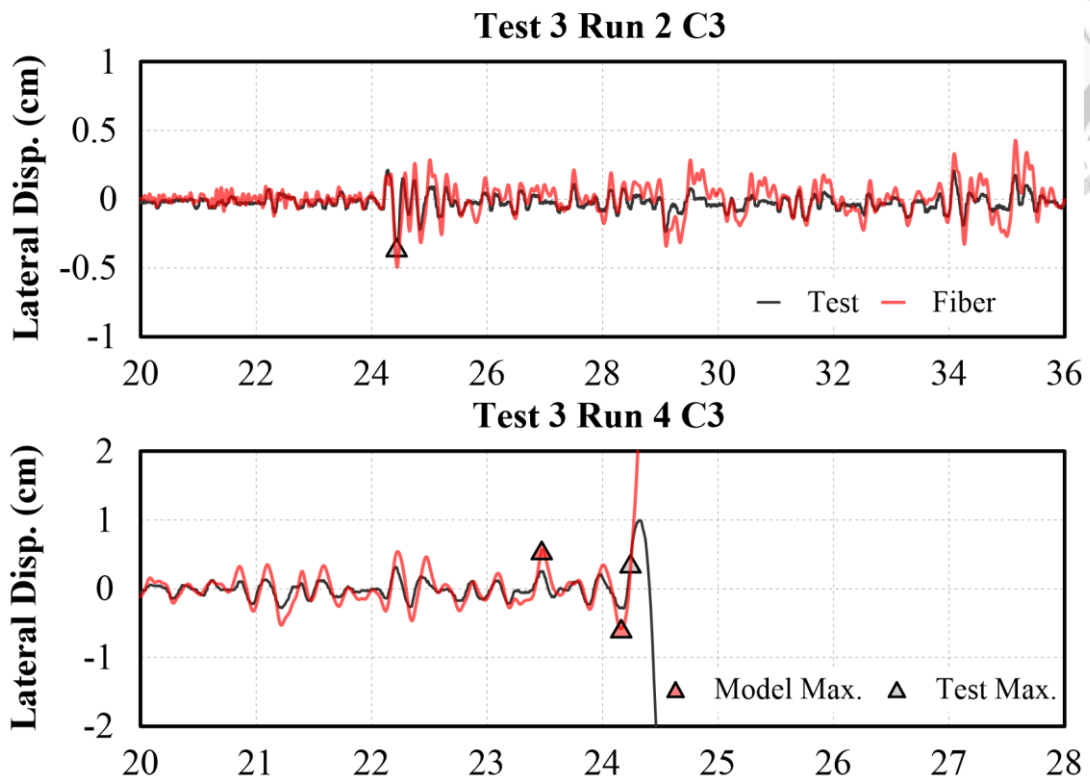
Figure 6-82. Comparison on T3 C3 lateral displacement for Fiber model
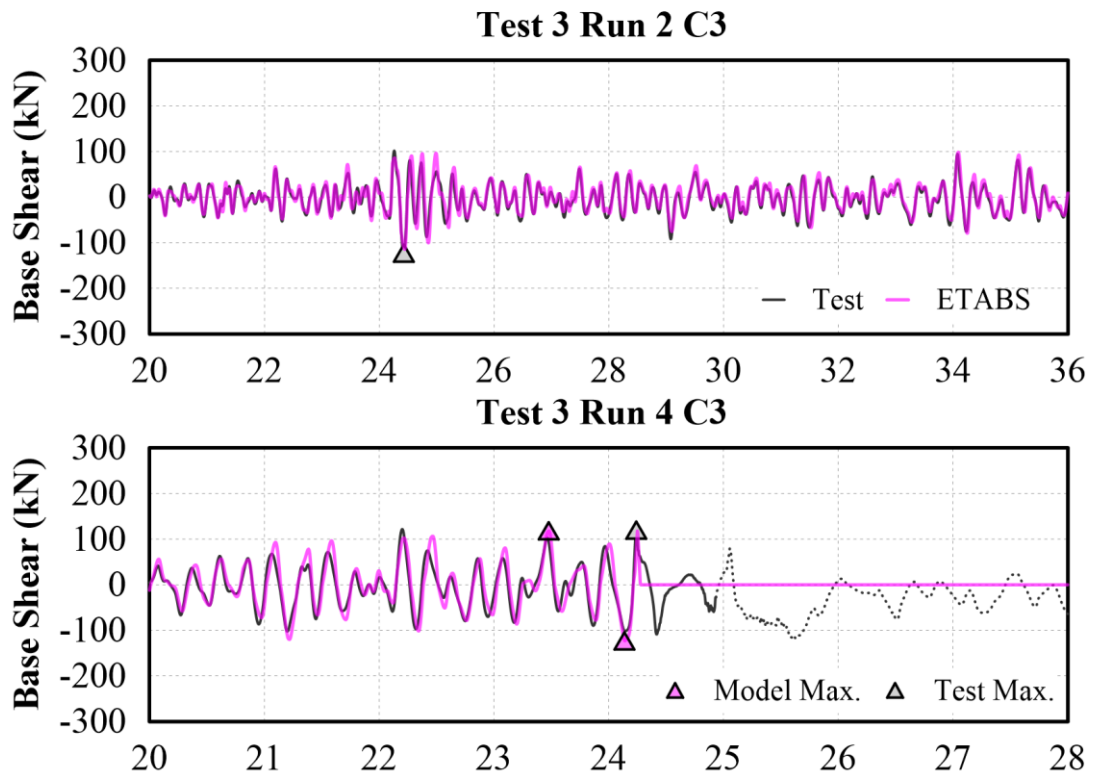
Figure 6-83. Comparison on T3 C3 base shear for ETABS model

538

Test 3 Run 2 C3

Test 3 Run 4 C3
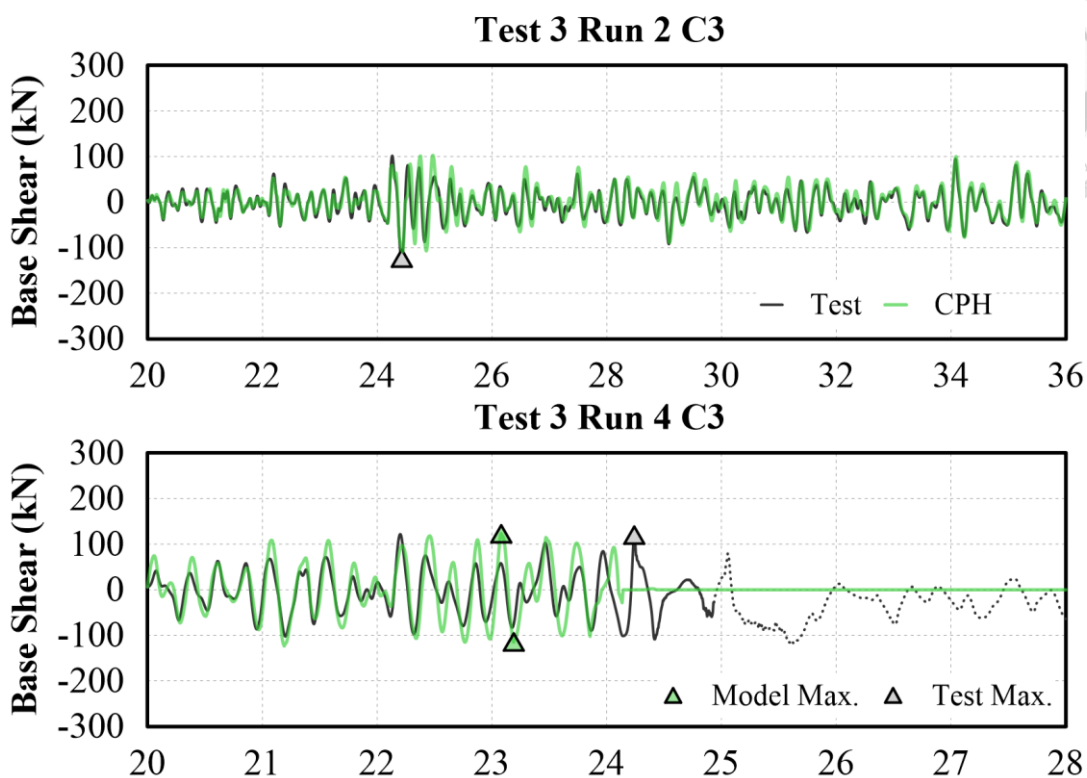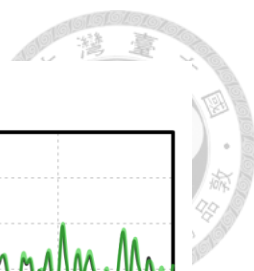
Figure 6-84. Comparison on T3 C3 base shear for CPH model

Test 3 Run 2 C3

Test 3 Run 4 C3
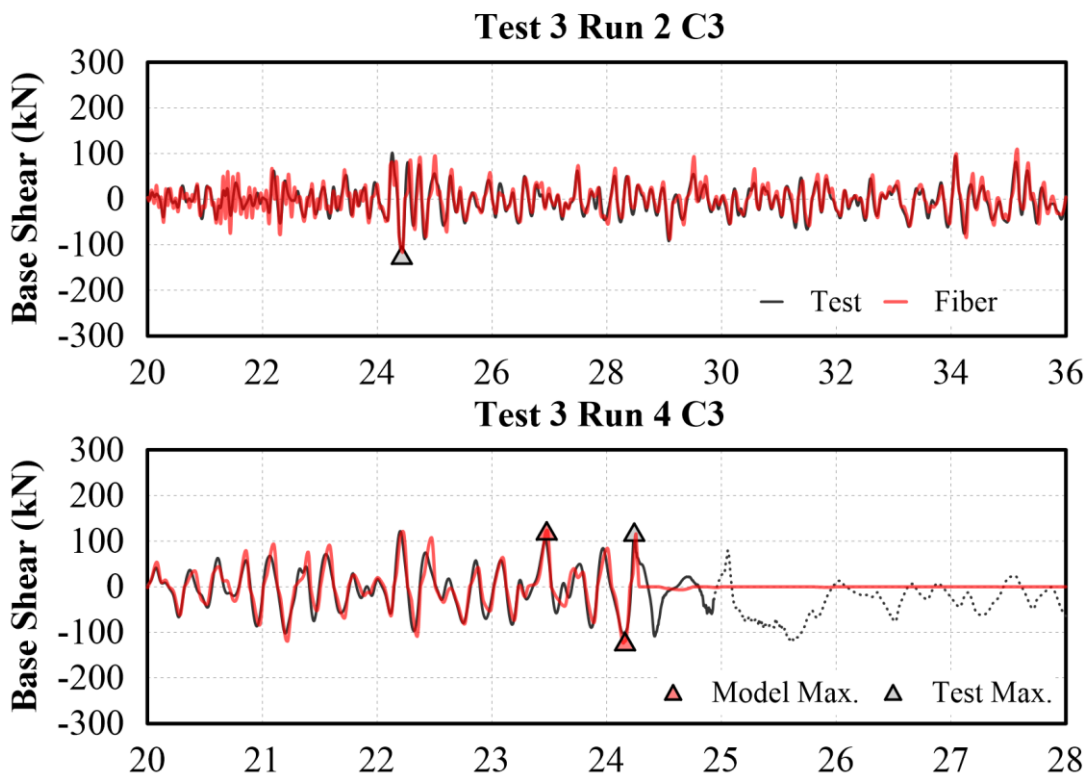
Figure 6-85. Comparison on T3 C3 base shear for Fiber model

539
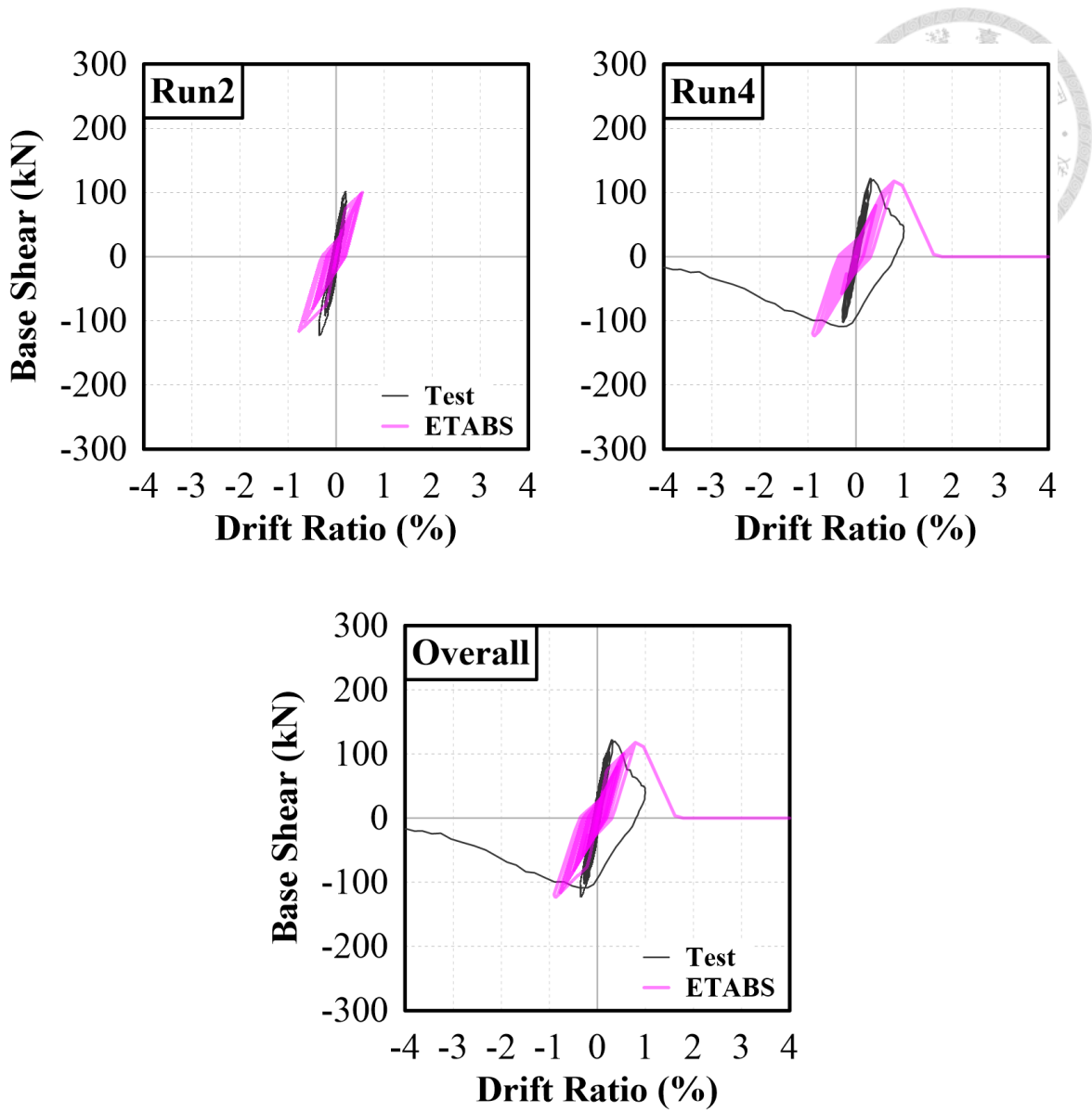
Figure 6-86. Comparison on T3 C3 hysteresis curve for ETABS model
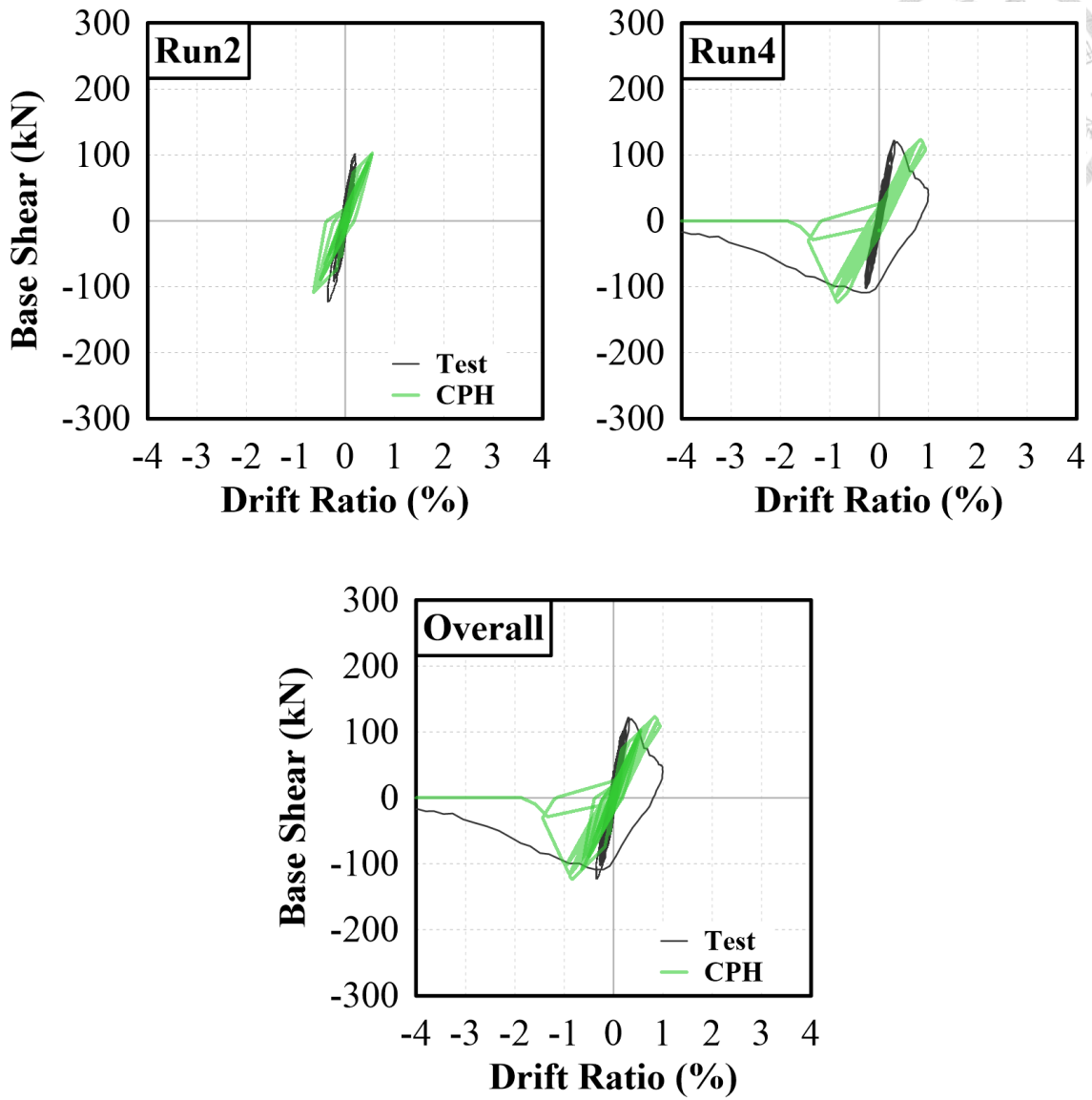
Figure 6-87. Comparison on T3 C3 hysteresis curve for CPH model
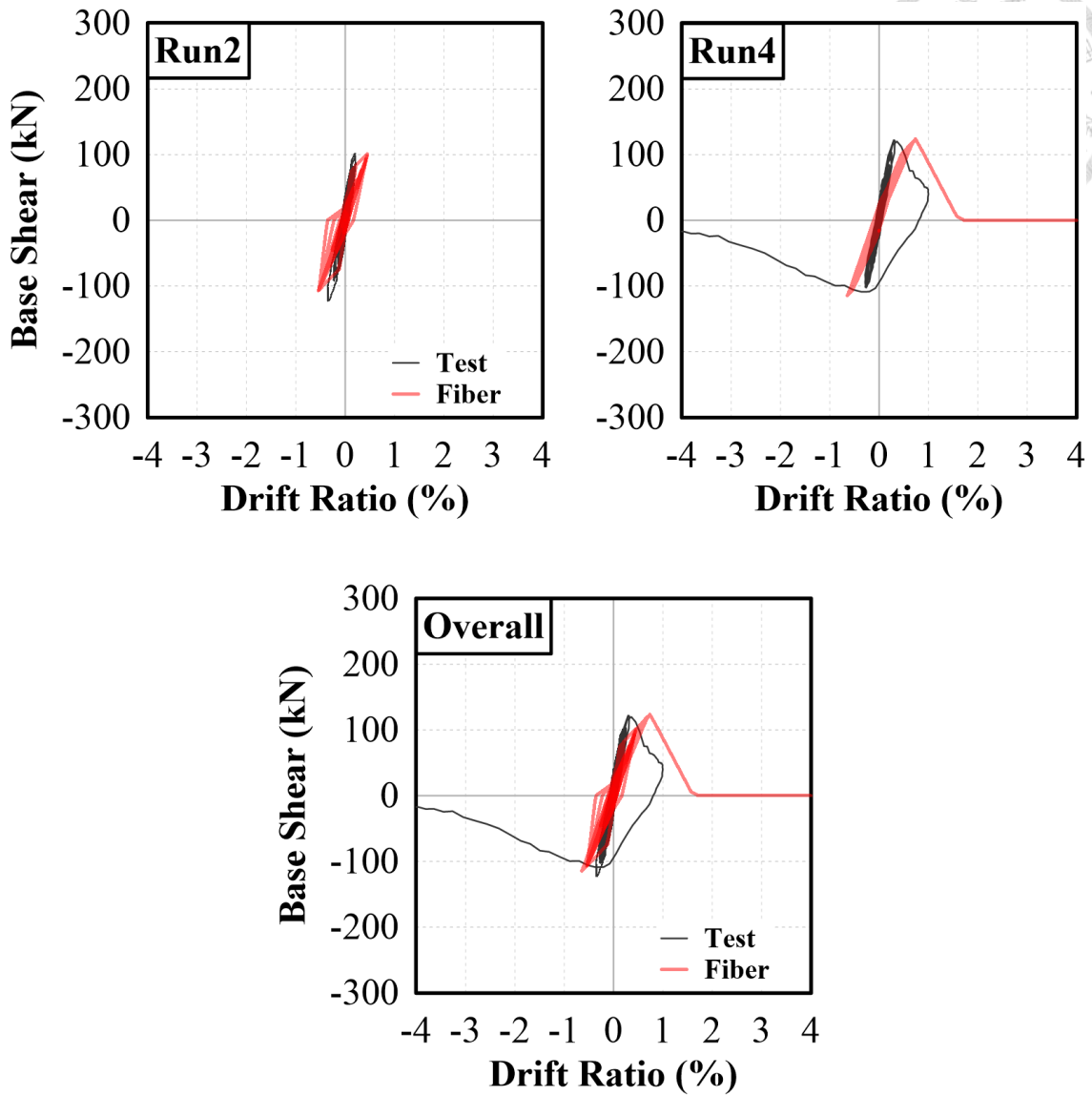
Figure 6-88. Comparison on T3 C3 hysteresis curve for Fiber model
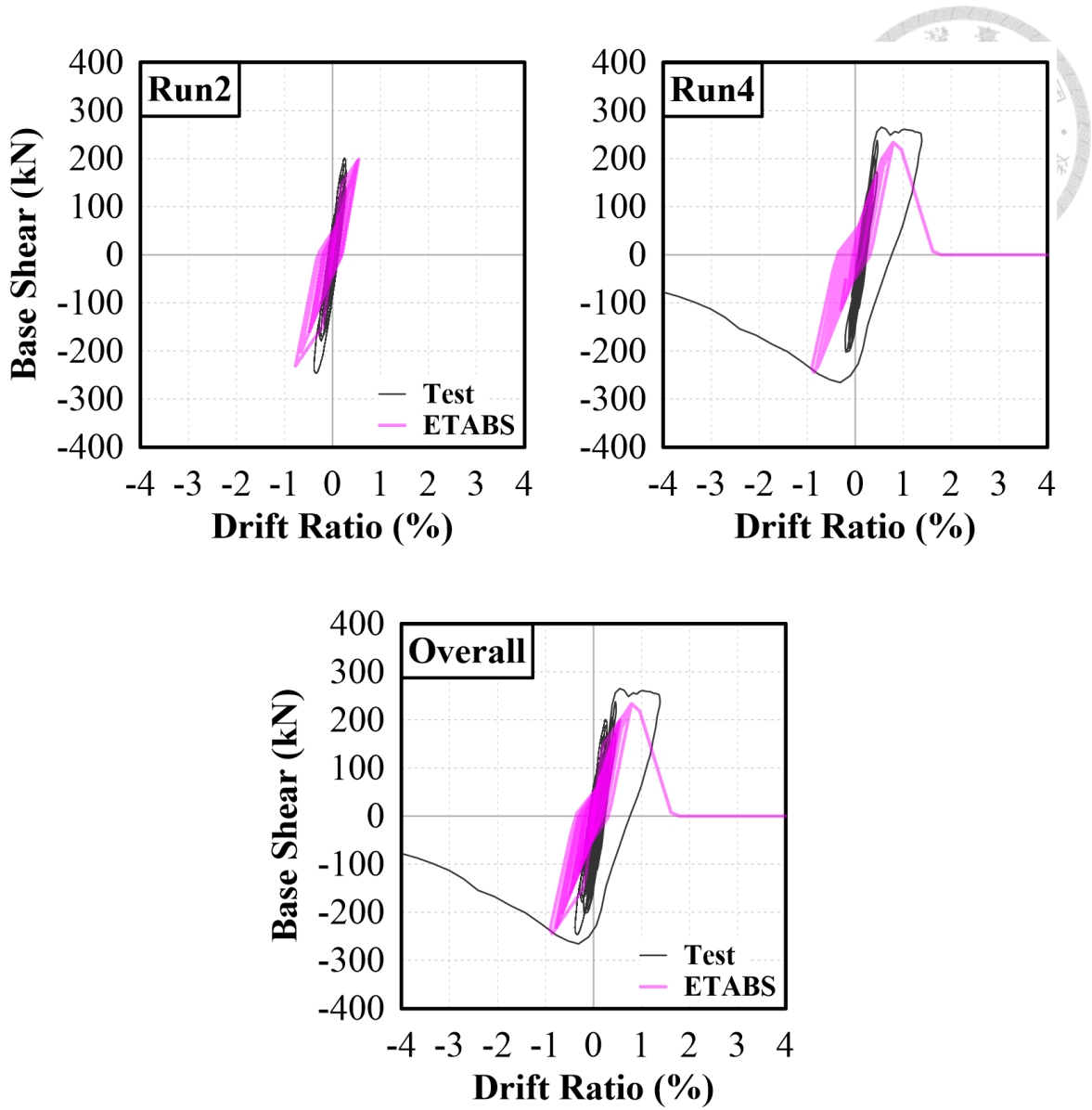
Figure 6-89. Comparison on T3 Frame hysteresis curve for ETABS model
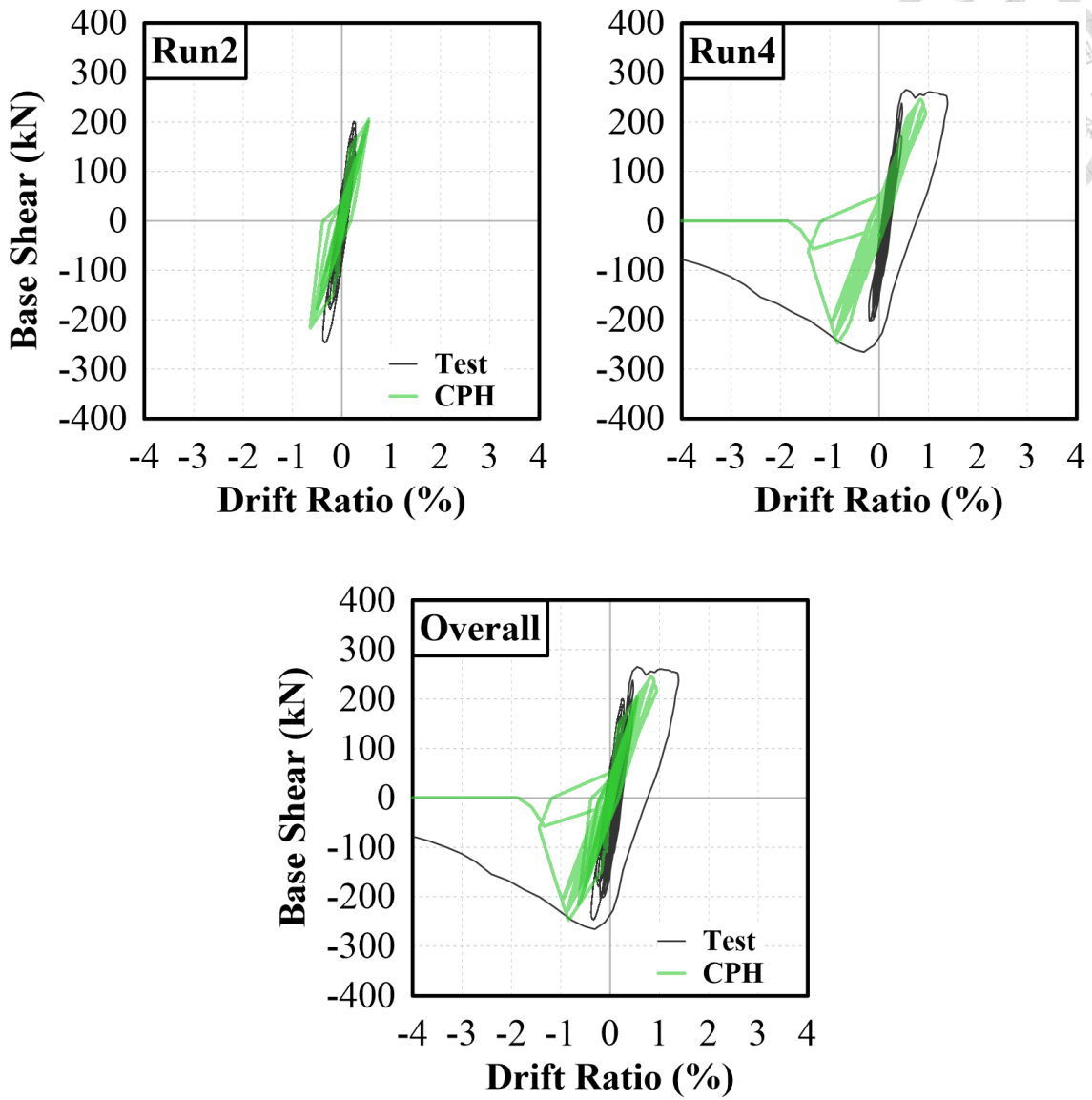
Figure 6-90. Comparison on T3 Frame hysteresis curve for CPH model

544
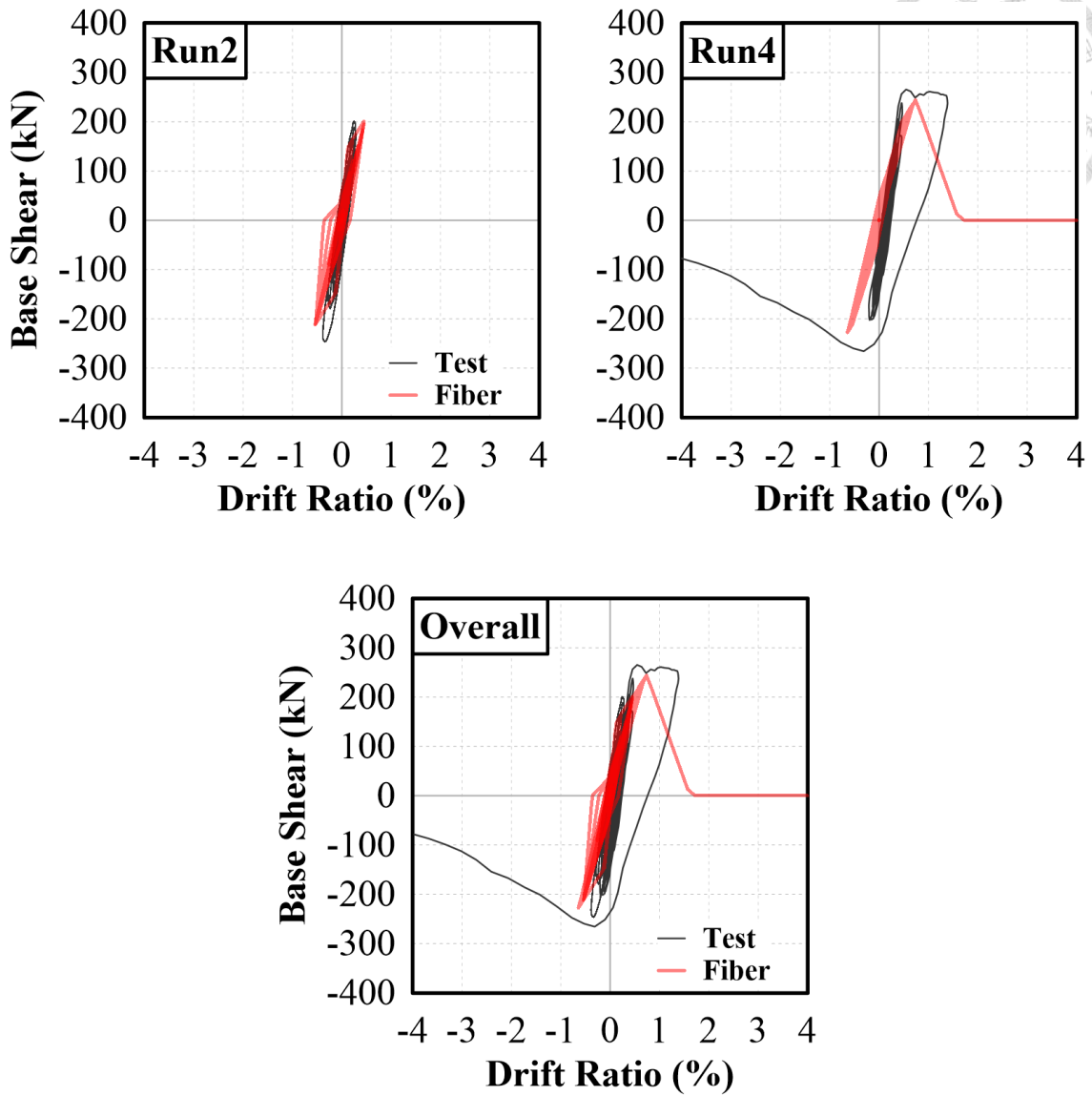
Figure 6-91. Comparison on T3 Frame hysteresis curve for Fiber model

545

Test 4 Run 2 C1

Test 4 Run 4 C1
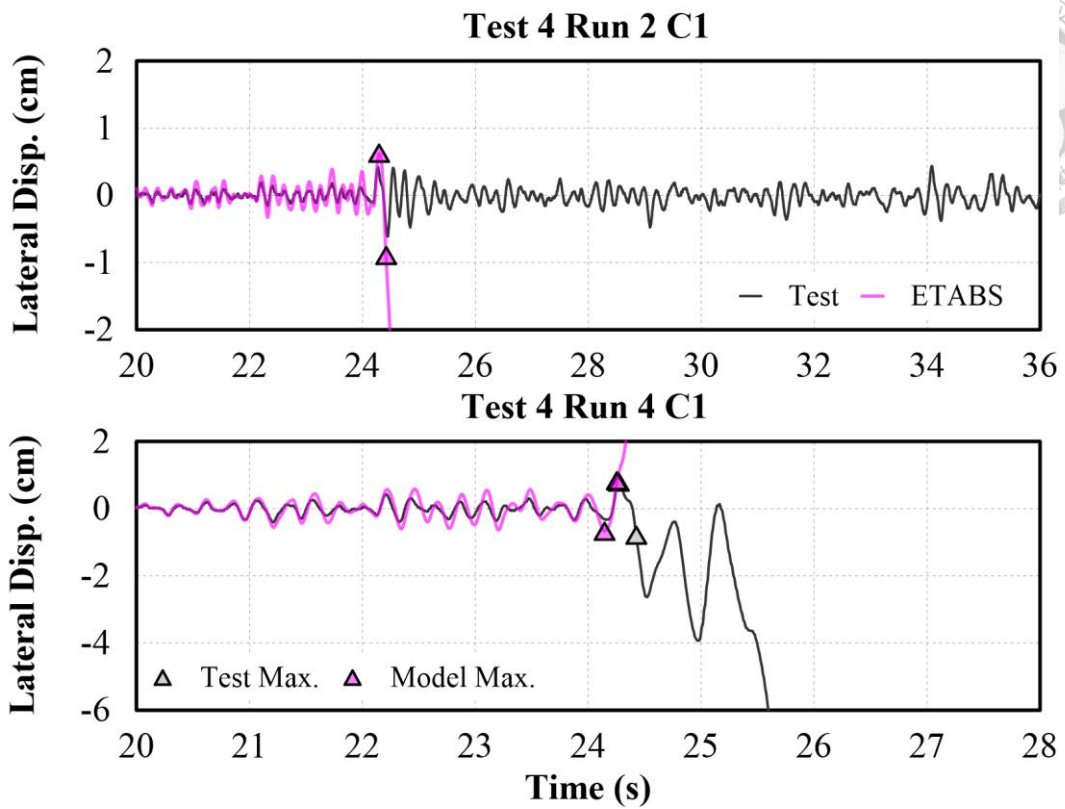
Figure 6-92. Comparison on T4 C1 lateral displacement for ETABS model

Test 4 Run 2 C1

Test 4 Run 4 C1
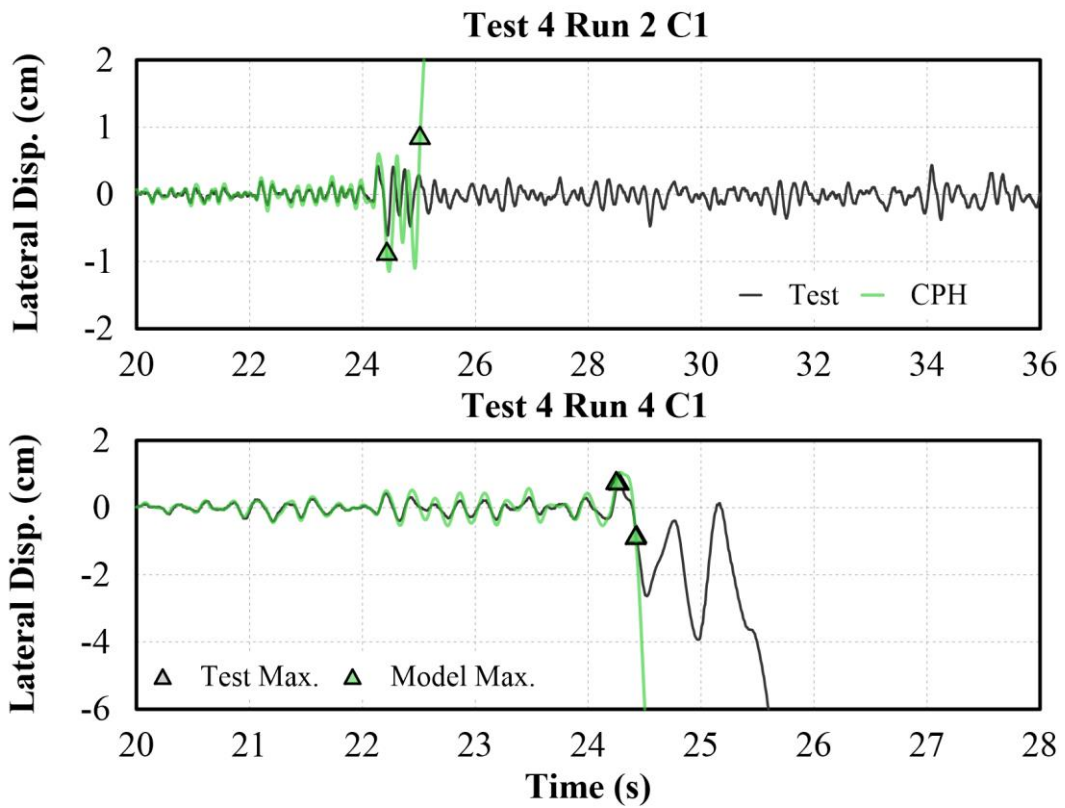
Figure 6-93. Comparison on T4 C1 lateral displacement for CPH model
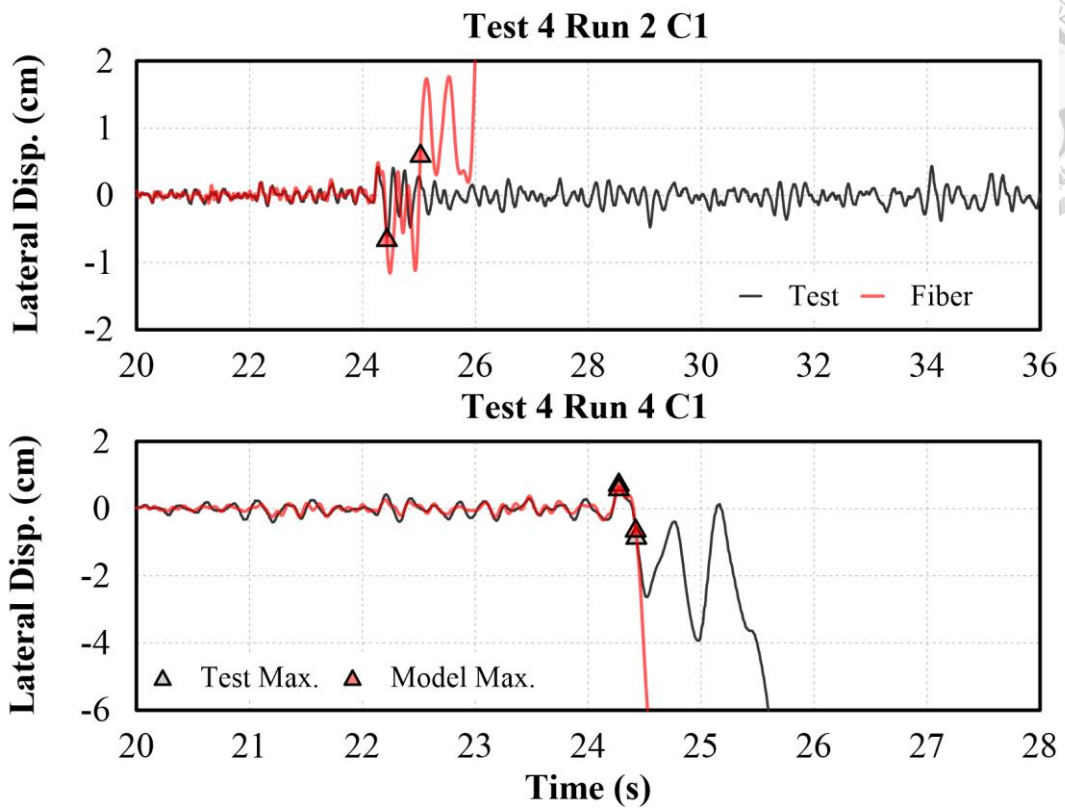
Figure 6-94. Comparison on T4 C1 lateral displacement for Fiber model
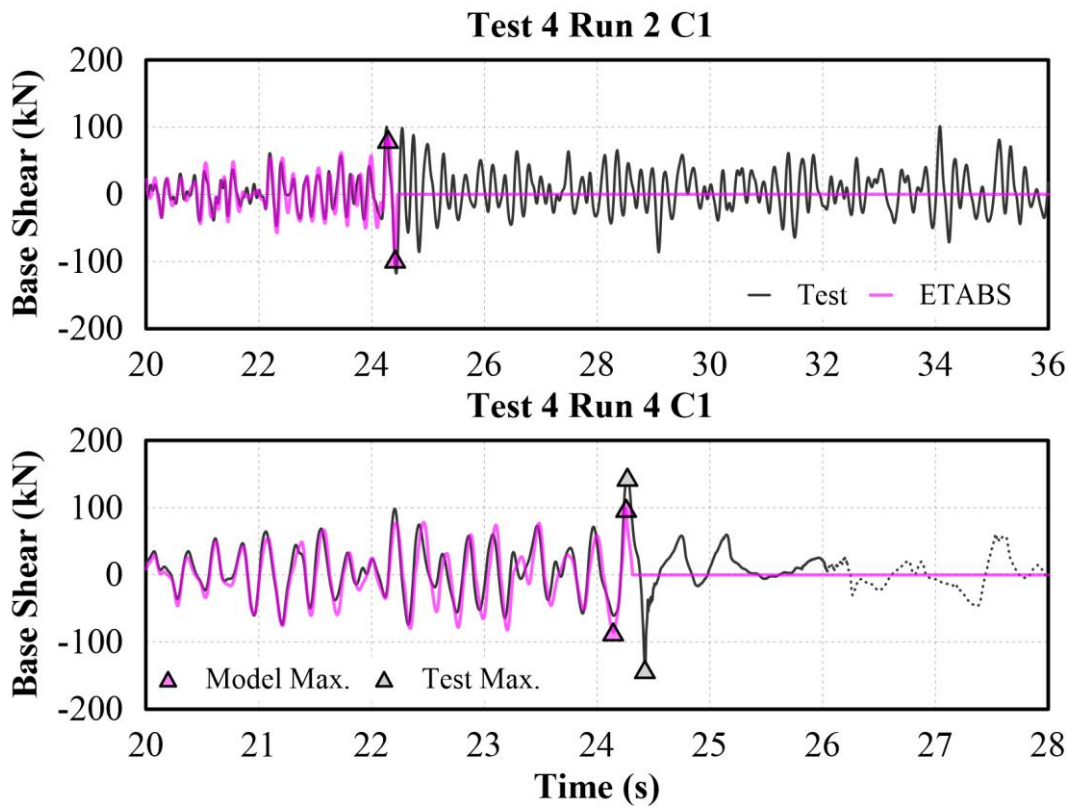
Figure 6-95. Comparison on T4 C1 base shear for ETABS model

547
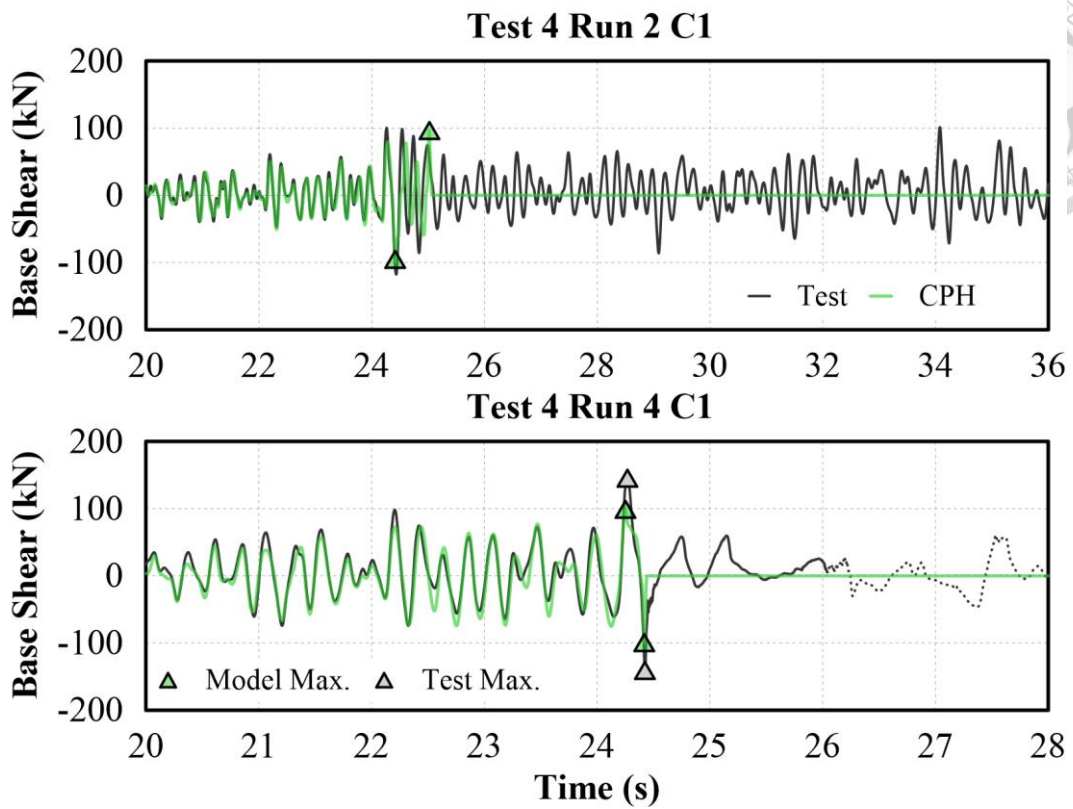
Figure 6-96. Comparison on T4 C1 base shear for CPH model
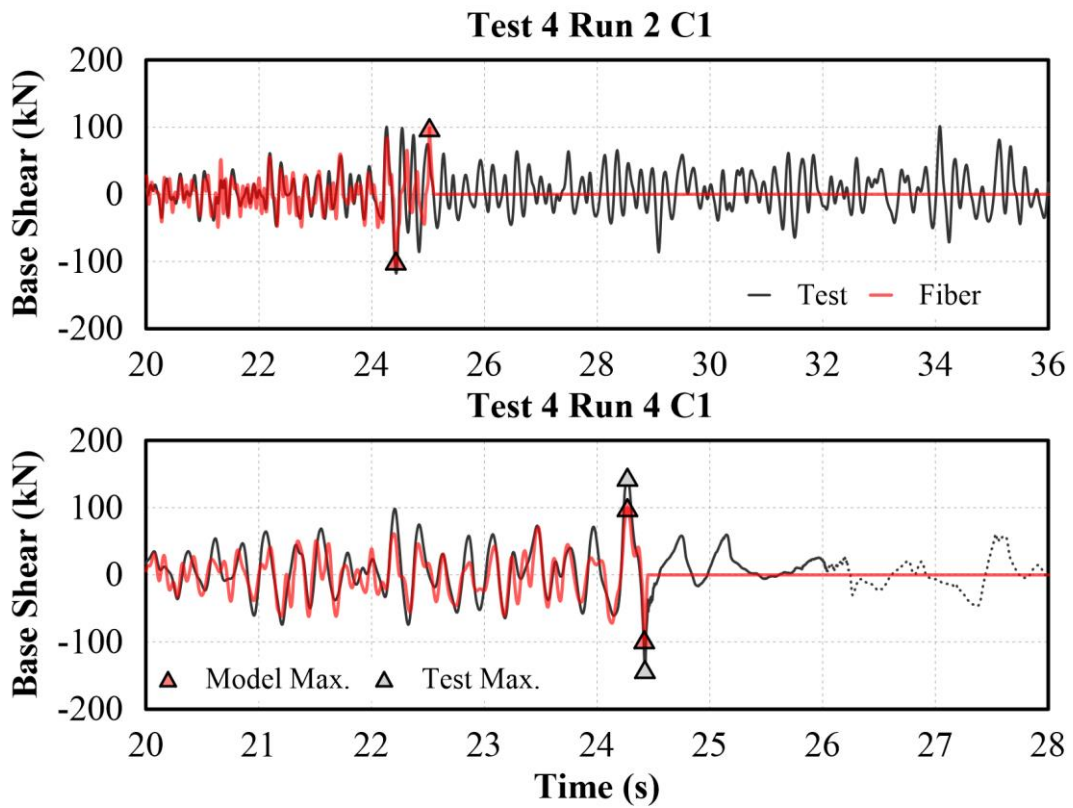
Figure 6-97. Comparison on T4 C1 base shear for Fiber model
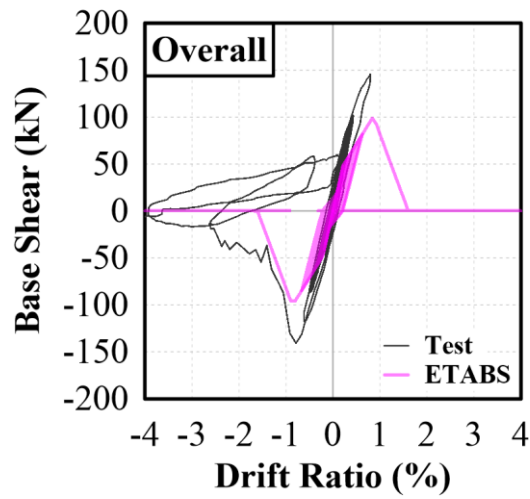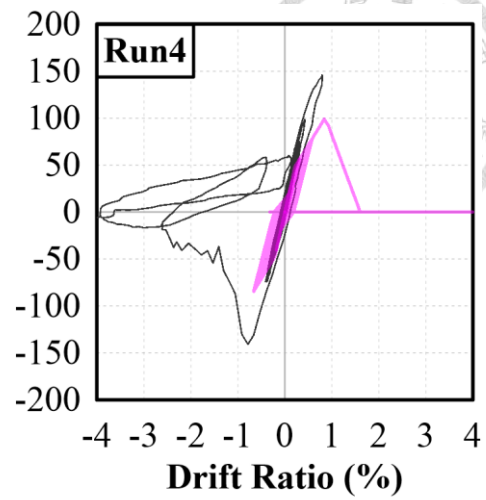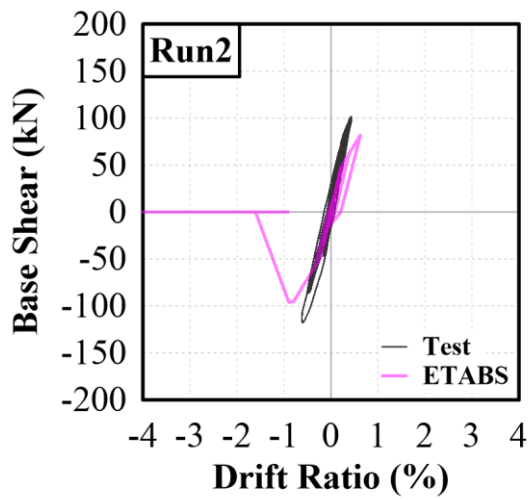
Figure 6-98. Comparison on T4 C1 hysteresis curve for ETABS model
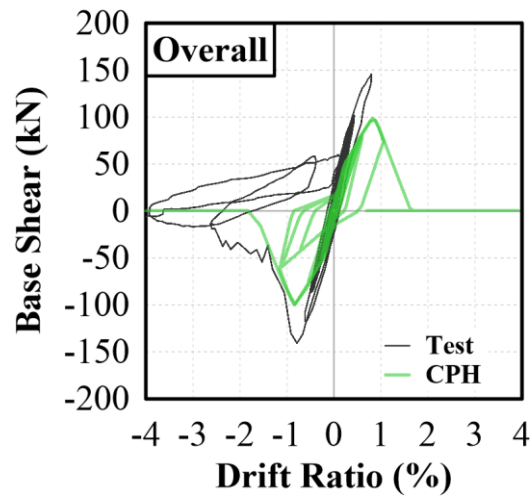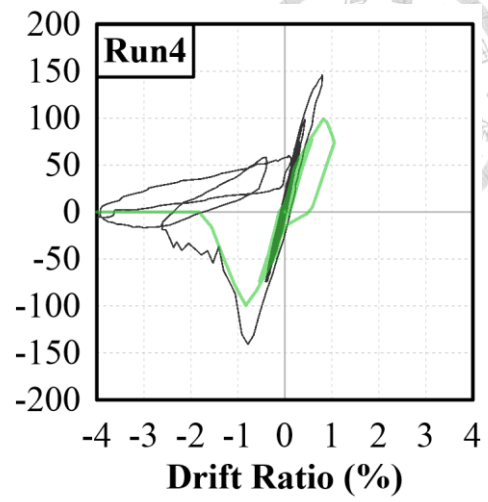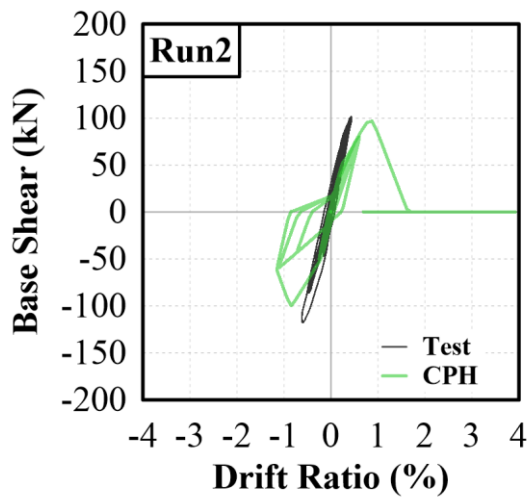
Figure 6-99. Comparison on T4 C1 hysteresis curve for CPH model

550
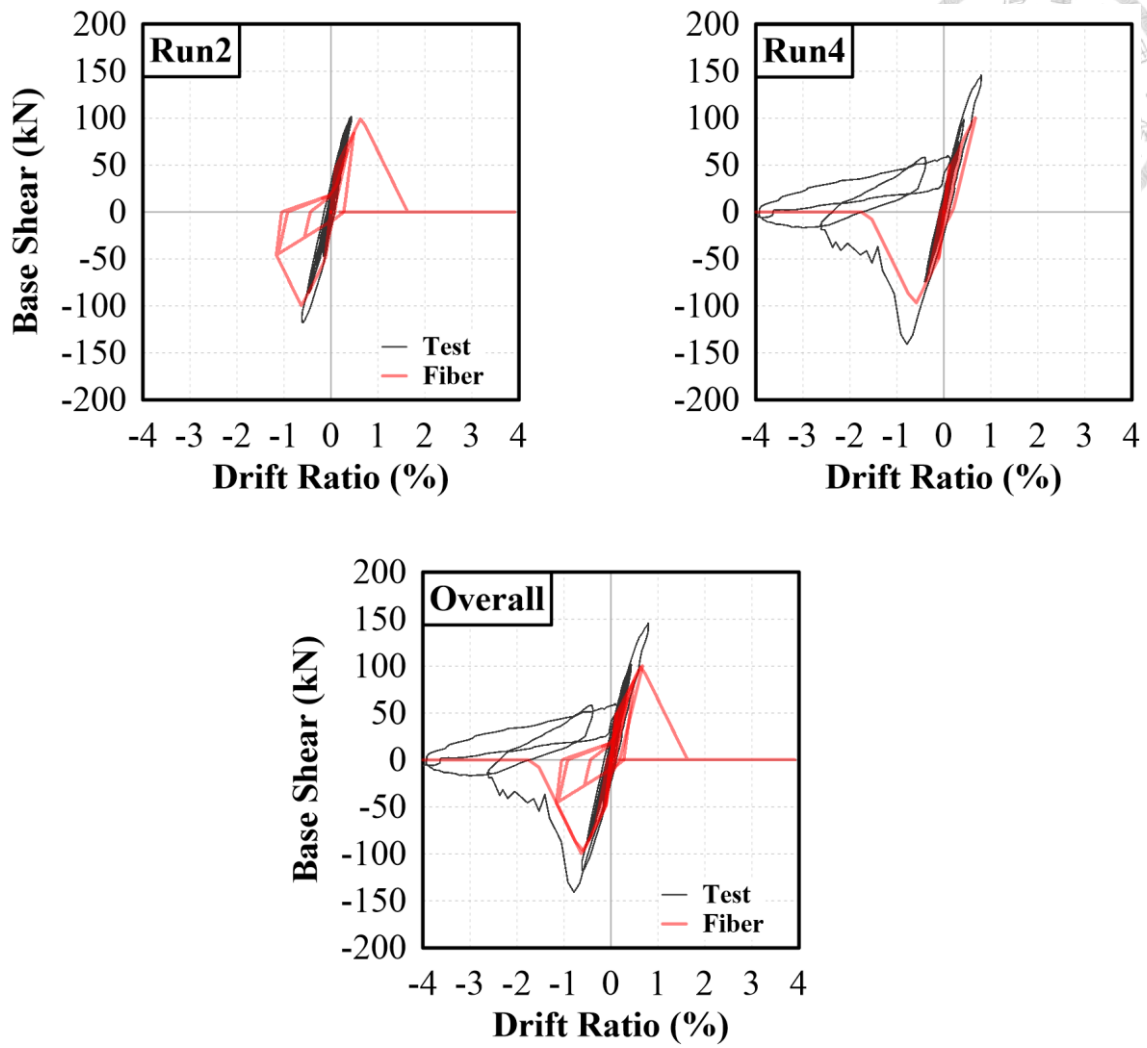
Figure 6-100. Comparison on T4 C1 hysteresis curve for Fiber model
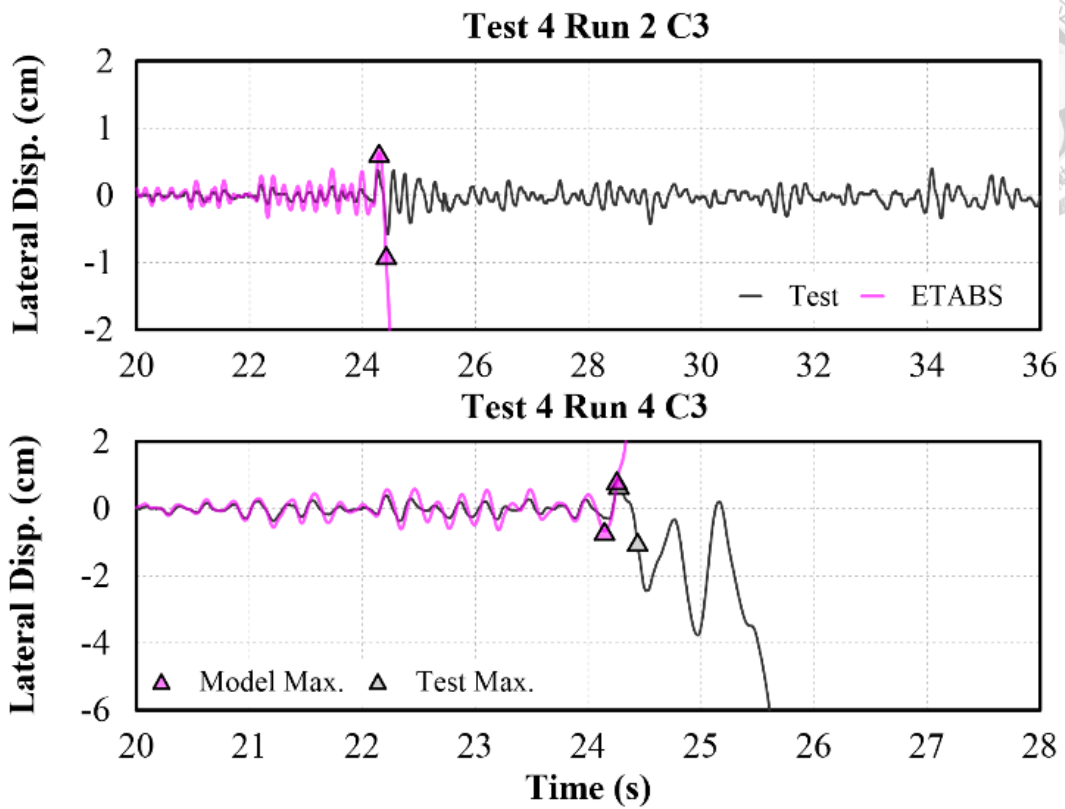
Figure 6-101. Comparison on T4 C3 lateral displacement for ETABS model

Figure 6-102. Comparison on T4 C3 lateral displacement for CPH model

552

Figure 6-103. Comparison on T4 C3 lateral displacement for Fiber model
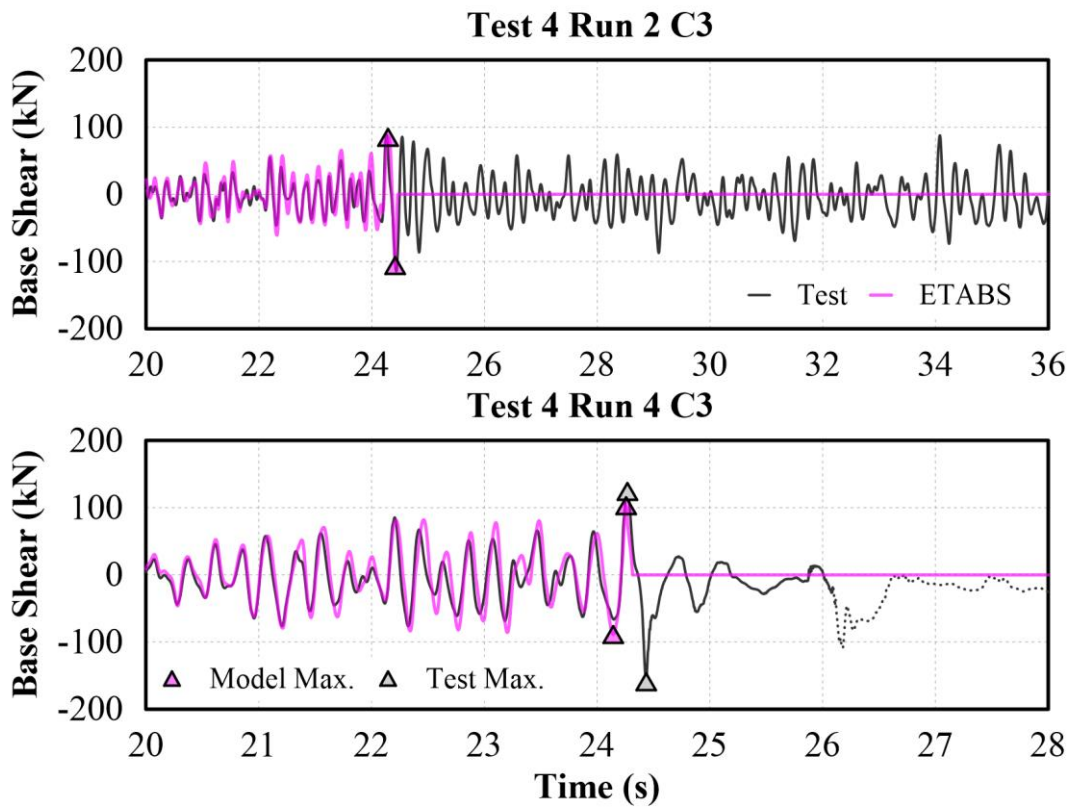
Figure 6-104. Comparison on T4 C3 base shear for ETABS model

553

Figure 6-105. Comparison on T4 C3 base shear for CPH model

Figure 6-106. Comparison on T4 C3 base shear for Fiber model

554

Figure 6-107. Comparison on T4 C3 hysteresis curve for ETABS model

555

Figure 6-108. Comparison on T4 C3 hysteresis curve for CPH model

556

Figure 6-109. Comparison on T4 C3 hysteresis curve for Fiber model

557

Figure 6-110. Comparison on T4 Frame hysteresis curve for ETABS model

558

Figure 6-111. Comparison on T4 Frame hysteresis curve for CPH model

559
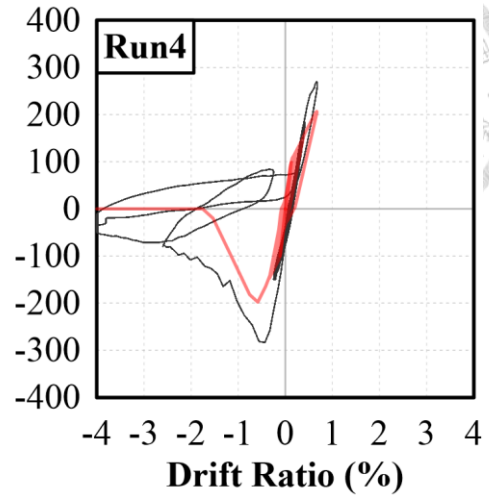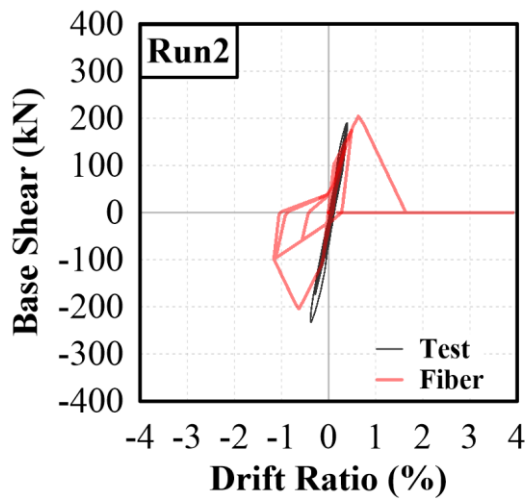
Figure 6-112. Comparison on T4 Frame hysteresis curve for Fiber model

560
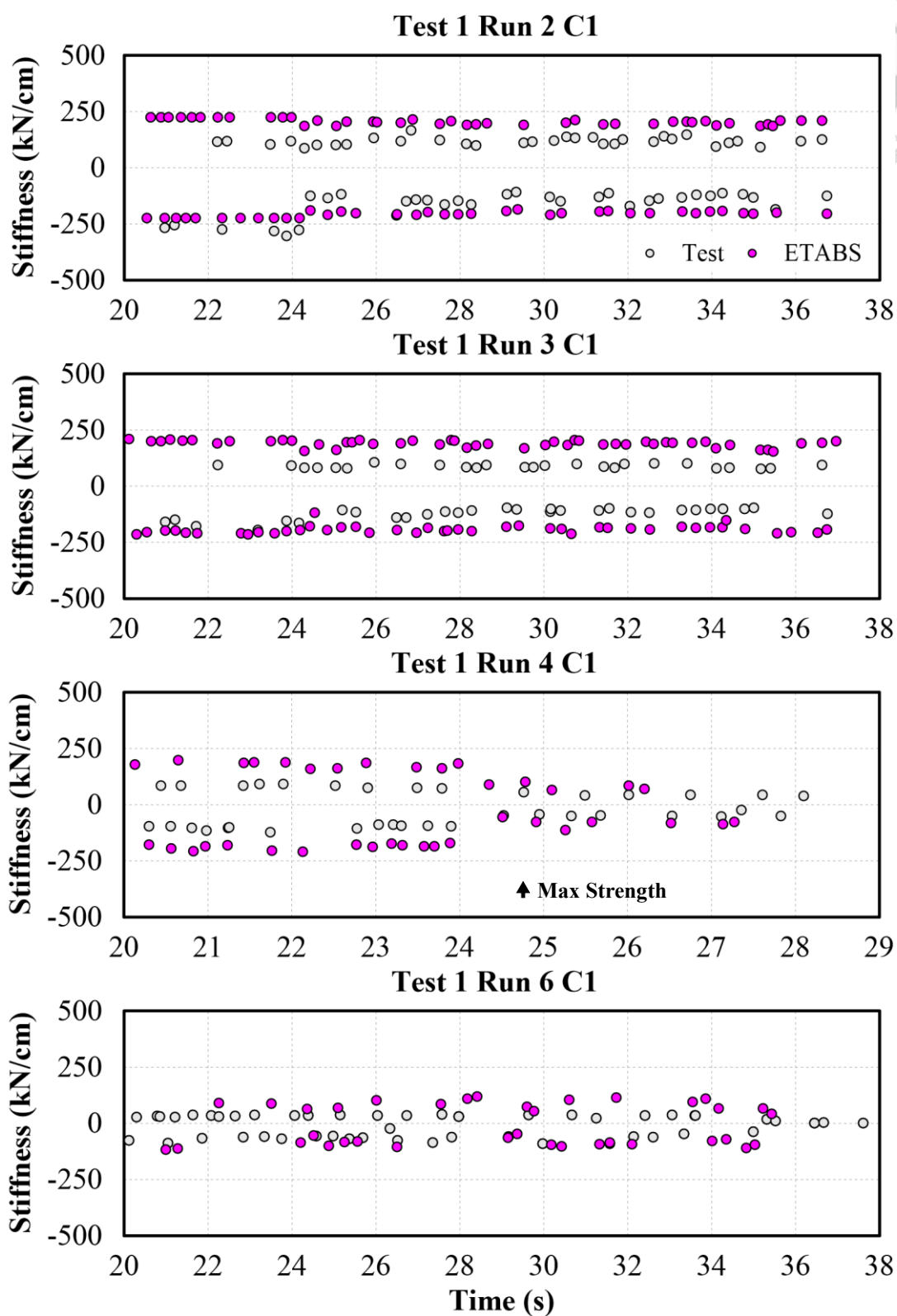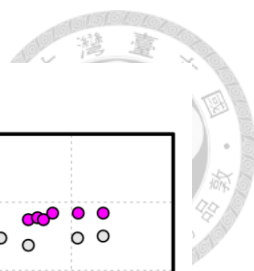
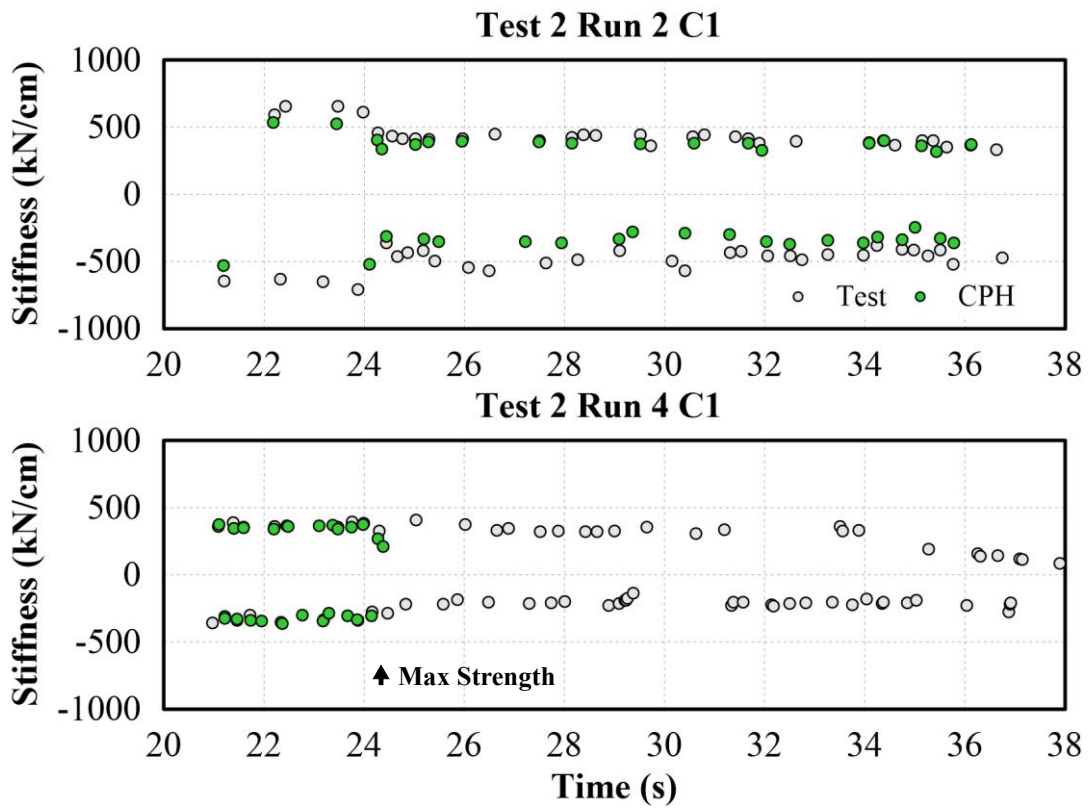**Figure 6-113. Comparison on T1 C1 stiffness response for ETABS model**
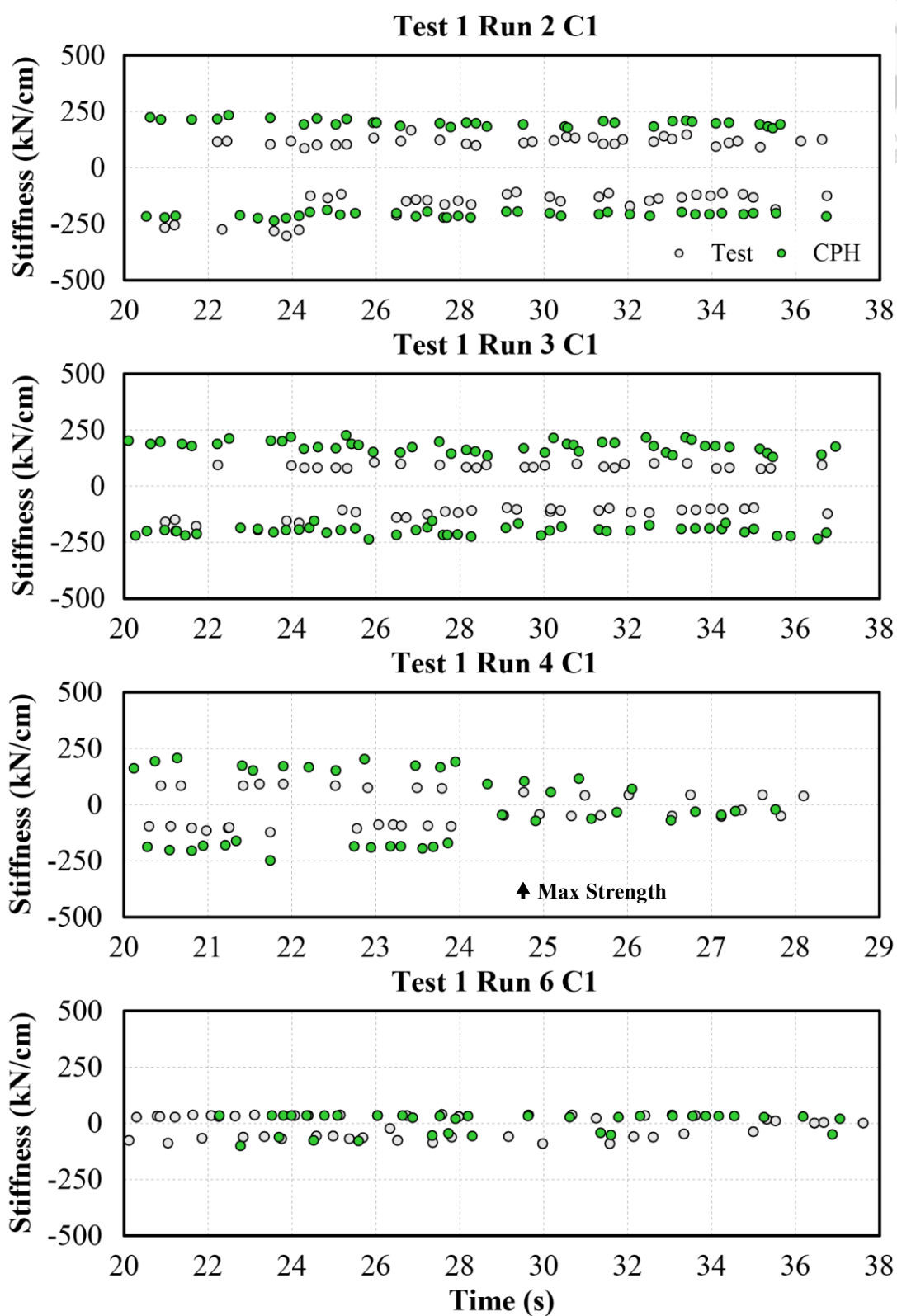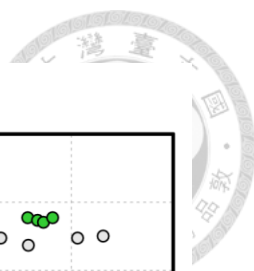
Figure 6-114. Comparison on T1 C1 stiffness response for CPH model
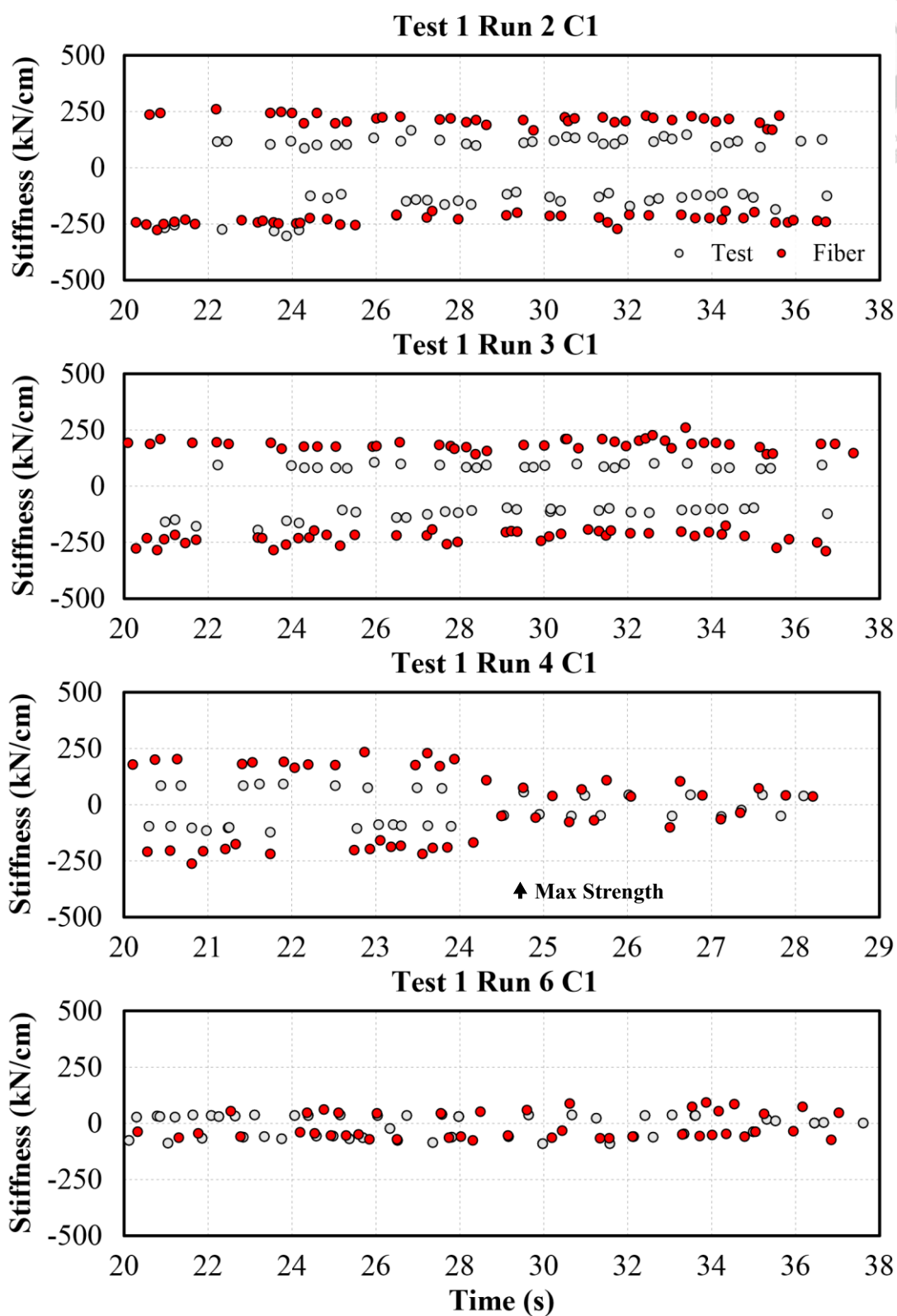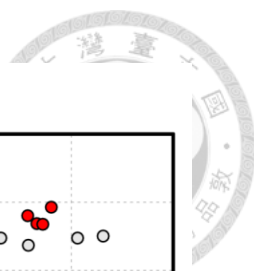
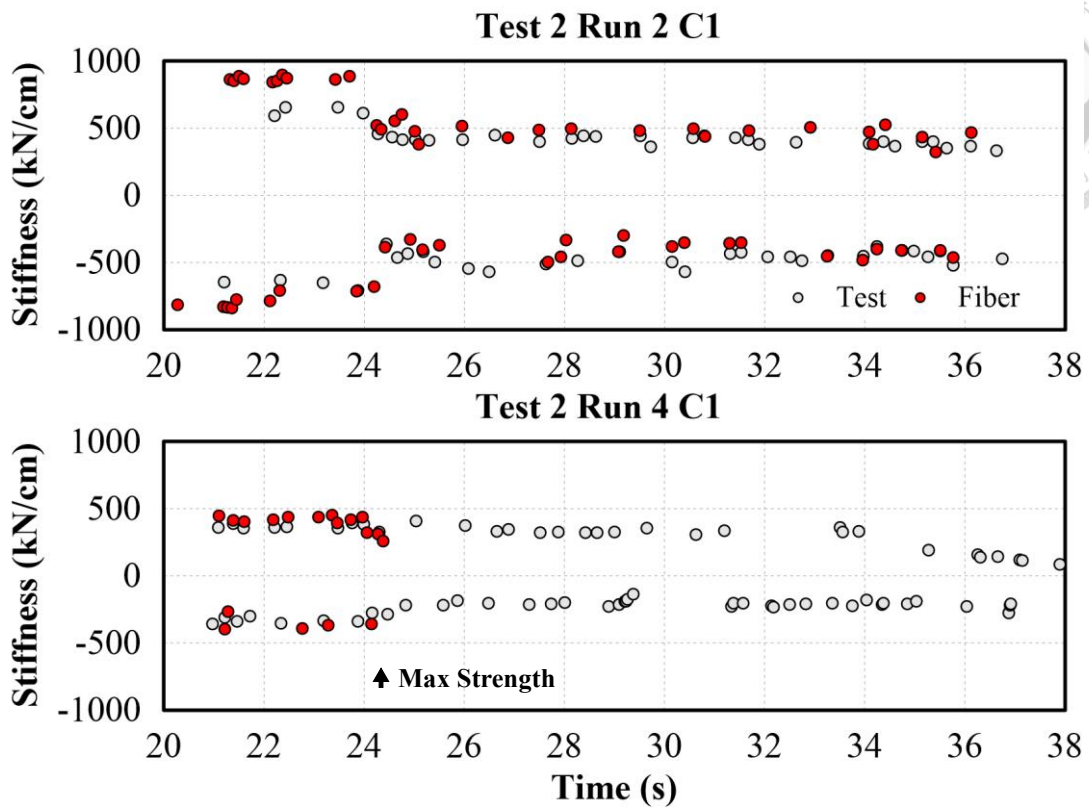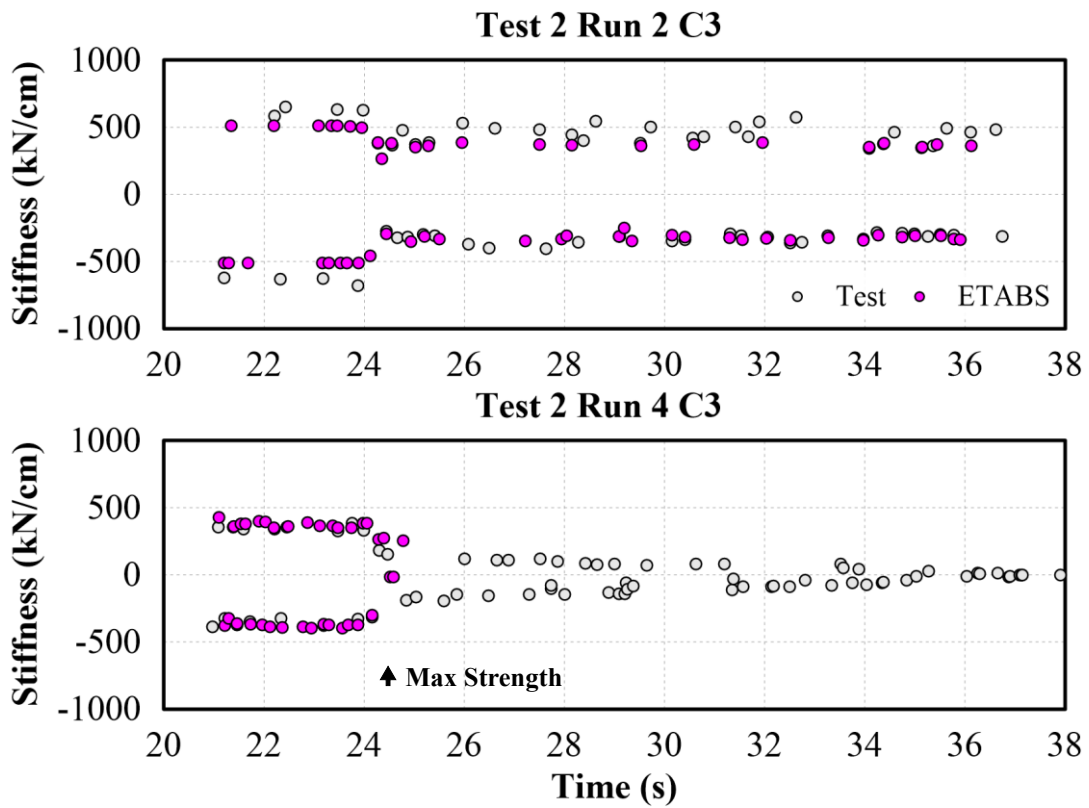**Figure 6-115. Comparison on T1 C1 stiffness response for Fiber model**
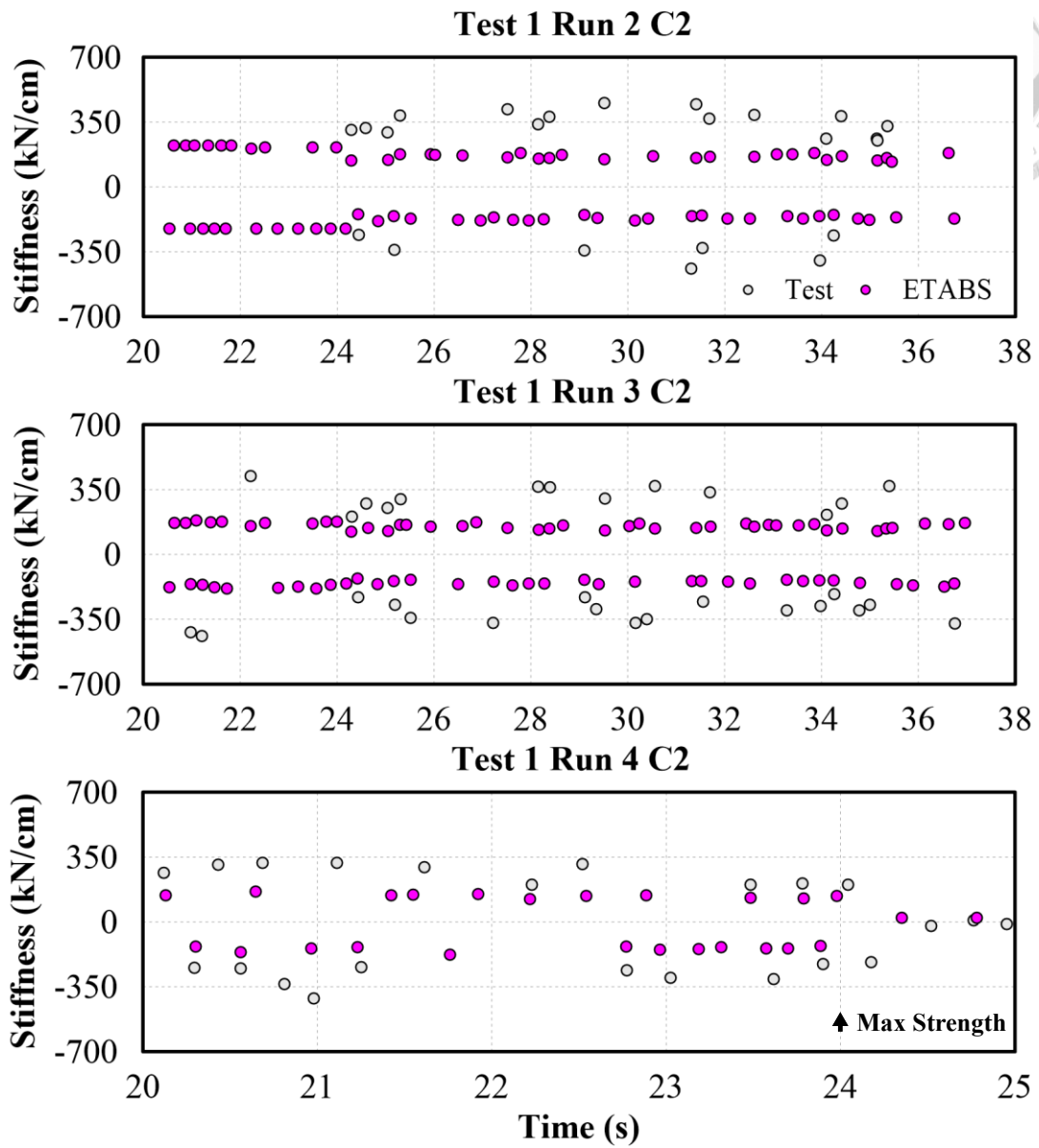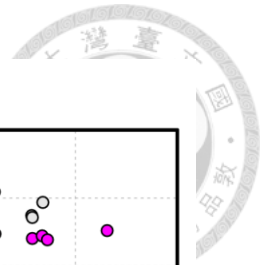
Figure 6-116. Comparison on T1 C2 stiffness response for ETABS model

564
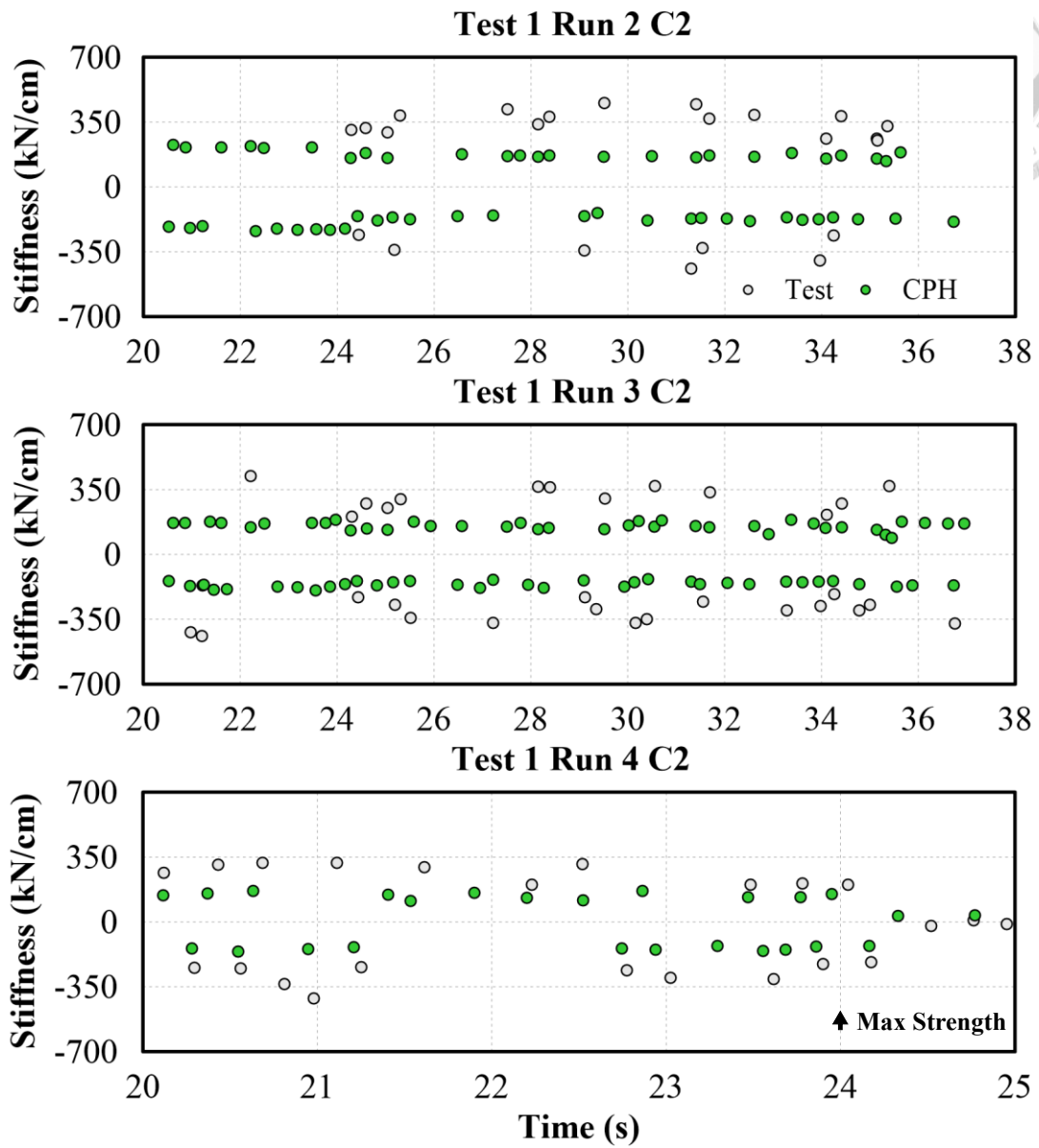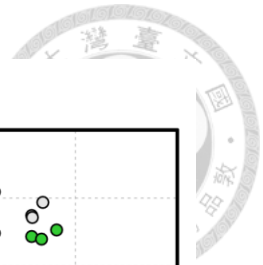
Figure 6-117. Comparison on T1 C2 stiffness response for CPH model

565
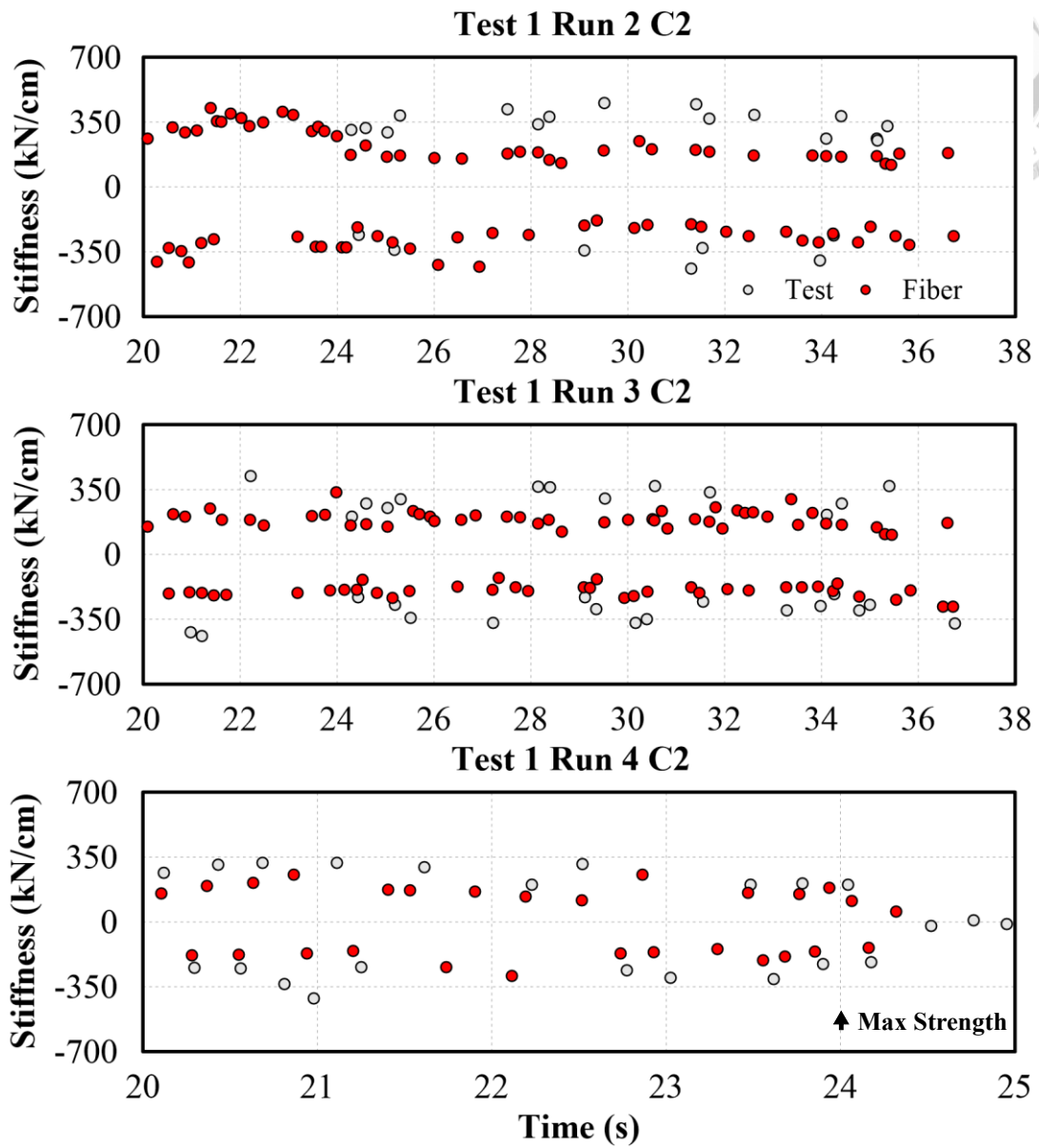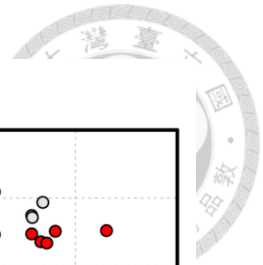
Figure 6-118. Comparison on T1 C2 stiffness response for Fiber model
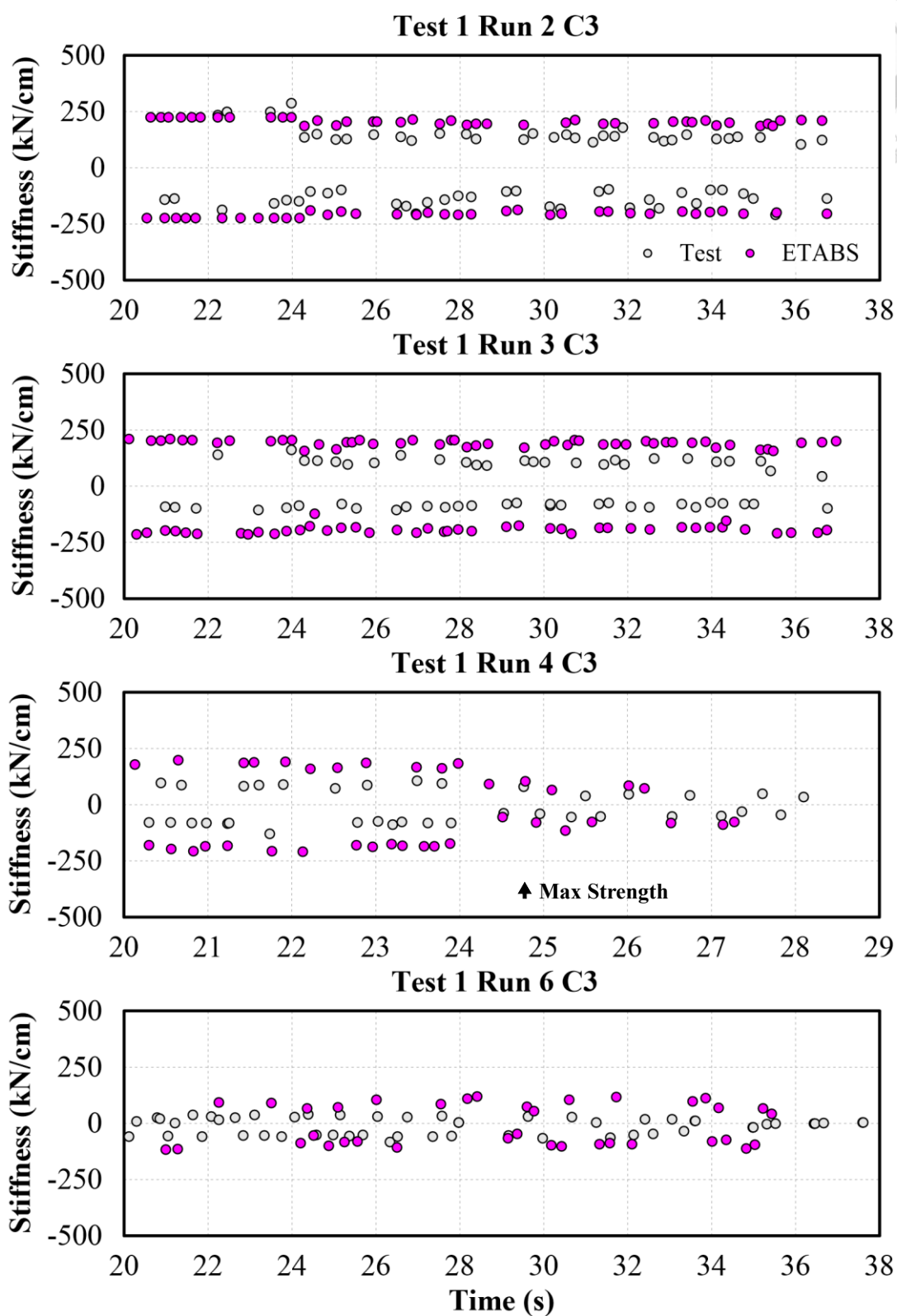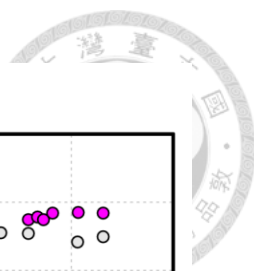
Figure 6-119. Comparison on T1 C3 stiffness response for ETABS model
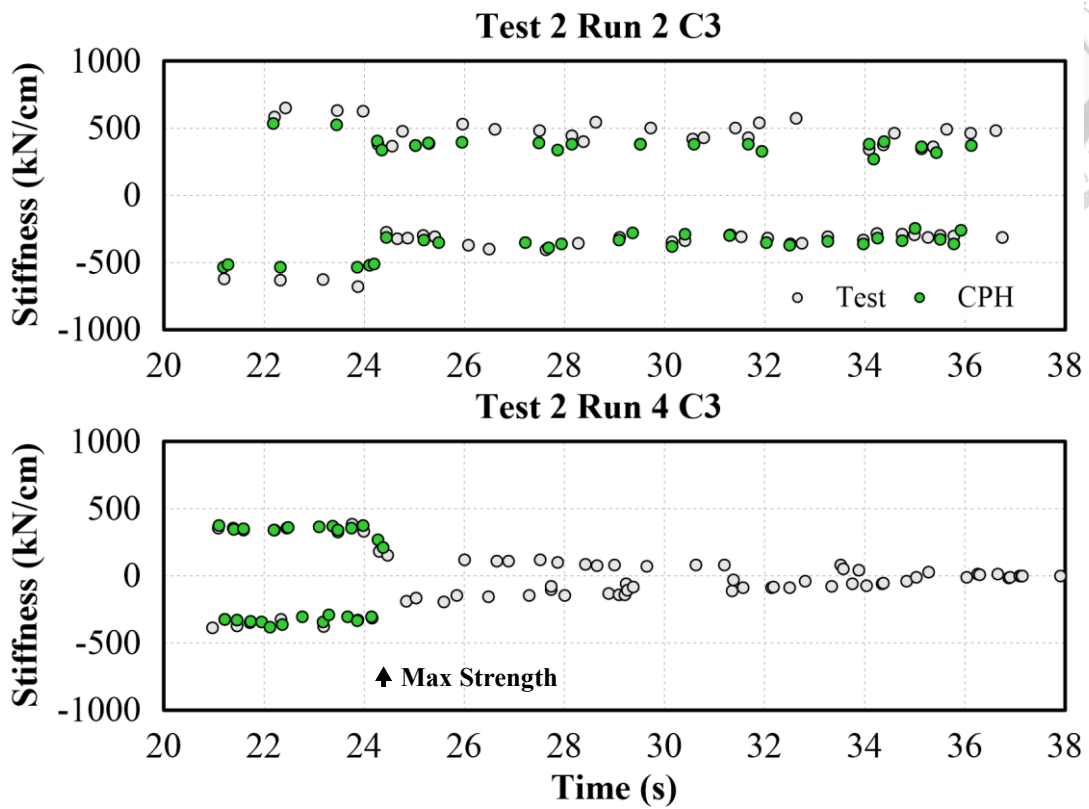
567
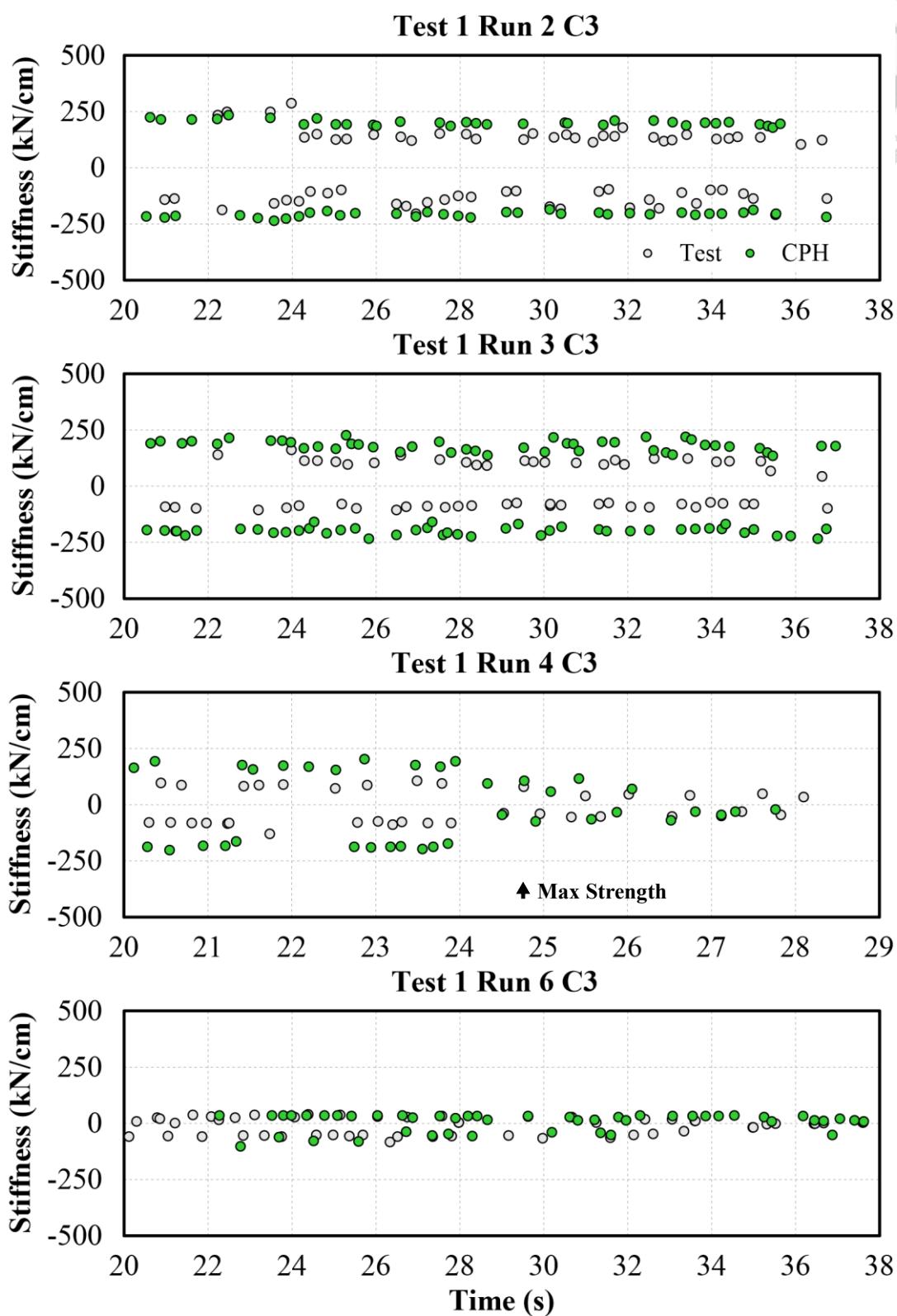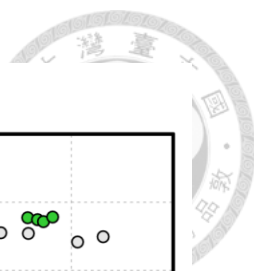
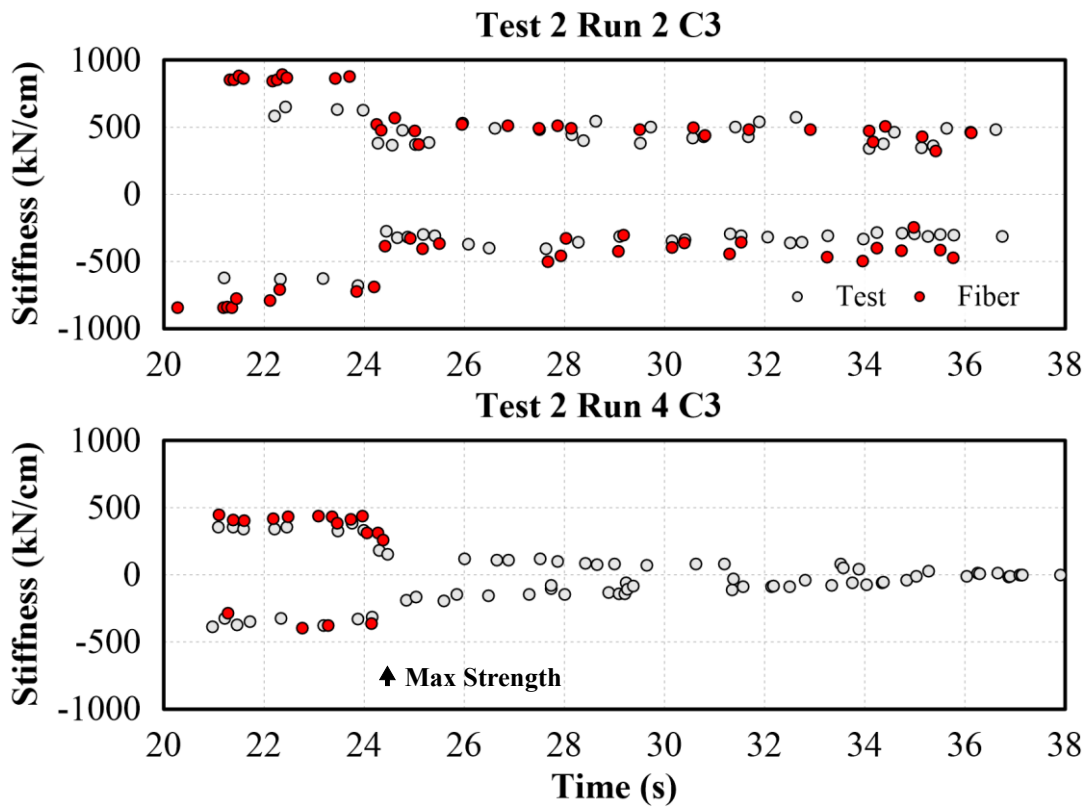**Figure 6-120. Comparison on T1 C3 stiffness response for CPH model**
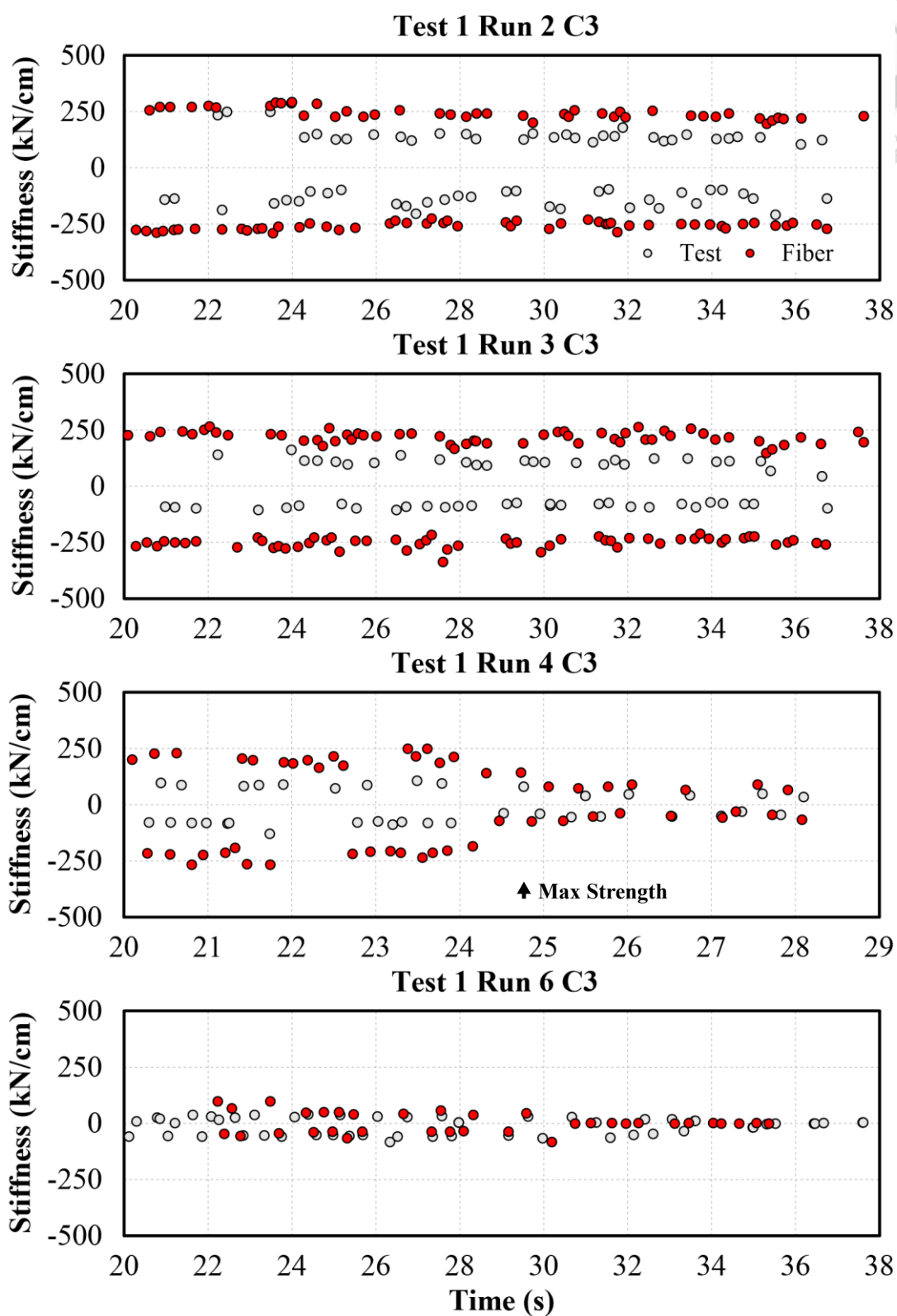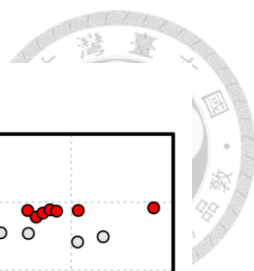
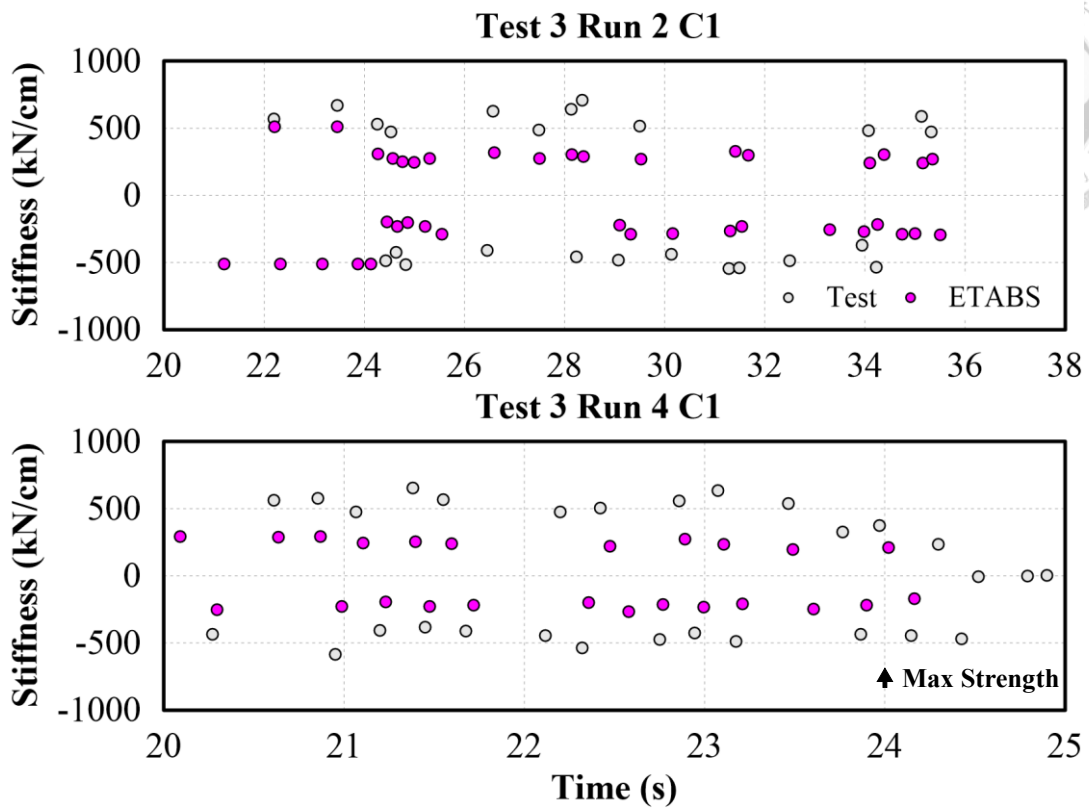**Figure 6-121. Comparison on T1 C3 stiffness response for Fiber model**
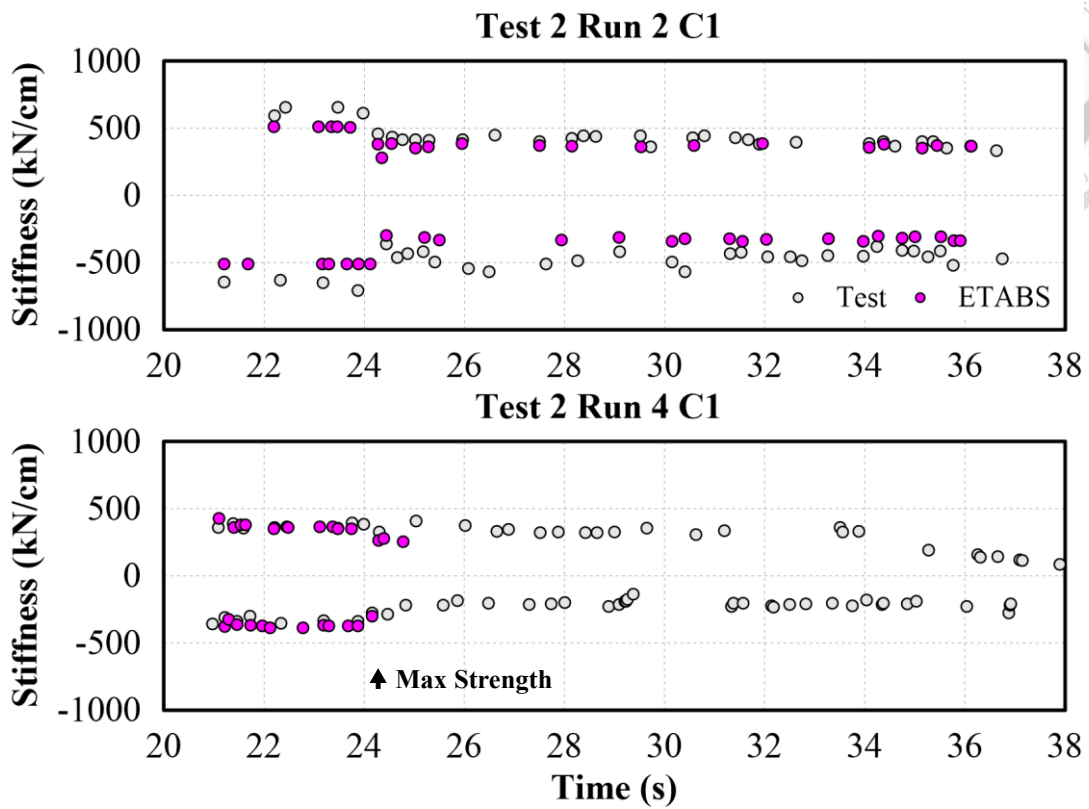
Figure 6-122. Comparison on T2 C1 stiffness response for ETABS model

Figure 6-123. Comparison on T2 C1 stiffness response for CPH model

570

Figure 6-124. Comparison on T2 C1 stiffness response for Fiber model

Figure 6-125. Comparison on T2 C3 stiffness response for ETABS model

571

Figure 6-126. Comparison on T2 C3 stiffness response for CPH model

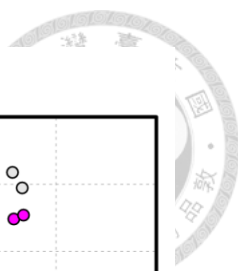**Figure 6-127. Comparison on T2 C3 stiffness response for Fiber model**

572

Figure 6-128. Comparison on T3 C1 stiffness response for ETABS model

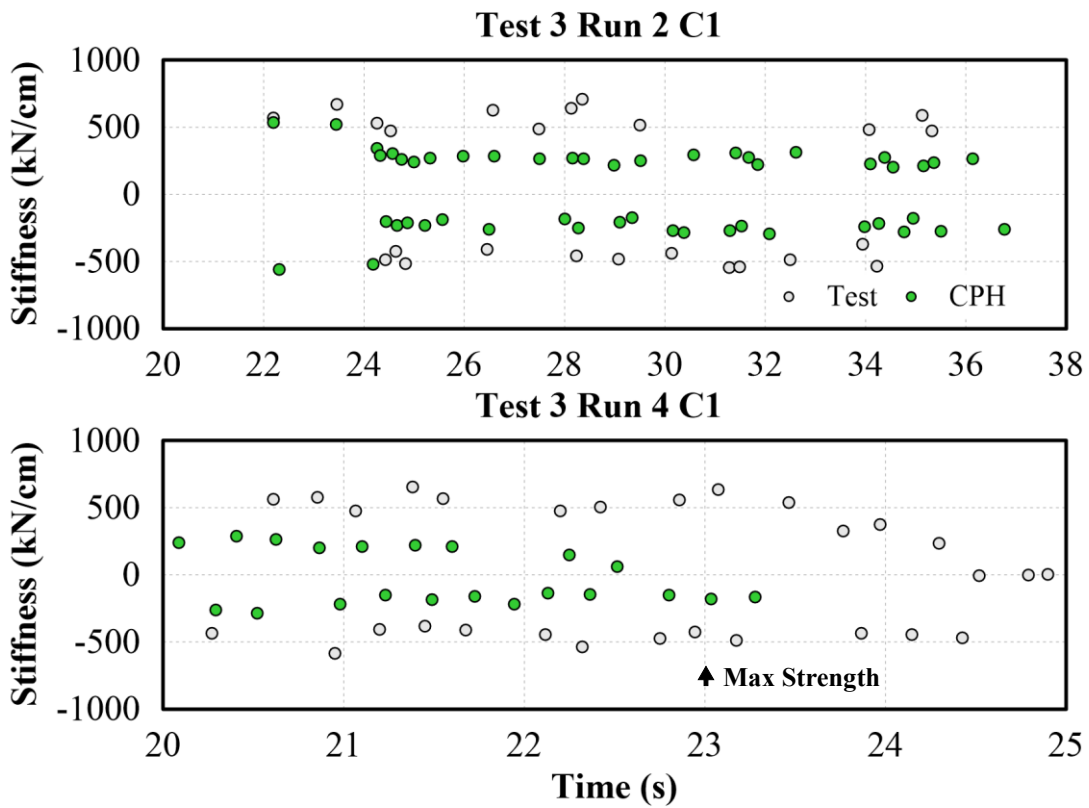**Figure 6-129. Comparison on T3 C1 stiffness response for CPH model**
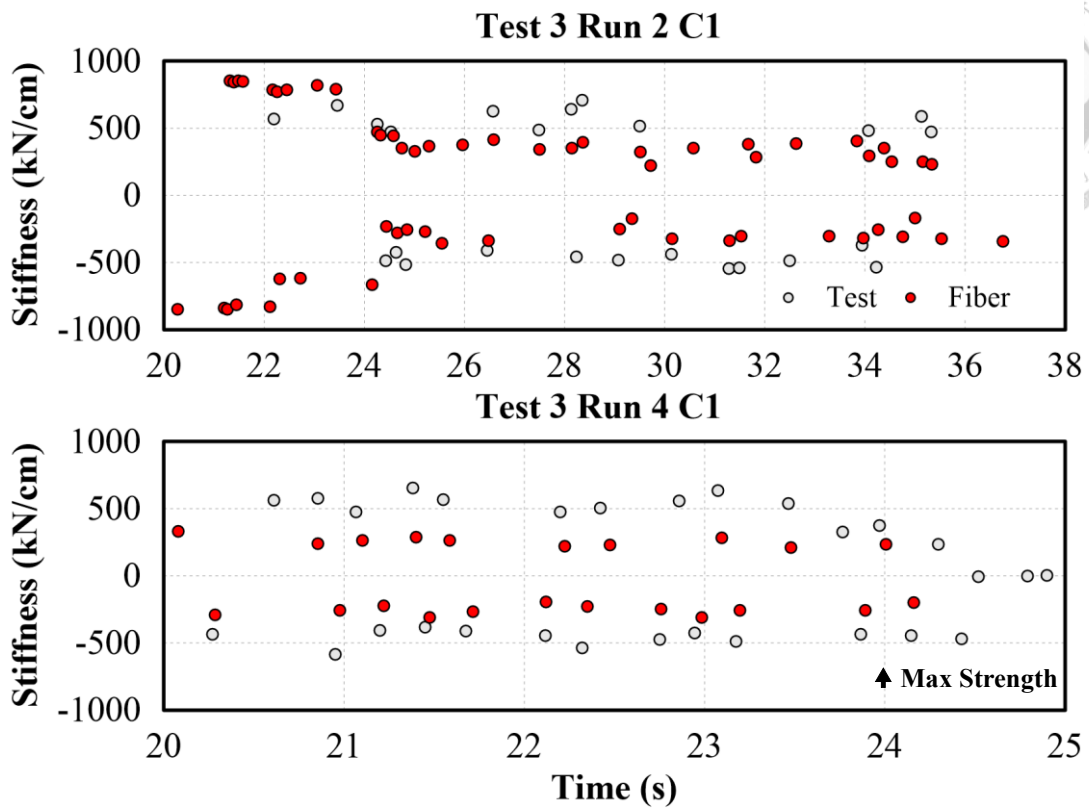
573

Figure 6-130. Comparison on T3 C1 stiffness response for Fiber model
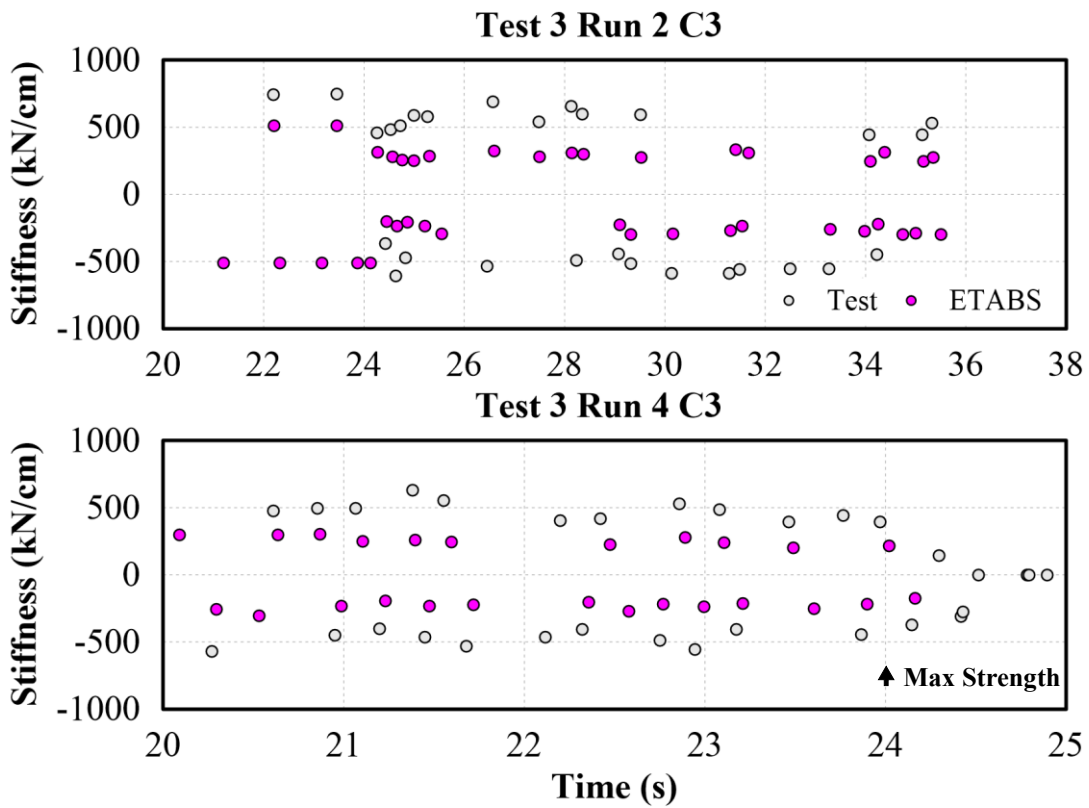

Figure 6-131. Comparison on T3 C3 stiffness response for ETABS model

Figure 6-132. Comparison on T3 C3 stiffness response for CPH model

Figure 6-133. Comparison on T3 C3 stiffness response for Fiber model

575

Figure 6-134. Comparison on T4 C1 stiffness response for ETABS model

Figure 6-135. Comparison on T4 C1 stiffness response for CPH model

576

Figure 6-136. Comparison on T4 C1 stiffness response for ETABS model

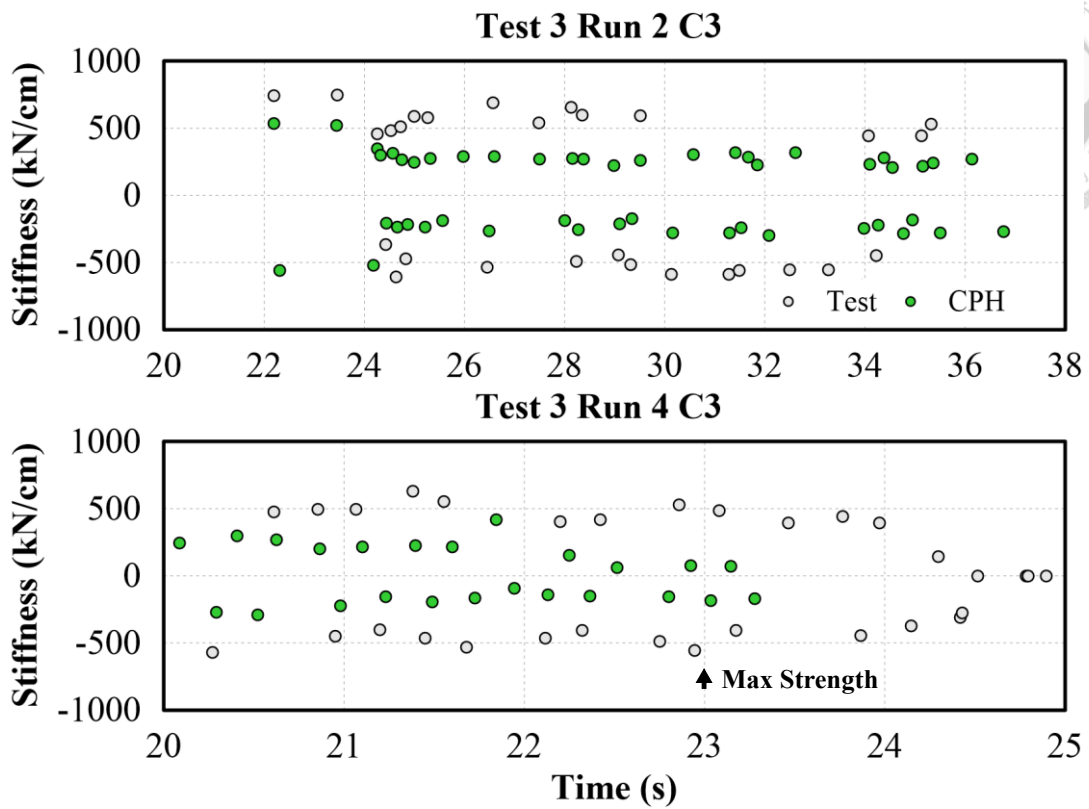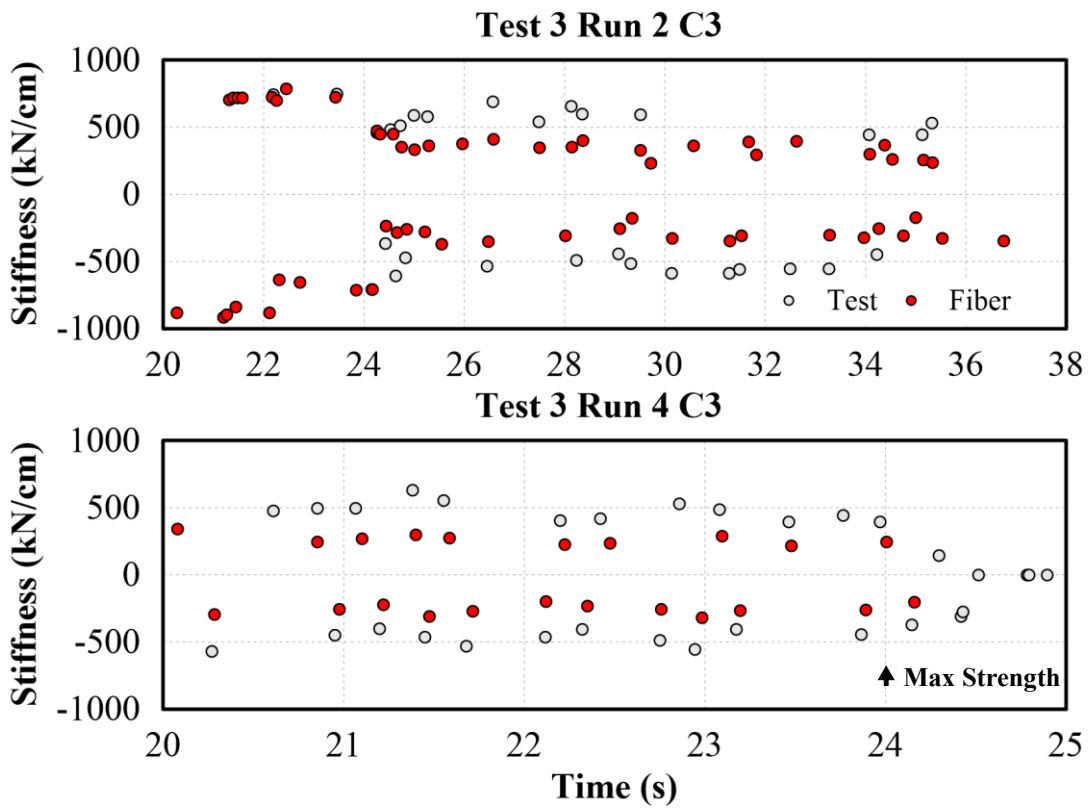**Figure 6-137. Comparison on T4 C3 stiffness response for ETABS model**

577

Figure 6-138. Comparison on T4 C3 stiffness response for CPH model

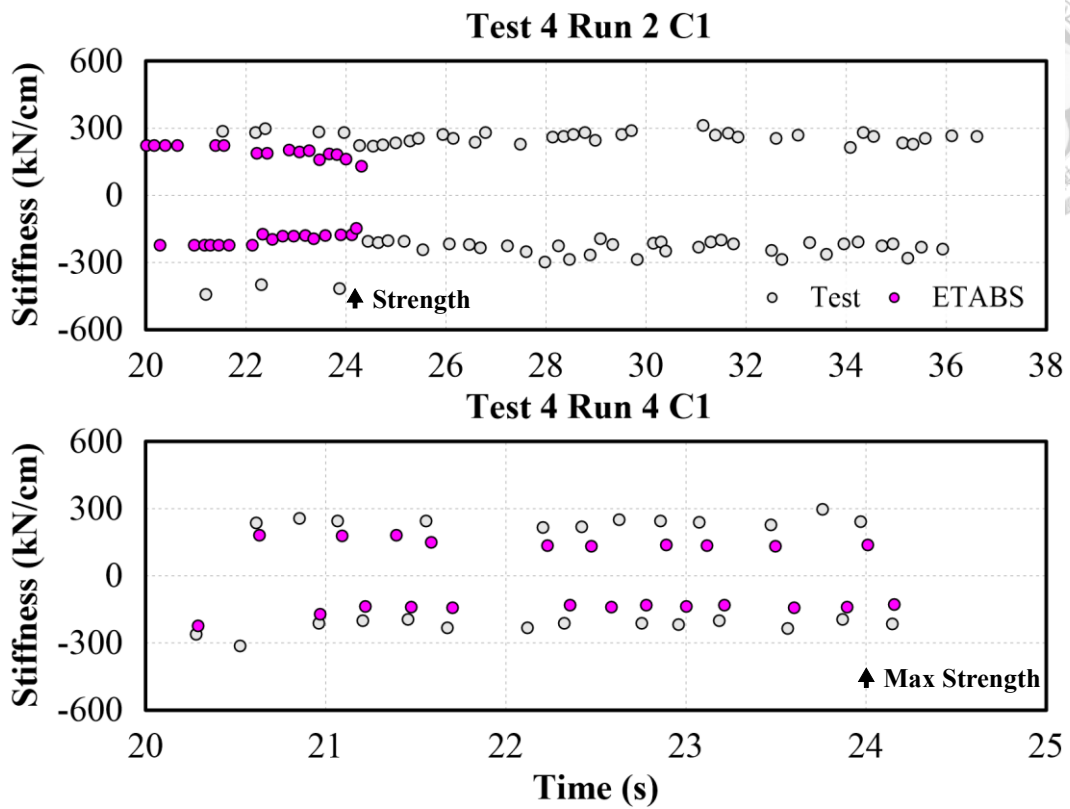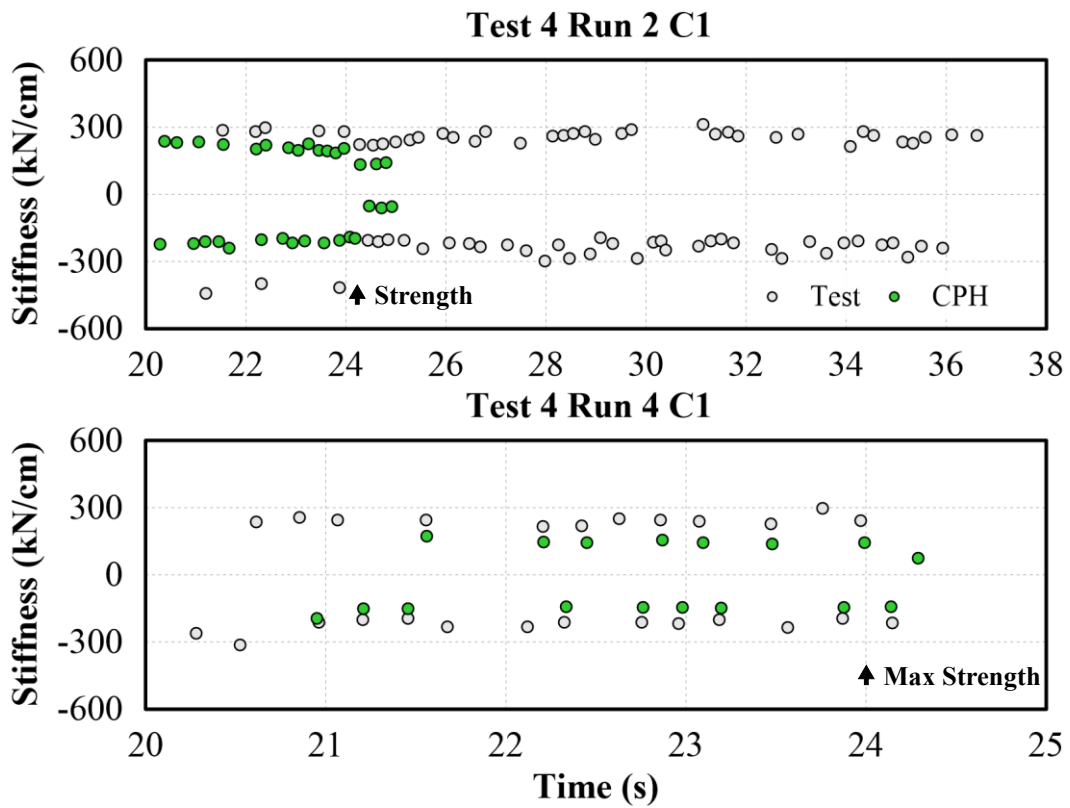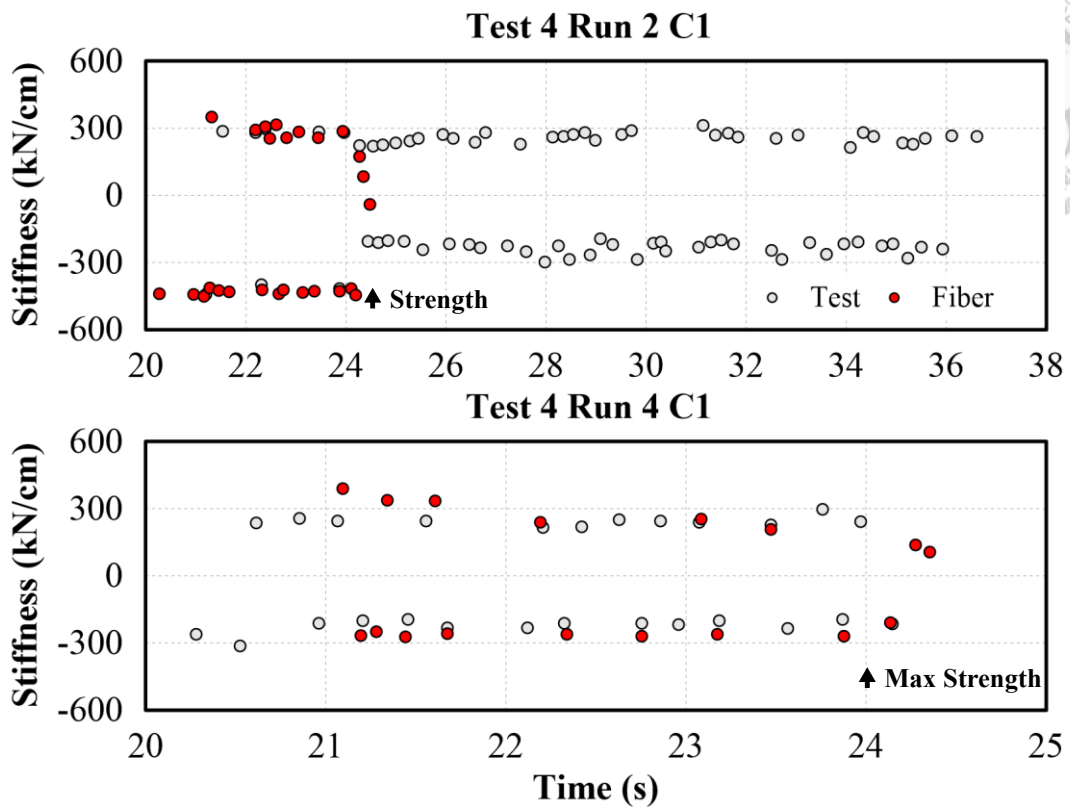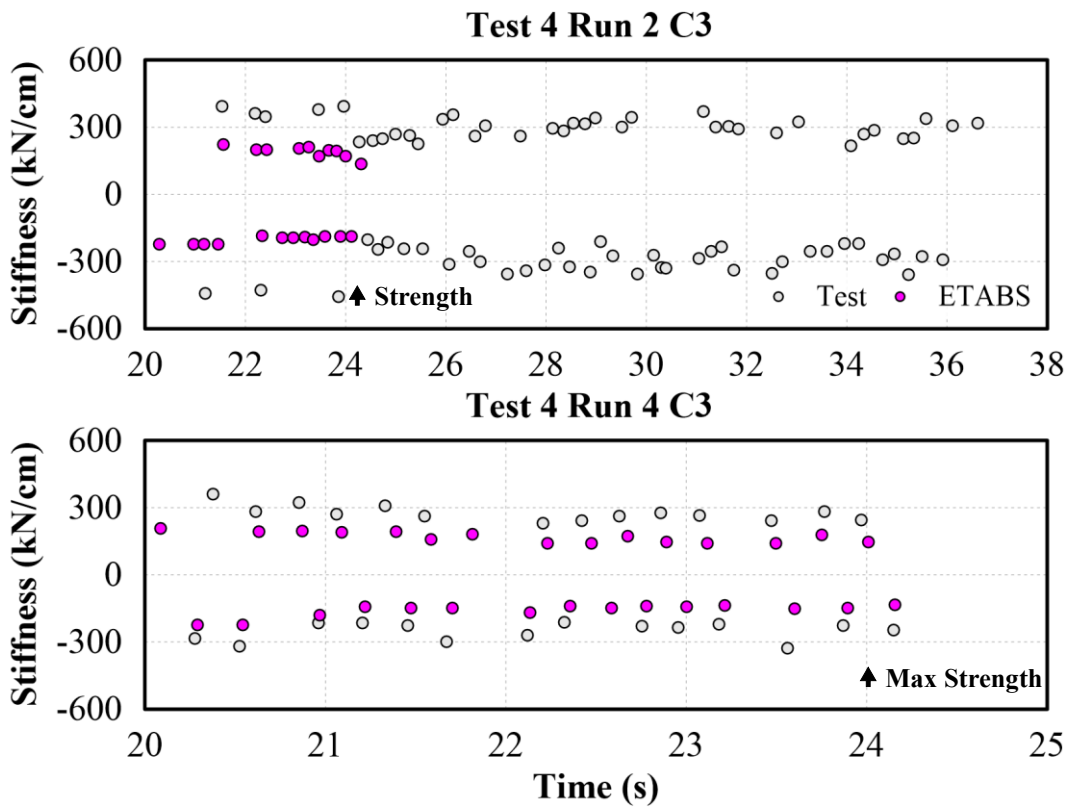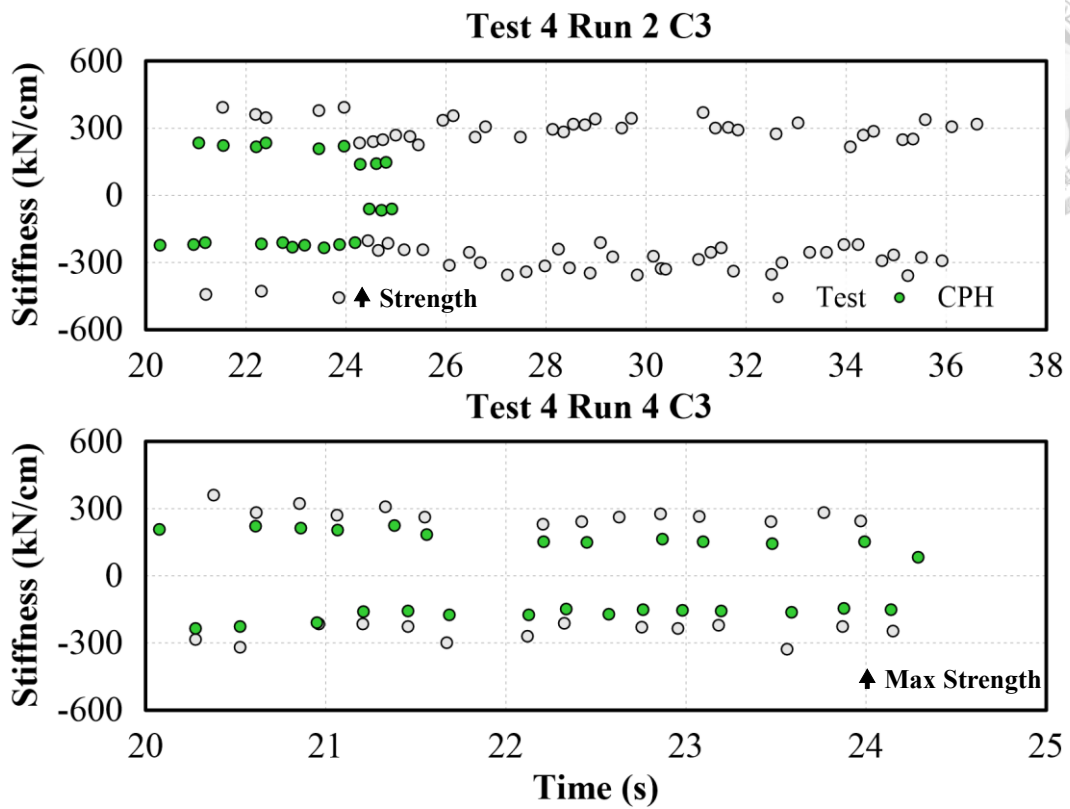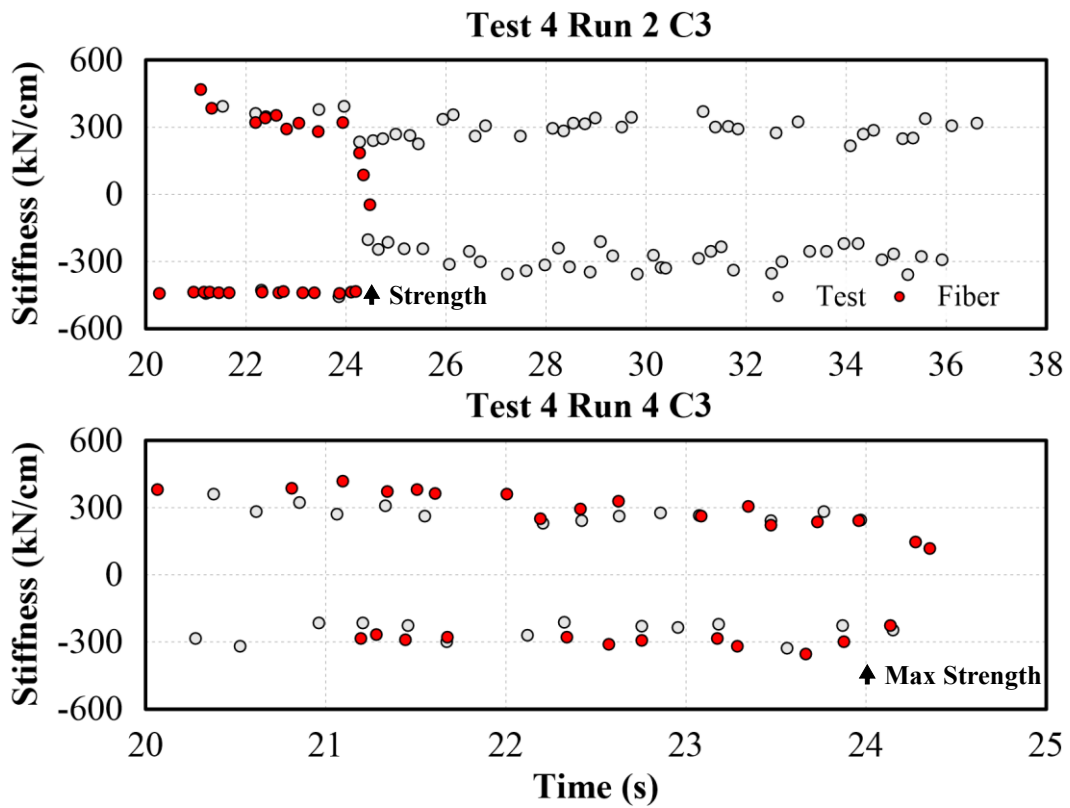**Figure 6-139. Comparison on T4 C3 stiffness response for Fiber model**

578

APPENDIX: SHAKING TABLE TEST COLUMN DATABASE

PROPERTIES OF THE SHAKING TABLE TEST COLUMN DATABASE

	Column Information			Geometry				Long. Rein.			Trans. Rein.			
	Specimen	Column	Scale	h	b	H	f'_c	d_ℓ	$f_{y\ell}$	ρ_ℓ	d_t	s	f_{yt}	ρ_t
				mm	mm	mm	MPa	mm	MPa	%	mm	mm	MPa	%
Guo (2008)														
1	P1	C1	1/3	150	150	1000	33.8	9.53	470.9	2.53	3.2	100	548.1	0.16
2	P1	C4	1/3	150	150	1000	33.8	6	231.7	1.39	5	33	661.9	0.16
3	L	C1	1/3	150	150	1000	32.3	9.53	470.9	2.53	3.2	100	548.1	0.16
4	L	C4	1/3	150	150	1000	32.3	6	231.7	1.39	5	33	661.9	0.16
5	P2	C1	1/3	150	150	1000	33.8	9.53	470.9	2.53	3.2	100	548.1	0.16
6	P2	C4	1/3	150	150	1000	33.8	6	231.7	1.39	5	33	661.9	0.16
Su (2007)														
7	T1	C1	1/2	250	250	1000	29.9	12.7	436.7	1.62	4	50	643.8	0.30
8	T1	C3	1/2	250	250	1000	29.9	12.7	436.7	1.62	4	50	643.8	0.30
Elwood (2003)														
9	S1	East	1/2	255		1475	24.6	12.7	479.3	1.99	9.53	50	689.7	1.12
10	S1	West	1/2	255		1475	24.6	12.7	479.3	1.99	9.53	50	689.7	1.12
11	S2	East	1/2	255		1475	23.9	12.7	479.3	1.99	9.53	50	689.7	1.12
12	S2	West	1/2	255		1475	23.9	12.7	479.3	1.99	9.53	50	689.7	1.12

TEST RESULTS OF THE SHAKING TABLE TEST COLUMN DATABASE

	Column Information		Test Strength		Calculated Strength		
	Specimen	Column	(−)	(+)	$V_{mn,(i)}$	$V_{mn,(-)}$	$V_{mn,(+)}$
			kN		kN	kN	kN
Guo (2008)							
1	P1	C1	42.40	32.52	33.44	35.72	31.07
2	P1	C4	40.46	43.44	36.36	35.50	35.50
3	L	C1	20.31	28.29	18.62	17.06	22.60
4	L	C4	19.47	27.55	19.53	18.38	21.44
5	P2	C1	43.23	34.73	33.40	35.23	32.19
6	P2	C4	41.66	39.85	36.60	35.50	35.50
Su (2007)							
7	T1	C1	136.12	130.86	118.18	167.85	149.82
8	T1	C3	127.21	135.21	119.81	150.15	167.49
Elwood (2003)							
9	S1	East	65.77	57.72	53.00	57.89	52.55
10	S1	West	55.31	72.05	53.00	50.82	60.52
11	S2	East	65.28	53.31	53.76	57.89	52.55
12	S2	West	51.49	70.00	53.76	50.91	60.52

579